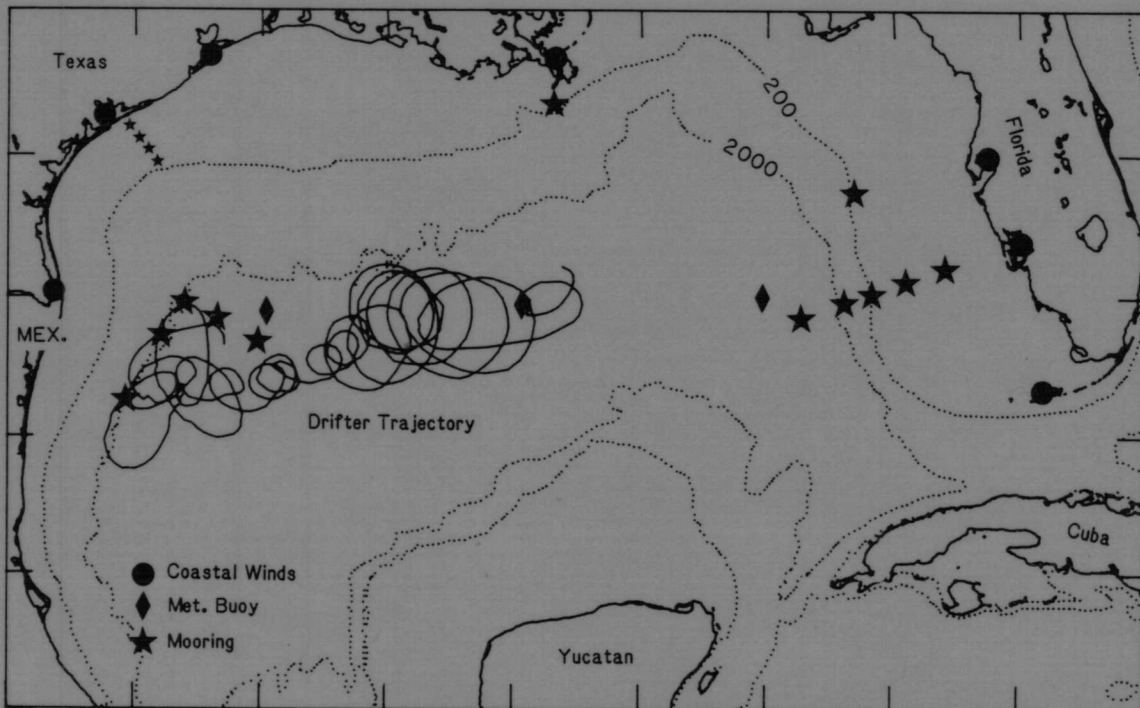


OCS STUDY
MMS 85-0094

COR
COPY

Gulf of Mexico Physical Oceanography Program Final Report: Years 1 and 2 Volume II: Technical Report



GULF OF MEXICO
PHYSICAL OCEANOGRAPHY PROGRAM
FINAL REPORT
YEARS 1 and 2

VOLUME II: TECHNICAL REPORT

Program Manager:
Evans Waddell, Ph.D.
Science Applications International Corp.
Raleigh, North Carolina 27606

Project Officer:
Murray L. Brown, Ph.D.
Minerals Management Service
Gulf Regional OCS Office

Prepared by :
Science Applications International Corp.
under
Contract No. 14-12-0001-29158

for

Minerals Management Service
Gulf of Mexico Regional OCS Office
Department of the Interior
3301 N. Causeway Blvd.
Metairie, Louisiana 77843

February, 1986

TABLE OF CONTENTS

<u>Section</u>	<u>Page</u>
Table of Contents	i
List of Figures	vi
List of Tables	xxiv
I. INTRODUCTION	1
1.1 Program Objectives	1
1.2 Program Background	1
1.3 Program Elements and Participants	1
1.4 Report Organization	3
II. DATA ACQUISITION AND METHODOLOGY	5
2.1 Introduction	5
2.2 Lagrangian Drifters	5
2.2.1 Introduction	5
2.2.2 Drifting Buoys	6
2.2.2.1 Drifting Buoys	6
2.2.2.2 Data Path	6
2.2.3 Position Data	6
2.2.4 Thermistor Data	11
2.3 Satellite Imagery	11
2.3.1 Introduction	11
2.3.2 Satellite Specifications	14
2.3.3 Data Sources and Availability	16
2.4 Hydrography	17
2.4.1 Introduction	17
2.4.2 Cruise Summaries	17
2.4.2.1 Year 1, Cruise 1	17
2.4.2.2 Year 1, Cruise 2	21
2.4.2.3 Year 2, Cruise 1	21
2.4.3 Shipboard Equipment	22
2.4.3.1 Shipboard Sampling Methodology	22
2.4.3.2 Laboratory Methodology	32
2.4.4 Ametek-Straza Current Profiles	35
2.4.5 Year 2 - Aerial Survey	37

TABLE OF CONTENTS

<u>Section</u>	<u>Page</u>
2.4.5.1 Introduction	37
2.4.5.2 Field procedures	39
2.5 Subsurface Currents	40
2.5.1 Introduction	40
2.5.2 Mooring Locations	40
2.5.3 Mooring Design	42
2.5.4 Current Meters	44
2.5.4.1 General Oceanics Niskin Winged Current Meter	44
2.5.4.2 Florida State University Current Meter	44
2.5.4.3 ENDECO Type 174 Current Meter	45
2.5.5 Deployment Period and Data Return	45
2.5.6 Texas Shelf Near-Bottom Currents	45
2.6 Ships-of-Opportunity	53
2.6.1 Introduction	53
2.6.2 Equipment	53
2.6.3 SOOP Sections and Data Products	59
2.7 References for Chapter 2	62
III. DATA ANALYSIS	63
3.1 Introduction	63
3.2 Lagrangian Drifters	63
3.2.1 Introduction	63
3.2.1.1 Water Temperature Data Analysis	63
3.2.1.2 Kinematic Analysis	63
3.2.1.3 Dynamic Analysis	64
3.2.1.4 Ring Kinematics	64
3.2.1.5 Ring Dynamics	65
3.3 Satellite Data Processing	65
3.3.1 Introduction	65
3.3.2 Real-Time Processing	66
3.3.3 Post Processing	67
3.3.4 Analysis of Satellite Data	72
3.4 Hydrography	76
3.4.1 Introduction	76

TABLE OF CONTENTS

<u>Section</u>	<u>Page</u>
3.4.2 Procedures for Handling the Ship-Based Hydrographic Data	76
3.4.3 Hydrographic Data Products	76
3.4.3.1 Ship-Based Data	76
3.4.3.2 Air-Deployable Probe Data	81
3.4.4 Ametek-Straza Current Profiles	89
3.4.4.1 Introduction	89
3.5 Subsurface Currents - Time Series Analysis	90
3.5.1 Introduction	90
3.5.1.2 West Texas Shelf	96
3.5.1.3 Spectral Analysis	96
3.6 References for Chapter 3	101
IV. SYNTHESIS AND INTERPRETATION	103
4.1 Introduction	103
4.2 Lagrangian Drifters	103
4.2.1 Introduction	103
4.2.2 Analysis of Trajectories and Sea-Surface Temperatures	103
4.2.2.1 Water Temperature Data	103
4.2.2.2 Divergence	124
4.2.2.3 Vorticity, Normal and Shear Deformation Rates	124
4.2.2.4 Ring Shape and Orientation	124
4.2.2.5 Ring Translation Velocity	138
4.2.2.6 Balances with Respect to the Ring Center	138
4.2.2.7 Motion of the Ring Center	138
4.2.3 Ring Movement	156
4.2.4 Sea-Surface Temperature Maps	156
4.2.5 Ring Kinematic Parameters	161
4.2.6 Ring Dynamics	161
4.2.7 Recommendations	162
4.2.7.1 Tracking Additional Rings	162
4.2.7.2 Kinematic Analysis	162
4.2.7.3 Ring Dynamics	162
4.3 Satellite Thermal Imagery	163

TABLE OF CONTENTS

<u>Section</u>	<u>Page</u>
4.3.1 Eastern Gulf of Mexico: 1983-1984	163
4.3.2 Cold-Core Perturbations in the Eastern Gulf of Mexico (1983-1984)	166
4.3.3 Cold Perturbations in the Eastern Gulf of Mexico (March through May 1983)	170
4.3.3.1 Introduction	170
4.3.3.2 Analysis Results	170
4.3.4 Cold Perturbations in the Eastern Gulf of Mexico (18 March through 7 May 1984)	184
4.3.4.1 Introduction	184
4.3.4.2 Analysis Results	184
4.3.5 Variations of the Loop Current Boundary (1980-1984)	201
4.3.5.1 Introduction	201
4.3.5.2 Analysis Results	203
4.3.6 Warm Rings in the Gulf of Mexico	203
4.3.6.1 Introduction	203
4.3.6.2 Temperature Structure	206
4.3.6.3 Path of the Warm Ring	211
4.3.6.4 Speed of the Warm Rings	215
4.3.6.5 Decay of Ring Size	219
4.3.6.6 Analysis Results	223
4.4 Hydrographic Data	224
4.4.1 March 1983	224
4.4.2 November 1983	231
4.4.3 May 1984	231
4.4.3.1 Aerial Survey	231
4.4.3.1.1 Introduction	231
4.4.3.1.2 Horizontal Configuration	239
4.4.3.1.3 Vertical Configuration	239
4.4.3.2 Ship-Based Hydrography	246
4.4.3.3 Time Series	252
4.5 Subsurface Currents	265
4.5.1 Introduction	265
4.5.2 Tidal and Inertial Currents	265
4.5.3 Wind-Driven Currents	268

TABLE OF CONTENTS

<u>Section</u>	<u>Page</u>
4.5.3.1 Observed Winds	273
4.5.3.2 Response of Shelf Currents to Wind Forcing	273
4.5.3.2.1 Currents at Mooring F: Coherence with Sea Level and with Winds	276
4.5.3.2.2 Coherence between Mooring D and Coastal Sea Level	288
4.5.3.2.3 Coherence between Moorings F and D	292
4.5.3.3 Response Between Wind and Currents: Selected Details	292
4.5.3.3.1 Response of Currents to Winds: Second Deployment, May-July 1983	295
4.5.3.3.2 Response of Currents to Winds: Third Deployment, August-October 1983	295
4.5.3.3.3 Response of Currents to Winds: Fourth Deployment, November 1983-January 1984	298
4.5.3.3.4 Wind Forcing at Mooring D: Summary	298
4.5.4 Coherence Across the Shelf: Tide Gauge to the Shelf Break	299
4.5.5 Mean Values Over Two Years: 1983-1984	299
4.5.6 Variability at Moorings A and G	307
4.5.7 Motions at Longer Periods: 30 Days or More	310
4.5.8 Forcing by the Loop Current	320
4.6 Analysis of Louisiana Shelf Current Meter Observations	328
4.6.1 Introduction	328
4.6.2 Discussion	330
4.7 Analysis of South Texas Continental Shelf Current Meter Observations: July to December, 1984	341
4.7.1 Introduction	341
4.7.2 General Geologic and Oceanographic Setting	349
4.7.3 Low Frequency Currents and Winds	352
4.7.3.1 July to October	352
4.7.3.2 October to July	355
4.7.4 Boundary Shear Stress	358
4.7.5 Forcing Mechanisms	367
4.7.6 Conclusions	367
4.8 References for Chapter 4	371

LIST OF FIGURES

<u>Figure No.</u>	<u>Caption</u>	<u>Page</u>
1.2-1.	Gulf of Mexico bathymetric map showing the nominal partition of the eastern and western Gulf of Mexico study areas	2
1.3-1.	Management structure for Program Years 1 and 2 . . .	4
2.2-1.	Physical characteristics of the Lagrangian buoy used in this study	7
2.2-2.	Data transmission path for data from the Lagrangian drifters	8
2.2-3.	Trajectories for Drifters (a) 1599, and (b) and (c) 3374	9
2.2-4.	Trajectories for Drifters (a) 3375 and (b) 3350 . . .	10
2.4-1.	Cruise track showing XBT and CTD station locations for R/V SUNCOASTER cruise from 7-22 March 1983 . . .	19
2.4-2.	Cruise track showing XBT, CTD, and thermosalinograph station locations for R/V SUNCOASTER cruise from 10-21 November 1983	22
2.4-3.	Cruise track showing XBT and CTD station locations, Stations 1-102, for R/V CAPE FLORIDA cruise from 5-18 May 1984	25
2.4-4.	Cruise track showing XBT and CTD station locations, Stations 103-188, for R/V CAPE FLORIDA cruise from 5-18 May 1984	26
2.4-5.	Cruise track showing XBT and CTD station locations, Stations 189-223, for R/V CAPE FLORIDA cruise from 5-18 May 1984	27
2.4-6.	Cruise track showing XBT and CTD station locations, Stations 224-268, for R/V CAPE FLORIDA cruise from 5-18 May 1984	28
2.4-7.	Schematic of CTD system used during hydrographic cruise	33
2.4-8.	Location of AXBT/AXCP drops during the May 1984 hydrographic survey	41
2.5-1.	Location of moorings deployed in the eastern Gulf for Years 1 and 2 of the MMS sponsored Gulf of Mexico Physical Oceanography Study	44

LIST OF FIGURES

<u>Figure No.</u>	<u>Caption</u>	<u>Page</u>
2.5-2.	Time line of the deployment periods and data return for each current meter level for instruments deployed in the eastern Gulf	51
2.5-3.	Location of current meters and NODC Buoy 42002	54
2.5-4.	Schematic diagram of deep water (74, 140 m) arrays	56
2.5-5.	Schematic diagram of shallow water (12, 18 and 34 m) arrays	57
2.6-1.	Examples of the cruise tracks for the repeated MMS and the NMFS/MMS Ship-of-Opportunity sections in the eastern Gulf	62
2.6-2.	Examples of data products generated for each SOOP cruise: (a) surface parameters (b) vertical temperature	63
3.3-1.	Schematic of atmospheric radiation processes relative to a satellite	71
3.3-2.	Schematic of cross-flow (L_c) and along-flow (L_a) length parameters determined for cold perturbations at the boundary of the Loop Current	75
3.3-3.	"Wave Staff" method of evaluating lateral fluctuations in Loop Current boundary locations	77
3.4-1.	T-S plot for November 1983 eastern Gulf of Mexico hydrography cruise	79
3.4-2.	Vertical plot of temperature for Stations 70 through 94 for November 1983	80
3.4-3.	Vertical plot of dissolved oxygen concentration for Stations 71 through 94 for November 1983	81
3.4-4.	Vertical plot of total chlorophyll concentration for Stations 71 through 94 for November 1983	82
3.4-5.	Nitrate versus phosphate plot for November 1983	84
3.4-6.	Nitrate versus temperature plot for November 1983	85
3.4-7.	Silicate versus sigma-t plot for November 1983	86

LIST OF FIGURES

<u>Figure No.</u>	<u>Caption</u>	<u>Page</u>
3.4-8.	Oxygen versus sigma-t plot for November 1983	87
3.4-9.	Surface oxygen plot for March 1983 eastern Gulf of Mexico hydrography cruise	88
3.4-10.	Surface total chlorophyll plot for March 1983 eastern Gulf of Mexico hydrography cruise	89
3.4-11.	Horizontal dynamic height plot for 0-500 meters for March 1983 eastern Gulf of Mexico hydrography cruise .	90
3.4-12.	Comparison of PDR determined station depth and Ametek-Straza determined station depth	93
3.5-1.	Filtered time series using 3 and 40-hour low-pass (HLP) smoothing	95
3.5-2.	Stick plots of vector quantities and time series plots of scalar quantities	96
3.5-3.	Spectra of 3 and 40 HPL time series	97
3.5-4.	Energy density ($\text{cm}^2/\text{sec}^2/\text{CPD}$) spectra of the along-shelf(v) component of the currents at location C' (34m)	99
3.5-5.	Energy density ($\text{cm}^2/\text{sec}^2/\text{CPD}$) spectra of the along-shelf(v) component of the wind recorded at Horace Caldwell Pier, Port Aransas, Texas	101
3.5-6.	Coherence and phase spectra for along-shelf (v) components of the Port Aransas wind and currents at various locations across the STOCS.	102
4.2-1.	Transect of the E.M. QUEENY Ship-of-Opportunity cruise which surveyed Ring 3374	106
4.2-2.	Vertical temperature structure of Ring 3374	107
4.2-3.	Transect of the M/V NORDIC WASA Ship-of-Opportunity cruise which surveyed the Loop Current extension that became Ring 3350	108
4.2-4.	Vertical temperature structure of the Loop Current extension that became Ring 3350	109
4.2-5.	Transect of the buoy deployment cruise which sampled Ring 3350	110

LIST OF FIGURES

<u>Figure No.</u>	<u>Caption</u>	<u>Page</u>
4.2-6.	Vertical temperature structure of Ring 3350	111
4.2-7.	Sea-surface temperature (°C) analysis for 8 November 1983	113
4.2-8.	Sea-surface temperature (°C) analysis for 15 November 1983	114
4.2-9.	Sea-surface temperature (°C) analysis for 22 November 1983	115
4.2-10.	Sea-surface temperature (°C) analysis for 29 November 1983	116
4.2-11.	Sea-surface temperature (°C) analysis for 11 December 1983	117
4.2-12.	Sea-surface temperature (°C) analysis for 18 December 1983	118
4.2-13.	Sea-surface temperature (°C) analysis for 25 December 1983	119
4.2-14.	Sea-surface temperature (°C) for 8 January 1984	120
4.2-15.	Sea-surface temperature (°C) for 15 January 1984	121
4.2-16.	Sea-surface temperature (°C) for 30 January 1984	122
4.2-17.	Sea-surface temperature (°C) for 5 February 1984	123
4.2-18.	Sea-surface temperature (°C) for 12 February 1984	124
4.2-19.	Sea-surface temperature (°C) for 19 February 1984	125
4.2-20.	Calculated divergence for Ring 1599	127
4.2-21.	Calculated divergence for Ring 3374 to mid-February 1983	128
4.2-22.	Calculated divergence for Ring 3374 after mid-March 1983	129
4.2-23.	Calculated divergence for Ring 3350	130

LIST OF FIGURES

<u>Figure No.</u>	<u>Caption</u>	<u>Page</u>
4.2-24.	Divergence calculated from the trajectory of Drifter 3375	131
4.2-25.	Time histories of ζ , S and N for Ring 1599	132
4.2-26.	Time histories of ζ , S and N for Ring 3374 to mid-February 1983	133
4.2-27.	Time histories of ζ , S and N for Ring 3374 after mid-March 1983	134
4.2-28.	Calculated vorticity for Ring 3350	135
4.2-29.	Vorticity calculated using the trajectory of Drifter 3375	136
4.2-30.	Time histories of ring eccentricity and orientation for Ring 1599	137
4.2-31.	Time histories of ring eccentricity and orientation for Ring 3374 to mid-February 1983	138
4.2-32.	Time histories of ring eccentricity and orientation for Ring 3374 after mid-March 1983	139
4.2-33.	Calculated velocity of the center of Ring 1599	141
4.2-34.	Calculated velocity of the center of Ring 3374 to mid-February 1983	142
4.2-35.	Calculated velocity of the center of Ring 3374 after mid-March 1983	143
4.2-36.	Time history of $(\zeta + f)$ for Ring 1599	144
4.2-37.	Time history of $(\zeta + f)$ for Ring 3374 to mid-February 1983	145
4.2-38.	Time history of $(\zeta + f)$ for Ring 3374 from mid-March 1983	146
4.2-39.	Time history of $D(f + \zeta)$ for Ring 1599	147
4.2-40.	Time history of $D(f + \zeta)$ for Ring 3374 to mid-February 1983	148
4.2-41.	Time history of $D(f + \zeta)$ for Ring 3374 after mid-March 1983	149

LIST OF FIGURES

<u>Figure No.</u>	<u>Caption</u>	<u>Page</u>
4.2-42.	Time history of $(\zeta + f) + D(f + \zeta)$ for Ring 1599 . . .	150
4.2-43.	Time history of $(\zeta + f) + D(f + \zeta)$ for Ring 3374 to mid-February 1983	151
4.2-44.	Time history of $(\zeta + f) + D(f + \zeta)$ for Ring 3374 after mid-March 1983	152
4.2-45.	Trajectory for the center of Ring 1599	153
4.2-46.	Trajectory for the center of Ring 3374 to mid-February 1983	154
4.2-47.	Trajectory for the center of Ring 3374 from mid-March 1983	155
4.2-48.	Calculated divergence of the motion of the center of Ring 1599	156
4.2-49.	Calculated vorticity of the motion of the center of Ring 1599	157
4.2-50.	Trajectories for Drifters (a) 1599, (b) and (c) 3374	159
4.2-51.	Trajectories for Drifters (a) 3375 and (b) 3350 . . .	160
4.2-52.	Path of the March 1983 ring as determined by infrared imagery and weekly oceanographic satellite data analysis	161
4.3-1a.	Monthly frontal analyses in the eastern Gulf of Mexico for the period from January through April 1983	166
4.3-1b.	Monthly frontal analyses in the eastern Gulf of Mexico for the period from May through December 1983	167
4.3-1c.	Monthly frontal analyses in the eastern Gulf of Mexico for the period from January through April 1984	169
4.3-1d.	Monthly frontal analyses in the eastern Gulf of Mexico for the period from May through December 1984	170
4.3-2.	Frontal analysis in the eastern Gulf of Mexico using satellite data for the period from 1 November to 8 December 1983	173

LIST OF FIGURES

<u>Figure No.</u>	<u>Caption</u>	<u>Page</u>
4.3-3.	Frontal analysis in the eastern Gulf of Mexico using satellite data for the period from 25 January to 26 April 1984	174
4.3-4.	(A) Sea-surface temperature ($^{\circ}\text{C}$) analysis for 9 March 1983	175
	(B) Sea-surface temperature ($^{\circ}\text{C}$) analysis for 19 March 1983	175
4.3-5.	Temperature ($^{\circ}\text{C}$) analysis along transect ZY indicated in Figure 4.3-4a	177
4.3-6.	(A) Temperature ($^{\circ}\text{C}$) analysis along transect XW . . .	178
	(B) Geostrophic current (cm s^{-1}) analysis along transect XW	178
4.3-7.	(A) Temperature ($^{\circ}\text{C}$) analysis along transect VU . . .	179
	(B) Geostrophic current (cm s^{-1}) analysis along transect VU	179
4.3-8.	Sea-surface temperature ($^{\circ}\text{C}$) analysis for 3 April 1983	180
4.3-9.	(A) Temperature ($^{\circ}\text{C}$) analysis along transect TS . . .	182
	(B) Geostrophic current (cm s^{-1}) analysis along transect TX	182
4.3-10.	Sea-surface temperature ($^{\circ}\text{C}$) analysis for 12 April 1983	183
4.3-11.	Sea-surface temperature ($^{\circ}\text{C}$) analysis for 26 April 1983	185
4.3-12.	(A) Temperature ($^{\circ}\text{C}$) analysis along transect PO . . .	187
	(B) Geostrophic current (cm s^{-1}) analysis along transect PO	187
4.3-13.	(A) Temperature ($^{\circ}\text{C}$) analysis along transect ON . . .	188
	(B) Geostrophic current (cm s^{-1}) analysis along transect ON	188
4.3-14.	Sea-surface temperature ($^{\circ}\text{C}$) analysis for 13 May 1983	189

LIST OF FIGURES

<u>Figure No.</u>	<u>Caption</u>	<u>Page</u>
4.3-15.	Sea-surface temperature ($^{\circ}$ C) analysis for 18 March 1984	191
4.3-16.	Sea-surface temperature ($^{\circ}$ C) analysis for 22 March 1984	192
4.3-17.	Temperature ($^{\circ}$ C) analysis along transect AB	193
4.3-18.	Analysis of the depth (m) of the 10° C isotherm along transect AB	194
4.3-19.	Sea-surface temperature ($^{\circ}$ C) analysis for 20 April 1984	195
4.3-20.	Sea-surface temperature ($^{\circ}$ C) analysis for 28 April 1984	197
4.3-21.	Temperature ($^{\circ}$ C) analysis along transects (A) CD and (B) DE	198
4.3-22.	Temperature ($^{\circ}$ C) analysis along transect FG	199
4.3-23.	Analysis of the depth (m) of the 10° C isotherm using data along transects CD, DE and FG	200
4.3-24.	Sea-surface temperature analysis for 7 May 1984	201
4.3-25.	Temperature ($^{\circ}$ C) analysis along transects (A) HI, (B) JK and (C) LM	202
4.3-26.	Analysis of the depth (m) of the 10° C isotherm using data along transects HI, JK and LM	204
4.3-27.	Mean deviation (km) of the Loop Current western and eastern boundary from their mean position versus latitude	206
4.3-28.	Mean 4-year position of Loop Current and positive and negative directions of Loop Current boundary between 25° N and 27° N	207
4.3-29.	Mean deviation (km) of the Loop Current western and eastern boundary from the mean position at 25° N, 26° N and 27° N	208
4.3-30.	Surface frontal analysis using NOAA infrared data for (A) 13 December 1983 and (B) 13 January 1984	210
4.3-31.	(A) Cruise path and station location for and (B) temperature ($^{\circ}$ C) section from data collected by the NORDIC WASA on 7-8 January 1984	211

LIST OF FIGURES

<u>Figure No.</u>	<u>Caption</u>	<u>Page</u>
4.3-32.	(A) Surface frontal analysis from the NOAA infrared data for 21 May 1982	212
	(B) Cruise path and station locations for and (C) temperature (°C) section from data collected by the E. QUEENY on 7-8 June 1982	212
4.3-33.	(A) Surface frontal analysis from the NOAA infrared data for 8 June 1982	213
	(B) Cruise path and stations for and (C) temperature (°C) section from data collected by the E. QUEENY on 7-8 June 1982	213
4.3-34.	(A) Cruise path and station locations for and (B) temperature (°C) section from data collected by the E. QUEENY on 26-27 August 1982	215
4.3-35.	Linear paths based on the connection of endpoints for the long term paths	216
4.3-36.	Characteristic paths of warm rings in the western Gulf of Mexico and the position of warm ring centers	217
4.3-37.	Path of a warm ring that is located in the northwestern Gulf of Mexico	219
4.3-38.	The path of three warm rings in the Gulf of Mexico which conform to the three characteristic paths presented in Figure 4.3-35	220
4.3-39.	Speed of the warm rings (km day ⁻¹) that are presented in Figure 4.3-37 as a function of time . . .	221
4.3-40.	Frequency distribution of warm ring speeds in the Gulf of Mexico	223
4.3-41.	Warm ring diameter (km) versus time for the three rings presented in Figure 4.3-37	224
4.3-42.	Time variation of the warm ring diameter	225
4.4-1.	Cruise track showing XBT and CTD station locations for R/V SUNCOASTER cruise from 7-22 March 1983	228
4.4-2.	Temperature, salinity, density and geostrophic velocities (1000-m level surface) for section Stations 1-38 for 9-14 March 1983	229

LIST OF FIGURES

<u>Figure No.</u>	<u>Caption</u>	<u>Page</u>
4.4-3.	Temperature, salinity, density and geostrophic velocities (1000-m reference level surface) for stations 45-76 and 121-144	230
4.4-4.	Temperature, nitrate, phosphate, silicate, oxygen, and total chlorophyll from the southern section in March 1983	231
4.4-5a.	Temperature, nitrate, phosphate, silicate, oxygen, and total chlorophyll from the northern section in March 1983	232
4.4-5b.	Continued	233
4.4-6.	Sea-surface temperature ($^{\circ}$ C) analysis for 19 March 1983	235
4.4-7.	Cruise track showing XBT, CTD and thermosalinograph station locations for R/V SUNCOASTER cruise from 10-21 November 1983	236
4.4-8.	Vertical plots of temperature, salinity and sigma-t for Stations 8 through 31 for November 1983	237
4.4-9.	Vertical plots of temperature, salinity and sigma-t for Stations 38 through 64 for November 1983	238
4.4-10.	Vertical plots of temperature, salinity and sigma-t for Stations 70 through 94 for November 1983	239
4.4-11.	Vertical plots of temperature, salinity and sigma-t for Stations 100 through 128 for November 1983	240
4.4-12.	Vertical plots of oxygen, nitrate and chlorophyll for Stations 9 through 31 for November 1983	241
4.4-13.	Sampling scheme for aerial XBT/XCP survey	243
4.4-14.	Horizontal contours of temperatures at 200 m below the surface	244
4.4-15.	Trajectory of a drifting buoy around a major cold pool located SW of the southwest Florida shelf	245
4.4-16.	Contours of transect normal velocity component at indicated stations on Section 2A	247

LIST OF FIGURES

<u>Figure No.</u>	<u>Caption</u>	<u>Page</u>
4.4-17.	Representative 40 HLP filtered velocities at mooring indicated in Figure 4.4-16	248
4.4-18.	Contours of transect normal velocity along Section 1A	250
4.4-19.	Temperature along Section 1A	251
4.4-20.	Three sections through the cold perturbation for the period from 5-18 May 1984	252
4.4-21.	Temperature section down the axis of the cold perturbation at both 1000-m and 200-m scales with sea-surface temperature profile (Stations 1-12)	253
4.4-22.	Temperature section across the cold perturbation of both 1000-m and 200-m scales with sea-surface temperature profile (Stations 14-24)	254
4.4-23.	Temperature section across the cold perturbation at both 1000-m and 200-m scales with sea-surface temperature profile (Stations 254-268)	256
4.4-24.	Stick plots of ADCP velocity at 20-m depth in the cold dome feature southwest of the Dry Tortugas, 6 May 1984	257
4.4-25.	Stick plots of ADCP velocity at 100-m depth in the cold dome feature southwest of the Dry Tortugas, 6 May 1984	258
4.4-26.	Stick plots of ADCP velocity at 200-m depth in the cold dome feature southwest of the Dry Tortugas, 6 May 1984	259
4.4-27.	Stick plots of ADCP velocity at 20-m depth in the cold dome feature southwest of the Dry Tortugas, 17-18 May 1984	260
4.4-28.	Cruise track showing XBT and CTD station locations, Stations 189-223, for R/V CAPE FLORIDA cruise from 5-18 May 1984	262
4.4-29.	Temperature sections and sea-surface temperature profiles for time series I	263
4.4-30.	Temperature sections and sea-surface temperature profiles for time series II	264

LIST OF FIGURES

<u>Figure No.</u>	<u>Caption</u>	<u>Page</u>
4.4-31.	Stick plots of ADCP velocity at 20-m depth for section XI of time series I	265
4.4-32.	Stick plots of ADCP velocity at 20-m depth for section XV of time series I	266
4.4-33.	Stick plots of ADCP velocity at 20-m depth for section XVII of time series I	267
4.4-34.	Stick plots of ADCP velocity at 50-m depth for section XV of time series I	269
4.4-35.	Stick plots of ADCP velocity at 100-m depth for section XV of time series I	270
4.5-1.	Fluctuations in pressure at the bottom of Mooring C and E for about the first 50 days	273
4.5-2.	Rotary spectra of velocity at the upper current meter, depth of 50 m at Mooring C (a) and 60 m at Mooring D (b), for the first 4 moorings	274
4.5-3.	Velocity components at Mooring D, lower current meter (60 m), during the 2nd setting	275
4.5-4.	Cross spectra between longshore wind at Fort Meyers, FL and the tidal height at Naples	277
4.5-5.	Cross spectra between longshore wind at Tampa, FL and the tidal height at Clearwater	278
4.5-6.	(a) Spectral amplitudes for the second year of data for longshore wind component at Tampa, tidal height at Clearwater, longshore current component at Mooring F (in 50-m depth) at the 17-m and 40-m instruments	280
	(b) Cross spectral coherence and phase between longshore velocity component at the 17-m instrument at Mooring F and the longshore wind at Tampa	281
	(c) Cross spectral coherence and phase between longshore velocity component at the 40-m instrument at Mooring F and the longshore wind at Tampa	281
	(d) Cross spectral coherence and phase between longshore velocity component at the 17-m instrument at Mooring F and the Clearwater tide gauge	282

LIST OF FIGURES

<u>Figure No.</u>	<u>Caption</u>	<u>Page</u>
4.5-6.	(e) Cross spectral coherence and phase between longshore velocity component at the 40-m instrument at Mooring F and the Clearwater tide gauge	282
4.5-7.	(a) Spectral amplitudes for the "winter" season of the second year of data	284
	(b) Cross spectral coherence and phase between longshore velocity component for the 17-m instrument at Mooring F and the winds at Tampa	285
	(c) Cross spectral coherence and phase between longshore velocity component for the 40-m instrument at Mooring F and the winds at Tampa	285
4.5-8.	(a) Spectral amplitudes for the "spring" season of the second year of data	286
	(b) Cross spectral coherence and phase between longshore velocity component at the 17-m instrument at Mooring F and the winds at Tampa	287
	(c) Cross spectral coherence and phase between longshore velocity component at the 40-m instrument at Mooring F and the winds at Tampa	287
4.5-9.	(a) Spectral amplitudes for the "summer" season of the second year of data	288
	(b) Cross-spectral coherence and phase between longshore velocity component at the 17-m instrument at Mooring F and the winds at Tampa	289
	(c) Cross-spectral coherence and phase between longshore velocity component at the 40-m instrument at Mooring F and the winds at Tampa	289
4.5-10.	(a) Spectral amplitudes for the "fall" season of the second year of data	290
	(b) Cross-spectral coherence and phase between longshore velocity component at the 17-m instrument at Mooring F and the winds at Tampa	291
	(c) Cross-spectral coherence and phase between longshore velocity component at the 40-m instrument at Mooring F and the winds at Tampa	291

LIST OF FIGURES

<u>Figure No.</u>	<u>Caption</u>	<u>Page</u>
4.5-11.	Cross spectra between the long-shelf current component at Mooring D, upper current meter (30 m) and sea level at the coast (Naples)	292
4.5-12.	Cross spectra between the (a) cross-shelf and (b) long-shelf current component at Mooring D, upper current meter (30 m), and sea level at the coast . . .	294
4.5-13.	Cross spectra between the (a) cross-shelf and (b) long-shelf current component at Mooring D, upper current meter (30 m), and sea level at the coast . . .	295
4.5-14.	(a) Spectra, phase and coherence at upper and lower instruments on Mooring F, (b) same analysis for Mooring D between the 17- and 50-m instruments, (c) C at Mooring D, between 50- and 71-m instruments	296
4.5-15.	Cross spectra between long-shelf components at (a) the upper current meters (17 m), (b) the lower current meters (40 m, 50 m), and (c) and between cross-shelf components at the upper current meters (17 m), at Moorings D and F for winter 1984 data	298
4.5-16.	Cross spectra between longshore wind component at the Met Buoy and currents at 60 m, Mooring D . . .	299
4.5-17.	Cross spectra between longshore wind component at the Met Buoy and the cross-shelf currents at 100 m, Mooring C	300
4.5-18.	(a) Cross spectra between bottom pressure at Mooring C (179 m) and sea level at Naples, FL, for "winter" data	303
	(b) Cross spectra between bottom pressure at Mooring E (179 m) and sea level at Clearwater, FL, for "winter" data	304
	(c) Cross spectra between bottom pressure at Mooring E (179 m) and sea level at Clearwater, FL, for "fall" data	305
4.5-19.	Cross spectra between currents 1 m above the bottom at Mooring E (179 m) and winds at Tampa, FL	306

LIST OF FIGURES

<u>Figure No.</u>	<u>Caption</u>	<u>Page</u>
4.5-20.	Scatter plot of velocity (U, V components) at the upper current meter (50 m) at Mooring C for the first emplacement	308
4.5-21.	Scatter plot of velocity (U, V components) at the upper current meter (30 m) at Mooring D for the first emplacement	309
4.5-22.	A comparison between mean values computed from individual 3-month mooring records (plus signs) and the cumulative mean for the entire record	310
4.5-23.	(a) Stick plots of currents at Mooring G (in 3200 m), (b) at Mooring C (in 180 m), (c) at Mooring D (in 75 m), summer 1984	313
4.5-24.	Vertical coherence at Mooring A (a) between currents at 170 m and 400 m, in the long-shelf component, (b) between temperature measured at 170 m and 400 m	314
4.5-25.	Vertical coherence at Mooring A between currents at 400 m and 740 m in the long-shelf component	315
4.5-26.	Vertical coherence at Mooring G between currents at 357 m and 1565 m in the long-shelf component . . .	316
4.5-27.	(a) Vertical coherence of U components at Mooring G between currents at 1565 m and 2364 m for the period beginning on 9 February 1984, (b) for V components, (c) for U components for the period beginning 24 October 1984, (d) for V components for the period beginning 24 October 1984	317
4.5-28.	(a) Vertical coherence of U components at Mooring G between currents at 2364 m and 3174 m for the period beginning on 9 February 1984. (b) for V components, (c) for U components for the period beginning 24 October 1984, (d) for V components for the period beginning 24 October 1984	318
4.5-29.	Coherence of the V components at Mooring G between currents at 357 m and 3174 m for the period beginning on 24 October 1984	319

LIST OF FIGURES

<u>Figure No.</u>	<u>Caption</u>	<u>Page</u>
4.5-30.	Coherence between the long-shelf velocity component (V) and temperature at Mooring G, 1565 m, for the period beginning on 9 February 1984	321
4.5-31.	Coherence between the long-shelf velocity component (V) and temperature at Mooring G, 2364 m for the period beginning on 9 February 1984	322
4.5-32.	Coherence in temperature at Mooring G between observations at 2364 m and 3174 m for the period beginning on 24 October 1984	323
4.5-33.	Very low frequency scatter plot of wind stress at Tampa versus currents at Mooring D, upper current meter (30 m), for the long-shelf components	324
4.5-34.	Very low frequency scatter plot of wind stress at Tampa versus currents at Mooring D, lower and middle current meters, for the long-shelf components	325
4.5-35.	Very low frequency scatter plot of wind stress at Tampa versus currents at Mooring E, middle current meter (100 m), for the long-shelf components	326
4.5-36.	Very low frequency scatter plot of wind stress at Tampa versus currents at Mooring A, upper current meter (170 m), for the long-shelf components	327
4.5-37.	Very low frequency scatter plot of wind stress at Tampa versus currents at Mooring E, bottom current meter (179 m), for the long-shelf components	329
4.5-38.	(a) Positions of the Loop Current near the mooring array from the NOAA satellite images, January - March 1983	330
	(b) Positions of the Loop Current near the mooring array from the NOAA satellite images, March - April 1983	331
4.5-39.	Spectrum of east-west fluctuations of the inshore edge of the Loop Current at 25°N from the maps of Figure 4.5-38 et. seq	332
4.6-1.	Spectra of current velocity components for meter MD 4 (70 m) from 23 February to 10 May	334

LIST OF FIGURES

<u>Figure No.</u>	<u>Caption</u>	<u>Page</u>
4.6-2.	Spectra of current velocity components for meter MD 4 (70 m) from 10 May to 27 July	335
4.6-3.	Spectra of current velocity components for meter MD 4 (70 m) from 27 July to 29 October	336
4.6-4.	Spectra of temperature for meter MD 4 (70 m) from 23 February to 20 May	337
4.6-5.	Spectra of temperature for meter MD 4 (70 m) from 10 May to 27 July	338
4.6-6.	Spectra of temperature for meter MD 4 (70 m) from 27 July to 29 October	339
4.6-7.	Coherence squared (above) and phase (below) between velocity components at meter MD 4 (70 m) from 23 February to 10 May	340
4.6-8.	38-hour low passed current stick plots from the initial MD deployment (23 February to 10 May 1984)	345
4.6-9.	38-hour low passed current stick plots from the second MD deployment (10 May to 27 July 1984)	346
4.6-10.	38-hour low passed current stick plots from the third MD deployment (27 July to 8 November 1984)	347
4.6-11.	Line plots of the 38-hour low-passed temperature records from the initial MD deployment (23 February to 10 May 1984)	348
4.6-12.	Line plots of the 38-hour low-passed temperature records from the second MD deployment (10 May to 27 July 1984)	349
4.6-13.	Line plots of the 38-hour low-passed temperature records from the third MD deployment (27 July to 8 November 1984)	350
4.7-1.	Gravity core transect across the STOCS near the study area	352
4.7-2.	General bathymetric map of STOCS showing locations of current meters	353
4.7-3.	Monthly mean water discharges for the Brazos River	354

LIST OF FIGURES

<u>Figure No.</u>	<u>Caption</u>	<u>Page</u>
4.7-4.	40-hour low-passed Eulerian data, 24 July to 4 October 1984	356
4.7-5.	Extratropical storm on 19 September 1984	358
4.7-6.	Inferred low frequency Lagrangian motion at current meter A (12 m), B (18 m), C (34 m), D (74 m) and E (140 m), 23 July to 4 October 1984	359
4.7-7.	40-hour low-passed Eulerian data, 4 October to 7 December 1984	360
4.7-8.	Inferred low frequency Lagrangian motion at current meter C' (34 m) and E (140 m), 4 October to 7 December 1984	362
4.7-9.	Boundary shear stress due to combined wave and current interaction at current meter locations on the STOCS 16 July to 4 October 1984	364
4.7-10.	Boundary shear stress due to combined wave and current interaction at current meter locations on the STOCS, 16 October to 9 December 1984	365
4.7-11.	Grain size distributions of samples from boxcore CB-1 (26 m) and from beach at Mustang Island	366
4.7-12.	Modified Shields diagram	367
4.7-13.	Inferred Lagrangian displacement of sand, 16 July to 4 October 1984	369
4.7-14.	Inferred Lagrangian displacement of sand, 4 October to 8 December 1984	370
4.7-15.	Inferred Lagrangian motion of low frequency wind, 23 July to 5 December 1984	371
4.7-16.	Unfiltered shear stress due to currents at 12 m, 18 m, and 34 m	372

LIST OF TABLES

<u>Table No.</u>	<u>Caption</u>	<u>Page</u>
2.2-1	Depths of the 9 thermistors on the line on drifter 1599	12
2.2-2	Chronology of events for Loop Current eddies containing drifters	13
2.3-1.	TIROS-N AVHRR Channel Characteristics	15
2.4-1.	Summary of stations according to sampling time and section number for R/V SUNCOASTER cruise from 7-22 March 1983	18
2.4-2.	Summary of samples taken during R/V SUNCOASTER cruise from 7-22 March 1983	20
2.4-3.	Summary of stations according to sampling time and section number for R/V SUNCOASTER cruise from 10-21 November 1983	23
2.4-4.	Summary of samples taken during R/V SUNCOASTER cruise from 10-21 November 1983	24
2.4-5.	Summary of stations according to sampling time and section number for R/V CAPE FLORIDA cruise from 5-18 May 1984	29
2.4-6.	Summary of samples taken during R/V CAPE FLORIDA cruise from 5-18 May 1984	31
2.4-7.	List of components of CTD system used during hydrographic cruises	34
2.4-8.	Recommended sampling depths for depths less than 100 meters	35
2.4-9.	Recommended sampling depths for depths greater than 100 meters	36
2.4-10.	CTD Salinity and Temperature Calibration Results . .	38
2.5-1.	Mooring locations in the eastern Gulf for Years 1 and 2 of the MMS sponsored Gulf of Mexico Physical Oceanography Study	45
2.5-2.	Specifications for General Oceanics, Inc. Model 6011-T (MK1) Niskin winged current meter	48
2.5-3.	Specifications for ENDECO Type 174 digital magnetic tape recording tethered current meter	49

LIST OF TABLES

<u>Table No.</u>	<u>Caption</u>	<u>Page</u>
2.5-4.	Deployment periods and instrument types for each current meter level for moorings in the eastern Gulf	52
2.5-5.	Data return for moorings in the eastern Gulf for the period from 26 January 1983 through 25 January 1985	53
2.5-6.	Current meter locations in the western Gulf on the south Texas continental shelf	55
2.5-7.	Texas shelf current meter deployment histories	58
2.6-1.	MMS and NMFS/MMS Ship-of-Opportunity sections through 25 January 1985	60
2.6-2.	Additional MMS Ship-of-Opportunity data sets through 25 January 1985	61
4.3-1.	Statistics on Cold Perturbations in the Gulf of Mexico for 1983-1984	171
4.4-1.	Time Series sections for R/V CAPE FLORIDA cruise, 4-19 May 1984	261
4.5-1.	Tidal constituents of currents at C1 and D2 and the observed tidal heights at Clearwater	272
4.5-2.	Compilation of means over the available record lengths for the shelf moorings	311
4.6-1.	Velocity Component Statistics for 3-Hour Low-Passed Records for Louisiana shelf Mooring MD	342
4.6-2.	Temperature Statistics for 3-Hour Low-Passed Records for Louisiana shelf Mooring MD	343
4.6-3.	Velocity Component Variance ($\text{cm}^2 \text{s}^{-2}$) within Three Frequency Bands for Total 3-Hour Low-Pass Filtered Records for each of three deployments on the Louisiana shelf	344

I. INTRODUCTION

1.1 Program Objectives

The Gulf of Mexico Physical Oceanography Program (GMPOP), a Minerals Management Service (MMS) study funded under contract with Science Applications International Corp. (SAIC), has as its objective the development of an improved understanding of primary Gulf circulation patterns and the mechanisms producing these patterns. It is expected that insights from this program will provide an expanded basis for making informed management decisions related to Outer Continental Shelf (OCS) oil and gas exploration, production and transportation. This objective is in keeping with the OCS Lands Act requirements that the Dept. of the Interior conduct appropriate studies to evaluate the environmental impacts of offshore oil and gas development.

1.2 Program Background

In 1982, a multi-year investigation was initiated of physical oceanographic conditions related to or resulting from deep circulation patterns in the Gulf of Mexico. The program was designed with a phased regional emphasis. During Program Years 1 and 2 measurements and associated interpretation focused on circulation in the eastern Gulf with special emphasis on the Loop Current and its interaction with the adjacent west Florida shelf and slope (Figure 1.2-1). As discussed in Chapter 2, two years of shelf and slope field measurements were completed and provide the basis for the present report. These measurements were designed to document the patterns and processes which occurred both along and across the slope and outer half of the west Florida shelf.

1.3 Program Elements and Participants

To achieve the program objectives, five major measurement tasks were undertaken over a two year period. These include:

- Subsurface currents/temperature and pressure across and along the west Florida shelf and across the slope into the region often occupied by the Loop Current. Subsurface currents on the Louisiana and south Texas shelf.
- Several regional and process oriented hydrographic surveys on and adjacent to the west Florida slope. These were designed to document conditions reflecting and affecting circulation and exchange along the eastern half of the Loop Current and shoreward to the outer half of the shelf. This included studies of Loop Current boundary waves and perturbations.
- Use of satellite thermal imagery to define the spatial extent and time-dependent characteristics of the Loop Current boundary and related features.

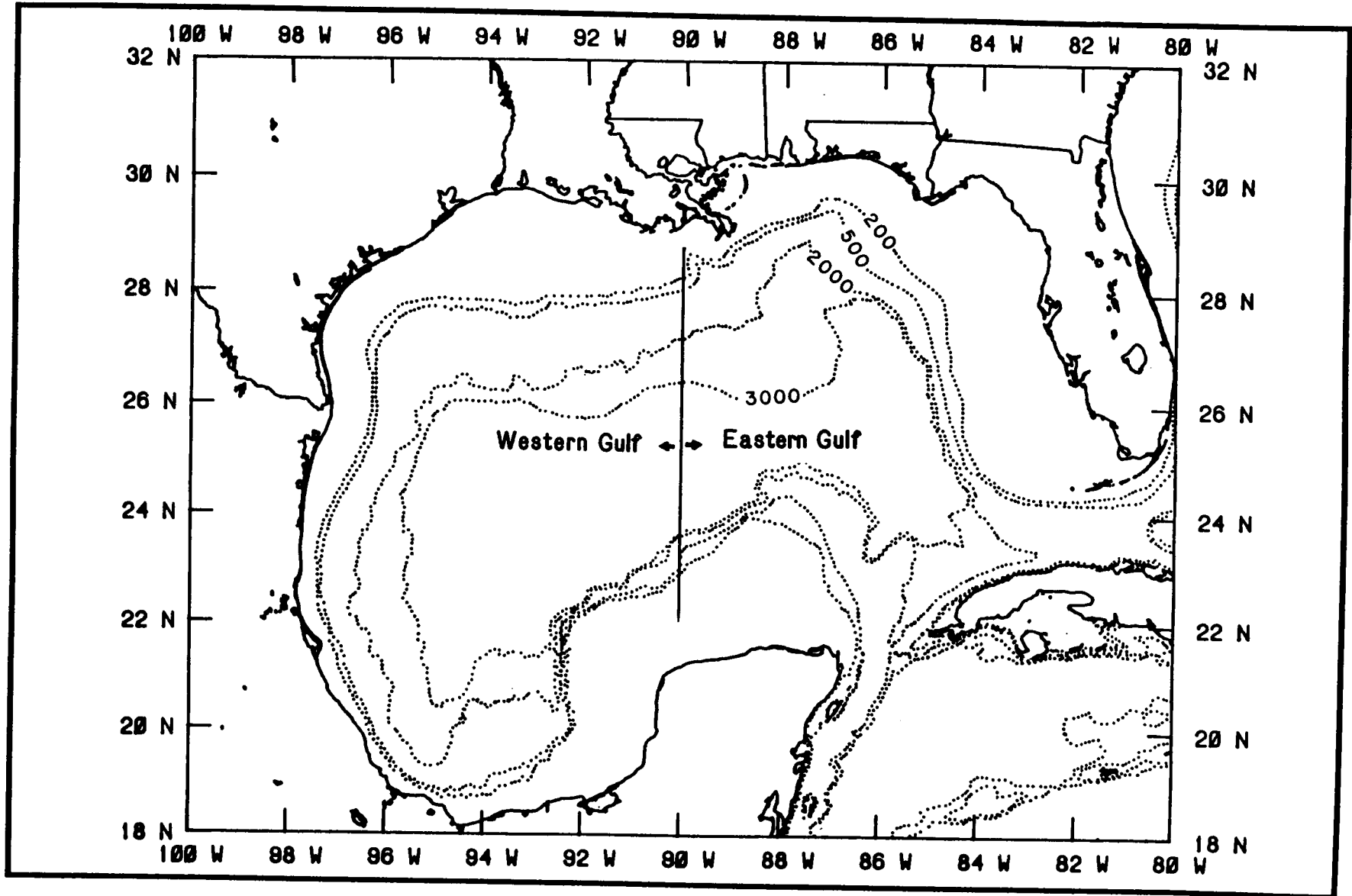


Figure 1.2-1. Gulf of Mexico bathymetric map showing the nominal partition of the eastern and western Gulf of Mexico study areas. This also partitions the emphasis on the Loop Current and Loop Current eddies.

- Tracking Lagrangian drifters deployed in major Loop Current eddies to document and partition the dynamic and kinematic characteristics of eddies shed by the Loop Current.
- Periodic and site-specific vertical temperature sections as estimated from expendable temperature probes dropped from Ships-of-Opportunity (SOOP) on regularly scheduled routes and on one-time opportunistic cruises.

These data are combined with routinely available observations such as coastal and at-sea (buoy) winds obtained from the National Weather Service and coastal waterlevel from the National Ocean Survey. Taken as a group, the above provided the data base necessary to develop the needed improved understanding of conditions in the eastern Gulf.

This data base also provides a standard against which the results of a concurrent numerical circulation modeling study can be compared. The modeling work is also MMS funded with time lines and deliverables coordinated with those on the present program.

To extract the important patterns and processes from the comprehensive multi-variate data set, a team of highly qualified scientists was established to work both independently and in collaboration. Presented alphabetically with their affiliation and primary area of responsibility these included:

- Dr. L. Atkinson, Skidaway Institute of Oceanography (SKIO), hydrography
- Dr. J. Lewis, SAIC, Lagrangian drifters
- Dr. W. Sturges, FBN Oceanography Inc. (FBN), subsurface currents
- Dr. F. Vukovich, Research Triangle Institute (RTI), satellite thermal imagery

As shown in Figure 1.3-1, these principal investigators were supported by a range of scientists and engineers, most of whom are from SAIC. The above program was supplemented by Dr. W. Wiseman (LSU) who was responsible for making subsurface current measurements on the Louisiana outer shelf. Dr. D. Nummedahl and John Snedden, Department of Geology, Louisiana State University, and A. Amos with the University of Texas, Marine Sciences Institute, Port Aransas, Texas, were responsible for the south Texas shelf current measurements.

1.4 Report Organization

This report is organized to group comparable and relevant material and to provide interpretative material without a simultaneous presentation of background information such as methodology. Chapter 2 presents a discussion of the data used and how it was obtained. Chapter 3 describes much of the analysis used in evaluating the observations discussed in Chapter 2. Chapter 4 is the primary technical discussion which uses selected results of data analysis to describe salient features of conditions in the study area.

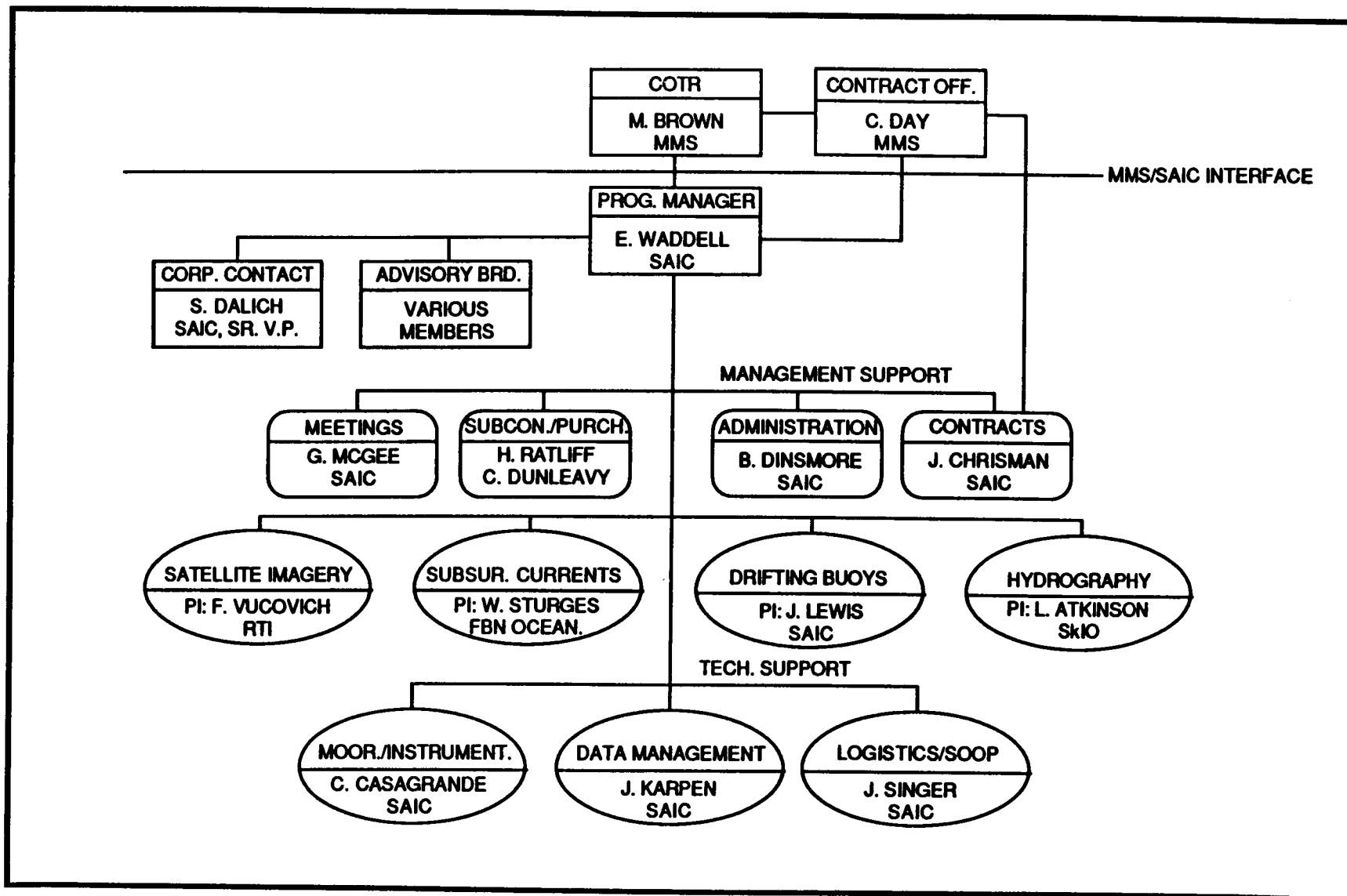


Figure 1.3-1. Management Structure for Program Years 1 and 2.

II. DATA ACQUISITION AND METHODOLOGY

2.1 Introduction

Presented below is an overview of when and how the various program observations were taken. Material is presented by program element so that a separate section exists for each of the major measurement or observational programs mentioned in Chapter I. This chapter will provide an overview of the extent of the data base available to the program principals and provide an understanding of methodology by which the observations were made or obtained.

2.2 Lagrangian Drifters

2.2.1 Introduction

The major Gulf of Mexico (GOM) circulation features are the Loop Current and large anticyclonic eddies or rings that are shed from it. The western movement of these rings results in the transport of a significant amount of heat, salt, and momentum into the western GOM (Elliot, 1979; Kirwan et al., 1984a). Dispersion within a ring is relatively small (Kirwan et al., 1984b); thus one could expect that material would tend to remain within the ring and be transported to the western GOM. For these reasons alone, it is critical that characteristics and movement of Loop Current rings be better understood. Knowing why they move along a particular path and determining the governing forces are particularly important. The goal of this study is to gain the ability to predict the speed and direction of movement of these rings, which is necessary information for determining if and when a ring will impact an area of concern.

Ring motion can be resolved or documented by several methods. Hydrographic surveys and current profiling provide the most direct and complete sets of data. However, the expense of such regular surveys of a ring over its lifetime (order of 1 year) is large. In many cases, satellite imagery can provide a more inexpensive means of ring tracking; however, it does not provide adequate dynamical information. Moreover, the location, and thus movement, of the warm-core ring is inferred using sea-surface temperature (SST) characteristics which cannot be discerned during summer or under clouds and can be significantly modified by frontal passages during the winter. One of the methods used in this project for following rings is tracking a Lagrangian drifter. In essence, a surface-constrained water parcel within a ring is tagged with a drifting buoy, and the motion of the buoy as it travels westward with the ring is used to study the kinematics and dynamics within the ring. This is the most inexpensive and accurate method for directly determining the following ring kinematics:

- (1) translation of the ring center,
- (2) swirl velocity, and
- (3) ring position.

In addition, recent theoretical advances in the analysis of Lagrangian data (Kirwan et al., 1984b) allow calculation of differential motion within the ring (vorticity, divergence, and deformation). This information can be used

to evaluate dynamic balances using the vorticity equation, a form of angular momentum balance.

2.2.2 Drifting Buoys

The drifting buoys used in this study are described below. In addition, the determination of the drifter's location and the data path are outlined.

2.2.2.1 Drifting Buoys

Buoys used were produced by the Polar Research Laboratory in Santa Barbara, California. Figure 2.2-1 shows the physical characteristics of the drifters, which are essentially short spar buoys with double conical flotation collars. Each drifter was drogued by a 200-m line with a ballast weight at the tail of the line. Communications and position fixing are the functions of an on-board electronic transmitter called a platform transmitter terminal (PTT) which includes an antenna, an RF modulator and power amplifier, message generation logic, a sensor interface unit, an ultra-stable oscillator, and a power supply. The PTT sends data to a specialized ARGOS electronics package on board a polar-orbiting satellite. Relative motion between the satellite and drifter produces a Doppler shift in the frequency of the RF link which is processed along with the satellite orbital track to derive the drifter position.

2.2.2.2 Data Path

The data transmission path is shown in Figure 2.2-2. In this case, the "users" are the NOAA Data Buoy Center (NDBC) and scientists involved in the present program. The complete data set of drifter positions is sent by Service ARGOS to NDBC on magnetic tape and forwarded to SAIC for analysis.

2.2.3 Position Data

Data used in this study are positions of drifters with ARGOS ID's 1599, 3374, 3375, and 3350. Drifters 1599, 3374, and 3350 were released in large rings while Drifter 3375 was placed in a smaller eddy in the northwestern GOM. In subsequent discussion, each ring will be referred to by the identification number of the drifter used to track the ring. Trajectories are shown in Figures 2.2-3 and 2.2-4.

Rings 1599, 3374, and 3350 tended to follow the deepest portion of the Gulf of Mexico. Drifter 3350 abruptly left its ring after three revolutions, while buoys in Rings 1599 and 3374 were tracked all the way to the Mexican slope, impacting at approximately 22°N. Drifter 1599 was still in its ring when the reporting system became inoperative, but Drifter 3374 left its ring after July 1983 and moved eastward at about 24°N.

Drifter 3375 was to be placed in a ring shed from the Loop Current in March 1983. Thermal frontal analysis indicated that the ring was centered at 26.5°N and 94°W, but a predeployment XBT survey indicated a weak thermal signature.

In spite of this, Drifter 3375 was released in this eddy and showed rotational characteristics for a short period before drifting southward. The drifter

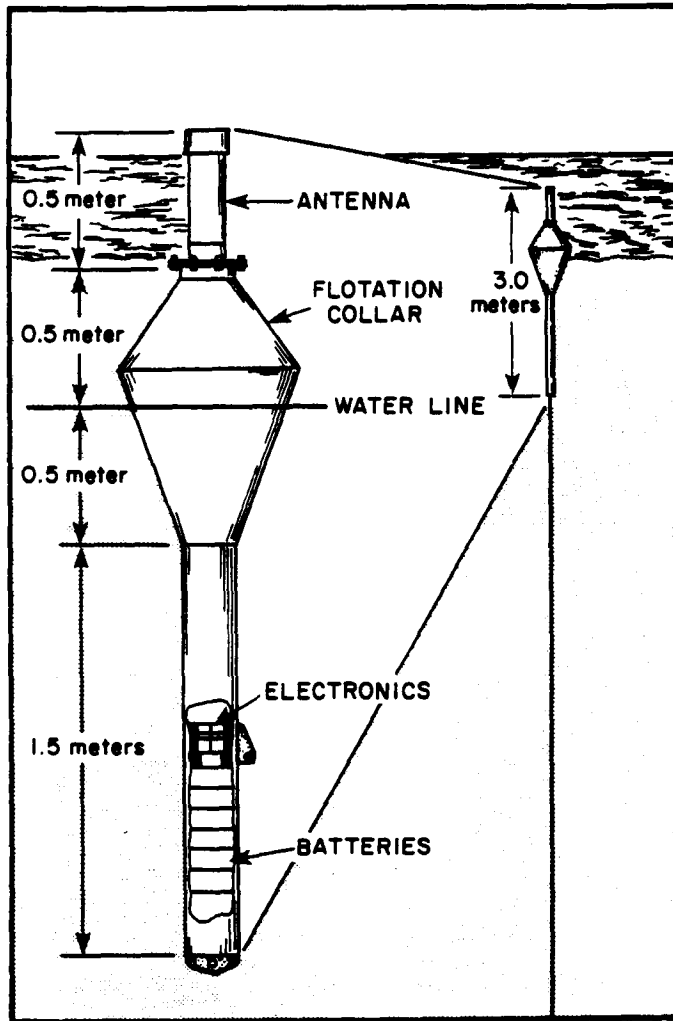


Figure 2.2-1. Physical characteristics of the Lagrangian buoy used in this study.

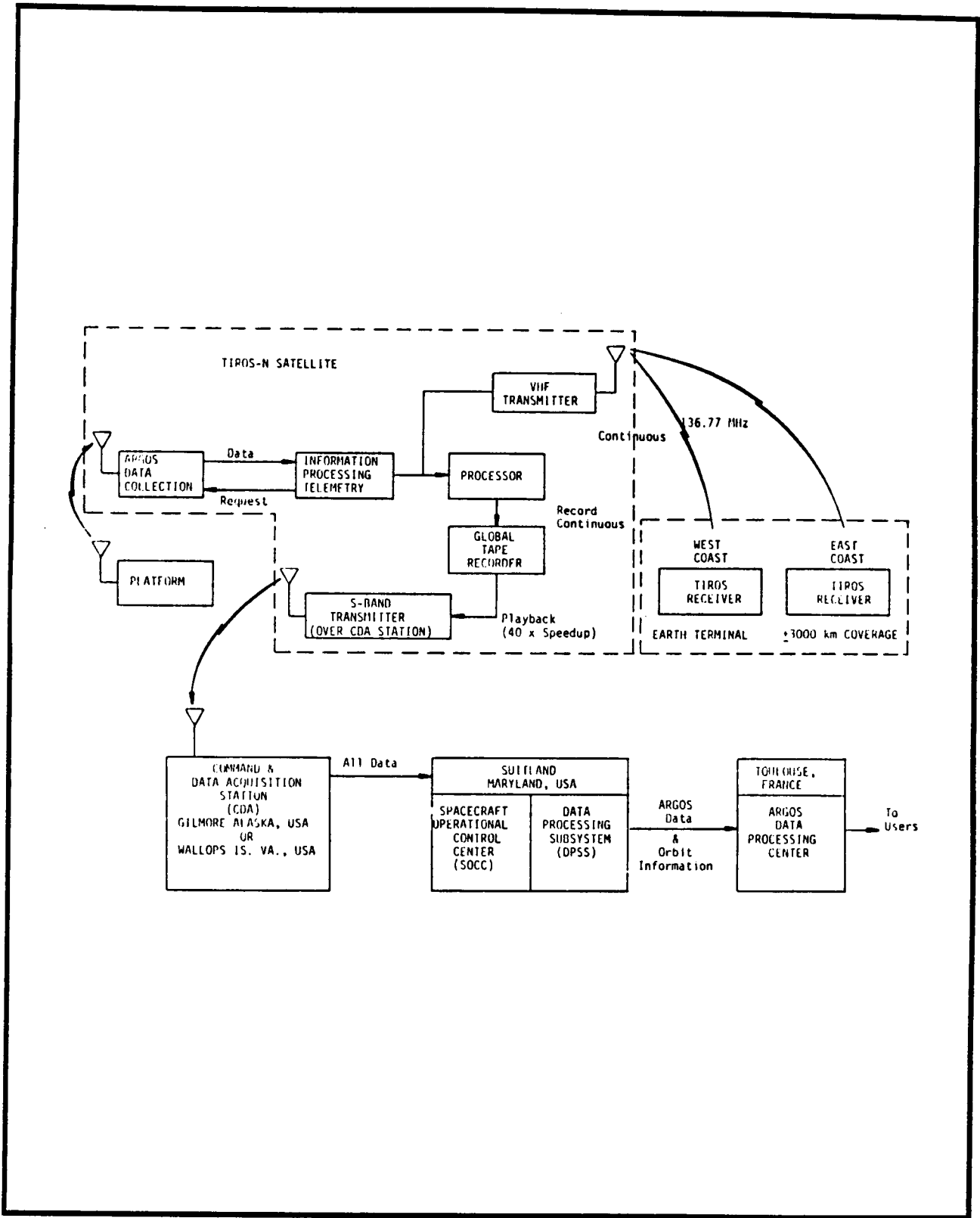
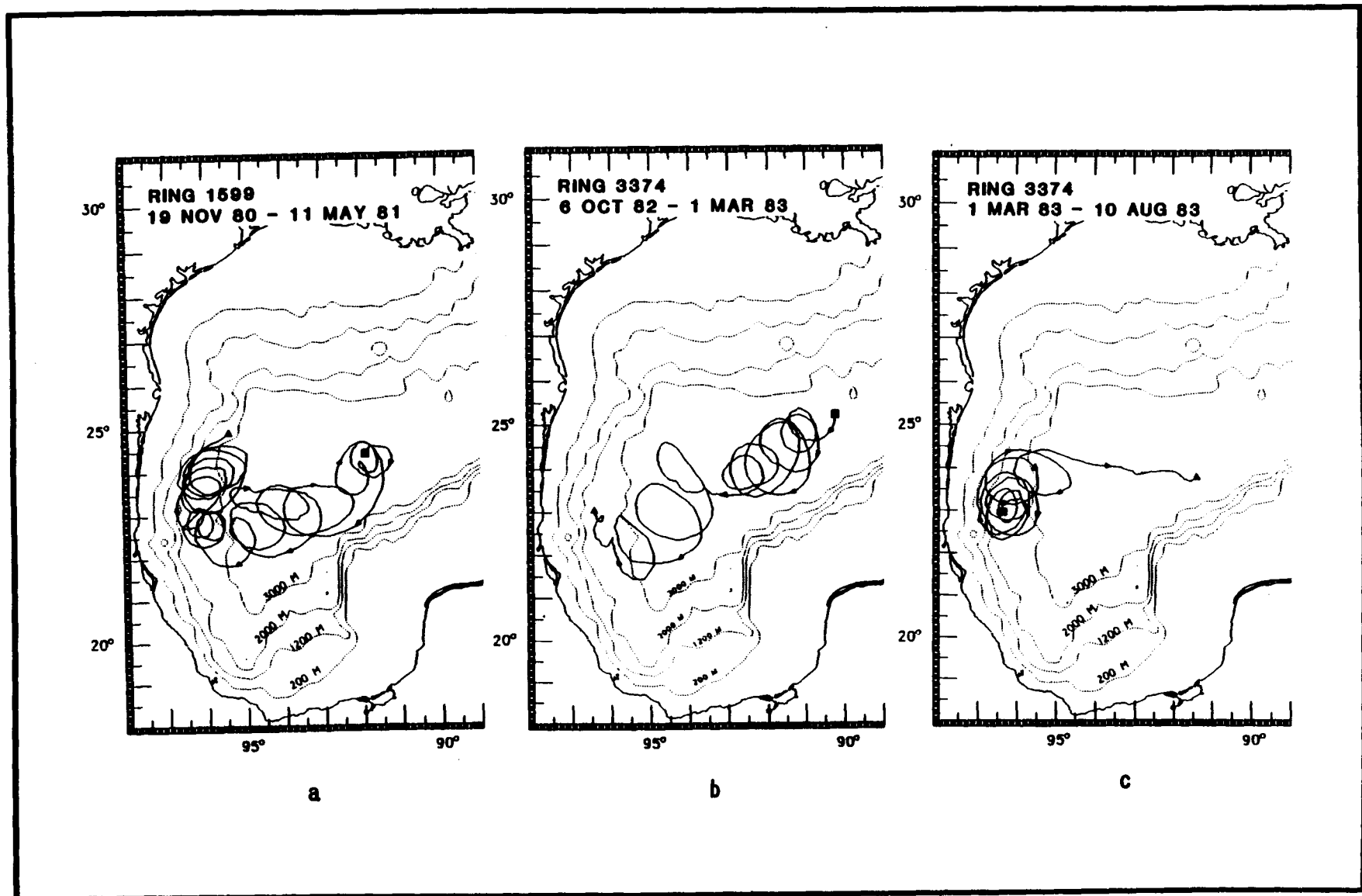


Figure 2.2-2. Data transmission path for data from the Lagrangian drifters used in this study.



Figures 2.2-3. Trajectories for drifters (a) 1599, and (b) and (c) 3374. Depth contours are in meters. The square and triangles denote the start and end positions, respectively.

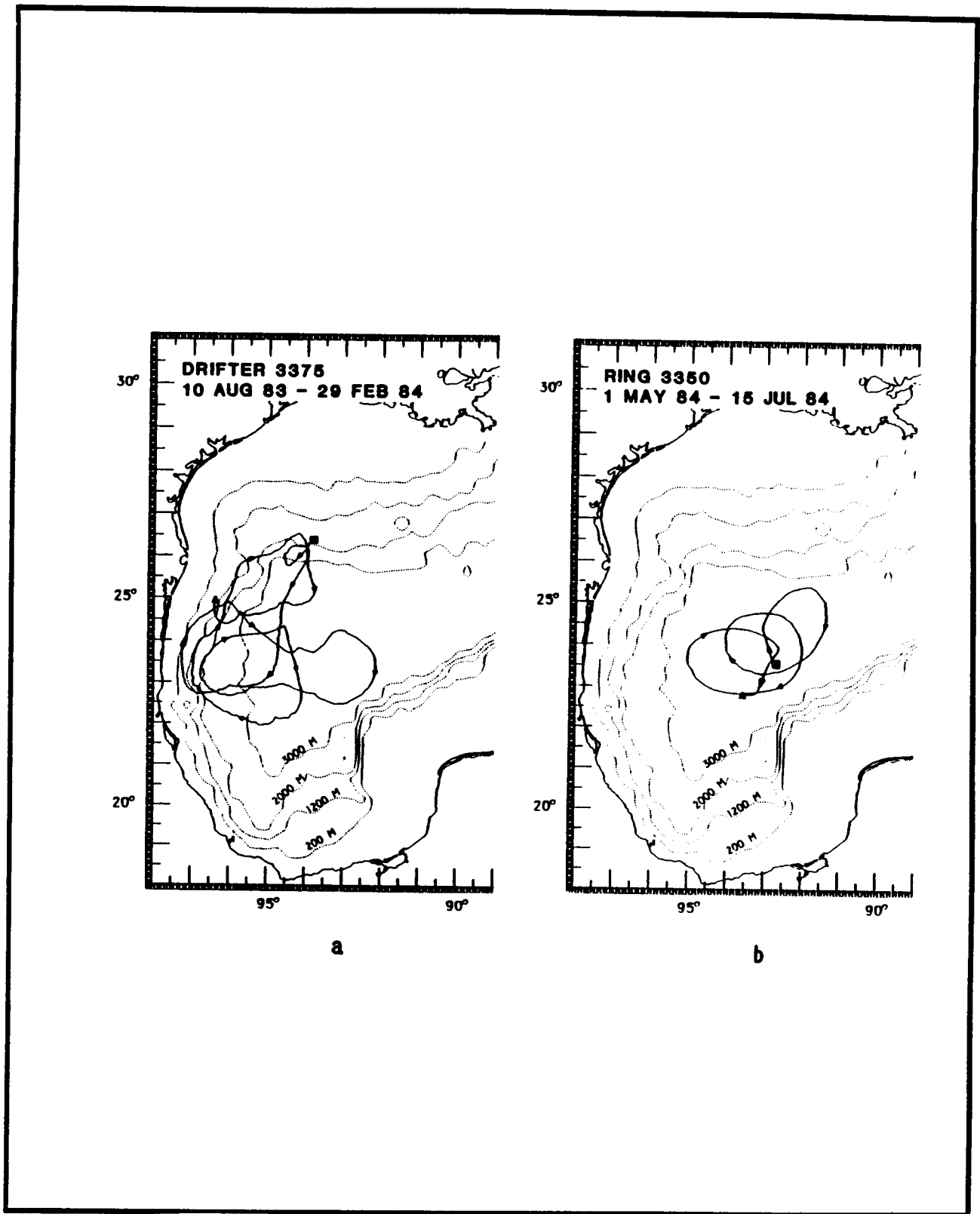


Figure 2.2-4. Trajectories for drifters (a) 3375 and (b) 3350. Depth contours are in meters. The squares and triangles denote the start and end positions, respectively.

eventually came under the influence of anticyclonic rotation at approximately 24°N and made three revolutions before entering water shallower than 200 m.

2.2.4 Thermistor Data

The 200-m line on Drifter 1599 had nine thermistors at the depths given in Table 2.2-1. In order to keep this line as straight as possible, a weight was attached to the end of the line. However, it was realized that some tilt with respect to the vertical would exist, and so a pressure gauge was also mounted at the end of the line to provide a means of estimating the tilt. The problem in using the thermistor data in the analysis of ring kinematics and dynamics deals with time scales. Our analyses indicate that the rings have dynamic variations on the order of 10 to 40 days. Ideally, these variations should be related to changes seen in the vertical temperature structure from the thermistor data. Unfortunately, there are considerable water temperature fluctuations on the order of 10 to 40 days that result from the atmospheric cooling and heating of the water column. These latter variations are relatively large and mask the variations induced by variations in ring force balances. Of course, atmospheric influences are less pronounced in deeper water, but unfortunately most of the deeper thermistors operated for only short periods of time.

The chronology of events of rings discussed in this report is presented in Table 2.2-2, which summarizes when the rings were shed from the Loop Current, dates of any subsequent XBT surveys, dates that the rings were seeded with the drifters, the locations for the seedings, and the times that the drifters were in the rings.

2.3 Satellite Imagery

2.3.1 Introduction

The primary application of satellite imagery to the present program has been to describe and define surface water masses and ocean fronts in the eastern Gulf of Mexico and hence to understand better the circulation in that region. A secondary application was to detect and locate oceanic phenomenon in support of the field operations associated with the program. The basic data used were infrared (IR) data from NOAA and GOES satellites.

Since for a given wavelength IR radiation is a function of temperature, over ocean surfaces IR imagery provides the distribution of sea-surface temperature. The satellite data in the visible portion of the radiation spectrum was also obtained, but was of secondary utility. The visible satellite data provided information on the reflectivity pattern of the ocean surface which is affected by waves and by suspended material at the surface. Under certain circumstances, visible data can be used to detect ocean fronts due to associated sharp horizontal gradients in suspended material concentration.

Table 2.2-1. Depths of the 9 thermistors on the line on drifter 1599.

Thermistor ID	Depth (m) of Thermistor
1	5
2	10
3	25
4	50
5	75
6	100
7	150
8	175
9	200

Table 2.2-2. Chronology of events for Loop Current eddies containing drifters.

Ring No	Approximate Time of Separation from Loop Current (Determined by Satellite Data)	Dates of XBT Surveys	Drifter Deployment Date and Location	Time that Drifter Was in Ring (mo) and Last Location
Ring 1599	Not Available	None Known	Nov. 1980 24.5° N 92° W	.6 25° N 95.5° W
Ring 3374	June 1982	Aug. and Dec., 1982	Oct. 1982 25° N 90° W	.9 24.5° N 95.5° W
March 1983 Ring	March 1983	None Known	Not Seeded
Ring 3350	Jan. 1984	Jan. 1984	May 1984 23.5° N 92.5° W	.1.5 24° N 92.5° W

2.3.2 Satellite Specifications

As previously indicated, IR data were obtained from two satellites. The present-day NOAA satellite series has been in operation since 1978 with the launch of TIROS-N. This polar-orbiting satellite provides twice-daily coverage over a given area. Two NOAA satellites have been in orbit at the same time giving four-a-day coverage. The orbital altitude of the NOAA satellite series is in the 800- to 900-km range.

One of the primary instruments on board the NOAA satellite is the Advanced Very High Resolution Radiometer (AVHRR). Table 2.3-1 provides specifications on the AVHRR system. The AVHRR, a five-channel radiometer, will provide data for real-time transmission in both Automatic Picture Transmission (APT) and High Resolution Picture Transmission (HRPT) modes. The data are available in four operational modes:

- (1) Direct readout to receiving stations of APT class at 4-km resolution of data in one visible and one IR channel.
- (2) Direct readout to receiving stations of the HRPT class at 1-km resolution of all spectral channels.
- (3) Global onboard recording of 4-km resolution data from all spectral channels for command readout at HRPT class stations.
- (4) On-board recording of data from selected portions of each orbit at 1-km resolution of all spectral channels.

The Geostationary Operational Environmental Satellites (GOES) are placed in a circular orbit at an altitude of 35,800 km. The orbital speed of the satellites is identical to the speed of rotation of the earth. Therefore, the satellites will remain stationary relative to a point on the earth. The data used by this program are from the Visible-Infrared Spin-Scan Radiometer (VISSR) which provides measurements of the earth in the 0.55-0.75 μm (visible) band during daylight and in the 10.5-12.5 μm (infrared) band both day and night. VISSR images of the global discs are generated by progressive stepping of a scan mirror and 1000 rpm rotation of the spacecraft. Approximately 18 min are required to scan the earth from northern to southern polar regions. The GOES visible image has a resolution of 1 km, and the IR image has a resolution of 9.3 km. In addition to the normal scan mode, the radiometer may be placed into a limited scan mode. This reduces the area of coverage but increases the frequency of imaging.

Usable IR images of the Gulf of Mexico can be obtained from these satellites about six to nine months of the year; i.e., in late fall, winter and spring periods. In summer and early fall, the sea-surface temperature gradient in the Gulf is generally weak and surface temperatures usually have very little relationship to circulation patterns. Summertime heating produces a mixed layer which acts like a buffer, preventing the satellite radiometers from "seeing" deeper frontal features. Furthermore, during summer and early fall, comparatively larger concentrations of water vapor exist in the boundary layer so that significantly more absorption of IR radiation from the sea-surface occurs. This tends to mask the true sea-surface temperature pattern. Absorption in the IR spectrum takes place in the late fall, winter and spring

Table 2.3-1. TIROS-N AVHRR Channel Characteristics

Channel	Wavelength (μm)	Primary Use
1	0.55 - 0.90	Daytime cloud and surface mapping
2	0.725 - 1.10	Surface water delineation
3	3.55 - 3.93	SST*, nighttime cloud mapping
4	10.5 - 11.5	SST, day/night cloud mapping
5	11.5 - 12.5	SST

* Sea-Surface Temperature

also; however, boundary layer water vapor content is not as significant as in the summer and early fall. Techniques exist for the correction of the infrared data for this absorption (Vukovich, 1983; Strong and McClain, 1984). But in the summer and early fall, the absorption of infrared radiation by water vapor is so large that the correction factor can be on the order of five larger than the sea-surface temperature gradient. Small errors in the correction factor can produce relatively large errors in the sea-surface temperature gradient. For this reason, IR imagery is of little use in the summer and early fall.

2.3.3 Data Sources and Availability

All NOAA and GOES infrared and visible imagery used for this project were obtained by the Research Triangle Institute (RTI) using the RTI's Satellite Receiving Station (RTI/SRS) which was established on RTI's campus in 1972. Direct readout IR data from the APT mode of the NOAA satellite were used. The APT signal receiver consists of a manual track, dual-yagi antenna and an APT/FM signal receiver.

RTI is also a primary (direct) user within the GOES system and, as such, maintains a direct communication line with the NOAA/National Earth Satellite Data and Information (NESDIS), Central Data Distribution Facilities (CDDF). The direct line provides user selection of 22 different standard sectorized (IR or visible) images from either GOES east or GOES west. Four of the image sectorizers are currently designated as "floating sectorizers" which can be focused on any geographical area to provide dedicated monitoring of unique environmental events or areas.

In order to develop sea-surface temperature analysis in particular situations, NOAA/AVHRR digital data tapes were obtained from NOAA/National Environmental Satellite Data and Information Service (NESDIS). Digital data are required to develop atmospherically corrected and spatially located sea-surface temperatures. Data obtained by the RTI/SRS are in analog form, but RTI possesses all algorithms necessary to transform the data to digital data tapes.

Other data used included satellite derived frontal analyses in the Gulf of Mexico performed by using either GOES or NOAA data. Dr. Steve Baig (NOAA/NESDIS) in Miami, Florida, develops frontal analyses for the eastern Gulf of Mexico using GOES data. These analyses were available for this program, on the average, every two to three days. NOAA/NESDIS also produces, on a daily basis, frontal analyses in the Gulf of Mexico using NOAA/AVHRR data.

Four primary data sources were used to derive the information on the warm rings in the Gulf of Mexico. These were:

- (1) NOAA infrared imagery on file at the Research Triangle Institute for the period 1973 through 1984;
- (2) Weekly oceanographic analysis prepared by NOAA/NESDIS based on NOAA satellite data and available for the period 1980 through 1984;

- (3) Biweekly oceanographic analysis prepared by NOAA/NESDIS/Miami, based on GOES satellite data; and
- (4) Information gleaned from publications GULFSTREAM and OCEANOGRAPHIC MONTHLY SUMMARY.

2.4 Hydrography

2.4.1 Introduction

The hydrographic component of the field program was designed to characterize the flow field and water masses in the study region and specifically to examine Loop Current/shelf water interaction. Hydrographic observations can be combined with more synoptic remote sensing observations and current meter measurements to provide a more complete picture of the ocean environment.

The key to the hydrographic sampling plan was cruise flexibility, with access to remote sensing before and during each cruise so that sampling strategies could be easily adjusted to accommodate relatively high-frequency changes in the Loop Current geometry. Sampling plans were based on satellite thermal imagery and sea-surface temperature maps that were routinely available on board during each cruise. At least one hydrographic section during each cruise coincided with a mooring line so that hydrographic data could be combined with current meter/temperature sensor data. The cruises were scheduled in March, November, and May, when cloud cover is expected to be at a minimum and surface thermal contrast to be high, so that high quality satellite IR imagery could be obtained. Each cruise was about twelve days long to insure coverage of at least one eddy event. Station spacing was generally tighter across the shelfbreak and in the vicinity of fronts where more intense density gradients were expected. The station spacing and a combination of CTD and XBT casts provided the coverage necessary to characterize regional hydrography and water masses and to compute geostrophic velocities and transports.

For at least a week prior to each cruise, Loop Current movement was monitored with standard NOAA/NESDIS products, and this information was used to finalize the cruise plan. During each cruise, data were plotted for continuous analysis so that the cruise plan could be modified if oceanographic conditions changed. Also, satellite imagery and SST maps were evaluated daily during each cruise and sampling plans were adjusted if necessary.

2.4.2 Cruise Summaries

2.4.2.1 Year 1, Cruise 1

The first cruise in the eastern Gulf of Mexico took place from 7-22 March 1983 on board the R/V SUNCOASTER. Severe weather forced changes in the cruise schedule and sampling plan while at sea. The final cruise track is shown in Figure 2.4-1, which indicates CTD and XBT station locations. Table 2.4-1 summarizes these stations, and Table 2.4-2 summarizes the samples taken on each section.

Table 2.4-1. Summary of stations according to sampling time and section number for R/V SUNCOASTER cruise from 7-22 March 1983.

Section	Date (EST)	Station Numbers
I	9-10 March	1X, 2C, 3X, 4C, 5X, 6C, 7C, 8C, 9C, 10C, 11C, 12X, 13C, 14X, 15C, 16X, 17C, 18X, 19C, 20C
I	12-14 March	21C, 22X, 23C, 24X, 25C, 26X, 27C, 28X, 29C, 30X, 31C, 32C, 33C, 34C, 35C, 36C, 37C, 38C
*II	14-16 March	45C, 46X, 47C, 48C, 49C, 50X, 51C, 52C, 53X, 54X, 55X, 56X, 57X, 58X, 59C, 60X, 61X, 62C, 64C, 65X, 66C, 67X, 68C, 69X, 70C, 71X, 72C, 73X, 74C, 75X, 76C
**III	19-21 March	121C, 122C, 123X, 124C, 125C, 126X, 127C, 128X, 129C, 130X, 132X, 133C, 134X, 135C, 136X, 137C, 138C, 139X, 140C, 141X, 142C, 143C, 144C, 145X, 146X, 147X, 148X, 149X

* Between Sections I and II, surface temperature data were collected at hourly intervals: Stations 39TS-44TS and 41X.

** Before and after Section III surface temperature data were collected at half hour intervals while steaming to and from Tampa/St. Petersburg. Stations 77TS-120TS and 151TS-181TS.

*** X = XBT drop; C = CTD cast; TS = Thermosalinograph station.

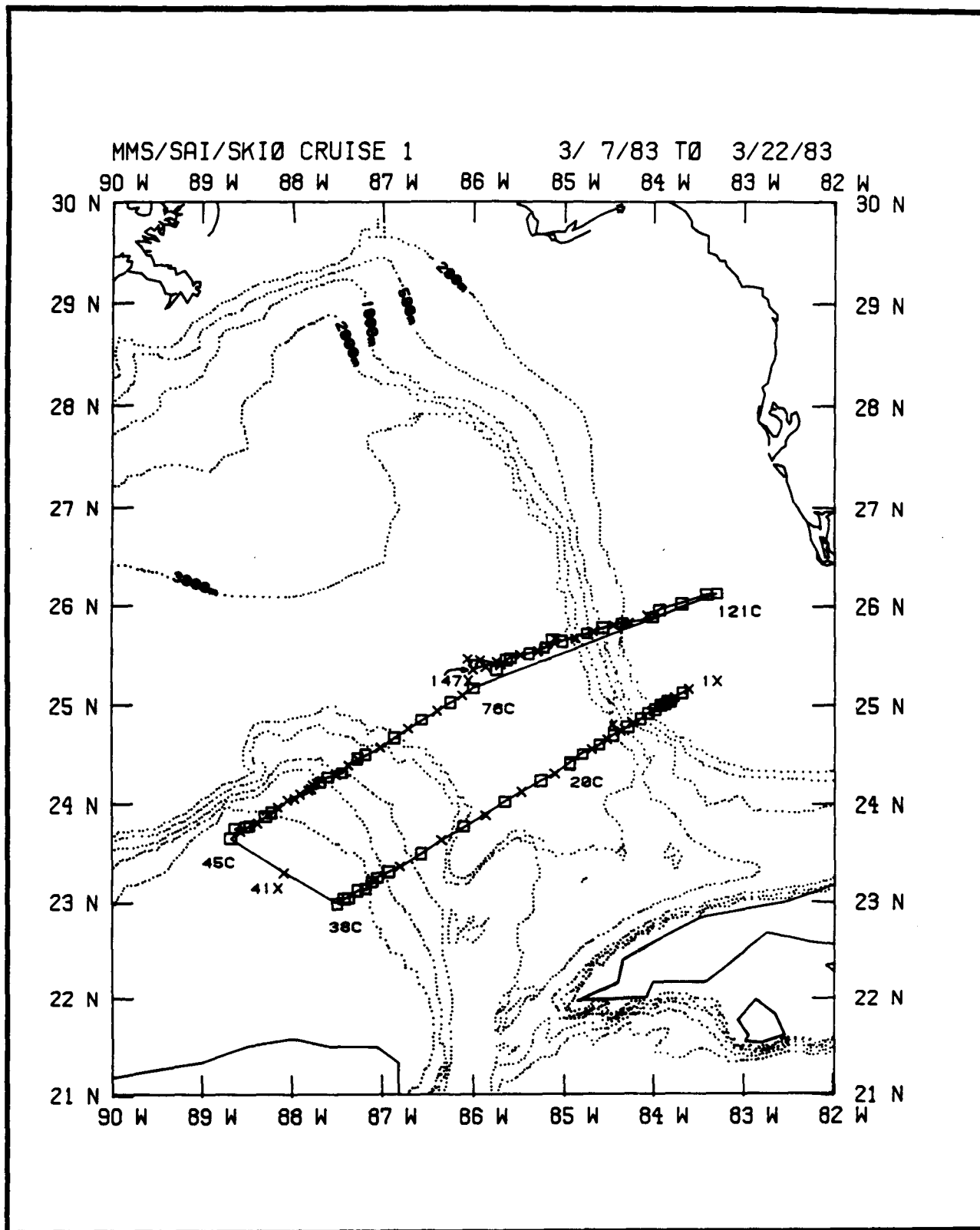


Figure 2.4-1. Cruise track showing XBT and CTD station locations for R/V SUNCOASTER cruise from 7-22 March 1983.

Table 2.4-2. Summary of samples taken during R/V SUNCOASTER cruise from 7-22 March 1983. Nuts = nutrients.

Section	CTD	XBT	Nuts	O ₂	Chlorophyll	Salinity
I (1X-20C)	13	7	94	94	47	22
I (21C-38C)	13	5	106	106	48	27
II (41X-76C)	15	18	127	128	55	21
III (121C-149X)	<u>15</u>	<u>14</u>	<u>142</u>	<u>142</u>	<u>57</u>	<u>20</u>
Totals	56	44	469	470	207	90

The original cruise plan called for three sections of approximately 30 CTD/XBT stations each. During the cruise a series of meteorological cold fronts moved through the area every two to three days, causing several sampling interruptions due to weather. As a result, only two transects across the southern Gulf from the west Florida shelf to the Yucatan Peninsula were completed.

Hydrographic sampling began on 9 March and was suspended on 10 March because of bad weather. The ship anchored off Loggerhead Key from 10-11 March to wait out the storm. Sampling resumed on 12 March. On 15 March CTD operations were suspended because of high winds and seas, and on 16 March all sampling operations were suspended and the ship steamed for St. Petersburg for shelter from another storm. During the run to St. Petersburg, sea-surface temperatures were mapped. Sampling again resumed on 19 March and the ship steamed for St. Petersburg on 21-22 March doing sea-surface temperature mapping. Because of bad weather, a plan for XBT sampling along a more northerly track to St. Petersburg was canceled.

2.4.2.2 Year 1, Cruise 2

The second cruise on the R/V SUNCOASTER took place from 10-21 November 1983. The final cruise track, indicating CTD and XBT station locations, is shown in Figure 2.4-2. The northernmost transect was shortened because of bad weather which forced the ship to return to port one day early. Table 2.4-3 summarizes the stations, and Table 2.4-4 summarizes the samples taken on each section. In addition to CTD and XBT stations, sea-surface temperature and salinity data were collected hourly between all sections. Also, XBT drops were made hourly while steaming to Section V, and every two hours while steaming from Section V. Four transects and part of a fifth were completed from the west Florida shelf to the central eastern Gulf, covering most of the meridional extent of the shelf. Good weather held during most of this cruise. However, on 15 November adverse weather conditions caused CTD operations to be suspended, with XBT sampling continuing. CTD operations resumed on 16 November and were again terminated because of severe weather conditions on 19 November.

2.4.2.3 Year 2, Cruise 1

The Year 2 hydrographic survey combined ship-based spatially well-resolved observations with plane-based regional scale observations. This design provided a single synoptic regional characterization with time series and synoptic observations of dynamic features along the Loop Current eastern boundary. These two methodologies were coordinated to produce a comprehensive documentation of the Loop Current and its interaction with the west Florida shelf and slope.

The shipboard phase of this survey took place from 4-19 May 1984 on board the R/V CAPE FLORIDA. The final cruise track is shown in Figures 2.4-3 through 2.4-6. Table 2.4-5 summarizes cruise stations, and Table 2.4-6 summarizes samples taken on each section.

Good weather held through most of the cruise. Fifteen transects were made along the west Florida shelfbreak between 23° and 27°N, with most of the data obtained between 24° and 26°N. Time series of hydrographic data were obtained on two sections, while three synoptic maps were made using mostly XBT drops

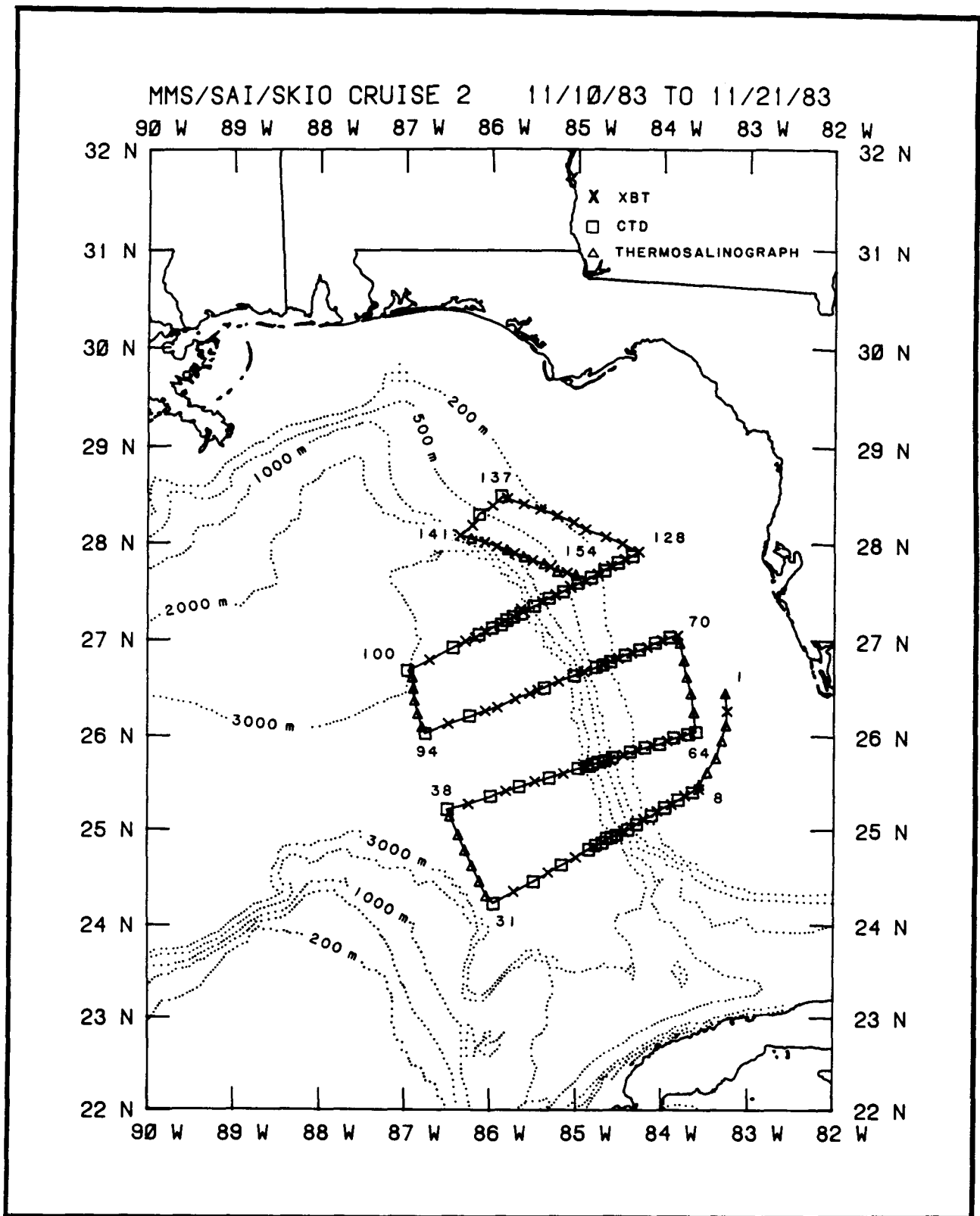


Figure 2.4-2. Cruise track showing XBT, CTD, and thermosalinograph station locations for R/V SUNCOASTER cruise from 10-21 November 1983.

Table 2.4-3. Summary of stations according to sampling time and section number for R/V SUNCOASTER cruise from 10-21 November 1983.

Section	Date (EST)	Station Numbers
I	11-13 November	2X*, 8X, 9C, 10X, 11C, 12X, 13C, 14X, 15C, 16X, 17C, 18C, 19X, 20C, 21C, 22C, 23C, 24C, 25C, 26X, 27C, 28X, 29C, 30X, 31C
II	13-14 November	38C, 39X, 40C, 41X, 42C, 43X, 44C, 45X, 46C, 47X, 48C, 49C, 50C, 51C, 52X, 53C, 54X, 55C, 56X, 57C, 58X, 59C, 60X, 61C, 62X, 63C, 64C
III	15-16 November	70X, 71C, 72X, 73C, 74X, 75C, 76X, 77C, 78X, 79C, 80X, 81C, 82C, 83X, 84C, 85X, 86C, 87X, 88X, 89X, 90X, 92C, 93X, 94C
IV	17-18 November	100C, 101X, 102C, 103X, 104X, 105C, 106X, 107C, 108C, 109C, 110C, 111C, 112X, 113C, 114X, 115C, 116X, 117C, 118X, 119C, 120X, 121C, 122X, 123C, 124X, 125C, 126X, 127C, 128X
(To) V	18-19 November	129X, 130X, 131X, 132X, 133X, 134X, 135X, 136X
V	19 November	137C, 138X, 139C, 140X, 141X
(From) V	19 November	143X, 145X, 147X, 149X, 151X, 153X

* Dropped while enroute to Section I.

Between sections, surface temperature and salinity were collected at hourly intervals:

Stations 1TS - 7TS (To Section I)
 Stations 32TS - 37TS (To Section II)
 Stations 65TS - 69TS (To Section III)
 Stations 95TS - 99TS (To Section IV)
 Stations 142Ts, 146TS, 148TS, 150TS, 152TS (From Section V)

Table 2.4-4. Summary of samples taken during R/V SUNCOASTER cruise from 10-21 November 1983.

Section	CTD	XBT	Nutrients	Oxygens	Chlorophyll		Salinity
					In Vivo	Filtered	
I (8X-31C)	15	*10	143	143	58	44	14
II (38C-64C)	16	11	135	135	60	46	15
III (70X-94C)	11	14	85	85	45	33	12
IV (100C-128X)	16	13	131	134	56	44	14
(To) V (129X-136X)	0	8	0	0	0	0	0
V (137C-141X)	2	3	14	14	8	6	2
(From) V (143X-153X)	0	6	0	0	0	0	0
TOTALS	60	65	508	511	227	173	57

* Includes XBT dropped at Station 2X to test Bathy Systems unit.

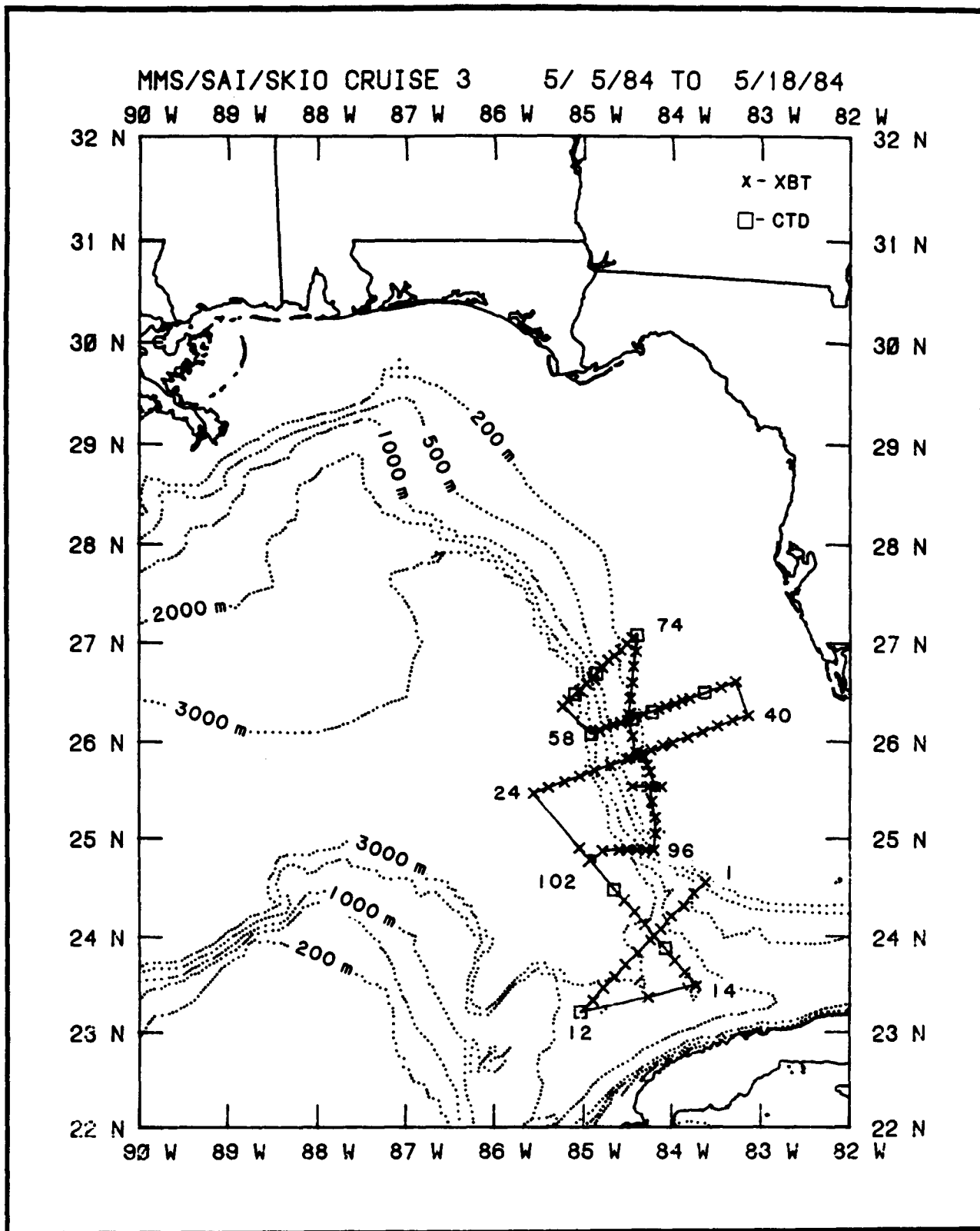


Figure 2.4-3. Cruise track showing XBT and CTD station locations, Stations 1-102, for R/V CAPE FLORIDA cruise from 5-18 May 1984.

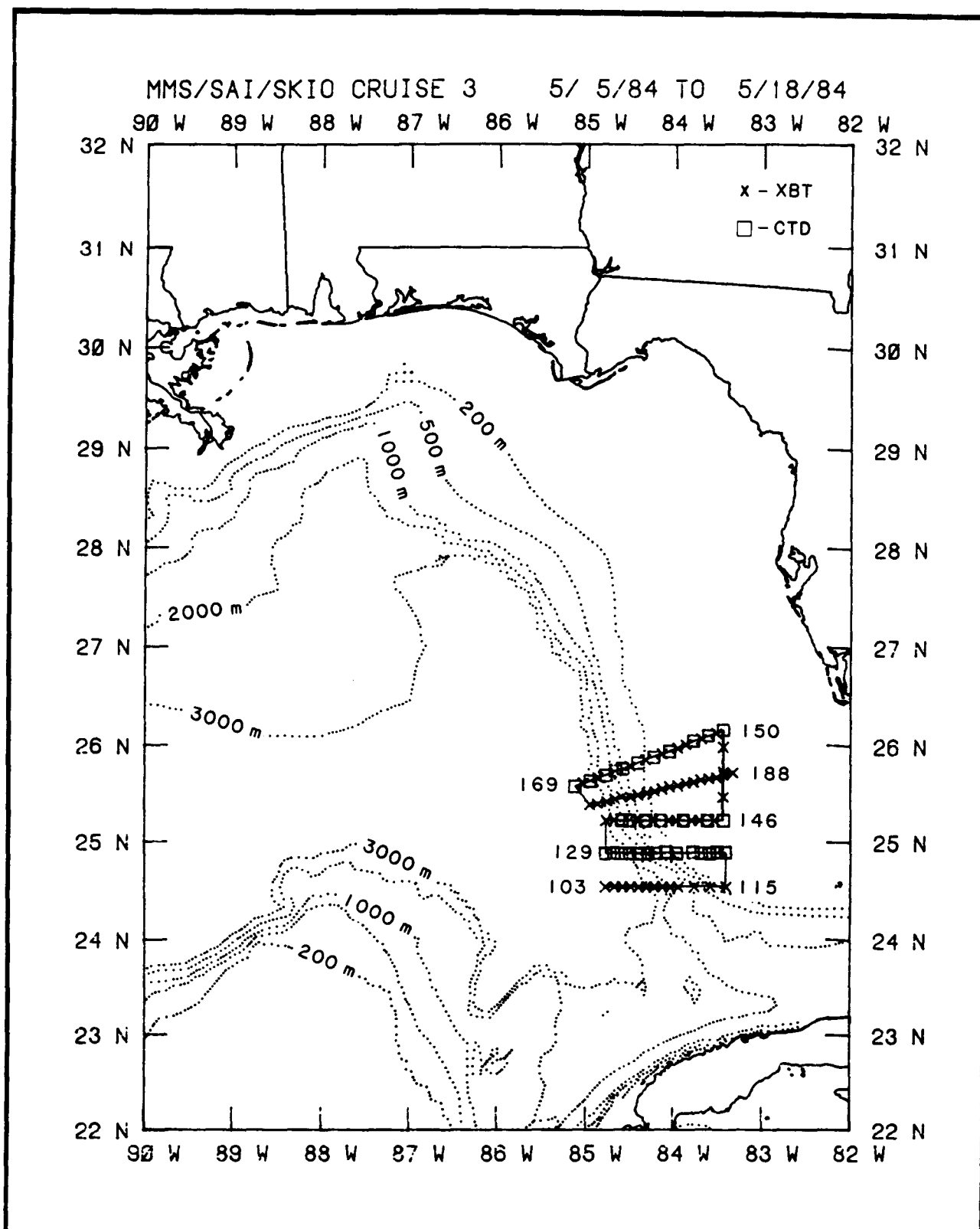


Figure 2.4-4. Cruise track showing XBT and CTD station locations, Stations 103-188, for R/V CAPE FLORIDA cruise from 5-18 May 1984.

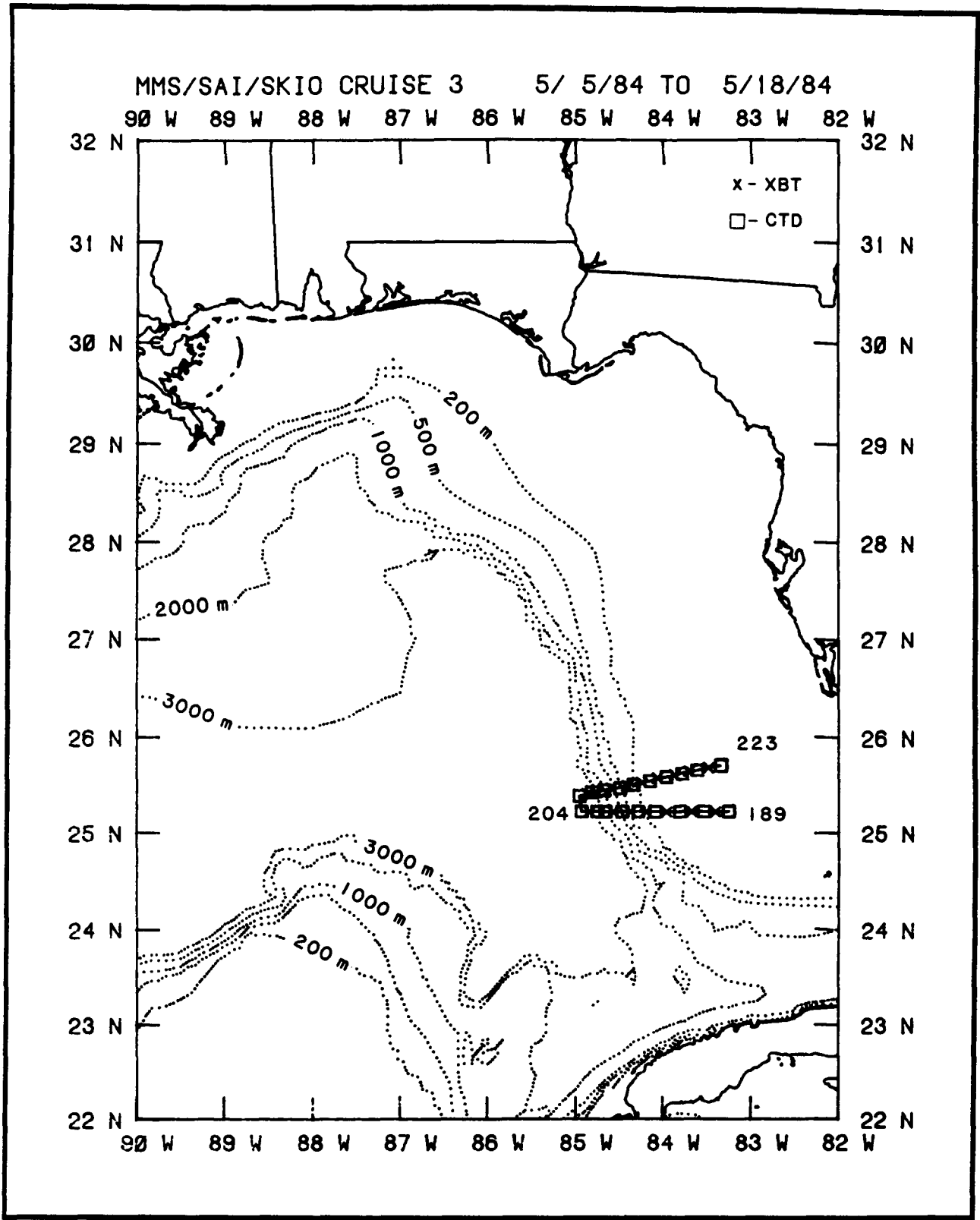


Figure 2.4-5. Cruise track showing XBT and CTD station locations, Stations 189-223, for R/V CAPE FLORIDA cruise from 5-18 May 1984.

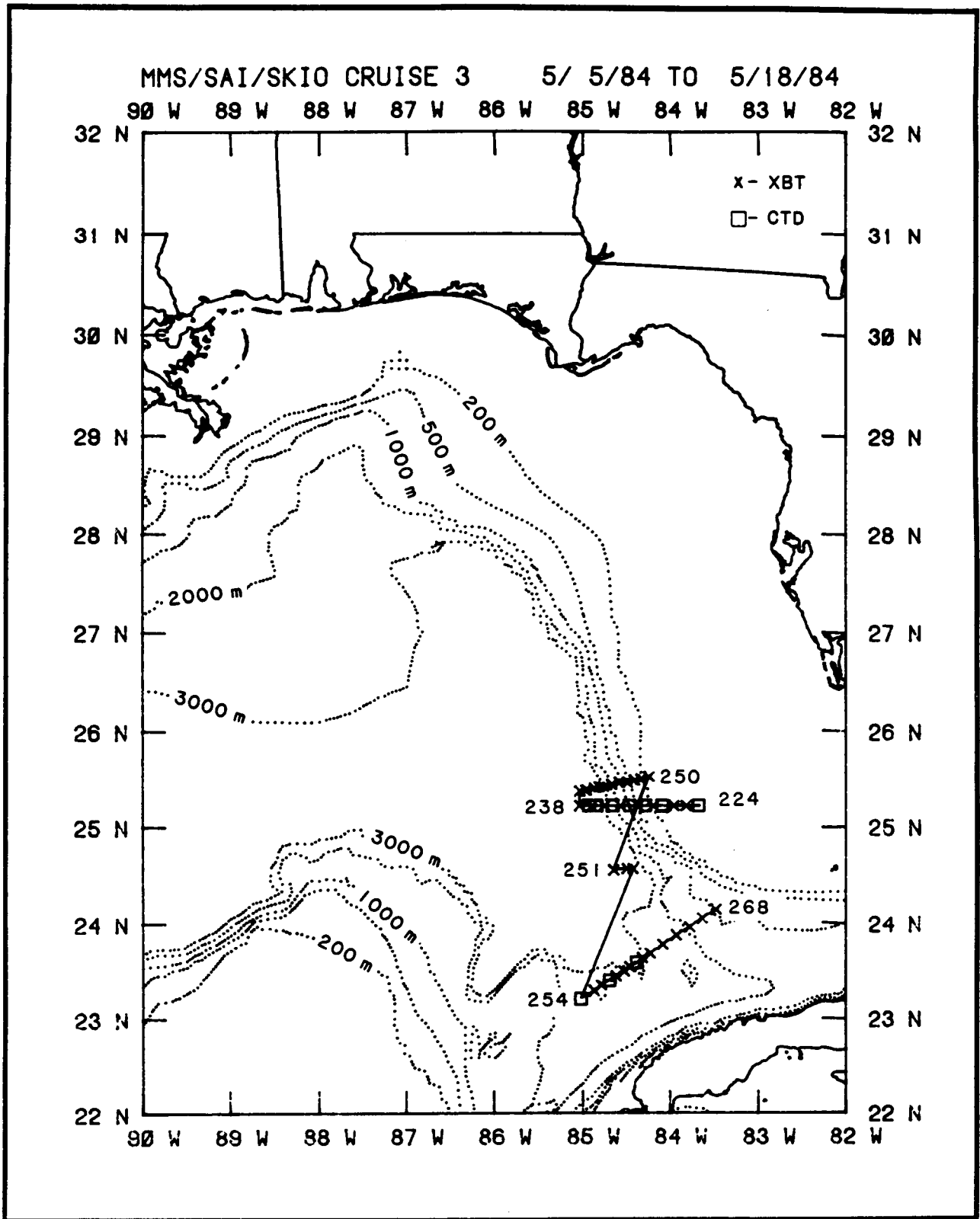


Figure 2.4-6. Cruise track showing XBT and CTD station locations, Stations 224-268, for R/V CAPE FLORIDA cruise from 5-18 May 1984.

Table 2.4-5. Summary of stations according to sampling time and section number for R/V CAPE FLORIDA cruise from 5-18 May 1984.

Section	Date (GMT)	Station Numbers
I	5-6 May	1X, 2X, 3X, 4X, 5X, 6X, 7X, 8X, 9X, 10X, 11X, 12C
II	6-7 May	*13X, 14X, 15X, 16X, 17C, 18X, 19X, 20X, 21X, 22C, **23X
III (Mooring Line)	7-8 May	24X, 25X, 26X, 27X, 28X, 29X, 30X, 31X, 32X, 33X, 34C, 35X, 36X, 37X, 38X, 39X, 40X
IV	8 May	41X, 42X, 43X, 44X, 45X, 46X, 47X, 48X, 49C, 50X, 51X, 52C, 53X, 54X, 55X, 56X, 57X, 58C
V	9 May	59X, 60X, 61C, 65X, 63X, 66X, 67C, 68X, 69X, 70X, 71X, 72X, 73X, <u>74C</u>
VI-A	9 May	<u>74C</u> , 75X, 76X, 77X, 78X, 79X, <u>80X</u>
VI-B	9 May	<u>80X</u> , 81X, 83X, 84X
VI-C	9-10 May	85X, 86X, 87X, 88X
VII	10 May	89X, 88X, <u>92X</u> , 91X
VI-D	10 May	<u>92X</u> , 93X, 94X, 95X, <u>96X</u>
VIII	10 May	<u>96X</u> , 97X, 98X, 99X, 100X, 102X
IX	10 May	103X, 104X, 105X, 106X, 107X, 108X, 109X, 110X, 111X, 112X, 113X, 114X, 115X
X	10-11 May	116C, 117c, 118C, 119C, 120C, 121C, 122C, 123C, 124C, 125C, 126C, 127C, 128C, 129C
XI	11-12 May	130X, 131X, 132C, 133C, 134X, ***135X, 136C, 137X, 138C, 139X, 140X, 141C, 142X, 143X, 144C, 145X, <u>146C</u>
XII	12 May	<u>146C</u> , 147X, 148X, 149X, <u>150C</u>
XIII (Mooring Line)	12-13 May	<u>150C</u> , 151X, 152C, 153X, 154C, 155X, 156X, <u>157C</u> , 158X, 159C, 160X, 161C, 162X, 163C, 164C, 165C, 166X, 167C, 168X, 169C
XIV	13 May	170X, 171X, 172X, 173X, 174X, 175X, 176X, 177X, 178X, 179X, 180X, 181X, 182X, 183X, 184X, 185X, 186X, 187X, 188X

Table 2.4-5. (Continued)

Section	Date (GMT)	Station Numbers
XV	14 May	189C, 190X, 191C, 192X, 193C, 194X, 195C, 196X, 197C, 198X, 199C, 200X, 201C, 202C, 203X, 204C
XVI	14-15 May	205C, 206X, 207C, 208X, 209C, 210X, 211C, 212X, 213C, 214X, 215C, 216X, 217C, 218X, 219C, 220X, 221C, 222X, 223C
XVII	15-16 May	224C, 225X, 226X, 227C, 228X, 229C, 230X, 231C, 232X, 233C, 234X, 235C, 237X, 236C, 238X
XVIII	16 May	239X, 240X, 241X, 242X, 243X, 244X, 245X, 246X, 247X, 249X, 250X
XIX	17 May	251X, 252X, 253X
XX	17-18 May	254C, 255X, 256X, 257C, 258X, 259X, 260X, 261C, 262X, 263X, 264X, 265X, 266X, 267X, 268X

* Actually between Sections I and II.

** Actually between Sections II and III but along Line II.

*** Stations 135X and 136C are at the same location.

Table 2.4-6. Summary of samples taken during R/V CAPE FLORIDA cruise from 5-18 May 1984.

Section	CTD	XBT	Nutrients	Oxygens	Salinity
I	1	11	13	13	0
II	2	*9	26	25	2
III	0	17	0	0	0
IV	4	14	35	36	4
V	3	11	29	29	3
VI-A	0	6	0	0	0
VI-B	0	3	0	0	0
VI-C	0	4	0	0	0
VII	0	3	0	0	0
VI-D	0	4	0	0	0
VIII	0	5	0	0	0
IX	0	13	0	0	0
X	14	0	67	67	8
XI	7	10	56	55	8
XII	1	3	5	5	1
XIII	10	9	82	83	10
XIV	0	19	0	0	0
XV	9	7	66	66	9
XVI	10	9	81	81	10
XVII	7	8	70	70	8
XVIII	0	11	0	0	0
XIX	0	3	0	0	0
XX	3	12	38	39	3
TOTALS	71	191	568	569	66

with occasional CTD casts. During the entire cruise AMETEK STRAZA current profiles and sea-surface temperature and salinity data were obtained. Because of deteriorating weather on 17 May, CTD operations were suspended and the final transect was completed with XBT drops.

2.4.3 Shipboard Equipment

2.4.3.1 Shipboard Sampling Methodology

The CTD system used during the cruises is shown schematically in Figure 2.4-7 and a component list is provided in Table 2.4-7. Basically, the CTD system consists of four major components:

- (1) the underwater unit equipped with depth, conductivity, and temperature sensors
- (2) the winch, conductor cable wire, and Rosette Multi-Bottle Array fitted with twelve 1.7 liter Niskin sampling bottles
- (3) the deck units that power the Rosette and CTD sensors
- (4) the data processing system that does real-time data processing, and stores and displays the data in a variety of modes (i.e., HP flexible disk, plotter, and printer)

Prior to arriving on station, the CTD system, bottles, and thermometers were checked, the Rosette cocked, and the station sheets initially filled in. The Neil Brown CTD and the General Oceanics Rosette supporting 1.7 liter Niskin bottles (the combined unit is known as the 'fish') were then lifted from the deck and lowered to 1-3-m depth, depending on the sea state. The bottom depth was checked and the cast started. All operations were timed and prompted by the HP 9825A calculator. The normal ship's heading was with the wind on the starboard aft quarter to keep the wire away from the ship.

During the downcast, temperature versus depth was plotted on an HP plotter. All data were continuously recorded on an HP flexible disk. The fish was held at the bottom depth for a four-minute soak while the reversing thermometers equilibrated. This was timed by the HP system, which also printed out soak data. During this time the sample depths for the upcast were selected based on the downcast temperature and salinity profiles. The upcast procedure was identical to the downcast procedure except that the CTD fish was stopped and the Rosette was tripped at selected depths. Soak data were printed during this operation.

Table 2.4-8 lists recommended sampling depths for shallow stations and Table 2.4-9 lists recommended sampling depths for deep stations. Because of special situations, depths were often added or deleted to sample more sensibly the water column for water less than 100-m total depth. This is because the waters of the west Florida shelf often exhibit complex temperature and salinity structure. This variability combined with the dominant effects of the Loop Current makes strict adherence to a specific sampling criteria difficult and often scientifically unjustified.

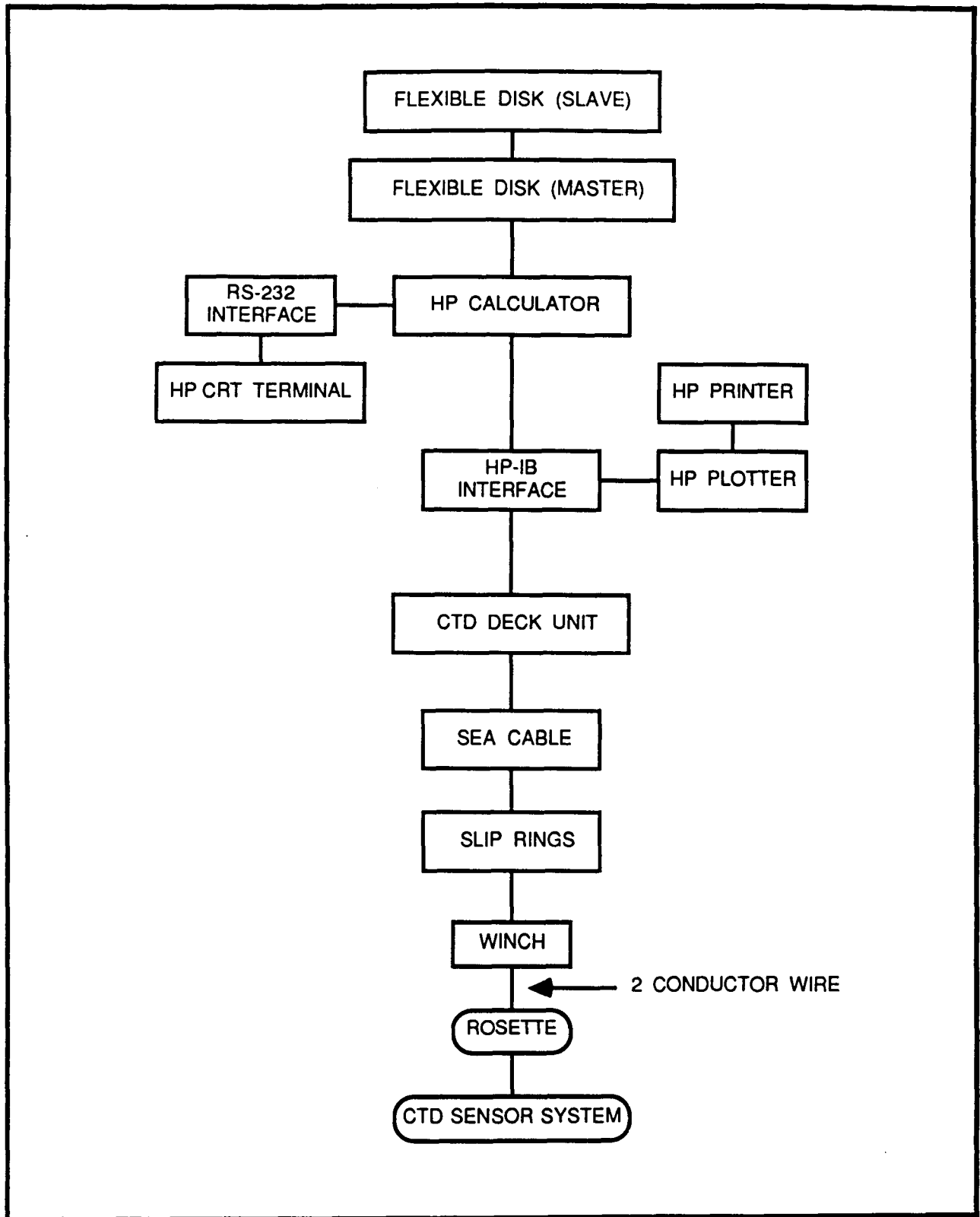


Figure 2.4-7. Schematic of CTD system used during hydrographic cruise.

Table 2.4-7. List of components of CTD system used during hydrographic cruises.

Neil Brown CTD

Neil Brown 1150 Deck Unit

General Oceanics Rosette Multi-Bottle Array Model 1015 Mark V

HP 9825A Calculator

HP 9885M Flexible Disk Drive

HP 9885S Flexible Disk Drive

HP 98034A HP-IB Interface

HP 9872A Plotter

HP 2631A Printer

HP 98036A RS-232 Interface

HP 2621P CRT

Table 2.4-8. Recommended Sampling Depths For Depths less than 100 meters.

- Depths less than 50 m
 - Mixed - surface and bottom
 - Two layer - surface, bottom of thermocline, bottom

- Depths greater than 50 m, less than 100 m
 - surface, 25 m, 50 m, 75 m, bottom

Table 2.4-9. Recommended sampling depths for water depths greater than 100 meters.

<600m	<900m	<1200	>1200m
Surface	Surface	Surface	Surface
50	50	50	50
100	100	100	100
150	150	150	150
200	200	200	200
250	-	-	-
300	300	300	300
400	400	400	400
500	500	500	500
600	600	600	600
<u>12 Bottles Max</u>	700	-	-
	800	800	800
	900	900	-
	<u>12 Bottles Max</u>	1000	1000
		1200	1200
		<u>13 Bottles Max</u>	1500
			<u>13 Bottles Max</u>

Once a cast was completed, the dissolved oxygen samples were drawn first, using normal precautions. The reagents were added, the ground glass stopper replaced, and the sample stored in a dark case until shipboard analysis was completed, generally within a few hours. Analysis was performed strictly according to the method described by Strickland and Parsons (1972). Nutrient samples were drawn into 125-ml poly bottles after two rinses and stored in a freezer for subsequent laboratory analysis by standard Technicon Autoanalyzer techniques. Salinity samples were drawn into 250-ml glass bottles after two rinses and stored for subsequent laboratory analysis using a Plessey portable laboratory salinometer. Samples collected for chlorophyll-a were filtered on glass fiber filters, which were then frozen for subsequent laboratory analysis using the fluorometric method of Yentsch and Menzel (1963) as described by Strickland and Parsons (1972). Finally, the reversing thermometers were read after equilibration to ambient temperature.

During the March and November 1983 cruises, sea-surface temperature and salinity were monitored along the cruise track with a Plessey CTD in a flow-through arrangement using water from the ship's sea chest. During the May 1984 cruise, sea-surface temperature and salinity were continuously recorded with the R/V CAPE FLORIDA Serial ASCII Interface Loop (SAIL) system.

2.4.3.2 Laboratory Methodology

Salinity, temperature, and depth recorded by the CTD system described in the previous section were calibrated against bottle casts. Likewise, calibrations were performed for dissolved oxygen, nutrients, and chlorophyll-a concentrations.

CTD salinity calibration data were obtained from upcast bottle and CTD samplings after the downcast. Temperature calibration data were obtained from the CTD and reversing thermometer readings. The salinity and temperature mean differences and standard deviations are given in Table 2.4-10. These differences are within the range of accuracy of the instruments used for calibration so no correction has been applied to the data. A calibration by Neil Brown, Inc. in June 1983 measured the CTD pressure (depth) sensor to within its rated accuracy and no correction has been applied there either. The XBT drops were checked periodically during the cruises against an internal recorder calibration and were found to be within the accuracy range of the system ($\pm 0.1^{\circ}\text{C}$). Thus no temperature offset was applied to the XBT data.

Dissolved oxygen calibrations were made during each run on each cruise. The thiosulfate was calibrated against standard potassium bi-iodate. The F-factor varied from 1.00 to 1.01 over the first cruise, 1.848 to 1.907 over the second cruise, and 4.31 to 4.49 over the third cruise. The blank value varied from 0.00 to 0.01, -0.001 to +0.005, and 0.00 to 0.01 ml during the first, second, and third cruises, respectively. The fluorometer used for chlorophyll-a measurement was calibrated following the procedure from Strickland and Parsons (1972).

Table 2.4-10. CTD Salinity and Temperature Calibration Results

Cruise	Salinity		Temperature	
	Mean	Std Dev	Mean	Std Dev
March 1983	-0.007	+/-0.010	+0.03	+/-0.02
Nov 1983	-0.010	+/-0.013	+0.02	+/-0.02
May 1984	+0.006	+/-0.026	+0.03	+/-0.03

Note: Mean salinity differences are bottle sample readings minus CTD downcast values. Mean temperature differences are reversing thermometer readings minus CTD downcast values.

2.4.4 Ametek-Straza Current Profiles

The Ametek-Straza DCP-4400, a hull-mounted acoustic doppler current profiler (ADCP), yields a vertical profile of the horizontal velocity field from the sea surface to about 200-m depth. During the May 1984 R/V CAPE FLORIDA cruise (CF8405) a 115kHz three beam ADCP was used to obtain velocity data approximately every 160 seconds quasi-continuously throughout the duration of the cruise.

The underwater portion of this system is configured such that the three acoustic transducers are oriented 120 degrees from each other in the horizontal and downward about 30 degrees from vertical. One transducer is aimed towards the bow of the ship, leaving the other two facing slightly aft on the port and starboard sides. At an operating frequency of 115kHz, the acoustic beams generated by the transducers are narrow (conical spreading is about three degrees); therefore, they remain distinct from each other well beyond the depths of interest. After acoustic pulses are generated simultaneously at the three transducers, the system directs the transducers to listen for the back-scattering of sound waves along each beam in a time-gated fashion. This back-scattering occurs because of density discontinuities in the water column due to the presence of fish, plankton, microstructure, turbulence, etc. These reflectors are assumed to be passively advected and the velocity field is assumed to be uniform in the horizontal in the region between the acoustic beams.

Time gating has the effect of dividing the distance along each beam into bins. Since the angle of the beams from the vertical and the speed of sound in seawater are known, time bins can be converted to depth bins below the in-hull transducer. The frequency of the back-scattered sound in each bin of the three beams is determined and its doppler shift from the original 115kHz is stored in memory. A positive shift results from water flowing closer to the beam, a negative one from water flowing further from the beam. For each particular bin the doppler data from all three beams are combined to yield fore and port components of the doppler shift vector and these are combined with data from the ADCP's internal compass to yield the doppler vector relative to the ship in geodetic (north and east) components. The results from several data collection cycles can be averaged to increase statistical confidence. The percentage of successful back-scatter detections is calculated at the end of the averaging cycle and is merged with the doppler vector for each depth bin. For this study over 60 cycles were averaged. After averaging, the doppler data (in units of 1/8 Hz) as a function of depth as well as a header record containing time, date, bottom depth and sea-surface temperature are stored on magnetic media for later retrieval and transformation into velocity profiles (the details of which are described in section 3.4.3).

The DCP-4400 has a fixed number of bins (63) for measuring velocity in the water column relative to the ship, plus one bin which is reserved for tracking the movement of the ship relative to the bottom. The size of the bins is user-selectable from a software controlled menu. Choices include 1.0, 3.2, 6.4 and 12.8 m per bin. Since past experience with this system indicated that its ability to detect back-scattered acoustic energy from planktonic reflectors at depths deeper than 200-250 m is marginal, the 3.2 m bin size which yields coverage to 200-m depth was chosen. As will be shown in Section 3.4.3,

bottom tracking capabilities extend somewhat deeper, presumably because the sediment-water interface is a much stronger reflector than those in the water column. When these bottom tracking data are available it is straightforward to subtract the ship motion out of the profile to yield absolute water velocities relative to the earth. When data are collected in regions where the water is too deep for the ADCP's bottom tracking capabilities, ship motion is calculated from LORAN-C data and recorded on a Serial ASCII Interface Loop (SAIL) system. These same LORAN-C data are used to determine the geographic location of each velocity profile obtained.

Initial analysis of the CF8405 Ametek-Straza ADCP data set is complete. The ADCP data have been merged with the corresponding SAIL data and horizontal maps of velocity at any particular depth for any particular time frame are routinely produced. The weakest link in the present data processing procedure is the technique required for extracting a low-noise ship motion signal from LORAN-C data for use in removing ship motion from the doppler data. Additional refinement of this technique and additional development of data display techniques are in progress.

2.4.5 Year 2 - Aerial Survey

2.4.5.1 Introduction

The aerial survey was made on 11-14 May 1984, with limited measurement on the last day. Two types of expendable probes were deployed:

- temperature profilers (AXBT's)
- current profilers (AXCP's)

The distribution of these profiles is shown in Figure 2.4-8 where the dots are AXBT locations and squares are AXCP locations. The position of the Loop Current boundary on 7 May 1984 is also shown and was used when designing the probe release pattern.

The design goal was to establish a series of transects which cross the entire Loop Current approximately normal to the local frontal boundary. The across-transect station spacing varied from 10 to 30 nautical miles, depending on proximity to an expected frontal position. Away from fronts 20 and 30 nmi spacing was used. AXCP's were released along two transects:

- Through a cold pool and across the base of the Loop Current - (Section 1).
- Along the transect adjacent to subsurface mooring locations - (Section 2).

Section 1 consisted of alternating AXBT's and AXCP's at 10-nmi separation. Since AXCP's also provide temperature this produced 10-nmi spaced temperature profiles and 20-nmi velocity profiles. On Section 2 AXCP's were released adjacent to deep current meter moorings and inside of the expected eastern and western Loop Current front. Maximum currents were expected in this region.

AXBT's provided temperature information to 760 m. AXCP's had a normal profile depth of 1600 m but most went only to 1100 or 1500-m depth.

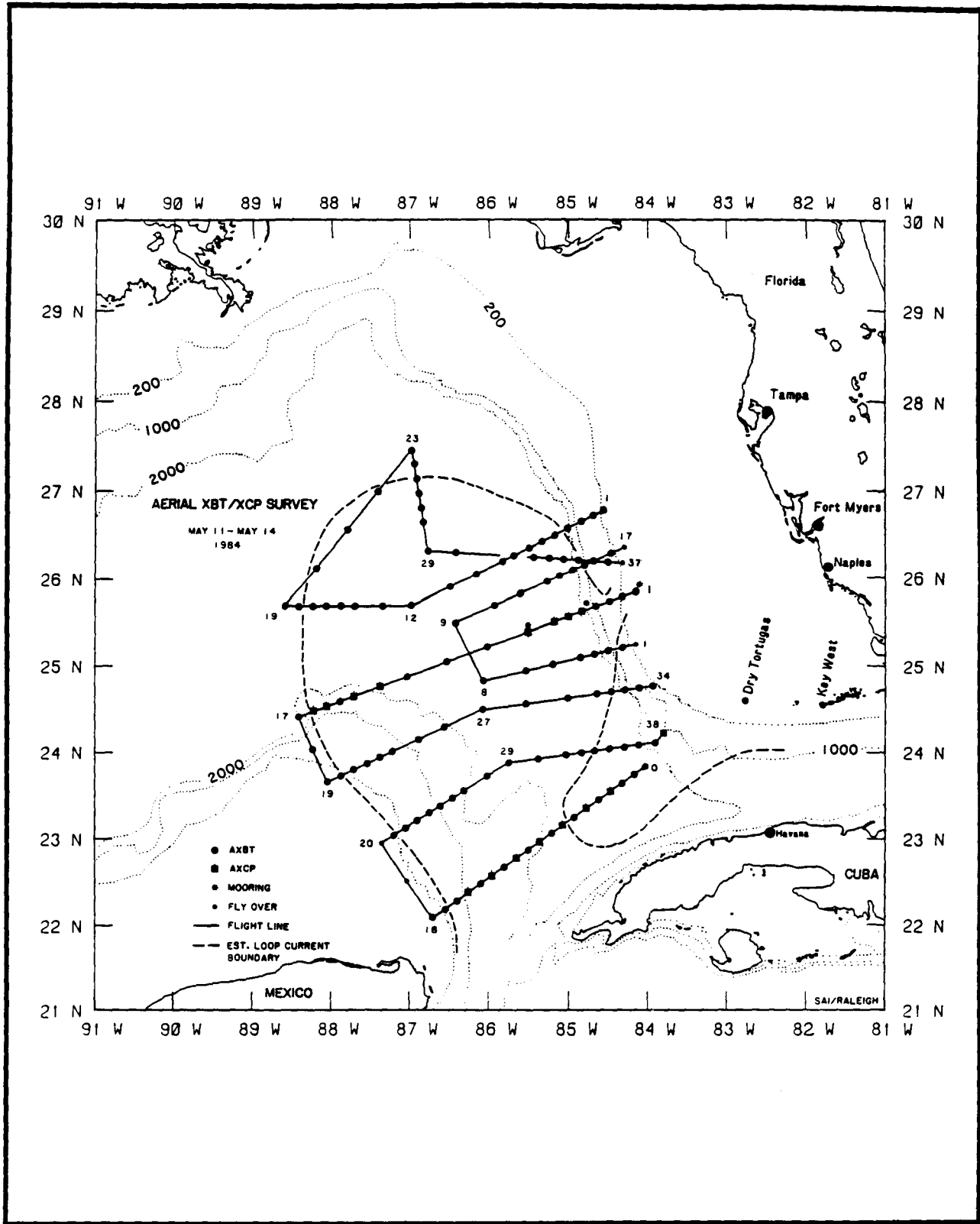


Figure 2.4-8. Location of AXBT/AXCP drops during the May 1984 hydrographic survey. Note that current profilers were dropped along two transects which extended across the entire Loop Current.

Seventeen AXCP's and 112 AXBT's were used. Two AXCP's failed and several others provided only partial profiles. Two AXBT's did not function properly. With the equipment on board the plane, probe function was evaluated in real time. Any station at which a malfunctioning AXBT was dropped was immediately reseeded. For AXCP's this was only done if the recalcitrant probe was released at a few key stations, e.g. adjacent to a current meter mooring. The scheme provided an excellent synoptic characterization of the Loop Current temperature field and selected features of the velocity field.

The plane and on-board equipment and personnel were obtained from Aero Marine Surveys (AMS). When AXCP's were released on two of the four daily flights, Horizon Marine also had a technician and back-up analogue recorders which received data on the AXCP channel. The plane and equipment provided by AMS had completely redundant positioning (aerial LORAN-C) receiving and recording capability specifically configured for aerial, expendable probe surveys.

2.4.5.2 Field procedures

Using the Loop Current frontal map from 7 May 1984, a series of possible sampling schemes were evaluated and the final pattern shown in Figure 2.4-8 was selected. Prior to each daily flight the pilot and two on-board operators were provided with:

- station identification numbers
- latitude and longitude of each station
- type and frequency of the probe to be deployed at each station
- the direction and distance between successive stations.

This was used by the pilot to fly the proposed route and by the on-board personnel to assure that the correct probes were dropped at the selected location. All flights originated in Naples, Florida. Data from each profile were sent from the water surface to the plane by radio link over one of three available channels (12, 14, 16), all of which could be received and recorded simultaneously. The observational information is contained in the modulation of the carrier frequency. Assigning a radio channel to a given station depended on consideration of station spacing, groundspeed of the plane, distance from the prior station and time required for completion of transmission from previously and subsequently released probes. If position, timing and channel selection were not proper, proximate data links could be broadcasting simultaneously on the same channel (i.e. "on top" of one another) which ruins data from both profiles.

Under these constraints and not knowing in advance the Loop Current geometry, it was guesswork ordering well in advance the number of probes needed in each transmission frequency channel. Also, the AXCP's all broadcast in the same channel.

The final flight pattern and sample spacing were in part guided by the real constraints of avoiding transmission overlap while using probes on hand.

Prior to each flight, the daily station and probe frequency information was used by the ground support personnel to load and arrange probe cannisters in on-board racks in the reverse order of deployment, i.e. last loaded = first deployed. To accommodate limited redeployments, an additional small storage rack contained several back-up probes (generally one in each broadcast frequency). Because of space limitations and the channel sequencing necessary the order of probe release could not be altered once the flight began.

2.5 Subsurface Currents

2.5.1 Introduction

Measurements of subsurface current/temperature/pressure are pivotal to the goals and success of this field program. The experimental design involved placing sensors at specific water depths on an array of tautline moorings which emphasized the outer-shelf, shelf-break and slope. Instruments were distributed vertically to provide appropriate documentation of the three-dimensional circulation. The program has been fortunate to have relatively few instrument losses considering the two-year deployment duration and the shelf location. Except as resulting from defects in new equipment, there was relatively little data loss. As a result, the program has available to it a data base which is providing valuable and fundamental insights to circulation patterns and processes on and adjacent to the west Florida shelf.

2.5.2 Mooring Locations

Current meter data were collected in two general areas during this study. The major effort was on the west Florida shelf where six moorings were deployed. A seventh mooring was deployed on the Louisiana shelf. The west Florida shelf moorings ranged in depth from 50 to 3275 m (Figure 2.5-1). Here, the isobaths trend NNW to SSE along a broad flat shelf that slopes steeply seaward beginning around 350 m. Five of the moorings were deployed along a line across the shelf near 26°N angling slightly to the WSW and the sixth was deployed some 90 nautical miles (167 km) to the north on the 180-m isobath.

The Louisiana shelf mooring was deployed in 81 m of water immediately south of Conoco's platform SP-55A where the isobaths trend ENE to WSW and the bottom slopes steeply seaward. This site is located approximately one-third of the way from Southwest Pass to South Pass and slightly offshore of a line drawn between the mouths of the two passes. The proximity to the platform prevented interference with the instrumentation by shrimp trawlers. All mooring locations are presented in Table 2.5-1.

2.5.3 Mooring Design

Mooring design involved a process of successive iterations. The first step consisted of defining representative vertical current profiles likely to prevail at the sites. This task required a review of existing literature relevant to the area of interest and of data sets actually collected at the sites, in their near vicinity, or in dynamically similar environments. These data were then entered as inputs to SAIC's taut-wire mooring design computer program, a variation of that originally developed by WHOI (Moller, 1976). The second step consisted of defining a theoretical mooring configuration suitable

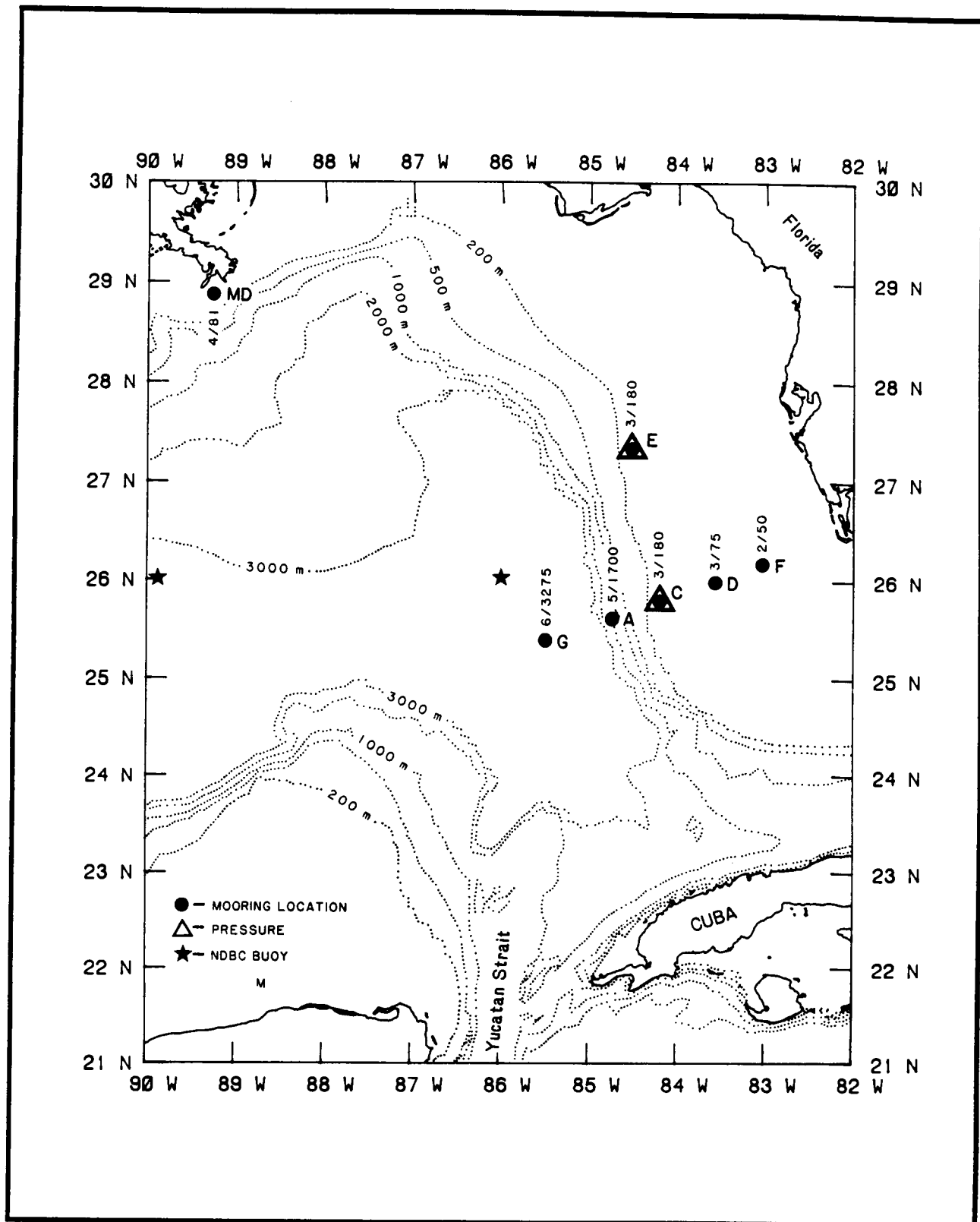


Figure 2.5-1. Location of moorings deployed in the eastern Gulf for years 1 and 2 of the MMS sponsored Gulf of Mexico Physical Oceanography Study. Numbers represent number of current meters and depth.

Table 2.5-1. Mooring locations in the eastern Gulf for years 1 and 2 of the MMS sponsored Gulf of Mexico Physical Oceanography Study.

Mooring	Location		Depth(m)	Nominal Instrument Depths (m)
	Latitude	Longitude		
A	25°42.9'N	84°53.1'W	1697	172, 400, 738, 1100, 1600
C	25°53.2'N	84°19.2'W	180	50, 100, 179
D(DA)	26°05.5'N	83°41.9'W	75	30, 60 (17, 50, 71)
E	27°25.2'N	84°37.5'W	180	50, 100, 179
F	26°14.5'N	83°13.3'W	50	17, 40
G	25°36.2'N	85°29.8'W	3200	177, 397, 703, 1565, 2364, 3174
*MD	28°51.9'N	89°16.8'W	81	13, 25, 45, 70

* Changed to DM and DMM on subsequent deployments.

for the environment in which it would be deployed, based on the experience of the design team.

In the third step, the adequacy of the mooring design defined in step two was checked by running the computer program. It calculated the deflection of the current meter array, the tensile load, the reserve buoyancy and the elevation of every mooring element when submitted to the current profile defined in step 1.

When some criteria (e.g. maximum allowable inclination) were violated, the mooring configuration was modified (step two), and step three repeated until the final configuration was such that the criteria on instrument inclination, reserve buoyancy, and tensile loads were all met for the input current profiles selected in step one.

The following additional design criteria were also met:

- (1) The inclination angle of each current meter mooring segment was not to exceed 25° from the vertical.
- (2) All instruments were shackled to glass or steel flotation sufficient to raise the instruments and associated hardware in the event of a mooring failure at any location along the mooring line.
- (3) Insofar as possible, galvanized steel was used in the mooring components. Where not possible, dissimilar materials were isolated from one another.
- (4) Acoustically actuated release devices were used to detach the anchor from the rest of the mooring system in order to recover the instruments. Paired acoustic release mechanisms were employed on the deep (> 200 m) moorings.
- (5) The weight of the anchor was designed to insure that the mooring would drag before the mooring wire would be subjected to a strain near its elastic limit.

2.5.4 Current Meters

Three types of current meters were used: the General Oceanics Model 6011 Niskin Winged Current Meter which was used on all of the moorings, the Florida State University modified Geodyne Type 101 current meter which was used near bottom on three of the west Florida shelf moorings, and the ENDECO Type 174 current meter which was used on the Louisiana shelf. A comprehensive description of each follows.

2.5.4.1 General Oceanics Niskin Winged Current Meter

The Niskin Winged Current Meter (NWCM) Model 6011-T is a solid state recording meter with no external moving parts. The meter is attached with a swivel on a mooring standoff and hangs vertically in the absence of a current. In the presence of a current, the instrument is tilted downstream. The angle of tilt varies with the speed of the current. The greater the current, the greater the angle of tilt. Operation of the instrument is unaffected by mooring tilt.

The instrument is fitted with a wing-like structure which stabilizes and orients the instrument in the direction of current flow. The housing contains a tilt sensor (a force balanced inclinometer), three orthogonally mounted Hall effect sensors for compass direction, and a thermistor for temperature.

During the mooring period, signals from the sensors are digitized and placed in a 64-bit parallel-in/serial-out shift register together with an associated time code and instrument serial number. The information is then shifted serially and recorded in serial form on a Phillip style magnetic tape cassette. The sampling rate is user selected, and a burst sampling option helps suppress observational noise.

The cassette is read and input directly to a computer where current velocity is calculated directly from tilt by converting tilt angle to current speed, using an experimentally determined calibration curve. The three vector components of the earth's magnetic field provided by the Hall effect sensors are combined in an appropriate equation to produce magnetic headings.

The results are displayed on strip charts and/or transcribed to a 9-track magnetic tape for further processing. Specifications for the MK1 model of this instrument are presented in Table 2.5-2. The MK2 version is similar except that it has an improved time reference accuracy ($\pm 0.1 \text{ secday}^{-1}$), vector averaging of burst samples, and conductivity and pressure options.

2.5.4.2 Florida State University Current Meter

The Florida State University (FSU) current meter is fabricated locally from a Geodyne Type 101 current meter. The internal electronics package has been replaced using modern, low-current drain circuitry available from Sea Data Corp. The magnetic tape recorder is the standard Sea Data unit.

The current speed and direction are determined by a vane and Savonius rotor. Burst sampling is used, in which a compass and vane reading are made many times per minute, and the rotor turns are counted during each small increment. The recording interval is programmable, but a reasonable trade-off is reached at about 2.5 seconds. This interval is used because the rotor does not respond well to higher frequencies. The number of one-minute increments per hour used in the burst sampling is programmable also. The instrument is equipped with a Parascientific Digiquartz pressure gauge.

2.5.4.3 ENDECO Type 174 Current Meter

The ENDECO TYPE 174 digital recording current meter is a self-contained magnetic-tape recording meter that measures current speed and direction, and water temperature and conductivity. It is an axial-flow, ducted-impeller meter that is trimmed for neutral buoyancy, and connected to the mooring wire by a slack tether assembly. Full 360° swivel rotation is provided by a "Cook Clamp" connection to a bushing on the mooring wire. Sampling intervals from two to ten minutes for deployment periods of 35 to 80 days respectively are possible. The instrument measures an average speed over the sampling interval. Specifications for the Type 174 instrument are presented in Table 2.5-3.

Table 2.5-2. Specifications for General Oceanics, Inc. Model 6011-T
(MK1) Niskin Winged Current Meter.

Current Speed:	Sensor: Housing tilt Threshold: 2 cm s ⁻¹ Maximum: 300 cm s ⁻¹
Current Direction:	Compass: 3 Hall generation; resolution 1°, accuracy ± 2°
Temperature:	Yellow Springs aged linear thermistor; resolution ± 1/64°C, accuracy ± .25°C
Time Reference:	Solid state crystal oscillator; accuracy ± 10 sec/day
Sampling Interval:	10 position switch selects from 1 to 512 readings per hour. At 8 readings/hour unit can operate for 89 days. At 4 readings/hour unit can operate for 177 days.
Burst Sampling:	4, 8, 16, 32 readings per burst at intervals of 1.3, 2.6, 5.3 and 10.6 seconds
Data Storage:	Tape Recorder: Digital Capacity: 19,000 readings
Battery Life:	12 months
Mechanical:	Pressure Housing: 51.3 mm long x 10.5 mm diameter 7075-T6 aluminum, hard coat anodized 6000 meter operating depth
Weight:	20 lbs in air, 10.7 lbs in water
Corrosion protection:	Zinc Anode

Table 2.5-3. Specifications for ENDECO Type 174 digital magnetic tape recording tethered current meter.

Current Speed:	Sensitivity: 50.1 rpm/51.4 cm/sec (50.1 rmp/knot) Speed Range: Dependent on sampling interval (user selectable), 0-257.2 cm/sec (0-5.0 knots) at standard 2 min interval.
Current Direction:	Magnetic Direction: 0-360° Resolution: 1.4° Accuracy: $\pm 7.2^\circ$ above 2.57 cm/sec (0.05 knot)
Temperature:	Range: -5° to $+45^\circ\text{C}$ (23° to 113°F) Resolution: 0.098°C (0.216°F) Accuracy: $\pm 0.2^\circ\text{C}$ (0.4°F)
Conductivity:	Range 5 to 55 mmhos/cm Resolution: 0.098 mmhos/cm Accuracy: ± 0.55 mmhos/cm
Depth:	Various sensor types available to meet application requirements
Sampling Interval:	Rate: one reading of 4 parameters every 2 min. (other rates available) Period: 35 days at standard interval

2.5.5 Deployment Period and Data Return

In January 1983 five moorings (A, B, C, D and E) were deployed on the west Florida shelf and slope in depths of 1700, 600, 180, 75 and 180 m respectively. During the first six-month rotation in July 1983 it was discovered that Mooring B had been destroyed by long-line fishing activity and that the two current meters were lost. This mooring was later replaced by a deeper mooring, Mooring G (3275 m), in February 1984. Also in February, the configuration of Mooring D was changed to that of Mooring DA and an additional mooring (Mooring F) was deployed further up on the shelf in 50-m depth. It was at this time that measurements were also begun on the Louisiana shelf with Mooring MD in 81-m depth.

A time line of the deployment periods and data return for each current meter level is presented in Figure 2.5-2 and the type of instrument used for each period is indicated in Table 2.5-4. The percent data return for each of these levels by parameter (current and temperature, and pressure when applicable) is summarized in Table 2.5-5. The overall data return for the two year period was 81%. This percentage was substantially degraded by the poor performance of the MK2 version of the General Oceanics, Inc. Niskin winged current meter when first deployed at all levels of Mooring A for February through October 1984. Some data loss was also realized during the first deployment of Mooring MD when three of the ENDECO Type 174 instruments flooded through their conductivity sensors.

2.5.6 Texas Shelf Near-bottom Currents

Near-bottom currents on the South Texas continental shelf were monitored during 145 days in the summer, fall and early winter of 1984 on the south Texas continental shelf (STOCS) in hopes of characterizing some of the near-bottom current patterns.

The data were collected by five ENDECO TYPE 105 current meters located 1 to 2 meters above the bottom in 12-, 18-, 34-, 74-, and 140-m depth water (Figure 2.5-3, Table 2.5-6). The instrument used is an axial flow ducted impeller device similar to the TYPE 174 instrument discussed earlier. However, it records the current speed and direction on 16 mm film every 30 minutes at the speed range selected as opposed to a magnetic tape. According to the manufacturer, the device has an accuracy of $\pm 2.5 \text{ cm s}^{-1}$ and 7° of direction.

The current meters were attached to free-standing taut line moorings. At 74 and 140 m the arrays included an acoustic release (Figure 2.5-4). At the shallower locations (12, 18, and 34 m) the arrays were diver deployed and retrieved (Figure 2.5-5). The shallow arrays were located next to oil rigs to avoid interference due to shrimping activity. In all cases, the current meters were mounted some 1.5 m above the bottom. Measurements of deep water wave height and period were recorded hourly by NODC Buoy 42002. Wind speed and direction were measured hourly at Horace Caldwell Pier, Port Aransas, Texas. The data were made available by Dr. David Gilhousen.

Table 2.5-7 shows the deployment histories for the current meters. Current meter C (34 m) was pulled up by a shrimp boat on or about 20 August 1984. It was redeployed on 23 August near a production platform at location C', also at 34-m depth. Current meter D (74 m) was grabbed by a shrimper's nets around 26

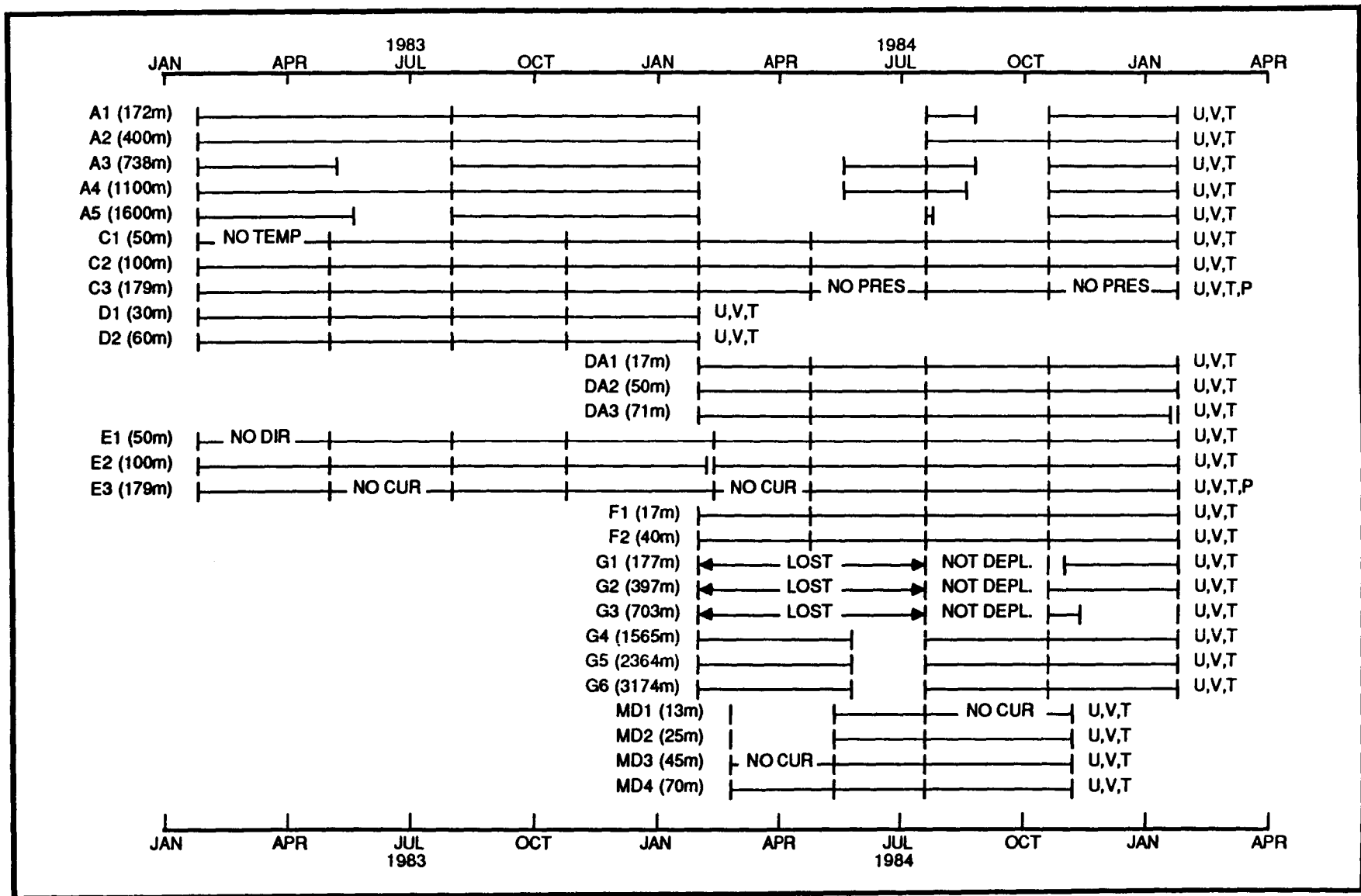


Figure 2.5-2. Time line of the deployment periods and data return for each current meter level for instruments deployed in the eastern Gulf for years 1 and 2 of the MMS sponsored Gulf of Mexico Physical Oceanography Study.

METER ID (DEPTH)	DEPLOYMENT PERIOD AND INSTR. TYPE										
	1	2	3	4	5	6	7	8			
A1 (172m)	MK1		MK1		MK2		MK2	MK2			
A2 (400m)	MK1		MK1		MK2		MK2	MK1			
A3 (738m)	MK1		MK1		MK2		MK2	MK1			
A4 (1100m)	MK1		MK1		MK2		MK2	MK1			
A5 (1600m)	MK1		MK1		MK2		MK2	MK2			
C1 (50m)	MK1	MK1	MK1	MK1	MK1	MK1	MK1	MK1			
C2 (100m)	MK1	MK1	MK1	MK1	MK1	MK1	MK1	MK1			
C3 (179m)	FSU	FSU	FSU	FSU	FSU	FSU	FSU	FSU			
D1 (30m)	MK1	MK1	MK1	MK1							
D2 (60m)	MK1	MK1	MK1	MK1							
DA1 (17m)					MK1	MK1	MK1	MK1			
DA2 (50m)					MK1	MK1	MK1	MK1			
DA3 (71m)					FSU	FSU	FSU	FSU			
E1 (50m)	MK1	MK1	MK1	MK1	MK1	MK1	MK1	MK1			
E2 (100m)	MK1	MK1	MK1	MK1	MK1	MK1	MK1	MK1			
E3 (179m)	FSU	FSU	FSU	FSU	FSU	FSU	FSU	FSU			
F1 (17m)					MK1	MK1	MK1	MK1			
F2 (40m)					MK1	MK1	MK1	MK1			
G1 (177m)					MK1						MK2
G2 (397m)					MK1						MK1
G3 (703m)					MK1						MK2
G4 (1565m)					MK1				MK1	MK1	MK1
G5 (2364m)					MK1				MK1	MK1	MK1
G6 (3174m)					MK1				MK1	MK1	MK1
MD1 (13m)									174	174	MK2
MD2 (25m)									174	174	MK2
MD3 (45m)					174	174	MK2				
MD4 (70m)					174	174	MK2				

WEST FLORIDA SHELF

PERIOD 1 : 1/26/83 - 4/30/83
 PERIOD 2 : 4/30/83 - 7/31/83
 PERIOD 3 : 7/31/83 - 10/23/83
 PERIOD 4 : 10/23/83 - 2/3/84
 PERIOD 5 : 2/3/84 - 4/26/84
 PERIOD 6 : 4/26/84 - 7/19/84
 PERIOD 7 : 7/19/84 - 10/19/84
 PERIOD 8 : 10/19/84 - 1/25/85

LOUISIANA SHELF (MOORING MD)

PERIOD 5 : 2/23/84 - 5/10/84
 PERIOD 6 : 5/10/84 - 7/27/84
 PERIOD 7 : 7/27/84 - 11/8/84

Table 2.5-4. Deployment periods and instrument types for each current meter level for moorings in the eastern Gulf for the period from 26 January 1983 through 25 January 1985.

DATA RETURN			
INSTRUMENT	CURRENTS	TEMPERATURE	PRESSURE
A1 (172m)	70%	70%	
A2 (400m)	77%	77%	
A3 (738m)	66%	66%	
A4 (1100m)	76%	76%	
A5 (1600m)	56%	56%	
C1 (50m)	100%	87%	
C2 (100m)	100%	100%	
C3 (179m)	100%	100%	75%
D1 (30m)	100%	100%	
D2 (60m)	100%	100%	
DA1 (17m)	100%	100%	
DA2 (50m)	100%	100%	
DA3 (71m)	100%	100%	
E1 (50m)	*100%	100%	
E2 (100m)	100%	100%	
E3 (179m)	78%	100%	100%
F1 (17m)	100%	100%	
F2 (40m)	100%	100%	
G1 (177m)	**34%	**34%	
G2 (397m)	**37%	**37%	
G3 (704m)	**11%	**11%	
G4 (1565m)	84%	84%	
G5 (2364m)	85%	85%	
G6 (3174m)	84%	84%	
MD1 (13m)	30%	70%	
MD2 (25m)	60%	60%	
MD3 (45m)	70%	100%	
MD4 (70m)	96%	96%	

*Speed only for first deployment.

**Excludes not-deployed period from 18 July to 18 October 1984, but does include instrument loss during prior deployment.

Table 2.5-5. Data return for moorings in the eastern Gulf for the period from 26 January 1983 through 25 January 1985.

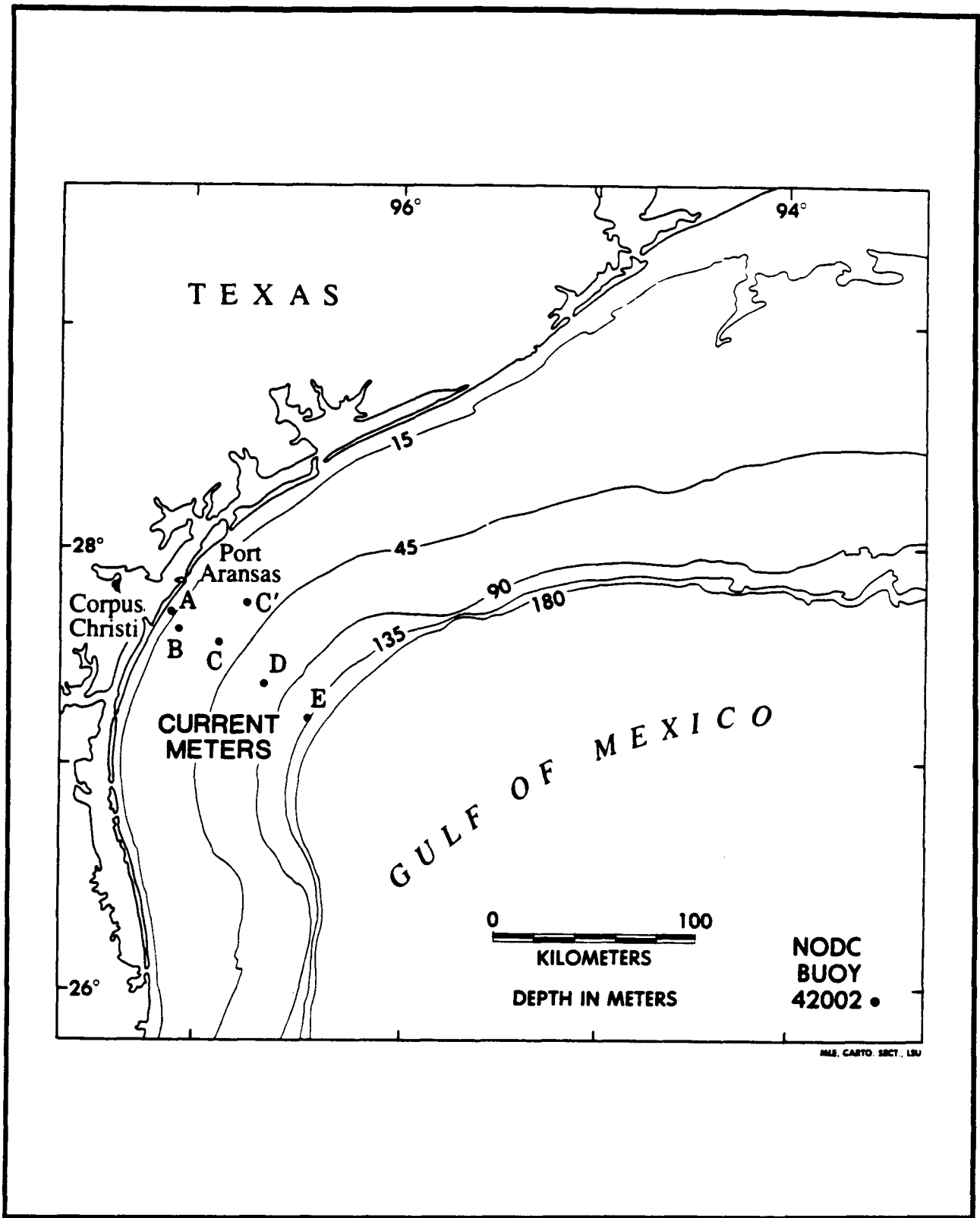


Figure 2.5-3. Location of current meters and NODC buoy 42002.

Table 2.5-6. Current meter locations in the western Gulf on the south Texas continental shelf.

Current Meter	Location		Water Depth(m)
	Latitude	Longitude	
A	27°42.52'N	97°06.20'W	12
B	27°37.81'N	97°04.12'W	18
C	27°32.90'N	96°52.70'W	34
C'	27°43.97'N	96°42.78'W	34
D	27°22.40'N	96°35.30'W	74
E	27°12.18'N	96°23.61'W	140

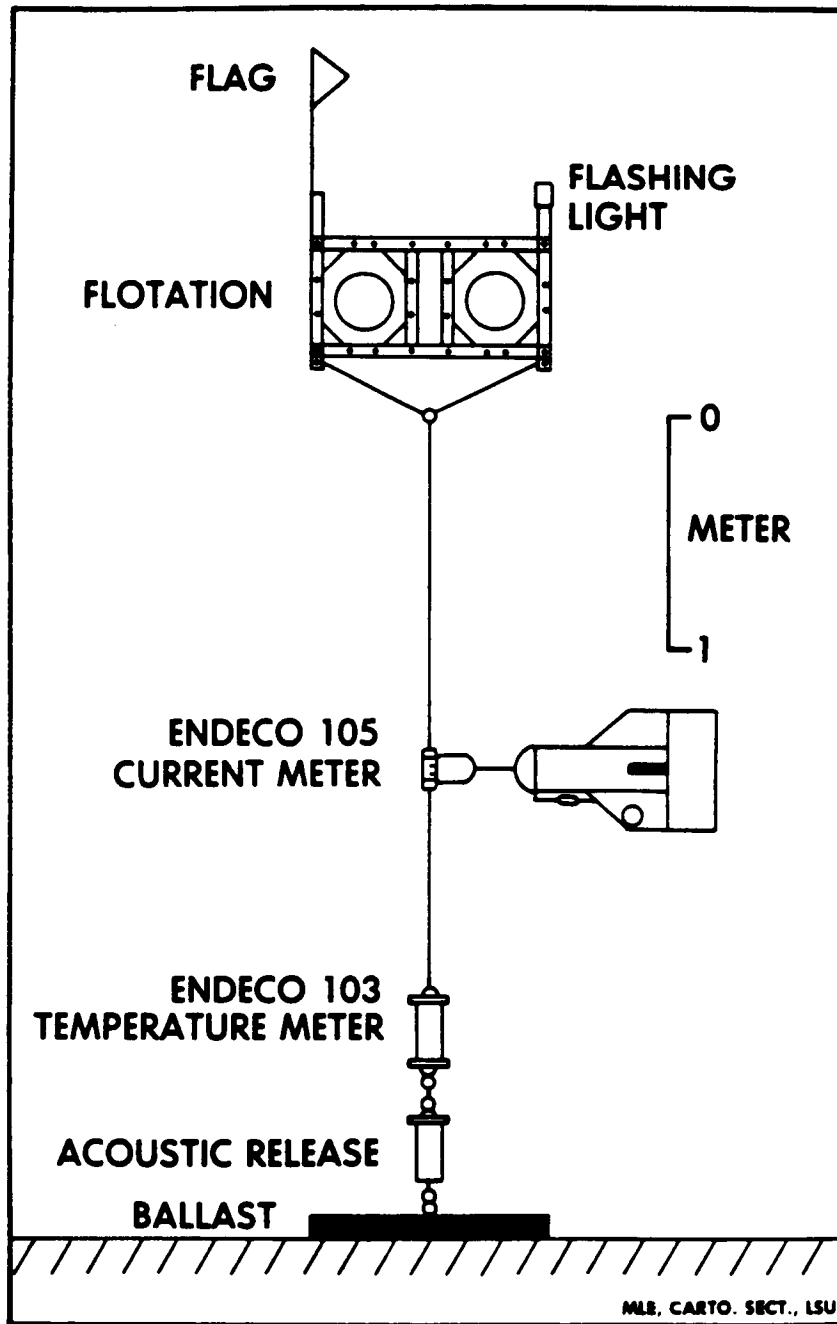


Figure 2.5-4. Schematic diagram of deepwater (74, 140 m) arrays. ENDECO 103 temperature meter was not used during this study.

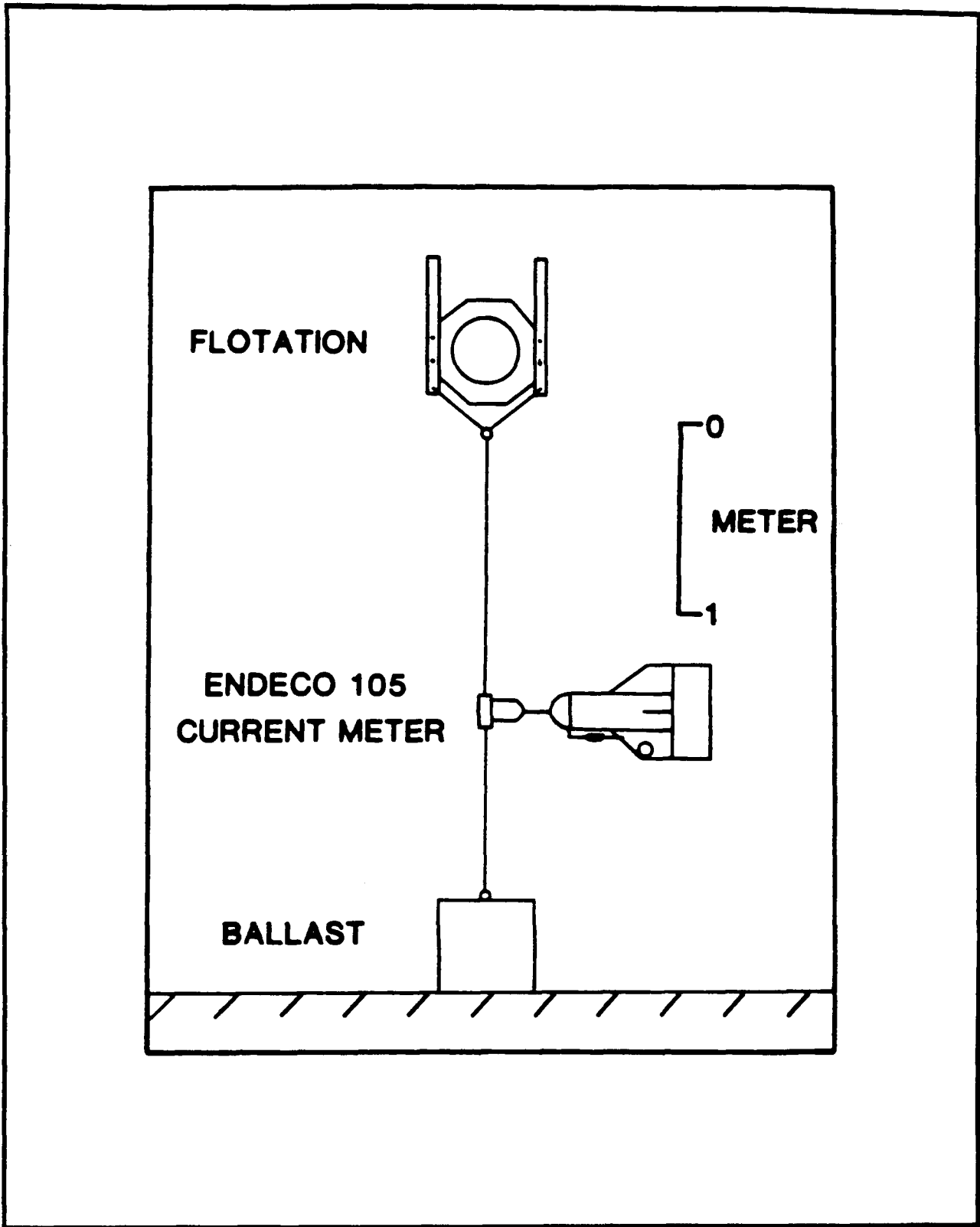


Figure 2.5-5. Schematic diagram of shallow water (12, 18 and 34 m) arrays.

Table 2.5-7. Texas shelf current meter deployment histories.

Current Meter	Start	Finish
A	1000 July 18, 1984	1300 Oct. 2, 1984
B	1030 July 18, 1984	2200 Sept. 27, 1984
C	1600 July 17, 1984	0600 Aug. 20, 1984
C'	1200 Aug. 23, 1984	0800 Dec. 9, 1984
D	1400 July 17, 1984	1300 Sept. 26, 1984
E	1000 July 17, 1984	1700 Nov. 5, 1984
E*	1900 Nov. 9, 1984	0000 Dec. 13, 1984

* Made available by A. Amos of UTMSI

September and was not redeployed due to extensive damage to the acoustic release.

Current meters A and B (12 and 18 m) were set for 30-minute interval recording intervals and ran out of film near the end of September. Current meter E (140 m) was retrieved on 5 November. It was later redeployed as part of another project.

2.6 Ships-of-Opportunity

2.6.1 Introduction

As part of the field effort in the Gulf of Mexico, MMS sought out merchant and research vessels passing through the Gulf which were willing to deploy XBT's while under way. One company, Coordinated Caribbean Transport, Inc. (CCT) operating out of New Orleans, Louisiana, made vessels along one of its routes available for such activities. Data collection along a track between New Orleans and the Yucatan Straits began in May 1983 and is continuing. Other vessels (primarily research vessels) periodically were provided with and dropped XBT's to support the measurement program. The NMFS/MMS provided data from the E. M. QUEENY Ship-of-Opportunity (SOOP) cruises which dropped XBT's in an east-west direction running from approximately 83.5°W to 90.0°W. This track is also continuing. Tables 2.6-1 and 2.6-2 summarize these data sets.

2.6.2 Equipment

To implement the MMS/CCT SOOP track a Sippican MK-9 XBT digitizer and an HP-85B mini-computer were installed on the SOOP vessel. In addition an LM-3A handheld launcher was provided for the deployments. T-7 (760m) XBT probes and HP-85 data cartridges were routinely replaced following each cruise. The data obtained from the E. M. QUEENY were initially received as graphs from a Sippican MK2 recorder and were later received as digitized tapes similar to those obtained from the CCT vessel. Data obtained from the NMFS/MMS vessel were primarily on data cartridges collected with a Bathy Systems SA-810 digitizer similar to the MK-9 system, though some graph plots were obtained as well.

2.6.3 SOOP Sections and Data Products

Examples of the two main SOOP sections are presented in Figure 2.6-1. Data from these sections and others that became available (Tables 2.6-1 and 2.6-2) were routinely processed, generating vertical section plots and a surface temperature plot along the cruise track. In addition, many of the E. M. QUEENY surface section plots also included salinity. Examples of these data products are provided in Figure 2.6-2. Additional vertical temperature plots of the upper 200 m only were also generated for each section. Note that the E. M. QUEENY data has been archived and plotted for data sets beginning as early as February 1981.

Table 2.6-1. MMS and NMFS/MMS Ship-of-Opportunity sections through 25 January 1985.

Section	Ship	Dates	No. Trips
*I	OYSTER BAY	5/1/83 - 5/16/83	2
I	LION HEART	6/21/83 - 6/23/83	1
I	NORDIC WASA	8/31/83 - 4/10/84	17
I	NESTOR I	5/2/84 - ongoing	18
**II	E. M. QUEENY	2/14/81 - ongoing	50

* MMS section from New Orleans to the Yucatan Straits.

** NMFS/MMS section from 27.0°N 90.0°W to 24.5°N 83.5°W.

Table 2.6-2. Additional MMS Ship-of-Opportunity data sets through
25 January 1985.

Ship (Program)	Dates	Cruise ID
BELLOWS	3/24/83 - 3/25/83	B8304
BELLOWS	4/4/83 - 4/6/83	B8306
BELLOWS	4/22/83 - 4/27/83	B8309
BELLOWS	1/24/84 - 1/25/84	B8408
BELLOWS	2/26/84 - 2/26/84	B8401
BELLOWS	4/25/84 - 4/29/84	B8405
BELLOWS	5/7/84 - 5/12/84	B8406
GYRE	4/21/84 - 4/25/84	GYRE84G4II
GYRE	5/2/84 - 5/12/84	GYRE84G5
JUNE BOLLINGER	7/21/83 - 7/23/83	JB01
OREGON II	8/2/83 - 8/23/83	ORII 136
OREGON II	10/12/83 - 10/19/83	ORII 138
OREGON II	12/8/83 - 12/21/83	ORII 140
PRIME IV	11/8/83 - 11/20/83	PRIME IV
RESEARCHER	3/12/84 - 3/14/83	RE01
ROME IV	8/18/82 - 8/27/82	ROME IV 550146
ROME IV	9/19/82 - 9/23/82	ROME IV 550147
SEAMAP	4/23/83 - 5/23/83	MS01
SUNCOASTER	2/19/83 - 2/19/83	SC8301
SUNCOASTER	3/16/84 - 3/19/84	SC8404
SUNCOASTER	3/25/84 - 3/26/84	SC8405
YUCA I	5/31/84 - 6/6/84	YUCA 18401

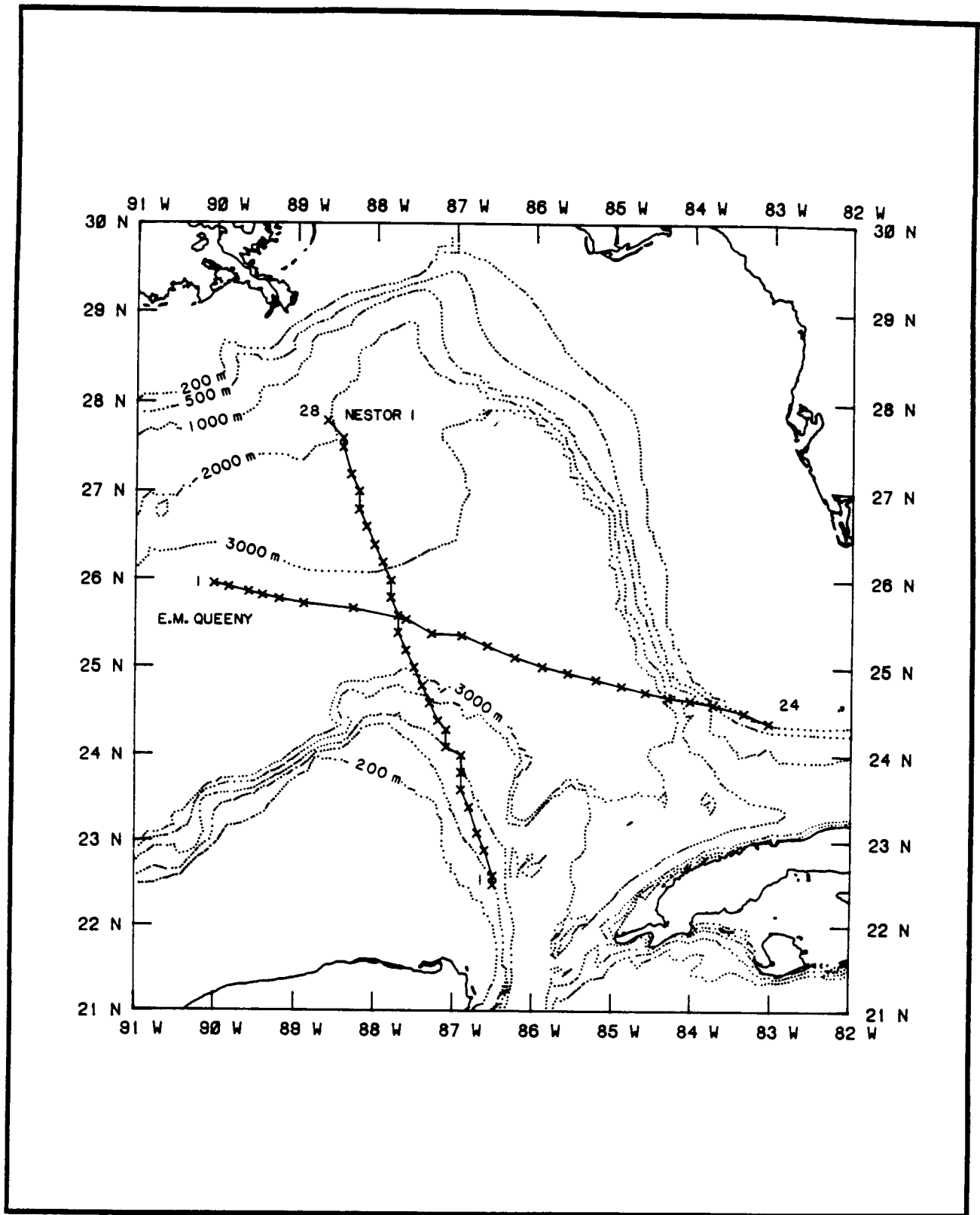


Figure 2.6-1. Examples of the cruise tracks for the repeated MMS and the NMFS/MMS Ship-of-Opportunity sections in the eastern Gulf.

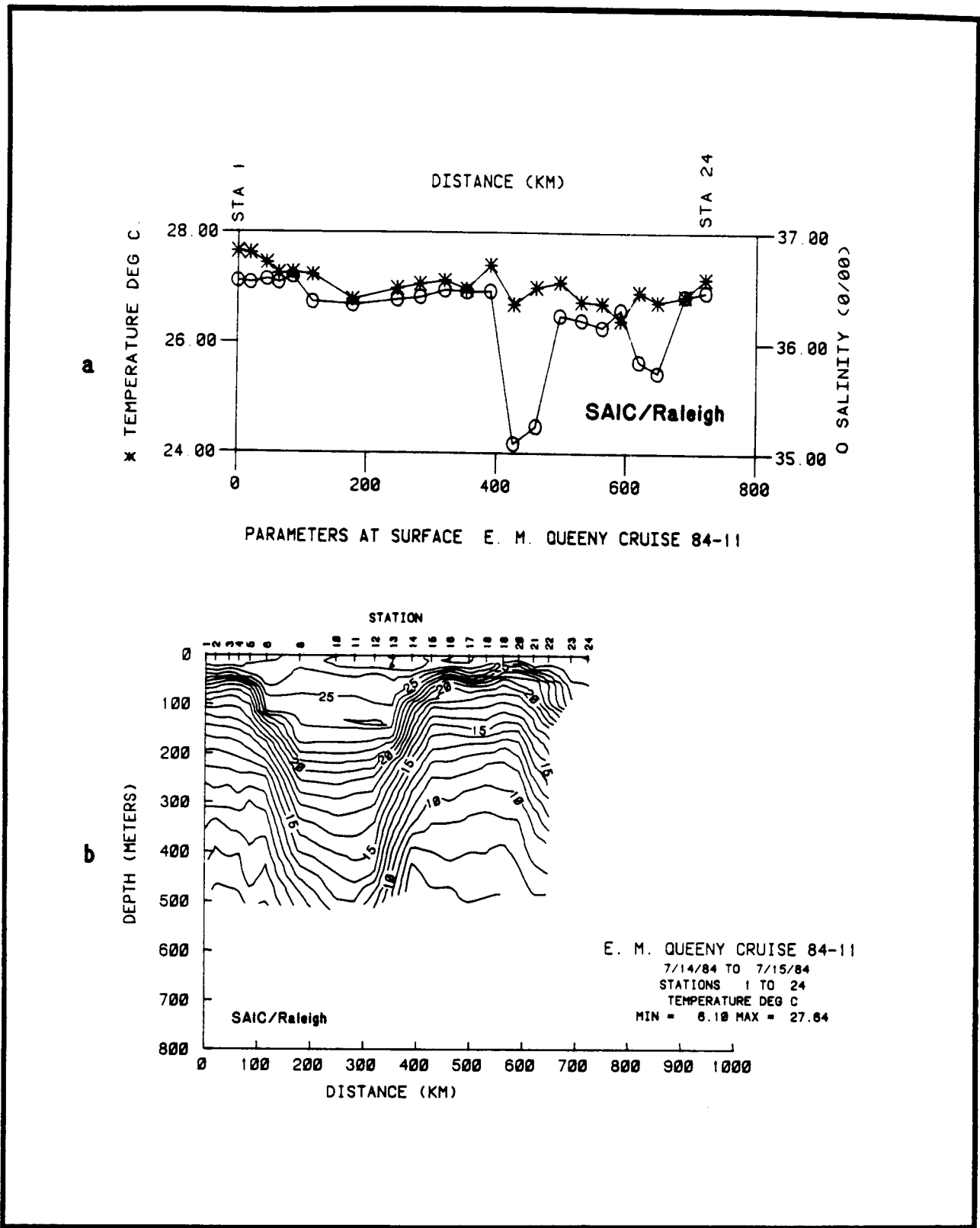


Figure 2.6-2. Examples of data products generated for each SOOP cruise: (a) surface parameters (b) vertical temperature.

2.7 References for Chapter 2

- Elliot, B. A., 1979. Anticyclonic rings and the energetics of the circulation of the Gulf of Mexico. Ph.D. dissertation, Texas A&M Univ., College Station, TX.
- Kirwan, A. D., Jr., W. J. Merrell, Jr., J. K. Lewis, and R. E. Whitacker, 1984a. Lagrangian observations of an anticyclonic ring in the western Gulf of Mexico. *J. Geophys. Res.* 89(C3): 3517-3424.
- Kirwan, A. D., Jr., W. J. Merrell, Jr., J. K. Lewis, R. E. Witaker, and R. Legeckis, 1984b. A model for the analysis of drifter data with an application to a warm core ring in the Gulf of Mexico. *J. Geophys. Res.* 89(C3): 3425-3438.
- Moller, Donald A., 1976. A computer program for the design and static analysis of single point subsurface mooring systems: NOYFB. Woods Hole Oceanographic Institution, Tech. Rep. 76-1.
- Strickland, J. D. H. and T. R. Parsons, 1972. *A Practical Handbook of Seawater Analysis*. Fisheries Research Board of Canada, Ottawa. 310 pp.
- Strong, A. E. and E. P. McClain, 1984. Improved ocean surface temperatures - comparison with drifting buoys. *Bull. Am. Metro. Society.* 65(2): 138-142.
- Vukovich, Fred M., 1983. An analysis of ground temperature and reflectivity patterns about St. Louis, Mo., using HCMM satellite data. *J. Climate and Appl. Meteorol.* 22(4): 560-571.
- Yentsch, C. and D. W. Menzel, 1963. A method for the determination of phytoplankton, chlorophyll, and phaeophytin by fluorescence. *Deep-Sea Res.* 10:221-231.

III. DATA ANALYSIS

3.1 Introduction

Chapter 3 presents a general description of analytical and numerical techniques used on the program data sets. This material is meant to provide the reader with a general appreciation of the various procedures and where needed to acquaint the reader with presentation or graphical formats. The chapter is organized so as to be internally consistent with the general order of presentation in Chapters 2 and 4.

3.2 Lagrangian Drifters

3.2.1 Introduction

The study of the ocean drifter data from rings consists of a consideration of water temperature data with respect to the ring's vertical structure and horizontal movement, a kinematic analysis which breaks the movement of the ring into the basic modes of motion, and a dynamic analysis which considers force balances in terms of angular momentum. These components will be introduced in this section and the results of the analyses described in the following sections.

3.2.1.1 Water Temperature Data Analysis

A number of water temperature data sets were considered in terms of ring structure and motion. The initial structure of some of the rings was determined using XBT data from Ship-of-Opportunity cruises and a buoy seeding cruise. Sea-surface temperature patterns were studied along with the corresponding buoy trajectories to gain insight into processes governing the ring motion. In addition, thermistor chain data from the buoy in Ring 3374 were studied. Unfortunately, these data were from the top 200 m of the water column, and seasonal cooling and heating of the water column appear to dominate the variations of the temperature. Moreover, several critical thermistors were lost during the latter part of the deployment (the 50-m, 75-m, and 100-m thermistors).

3.2.1.2 Kinematic Analysis

The kinematic analysis is based on the technique of Kirwan et al. (1984a) in which the motion of the ring (as seen by the drifter) is broken into the six basic modes of motion:

-
- U translation of the ring center,
-
- u swirl velocity of the water around the center of the ring,
- ζ vorticity (rotation rate),
- D divergence (area change),

- N normal deformation rate (due to forces acting normal to the ring boundary), and
- S shear deformation rate (due to forces acting parallel to the ring boundary).

In addition, the kinematic analysis uses N and S to calculate ellipticity of the ring plus the orientation of the ellipse in space. The goal of this study is to determine how the kinematic parameters vary in space and time and to relate these changes to various factors.

3.2.1.3 Dynamic Analysis

The last form of analysis is a dynamic analysis in terms of angular momentum balance. The time histories of the position of the ring center, ζ , and D are used to determine the left hand side of the following vertically-integrated vorticity equation:

$$(\zeta_T + f) + D_T(\zeta_T + f) = (-\text{curl}_z \tau + B) / H\rho \quad (3.2-1)$$

where ζ_T is total vorticity of the ring, f is the Coriolis parameter, and D_T is the total divergence of the ring. The right hand side of the equation represents the forces that would balance the expression, $\text{curl}_z \tau$ representing horizontal and vertical shearing forces, $B = \nabla \alpha \times \nabla P$ being the baroclinic torque with $\alpha =$ inverse of density ρ , $P =$ pressure, and H being the depth of the vertical integration. The goals of dynamic analysis are to determine what factors are the most important in the force balances of the rings and how the balance of terms varies in space and time.

3.2.1.4 Ring Kinematics

The trajectory data are the result of the influences of the anticyclones and other, higher frequency phenomena. Kirwan et al. (1984b) presented velocity energy spectra of ring 1599 which pointed out the sizeable effects of tides and basin-wide oscillations. To consider only ring kinematics following the lead of Kirwan et al., the trajectory data are filtered using a 100-h low-pass filter. These data are then used in the following analyses.

The ring parameters calculated using the drifter position data are vorticity ζ , divergence D, normal deformation rate N, and shear deformation rate S. These differential kinematic parameters (DKP) were determined: the translation velocity vector, U, of the ring center, the swirl velocity vector, u, of the ring, and position vector, X, of the drifter relative to the ring center. In addition, ring shapes and orientations were calculated to give X_{maj} , X_{min} , and A, which are the major axis length, the minor axis length, and the ellipse orientation, respectively. All calculations were based on the theory of Kirwan et al. (1984a) which gives the analytical solutions to the governing equations for drifter velocities. The calculations were made at six-h intervals with the assumption that the ring parameters were relatively constant over consecutive 18-h periods. However, the results indicated the presence of meteorological effects, so the DKP were smoothed using an

eight-day running average. These averages were then used to calculate the position vector X of the drifter, the translation velocity vector U of the ring center, and the swirl velocity vector u of the ring.

3.2.1.5 Ring Dynamics

Force balances were considered using the vertically-integrated vorticity equation

$$(\zeta_T + f) + D_T(\zeta_T + f) = (-\text{curl}_z \tau + B) / H\rho.$$

Two aspects of this expression should be pointed out. First, the total vorticity ζ_T and the total divergence D_T represent the sum of the vorticity ζ and divergence D relative to the ring center plus the vorticity ζ_C and divergence D_C of the ring center:

$$\zeta_T = \zeta + \zeta_C$$

$$D_T = D + D_C$$

The ring may be thought of as a spinning top with an axis of rotation which wobbles. Kinematic analysis provides information with respect to the center (axis) of rotation, but the total angular momentum of the ring includes any rotation (wobbling) of the ring center. Thus, ζ_C as well as D_C must be taken into consideration.

The second aspect of dynamic expression concerns the depth term H . The continuity equation that is vertically integrated over the entire water column yields

$$D = -H^{-1} dH/dt.$$

However, in this case, H is only the depth of the vertical integration. Since the ocean drifters were drogued by a 200-m line, calculated kinematic parameters represent some form of a 200-m average, which is the value of H .

3.3 Satellite Data Processing

3.3.1 Introduction

Real-time and post-processing techniques were used to process the satellite data for this program. Real-time processing can be divided into two parts: online processing and post processing. For online processing, the Automatic Picture Transmission (APT) and GOES IR satellite data were video-enhanced using an online computer called a Scanning Radiometer Data Manipulator (SRDM). The SRDM was applied to enhance the video contrast and the temperature range which defines the sea-surface temperature distribution.

If an important feature were detected in the initial imagery received by the RTI/SRS, the satellite data were transferred to the RTI image processing system where they were digitized for digital processing. The basic components of the RTI image processing system are a spatial data image processing terminal and a Micro PDP-11 computer. Through the image processing system,

satellite data can be enhanced to accentuate the temperature range that defines the sea-surface temperature, extraneous clouds can be removed, the data can be color processed, and isopleths of constant temperatures can be produced. These data, for the most part, were used to detect and locate significant perturbation and changes that occurred in the eastern Gulf of Mexico.

In the post-processing mode, digital tapes acquired at NASA's Wallop's Island Satellite Receiving Station were obtained from NOAA/NESDIS. Through analysis algorithms, these data were processed to produce atmospherically-corrected, cloud-free, and earth-located analysis of the sea-surface temperature in the region of interest. Application of these data provided more accurate analyses of the sea-surface temperature. Further aspects of both real-time and post-processing of the satellite data are discussed in the following sections.

3.3.2 Real-Time Processing

NOAA and GOES satellite IR data are received in real-time in the GOES tap mode or the APT mode. In either case, the IR data are from the 11 μm water vapor window band. In this band, absorption by water vapor, carbon dioxide, and ozone occurs, but the amount of energy absorbed is small compared to the energy in the original signal (i.e., the maximum signal is obtained from the radiating surface). Since, for the most part, the signal represents the signal from the radiating surface and since, for a given wavelength band, the energy from the radiating surface is a function of the temperature of the surface, the distribution of the infrared radiation obtained by the satellite represents the distribution of temperature of the radiating surface. The cloud-top temperatures (which can be as low as -40°C) and the land surface temperatures (which can be as high as $+40^{\circ}\text{C}$) represent the extreme ends of the temperature spectrum viewed by the satellite. Overall, the temperature range observed by the infrared radiometer can be as large as, or even larger than, 80°C . The sea-surface temperatures in the eastern Gulf of Mexico range, on the average, from 16 to 30°C (a 14°C range). This represents about 1/6th of the absolute range in temperature that the satellite's radiometer will generally detect.

In the normal mode of collection of GOES and NOAA IR data, the sea-surface temperature pattern is not well defined in the gray scale rendition of the data. This rendition uses sixteen shades which are spread over the 80°C range generally observed in the satellite data. Each shade of gray roughly represents a 5°C temperature range. Under these circumstances, the 14°C sea-surface temperature range in the eastern Gulf of Mexico is represented by two shades of gray. This rendition of the sea-surface temperature distribution makes analysis difficult, if not impossible.

In order to facilitate analysis of both the NOAA and GOES infrared data, an inline computer called a Scanning Radiometer Data Manipulator (SRDM) was used to enhance the imagery over the range of sea-surface temperatures observed in the eastern Gulf of Mexico. Essentially, the SRDM concentrates the 16 shades of gray over the 14°C range which is generally observed in the eastern Gulf. The SRDM also linearizes the data base so that horizontal distances in the north-south and east-west direction are equivalent. In this manner, the location of infrared data in latitude and longitude space is simplified since

a common grid can be used for all imagery. However, the linearization can only be accomplished on NOAA data received in the APT mode.

The enhanced NOAA and GOES imagery was used to detect frontal boundaries, water masses, and perturbations in the eastern Gulf of Mexico. The satellite data were studied on a daily basis, and a frontal analysis was developed on days when the skies were sufficiently clear to see the Loop Current and associated perturbations. On the average, there were about two to three reliable frontal analyses per week. These frontal analyses were used in various aspects of the research program. During the field program phase, they were used to detect and to identify features, and to locate them in space. In this manner, these data were used as an aide in guiding the field program for the collection of hydrographic data in features of interest. In the analysis phase, these data were used to develop statistics on the behavior of the Loop Current and on perturbations found on its boundary. The data were also used in conjunction with the analysis of hydrographic and current meter data to characterize perturbations of interest. Time series analyses were used to obtain translation speeds for and to study the evolution of various features.

3.3.3 Post-Processing

The sea-surface temperature distribution was obtained from NOAA satellite data using high resolution digital tapes acquired from the National Environmental Satellite Data and Information Service (NESDIS). The analyses of the sea-surface temperature distribution were obtained from satellite data in order to study the mesoscale or synoptic-scale temperature structure of the Loop Current or a specific Loop Current boundary event. In order to derive the sea-surface temperature distribution, two levels of processing were necessary. The first level involved the development of a cloud-free data set and the second, the correction of the infrared data for atmospheric effects.

Generally, clouds, which prevent radiation from the sea-surface from reaching the satellite, affect every image obtained in the eastern Gulf of Mexico. On any given day in the period 1983 through 1984, four NOAA images were obtained in the eastern Gulf of Mexico. Clouds do not generally affect each of the four images in the same manner. Clouds move, dissipate, and redevelop over a period of one day so that they are usually found in different areas of each image. Two, three, and even four satellite data sets can be integrated over a 24-hour period to obtain a cloud-free data set. The integration procedure tests each pixel (temperature) at a given location and retains the warmest one, which is presumably the clear-sky pixel. Sometimes this technique does not remove all the cloud effects and some residual cloud effects linger in the data sets. As long as these residual clouds are small in scale (areas less than $\frac{1}{2}$ degree longitude by $\frac{1}{2}$ degree latitude), they are removed on a cloud-by-cloud basis by testing the temperature and physically removing all temperatures less than some acceptable sea-surface temperature. The cloud temperatures are replaced by sea-surface temperatures using an interpolation routine and by those acceptable sea-surface temperatures surrounding the cloud. If larger scale clouds persist in the analysis after integration of satellite data sets over a 24-hour period, they are left in the subsequent analysis and identified.

After a cloud-free data set is obtained, these data must be corrected for atmospheric effects. The principal signal received by the satellite is

radiation emitted from the radiating surface regardless of whether that surface is the sea-surface, the continental surface, cloud-tops, etc. (Figure 3.3-1). A small amount of the energy emitted by the radiating surface is absorbed by three principal atmospheric constituents: water vapor, carbon dioxide, and ozone. In the infrared water vapor window band, the amount of absorption by water vapor, as well as the other absorbing gases, is minimized; but some lingering absorption still persists. Furthermore, all gases that absorb infrared radiation also emit it. Therefore, the satellite also receives a small portion of energy that is due to re-radiation by the same absorbing gases. The net effect is an overall reduction of the amount of energy received by the satellite in comparison to the amount of energy emitted at the surface. In terms of energy emitted from the sea-surface, the reduction in emitted energy leads to a 2 to 4°C temperature difference, on the average, between the equivalent black body temperature observed by the satellite and the actual sea-surface temperature based on the kind of air masses generally found in the Gulf of Mexico. Since in the eastern Gulf of Mexico there is about a 14°C range in temperature at the sea-surface, the atmospheric effect not only influences the absolute value of the temperature but also can affect the relative distribution of temperature. For this reason, these data must be corrected for atmospheric effects.

Two basic techniques were used to correct for the atmospheric effect: the single-channel and the dual-channel techniques. The dual-channel technique is considerably more powerful. However, in 1983, not all the NOAA satellites in orbit at that time collected the required information to apply the dual-channel technique. Therefore, the single-channel technique was applied on the 1983 data and the dual-channel technique on the 1984 data.

The theory on which single-channel technique is based follows. The radiation received by the satellite, N_s , can be determined through the radioactive transfer equation:

$$N_s = \int_{\lambda} \phi_{\lambda} \tau_{\lambda} R_{\lambda} d\lambda + \int_{\lambda} \phi_{\lambda} \int_{\tau_{\lambda}} R_{\lambda} d\tau_{\lambda} d\lambda, \quad (3.3.1)$$

where λ is the wavelength, ϕ_{λ} is the spectral response, τ_{λ} is the transmissivity, R_{λ} is the black body radiation from the surface, R_{λ}^{λ} is the black body radiation from the atmosphere. Letting

$$\tilde{\tau} = \int_{\lambda} \tau_{\lambda} d\lambda / \int_{\lambda} d\lambda, \quad (3.3.2)$$

and defining

$$N_o \equiv \int_{\lambda} \phi_{\lambda} R_{\lambda} d\lambda \quad (3.3.3)$$

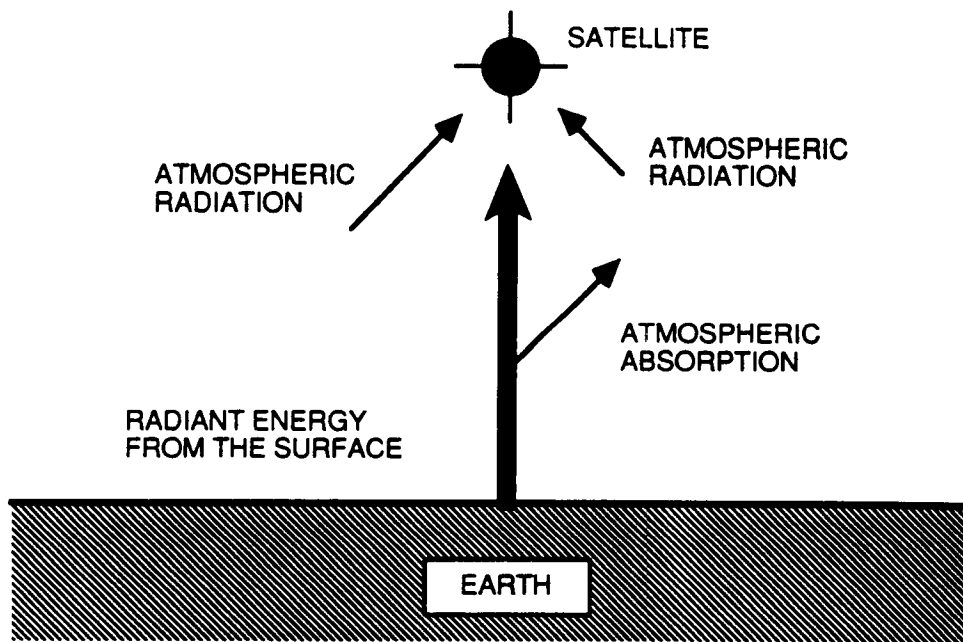


Figure 3.3-1. Schematic of atmospheric radiation processes relative to a satellite.

and

$$\delta N \equiv \int_{\lambda} \phi_{\lambda} \int_{\tau_{\lambda}} R_{\lambda} d\tau_{\lambda} d\lambda \quad , \quad (3.3.4)$$

where N_0 is the black body radiation emitted at the surface in the spectral interval and δN is the increment of radiation emitted by the atmosphere and received by the satellite in the spectral interval, then the following approximation is made:

$$\bar{N} \sim \bar{\tau} N_0 + \delta N \quad . \quad (3.3.5)$$

Assuming that δN is invariant in a small area (i.e., the air mass characteristics do not change markedly over a small area), differentiating Eq. 3.3.5 gives

$$\frac{dN_s}{dN_0} = \bar{\tau} \quad . \quad (3.3.6)$$

Equation 3.3.6 states that the gradient of radiation (or temperature) emitted from the ground will be reduced due to atmospheric absorption.

For the satellite infrared data, the digital counts C are related to radiation received by the satellite by a simple linear relationship, i.e.,

$$N_s = aC + b \quad , \quad (3.3.7)$$

where a and b are parameters derived from the satellite calibration data. In order to correct for the atmospheric absorption, the following procedure was used. Equation 3.3.6 was differentiated:

$$\frac{dN_s}{dC} = a \quad . \quad (3.3.8)$$

This differential equation was written in the following form:

$$\frac{dN_0}{dC} \frac{dN_s}{dN_0} = a \quad . \quad (3.3.9)$$

Substitution of Eq. 3.3.8 into Eq. 3.3.9 and integration gave

$$N_o = a'C + b' , \quad (3.3.10)$$

where $a' = a/\bar{\tau}$. The new intercept term b' , may be expressed as a function of the old intercept term b by combining Eqs. 3.3.5, 3.3.7, and 3.3.10:

$$b' = (b - \sigma N) \bar{\tau}^{-1} \quad (3.3.11)$$

Equation 3.3.10 gives the radiation emitted at the surface which is directly related to the ground temperature. The ground temperature was derived through the Planck function:

$$T_g = \lambda_o [\ln(\lambda_1/N_o + 1.0)]^{-1} , \quad (3.3.12)$$

where T_g is the surface temperature, and λ_o and λ_1 are the Planck constants whose values depend on the parameter dimensions that are used.

The mean transmissivity was determined by calculating the optical path for water vapor by using upper air data for various upper air weather stations surrounding the eastern Gulf of Mexico. The optical path for carbon dioxide was calculated by assuming that the carbon dioxide distribution was thoroughly mixed in the atmosphere and the mixing ratio was 0.5 g kg^{-1} (Haltiner and Martin, 1957). The optical paths for carbon dioxide and water vapor were used to develop the mean transmissivity in the water vapor window band used by the NOAA satellites. The transmissivity of Wyatt et al. (1964a, b) was used. The corrected intercept term b' may be computed using Eq. 3.3.11. An alternate approach uses in situ temperature and the Planck function to derive surface radiation in the spectral band sensed by the NOAA satellite. The derived value of the surface radiation is matched with the digital count located in that region. These two values were combined in Eq. 3.3.10 to determine the intercept term b' . This technique is described in more detail in papers presented in the literature by Vukovich (1983, 1984). According to comparisons made by Vukovich, the temperatures determined using the single-channel approach compared with in situ data with a correlation coefficient of 0.97 and a RMS difference of $\pm 1.0^\circ\text{C}$. These statistics are consistent with those found for the NOAA AVHRR using the dual-channel approach by McClain (1980) and for the GOES radiometer by Maul (1981). Maul suggested that a RMS difference of $\pm 1^\circ\text{C}$ or slightly less is probably the geophysical limit of accuracy of present generation infrared radiometers.

The dual-channel technique was applied to the 1984 data. It is much more powerful than the single-channel technique because it corrects each temperature for the local atmospheric effect which influences the radiation emitted at the particular position in space. The dual-channel technique makes use of the two water vapor window channels which are part of the AVHRR system: the $11 \mu\text{m}$ and $12 \mu\text{m}$ atmospheric water vapor window bands. Noise levels for

these two bands are exceptionally low. Because of this, the dual-channel technique can be used to correct the infrared temperature in the 11 μm band using the temperature difference between the 11 μm and 12 μm infrared temperatures. The temperature difference is a function of the absorption in the two bands. That difference is proportional to the atmospheric effect. The correction equation was empirically derived by comparison with in situ data (McClain et al., 1983). Subsequently, a linear regression equation was derived which corrects the 11 μm infrared temperature utilizing the infrared temperatures from the 11 μm and 12 μm bands. The statistics presented by Strong and McClain (1984) indicate that the RMS difference between the temperatures obtained using the dual-channel approach and in situ temperatures lies between ± 0.5 and $\pm 1.0^\circ\text{C}$.

3.3.4 Analysis of Satellite Data

Two principal products developed through analysis of satellite imagery are frontal analyses in the eastern Gulf of Mexico and statistics on features detected in that region. Frontal analyses are line drawings in latitude and longitude space that delimit boundaries between cold and warm water. These frontal analyses are used to define water masses, perturbations and major current systems. They are developed from enhanced GOES and NOAA satellite data. The GOES data are gridded when they are received through the GOES tap line. The positioning of the NOAA satellite data in latitude and longitude space was performed using grids developed at the Research Triangle Institute (RTI). In order to obtain the best possible analysis, these frontal analyses were compared with similar analyses developed by the NESDIS. Frontal analyses were produced on each day the skies were sufficiently clear to see a major portion of the eastern Gulf of Mexico. On the average, two to three of these analyses could be constructed each week. However, each analysis did not cover the entire eastern Gulf of Mexico. Characteristic frontal analyses were also developed for a given month. A monthly analysis was developed by integration of the daily analysis on clear-sky days for the given month. These analyses were used to describe the general oceanography for the month.

One of the principal uses for the frontal analyses was to derive statistics on features. A major feature for which statistics were produced was the cold perturbation that develops on the boundary of the Loop Current (Vukovich and Maul, 1985). The statistics developed for the cold perturbation were the dimensions and speed. The dimensions were defined by two characteristic lengths: the cross-flow length (L_c) and the along-flow length (L_a) (see Figure 3.3-2). The speed of the boundary perturbation was determined through analyses of a time series of the frontal analysis. The position of the center of the perturbation was determined as a function of time. The speed was defined as the time rate of change of the position of the center of the perturbation.

Warm rings which separated from the Loop Current were another major feature. Best estimates of the locations and diameters as a function of date/time for a warm ring were obtained for the estimated center of the ring. Diameters were determined only when the entire ring was evident in the satellite data. The ring size was characterized by a ring diameter, chosen on the basis of a best fit circle whose area was approximately equal to that of the ring at a given time. When continuous data were available, the position and diameter data were smoothed as a function of time using a polynomial regression procedure.

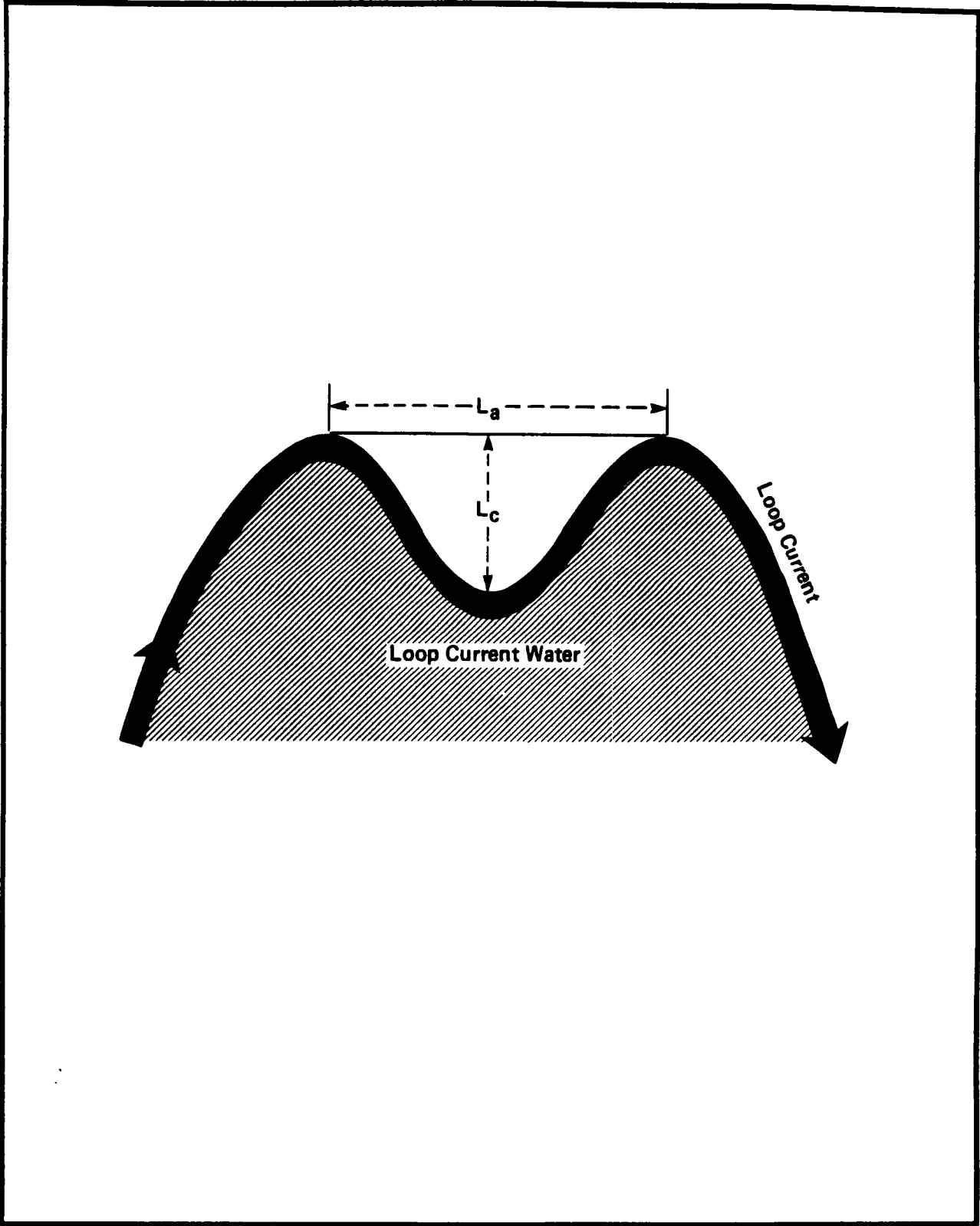


Figure 3.3-2. Schematic of cross-flow (L_c) and along-flow (L_a) length parameters determined for cold perturbations at the boundary of the Loop Current.

The smoothed position data, together with elapsed time, were used to obtain the speeds of the warm rings. Temperature data were obtained at randomly-spaced stations using expendable bathythermographs (XBT's) collected by the Ship-of-Opportunity programs (1982, NOAA; 1984, MMS). The life cycle of the warm ring, boundary perturbation, or any other feature detected in the eastern Gulf of Mexico was studied using a time series of the frontal analyses.

The frontal analyses were also used to study the variability of the eastern and western frontal boundaries of the Loop Current. In addition to the frontal analyses for 1983 and 1984, the frontal analyses for 1980, 1981, and 1982 were also used in this analysis. (The frontal boundary analyses for 1980, 1981, and 1982 were previously performed by RTI.) The variability of the eastern and western boundaries of the Loop Current was studied at 25°N, 26°N, and 27°N latitude. The variability was measured as a deviation from the mean position of the Loop Current relative to a fixed point in space.

In order to accomplish this analysis, distances were measured from either the eastern or western boundary of the Loop Current at a specific latitude to a fixed point on the latitude line. Figure 3.3-3 demonstrates the procedure and identifies the position of the fixed point relative to each latitude for measurements of distances for the western boundary and eastern boundary. These distances were determined for the periods from November through May in 1980-1981, 1981-1982, 1982-1983, and 1983-1984. In the November through May period, features could be distinguished in a continuous manner at the sea-surface using satellite infrared data. For each fixed point, after all distances had been measured, the average distance was calculated using all measurements within the period cited (i.e., monthly average, yearly average, or four-year average). After the period average was calculated, the average value of the absolute value of the deviation of each distance from the mean was computed for the given period (i.e., monthly average deviation, yearly average deviation, and four-year average deviation).

It should be noted that this analysis was only performed when a Loop Current boundary was distinguishable at each of the three latitudes used in the analysis. If for some reason data were not available at each of the three latitudes (for example, a major ring separated from the Loop Current and the Loop Current was only identifiable at 25°N), then the available data were not used in the determination of either the average front location or the average deviation.

This analysis provided information on the long-term variability of the Loop Current boundary, which, for the most part, is related to the cold perturbations that develop on that boundary. It established information on the latitudinal variation of these perturbations, on the nature of these perturbations on the western and eastern boundaries, and on the monthly variations of these perturbations over the period when infrared data could be used to identify frontal boundaries.

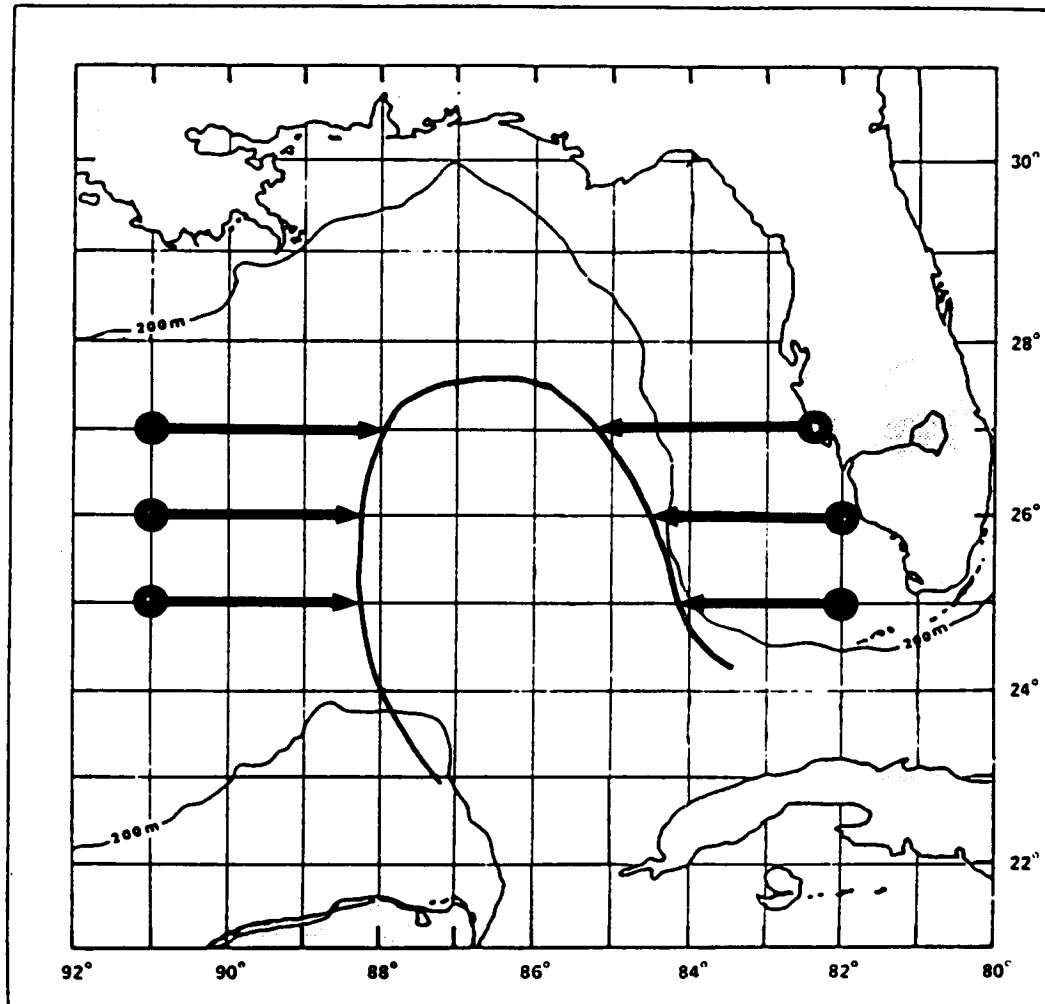


Figure 3.3-3. "Wave Staff" method of evaluating lateral fluctuations in Loop Current boundary locations. For available imagery, distances to LC boundary along a line of latitude are measured from a fixed point (●). Descriptive statistics of these measured distances can be used to estimate mean as well as LC boundary position variability.

3.4 Hydrography

3.4.1 Introduction

Much of the hydrographic data collected for this program was collected in conjunction with the three major hydrographic cruises in March and November 1983 and in May 1984. Also in May, an extensive AXBT survey was made of the Loop Current system. This section discusses the data handling methods and some of the standard data products generated in conjunction with these efforts.

3.4.2 Procedures for Handling the Ship-Based Hydrographic Data

During CTD casts an HP 9825T converted raw data counts from the Neil Brown CTD to scientific units and stored them on flexible disks. A log of time, position, and weather was maintained by the ship's personnel throughout each cruise, and periodically, data from the bridge log were entered into the computer and station headers were created. A program then read the headers and raw CTD data, averaged the data over 1-m intervals using only data where the CTD was moving downward, calculated salinity, and created a file consisting of a header and 1-m averaged temperature and salinity data. The station files were then ready for use in replotting casts, plotting vertical sections along a transect, and plotting horizontal maps.

After each cruise, headers and cast data were checked for errors and nutrient, oxygen, and chlorophyll data were entered into the station files following analyses. Duplicate salinity samples were sent to other oceanographic laboratories for intercomparison, and preliminary temperature versus salinity (T-S) plots of all CTD data were produced to check the data quality. Preliminary plots of temperature versus nutrient data were also generated to verify the quality of these data and to identify incorrectly entered values.

3.4.3 Hydrographic Data Products

3.4.3.1 Ship-based Data

A number of final data products were generated for each of the three major hydrographic cruises along the west Florida shelf. Examples of these are presented in this section. The general observations cited here apply to all three data sets.

A standard T-S plot was generated from the CTD data for each of the three cruises. The expected family of T-S relations for the eastern Gulf are presented in Figure 3.4-1. They show the characteristic salinity maximum of the Loop Current between 20 and 25°C and the presence of less saline shelf and slope waters (Continental Edge Water) at temperatures down to approximately 15°C. The salinity minimum between 5 and 8°C is characteristic of Antarctic Intermediate Water.

Vertical section plots of temperature, salinity, sigma-t, nitrate, phosphate, silicate, oxygen and total chlorophyll were also generated. Figures 3.4-2 through 3.4-4 provide examples for temperature, oxygen and total chlorophyll along one section. In this case, cool, low oxygen water had moved up onto the shelf along the bottom, and high total chlorophyll observations occurred in the upper 50 to 100 m over the shelf.

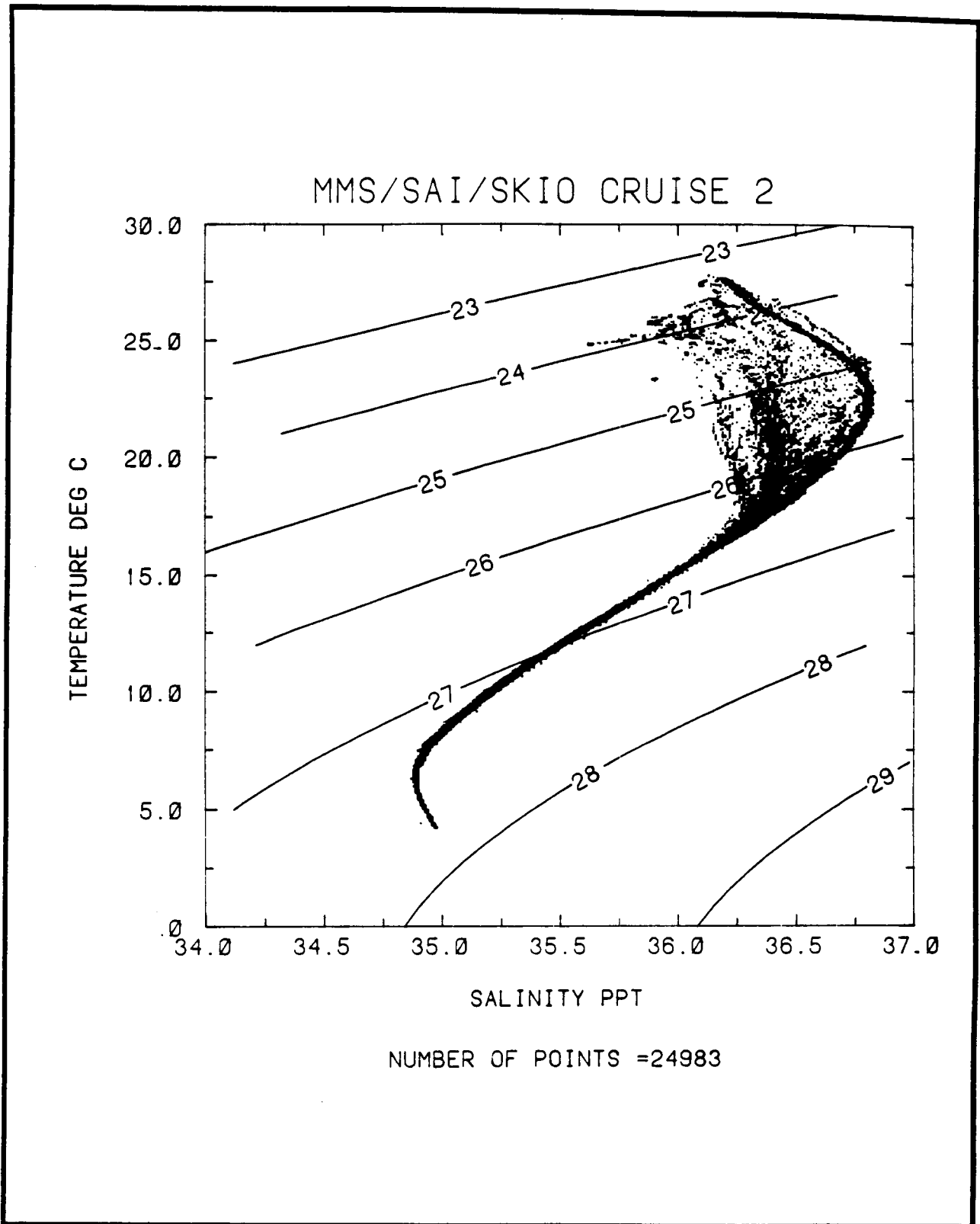


Figure 3.4-1. T-S plot for November 1983 eastern Gulf of Mexico hydrography cruise.

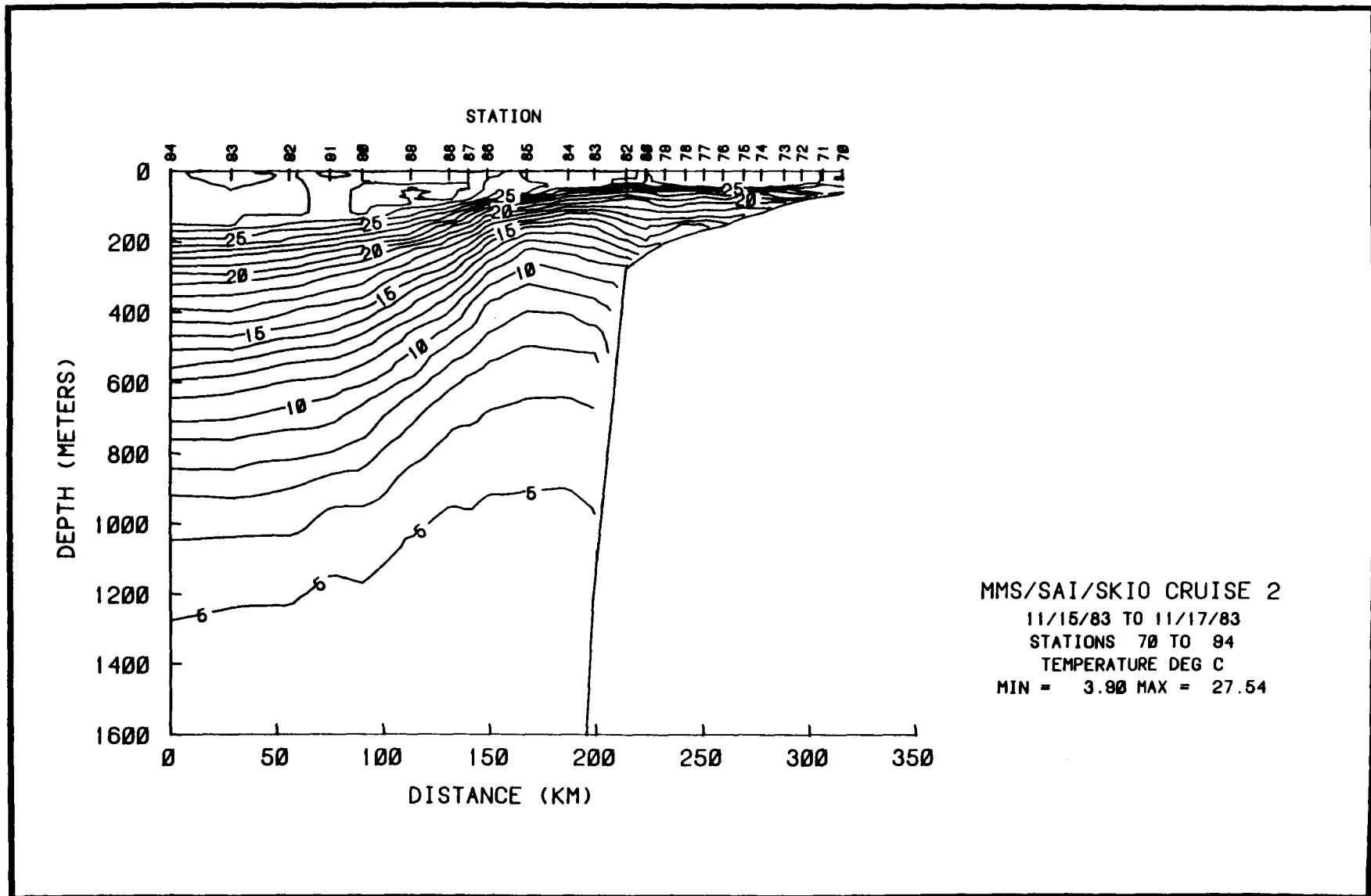


Figure 3.4-2. Vertical plot of temperature for Stations 70 through 94 for November 1983 eastern Gulf of Mexico hydrography cruise.

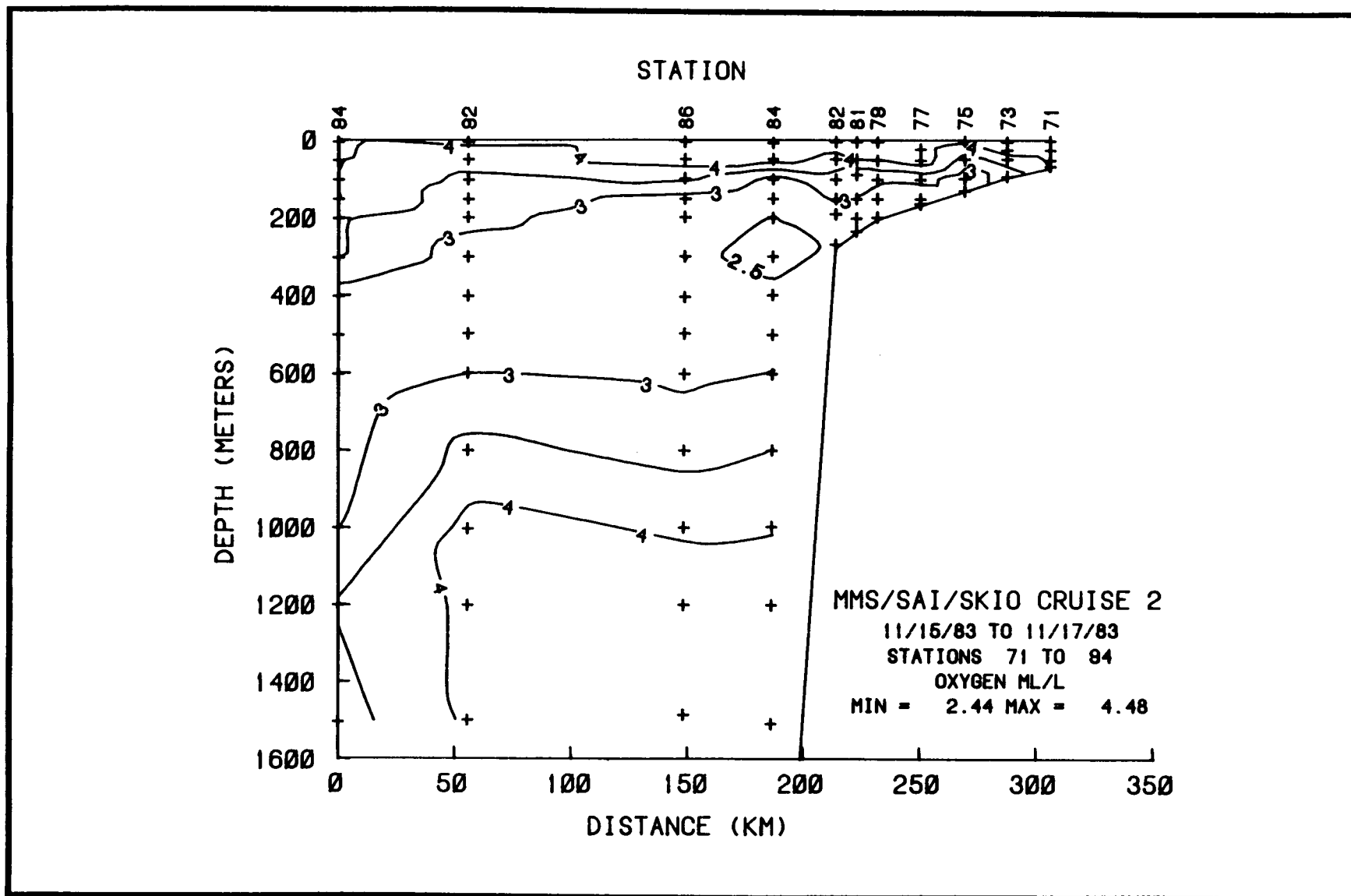


Figure 3.4-3. Vertical plot of dissolved oxygen concentration for Stations 71 through 94 for November 1983 eastern Gulf of Mexico hydrography cruise.

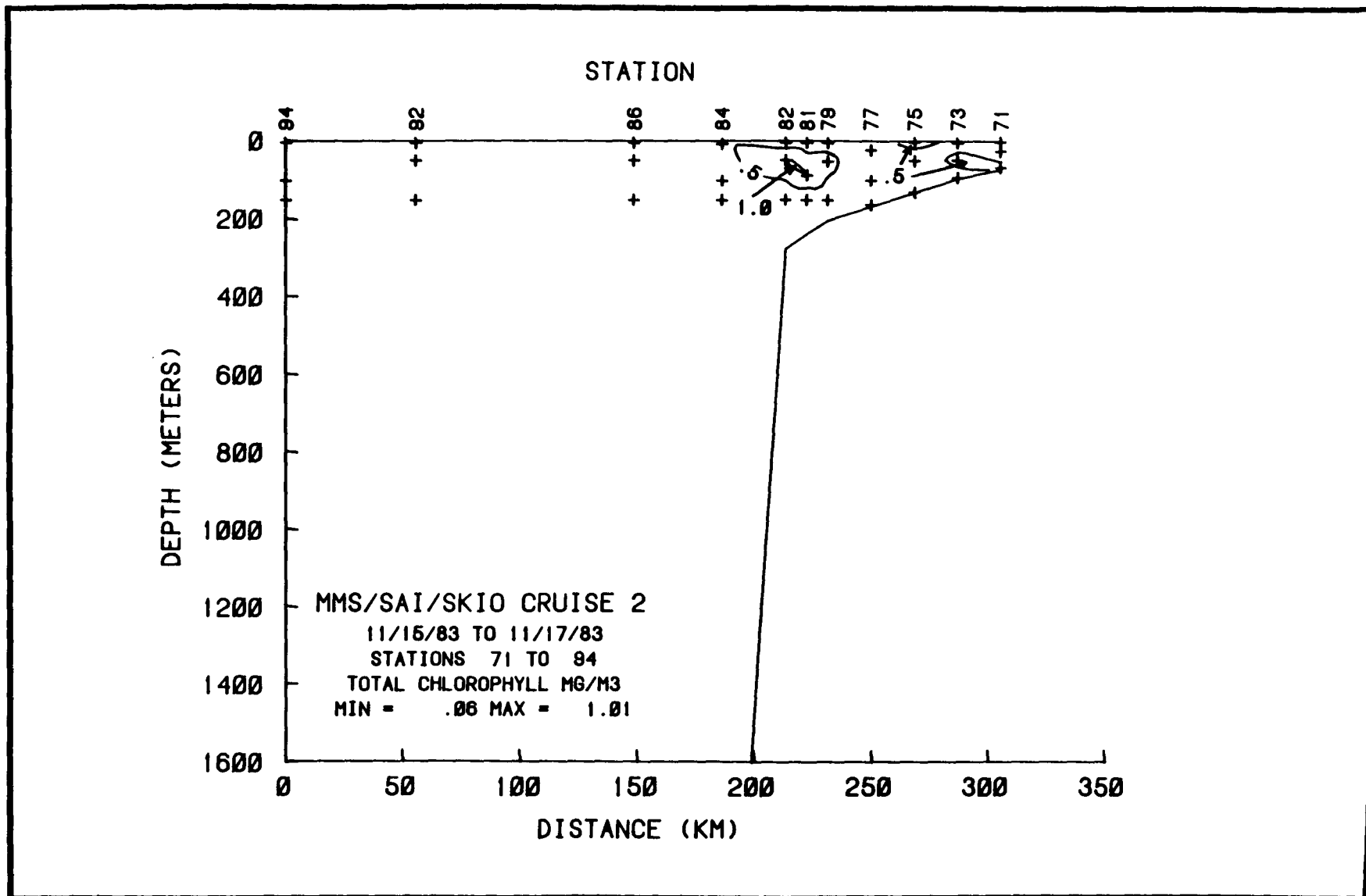


Figure 3.4-4. Vertical plot of total chlorophyll concentration for Stations 71 through 94 for November 1983 eastern Gulf of Mexico hydrography cruise.

Scatter plots of nutrient, oxygen and total chlorophyll data versus one another, and such other physical parameters as temperature, salinity and sigma-t were also made. Figures 3.4-5 through 3.4-8 provide examples of some of these. The nitrate versus phosphate plot of Figure 3.4-5 reveals that a nitrate to phosphate ratio on the order of 15 to 1 applied for much of these data. The nitrate versus temperature and silicate versus sigma-t plots of Figures 3.4-6 and 3.4-7 reveal that the highest concentrations of these nutrients occurred at depth at temperatures between 5 and 8°C and at sigma-t's near 27.5, respectively. The oxygen versus sigma-t plot of Figure 3.4-8 exhibits the characteristic minimum near 2.4 ml/l at a sigma-t near 27.2.

Horizontal plots of a number of parameters were also generated. Examples of some of these are presented in Figures 3.4-9 through 3.4-11. Figure 3.4-9 shows the surface distribution of oxygen. The lowest concentrations were found to occur in the warm Loop Current and higher concentrations occurred in cooler shelf waters to the northeast and southwest. Similarly, surface chlorophyll concentrations were highest on the two shelves (Figure 3.4-10). Finally, a horizontal dynamic height plot is presented in Figure 3.4-11 for the upper 500 m of the water column. It suggests a current flow to the north near 87°W and to the south near 85°W around a central high.

3.4.3.2 Air-deployable Probe Data

All AXBT data were processed using the Sippican equation for transforming frequency to temperature. Comparisons were made with other conversion schemes (Bane, 1983) with resulting differences to the general pattern being minimal. The various combinations of temperature profile data were combined to create transects which were then contoured.

The contouring routines used linear interpolation on a triangulation scheme. Thus, the regions between observations were estimated by linear gradients between any two encompassing points. This scheme overcomes problems of "over and under shoot" which can result when spline-let routines are used on irregularly spaced data. The linear interpolation occurs even between widely spaced observations, and under these circumstances is probably not a good estimate of actual horizontal gradients. In the vicinity of fronts, the linear interpolation scheme tends to "spread" what may be a much sharper gradient.

In the QA process each profile is evaluated individually. After contouring quality assured profiles, the pattern is evaluated for features that clearly result from isolated cases of a distorted fall velocity. These profiles can be eliminated as needed, and the corrected final contoured transect created.

The AXCP data were processed by Horizon Marine using computer routines which, at the time, were proprietary. Results of these analyses were profiles of magnetic north and east velocity components and temperature. These velocities were rotated to transect-normal and -parallel components.

Although presented as velocities, they are probably better considered as biased velocity estimates. Bias in this sense implies a directed velocity so the true local velocity may be the velocity sensed by this instrument plus some offset. The manufacturer and Horizon Marine generally assume that the

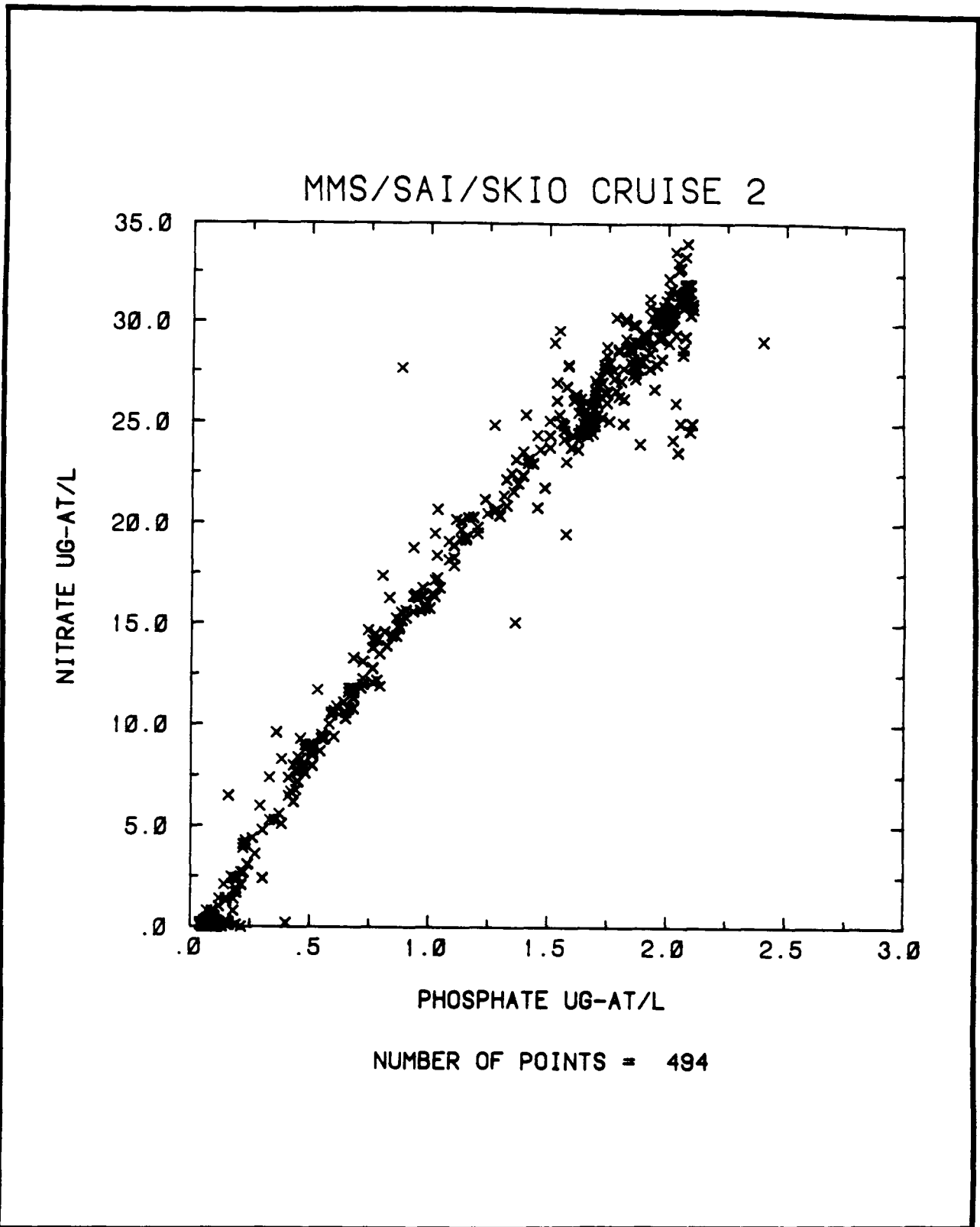


Figure 3.4-5. Nitrate versus phosphate plot for November 1983 eastern Gulf of Mexico hydrography cruise.

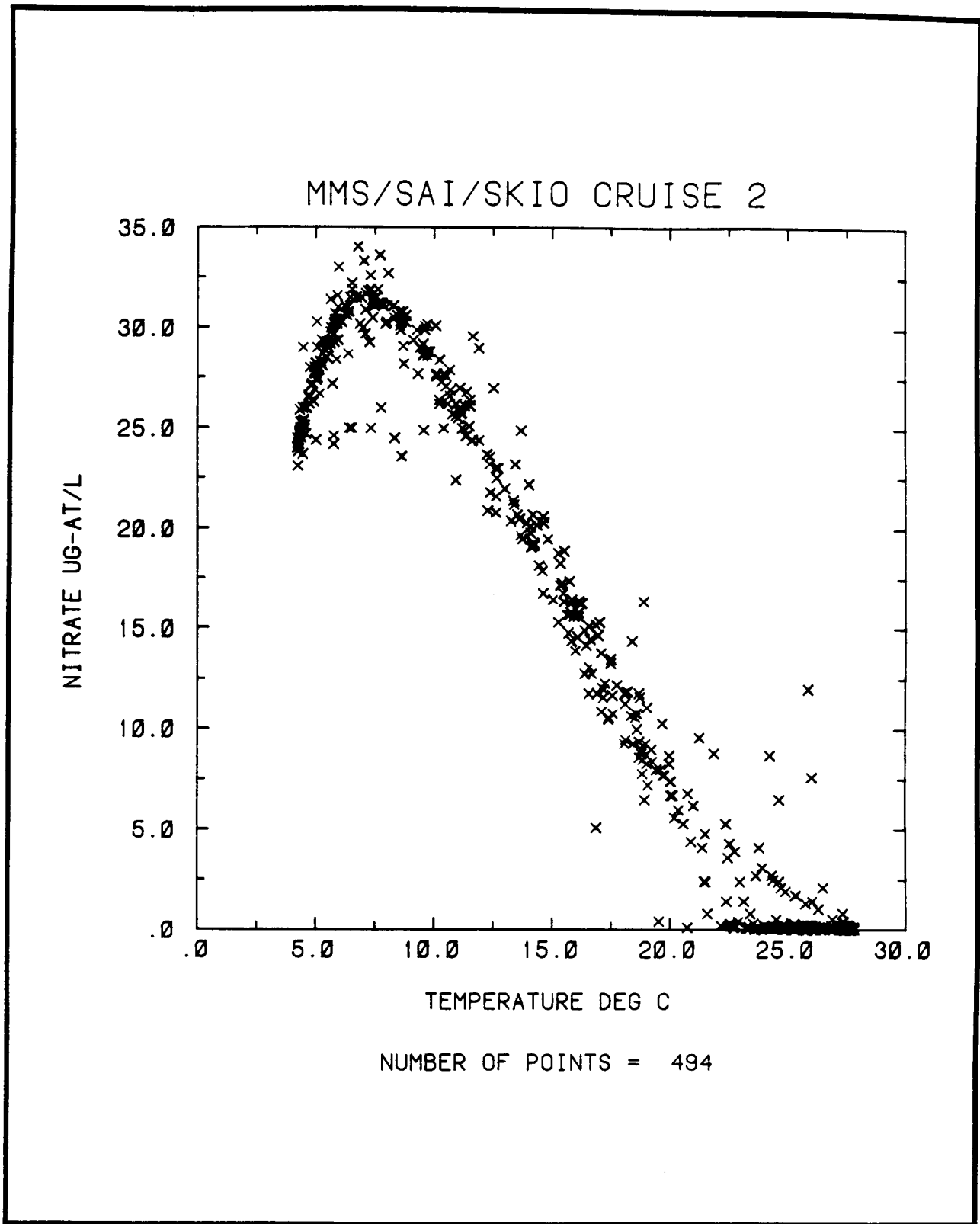


Figure 3.4-6. Nitrate versus temperature plot for November 1983 eastern Gulf of Mexico hydrography cruise.

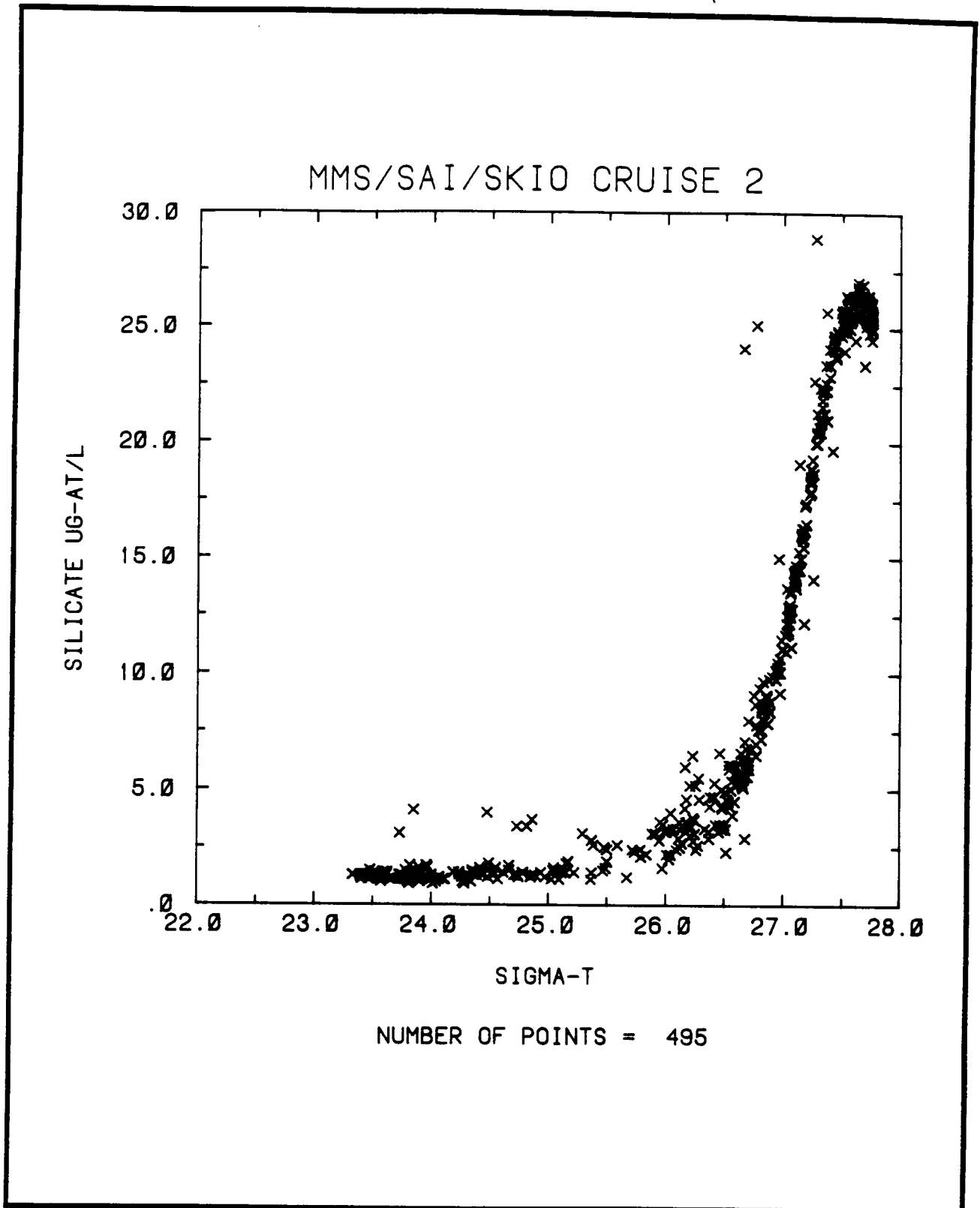


Figure 3.4-7. Silicate versus sigma-t plot for November 1983 eastern Gulf of Mexico hydrography cruise.

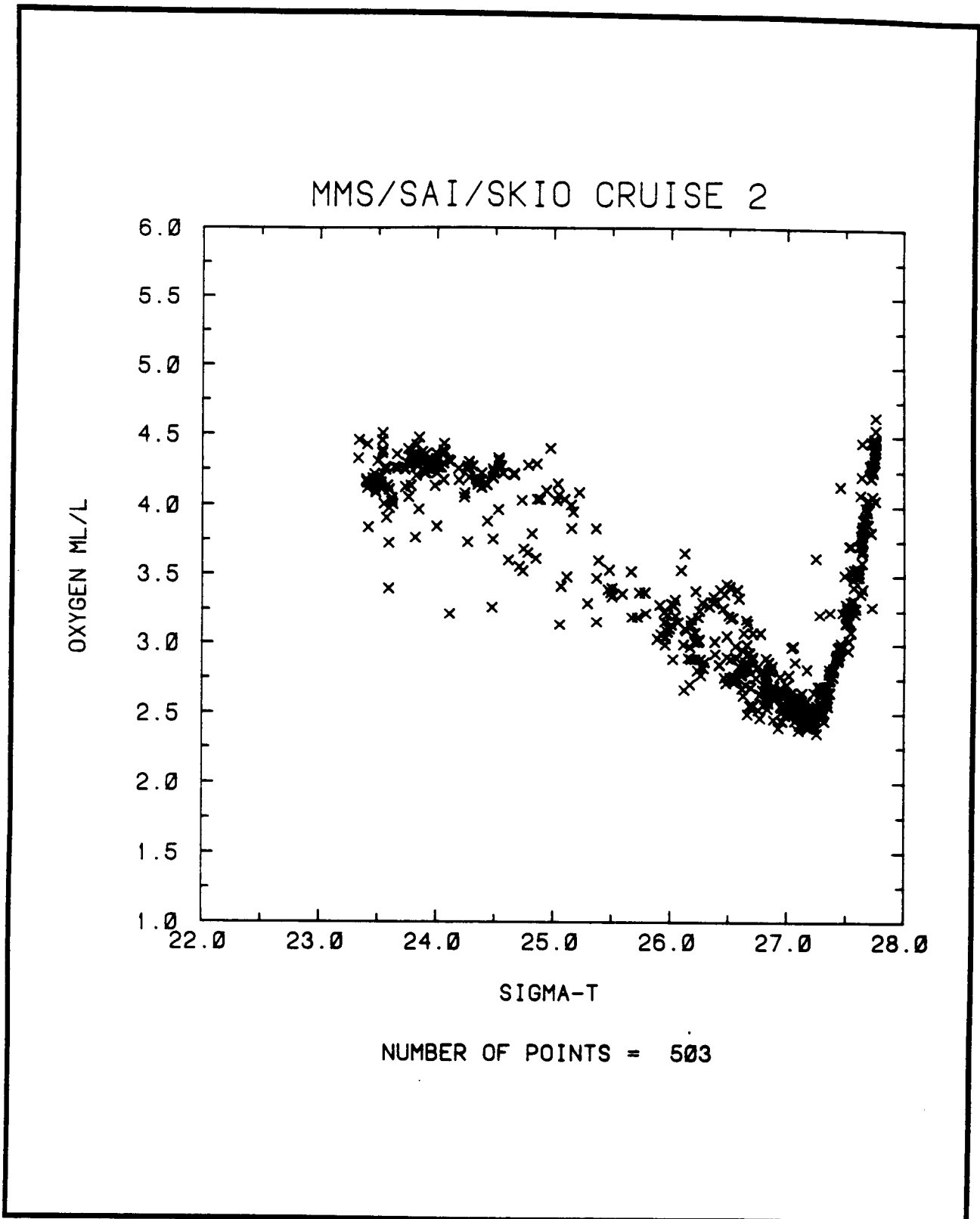


Figure 3.4-8. Oxygen versus sigma-t plot for November 1983 eastern Gulf of Mexico hydrography cruise.

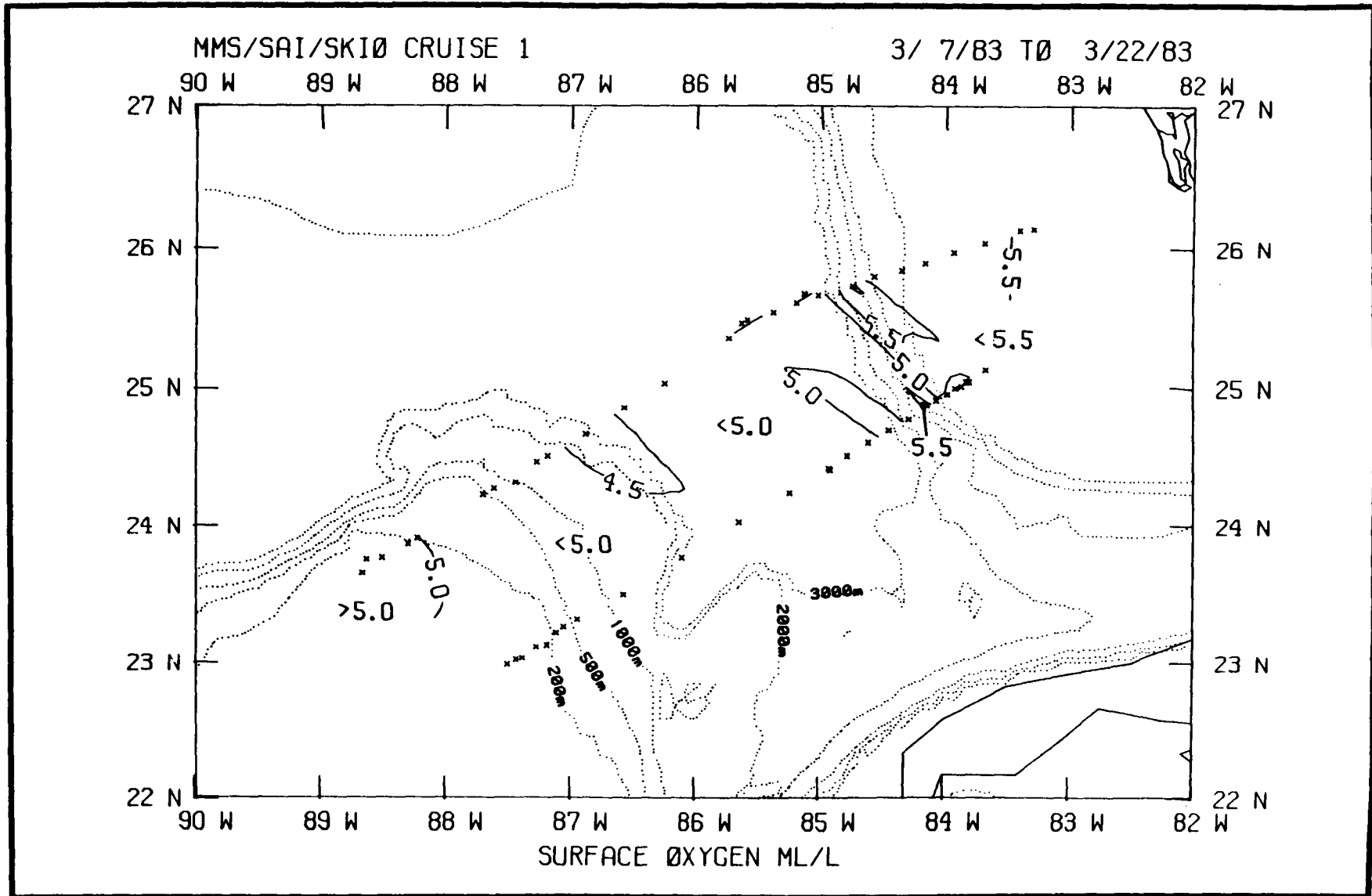


Figure 3.4-9. Surface oxygen plot for March 1983 eastern Gulf of Mexico hydrography cruise.

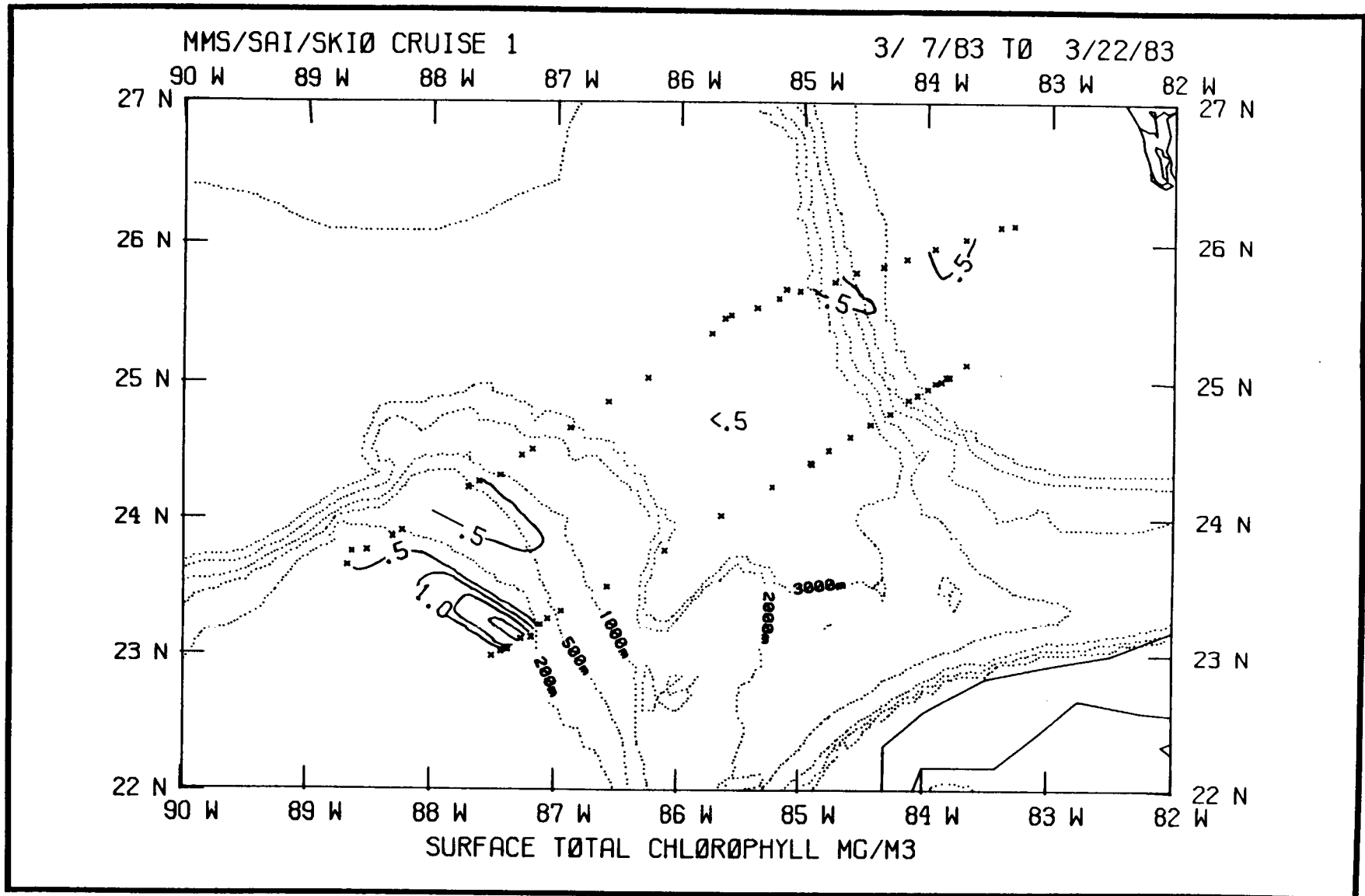


Figure 3.4-10. Surface total chlorophyll plot for March 1983 eastern Gulf of Mexico hydrography cruise.

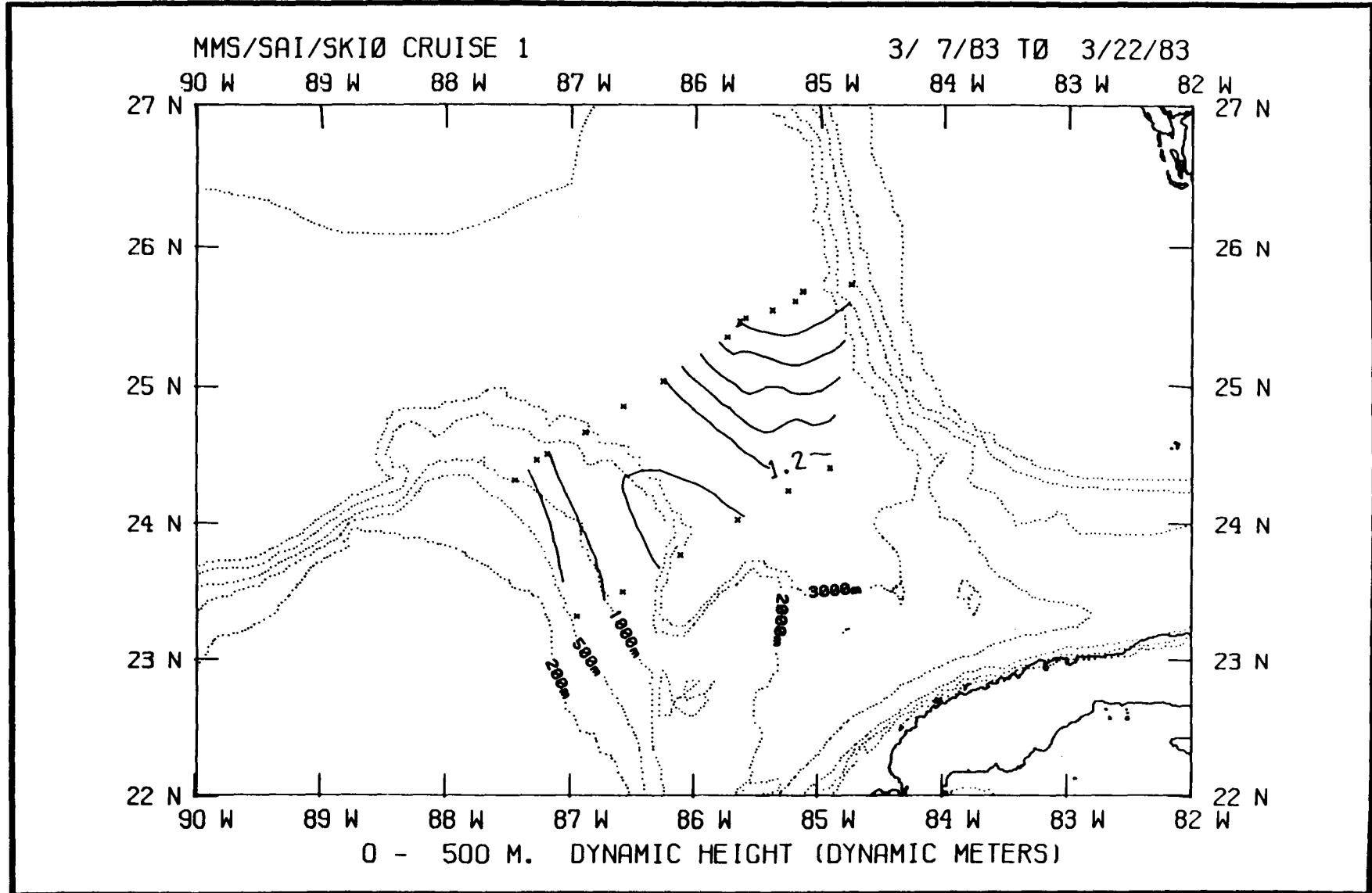


Figure 3.4-11. Horizontal dynamic height plot for 0-500 meters for March 1983 eastern Gulf of Mexico hydrography cruise.

bias is small, i.e. on the order of 10 cm s^{-1} . The sensed velocity gradient is probably an accurate estimate of vertical shear.

At present no effort has been made to estimate bias since (1) there are no assurances that this bias is spatially or temporally constant, and (2) these profiles were taken at widely separated sites over several days.

3.4.4 Ametek-Straza Current Profiles

3.4.4.1 Introduction

A total of 7035 vertical profiles of horizontal velocity data were measured and recorded by the Ametek-Straza DCP-4400 ADCP system (described in Section 2.4.4) during the May 1984 R/V CAPE FLORIDA cruise. After the cruise, these data (which are east and north components of the doppler shift vector recorded in units of $1/8 \text{ Hz}$) were uploaded to a mainframe computer. SAIL data including date, time, latitude and longitude were also uploaded to the same computer. Since the position data recorded by SAIL are required for the presentation of all ADCP data and essential for the analysis of ADCP data in regions where bottom tracking was not possible, the time-based intersection of these two data sets was determined and the remainder of both data sets was eliminated from further consideration.

A least-squares, third-order polynomial fit was computed for latitude and longitude over either one-hour time intervals (approximately 60 SAIL records) or the time interval between hydrographic stations, whichever was less. Only data obtained when the ship was on a relatively steady course and speed were used in this procedure; therefore all data during times when the ship was slowing down for, turning onto, sitting on and departing from station have been eliminated from analysis, resulting in a total of 3490 fully processed velocity profiles. (The elimination of data from station locations does not significantly reduce the geographic coverage. See Figures in 3.4.4.2.) This polynomial fitting procedure has two purposes: (1) it allows accurate alignment of the time bases of the two data sets since the polynomial fit to the SAIL data can be evaluated at the time of the corresponding ADCP data records to yield the geographic location of each velocity profile, and (2) while allowing for a modest amount of change in the ship's speed and direction, it effectively low-pass filters the position data, resulting in a reduction of LORAN-C measurement noise. This is desirable when ADCP bottom tracking data are not available and it is necessary to determine ship motion by time differencing the position data. Individual LORAN-C measurements are accurate to within about 0.01 nautical mile, which is good for positioning purposes but translates into an undesirably large error of about 12 cm s^{-1} when divided by the 160 cycle time of the ADCP. A comparison of record-to-record differences in position for both raw and fitted data shows a factor of three to seven reduction (the average factor was four) in standard deviation in the fitted data set, while the means were the same.

For those ADCP velocity profiles where there is no bottom tracking information, it is estimated that an additional error of about 3 to 4 cm s^{-1} is introduced into the absolute velocity calculation by the polynomial fitting process. This is larger than the approximately 2 cm s^{-1} bin to bin error within the profile resulting from the limitations of the acoustic signal processing hardware (Joyce et al., 1982). This 2 cm s^{-1} error is also

applicable to the bottom tracking data. Thus the total error in velocity at any given depth for non-bottom tracking cases is about 5 or 6 cm s⁻¹ while for the regions where bottom tracking was successful, the error is about 2 cm s⁻¹ less. Other potentially significant sources of error not quantified here include misalignment of the transducer assembly in the ship's hull and high frequency wave-induced motion of the ship. Error due to transducer misalignment is considered small since the difference in ship's heading recorded independently by SAIL and by the ADCP is very small. Joyce et al.(1982) argue that averaging over many wave periods should significantly reduce error due to wave effects and conclude that overall error in absolute velocity when LORAN-C data must be used in lieu of bottom tracking data to remove ship motion is 5 to 10 cm s⁻¹.

Water depth at each hydrostation as measured with a standard PDR has been compared to bottom depth measured by the ADCP while on station (Figure 3.4-12). All depth estimates greater than 500 m regardless of source were set equal to 450 m before plotting. Note the large number of cases where the station depth (i.e., the true depth) is greater than 500 m, but the corresponding ADCP depth ranges from near zero to 500 m. Also note the tight fit for true depth less than about 250 or 300 m. Thus, ADCP depth equals true depth for true depth less than 250 m, but the converse is not necessarily true. For this reason, water depth at each ADCP profile location was estimated by interpolating between hydrostations and, where this interpolated depth was less than 250 m, the ADCP measured depth was used. If water depth was less than 250 m and the percentage of successful detection of acoustic reflections was greater than 95 percent for the bottom tracking bin, then the ship motion was calculated from bottom tracking data. If not, the LORAN-C based estimate was used.

Once the best estimate of ship motion and bottom depth was determined for each ADCP profile, each component of the doppler shift vector was converted to velocity in centimeters per second relative to the ship via the following relationship:

$$V = DS * C(T)/18400$$

where V is velocity, DS is the doppler shift, and C(T) is the speed of sound in seawater as a function of sea-surface temperature. The ship motion was then subtracted from the velocity in each depth bin to yield the absolute east and north velocity components as a function of depth relative to the earth. Finally, each velocity profile was scanned for bins having less than 95 percent acoustic reflection detection success rate and for bins corresponding to depths greater than the bottom depth. The velocity in any such bins was set equal to a check value and they were thus eliminated from further analysis.

3.5 Subsurface Currents - Time Series Analysis

3.5.1 Introduction

After transcribing data tapes, the standard data analysis procedure listed below is initiated on time series data such as subsurface currents, winds, and water level.

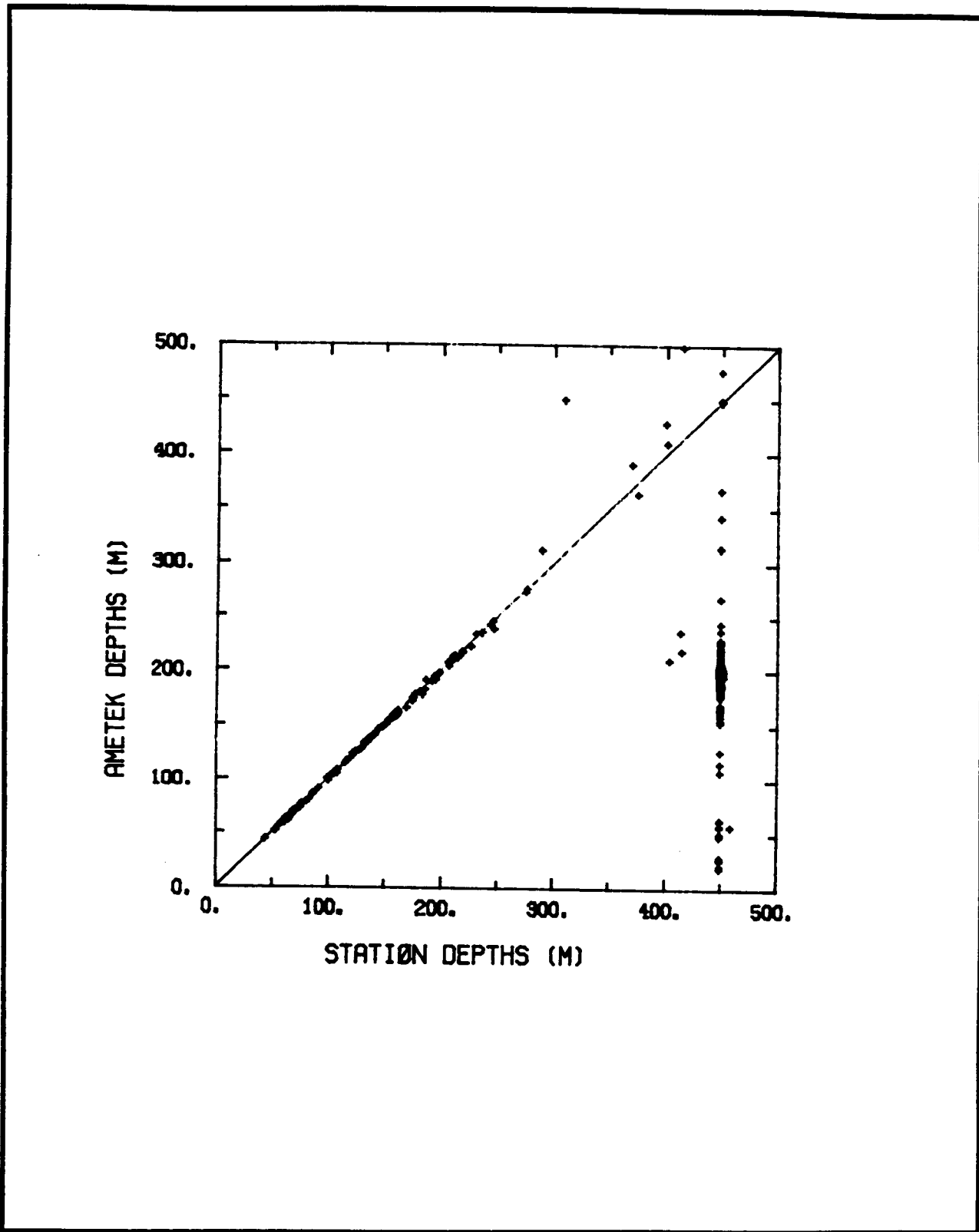


Figure 3.4-12. Comparison of PDR determined station depth and Ametek-Straza determined station depth. Ametek depth equals true depth for true depth less than 250 m.

- Review of raw data plots.
- QA of data, identify questionable observations and make corrections as appropriate.
- Filtering using 3 and 40 hour low pass (HLP) smoothing (Figure 3.5-1).
- Stick plots of vector quantities and time series plots of scalar quantities. Stick plots are of 40 HLP data (Figure 3.5-2).
- Spectra of 3 and 40 HLP time series (Figure 3.5-3).
- Biweekly statistics including means, variance, standard deviation, maximum and minimum for successive two week intervals and the entire record.
- Bivariate analysis which evaluates speed as a function of magnitude and direction.

As appropriate, coherence squared and phase relations are calculated between similar time series. Rotary spectra can also be calculated and displayed. SAIC works with program PI's in an effort to accommodate special analysis and graphic requirements.

Listed below is a brief summary of what some of the above mentioned analysis involves as well as what the results mean.

The magnitude of a variable as it changes with time produces a time series. Any such time series can be approximated by a trigonometric series, i.e. a Fourier series. The terms in such a series are sines and cosines which are weighted by specific magnitudes for each frequency. A given time series has a set of weighting values which is unique. The value of a variable at any given time is the linear superposition of the contribution of each periodic component.

The low-pass filtering mentioned above suppresses the amplitude of high-frequency elements in the trigonometric series. As a result, only lower frequency components contribute to the filtered time series. Visually, this tends to remove sharp peaks which might have been evident in the unfiltered time series. The more high-frequency components suppressed, i.e. the greater the filtering, the smoother the time series appears.

The spectrum of a time series decompose the record into the trigonometric or periodic components. The magnitude of the spectra at a given frequency is the value of the weighting function in the Fourier series mentioned above. Hence the greater the weighting function for a given frequency, the greater that frequency's contribution to the time series. It is stated without proof that the spectrum also is an indication of the time series' variance that is contributed by the frequency components. For a given frequency, the magnitude of a sinusoid determines the variance. Since the value of the spectral estimate reflects that amplitude, it also indicates the relative variance contributed at that frequency (higher peaks - more variance).

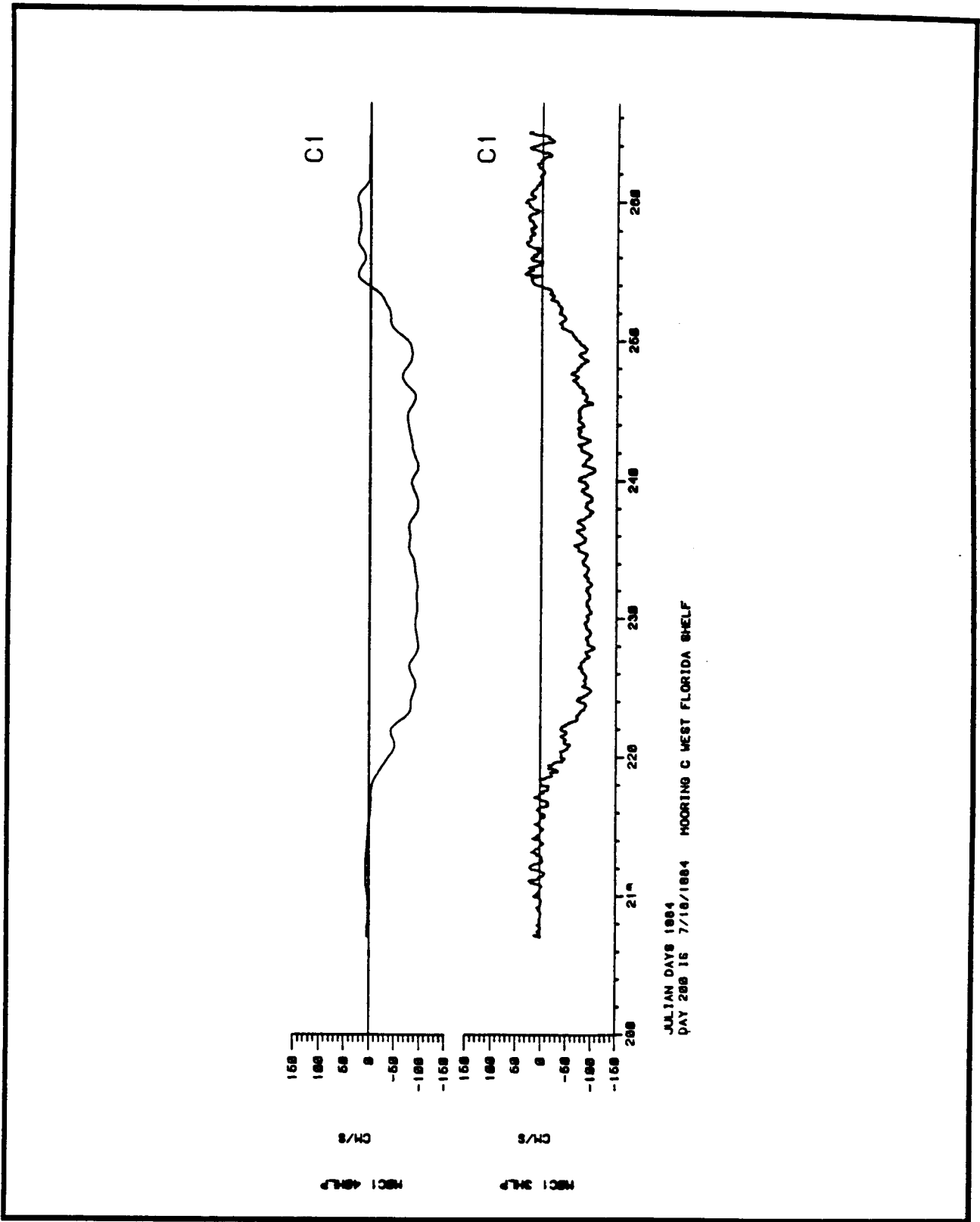


Figure 3.5-1. Filtered time series using 3 and 40-hour low-pass (HLP) smoothing.

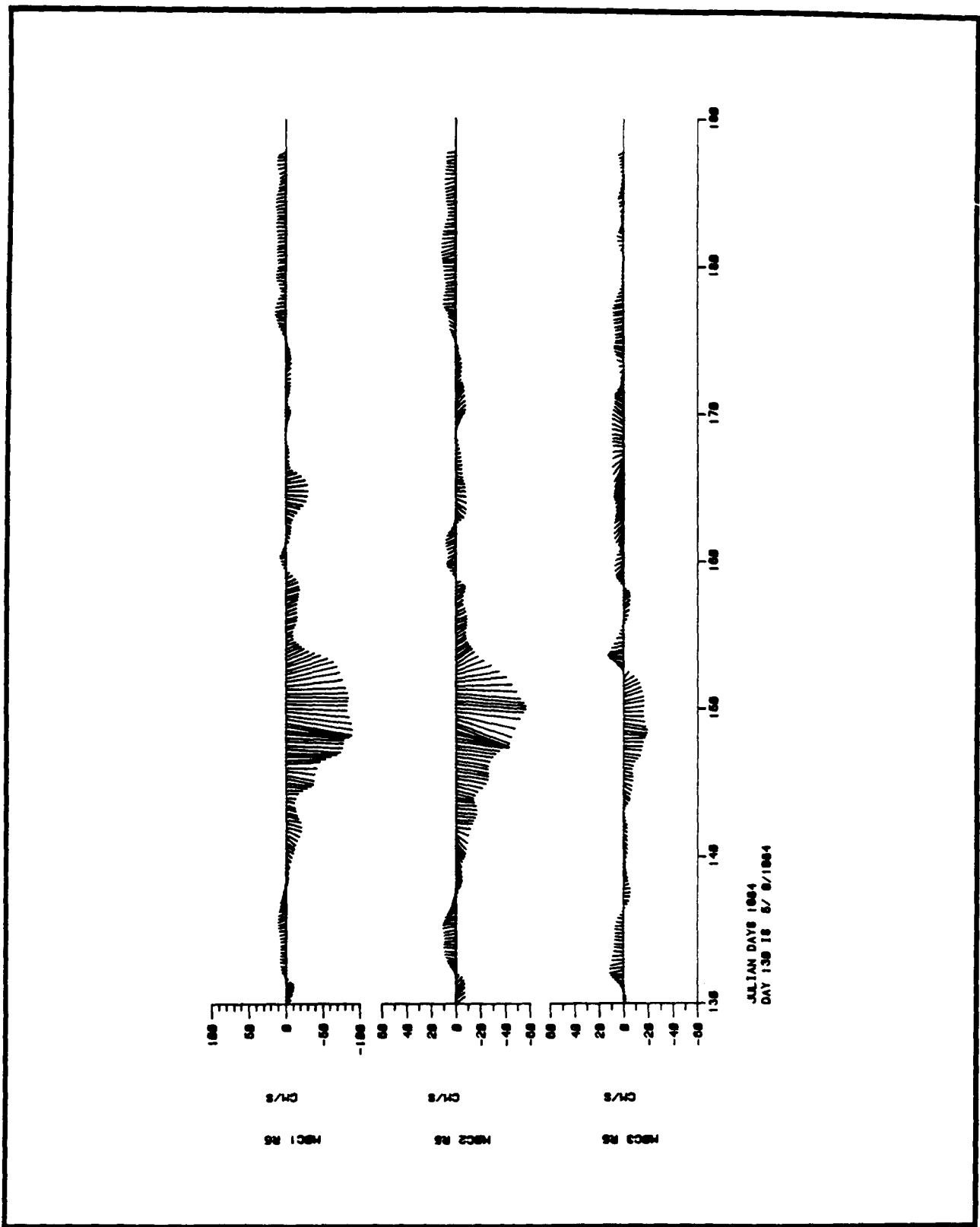


Figure 3.5-2. Stick plots of vector quantities and time series plots of scalar quantities.

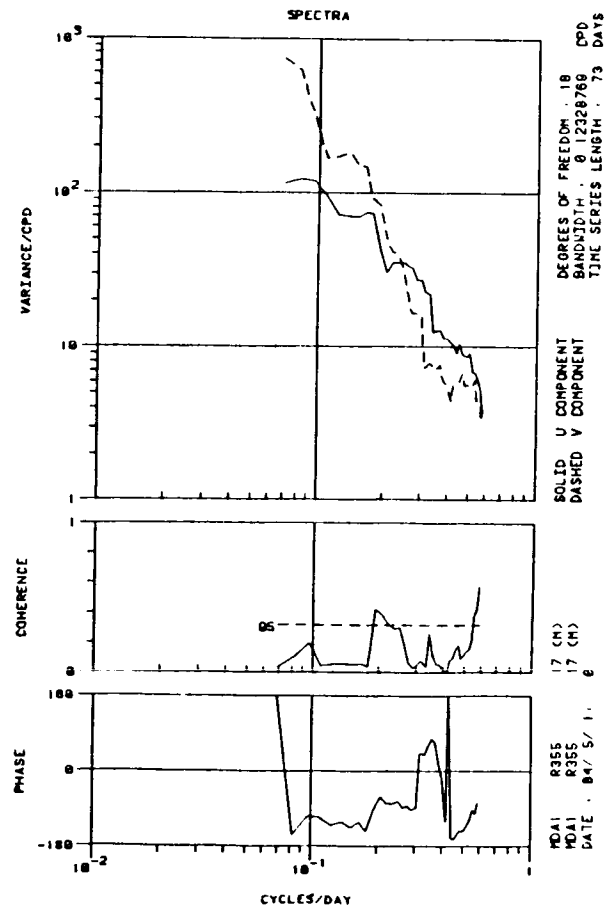
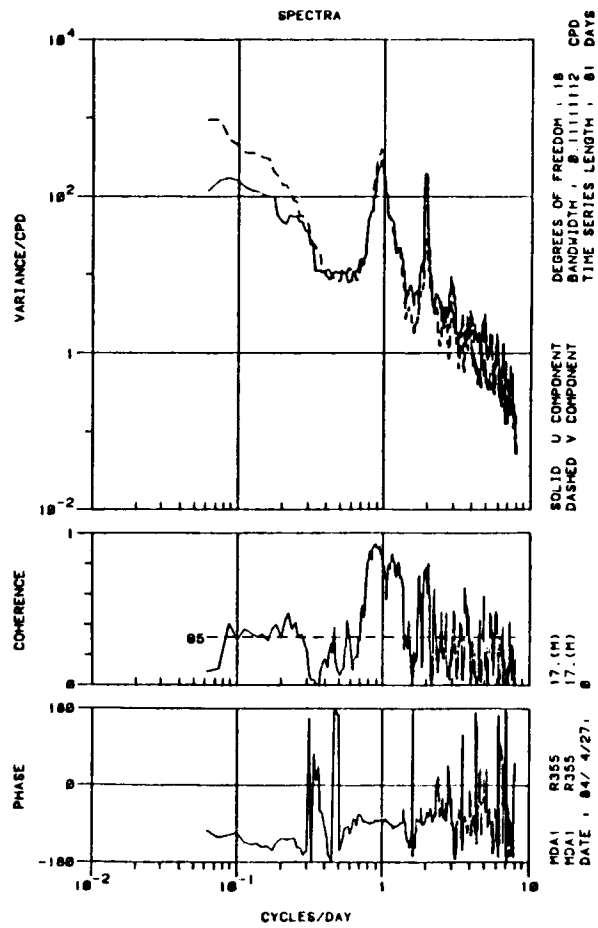


Figure 3.5-3. Spectra of 3 and 40 HPL time series.

The correlation between two time series can be done in the frequency or time domains. In the former, this correlation is between two sinusoids at the same frequency. If they are identical then they have a perfect correlation of one. If less than identical, the correlation coefficient is less than one. If they have little or no correlation, then the coefficient is close to zero and the value of one sinusoid is not related to the value of the other. In the frequency domain, this correlation coefficient is called coherence squared or, in this report, coherence.

Two sinusoids can be perfectly correlated (i.e. a coherence of one) but be out of phase. This occurs when they are offset in time. If one was shifted by a percent of the frequency two perfectly correlated sinusoids would overlap. This shift is the phase shift between the two time series. There is potentially a different value for each frequency. Certain motions tend to have particular phase relations between orthogonal velocity components. As an example, circular particle motion will produce a 90° phase shift between velocity components measured at a fixed point. In addition, knowing which component leads indicates the direction the circular motion is rotating.

Rotary spectra simply decomposes a time series into a cyclonic and anticyclonic component. The spectrum again indicates the relative variance contributed by that sense of rotation at that frequency. This information is important since most motions in the oceans rotate in a particular direction as dictated by the physics of the motion.

3.5.1.2 West Texas Shelf

This project was proposed and carried out with the intention of studying the kinematics and dynamics of shelf sediment transport. The data reduction and synthesis follow two lines of investigation: a general study of water parcel motion and detailed examination of the periods when boundary shear stress was clearly in excess of the threshold of motion for a pre-determined sand grain size.

3.5.1.3 Spectral Analysis

The time series of currents and winds were analyzed using the methods described by Fee (1969). First, the data were examined to determine if any instrumental effects (such as improper trim of the meters) were present, and none were found. They were then studied to identify and remove any trends and averaged and subtracted from that average to yield the variance. The amplitude of the variance was then subjected to a fast Fourier transform using a Parzen spectral window (as described by Chatfield, 1980). Figure 3.5-4 shows a typical power spectrum for the current meter data. Note the smooth decrease in energy levels with decreasing period (and increasing frequency) and the marginally significant increases in energy density at the inertial and tidal periods. Because of the location of the STOCS at 27°N latitude, there is very little frequency separation between the inertial period (26 h) and the diurnal tidal periods. Thus, they are represented by one peak. The semi-diurnal tidal peak is less well-developed, an expected result on this coast which is dominated by the diurnal tide (Smith, 1974). In fact, calculations by McGrail and Carnes (1983) indicate that on the Texas shelf near Flower Garden Banks, the K_1 tide has a maximum amplitude of 6.5 cm s^{-1} .

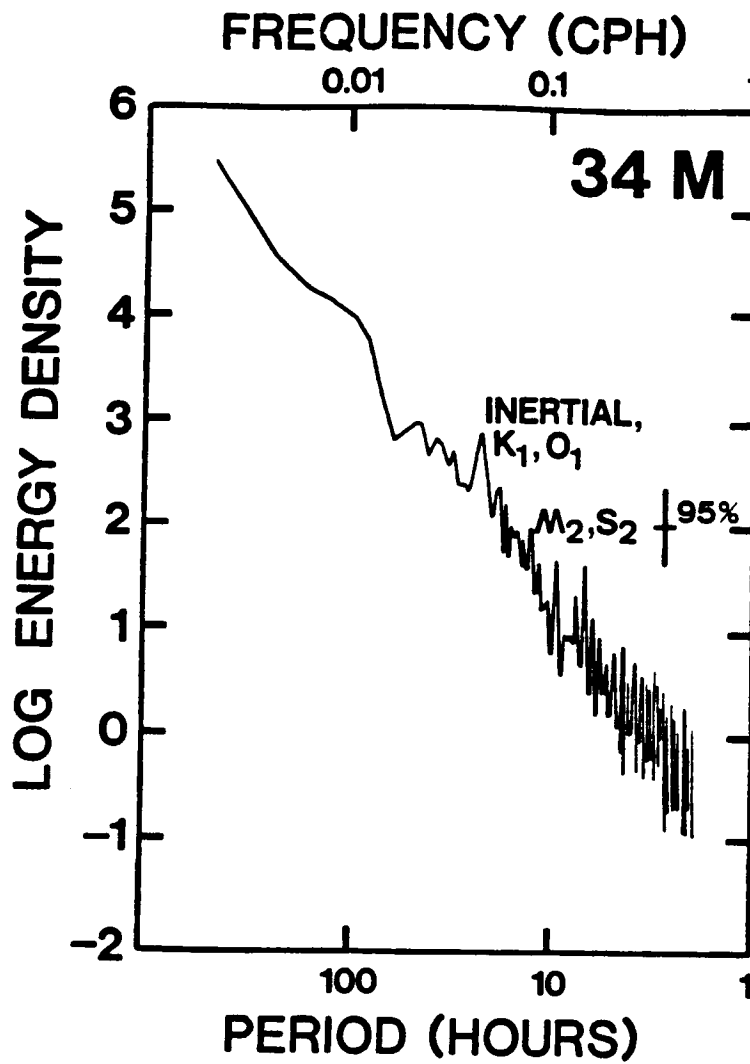


Figure 3.5-4. Energy density ($\text{cm}^2/\text{sec}^2/\text{CPD}$) spectra of the along-shelf (v) component of the currents at location C' (34m), 23 August to 9 December 1984. Degrees of freedom = 18.

and the M_2 tide of 2.6 cm s^{-1} . It is expected that these have a similar magnitude on the STOCS.

Spectral analysis of the wind records from Horace Caldwell Pier (HCP) at Port Aransas shows a similar decrease in energy level with decreasing period (Figure 3.5-5). A well-pronounced peak near the diurnal frequency probably corresponds to the sea-breeze effect. Another peak at 64 h has not been previously recognized on the Texas coast.

From this and the spectra of the other meters it was decided to use a 40-h low-pass (HLP) filter. This effectively removed the high frequency components from the wind and current meter data. It is quite evident that in doing so the majority of the variance in the wind and current time series still remained. The use of the 40-HLP filter allows the longer period forcing mechanisms, the mechanisms ultimately behind sediment transport on the STOCS, to be studied.

Coherence and phase spectra between along-shelf (V) and cross-shelf (U) components of the wind and currents were also computed. Generally, values of coherence were statistically significant only at the lower frequencies. The highest degree of coherence for these longer periods was between the V components of the wind and currents (Figure 3.5-6). As expected, there is a steady decrease in coherence from A (12 m) to E (140 m). A slight increase between D and E may be attributed to the longer record length of E. Clearly, the coupling between the wind and bottom current field decreases in an offshore direction. The phase spectra for the shallow locations (A, B, and C) show a slight lead for the wind, particularly at 100 h. At the deep locations (D, E) the phase spectra are highly variable, again suggestive of a poor coupling between the wind and the currents at these deeper depths.

The coherence spectra for the U components of the wind and current were lower, the highest value being 0.7 at 300 to 100 h at location A (12 m). Coherence between the V component of the current and the U component of the wind at long periods ($> 100 \text{ h}$) was even lower at each station.

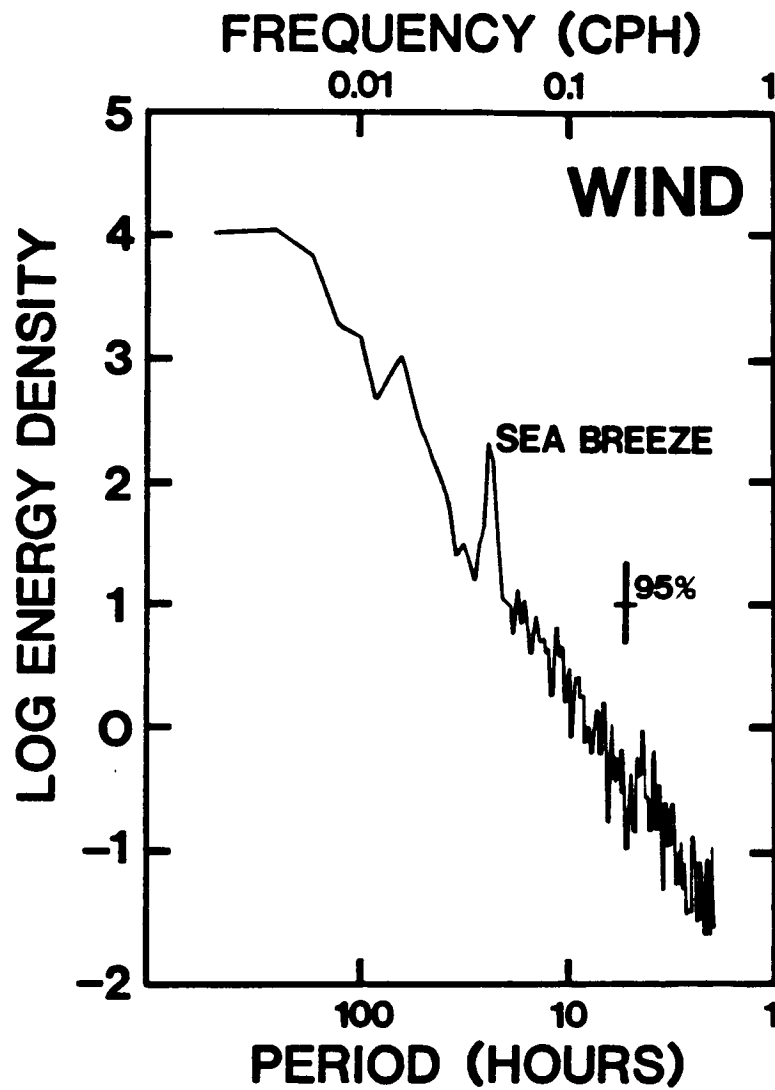


Figure 3.5-5. Energy density ($\text{cm}^2/\text{sec}^2/\text{CPD}$) spectra of the along-shelf (v) component of the wind recorded at Horace Caldwell Pier, Port Aransas, Texas, 23 August to 9 December 1984. Degrees of freedom = 18.

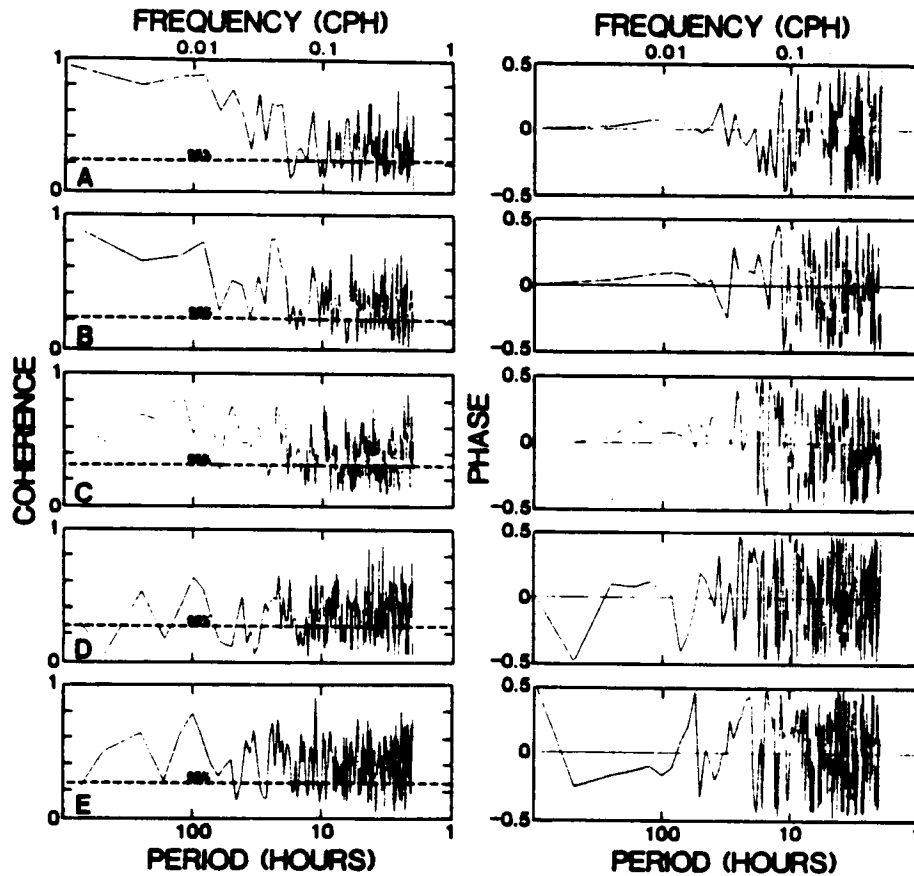


Figure 3.5-6. Coherence and phase spectra for along-shelf (v) components of the Port Aransas wind and currents at various locations across the STCS. Degrees of freedom range from 18-30. The phase is listed in fraction of a complete circle where 0 = 0 degrees, 1 = 360 degrees.

3.6 References for Chapter 3

- Bane, John M., 1983. A field performance test of the Sippican aircraft - deployed expendable bathythermograph. University of North Carolina at Chapel Hill, Tech. Rep. No. CMS-83-1, 6 pp.
- Chatfield, C., 1980. The Analysis of Time Series. Chapman and Hall, London, 270 pp.
- Fee, E., 1969. Digital computer programs for spectral analysis of time series. Univ. of Wisconsin Center for Great Lakes Studies, Special Report No. 6, 17 pp.
- Haltiner, G. J., and F. L. Martin, 1957. Dynamical and Physical Meteorology. McGraw-Hill, New York.
- Joyce, T. M., D. S. Bitterman, Jr. and K. E. Prada, 1982. Shipboard acoustic profiling of upper ocean currents. Deep-Sea Res. 29:903-913.
- Kirwan, A. D., Jr., W. J. Merrell, Jr., J. K. Lewis, R. E. Whitaker and R. Legeckis, 1984a. A model for the analysis of drifter data with an application to a warm core ring in the Gulf of Mexico. J. Geophys. Res. 89(C3): 3425-3438.
- Kirwan, A. D., Jr., W. J. Merrell, Jr., J. K. Lewis, and R. E. Whitaker, 1984b. Langrangian observations of an anticyclonic ring in the western Gulf of Mexico. J. Geophys. Res. 89(C3): 3417-3424.
- Maul, G. A., 1981. Application of GOES visible-infrared data to quantify mesoscale ocean temperatures. J. Geophys. Res. 86(C9): 8007-8021.
- McClain, E. P., 1980. Multiple atmospheric-window techniques for satellite-derived sea-surface temperatures. COSPAR/SCOR/IVCRM. Symposium on oceanography from space, Venice Italy, 26-30 May 1980, p. 20.
- McClain, E. P., W. G. Pichel, C. C. Walton, Z. Ahmad, and J. Sutton, 1983. Multichannel improvements to satellite-derived global sea-surface temperatures. Adv. Space Res. 216: 43-47.
- McGrail, D. W., and M. Carnes, 1983. Shelfedge dynamics and the nepheloid in the northwest Gulf of Mexico. In: D. J. Stanley and G. T. Moore (eds.), The Shelf Break: Critical Interface on Continental Margins. Soc. Econ. Paleo. Min. Spec. Pub. no. 33, 251-264 pp.
- Smith, N. P., 1974. Intracoastal tides of Corpus Christi Bay. Contrib. Mar. Sci. 18: 205-219.
- Strong, A. E. and E. P. McClain, 1984. Improved ocean surface temperatures - comparison with drifting buoys, Bull. Amer. Meteorol. Soc. 65(2): 138-142.

- Vukovich, F. M., 1983. An analysis of ground temperature and reflectivity patterns about St. Louis, Mo., using HCMM satellite data. *J. Climate & Appl. Meteorol.* 22(4): 560-571.
- Vukovich, F. M., 1984. A comparison of surface temperature derived from HCMM infrared measurements. *Remote Sensing of Environ.* 15: 69-76.
- Vukovich, F. M., and G. A. Maul, 1985. Cyclonic eddies in the eastern Gulf of Mexico. *J. Phys. Oceanogr.* 15(1): 105-117.
- Wyatt, P. J., G. N. Plass, and V. R. Stull, 1964a. The infrared transmittance of carbon dioxide. *J. Appl. Optics.* 3(2): 243-254.
- Wyatt, P. J., G. N. Plass, and V. R. Stull, 1964b. The infrared transmittance of water vapor. *J. Appl. Optics.* 3(2): 229-241.

IV. SYNTHESIS AND INTERPRETATION

4.1 Introduction

Presented in this chapter is a discussion of understandings and insights developed to date concerning conditions and processes associated with or resulting from circulation patterns on or adjacent to the west Florida shelf. In addition, information regarding the geometry and trajectories of previous eddies as determined from satellite thermal imagery is discussed as well as LC eddy kinematics and dynamics as deduced from motion of recent drifters' trajectories. As indicated previously, subsurface current measurements and western Gulf imagery and drifter trajectories are being investigated as part of ongoing program tasks.

4.2 Lagrangian Drifters

4.2.1 Introduction

In this section, the results of work with Lagrangian drifters are discussed and interpreted in terms of the processes and conditions important to being able to predict the speed and direction of movement of rings in the Gulf of Mexico. What answers this work provides as well as what remains to be determined are also discussed.

4.2.2 Analysis of Trajectories and Sea-Surface Temperatures

4.2.2.1 Water Temperature Data

Loop Current Ring 3374 was surveyed by the M/V E. M. QUEENY SOOP cruise on 31 August and 1 September 1982. Figure 4.2-1 shows the cruise track and Figure 4.2-2 shows the temperature structure from the XBT sampling. The ring is indicated by the the isotherm depression at Station 2 (89.5°W). The 22°C isotherm along the transect has a maximum depth of 160 m. A survey on 18 December 1982 showed a 22°C isotherm depth of 200 m.

The Loop Current extension that eventually became Ring 3350 was surveyed by the M/V NORDIC WASA SOOP cruise on 7-8 January 1984. The cruise track is shown in Figure 4.2-3 and the temperature structure is presented in Figure 4.2-4. The center of the extension is near Station 11 (26°N) and the maximum depth of the 22°C isotherm is ~215 m.

During the deployment of the buoy in Ring 3350, XBT data were collected on 21-23 April 1984 at Stations 1-38 shown in Figure 4.2-5. The ring's thermal structure is shown in Figure 4.2-6, with the 22°C isotherm being only 110 m at its deepest (Station 30). These and the data in Figure 4.2-3 indicate that the ring had decayed substantially over the approximately 4-month period.

During the period that Buoy 3375 was deployed, the National Environmental Satellite Data and Information Service (NESDIS) began producing an experimental isotherm contour chart for the entire Gulf of Mexico. Sea-surface temperature observations for a week were objectively analyzed by a weighted averaging scheme to produce a grid point SST field at each 1/8° latitude-longitude (14 km) intersection. The general patterns of these

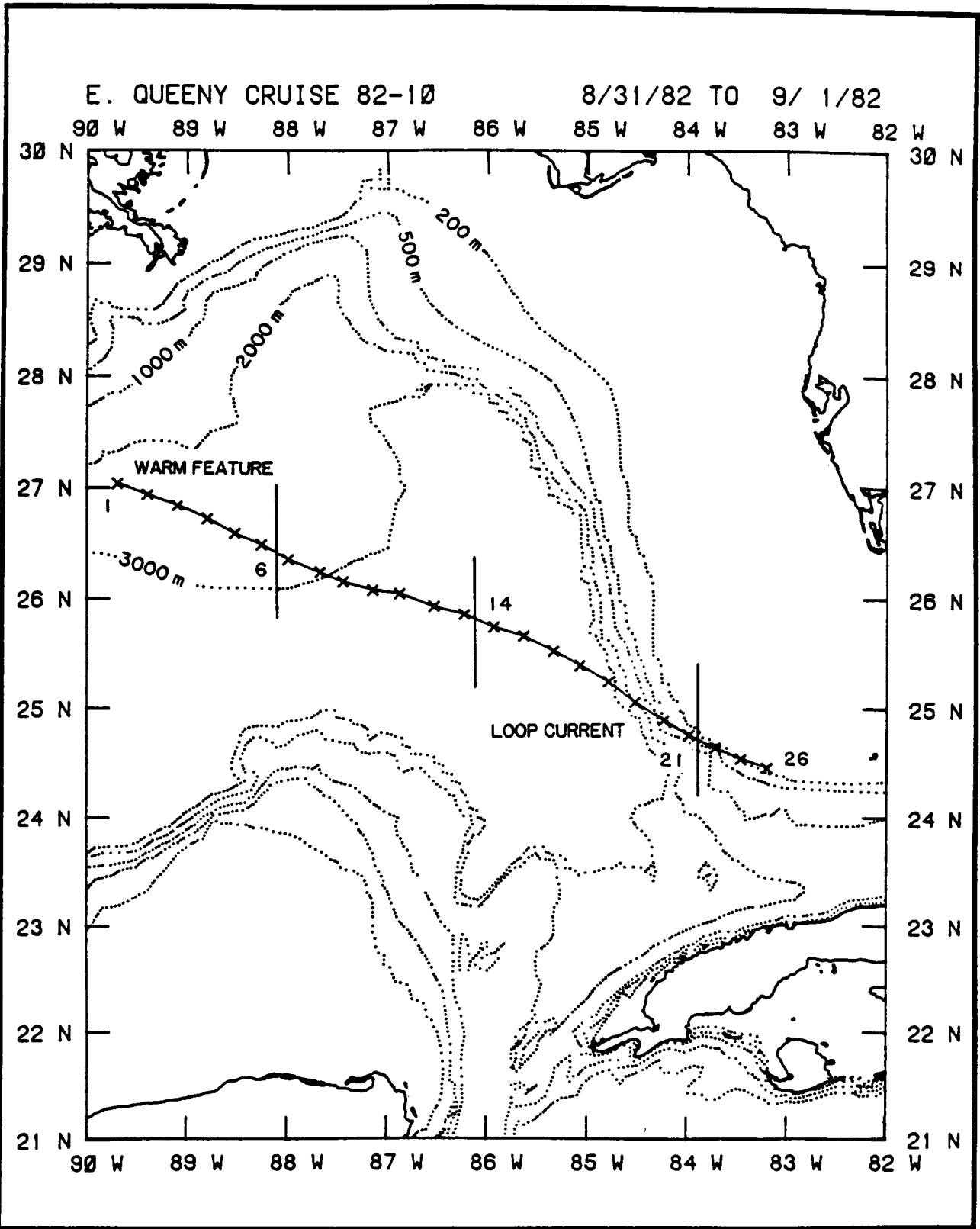


Figure 4.2-1. Transect of the E. M. QUEENY Ship-of-Opportunity cruise which surveyed Ring 3374. Sampling by XBT's is indicated by x's.

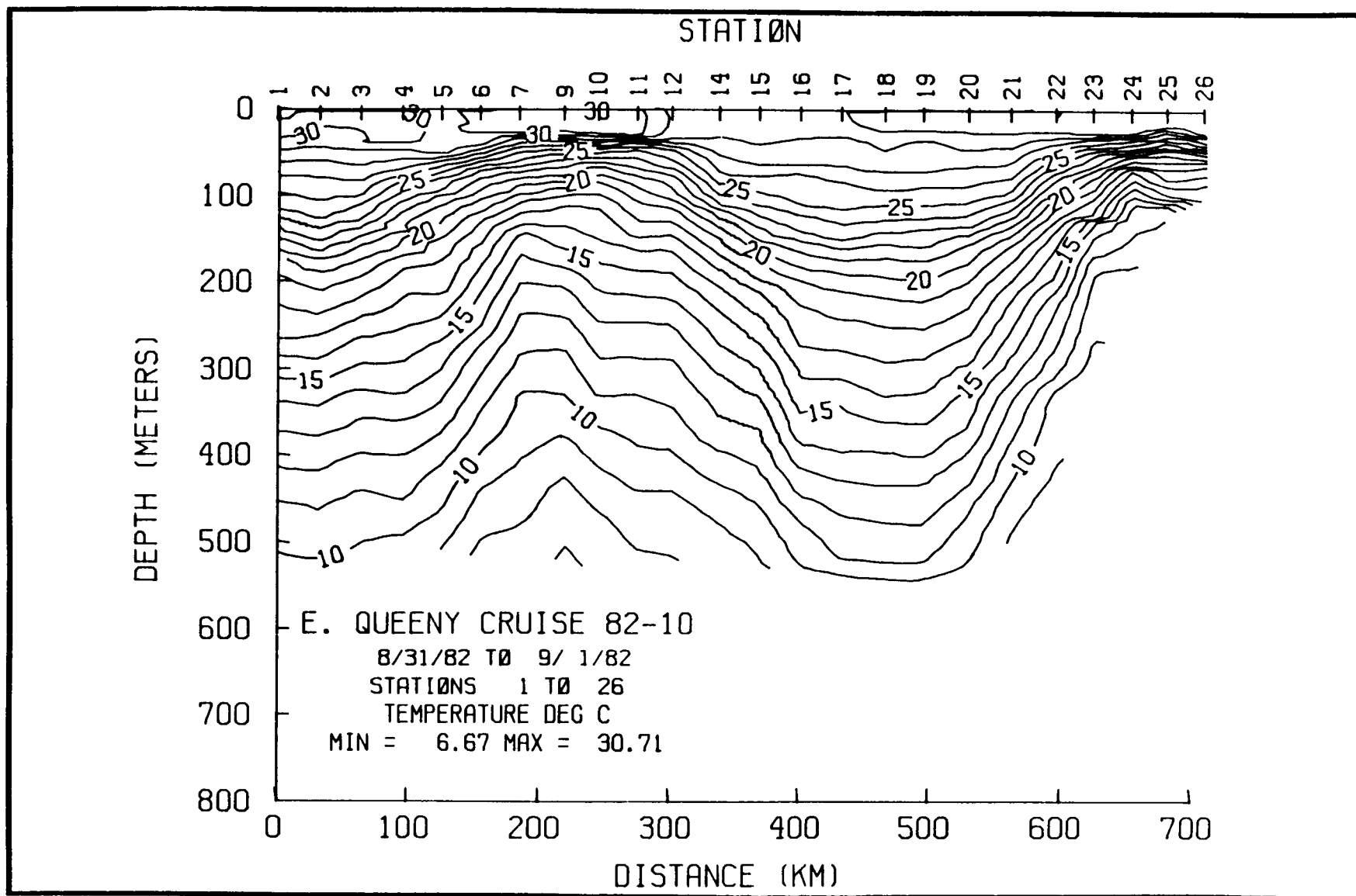


Figure 4.2-2. Vertical temperature structure of Ring 3374 from the transect shown in Figure 4.2-1.

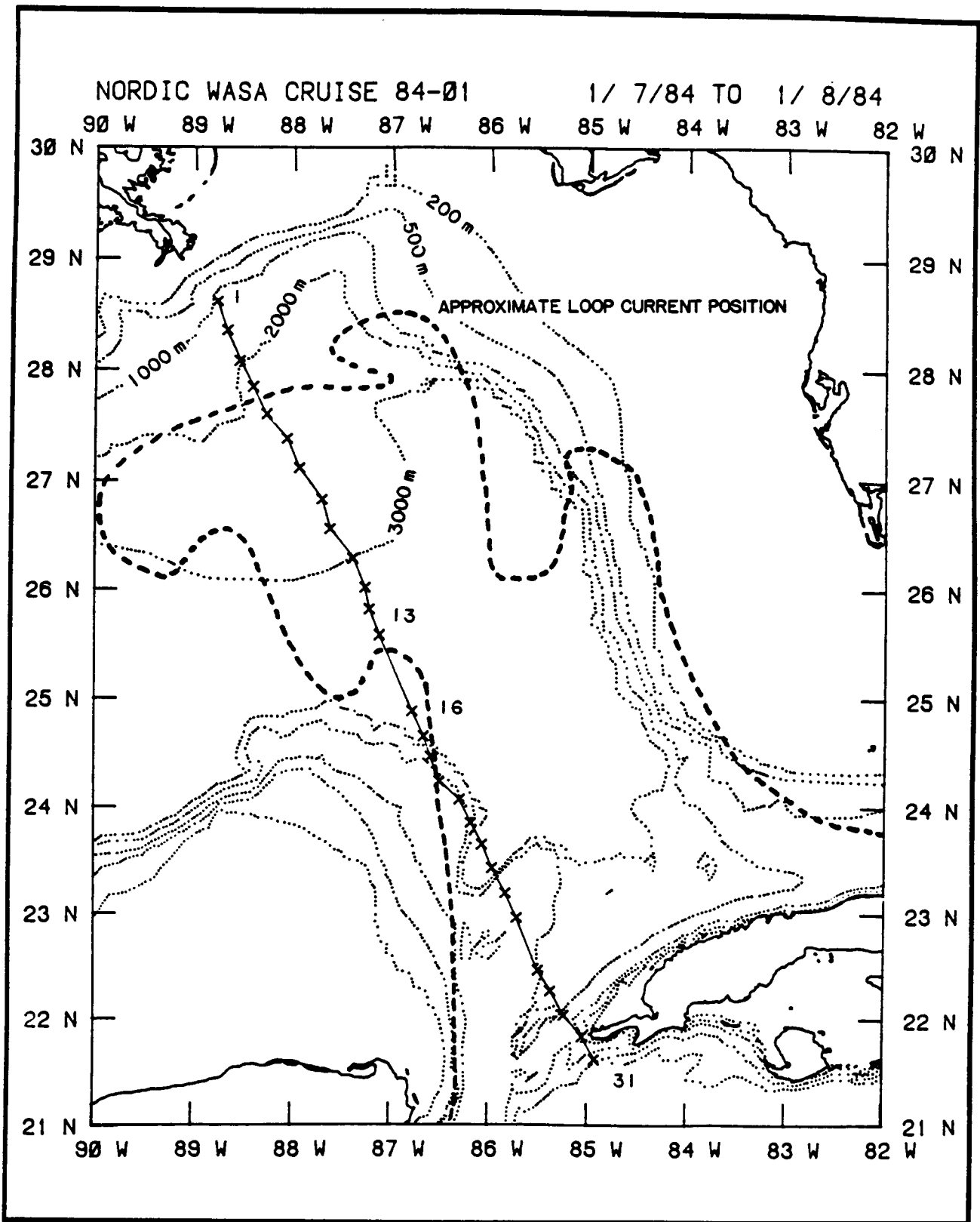


Figure 4.2-3. Transect of the M/V NORDIC WASA Ship-of-Opportunity cruise which surveyed the Loop Current extension that became Ring 3350. Sampling by XBT's is indicated by x's.

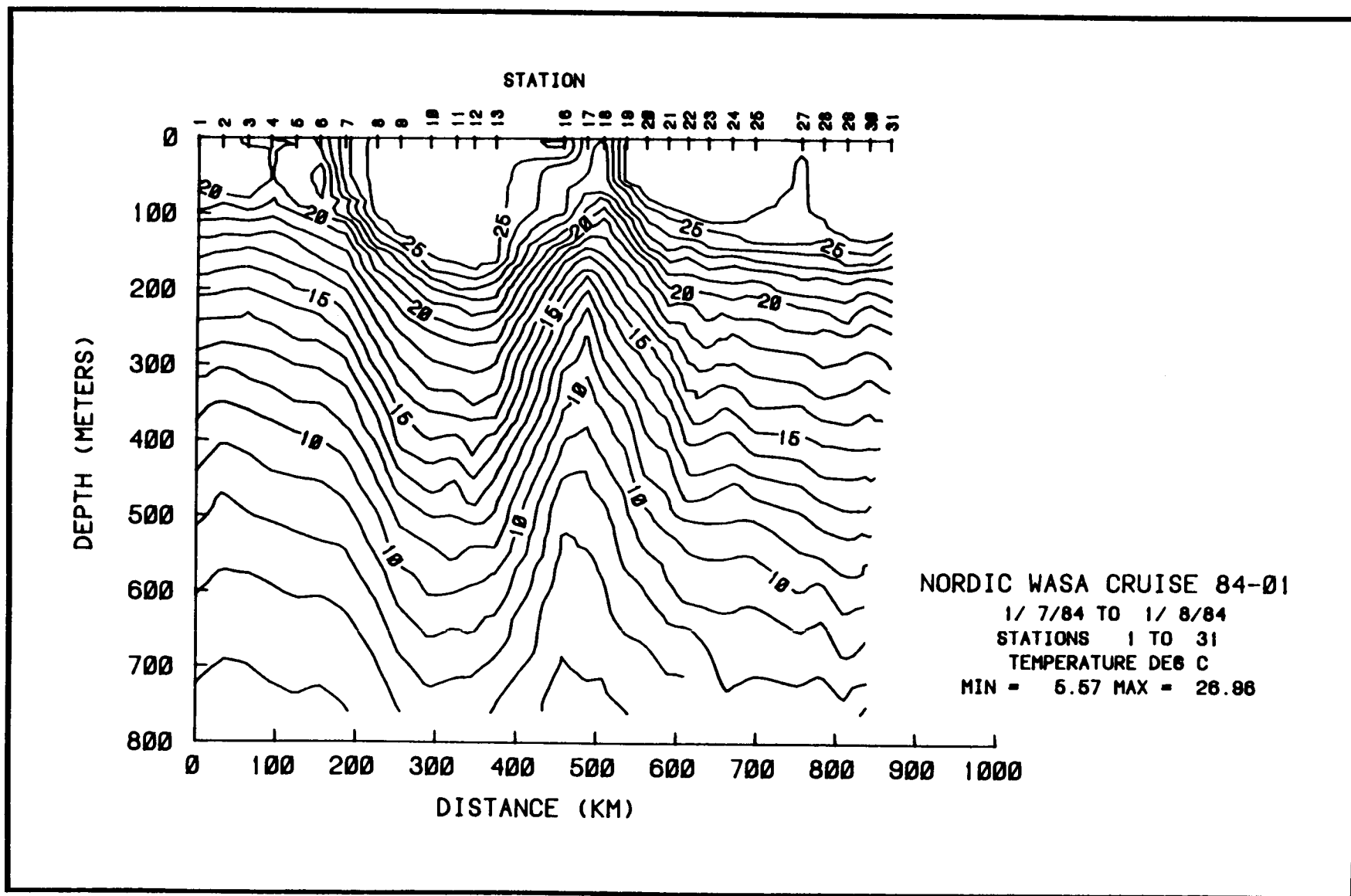


Figure 4.2-4. Vertical temperature structure of the Loop Current extension that became Ring 3350 from the transect shown in Figure 4.2-3.

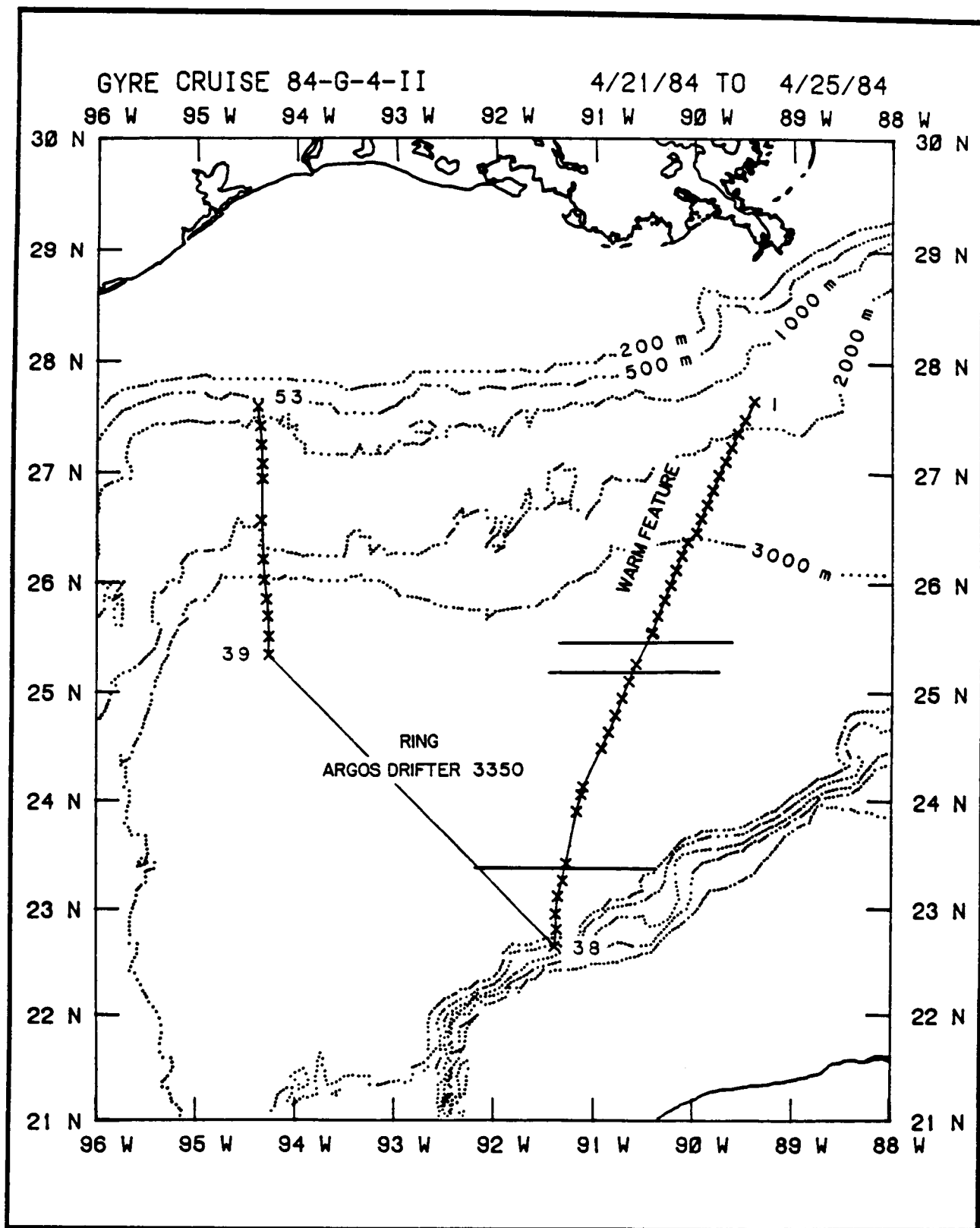


Figure 4.2-5. Transect of the buoy deployment cruise which sampled Ring 3350. Sampling of XBT's is indicated by x's.

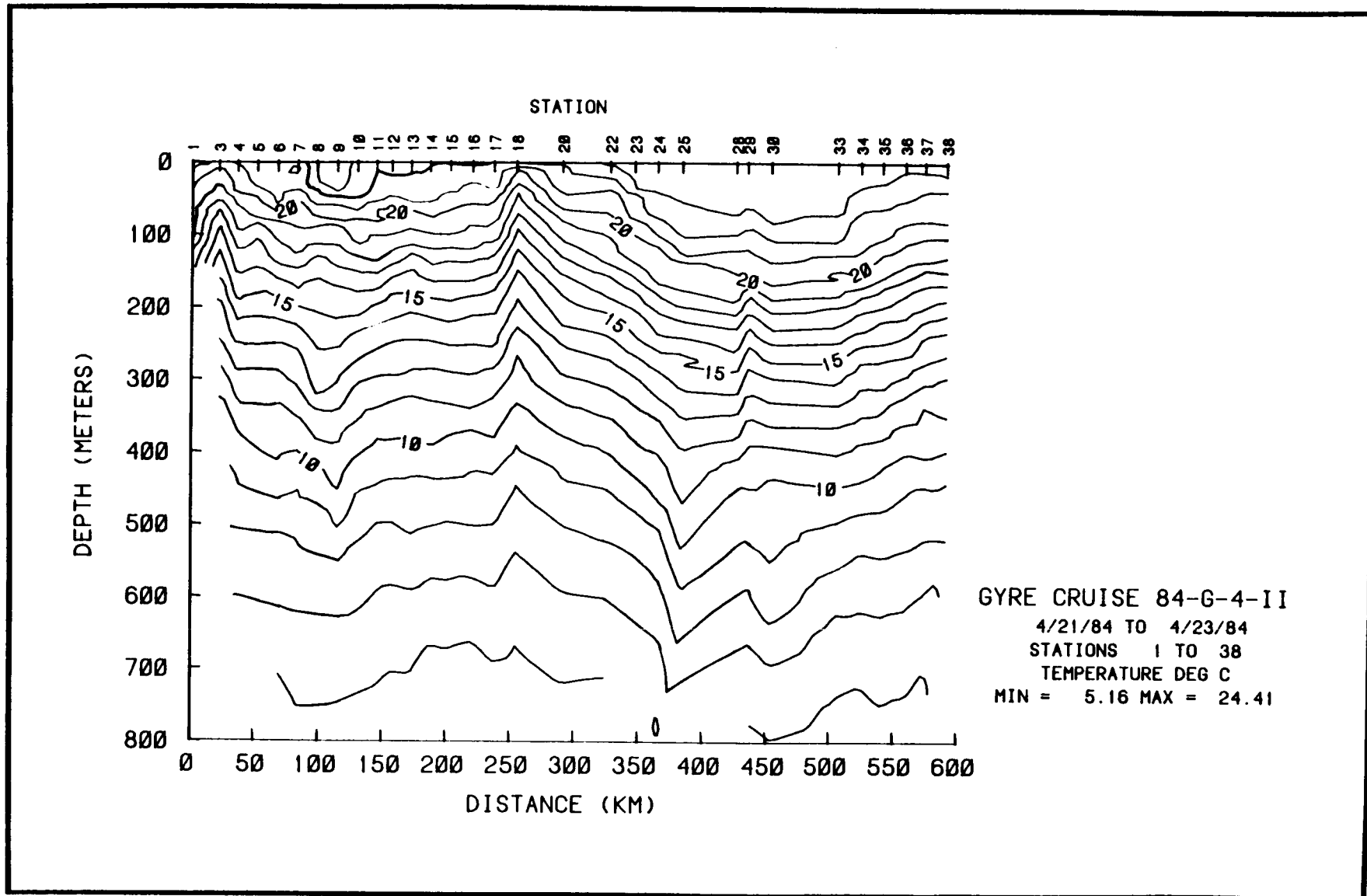


Figure 4.2-6. Vertical temperature structure of Ring 3350 from the transect shown in Figure 4.2-5.

experimental SST analyses are discussed here in terms of the anticyclonic movement of Buoy 3375.

Figure 4.2-7 shows a smoothed version of the SST composite for 7 days before 8 November 1983 along with the trajectory for the same 7 days for Drifter 3375. The drifter was moving eastward along the southern edge of a relatively cool tongue of 26°C water. The Loop Current was extended to 27°N and was intact. The composite of 15 November 1983 (Figure 4.2-8) shows the drifter heading south with a tongue of 26°C water pointing in the direction of the trajectory. The Loop Current appears somewhat convoluted, and cooler water was found along the coast of Mexico. The 22 November 1983 composite (Figure 4.2-9) shows the drifter moving westward, with the 26°C isotherm moving toward the Mexican coast and then northward. This pattern continued as shown in the 29 November 1983 composite (Figure 4.2-10). The Loop Current appeared less convoluted at these times.

These four composite periods showed an intrusion of relatively cool water offshore from the Louisiana shelf. By the 29 November 1983 composite, the tongue of 25°C water had reached southward to 25°N, and an anticyclonic feature (B) with a center at 26.5°N and 93.5°W is indicated. As will be show, this feature later joined with waters further south.

The 11 December 1983 composite (Figure 4.2-11) shows the drifter moving north and east along a tongue of 25°C water. The Loop Current appears to be in the process of pinching off a ring and the intrusion of cooler water off Louisiana resulted in 24°C water reaching down to 25.5°N. The 18 December 1983 composite (Figure 4.2-12) indicates the near-shedding of a ring by the Loop Current, and that the intrusion of cool water off Louisiana resulted in 23°C water near 26°N. Finally, note that the drifter had completed one anticyclonic rotation since the 8 November 1983 composite (Figure 4.2-7).

The SST composite of 25 December 1983 (Figure 4.2-13) shows the drifter heading south in a tongue of 25°C water. The Loop Current appears quite convoluted and a tongue of cooler water still intrudes from the Louisiana coast. In two weeks (Figure 4.2-14), the drifter headed west and north, with the Loop Current reaching to 90°W. Note a tongue of 22°C water off Louisiana reaching southward to 26°N. The composite of ±5 January 1984 (Figure 4.2-15) shows the drifter heading northward along the west side of a 23°C tongue of water that stretches all the way to 27°N, apparently connecting with the anticyclonic feature noted previously at 26.5°N. This indicates the merging of the anticyclonic feature, (A) which the drifter had been circling, with the more northerly anticyclone (B). After another two week period, the drifter is still seen to be heading north and east along the west side of a tongue of 22°C water (Figure 4.2-16). It also shows that the Loop Current had completely shed a new ring (Ring 3350), and the intrusion of colder water off the Louisiana coast was less pronounced. The 5 February 1984 SST composite indicates that the new Loop Current Ring 3350 can be defined by the 24°C sea-surface isotherm (Figure 4.2-17). Drifter 3375 headed east and then turned south during the seven days prior to 5 February 1984. The 12 February 1984 composite (Figure 4.2-18) shows the drifter heading south along the western edge of a 22°C tongue of water. Ring 3350 is much better organized. However, the 19 February 1984 SST composite shows no well-defined signature of this ring at the 1°C temperature contour interval (Figure 4.2-19).

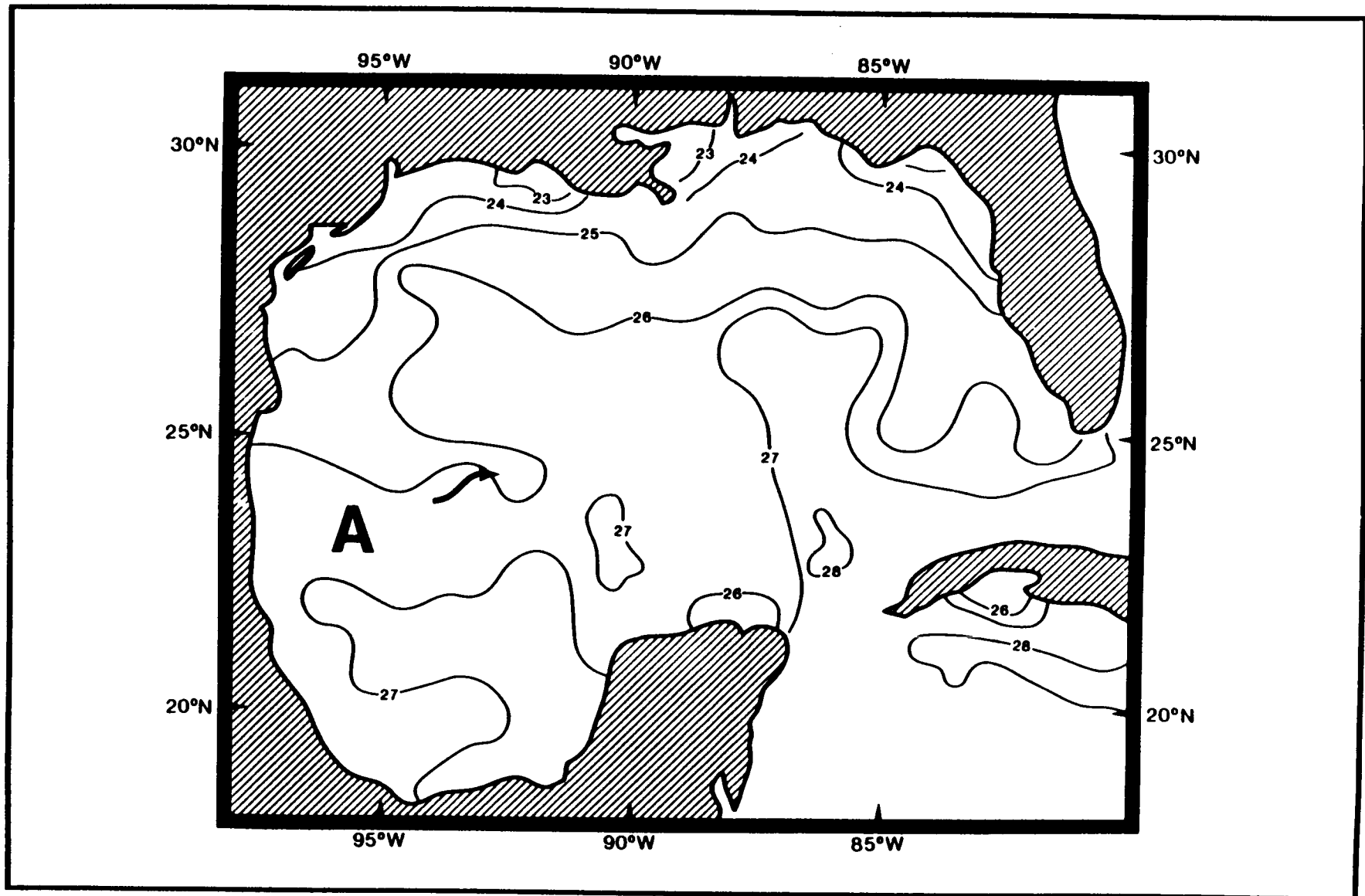


Figure 4.2-7. Sea-surface temperature ($^{\circ}\text{C}$) for 8 November 1983 from the 14-km charts produced by NESDIS. The corresponding trajectory of Drifter 3375 is shown by the dark arrow. The letter A represents the inferred location of Ring 3374.

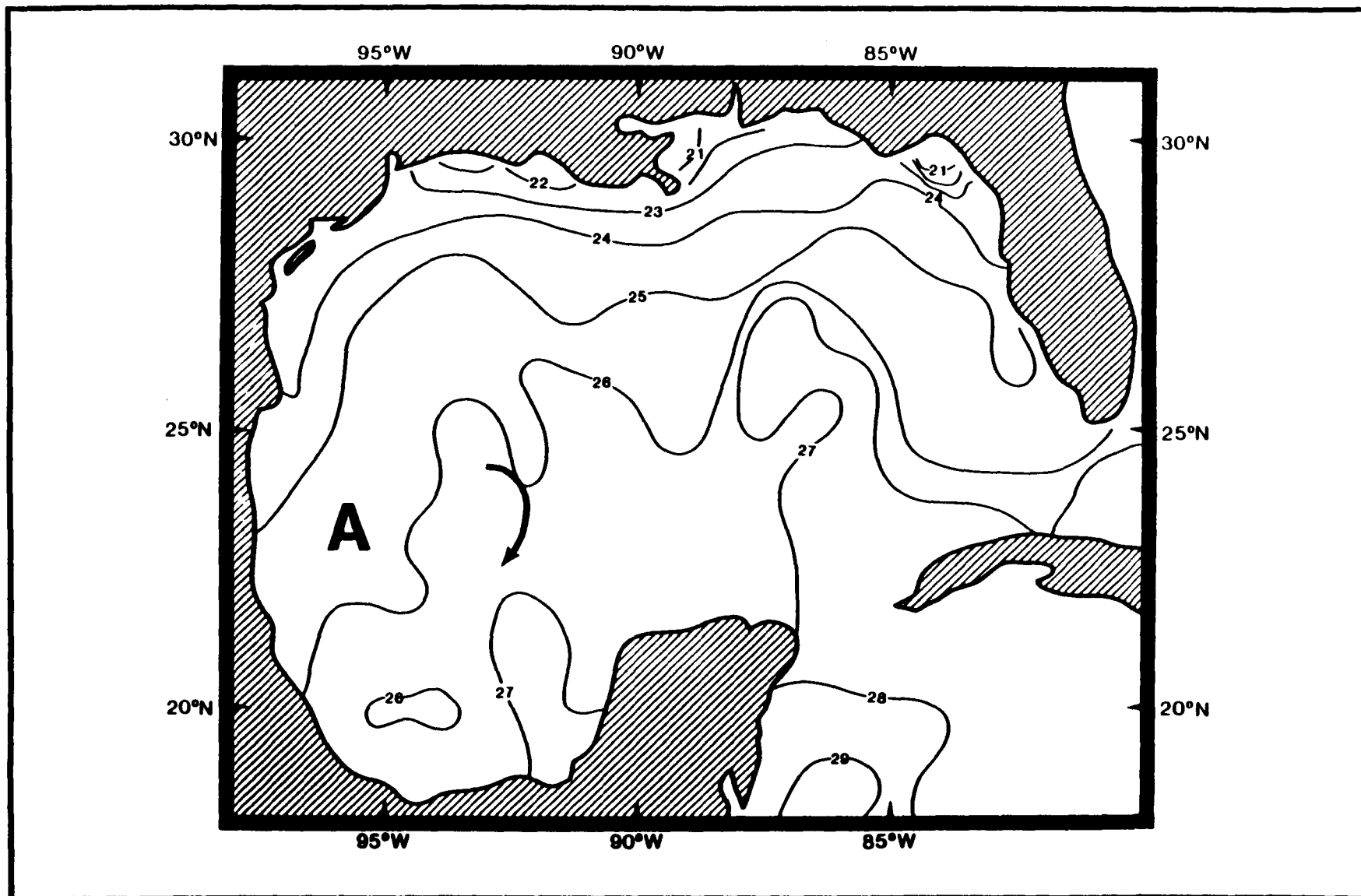


Figure 4.2-8. Sea-surface temperature ($^{\circ}\text{C}$) for 15 November 1983 from the 14-km charts produced by NESDIS. The corresponding trajectory of Drifter 3375 is shown by the dark arrow. The letter A represents the inferred location of Ring 3374.

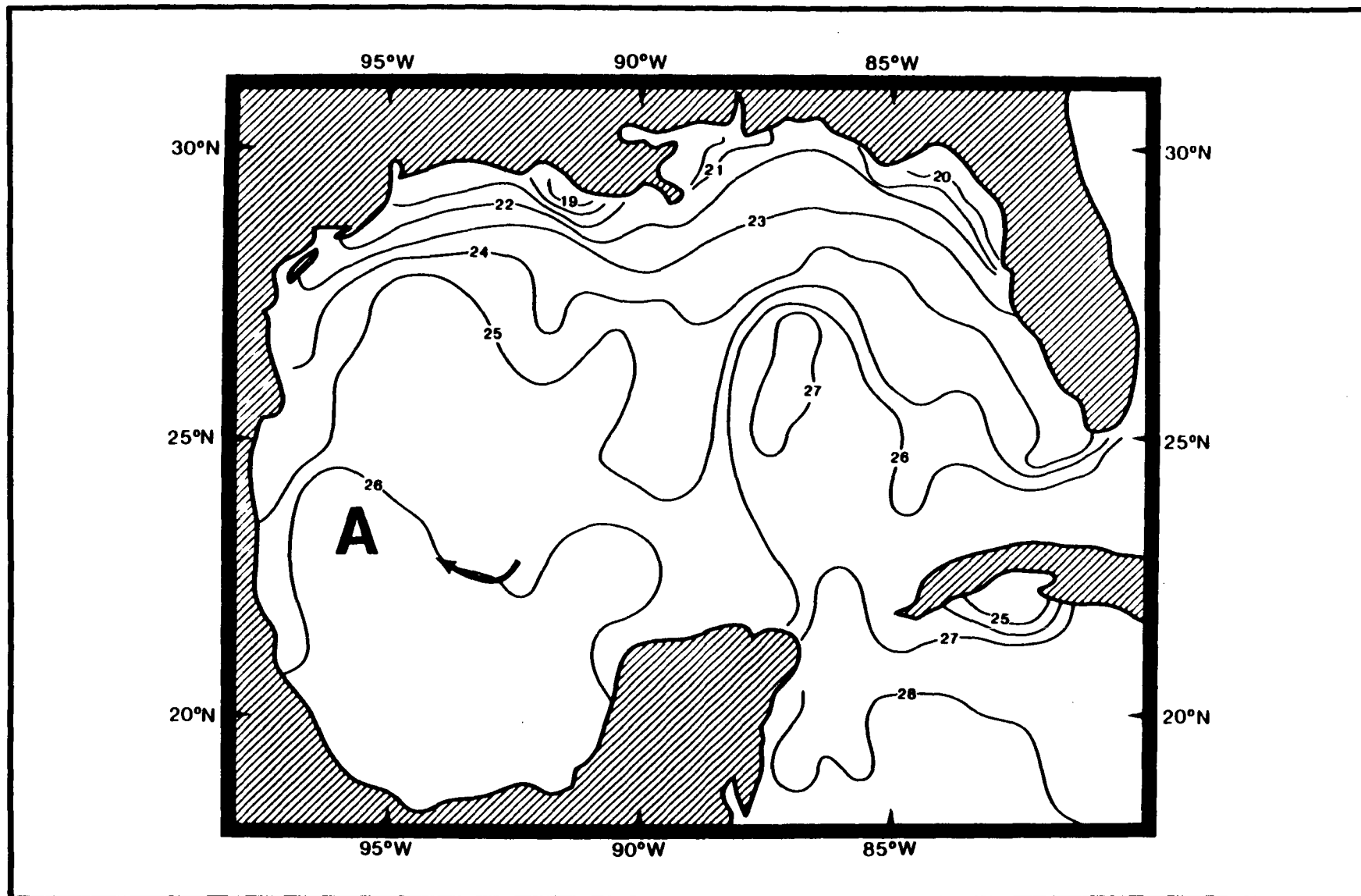


Figure 4.2-9. Sea-surface temperature ($^{\circ}\text{C}$) for 22 November 1983 from the 14-km charts produced by NESDIS. The corresponding trajectory of Drifter 3375 is shown by the dark arrow. The letter A represents the inferred location of Ring 3374.

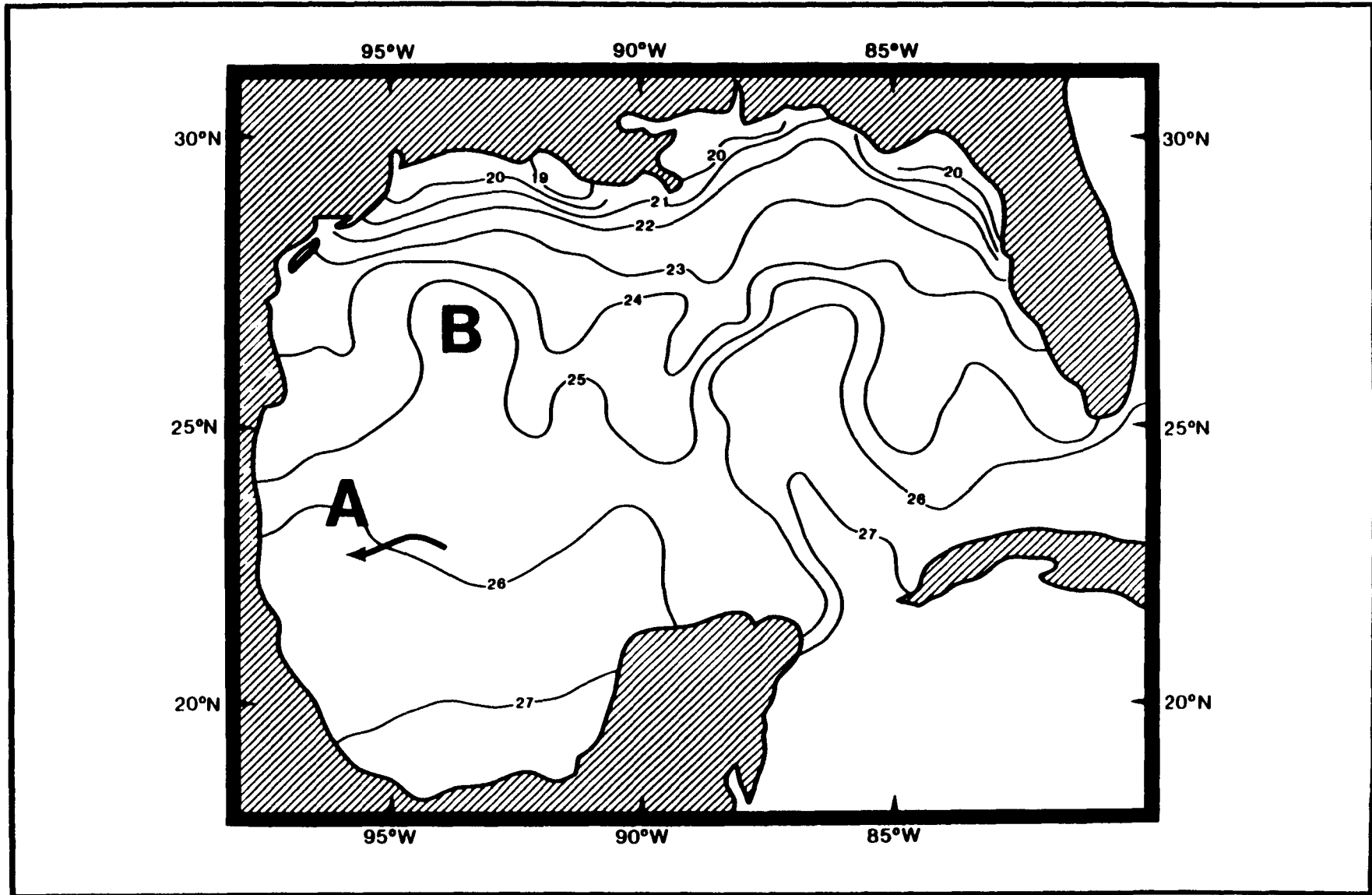


Figure 4.2-10. Sea-surface temperature ($^{\circ}\text{C}$) for 29 November 1983 from the 14-km charts produced by NESDIS. The corresponding trajectory of Drifter 3375 is shown by the dark arrow. The letters A and B represent the inferred locations of Ring 3374 and a more northerly anticyclone, respectively.

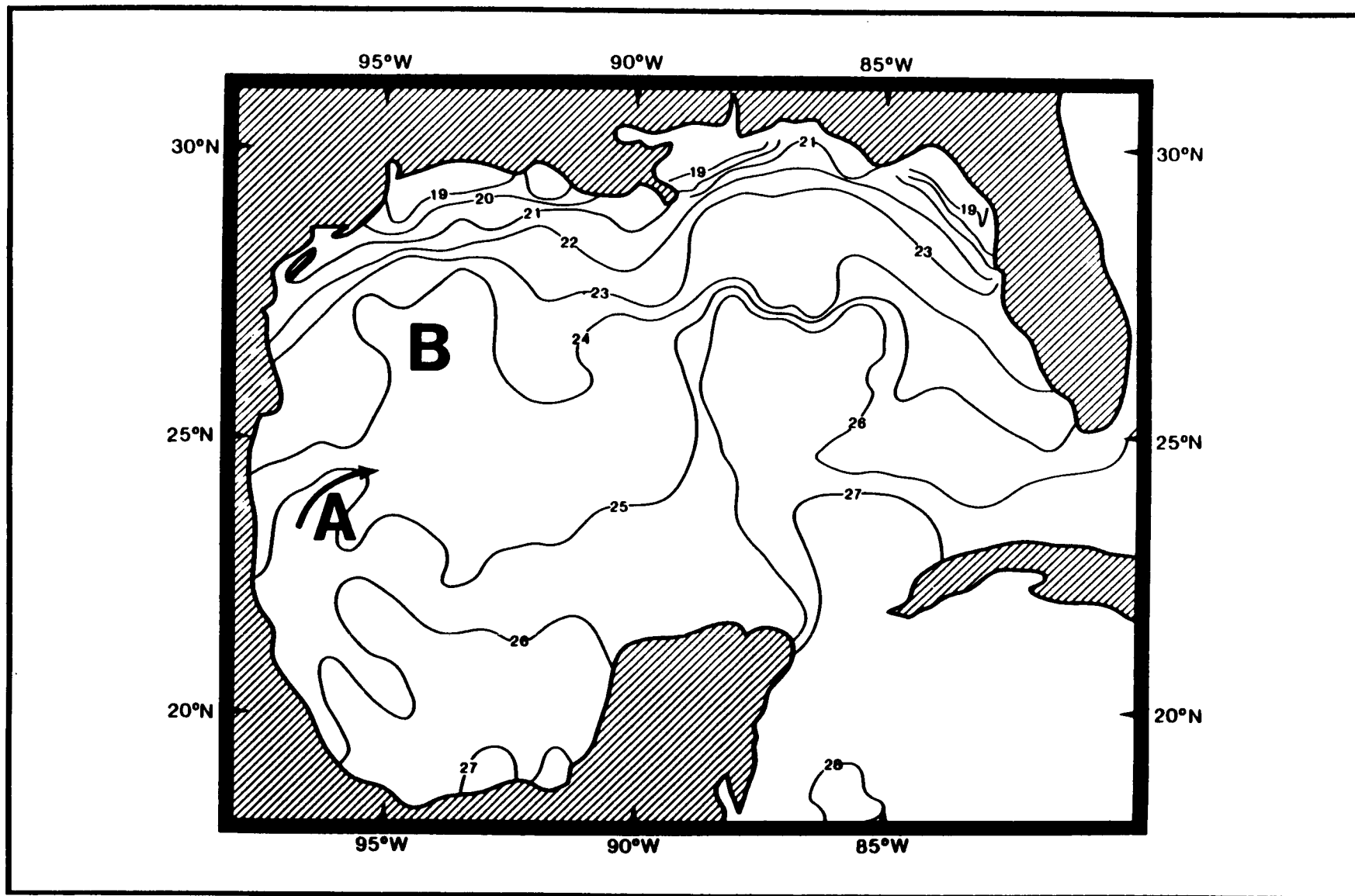


Figure 4.2-11. Sea-surface temperature ($^{\circ}\text{C}$) for 11 December 1983 from the 14-km charts produced by NESDIS. The corresponding trajectory of Drifter 3375 is shown by the dark arrow. The letters A and B represent the inferred locations of Ring 3374 and a more northerly anticyclone, respectively.

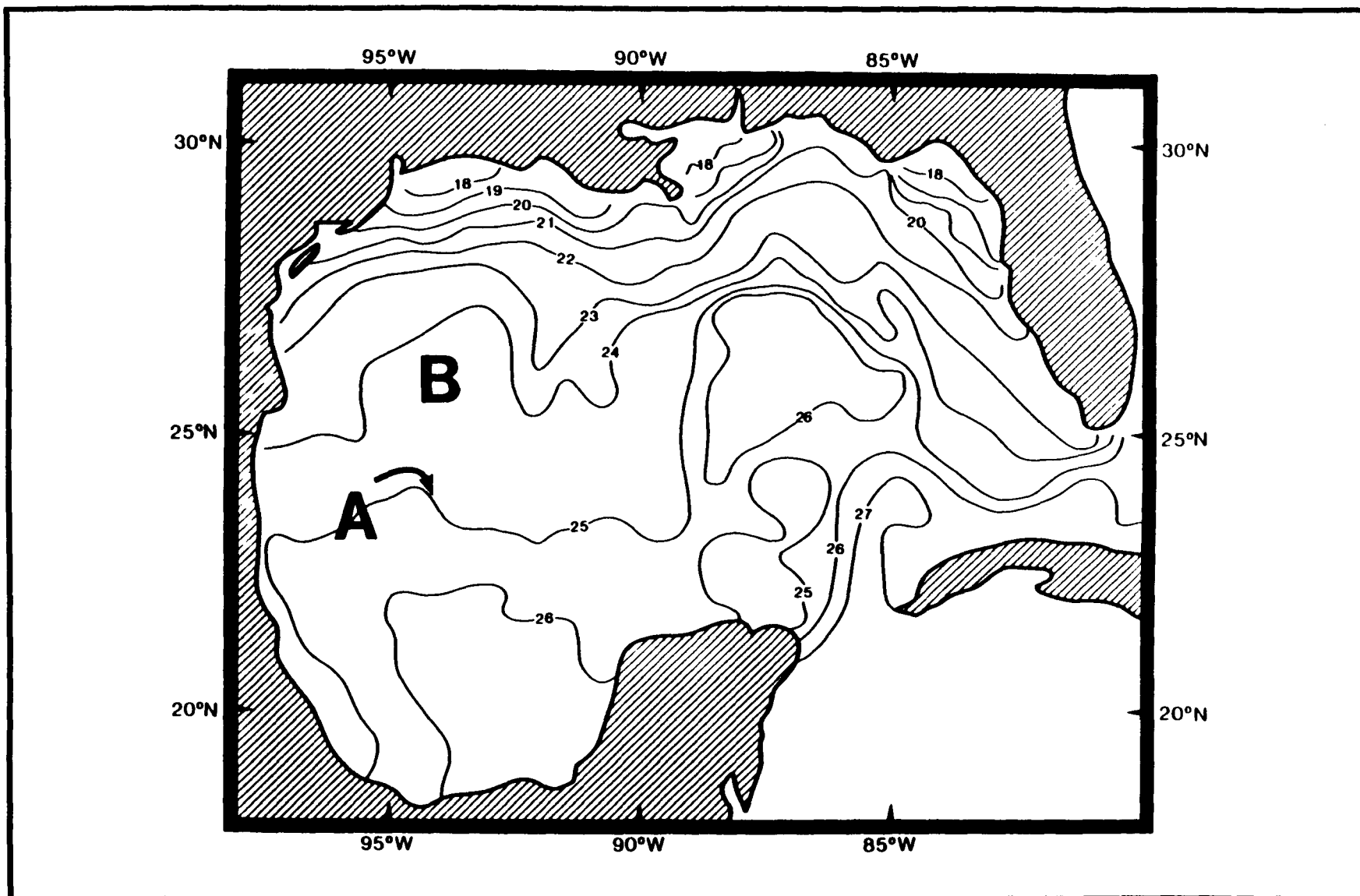


Figure 4.2-12. Sea-surface temperature ($^{\circ}\text{C}$) for 18 December 1983 from the 14-km charts produced by NESDIS. The corresponding trajectory of Drifter 3375 is shown by the dark arrow. The letters A and B represent the inferred locations of Ring 3374 and a more northerly anticyclone, respectively.

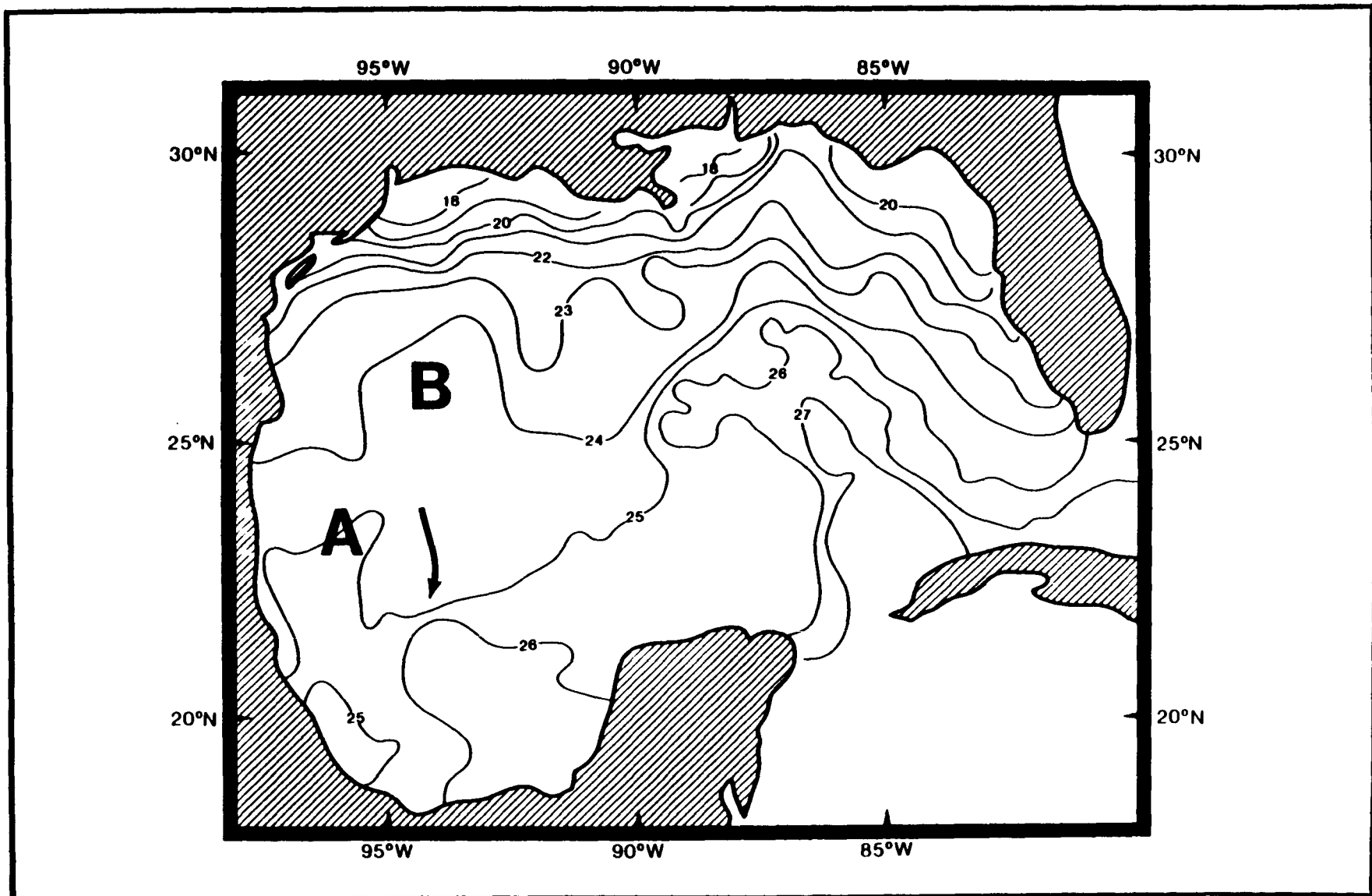


Figure 4.2-13. Sea-surface temperature ($^{\circ}\text{C}$) for 25 December 1983 from the 14-km charts produced by NESDIS. The corresponding trajectory of Drifter 3375 is shown by the dark arrow. The letters A and B represent the inferred locations of Ring 3374 and a more northerly anticyclone, respectively.

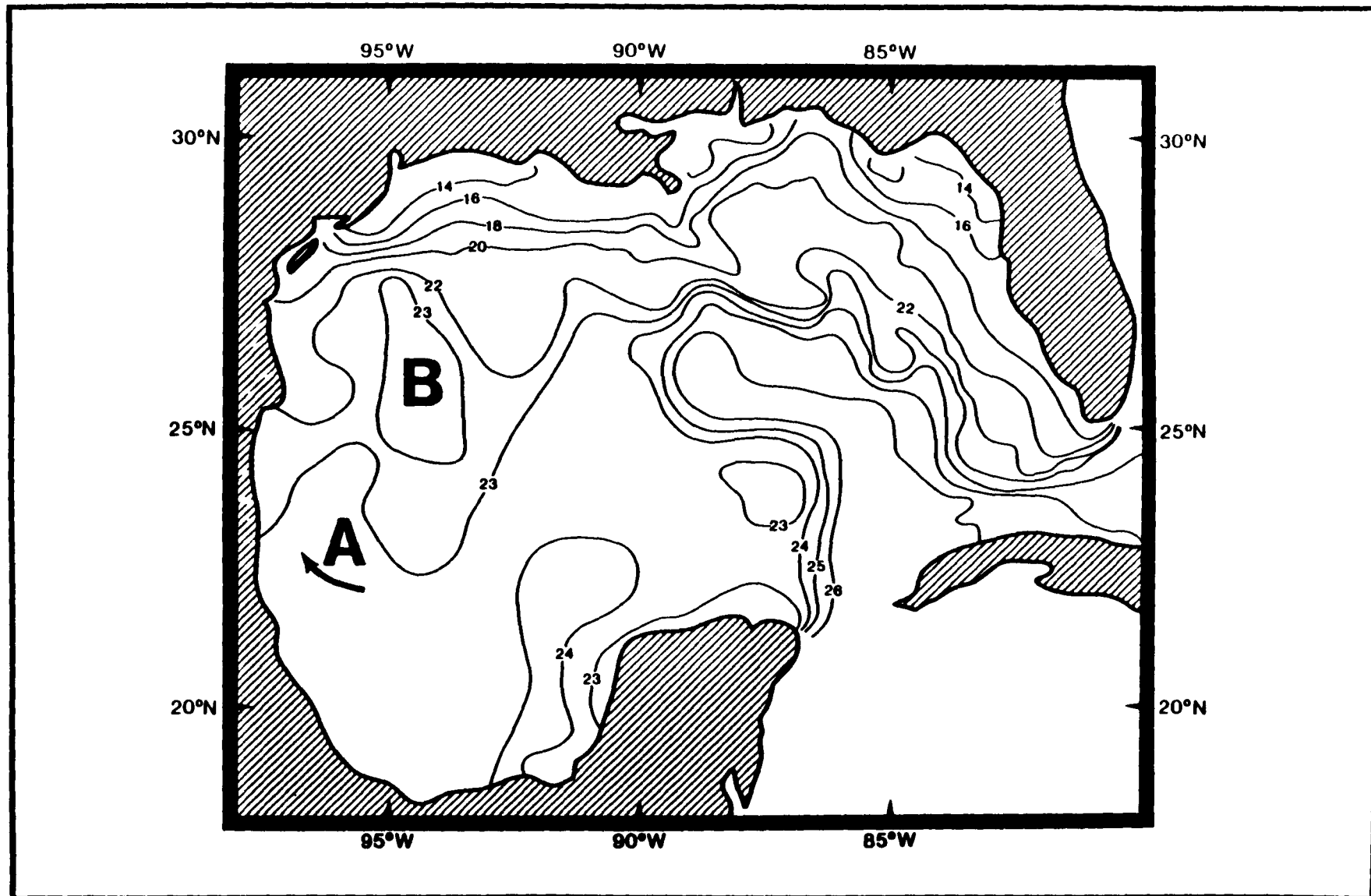


Figure 4.2-14. Sea-surface temperature ($^{\circ}\text{C}$) for 8 January 1984 from the 14-km charts produced by NESDIS. The corresponding trajectory of Drifter 3375 is shown by the dark arrow. The letters A and B represent the inferred locations of Ring 3374 and a more northerly anticyclone, respectively.

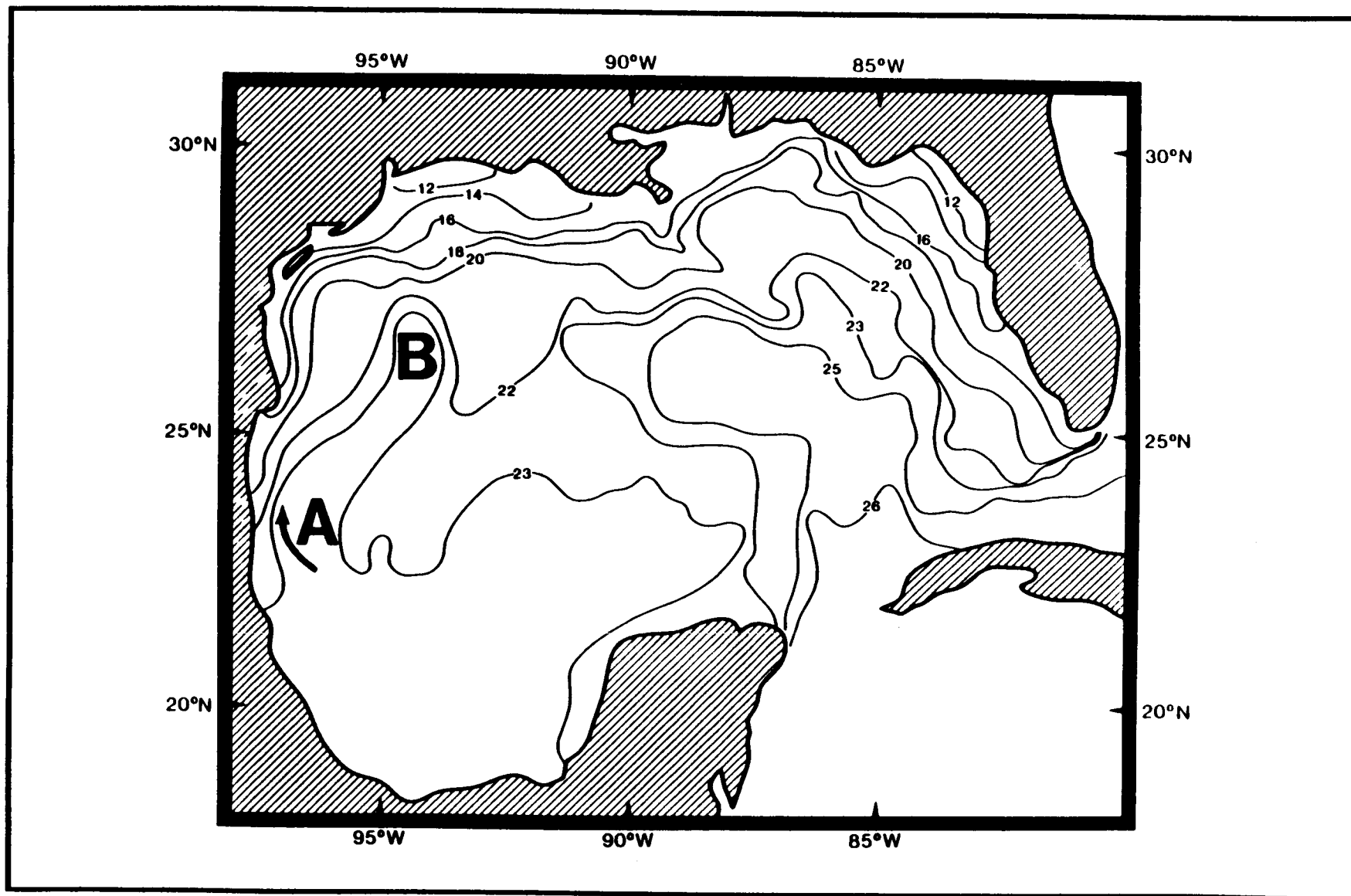


Figure 4.2-15. Sea-surface temperature ($^{\circ}\text{C}$) for 15 January 1984 from the 14-km charts produced by NESDIS. The corresponding trajectory of Drifter 3375 is shown by the dark arrow. The letters A and B represent the inferred locations of Ring 3374 and a more northerly anticyclone, respectively.

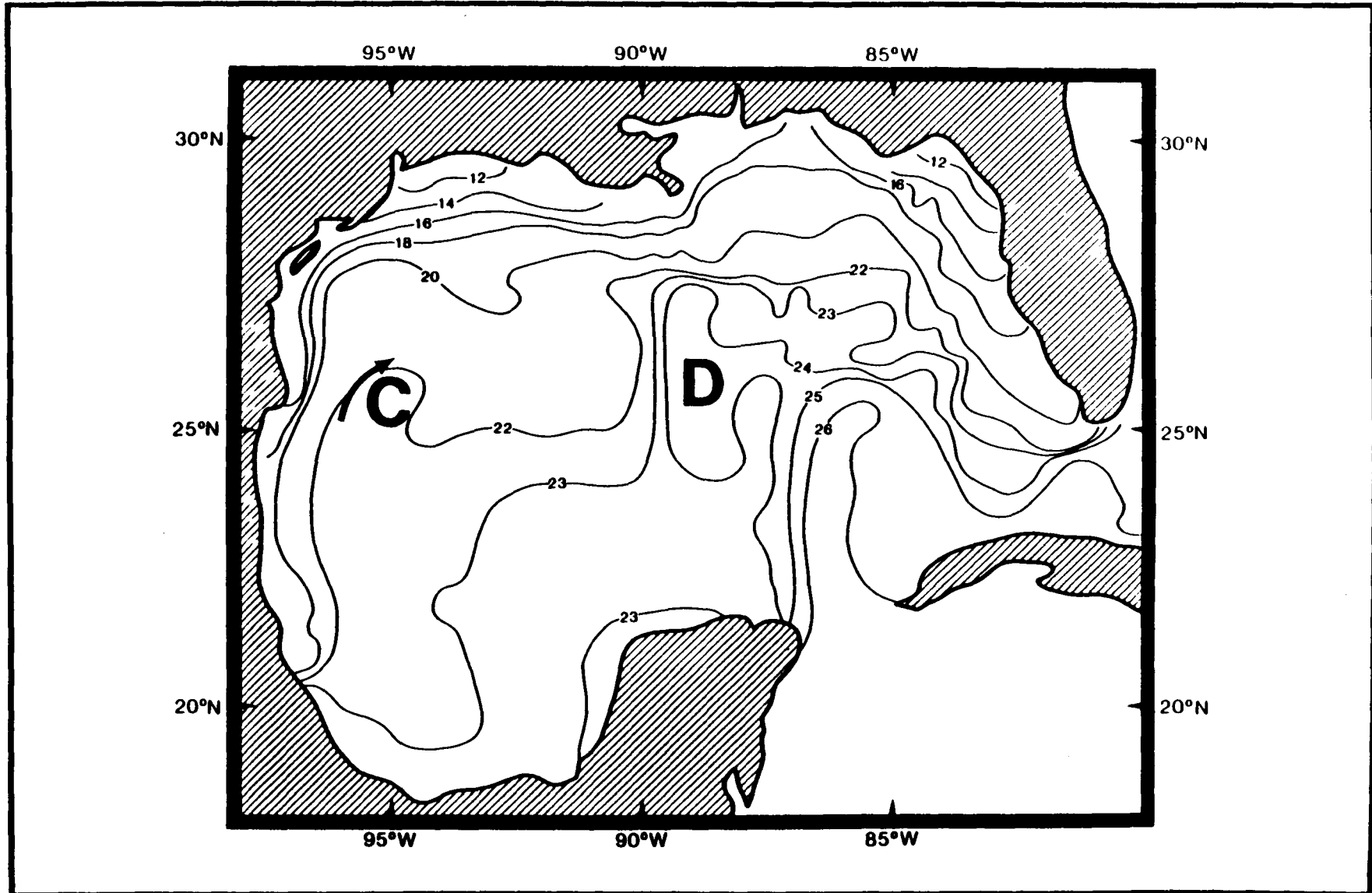


Figure 4.2-16. Sea-surface temperature ($^{\circ}\text{C}$) for 30 January 1984 from the 14-km charts produced by NESDIS. The corresponding trajectory of Drifter 3375 is shown by the dark arrow. The letters C and D represent the positions of the coalesced anticyclones and Ring 3350, respectively.

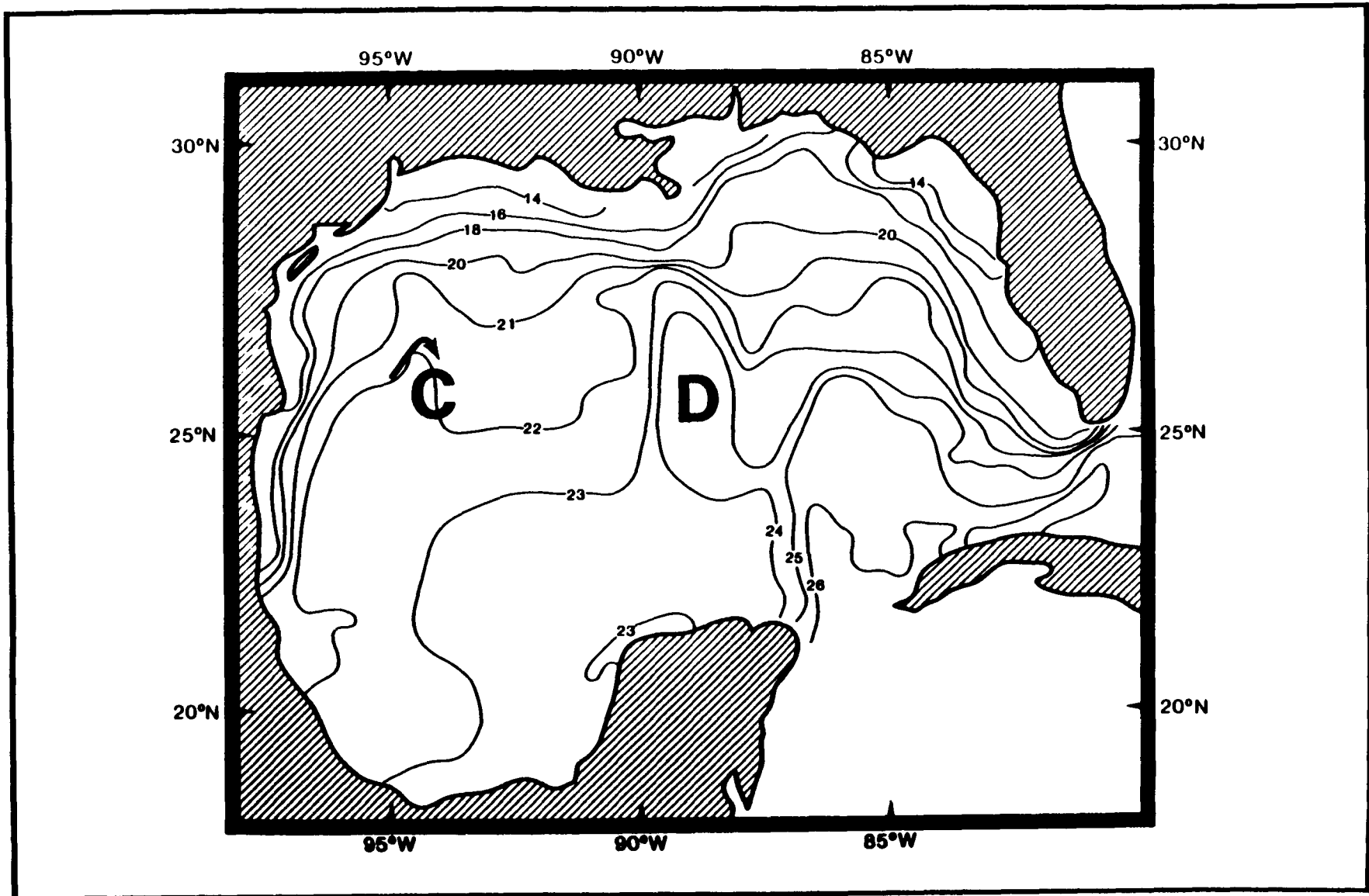


Figure 4.2-17. Sea-surface temperature ($^{\circ}\text{C}$) for 5 February 1984 from the 14-km charts produced by NESDIS. The corresponding trajectory of Drifter 3375 is shown by the dark arrow. The letters C and D represent the positions of the coalesced anticyclones and Ring 3350, respectively.

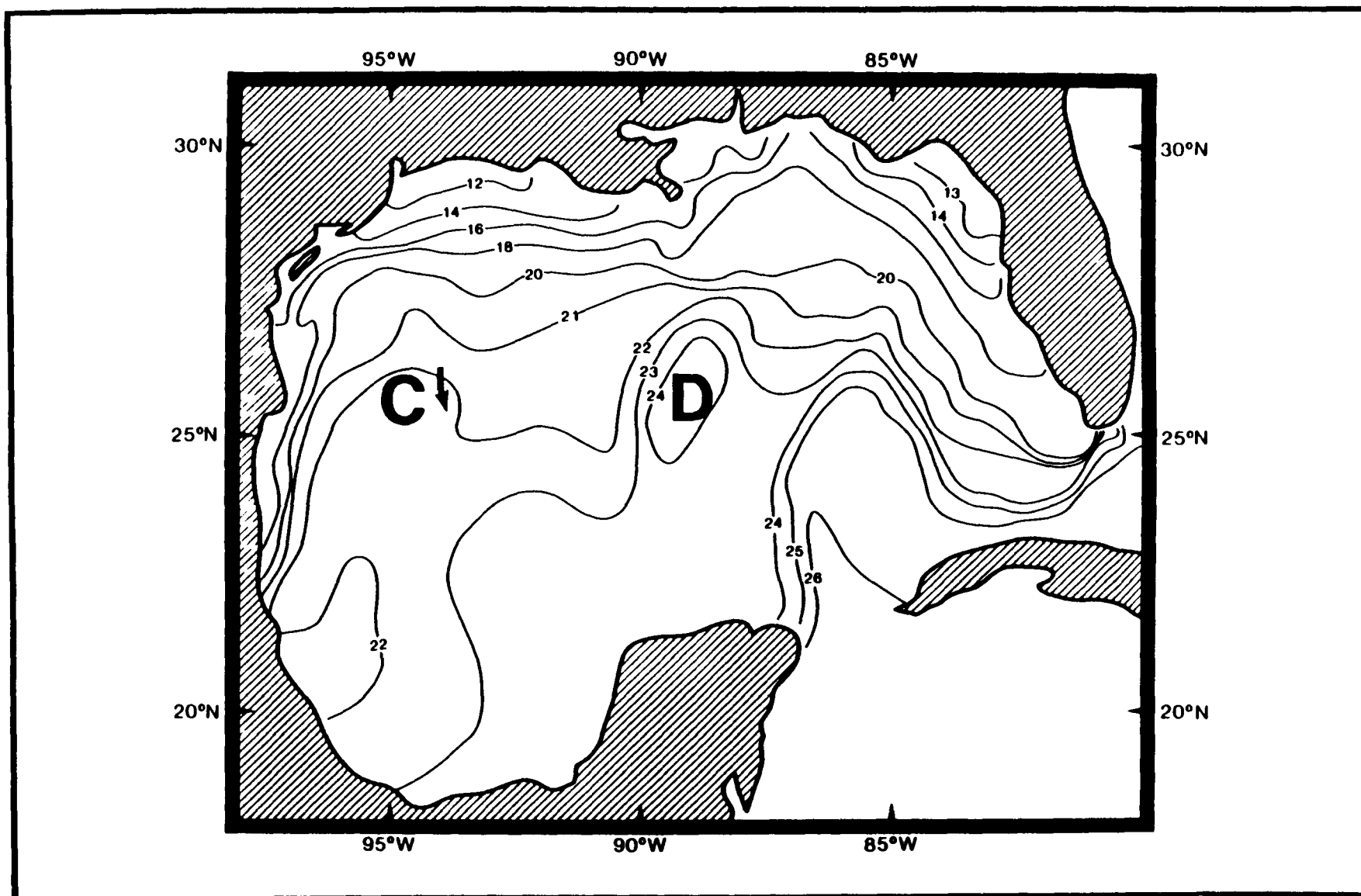


Figure 4.2-18. Sea-surface temperature ($^{\circ}\text{C}$) for 12 February 1984 from the 14-km charts produced by NESDIS. The corresponding trajectory of Drifter 3375 is shown by the dark arrow. The letters C and D represent the positions of the coalesced anticyclones and Ring 3350, respectively.

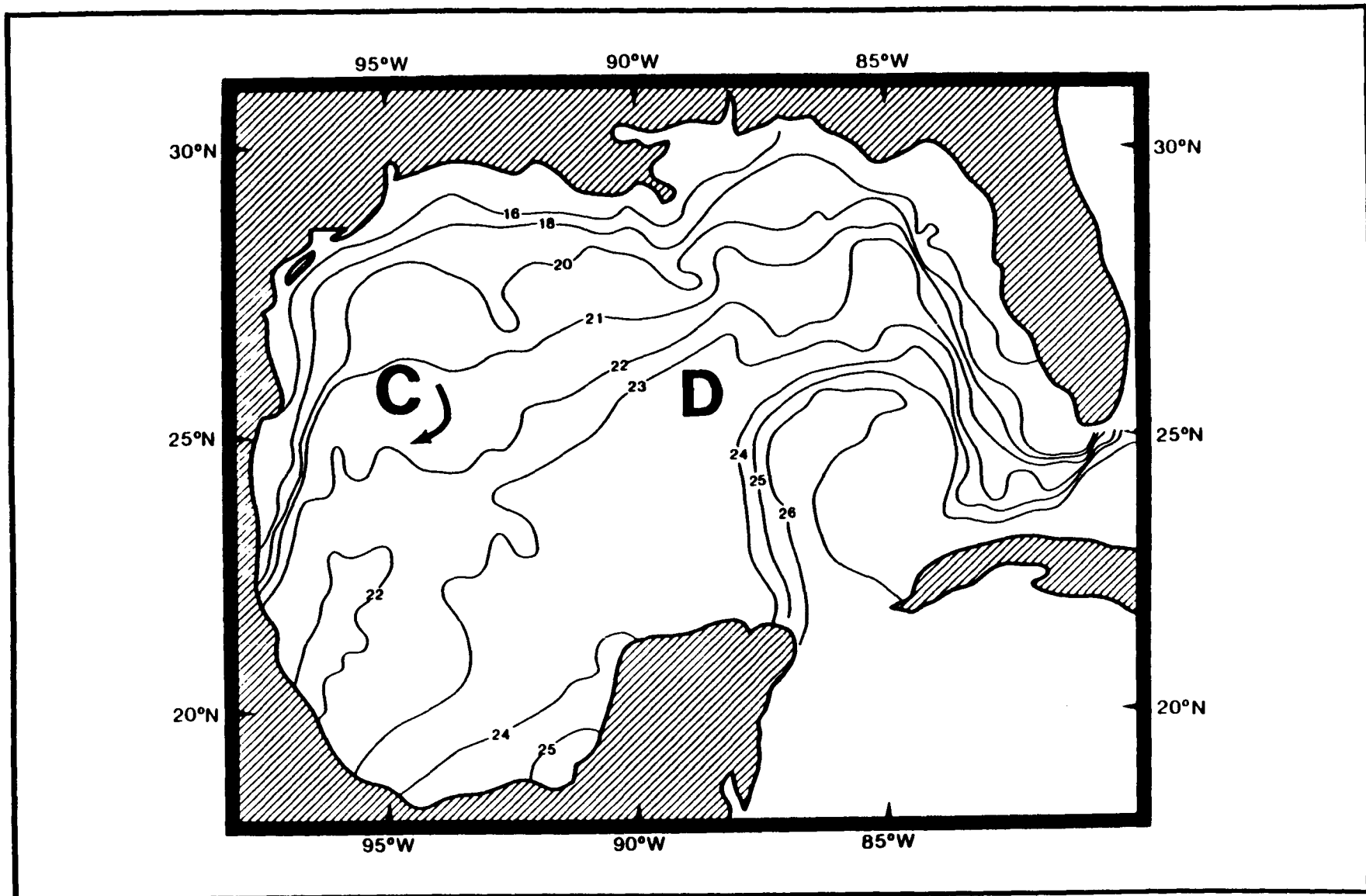


Figure 4.2-19. Sea-surface temperature ($^{\circ}\text{C}$) for 19 February 1984 from the 14-km charts produced by NESDIS. The corresponding trajectory of Drifter 3375 is shown by the dark arrow. The letters C and D represent the positions of the coalesced anticyclones and Ring 3350, respectively.

4.2.2.2 Divergence

Time histories of ring divergences with respect to the centers of the rings are shown in Figures 4.2-20 through 4.2-23. All the rings went through periods of convergence and divergence with amplitudes of the order of 10^{-5} s^{-1} . The classical concept of a decaying warm-core ring is that of a divergent mass field in the top layers of the ring. These data indicate that factors other than shearing stresses were influencing the mass field to produce periods of convergence. The divergence time history for Drifter 3375 is shown in Figure 4.2-24. This time history is quite similar to those from drifters in rings. The calculated mean divergence for all of the time histories was one to three orders of magnitude smaller than the fluctuations, essentially implying a zero net divergence.

4.2.2.3 Vorticity, Normal and Shear Deformation Rates

The time histories of ζ , N , and S for Rings 1599 and 3374 are shown in Figures 4.2-25 through 4.2-27. For these rings, vorticity is the dominant parameter, with a mean value of about $-2 \cdot 10^{-5} \text{ s}^{-1}$. For Ring 3350 (Figure 4.2-28), vorticity approached zero in two instances, implying that perhaps the drifter was seeded beyond the radius to maximum currents (i.e., beyond the region which is always dominated by the swirl of the ring). This implication is supported by the larger loops of the trajectory of Ring 3350 (Figure 2.2-4) compared to the corresponding loops of Rings 1599 and 3374 (Figure 2.2-3). This is probably the reason why the drifter left the ring.

The vorticity calculated from Drifter 3375 is shown in Figure 4.2-29. Here distinct periods of positive as well as negative vorticity, similar to Ring 3350, are seen. The negative vorticity has amplitudes of $-4 \cdot 10^{-5} \text{ s}^{-1}$, somewhat larger than the amplitudes from the rings. These data point out the tremendous effect that anticyclones have on water parcel motion in the western Gulf.

4.2.2.4 Ring Shape and Orientation

Ring eccentricity is represented by the parameter $e = X_{\text{maj}} / X_{\text{min}}$. The time histories of e along with the orientations of the major axis (angle A) are presented for Rings 1599 and 3374 in Figures 4.2-30 through 4.2-32. The 'x' marks the value of e while the dashed lines through the 'x' represent the orientation of the major axis (north is in the positive e direction and east is in the positive time direction.)

Ring 1599 was only slightly elliptical, with e having an average value of ~ 2 (Figure 4.2-30). After the ring encountered the Mexican coast, the eccentricity increased, with the average value of e being ~ 4 . The ring orientation is initially north/south, but this changes to more of an east/west orientation after approximately 25 days. However, the period encompassing days 450 through 480 shows a shift toward a north/south orientation along with an increase in e .

The eccentricity for Ring 3374 is initially not as consistent as that of Ring 1599. Figure 4.2-31 shows $e=2$ with a north/south orientation, but there are also large variations in e . After mid-March 1983 (Figure 4.2-32), the

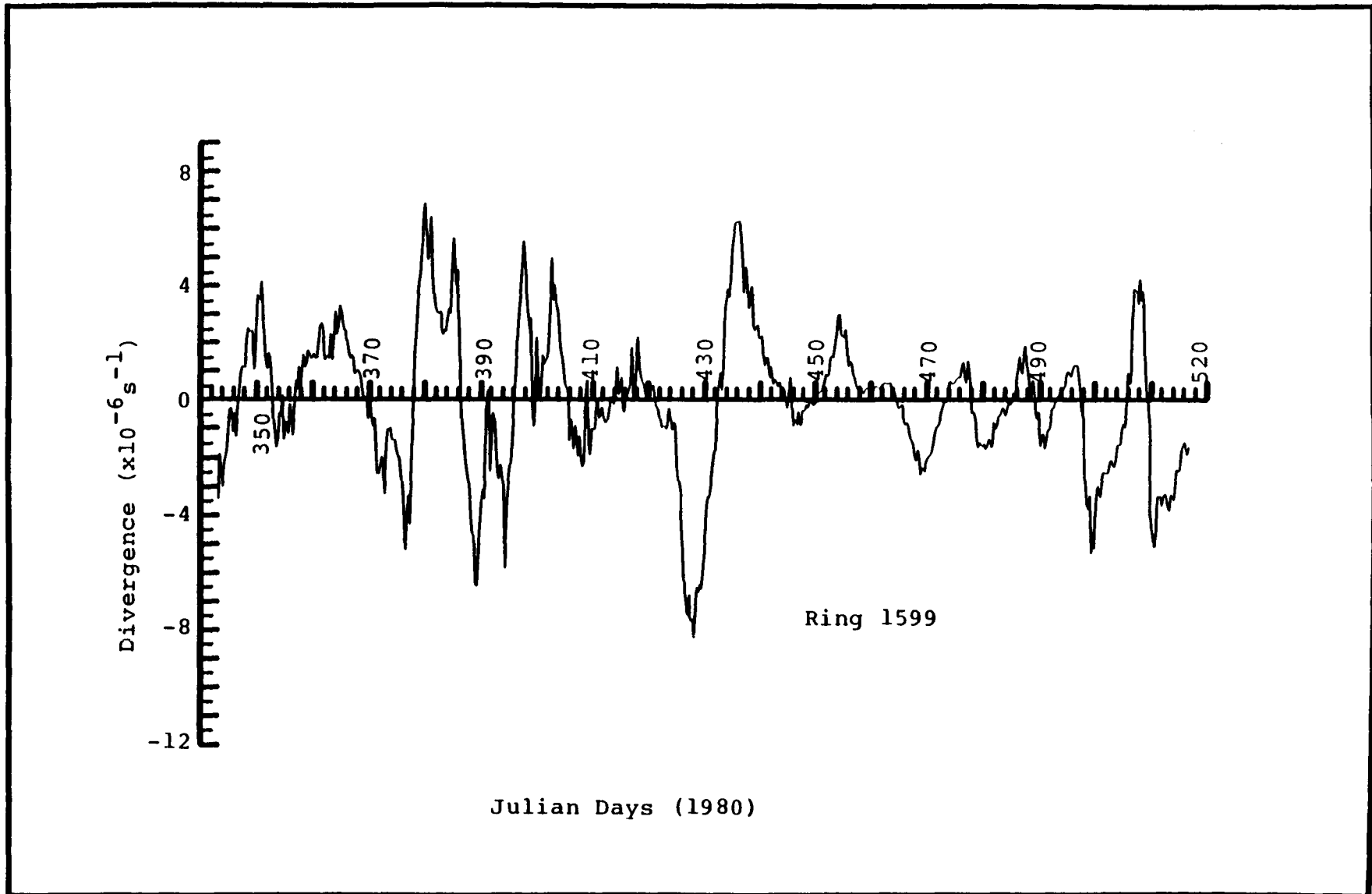


Figure 4.2-20. Calculated divergence for Ring 1599.

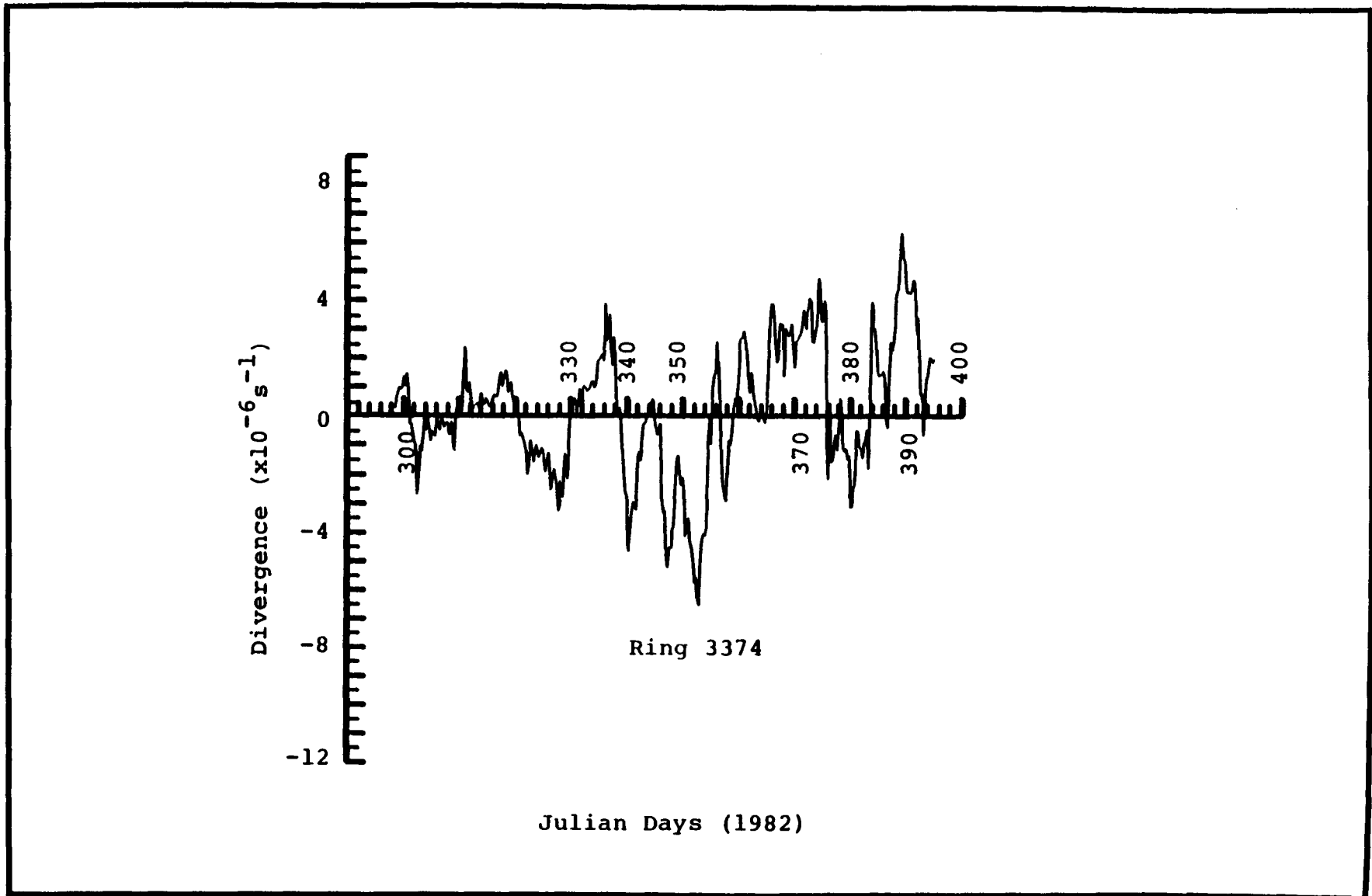


Figure 4.2-21. Calculated divergence for Ring 3374 to mid-February 1983.

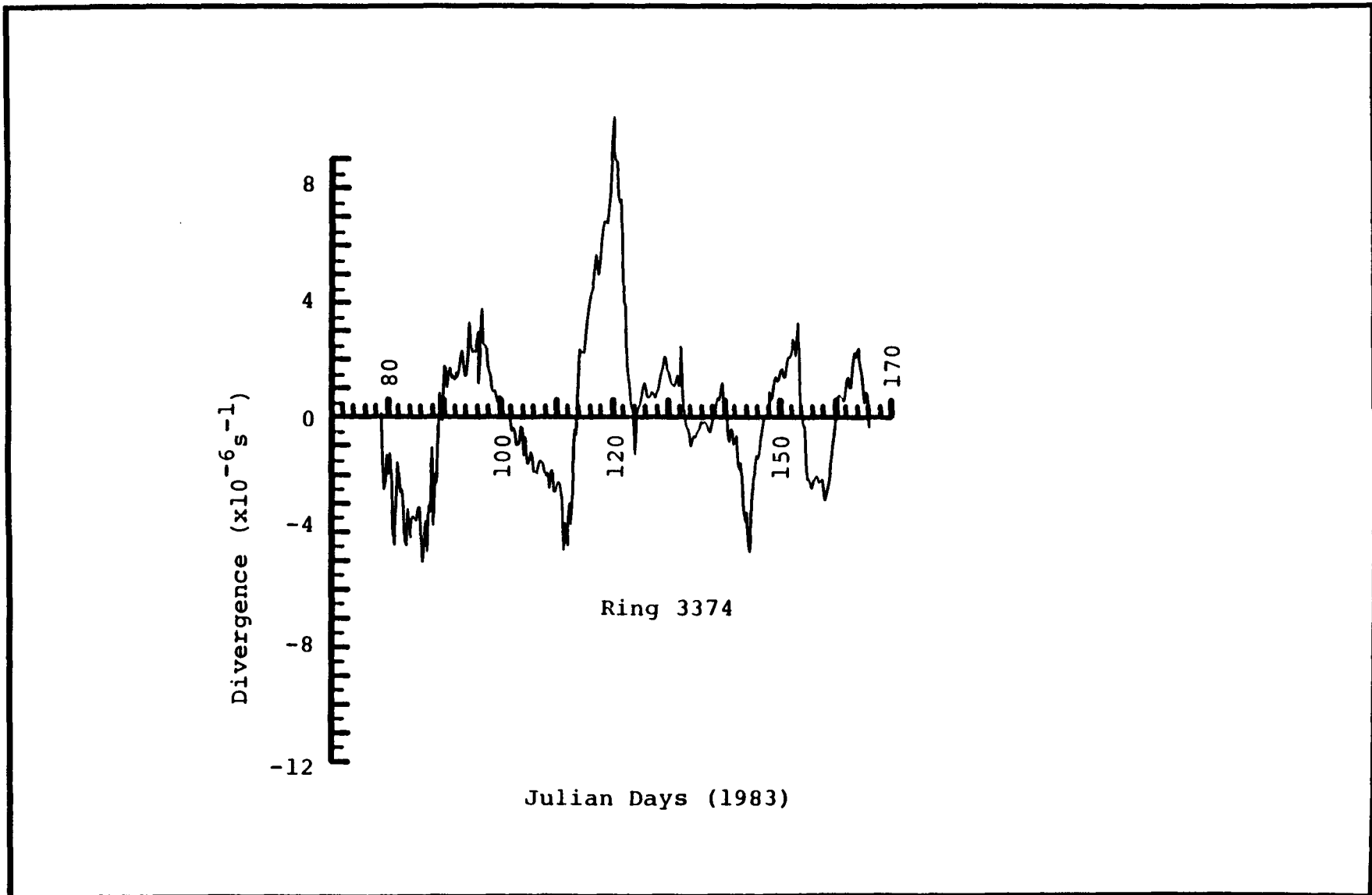


Figure 4.2-22. Calculated divergence for Ring 3374 after mid-March 1983.

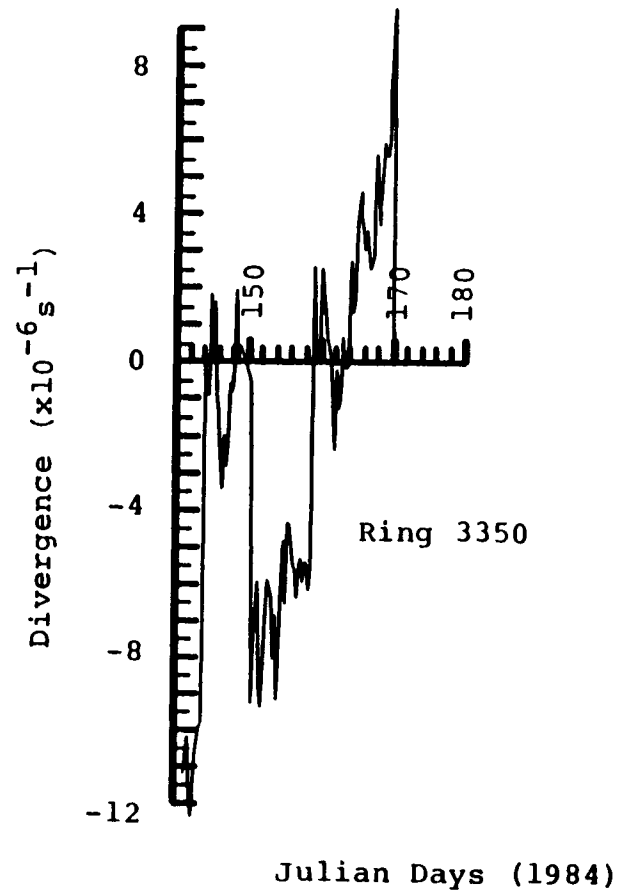


Figure 4.2-23. Calculated divergence for Ring 3350.

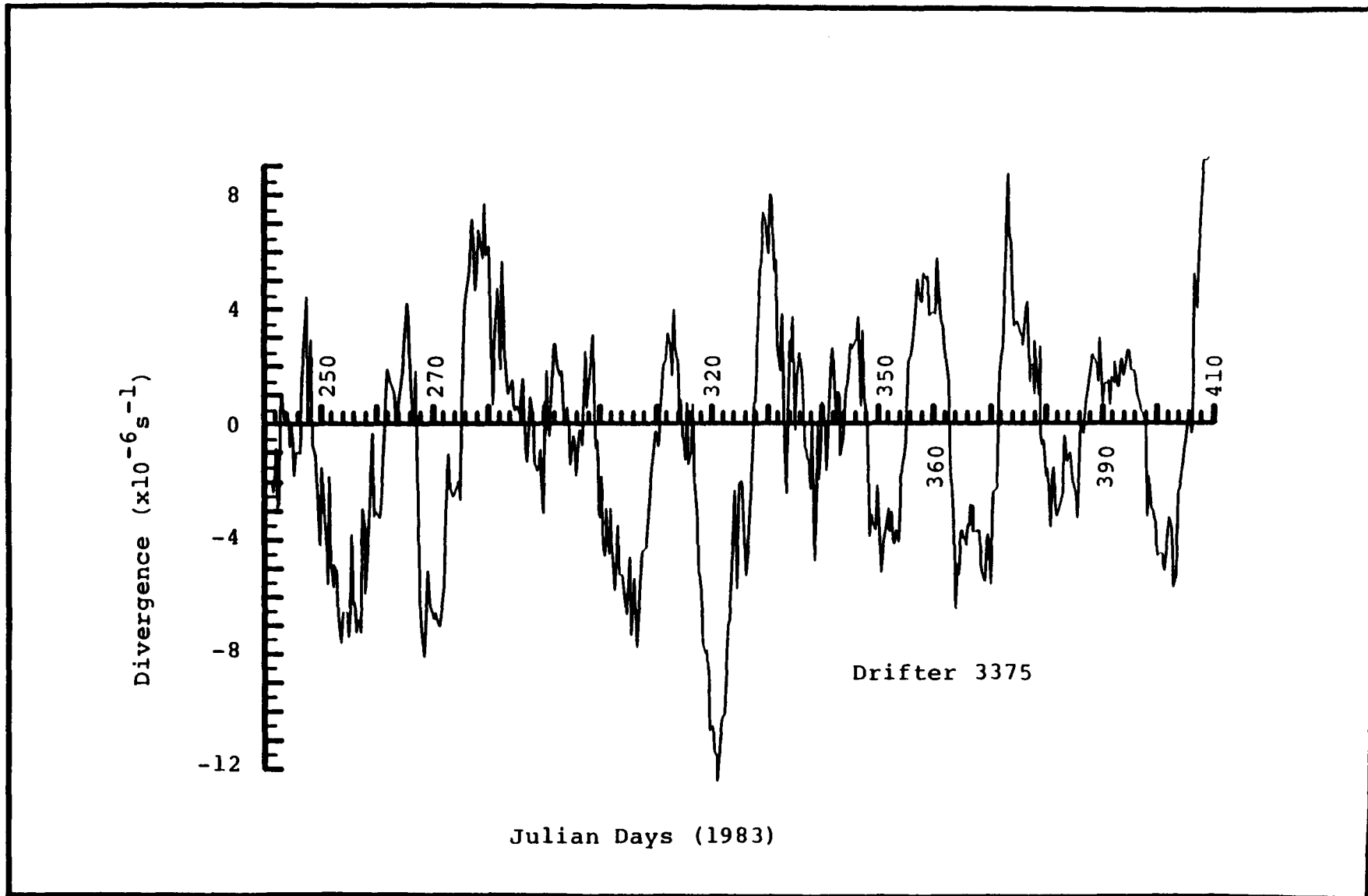


Figure 4.2-24. Divergence calculated from the trajectory of Drifter 3375.

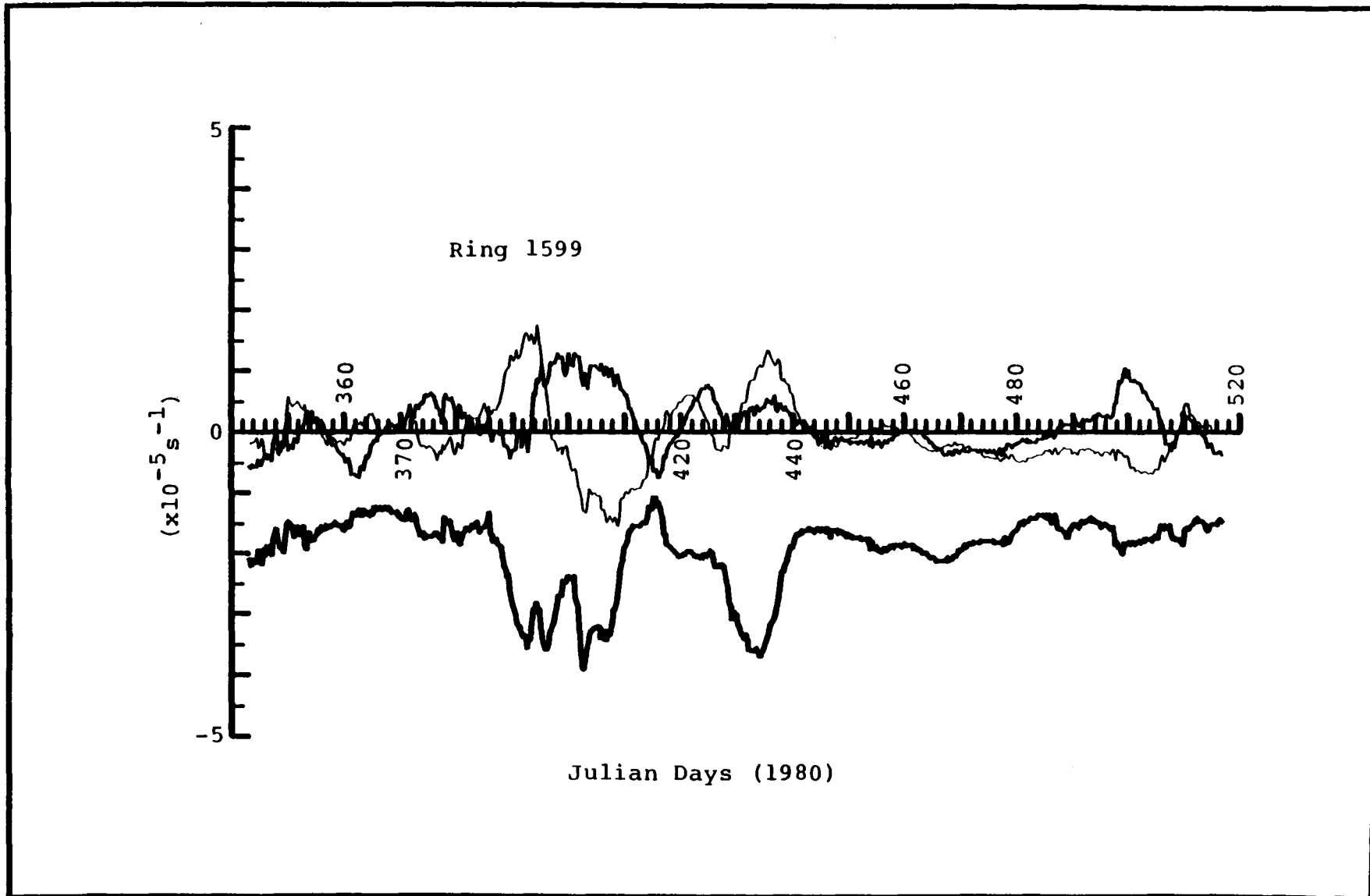


Figure 4.2-25. Time histories of ζ (darkest line), S (lighter line), and N (lightest line) for Ring 1599.

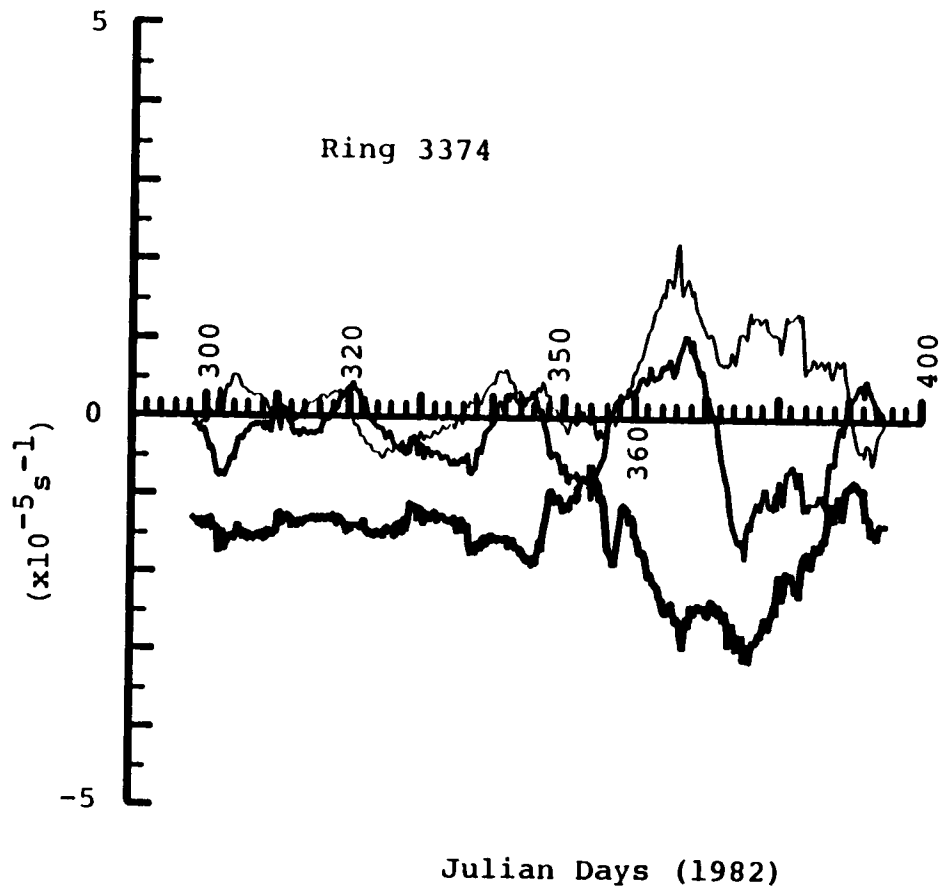


Figure 4.2-26. Time histories of ζ (darkest line), S (lighter line), and N (lightest line) for Ring 3374 to mid-February 1983.

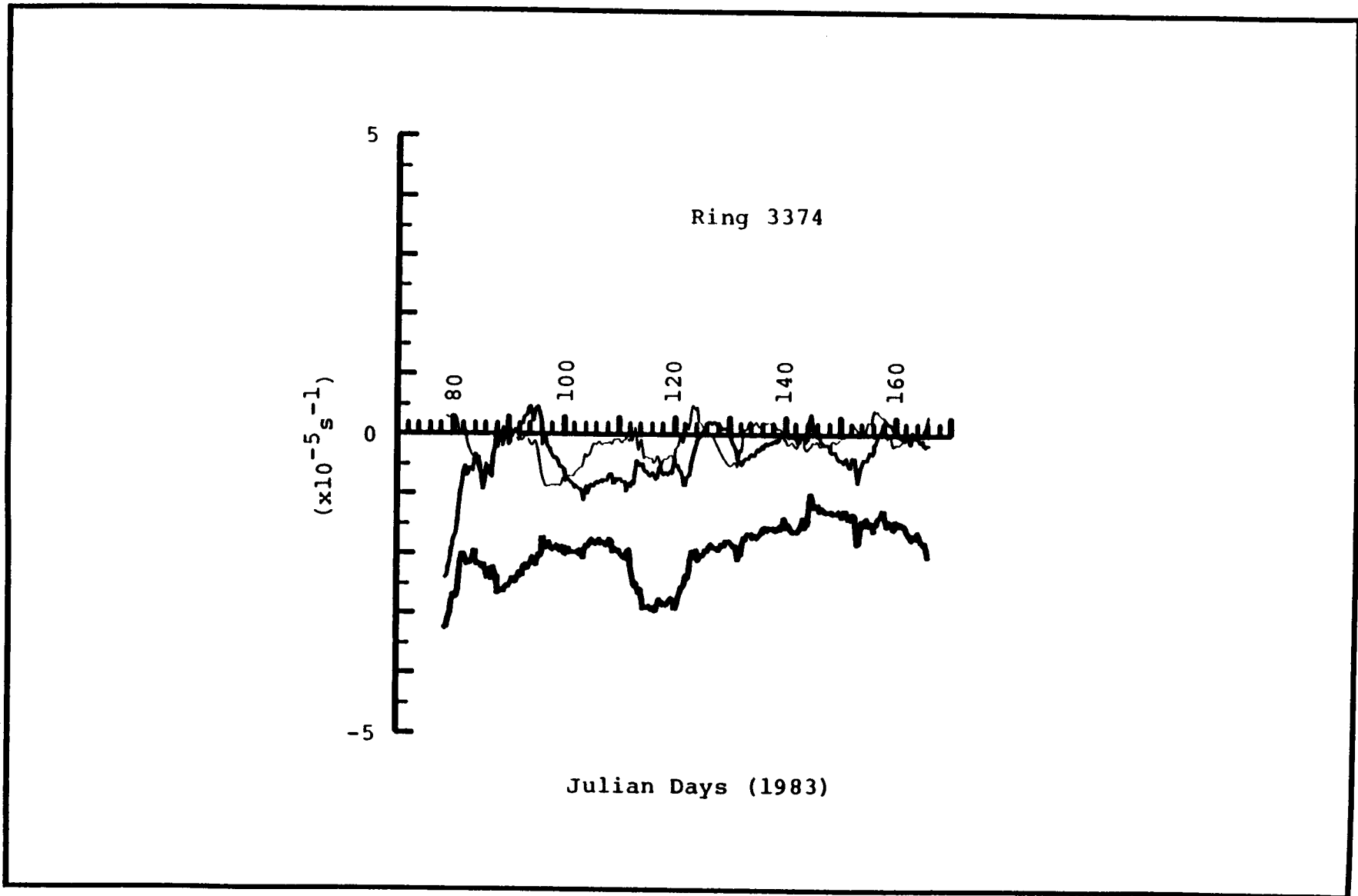


Figure 4.2-27. Time histories of ζ (darkest line), S (lighter line), and N (lightest line) for Ring 3374 after mid-March 1983.

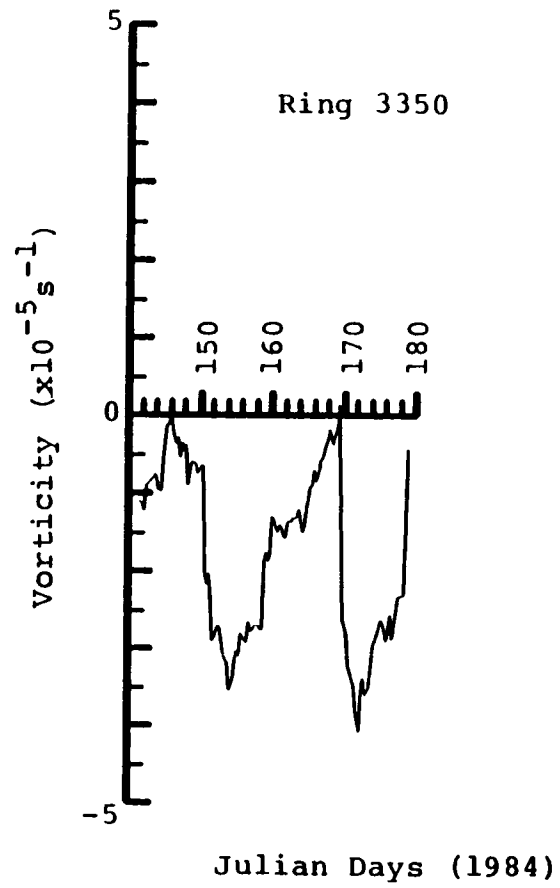


Figure 4.2-28. Calculated vorticity for Ring 3350.

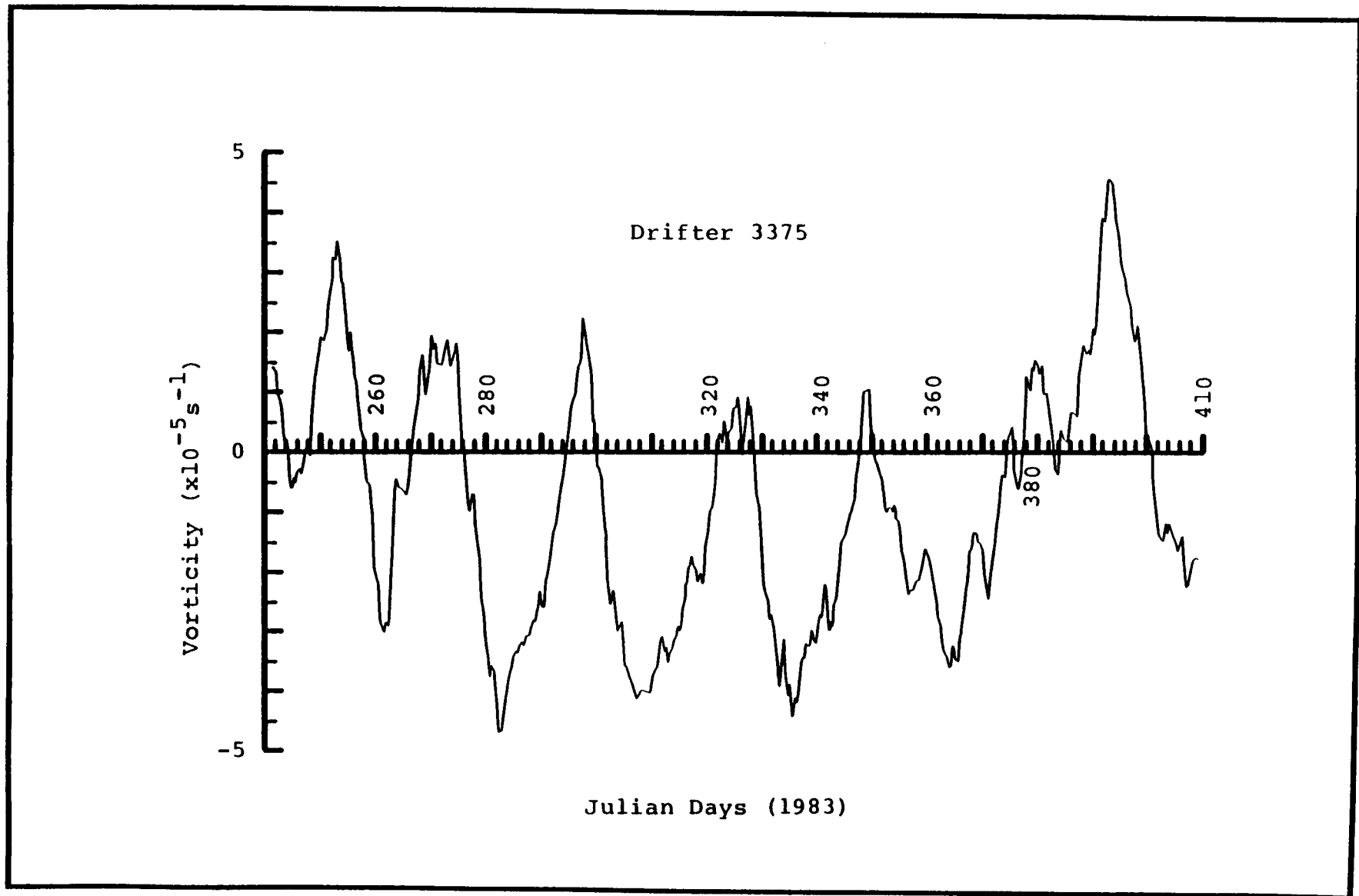


Figure 4.2-29. Vorticity calculated using the trajectory of Drifter 3375.

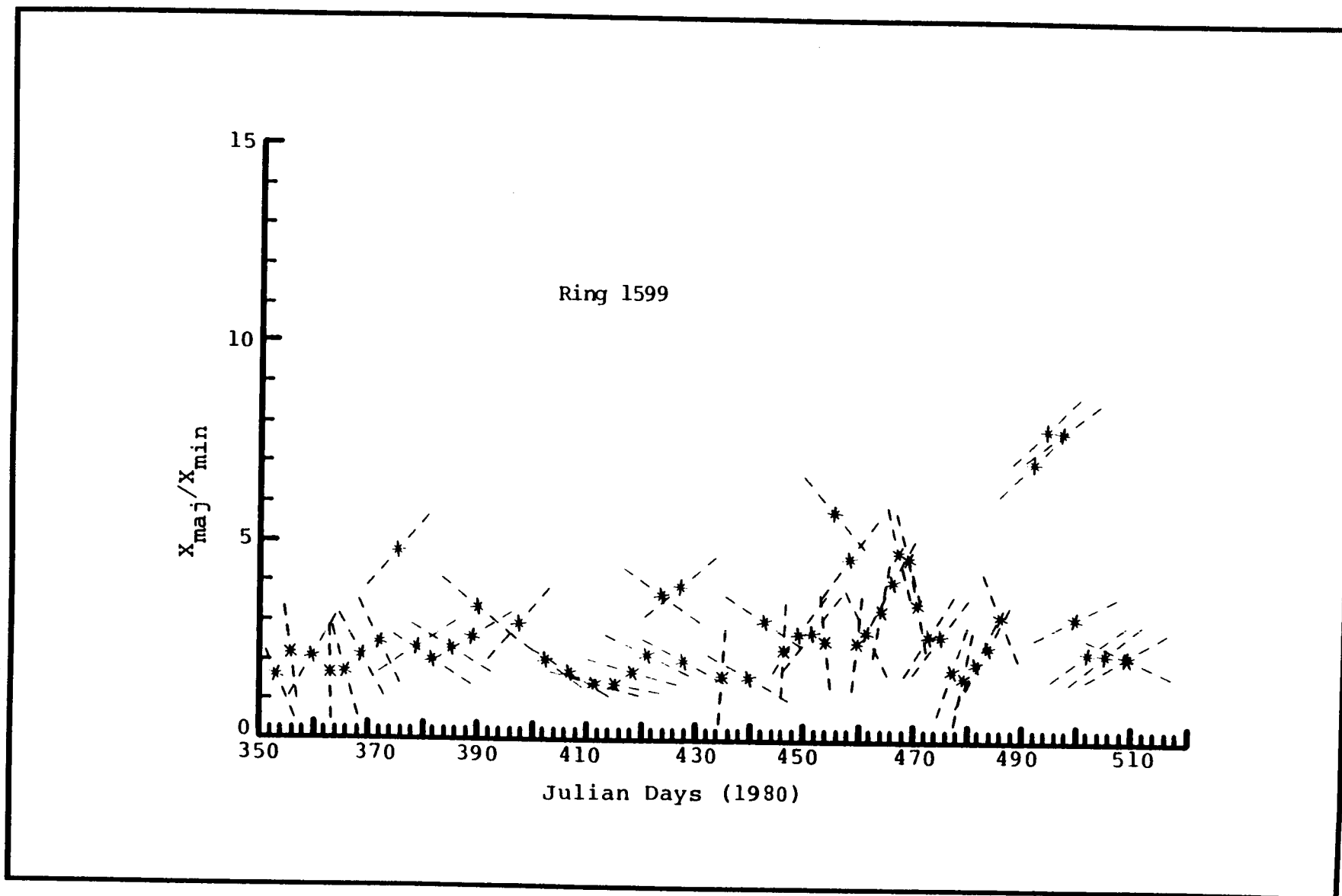


Figure 4.2-30. Time histories of ring eccentricity and orientation for Ring 1599.

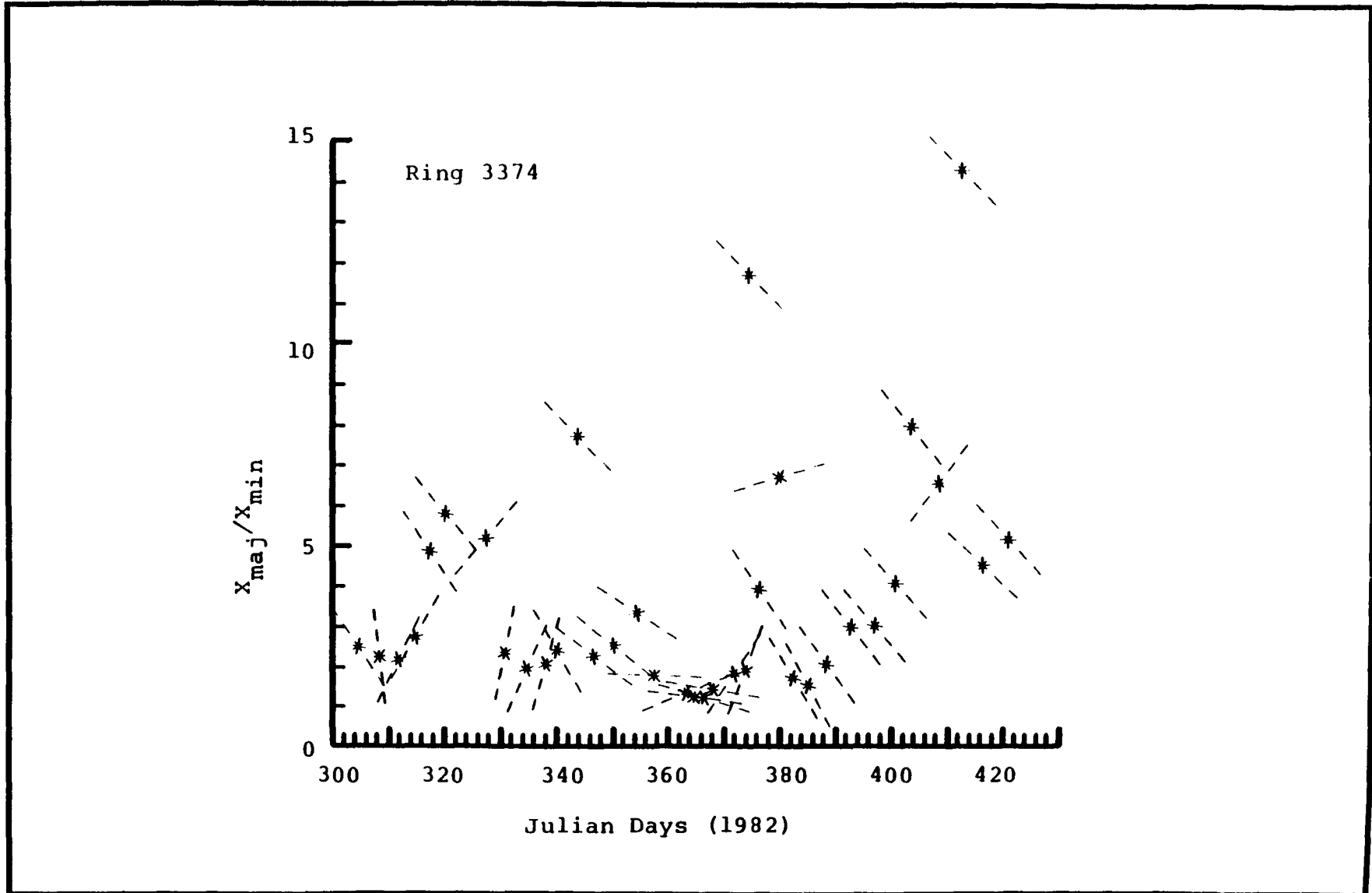


Figure 4.2-31. Time histories of ring eccentricity and orientation for Ring 3374 to mid-February 1983.

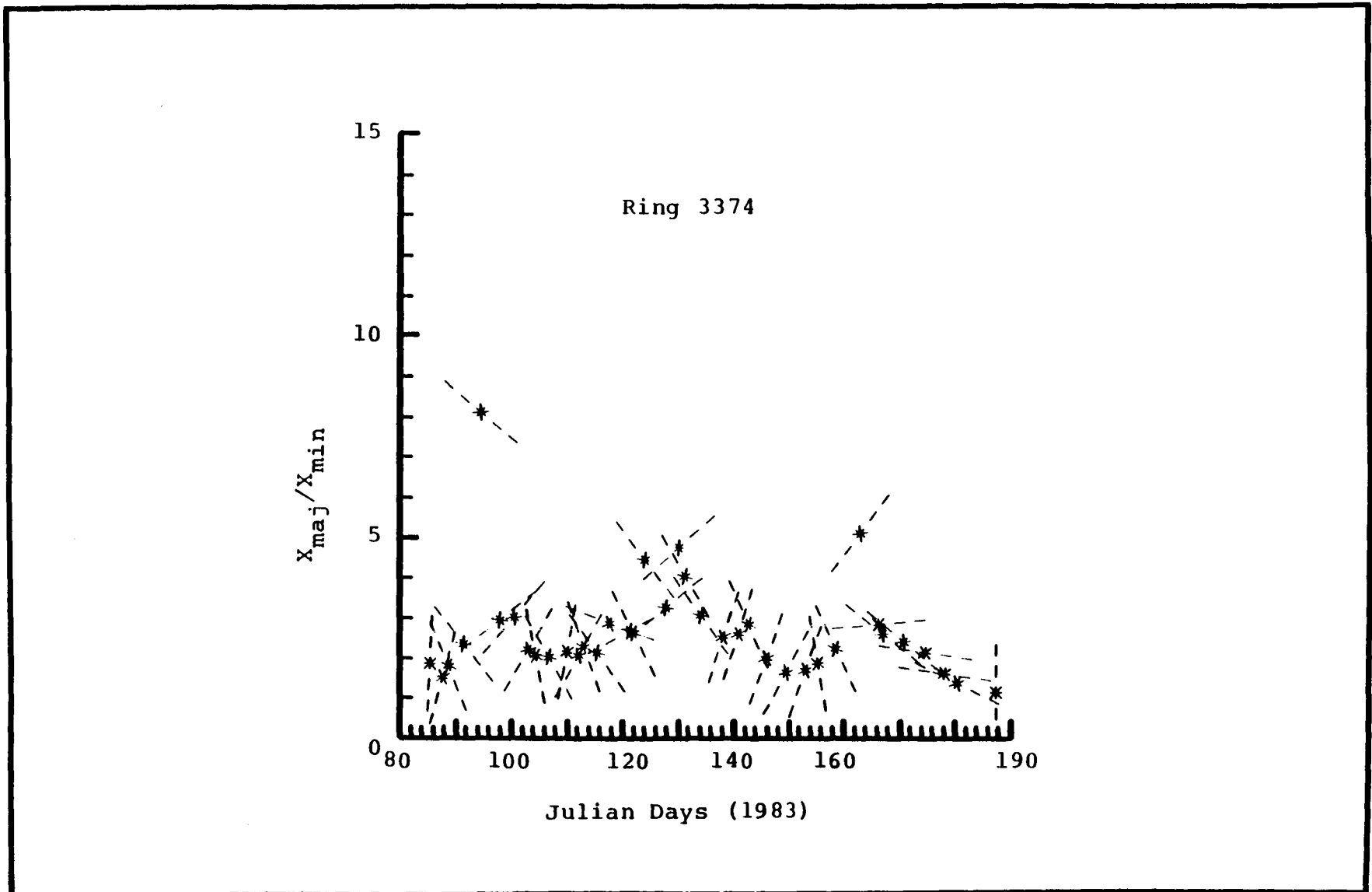


Figure 4.2-32. Time histories of ring eccentricity and orientation for Ring 3374 after mid-March 1983.

magnitude of e is similar to that of Ring 1599 after it had encountered the Mexican coast. The primary orientation is north/south.

4.2.2.5 Ring Translation Velocity

The translation velocity of the center of Ring 1599 is shown in Figure 4.2-33. The east/west motion is indicated by the lighter line, with east being positive. The movement is primarily westward, but with definite periods of eastward translation. Peak speeds are of the order of 25 cm s^{-1} . The oscillations continued even after the ring encountered the Mexican coast, but with a much smaller variance. The north/south motion (darker line with north being positive) fluctuates between positive and negative values also. The fluctuations in speed again diminished after the ring encountered the Mexican coast.

Translation velocities for Ring 3374 are shown in Figures 4.2-34 and 4.2-35. As with Ring 1599, there are periodic fluctuations with slightly smaller amplitudes ($\sim 20 \text{ cm s}^{-1}$). Rings 3374 and 1599 each show a very strong peak in velocity ($>75 \text{ cm s}^{-1}$). This occurs at about day 414 for Ring 1599 and day 352 for Ring 3374.

4.2.2.6 Balances with Respect to the Ring Center

With respect to the ring center, the dynamic balances are

$$(\zeta+f)+D(f+\zeta)=R \quad (\text{Eq. 4.2-2})$$

where R represents the residual of the summation of the two terms in the left hand side of Eq. 4.2-2. Figures 4.2-36 through 4.2-44 show the time histories of the time derivative term $(\zeta+f)$, the stretching term $D(f+\zeta)$, and R for Rings 1599 and 3374. The time derivative term (Figures 4.2-36 through 4.2-38) is small compared to the stretching term (Figures 4.2-39 through 4.2-41) except as $D \rightarrow 0$. Since $f > \zeta$, the stretching term oscillates with the sign of divergence D . The sum of the two terms (Figures 4.2-42 through 4.2-44) oscillates with a period of 10 to 20 days. These results indicate that equation 4.2-2 may be rewritten as

$$(\zeta+f)=0 \quad \text{or} \quad V=-\zeta/\beta \quad (\text{Eq. 4.2-3})$$

and

$$D(f+\zeta)=R \quad (\text{Eq. 4.2-4})$$

where V is the northward translation speed of the ring center and $\beta = \partial f / \partial y$ (y positive northward).

4.2.2.7 Motion of the Ring Center

The results of the kinematic analysis were used to calculate the trajectory of the center of Rings 1599 and 3374. These trajectories are shown in Figures 4.2-45 through 4.2-47. The ring centers have a considerable amount of rotation during various periods. These trajectories were run through the kinematic analysis routine to calculate ζ_C and D_C . An example of the results is shown in Figures 4.2-48 and 4.2-49. In general, vorticity and divergence

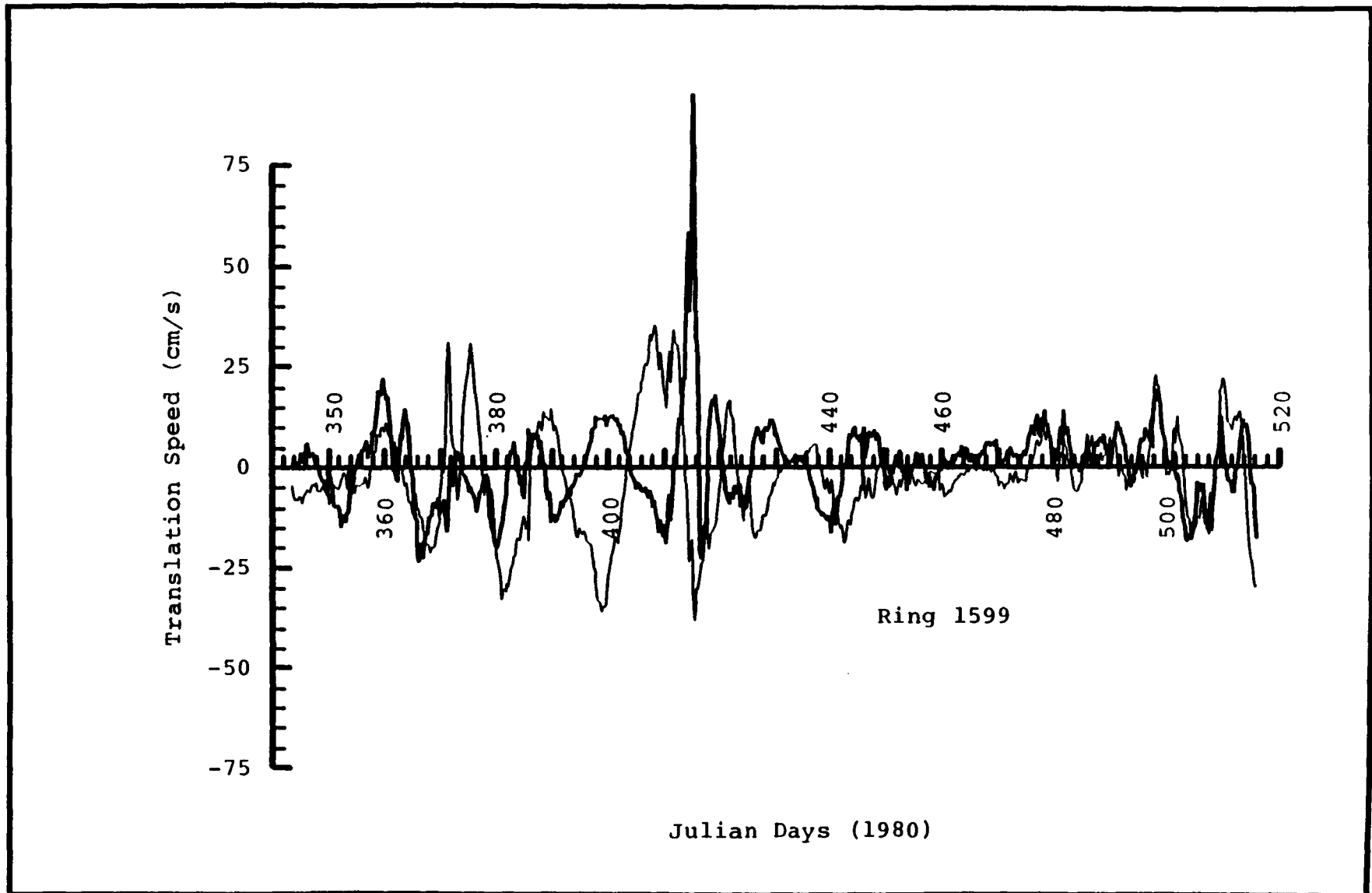


Figure 4.2-33. Calculated velocity of the center of Ring 1599: east/west speed (lighter line) and north/south speed (darker line).

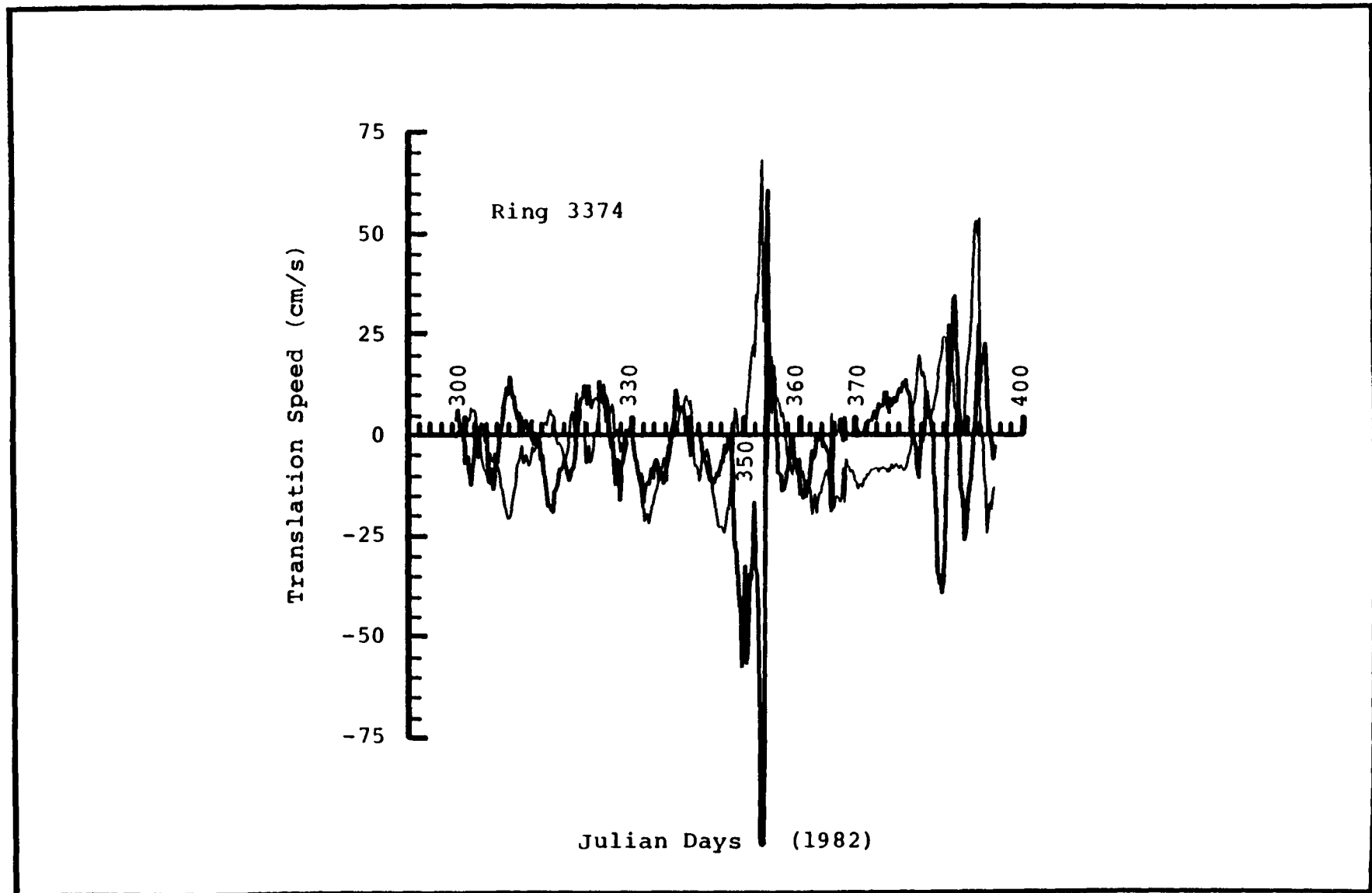


Figure 4.2-34. Calculated velocity of the center of Ring 3374 to mid-February 1983: east/west speed (lighter line) and north/south speed (darker line).

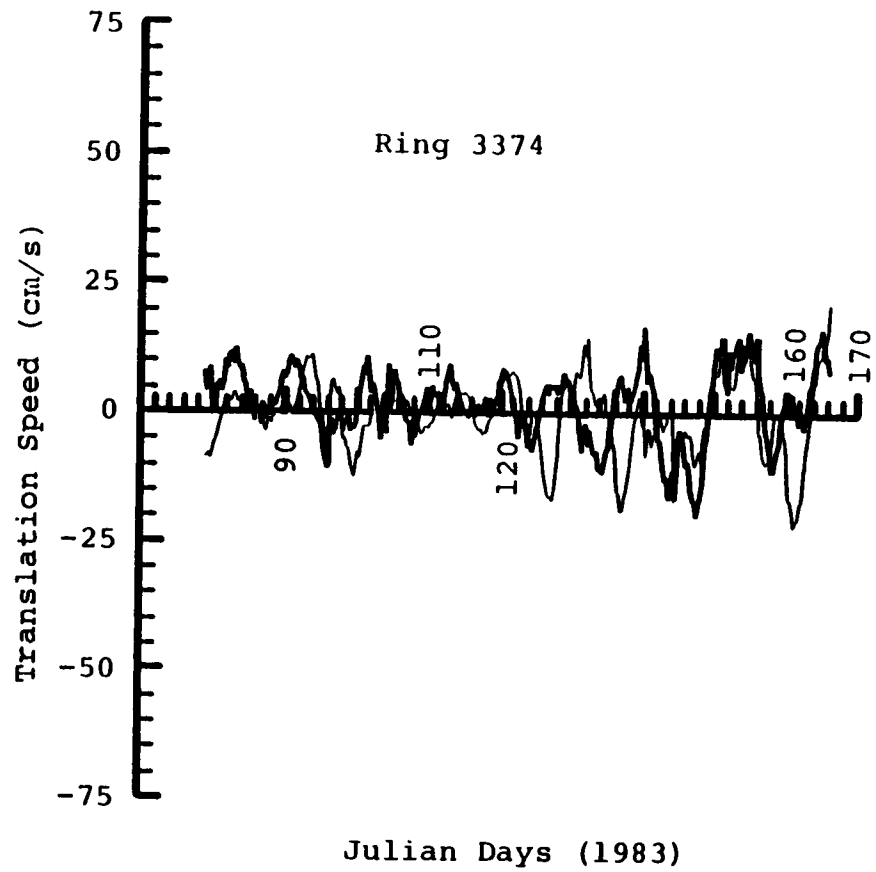


Figure 4.2-35. Calculated velocity of the center of Ring 3374 after mid-March 1983: east/west speed (lighter line) and north/south speed (darker line).

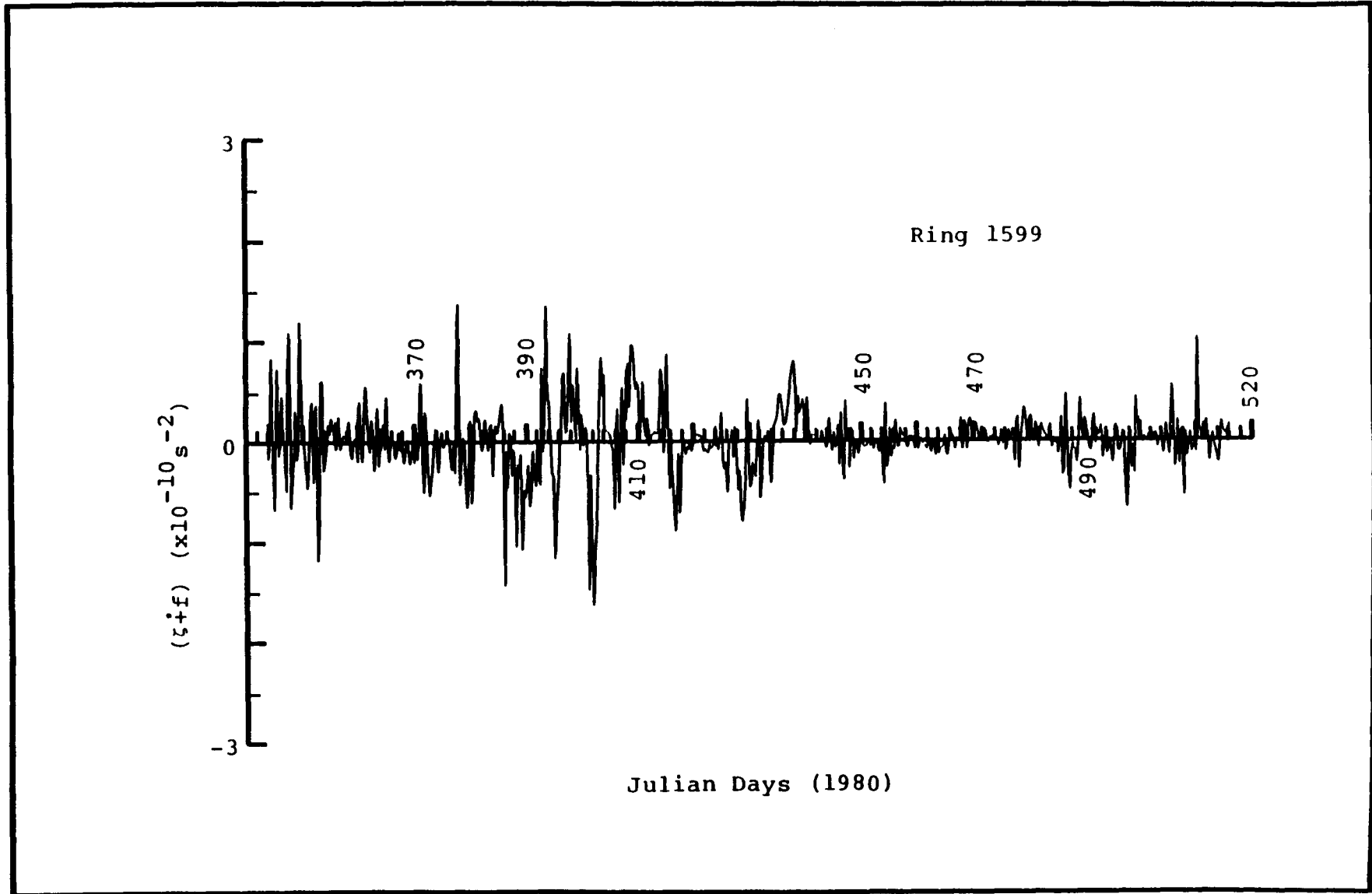


Figure 4.2-36. Time history of $(\zeta+f)$ for Ring 1599.

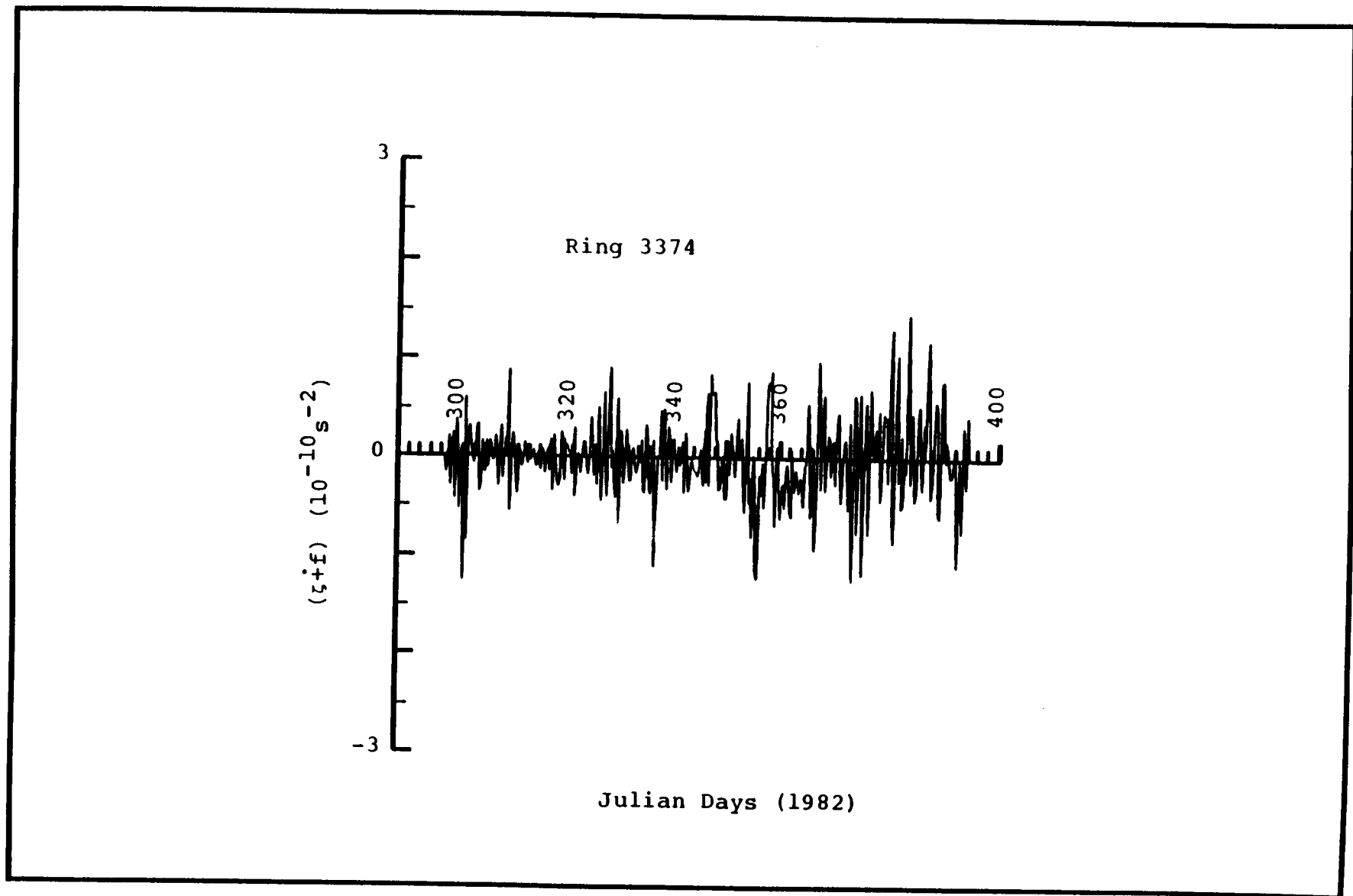


Figure 4.2-37. Time history of $(\zeta+f)$ for Ring 3374 to mid-February 1983.

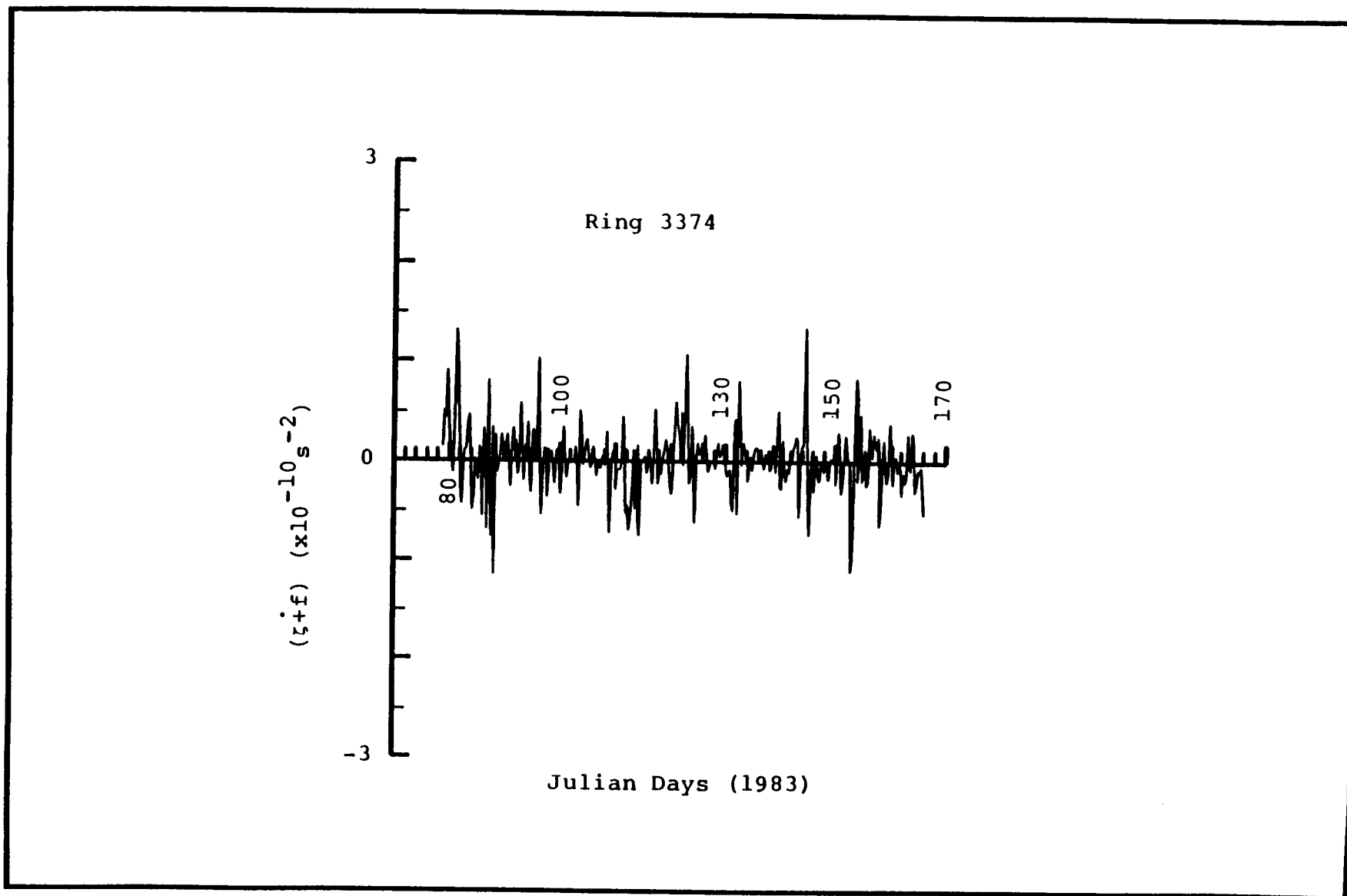


Figure 4.2-38. Time history of $(\zeta+f)$ for Ring 3374 from mid-March 1983.

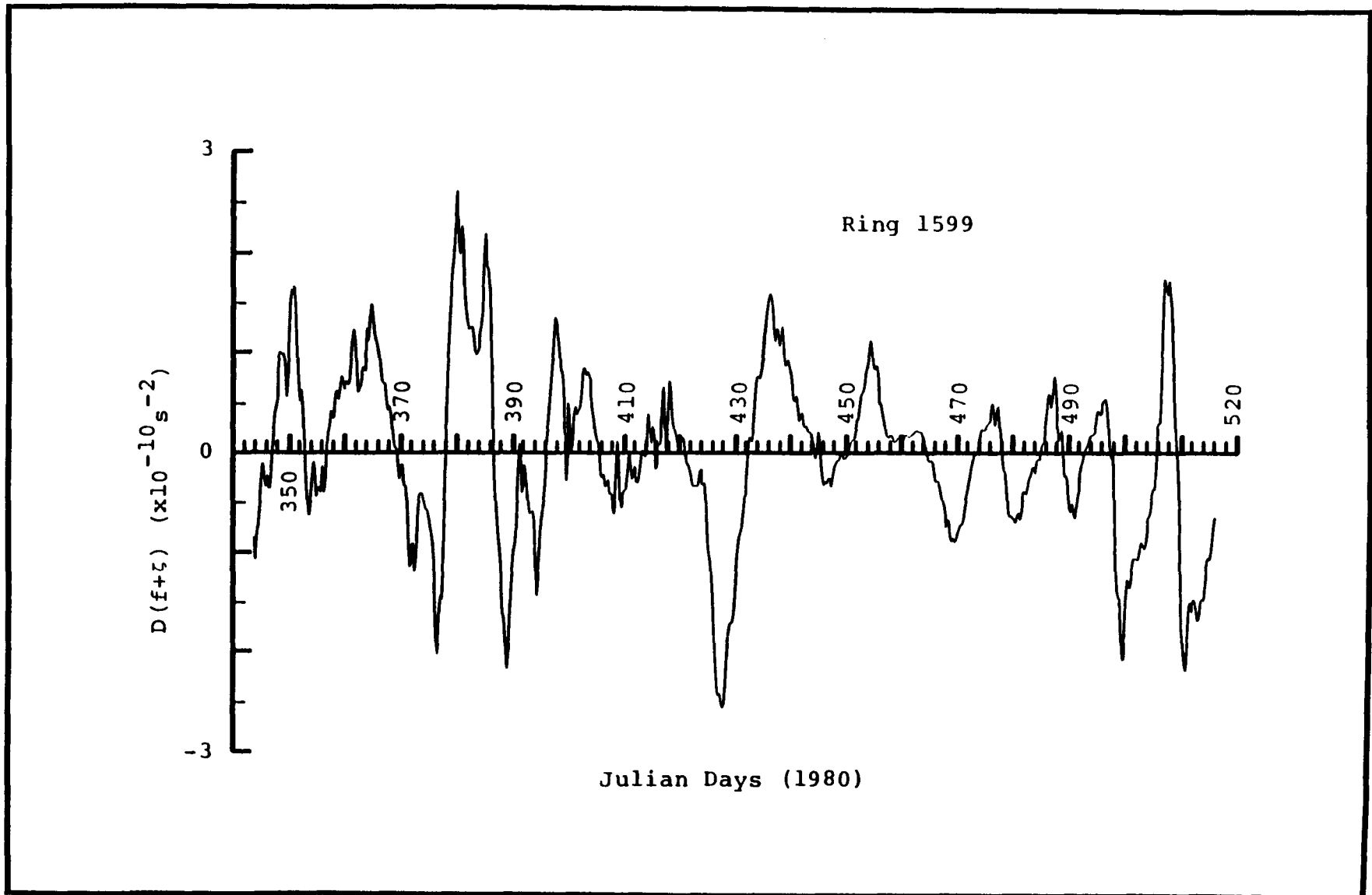


Figure 4.2-39. Time history of $D(f+\zeta)$ for Ring 1599.

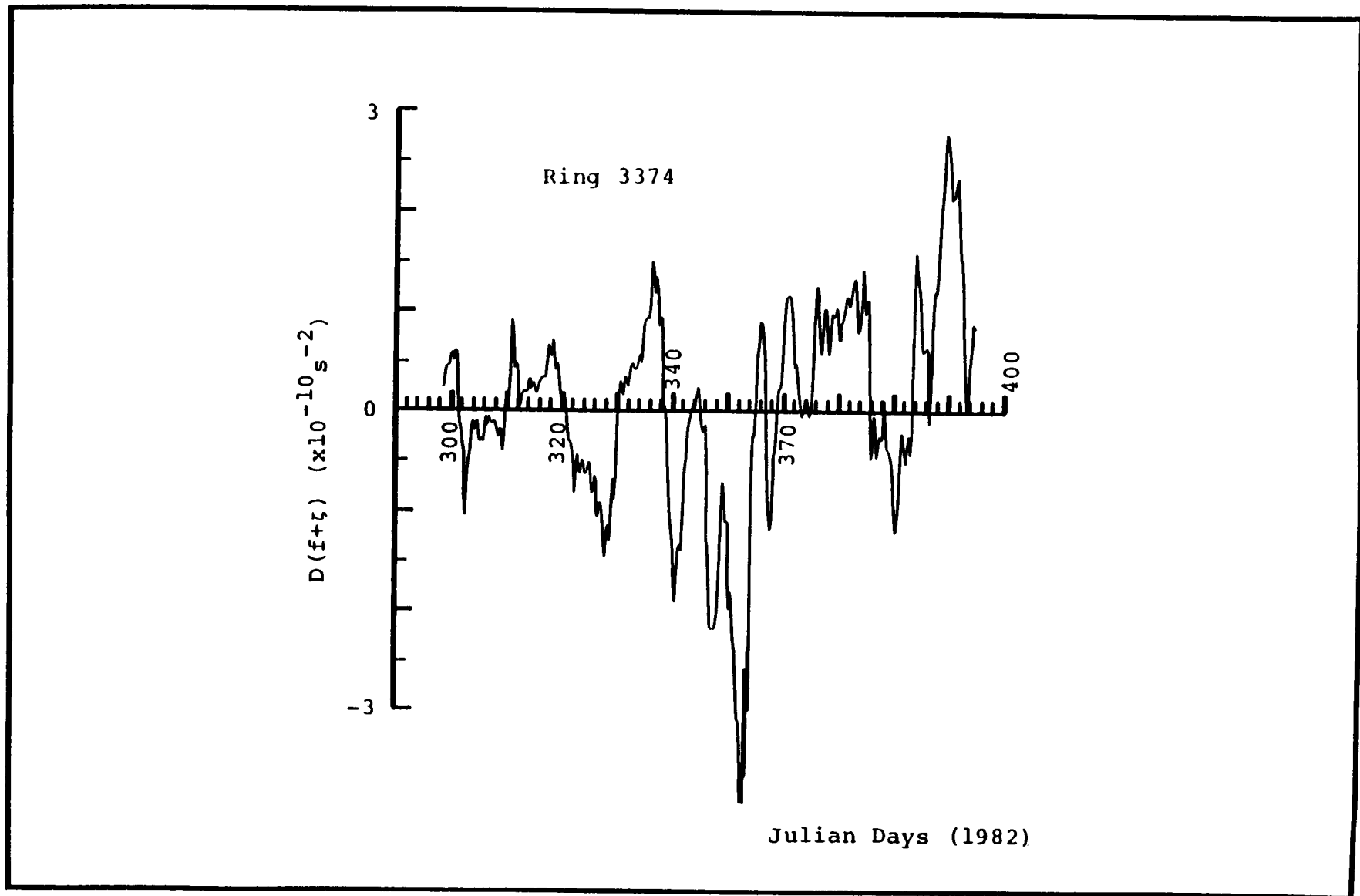


Figure 4.2-40. Time history of $D(f+\zeta)$ for Ring 3374 to mid-February 1983.

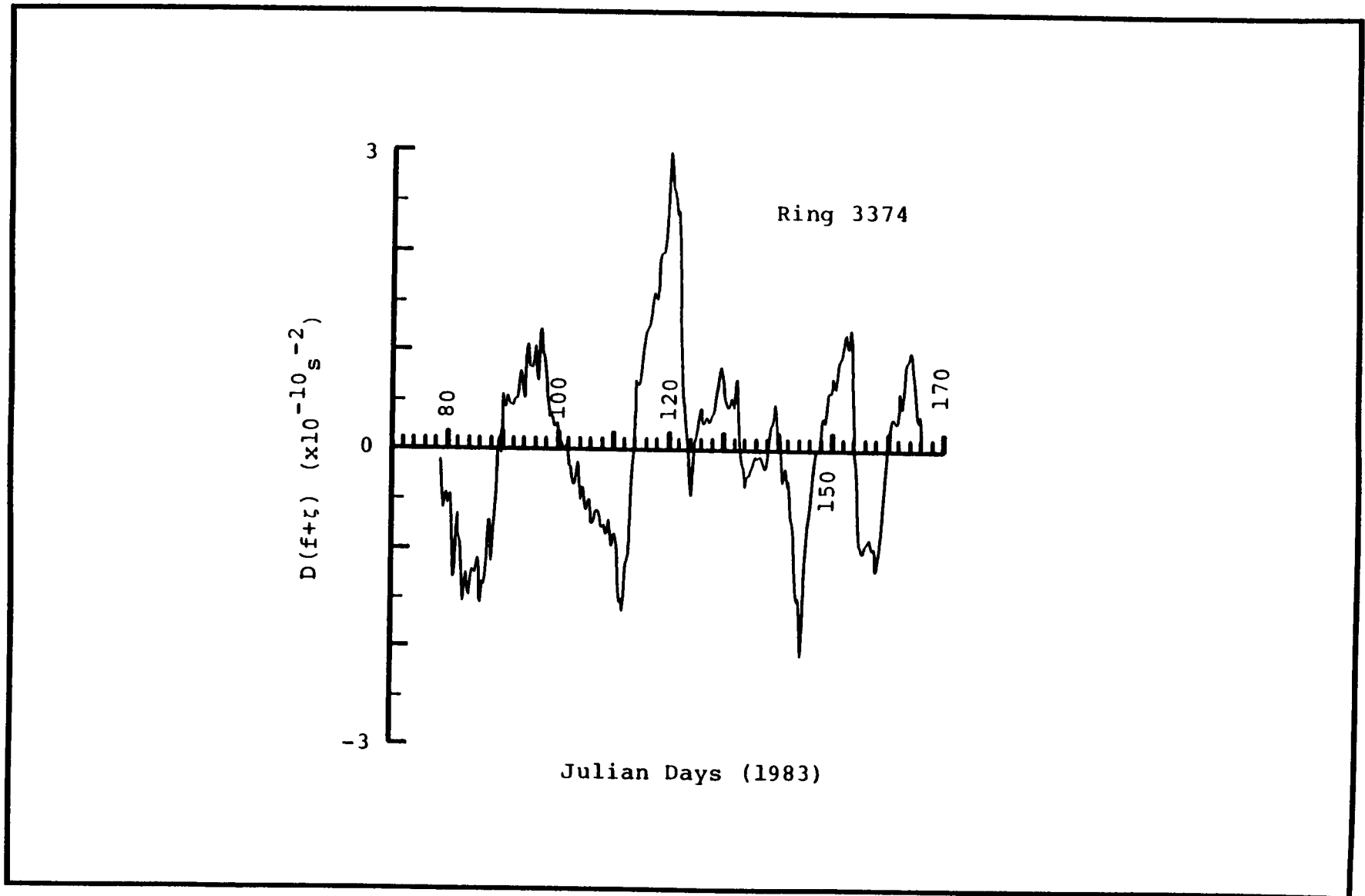


Figure 4.2-41. Time history of $D(f+\zeta)$ for Ring 3374 after mid-March 1983.

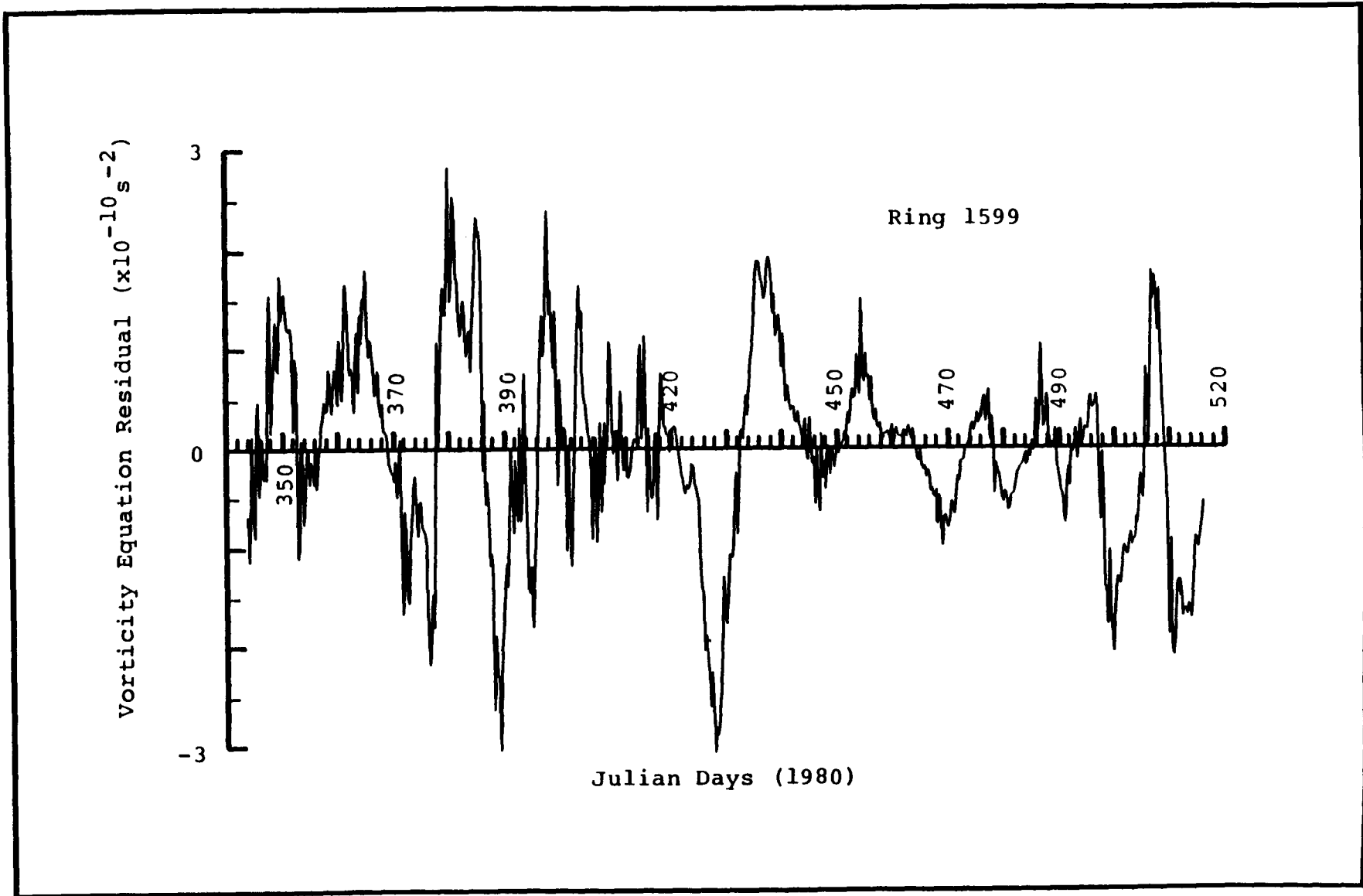


Figure 4.2-42. Time history of $(\zeta+f)+D(f+\zeta)$ for Ring 1599.

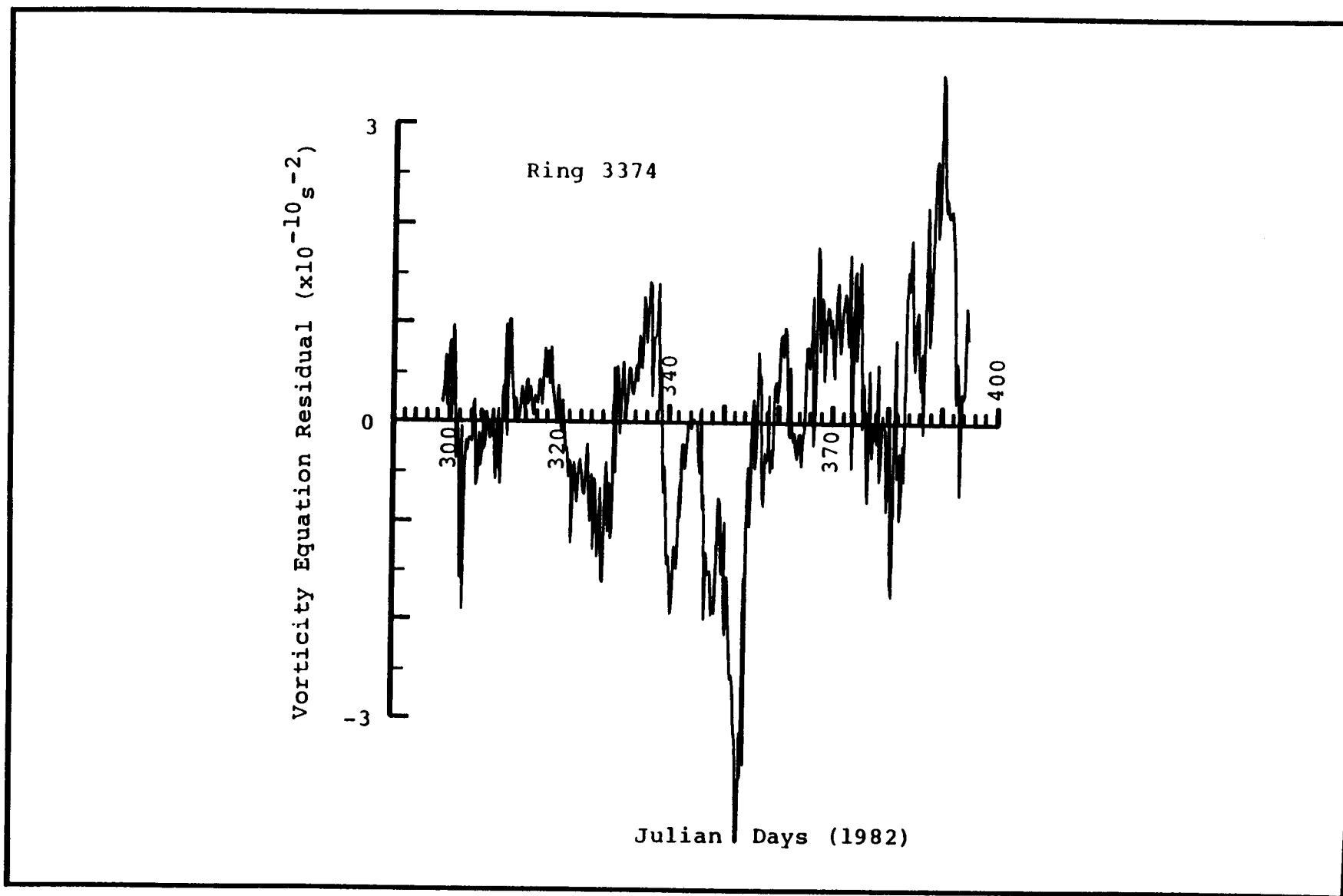


Figure 4.2-43. Time history of $(\zeta+f)+D(f+\zeta)$ for Ring 3374 to mid-February 1983.

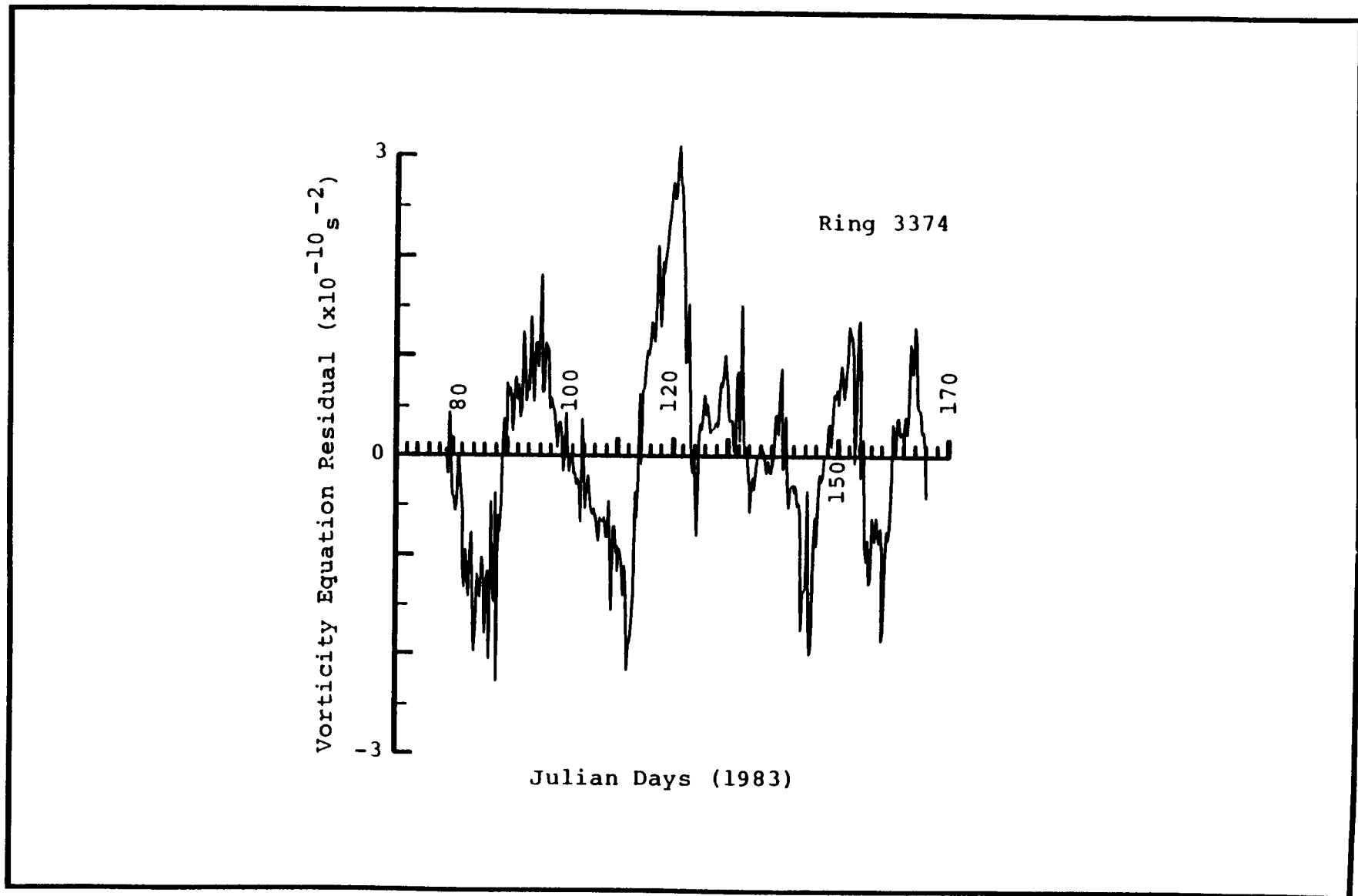


Figure 4.2-44. Time history of $(\zeta+f)+D(f+\zeta)$ for Ring 3374 after mid-March 1983.

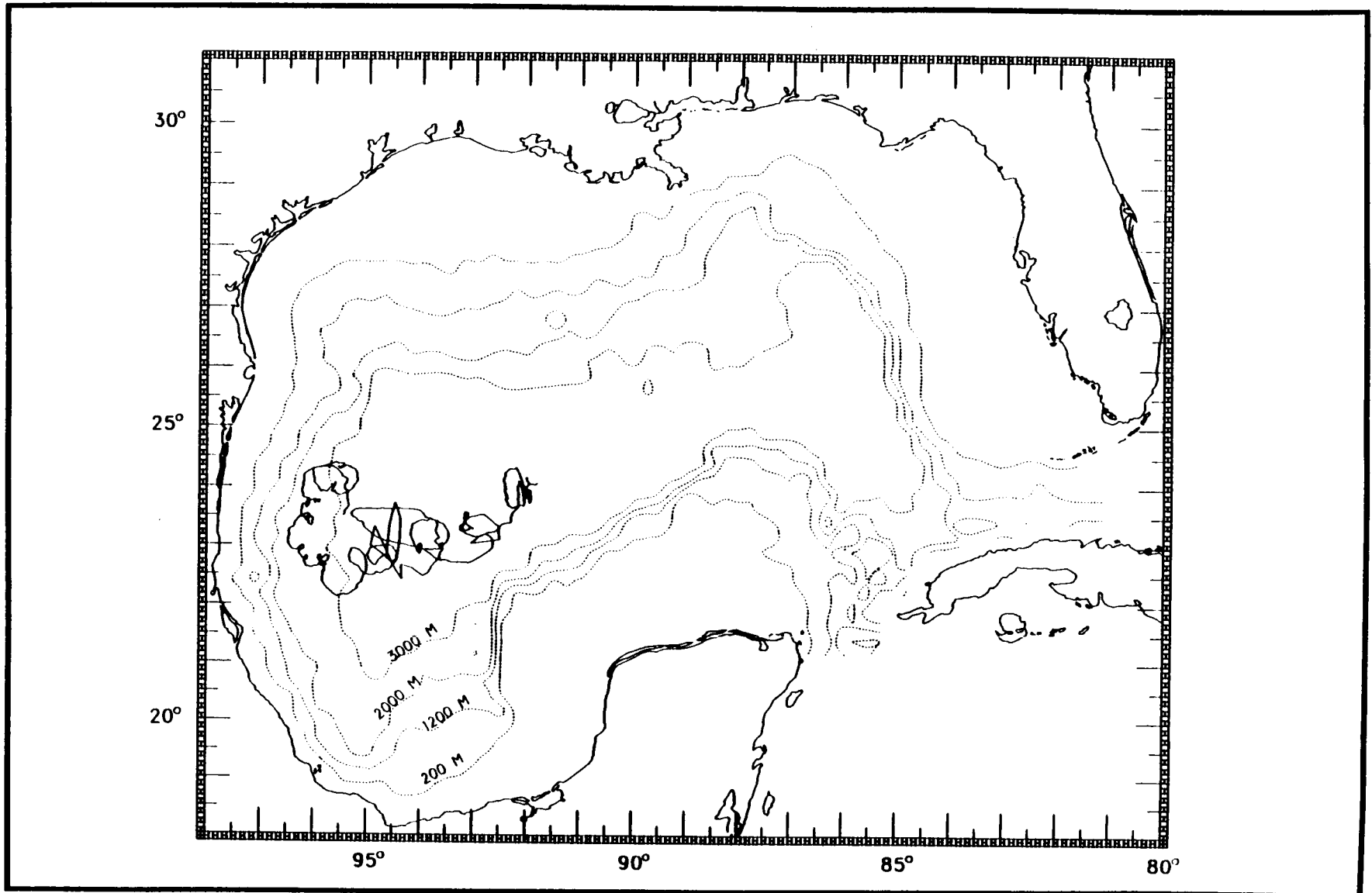


Figure 4.2-45. Trajectory for the center of Ring 1599.

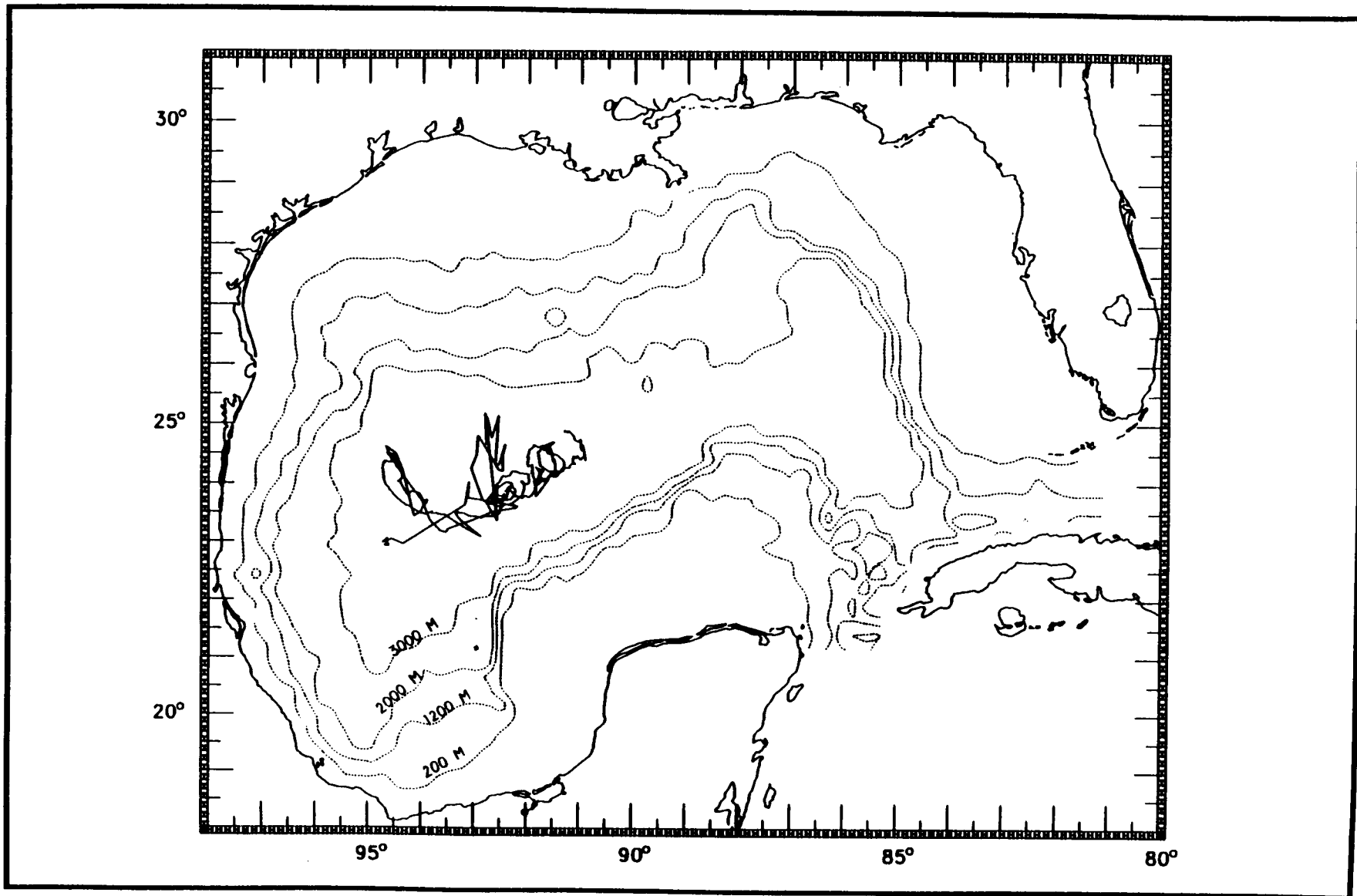


Figure 4.2-46. Trajectory for the center of Ring 3374 to mid-February 1983.

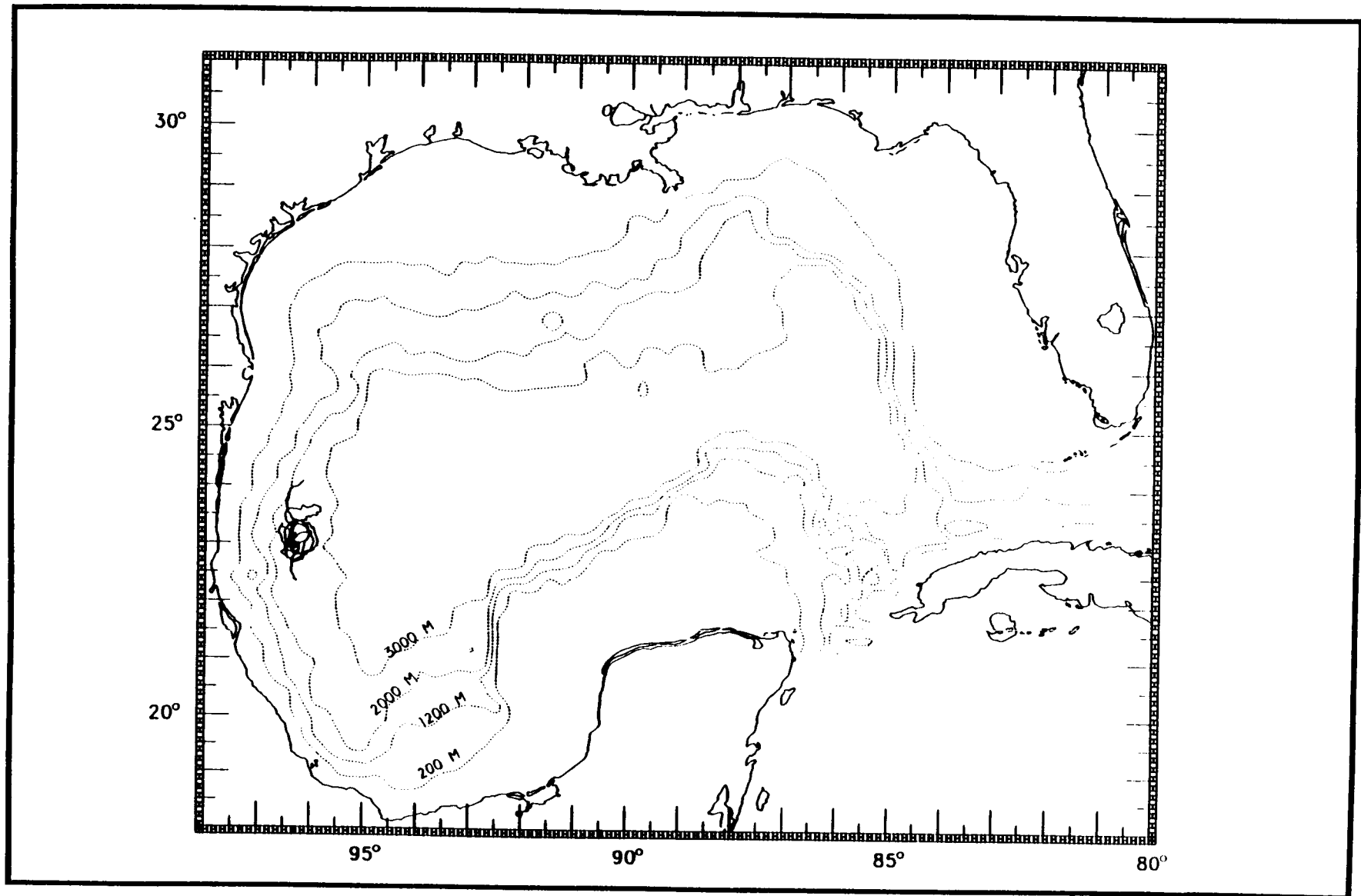


Figure 4.2-47. Trajectory for the center of Ring 3374 from mid-March 1983.

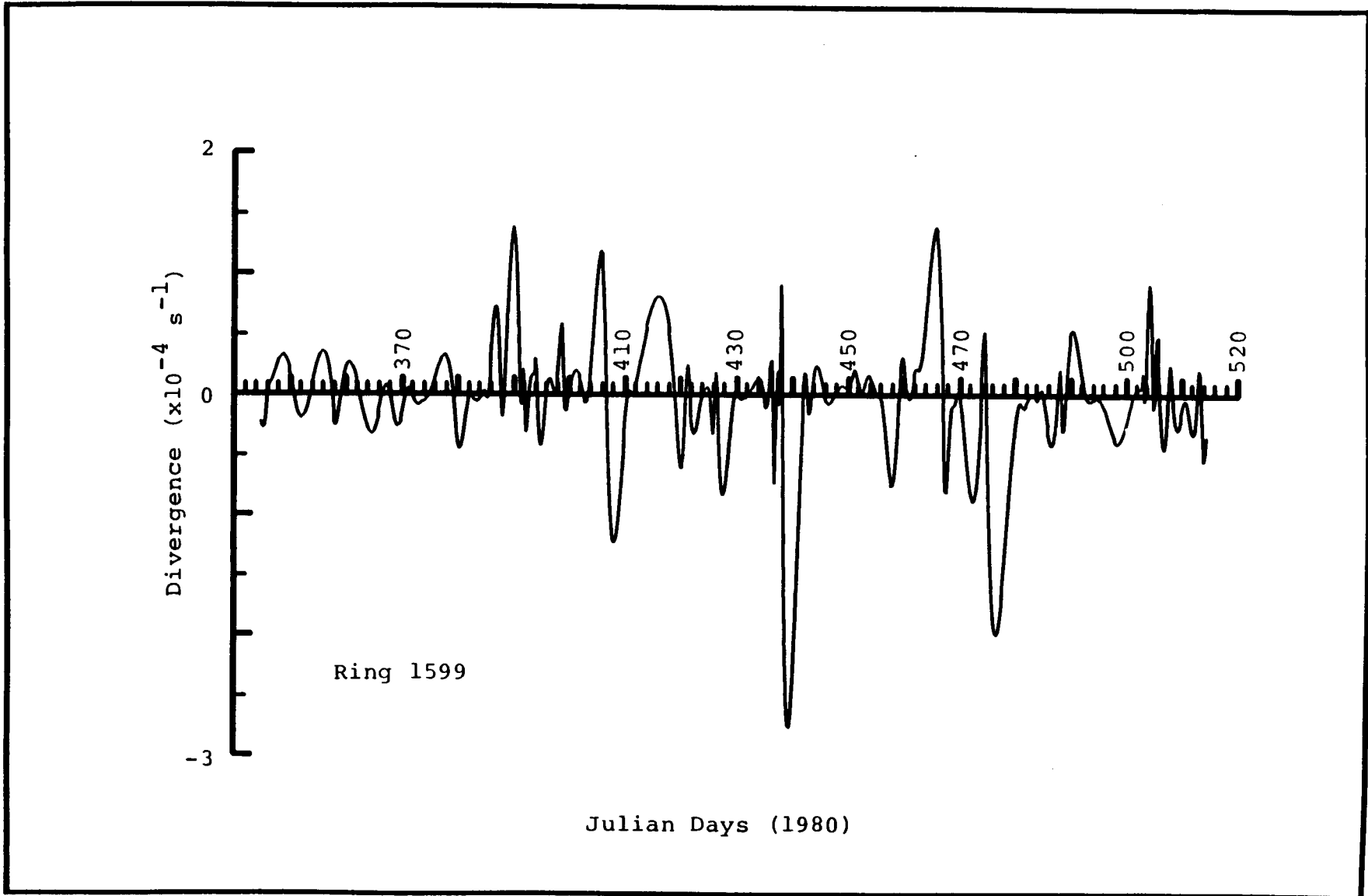


Figure 4.2-48. Calculated divergence of the motion of the center of Ring 1599.

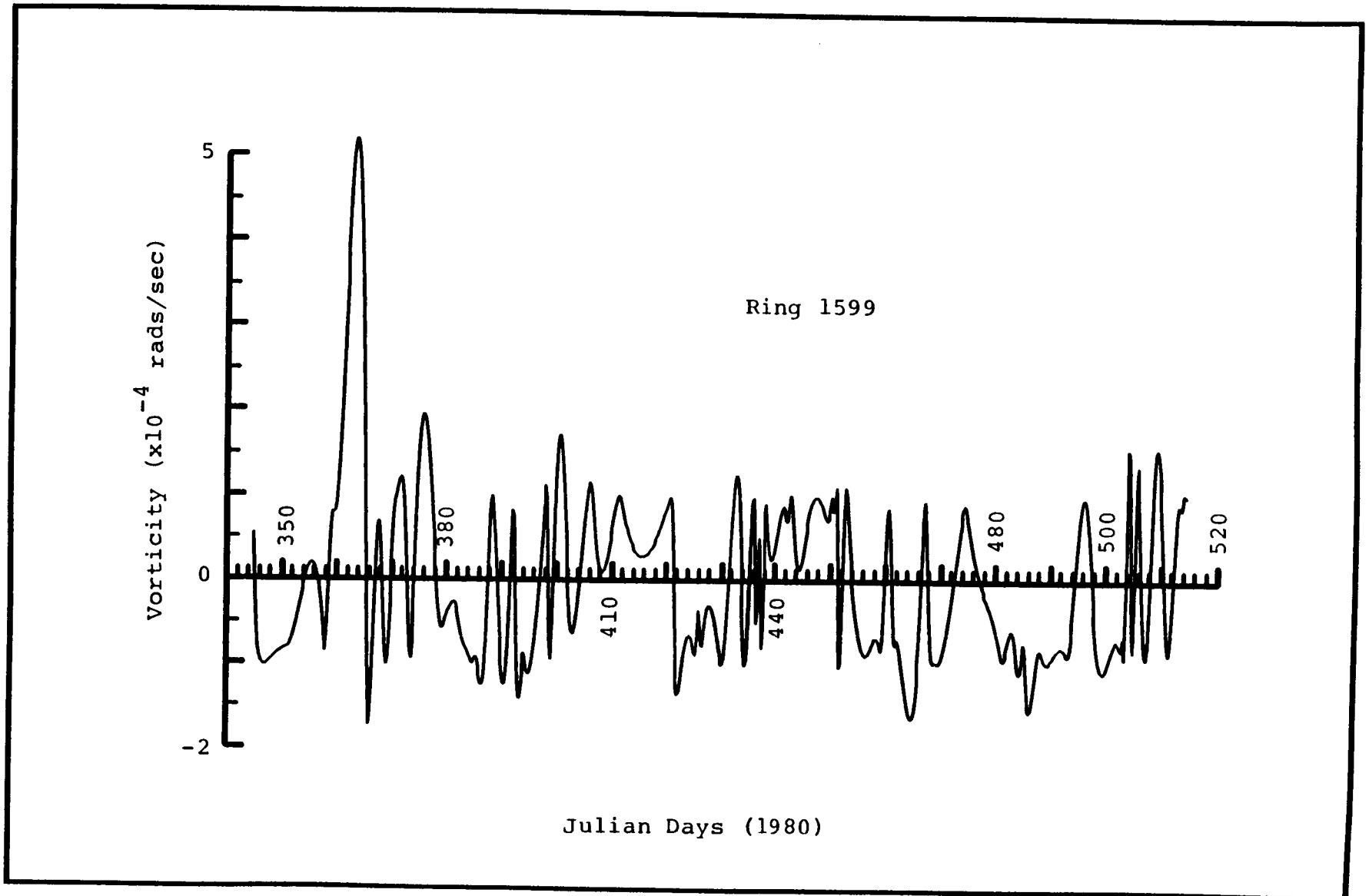


Figure 4.2-49. Calculated vorticity of the motion of the center of Ring 1599.

of the ring centers are approximately one to two orders of magnitude larger than ζ and D relative to the ring centers. In addition, ζ_C and D_C fluctuate at a higher frequency than ζ and D . Thus, these results would indicate that the angular momentum of the ring centers is important in the overall balance of forces.

4.2.3 Ring Movement

The general paths of Rings 1599, 3374 (Figure 4.2-50), and 3350 (Figure 4.2-51) are identical. The rings followed the deepest part of the Gulf of Mexico, a feature seen in the numerical modeling of the GOM by Hurlburt and Thompson (1980). Three months elapsed from the time Ring 3350 was shed until it was seeded. Rings 1599 and 3374 indicate a three to five month travel time from seeding until encountering the Mexican coast. These results indicate a total travel time across the Gulf of Mexico of six to eight months.

The trajectory data of Rings 1599 and 3374 show that the rings continued to persist for three to five months after interacting with the bathymetry of the Mexican shelf. This indicates a total ring life span of at least 9 to 13 months. The persistence of warm-core rings off a western boundary has been seen in numerical experiments and has been attributed to dynamics which cause an anticyclone to move offshore as it reaches shallower water (Smith and O'Brien, 1983). This supports the contention that the high dynamic topography at 23.5°N observed by numerous researchers (e.g. Nowlin and McClelland, 1967; Merrell and Morrison, 1981) is a result of rings from the Loop Current.

After July 1983, Drifter 3374 (Figure 4.2-50c) left its ring and moved toward the east. The location at which the drifter left the ring coincides almost exactly with a region where large eastward transports (30 Sverdrups) have been observed (Merrell and Morrison, 1981). This eastward flow is a result of a combination of the flow pattern of the anticyclone's northern limb and the southern limb of a cyclone which is typically found directly north of the anticyclone (Merrell and Morrison, 1981; Brooks and Legeckis, 1982; Merrell and Vazquez, 1983). Smith and O'Brien (1983) have shown numerically that such cyclones can be shed from anticyclones as the latter feels the effects of a western boundary.

Finally, the northward translation of the rings after encountering the western boundary should be noted. This can be seen in Figure 4.2-50, and similar motion is implied in Figure 4.2-51. Such northward ring translation has been documented in numerical studies of the Gulf of Mexico (Hurlburt and Thompson, 1980; Smith, 1985). The analysis of Smith and O'Brien (1983) indicates that the northward motion is the result of non-linear asymmetries in the flow field. The flow on the ring's western side is accelerated since it becomes confined between the ring center and the continental shelf. This apparently produces a net northward translation of the ring.

4.2.4 SST Maps

The trajectory of Drifter 3375 can be seen in Figure 4.2-51 and the corresponding SST contour maps in Figures 4.2-7 through 4.2-19. The intention was to place Drifter 3375 in the ring that was shed by the Loop Current in March 1983. Although temperature frontal analyses indicated that the ring had moved west across the northern GOM (see Figure 4.2-52), the XBT data from the

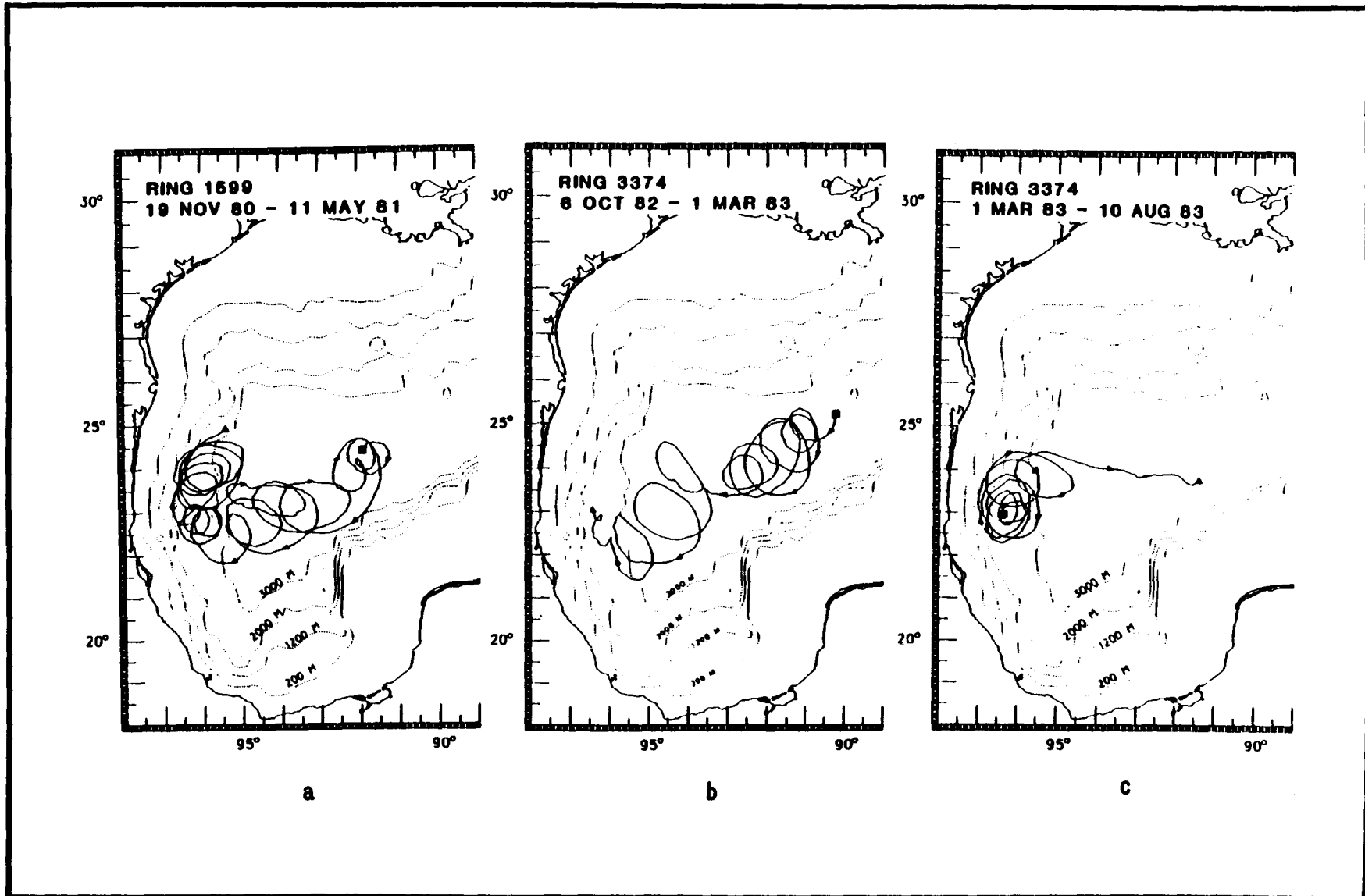


Figure 4.2-50. Trajectories for Drifters (a) 1599, and (b) and (c) 3374. Depth contours are in meters. The square and triangles denote the start and end positions, respectively.

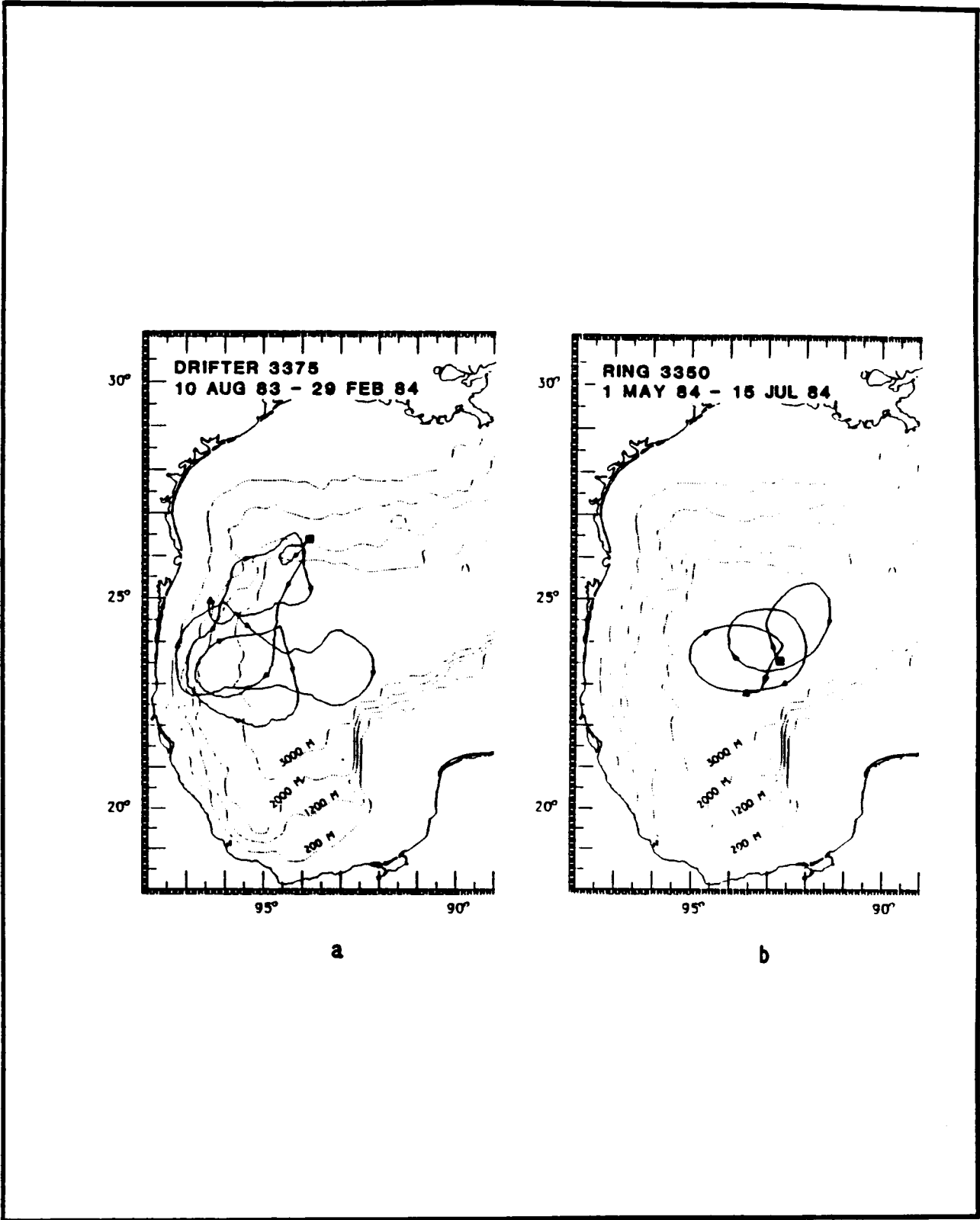


Figure 4.2-51. Trajectories for Drifters (a) 3375 and (b) 3350. Depth contours are in meters. The squares and triangles denote the start and end positions, respectively.

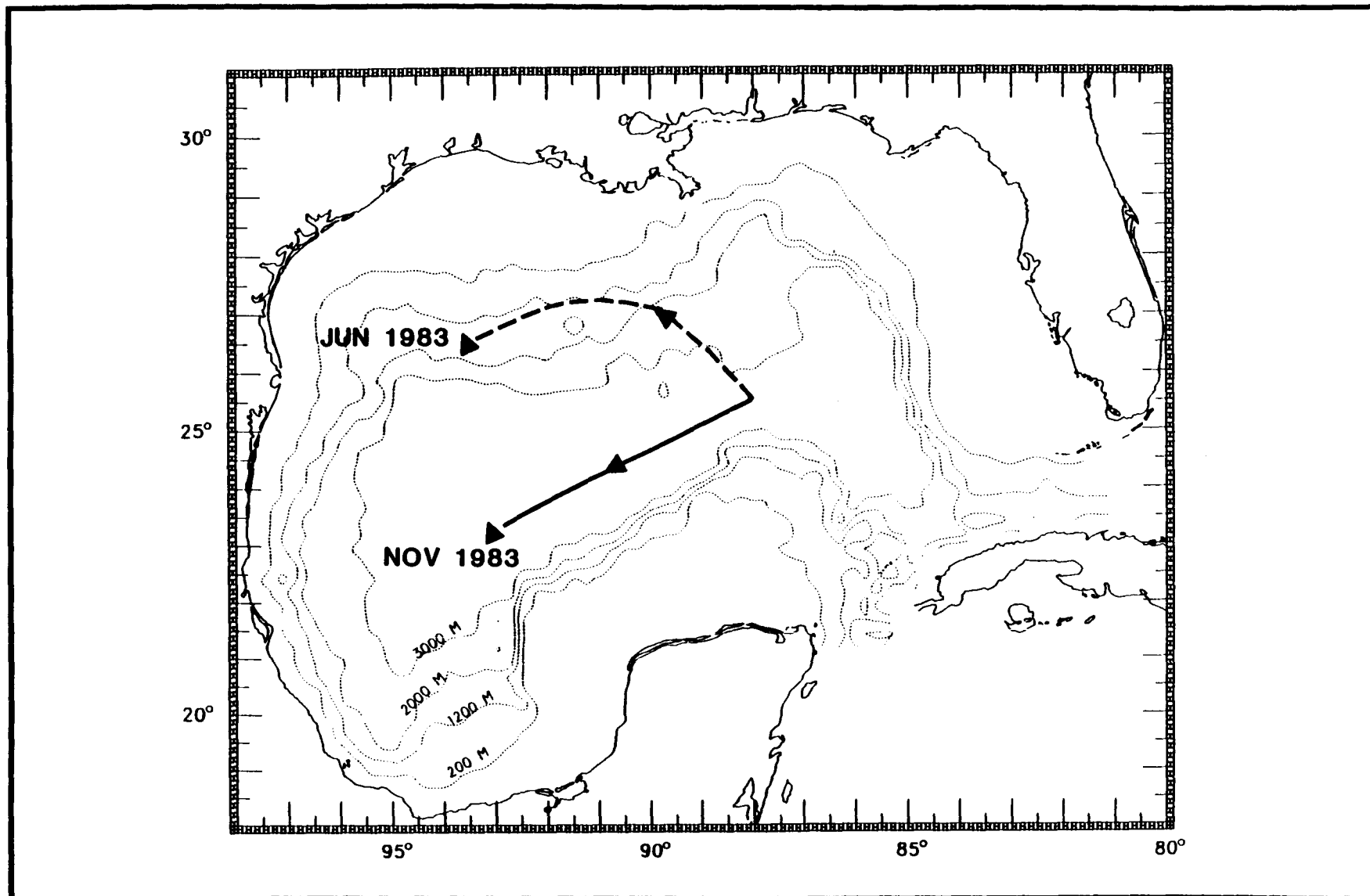


Figure 4.2-52. Path of the March 1983 ring as determined by infrared imagery and weekly oceanographic satellite data analysis from NOAA/NESDIS (dashed line) and as inferred by the results of this study (solid line).

drifter deployment cruise found no Loop Current ring. Numerical experiments by Hurlburt and Thompson (1980) and the ring trajectory data in Figures 4.2-50 and 4.2-51 would indicate that the March 1983 ring was probably considerably farther south, translating across the deeper portions of the Gulf. This situation demonstrates the care that must be taken in the interpretation of satellite thermal imagery, especially in the northern Gulf of Mexico where the presence of Mississippi River water (cooler temperatures in the winter, warmer temperatures in the summer) could mask the true dynamics of the system.

Drifter 3375 was deployed in a small eddy where the thermal frontal analysis had located the March 1983 ring. But after a few revolutions, Ring 3375 began heading south in August 1983 (Figure 4.2-51a), an unusual direction of flow considering the mean northwesterly wind flow for that month (Ropelewski, 1984). Hurricane Alicia did impact the upper Texas coast during mid-August 1983, and the associated cyclonic wind fields could have been responsible for some of the southward movement of Drifter 3375.

The trajectory of Ring 3375 began anticyclonic rotation right after the first of September 1983, with the center of rotation at approximately 24°N (Figure 4.2-51a). The question arises as to whether this first rotation was around Ring 3374 or the March 1983 ring. Several factors suggest that the rotation was around Ring 3374. First, the last recorded center of rotation for Ring 3374 (July 1983) was also at 24°N (see Figure 4.2-50c). In addition, Figures 4.2-50a and 4.2-50b indicate that initial ring impact tends to be several hundred km to the south along the Mexican coast. Thus, rotation around the March 1983 ring would be expected to be centered at 22°N . Moreover, the previously estimated time for a ring to travel across the Gulf indicates a western boundary impact time for the March 1983 ring of September to November 1983. A conjecture that the March 1983 ring was ~500 km east of the Mexican coast is supported by the continuation of the trajectory of Ring 3375 eastward into the Gulf of Mexico where it makes a large anticyclonic loop centered at 23°N and 93°W (Figures 4.2-51a and 4.2-7 through 4.2-9). All evidence indicates that this rotation was around the March 1983 ring (Figure 4.2-52).

To summarize, the data indicate the following scenario. The March 1983 ring was traveling across the deep portion of the Gulf of Mexico while Ring 3374 was against the Mexican coast. There was no evidence of a ring in the northwestern Gulf of Mexico during July and August 1983. During November 1983, the March 1983 ring had moved as far west as 93°W (Figures 4.2-7 through 4.2-9). An anticyclone moved into the northwestern Gulf of Mexico during this month, possibly a product of Ring 3374 (Figures 4.2-10 through 4.2-13). During January 1985, Ring 3374 and the anticyclone in the northwestern Gulf appeared to coalesce (Figures 4.2-14 through 4.2-16), with the center of rotation becoming approximately 26°N and 95°W . During February 1984, Ring 3350 totally pinched off from the Loop Current (Figures 4.2-17 and 4.2-18).

The coalescing of Ring 3374 with the more northerly anticyclone is likely a typical occurrence in the life history of a Loop Current ring. Modeling studies by Thompson (1985) show a similar process in which a ring spinning off the Mexican coast suddenly translates northward into the northwestern Gulf of Mexico. This rapid movement may be explained by the self-advection process within the ring itself. Smith and O'Brien (1983) have described how the accelerated flow on the western edge of a ring causes net northward translation. The approach of a more recently shed ring would further enhance

the ring asymmetry and greatly increase the tendency for northward translation. If it were not for this asymmetry and the resulting northward translation, the tendency would be for the older ring to coalesce with the approaching ring as opposed to the older ring (and its associated energy) moving northward onto the Texas shelf.

4.2.5 Ring Kinematic Parameters

The results of the kinematic calculations for Rings 1599 and 3374 show that differential motion is dominated by vorticity ζ , with deformation and divergence typically being much smaller than ζ . This would indicate that material in a Loop Current ring would tend to stay in the ring as it translates westward. If the material stays on the surface of the water, local winds could result in some of it leaving the ring. However, any part of the material floating some tens of meters below the water surface would tend to remain within the ring.

Rings 1599 and 3374 also show some amazing consistencies with the kinematic variables: a) the intensities of the circulation of both rings were $\sim 45 \text{ cm s}^{-1}$, b) both had oscillations of convergence/divergence about the ring center with a period of about 20 days, and c) the time series of vorticities (Figures 4.2-25 and 4.2-26) for both became more negative for approximately 30 days at 94°W . This agreement plus the identical paths of the rings indicates that a single process is responsible for governing much of the ring movement. Since the wind forcing over the life of each ring as well as its initial state may have been vastly different, it is logical to presume that bottom topography governs much of the ring motion as it translates westward. But whatever the mechanism may be, the results of the previous section indicate that ring/ring interaction must also be considered in the far western GOM.

4.2.6 Ring Dynamics

Dynamic calculations show periodic vortex stretching in the ring centers (convergence/divergence) which is not balanced by absolute vorticity variations, $(\zeta+f)$. It would not be unreasonable to attempt to relate variations in bottom topography to the periodic vortex stretching (i.e. topographic steering). However, the angular momentum of the movement of the ring center must also be considered, and initial calculations have shown that ζ_C and D_C are relatively large. This translates to the example of a wobbling top in which the spinning is almost constant compared to the wobble of the axis.

Since the angular momentum of the ring center is considerable, its influence must be added before attempting to relate variations in vorticity balance to variations in bottom topography. However, the calculations to date have been quite valuable and offer important information for modelers in the GOM. Specifically, vortex stretching is a dominant mechanism with a GOM ring and fluctuates with a period of about 20 days. In addition, the angular momentum of the ring centers appears to be considerable, with the position of a ring center moving westward in less than a smooth manner. These specifics can be translated directly to various model parameters. First, vortex stretching indicates the importance of a free water surface and variable layer depths within the model. More important, however, is the balance of the vortex stretching. Consider the situation in which $\zeta_C = D_C = 0$. This would indicate

that the vortex stretching must be balanced by a combination of shearing stresses and baroclinic torque. Thus, it is important that the model correctly specifies horizontal and vertical diffusion of momentum plus the horizontal and vertical variations of the pressure and density fields. This specification must not only be in terms of the parameterization of these variables but also in terms of the resolution (primarily horizontal resolution) of the parameters. Considering the scales of motion indicated by the Lagrangian drifters, a horizontal resolution of ~5 km would be appropriate.

4.2.7 Recommendations

4.2.7.1 Tracking Additional Rings

The results of present research indicate that Loop Current rings move westward through the deeper portions of the GOM, impact the Mexican shelf, and then translate northward. However, only three rings have been considered directly (Rings 1599, 3374, and 3350) and one ring indirectly (the March 1983 ring). This is a rather limited data set upon which to establish the basic kinematics of Loop Current rings; and thus, the seeding of additional rings with Lagrangian drifters should be pursued. In particular, the characteristics of rings that may take a more northerly path across the GOM need to be determined. In a study of satellite imagery, Vukovich and Crissman (1985) found indications of rings moving westward along the Texas/Louisiana shelf, although the preferred path was similar to that found in this study. Also, experiences within the offshore industry indicate numerous encounters with high-speed, ring-like currents along the Texas/Louisiana shelf. It would be highly desirable to study a more northerly moving ring in order to provide the best possible picture of the possible variations of Loop Current ring kinematics. This information would also provide the modelers with some indication of the frequency and characteristics of anomalous ring movement.

4.2.7.2 Kinematic Analysis

A continuation of this study and interpretation of the kinematic parameters of Rings 1599 and 3374 and any future rings that are tracked are recommended. Kinematic analysis not only provides the parameters for dynamic studies, but it also provides clues to the interaction of a ring with its environment. Further study of ring orientation and eccentricity as it travels through the deeper Gulf, approaches the western GOM shelf, and moves northward along the western shelf is specifically recommended. This could provide further indications of ring/topography and ring/ring interactions. In addition, the cause of the abrupt change in vorticity, seen as Rings 1599 and 3374 approached 94°W needs to be determined. This short-term change, which increased the negative vorticity by a factor of about two, strongly indicates the coupling of the flow fields of two anticyclonic rings. Thus, it is possible that these kinematics will indicate how two anticyclones begin to merge as one approaches another from the east.

4.2.7.3 Ring Dynamics

The results to date indicate a primary governing force for ring movement, possibly topographic steering. Force balances in terms of angular momentum were considered, and the results indicate that ring center motion must be

further studied. Additional vorticity calculations using ζ_T and D_T from Rings 1599 and 3374 and for any additional rings tracked in the future are recommended. Specifically, the importance of vortex stretching will be calculated and the relation of this stretching to depth variation (i.e. does $D_T = -H^{-1}dH/dt$) will be studied. The importance of shearing stresses and baroclinic torque in balancing the vorticity equation will also be studied.

4.3 Satellite Thermal Imagery

4.3.1 Eastern Gulf of Mexico: 1983-1984

Circulation in the eastern Gulf of Mexico is generally dominated by the highly variable Loop Current and related features (Leipper, 1970; Behringer, 1977; Maul, 1977; Molinari, 1977; Vukovich et al., 1979). To characterize this variability in the eastern Gulf of Mexico for 1983-1984, monthly thermal frontal maps were constructed using NOAA and GOES satellite infrared data. These were analyzed to present the most characteristic position of the Loop Current front and of any associated warm rings for the months of January, February, March, April, May, November, and December. For June, July, August, September, and October, satellite infrared data could not be used to define thermal boundaries because of the lack of spatial contrast of the sea-surface temperatures and because the high water vapor concentration in the marine boundary layer markedly affected the infrared signature of the sea-surface.

In January 1983 (Figure 4.3-1a), a major warm ring (diameter on the order of 400 km) was separating from the Loop Current. The separation process actually began in December 1982. The February frontal analyses suggest that the ring

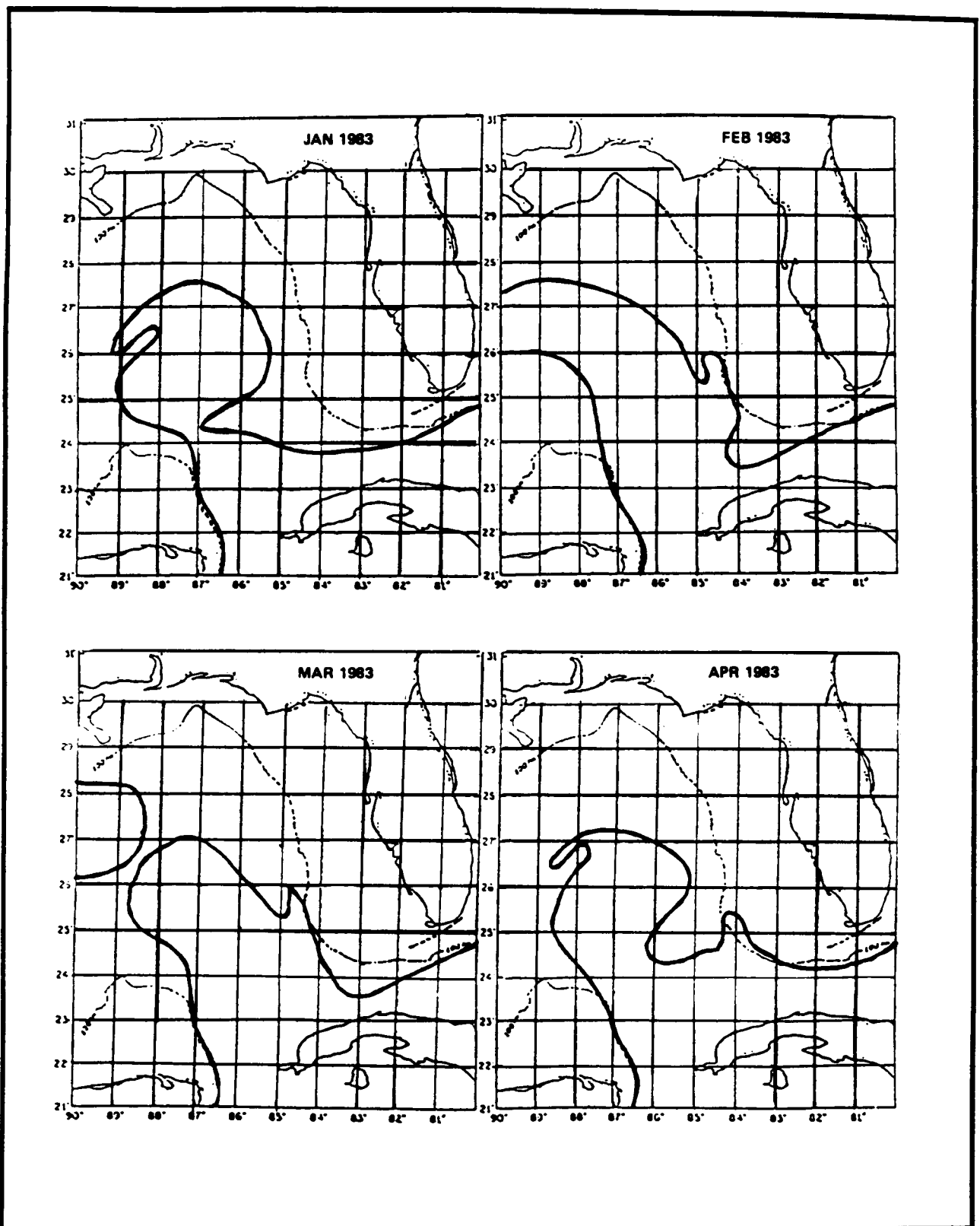


Figure 4.3-1a. Monthly frontal analyses in the eastern Gulf of Mexico derived from NOAA and GOES satellite data for the period from January through April 1983.

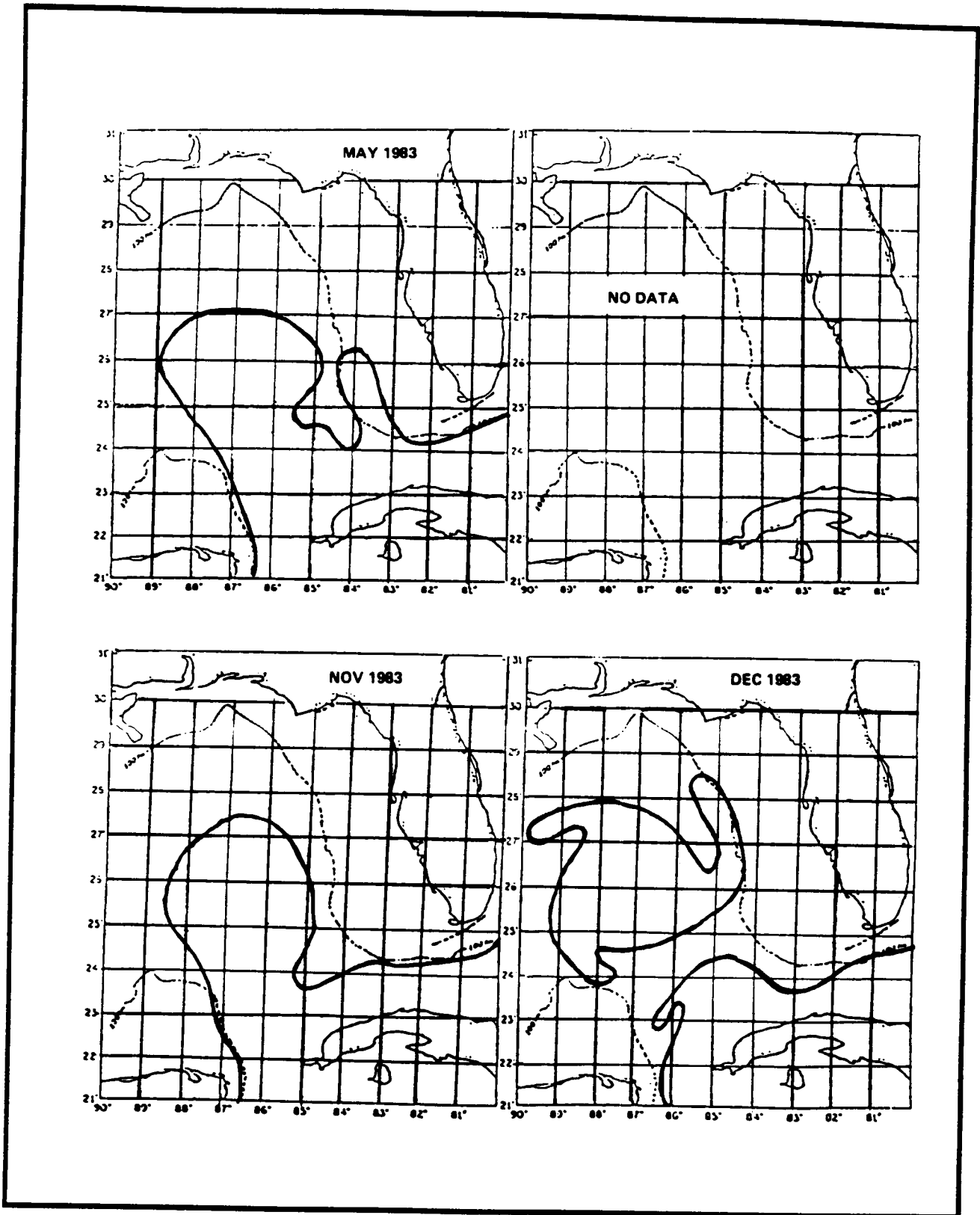


Figure 4.3-1b. Monthly frontal analyses in the eastern Gulf of Mexico derived from NOAA and GOES satellite data for the period from May through December 1983.

Like the period from January through May 1983, January through May 1984 (Figure 4.3-1c) was also characterized by a number of perturbations on the LC front which had a profound effect on the character of that boundary during that period. Aspects of these perturbations will be discussed later.

In November 1984 (Figure 4.3-1d), small warm rings were separating from the northern portion of the Loop Current. By December 1984, these rings (ring diameters on the order of 100 km) were evident in the central portions of the eastern Gulf of Mexico. However, there was no indication that a major warm ring was separating from the Loop Current as previously occurred in December 1982 and December 1983.

4.3.2 Cold-Core Perturbations in the Eastern Gulf of Mexico (1983-1984)

Cold-core perturbations which were detected on the boundary of the Loop Current and which affected the circulation in the eastern Gulf of Mexico have many characteristics. The most common of these are alternating cold and warm filament-like structures, cold tongues, and cold meanders (Vukovich and Maul, 1985). In the period 1983 through 1984, many perturbations were noted on the boundary of the Loop Current. Most of these only lasted a few days to one or two weeks. Eleven lasted more than two weeks and some lasted more than two months. The boundary features having longer life cycles were thought to be the cold-core perturbations described by Vukovich and Maul (1985). The shorter time-scale phenomena are believed to be shallow and may be associated with small time-scale effects; e.g., wind associated mixing.

Various statistics on the eleven cold-core perturbations detected in the period from 1983 through 1984 are presented in Table 4.3-1. Each perturbation has been labeled by a letter of the alphabet. Among the information given in the Table are the average horizontal dimensions and speed of the perturbation at the surface. The horizontal dimension was divided into two parts: the scale length parallel to the direction of the mean flow of the Loop Current (along-flow scale length) and the cross-flow scale length. The speed was determined by successive positions of the center of the perturbation given the time of each observation. The period of existence (the period over which the perturbation was detectable) of the perturbation and comments concerning the perturbation are also presented. Under the heading "Period of Existence", two dates are presented. The first is the date on which the perturbation was first observed. The perturbation may have existed previous to that date but it was not detected using satellite data. The second is the date on which the perturbation could no longer be detected in the satellite data. If no ending time is presented in the Table, it means that the temperature gradient at the sea-surface vanished under the influence of seasonal heating and that the outcome of the perturbation could not be determined.

Cold-core perturbations which are usually located along the northern and eastern boundaries of the Loop Current have, on the average, an along-flow scale length of about 190 km and a cross-flow scale length of about 130 km. The speed of these perturbations ranges from 6 to 24 km day⁻¹. The slower speeds are associated with those perturbations located off the Dry Tortugas. The life cycle of these boundary disturbances, which is based on satellite infrared observations, can be as small as 16 days and as large as four months. The shorter life cycles are generally associated with those whose life cycle was abruptly changed such as occurred in the period from March through May

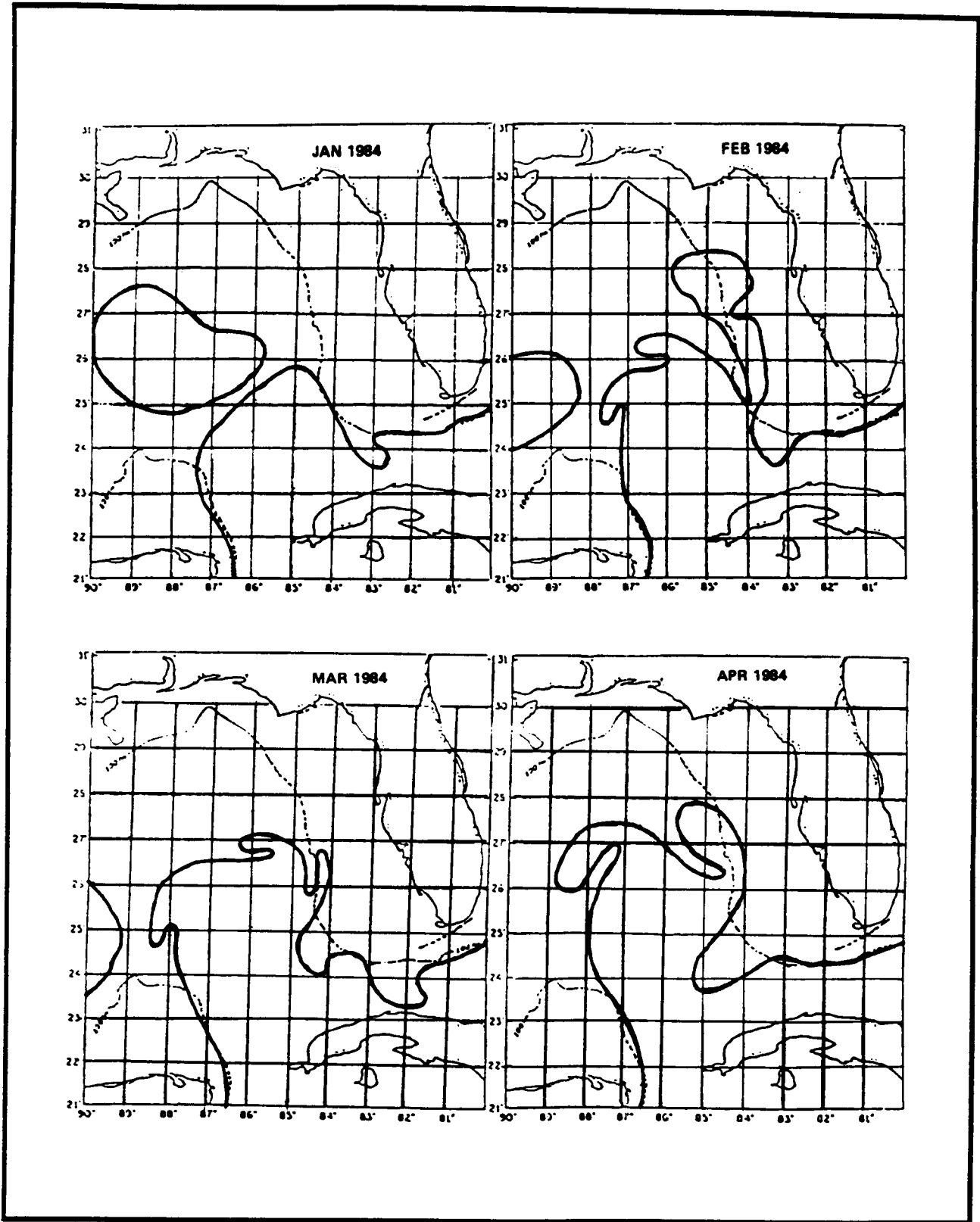


Figure 4.3-1c. Monthly frontal analyses in the eastern Gulf of Mexico derived from NOAA and GOES satellite data for the period from January through April 1984.

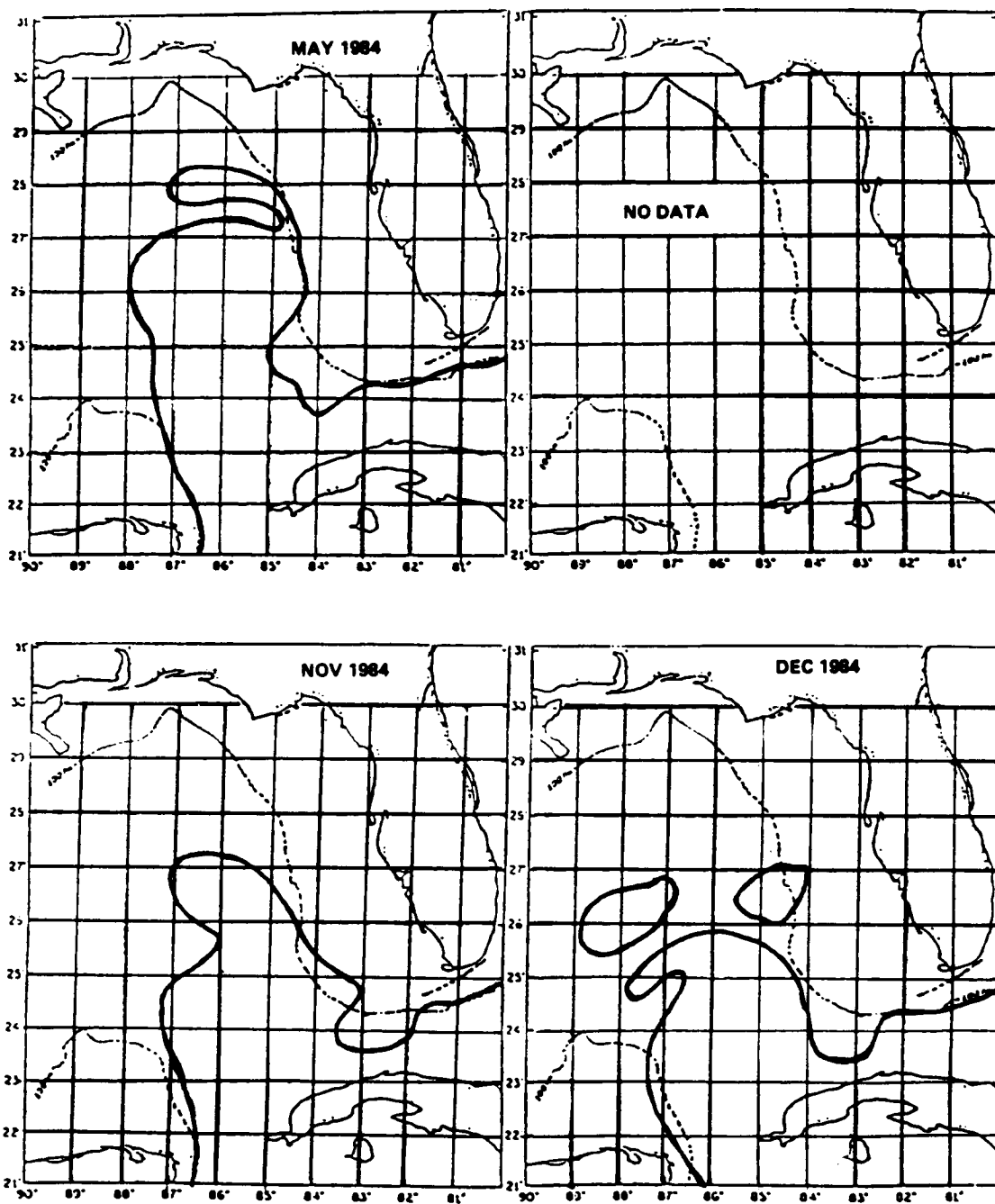


Figure 4.3-1d. Monthly frontal analyses in the eastern Gulf of Mexico derived from NOAA and GOES satellite data for the period from May through December 1984.

Table 4.3-1. Statistics on Cold Perturbations in the Gulf of Mexico for 1983-1984.
The averages are over the periods that the perturbation was detected.

Major Cold Perturbation	Average Along-flow Scale-length (km)	Average Cross-flow Scale-length (km)	\sim Average Speed (km/day)	Period of Existence	Comments
A	220	160	8	1 Mar - 10 Apr 1983	Merged with B or grew or dissipated.
B	170	70	8	24 Mar - 10 Apr 1983	Merged with A or grew or dissipated.
C	310	190	6	10 Apr - mid-June 1983	Meander developed as a result of either the merger of A and B, or A grew and B dissipated or A dissipated and B grew.
D	180	130	14	7 May 1983 -	Temperature gradient vanished before outcome could be determined.
E	190	180	10	1 Nov - 7 Dec 1983	Merged with F or dissipated.
F	240	200	10	28 Nov - 13 Dec 1983	Warm ring separated and cold perturbation was no longer detected.
G	200	120	11	15 Jan - 1 Apr 1984	Dissipated.
H	190	130	10	24 Jan - 21 May 1984	Dissipated.
I	130	60	10	14 Mar - 21 Apr 1984	Dissipated.
J	220	80	24	13 Apr - 5 May 1984	Dissipated.
K	200	80	20	18 May 1984 -	Temperature gradient vanished before outcome could be determined.

1983. In that period, three perturbations were discovered and the outcome of two of them could not be detected. It appeared that these latter two merged, forming one large one. This will be further discussed below.

Perturbations E and F, which were detected in the period from 1 November through 13 December 1983, also had short life cycles. It appears from the NOAA infrared imagery (Figure 4.3-2) that Perturbation E merged with Perturbation F around 8 December. By 13 December, a warm ring separated from the Loop Current and the cold perturbation which resulted from the merger of Perturbation E and F was no longer detectable.

Perturbations G and H, which had long life cycles, were first detected on the northwestern boundary of the Loop Current (Figure 4.3-3). These features traveled eastward along the northern boundary of the Loop Current until they reached the west Florida shelf, then moved southward until they reached the Dry Tortugas. Upon reaching the Dry Tortugas, their speed decreased appreciably and they become quasi-stationary. They also appeared to grow in size before dissipating. A more detailed discussion of the life history of Perturbation H will be given in Section 4.3.4. Examination of over ten years of satellite infrared imagery has indicated that these perturbations have never been observed to advect through the Florida Straits.

4.3.3 Cold Perturbations in the Eastern Gulf of Mexico (March through May 1983)

4.3.3.1 Introduction

In the spring of 1983, a series of hydrographic cruises were conducted in the eastern Gulf of Mexico as part of this and another program by the Florida Institute of Oceanography (FIO). The data from these cruises describe a significant portion of the life history of three cold perturbations. Analysis of hydrographic and current meter data was combined with the analysis of satellite data to study the evolution and circulation in the cold perturbations over a period of approximately 60 days.

Current meter data from two moorings located on or immediately off the west Florida shelf were used to study the flow characteristics in the perturbations. The first mooring was located at a depth of approximately 1700 m at 25.72°N and 84.88°W; (position A in Figure 4.3-4a), the second, at a depth of 180 m at 25.88°N and 84.32°W (position C). In both cases, data from the shallowest current meter were used (172 m for A and 50 m for C). The temperature pattern on the west Florida shelf was characterized by cold water to the north in the Apalachee Bay regions (see Figure 4.3-4a) with increasing temperature southward toward the Florida Keys.

4.3.3.2 Analysis Results

On 9 March 1983, the NOAA sea-surface temperature distribution (Figure 4.3-4a) indicated that a wavelike cold perturbation was centered around 25.7°N and 85.4°W. A warm filament had developed on the shoreward side as a result of northward advection of warm Loop Current water. The northward movement of water in the warm filament was indicated by the current meter data (i.e., north-northwest flow at approximately 35 cm s^{-1} was observed at current meter A, and northeast flow at approximately 13 cm s^{-1} , at current meter C).

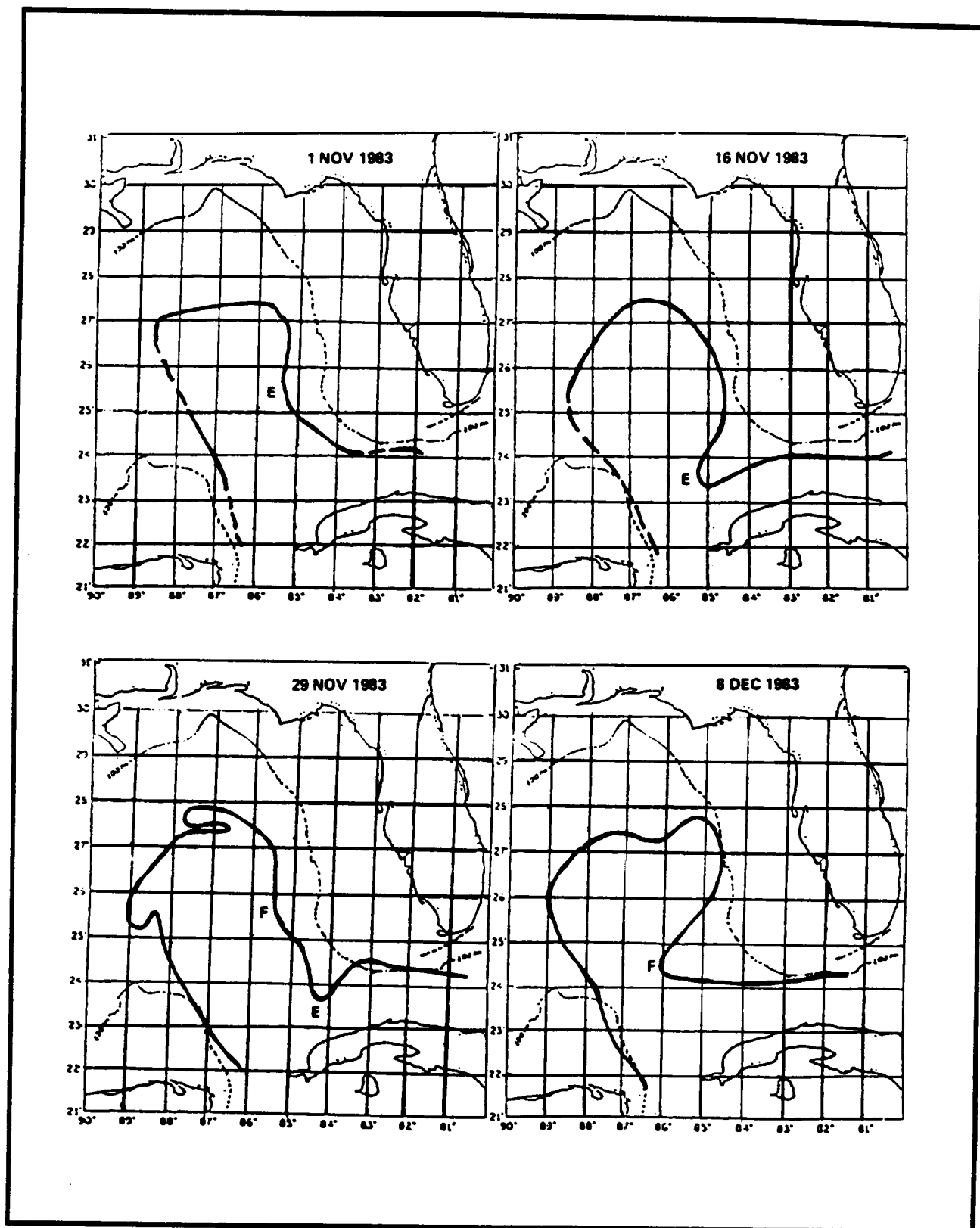


Figure 4.3-2. Frontal analysis in the eastern Gulf of Mexico using satellite data for the period from 1 November to 8 December 1983.

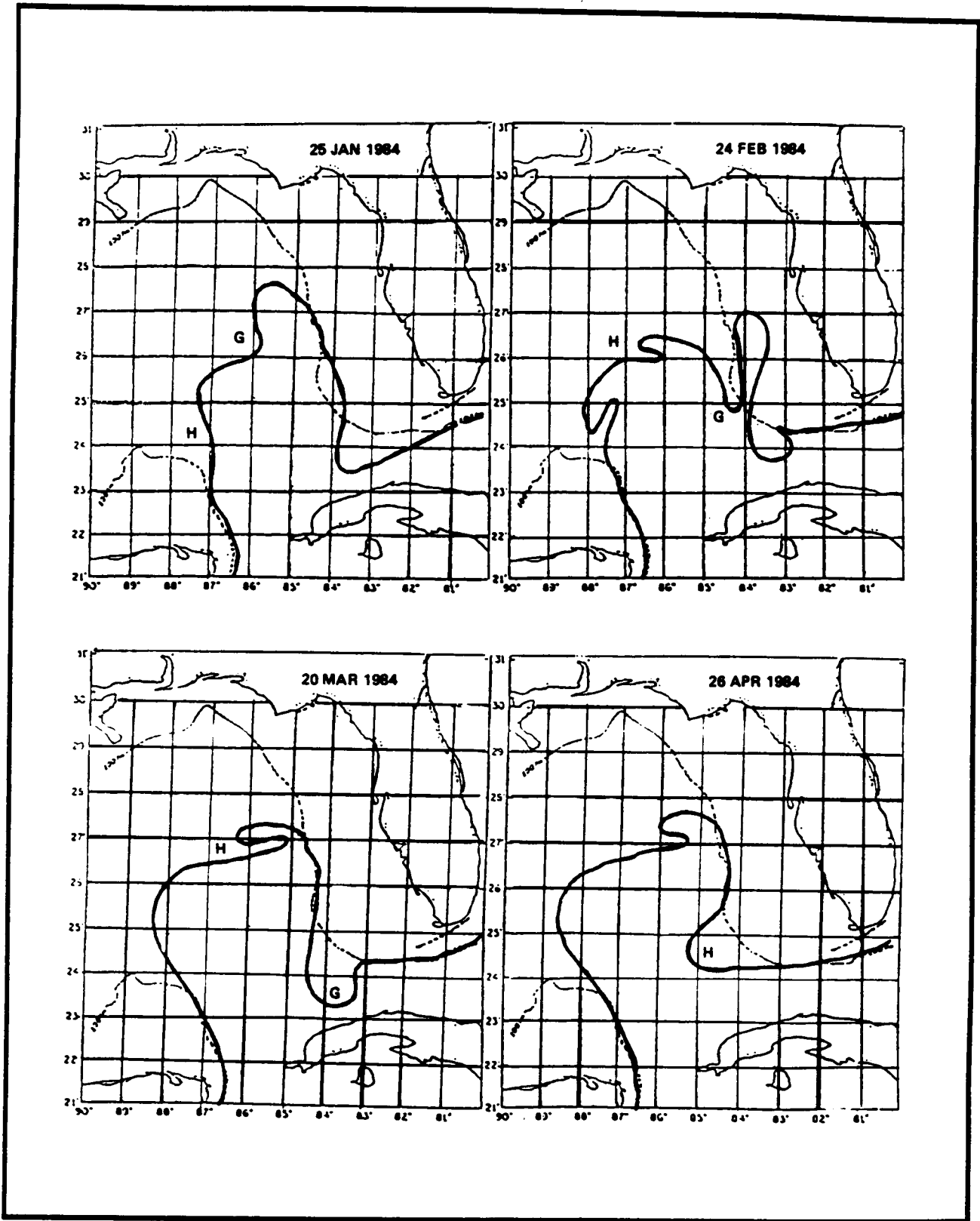
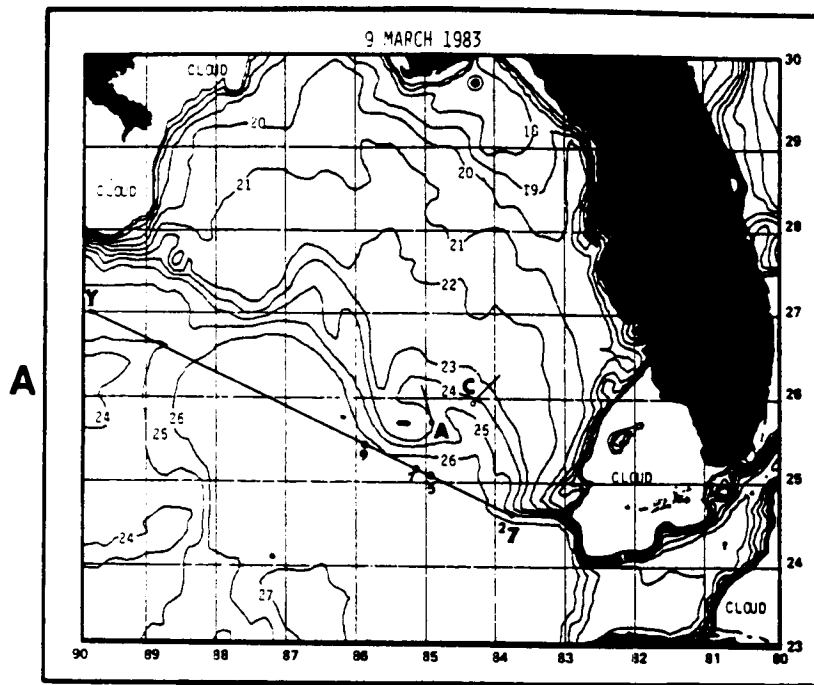
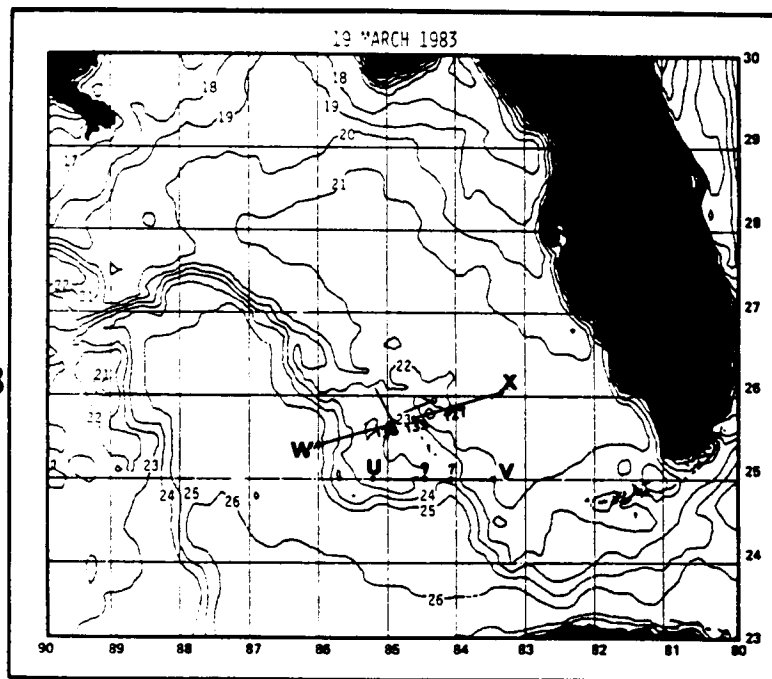


Figure 4.3-3. Frontal analysis in the eastern Gulf of Mexico using satellite data for the period from 25 January to 26 April 1984.



A



B

Figure 4.3-4. (A) Sea-surface temperature ($^{\circ}\text{C}$) analysis for 9 March 1983. Transect XY was performed by the E.M. QUEENY (7-8 March 1983). The large dot indicates the Apalachee Bay.

(B) Sea-surface temperature ($^{\circ}\text{C}$) analysis for 19 March 1983. Transect XW was performed by SAIC (19-21 March 1983). Transect VU was performed by FIO (24-25 March 1983).

The temperature section (Figure 4.3-5) along transect ZY (Figure 4.3-4a) shows that the leading edge of the cold perturbation is between Stations 7 and 9. There is no indication of the cold dome which characterizes these features (Vukovich and Maul, 1985), but this was expected since the transect is at the leading edge of the feature. It is important to note that the 24 and 25°C isotherms are horizontal between Stations 3 and 6 at the leading edge of the warm filament (see arrow in Figure 4.3-5).

The 19 March 1983 NOAA sea-surface temperature analysis (Figure 4.3-4b) indicated that the west Florida shelf was characterized by relatively the same pattern as on 9 March. The cold perturbation had moved southward at approximately 7 km day⁻¹. The warm filament had a length of about 150 km. North-northwestward flow at approximately 31 cm s⁻¹ was observed at the northern edge of the warm filament by current meter A, and west-southwestward flow at approximately 13 cm s⁻¹ on the east side of the filament by current meter C. Another wavelike cold perturbation was detected at approximately 26.2°N and 86.3°W.

Figure 4.3-6 presents the temperature and geostrophic analysis along transect XW (Figure 4.3-4b). The transect passed north of the center of a cold perturbation and essentially through the current meter mooring line. A deep cold dome is centered around Station 140 (Figure 4.3-6a). The warm filament noted in the satellite data is located between Stations 133 and 138. The transect passed through the northern edge of the warm filament, which appears to be very shallow (approximately 50 m deep). The depth of the warm filament was based on all cases on the determination of the depth of a line that passed through the maximum curvature of each isotherm in the filament. When an isotherm was reached that no longer had a curvature maximum, the maximum depth of the filament was assumed to be reached. A secondary, shallow warm feature is noted at Station 129, where current meter C was located.

Strong southward geostrophic currents (negative velocities) having a maximum speed of approximately 94 cm s⁻¹ at the surface are noted in the Loop Current centered near Station 144 (Figure 4.3-6b). Northward geostrophic currents (surface speed ~ 10 to 20 cm s⁻¹) are found in the warm filament in the region where current meter A was located. Southward geostrophic currents (surface speeds ~ 10 to 20 cm s⁻¹) were noted on the east side of the warm filament near the region where current meter C was located. It should be noted that the component of the near-surface current perpendicular to section XW measured by current meter C is approximately zero.

Transect VU (Figure 4.3-4b) crossed the mouth of the warm filament; i.e., that portion of the warm filament where warm Loop Current water was first being advected northward on the shoreward side of the cold perturbation. The mouth was located between Stations 7 and 10 in the temperature section (Figure 4.3-7a). The isotherm pattern shows a relatively warm feature centered at about Station 7 and extending to approximately the 350-m depth. Strong northward currents having a surface speed of approximately 100 cm s⁻¹ are noted on the western side of the warm filament (Figure 4.3-7b). Southward geostrophic currents having a surface speed of approximately 20 cm s⁻¹ are noted on the east side of the warm filament.

The 3 April 1983 NOAA sea-surface temperature distribution (Figure 4.3-8) shows two closely spaced cold perturbations on the eastern boundary of the

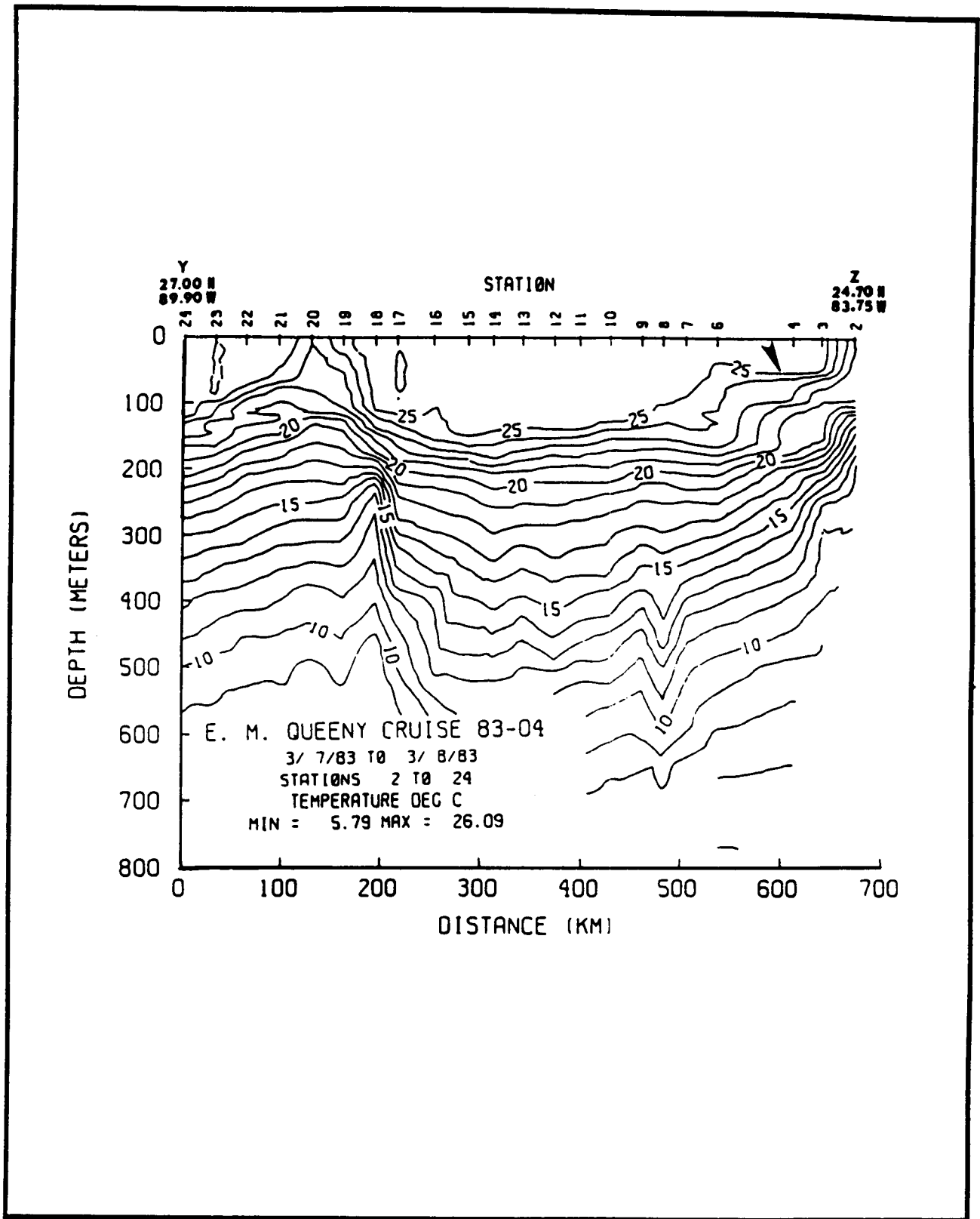


Figure 4.3-5. Temperature ($^{\circ}$ C) analysis along transect ZY indicated in Figure 4.3-4a.

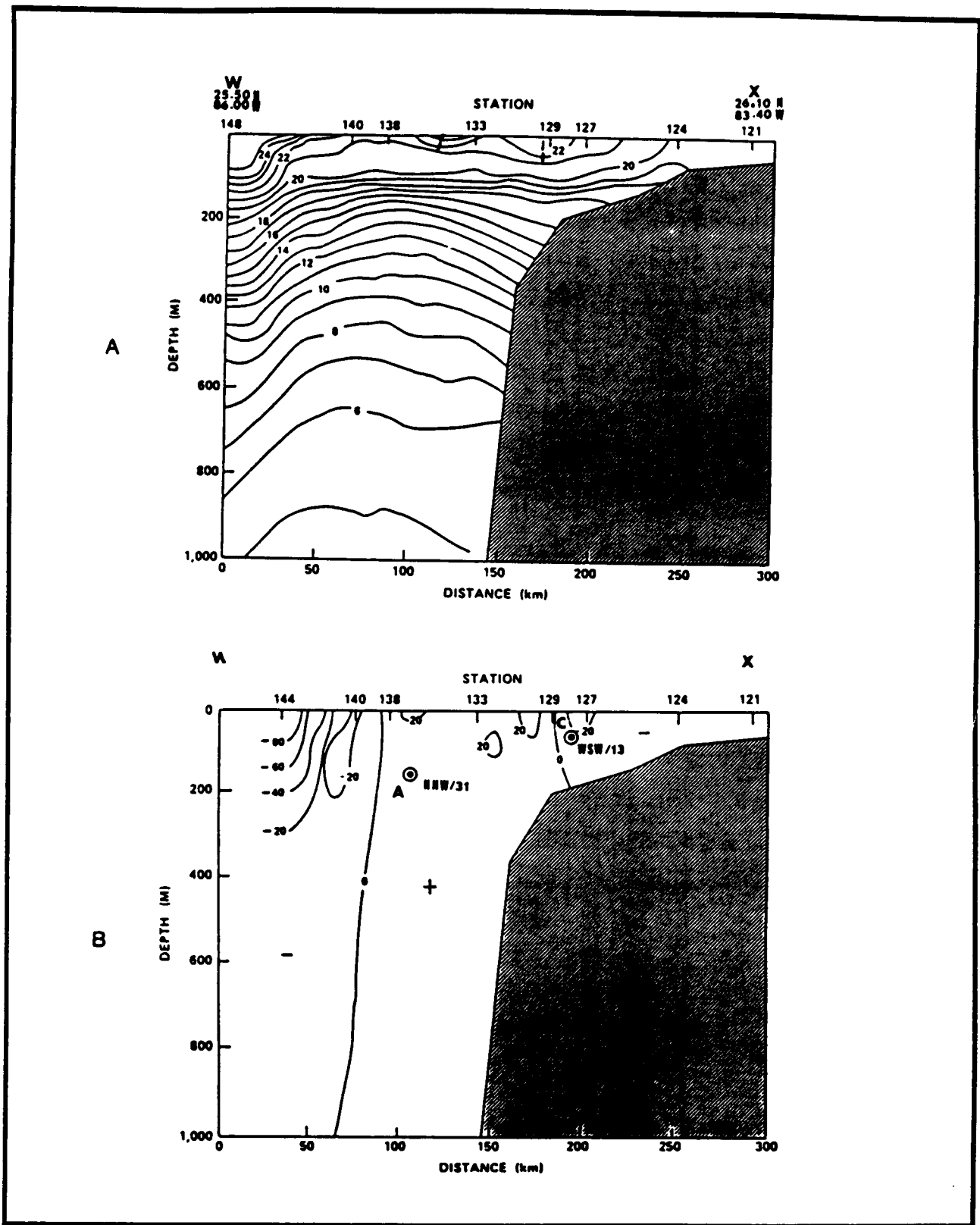


Figure 4.3-6. (A) Temperature ($^{\circ}\text{C}$) analysis along transect XW.
 (B) Geostrophic current (cm s^{-1}) analysis along transect XW.
 The transect was performed in the period of 19-21 March 1983 (see Figure 4.3-4b).

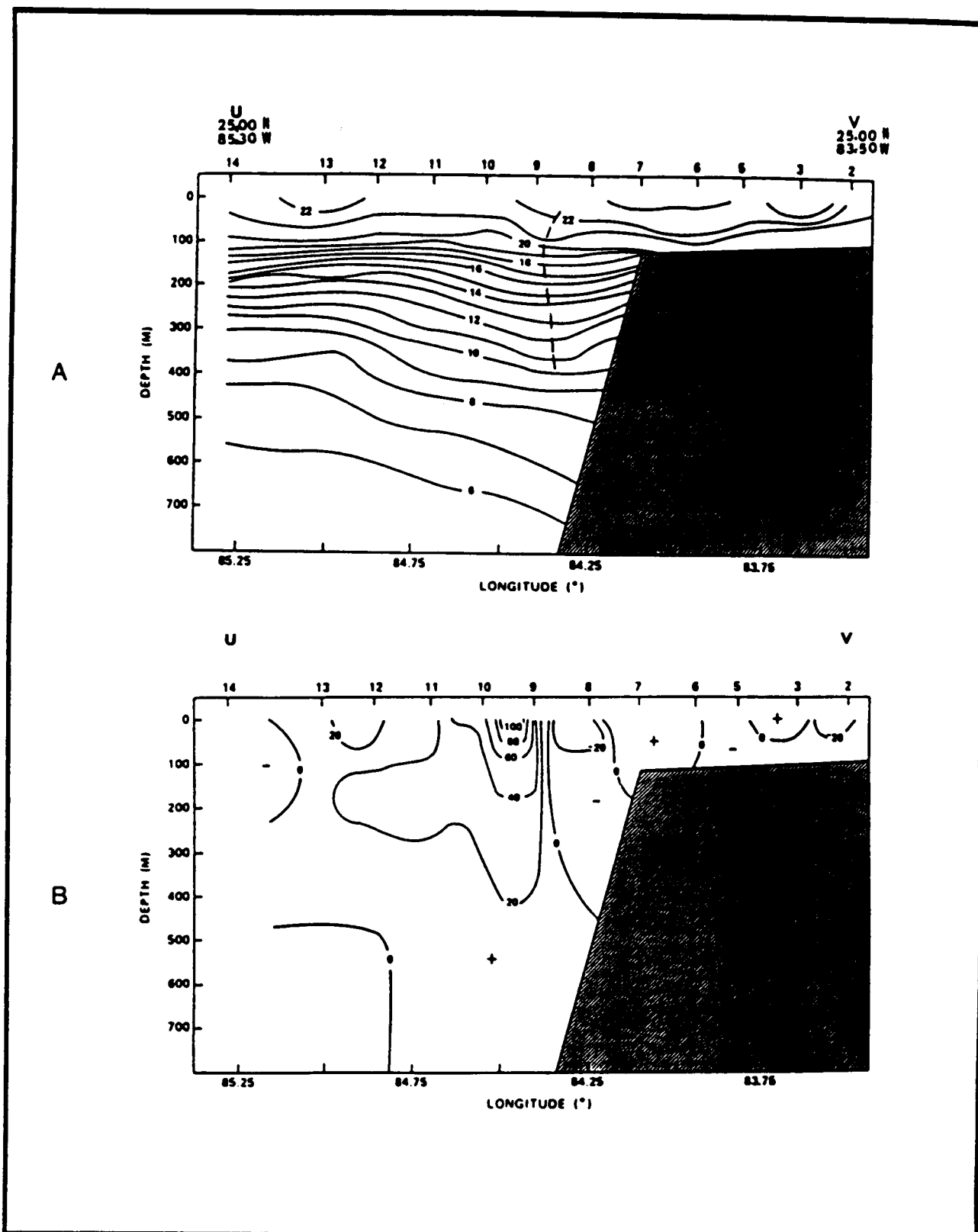


Figure 4.3-7. (A) Temperature ($^{\circ}\text{C}$) analysis along transect VU.
 (B) Geostrophic current (cm s^{-1}) analysis along transect VU.
 The transect was performed in the period of 19-21 March 1983 (see Figure 4.3-4b).

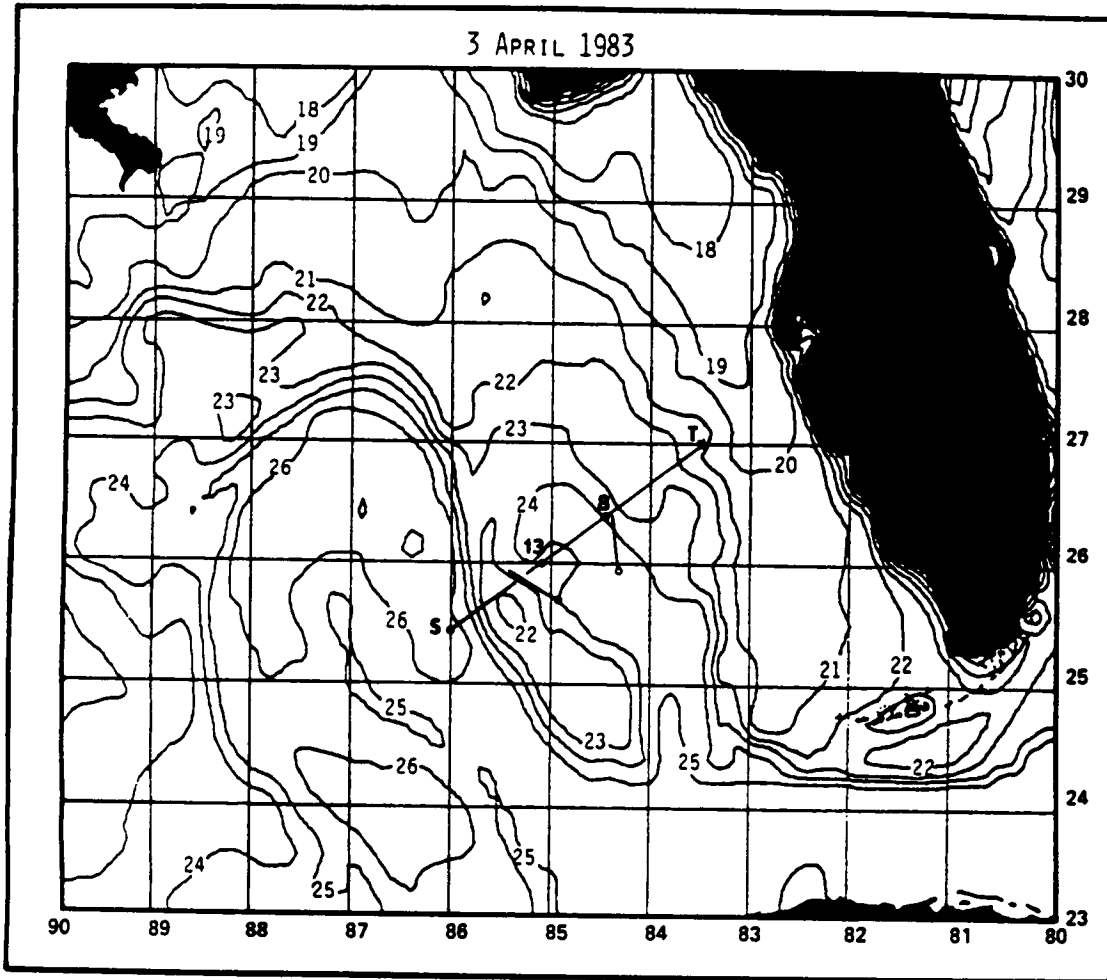


Figure 4.3-8. Sea-surface temperature ($^{\circ}\text{C}$) analysis for 3 April 1983. Transect TS was performed by F10 in the period of 4-5 April 1983.

Loop Current. The perturbation detected around 9 March had moved south-southeastward from its position on 19 March at approximately 8 km day^{-1} and was centered at about 24.9°N and 84.6°W , where there is a closed 22.5°C isotherm (dashed line). The second perturbation, which was detected on 19 March (and was traced back to the feature at 26.9°N and 86.4°W on 9 March using a time series of satellite data), also moved southeastward, but at about 10 km day^{-1} . It was centered at around 25.7°N and 85.4°W , where there is a closed 22.0°C isotherm.

An elongated warm filament that was oriented northwest-southeast developed on the shoreward side of these two perturbations. The warm filament had a length of approximately 300 km, which is at least a factor of two greater than the largest warm filament previously noted. Both current meters A and C were in the warm filament. The near-surface flow at current meter A was northwestward at approximately 30 cm s^{-1} ; at current meter C, the near-surface flow was to the north at approximately 3 cm s^{-1} . The general character of the surface temperature pattern on the west Florida shelf was similar to that previously observed.

The cold dome centered near Station 14 (Figure 4.3-9a) is associated with the newest perturbation. The cold dome is not pronounced because the transect did not pass through the center. The northern part of the warm filament, which is between Stations 8 and 13, is a shallow feature, having a depth of about 50 to 100 m. The maximum surface geostrophic current in the Loop Current (Figure 4.3-9b) has a speed of about 100 cm s^{-1} to the south. The surface geostrophic current in the northern part of the warm filament varied from 10 to 20 cm s^{-1} . Weak southward geostrophic currents were calculated on the east side of the filament where current meter C observed northward flow.

On 12 April 1983, only one large cold-core meander, centered at 24.8°N and 85°W , was detected (Figure 4.3-10). Whether this meander was the result of the coalescence of the two cold perturbations detected on 3 April or whether one of those perturbations dissipated while the other grew could not be determined from the available data. Both current meters A and C were north of the meander in a region where there was little or no temperature gradient. The flow at current meter A was southward at approximately 10 cm s^{-1} , and that at current meter C was eastward at approximately 14 cm s^{-1} .

In the previous sea-surface temperature analysis, the sea-surface temperature pattern on the west Florida shelf was characterized by cold water to the north in the Apalachee Bay region, and the temperature increased toward the Florida Keys. On 12 April, the sea-surface temperature pattern on the west Florida shelf was characterized by a series of isolated cold and warm patches. Although seasonal heating may be responsible for the change, this process generally increases the surface temperature gradually over a period of weeks to months and is usually not responsible for such an abrupt change in the relative distribution of temperature (Vukovich et al., 1978; Vukovich et al., 1980). The large warm patch centered at 28.5°N and 83.7°W had a center surface temperature greater than 24°C . A temperature of this magnitude was previously observed only in the Loop Current or in the warm filaments (which contain Loop Current water) associated with the cold perturbation. Unfortunately, in situ temperature and salinity data were not available in the feature to help determine the warm patch's origin.

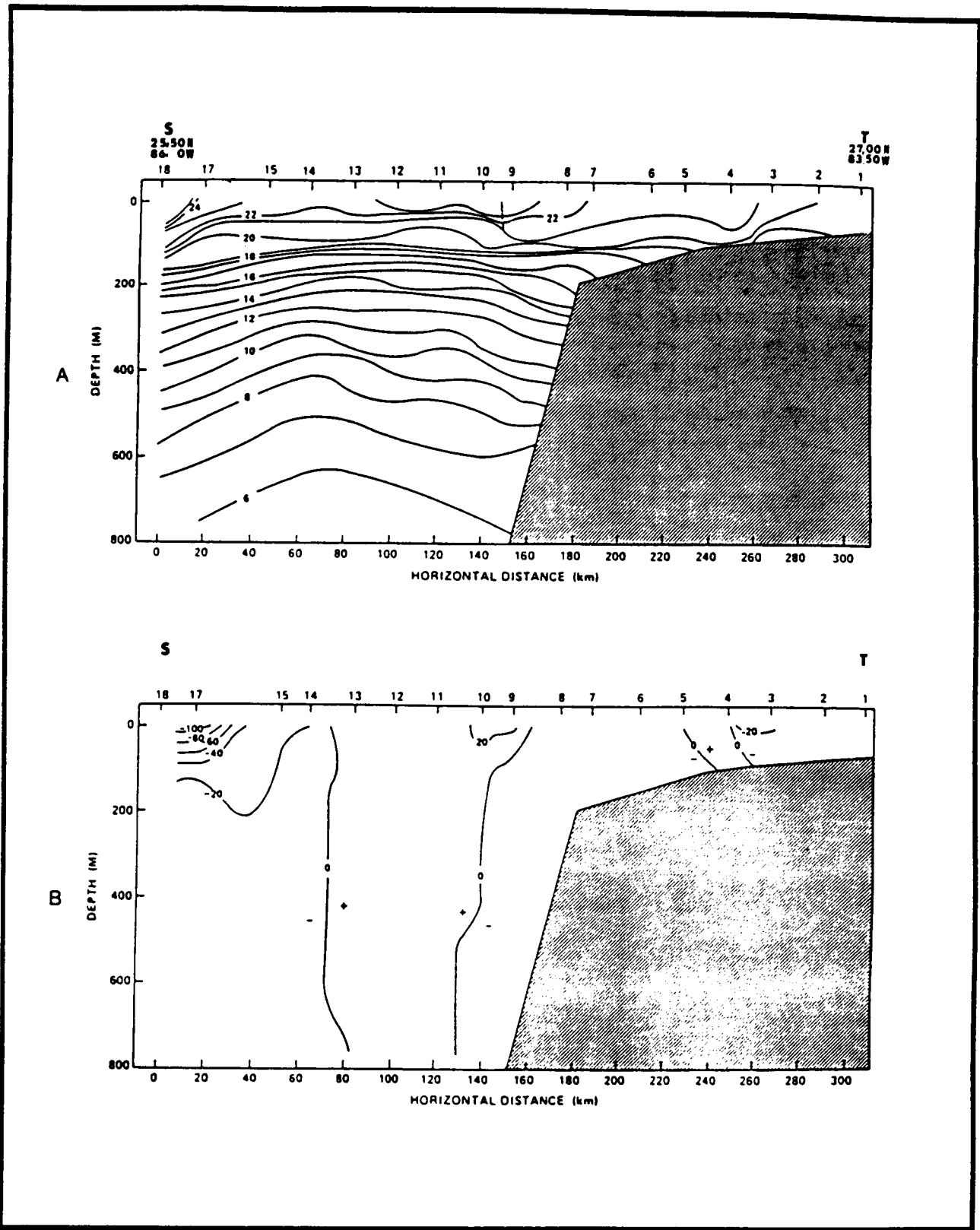


Figure 4.3-9. (A) Temperature ($^{\circ}\text{C}$) analysis along transect TS. (B) Geostrophic current (cm s^{-1}) analysis along transect TS. The transect was performed in the period of 4-5 April 1983. (See Figure 4.3-8).

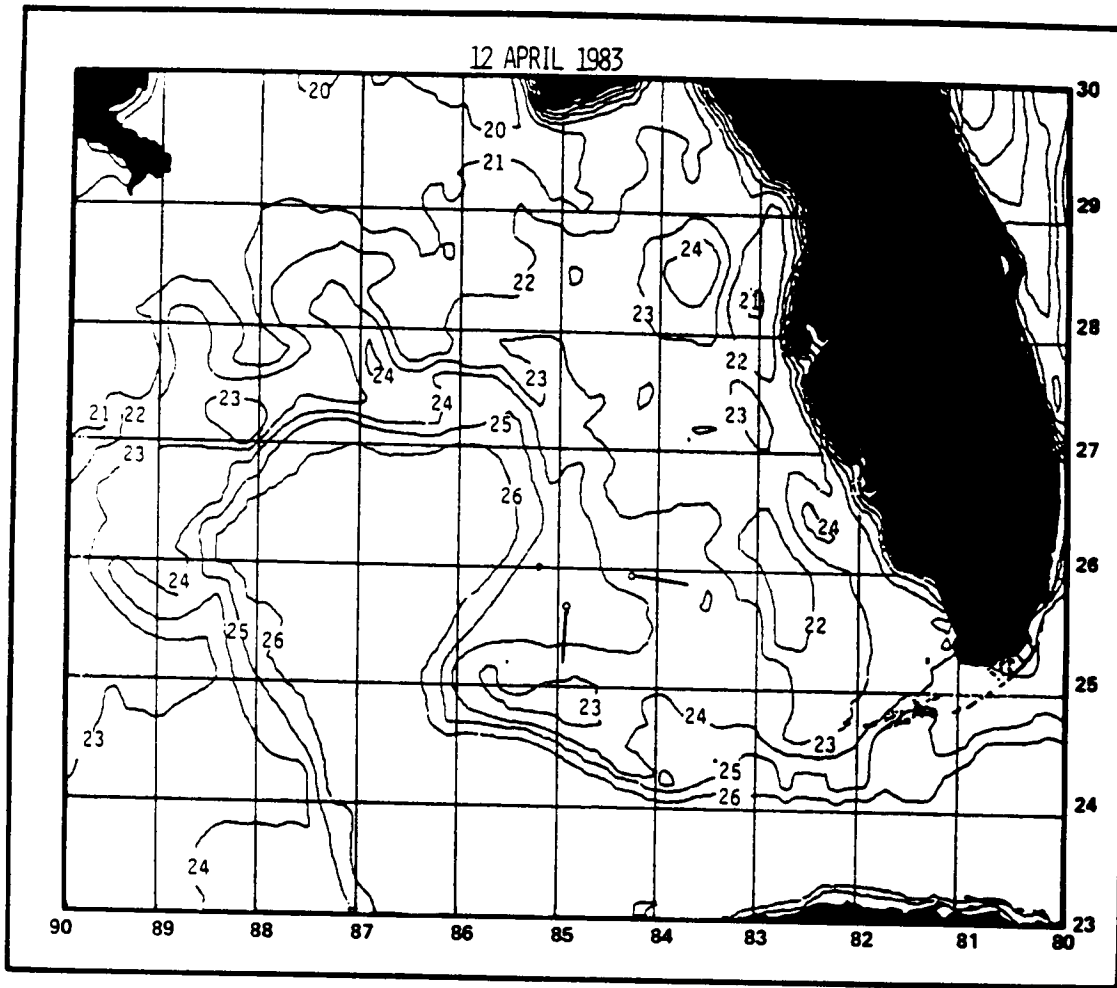


Figure 4.3-10. Sea-surface temperature (°C) analysis for 12 April 1983.

The meteorological data indicated that a major atmospheric cold front passed through the Gulf of Mexico between 6 and 10 April 1983. It is difficult to attribute the change on the west Florida shelf to a single meteorological event or the cumulative effect of a number of events since the winds and the pressure changes associated with that system or the series of systems before 12 April were not any stronger than those associated with systems that passed through the Gulf before or after 1 March. No significant change of the sea-surface temperature pattern on the west Florida shelf was observed between 1 March and 1 April. There was, however, a major difference in the oceanography off the west Florida shelf between the 1 March and 1 April period and the 1 and 12 April period. Large amounts of warm Loop Current water were being advected northward along the seaward boundary of the west Florida shelf (the 200-m isobath) in a large warm filament (Figure 4.3-8) between 1 and 12 April. A time series of satellite data indicated that the warm water in the filament moved onto the west Florida shelf in a northeastward direction. Between 2 and 9 April, the winds were persistent from the south and southeast which could account for the manner in which the warm Loop Current water moved to the northeast. The warm filament was present prior to and during the development of the large meander, but was no longer evident after the large meander developed. Though the evidence suggests that the change in the temperature pattern may have been a result of mixing between the Loop Current water contained in the large warm filament and the shelf water, the evidence is not conclusive.

By 26 April 1983 (Figure 4.3-11), the meander had moved to the south-southeast at approximately 4 km day^{-1} and was centered at about 24.7°N and 84.8°W . In the time period since the last sea-surface temperature analysis, a large warm filament, approximately 165 km in length, had developed on the shoreward side of the meander. The warm filament was identified in four clear-sky satellite images over a 5-day period. Current meter A was located at the surface manifestation of the Loop Current front and the near-surface flow at that position was south-southeastward at approximately 19 cm s^{-1} . Current meter C was located immediately north of the leading edge of the warm filament. The near-surface flow at current meter C was westward at about 7 cm s^{-1} .

The sea-surface temperature pattern on the west Florida shelf on 26 April was not significantly different from that on 12 April. The principal feature on the shelf was still the large warm patch which still had a central temperature greater than 24°C and which was now centered at 28.8°N and 83.7°W , or just north of its position on 12 April.

Transect RQ (Figure 4.3-11) passed near the mouth of a warm filament, and transect PO passed through the southern tip of the cold perturbation. Transect RQ was not properly located with respect to the flow into the filament and does not show any relevant information. A new developing cold perturbation was detected at around 26.7°N and 85.4°W (Figure 4.3-11). The determination that this was a developing cold perturbation was based on a time series of satellite images that showed a major cold perturbation that existed in this region 10 days later which could be traced back to this feature. Transect ON passed through the region downstream of the developing cold perturbation (presuming the perturbation was moving to the south-southeast, which other satellite data verified) where warm filaments typically develop.

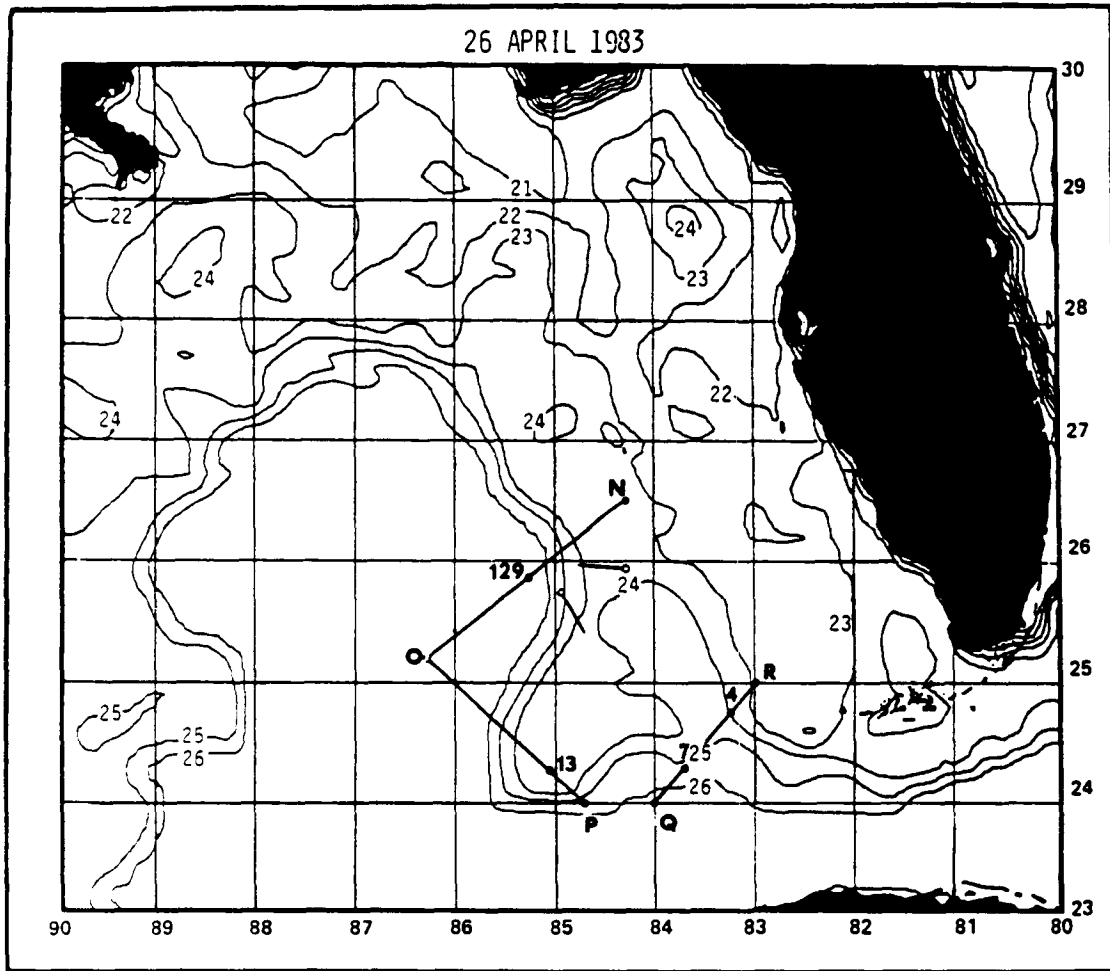


Figure 4.3-11. Sea-surface temperature ($^{\circ}\text{C}$) analyses for 26 April 1983. Transects RQ, PO, and ON were performed by FIO in the period of 22-28 April 1983.

Satellite data collected after 26 April showed that a warm filament did indeed develop.

The cold dome was located around Station 13 along transect P0 (Figure 4.3-12a). Strong geostrophic currents were detected on both sides of the cold dome (Figure 4.3.12b). The surface geostrophic current on the west side of the dome had a maximum speed of approximately 110 cm s^{-1} , and that on the east side of the dome, 125 cm s^{-1} . Two centers of strong southward geostrophic flow were detected along transect ON (Figure 4.3-13b). The Loop Current front is nearly horizontal between Station 27 and 29 in the surface layer (i.e., surface to the 100-m depth) (See arrow in Figure 4.3-13a). A similar feature was noted in Figure 4.3-5 near the mouth of a warm filament (Figure 4.3-4). This feature may be indicative of the effects of shallow advection in the warm filament. Time series of satellite images indicated that a warm filament existed in both cases. Whether this feature is due to the advection associated with the filament is speculation. But the fact remains that the Loop Current front was nearly horizontal near the mouth of the warm filament in both cases.

By mid-June, analyses of satellite data suggested that the large meander off the Dry Tortugas had dissipated. There were indications on 13 May (Figure 4.3-14) that the sea-surface temperature pattern on the west Florida shelf was reestablishing its previous character (relatively cold water in the Apalachee Bay region with increasing temperature southward to the Florida Keys). The major warm patch in the Apalachee Bay region had almost completely dissipated. If seasonal heating were responsible for the change in the sea-surface pattern on the west Florida shelf on or about 12 April, the rather complex pattern of 12 April should have persisted since the seasonal heating persisted. The feature centered at 24.8°N and 85.3°W (where the closed 25°C isotherm is) is the cold perturbation that was traced back to the feature located at 26.7°N and 85.4°W on 26 April.

4.3.4 Cold Perturbations in the Eastern Gulf of Mexico (18 March through 7 May 1984)

4.3.4.1 Introduction

In the period from 18 March through 7 May, a series of hydrographic cruises were performed in the eastern Gulf of Mexico during the life cycle of a cold perturbation that was first detected around 18 March 1984; i.e., Perturbation H in Table 4.3-1. The hydrographic data were collected by FIO, SAIC and the Minerals Management Service's Ship-of-Opportunity Program (the NORDIC/WASA). Satellite data were collected and analyzed by the Research Triangle Institute. The hydrographic data were combined with the analyses of satellite data to study the life history of the cold perturbation.

This portion of this report discusses the life cycle of a cold perturbation that was located on the boundary of the Loop Current in the period 18 March through 7 May 1985. It focuses on the areal dimensions of the perturbation and the change in these dimensions as it moved from the northern boundary of the Loop Current and became quasi-stationary off the Dry Tortugas.

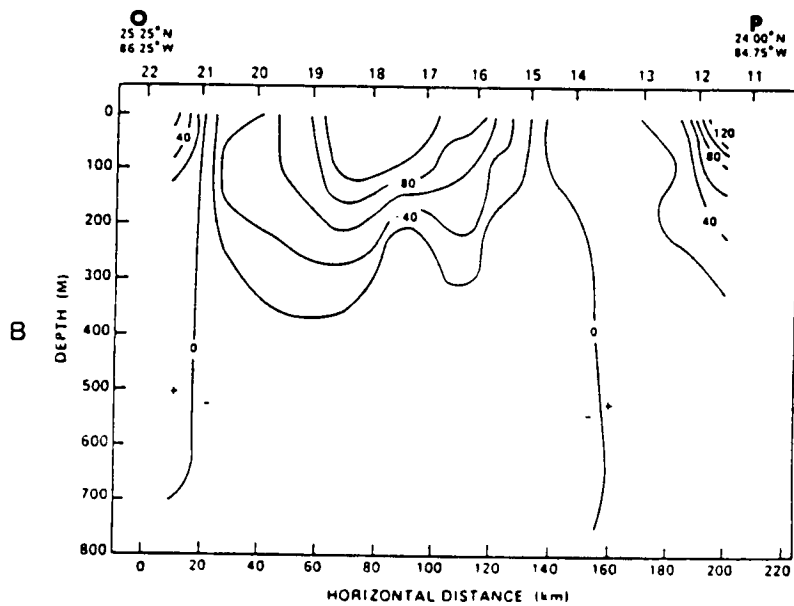
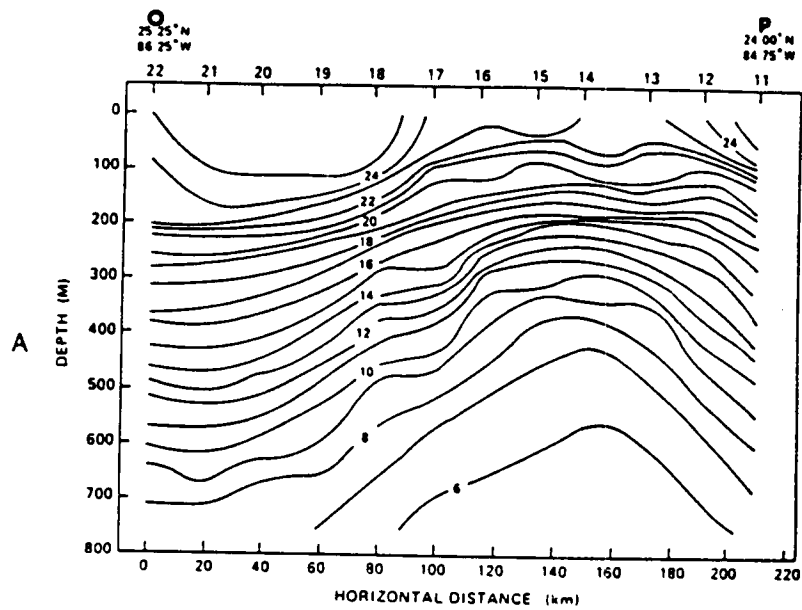


Figure 4.3-12. (A) Temperature ($^{\circ}\text{C}$) analysis along transect P0.
 (B) Geostrophic current (cm s^{-1}) analysis along transect P0.
 The transect was performed between 23 and 25 April 1983.
 (See Figure 4.3-11).

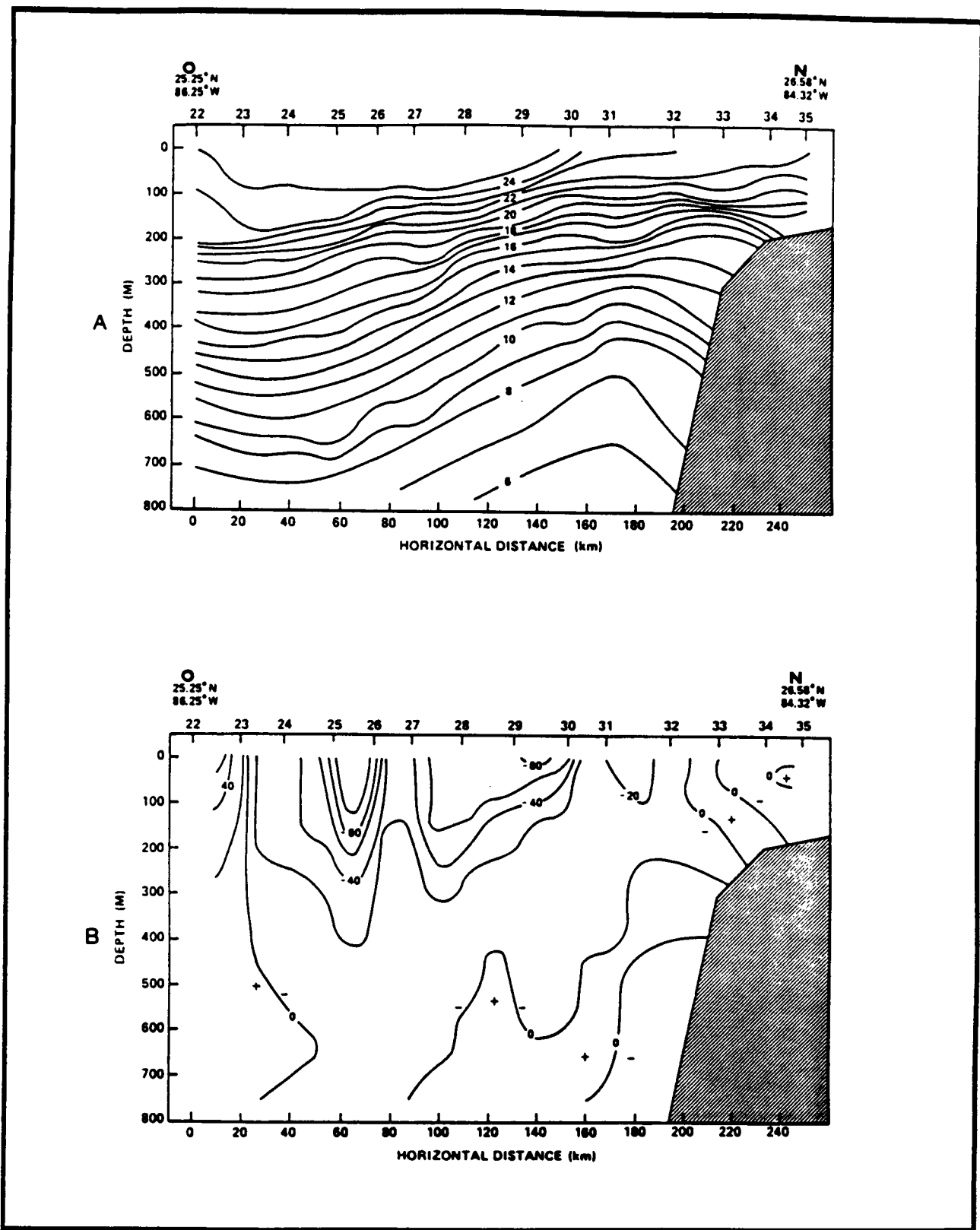


Figure 4.3-13. (A) Temperature ($^{\circ}\text{C}$) analysis along transect ON.
 (B) Geostrophic current (cm s^{-1}) analysis along transect ON.
 This transect was performed in the period of 25-28 April 1983. (See Figure 4.3-11).

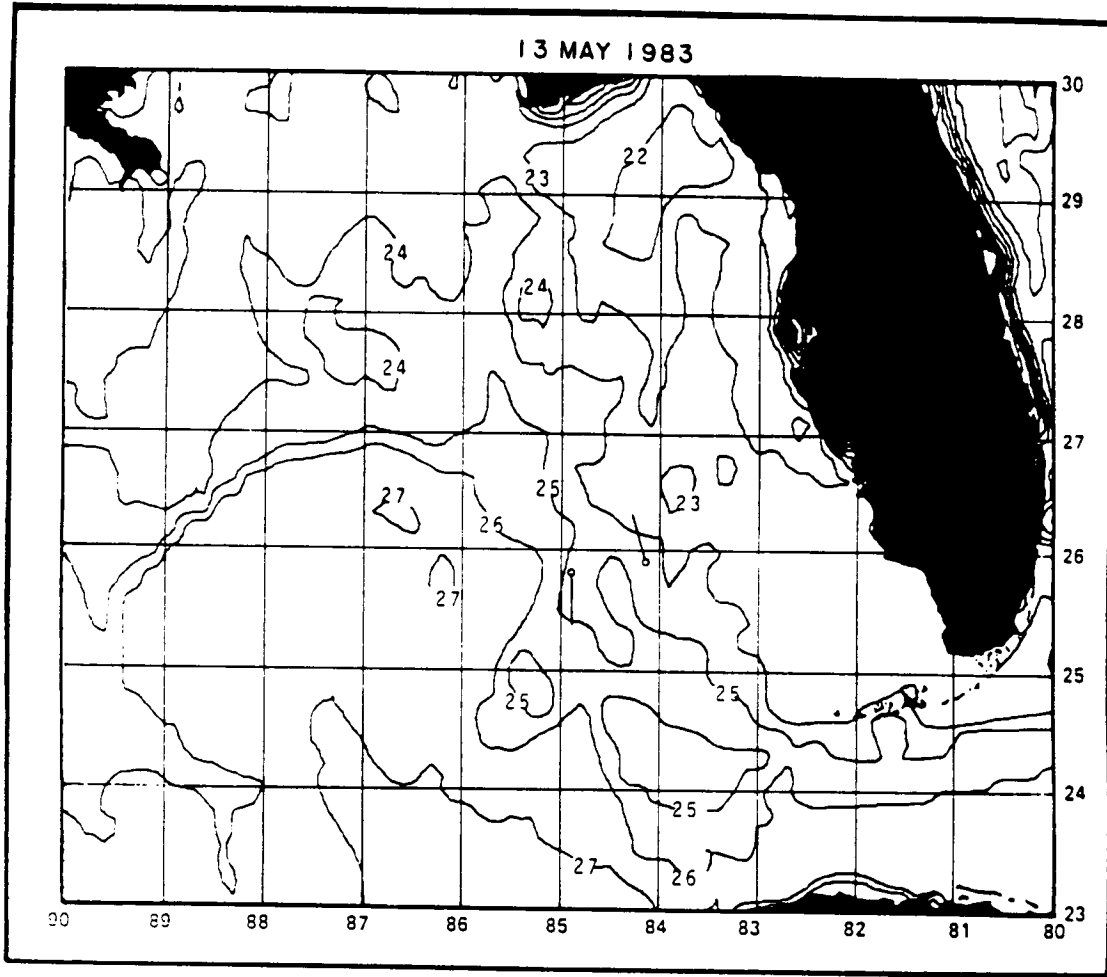


Figure 4.3-14. Sea-surface temperature ($^{\circ}\text{C}$) analyses for 13 May 1983. NOAA satellite data were used for the surface temperature analyses. The current directions for current meters A' and B' are indicated.

4.3.4.2 Analysis Results

Perturbation H (See Table 4.3-1) was initially detected on the northern boundary of the Loop Current on 18 March 1984 (Figure 4.3-15) with its center located at 26.7°N and 86.7°W. At this northern boundary, the current generally flows west to east and these cold core features are usually elongated in a direction parallel to the flow. At the surface, the perturbation had an along-flow scale length of approximately 200 km and a cross-flow scale length of approximately 100 km. The perturbation moved eastward at approximately 7 km day⁻¹, and on 22 March, the center was located at 27°N and 86°W (Figure 4.3-16). At this time, the along-flow scale length was still 200 km and the cross-flow scale length had increased to about 120 km.

A section comprised of XBT's and CTD's was performed in the period 25 to 26 March (transect AB in Figure 4.3-16). The transect focused on the warm filament on the eastern and northern side of the cold perturbations though portions of the transect passed through the leading edge of the cold perturbation. The cold dome generally associated with these cold perturbations (Vukovich and Maul, 1985) is centered at around Station 13 (Figure 4.3-17). The isotherm configuration suggests that the cold dome exceeds the 800-m maximum depth in the analysis. The warm filament, centered at about Station 8, was not much more than 200-m deep (the local depth of the shelf). It should be noted that the center of the warm filament in the hydrographic data is east of the center of the warm filament in the satellite data. This is, for the most part, a result of the perturbation's eastward movement in the intervening three days between the collection of the hydrographic data and the collection of the satellite data.

Analysis of the 10°C isotherm depth (Figure 4.3-18) indicated that the isotherm rose from approximately 580-m depth in the Loop Current to about 290-m depth at the center of the cold dome. On the shoreward side of the cold dome, the isotherm descended to approximately 390-m depth. At about 150 km northeast of point B along the transect AB (Figure 4.3-16), the 10°C isotherm intersected the shelf slope. According to this analysis, the cross-flow scale length of the perturbation is approximately 60 km at the 350-m depth, which is about one-half of that determined at the surface. This difference is expected since the transect did not pass through the center of the perturbation.

From a time series of satellite data, it was noted that the perturbation moved eastward until it reached the shelf slope off the west Florida shelf where it moved southward at speeds of about 8 to 10 km day⁻¹. Based on the surface manifestation of the perturbation from the satellite data, the along-flow scale length of the perturbation remained about 200 km, and the cross-flow scale length about 100 km during this period. On 20 April, the perturbation became quasi-stationary off the Dry Tortugas (Figure 4.3-19). In this region, the Loop Current changes from a general southward direction immediately west of the west Florida shelf to an eastward direction in the Florida Straits. At this time, a general change in the characteristics of the perturbation occurred. The along-flow scale length (east-west scale length) was approximately 130 km, which was approximately equivalent to the cross-flow scale length measured in the perturbation when it was located along the northern and eastern boundaries of the Loop Current. The cross-flow scale length is approximately 180 km, which is about equivalent to previous measurements of the along-flow scale length.

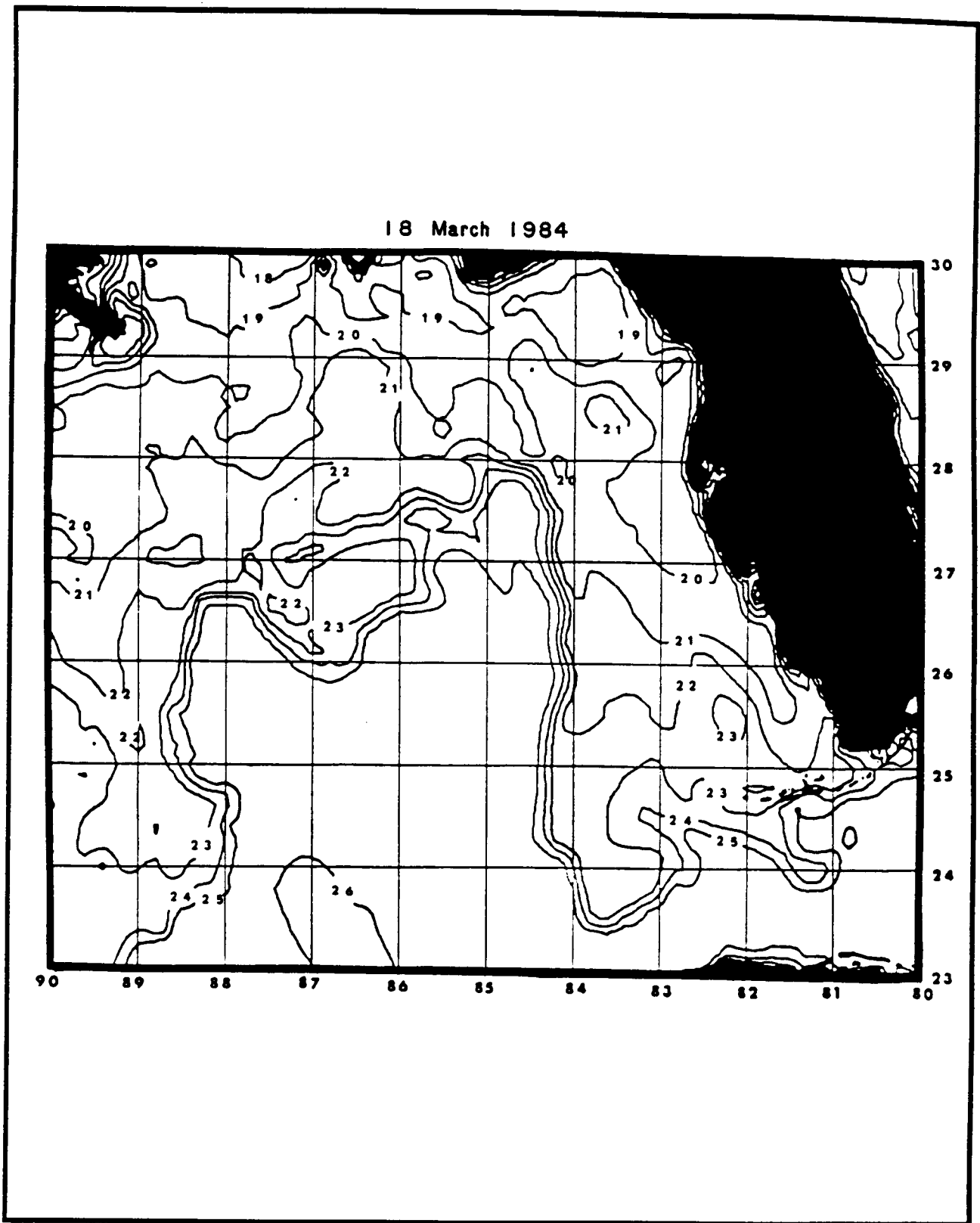


Figure 4.3-15. Sea-surface temperature ($^{\circ}\text{C}$) analysis for 18 March 1984.

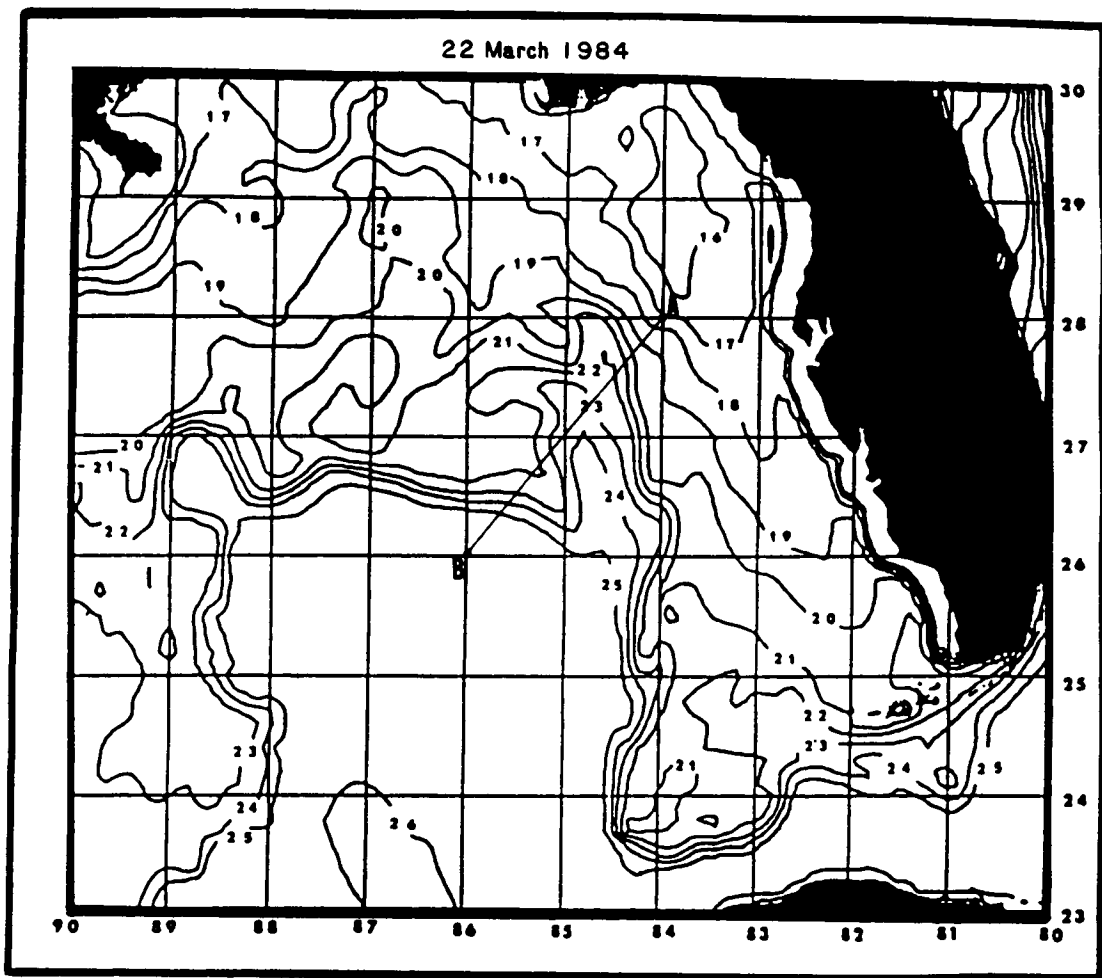


Figure 4.3-16. Sea-surface temperature ($^{\circ}\text{C}$) analysis for 22 March 1984. Transect AB was performed by the Florida Institute of Oceanography (FIO) in the period of 25-26 March 1984.

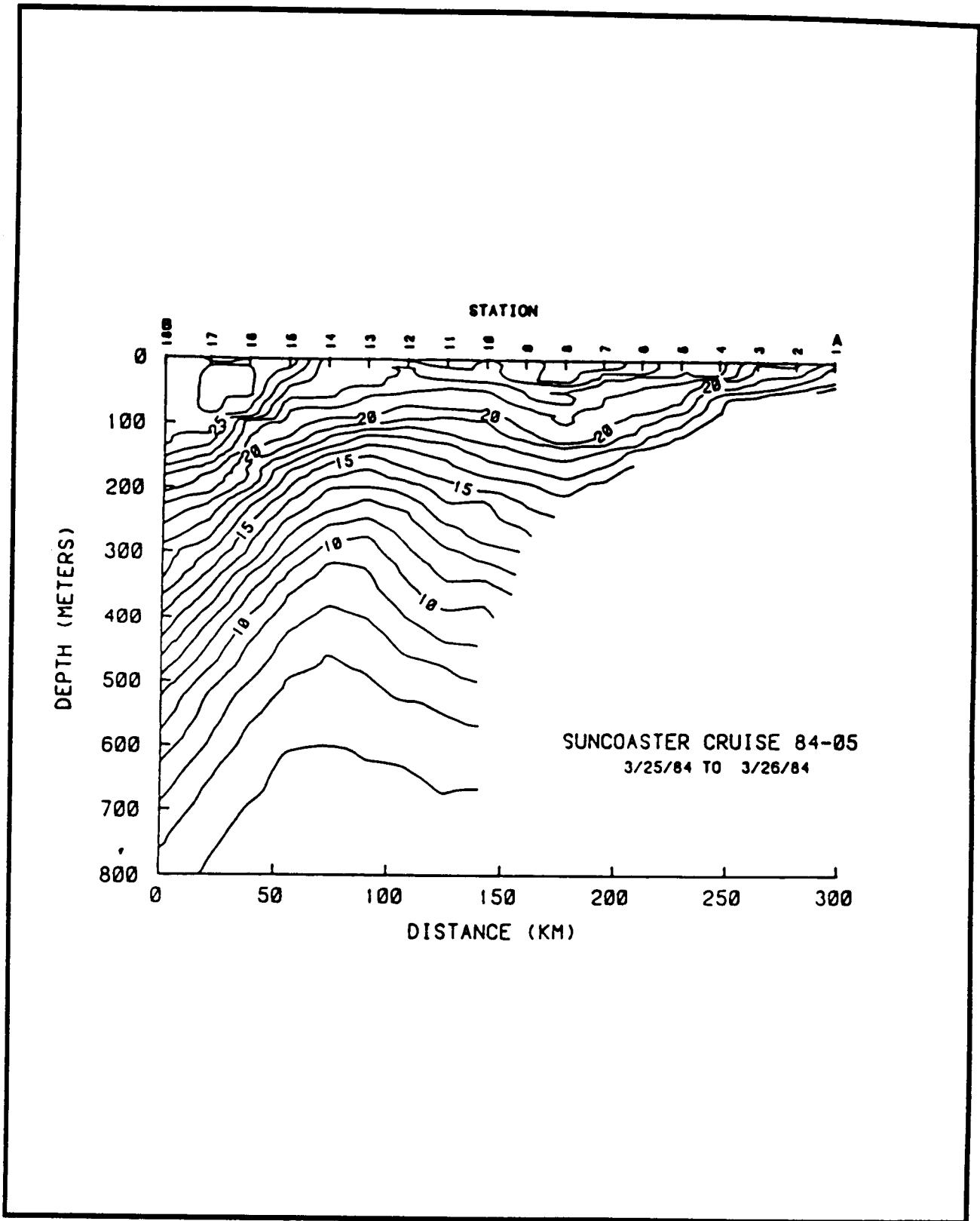


Figure 4.3-17. Temperature ($^{\circ}\text{C}$) analysis along transect AB indicated in Figure 4.3-16.

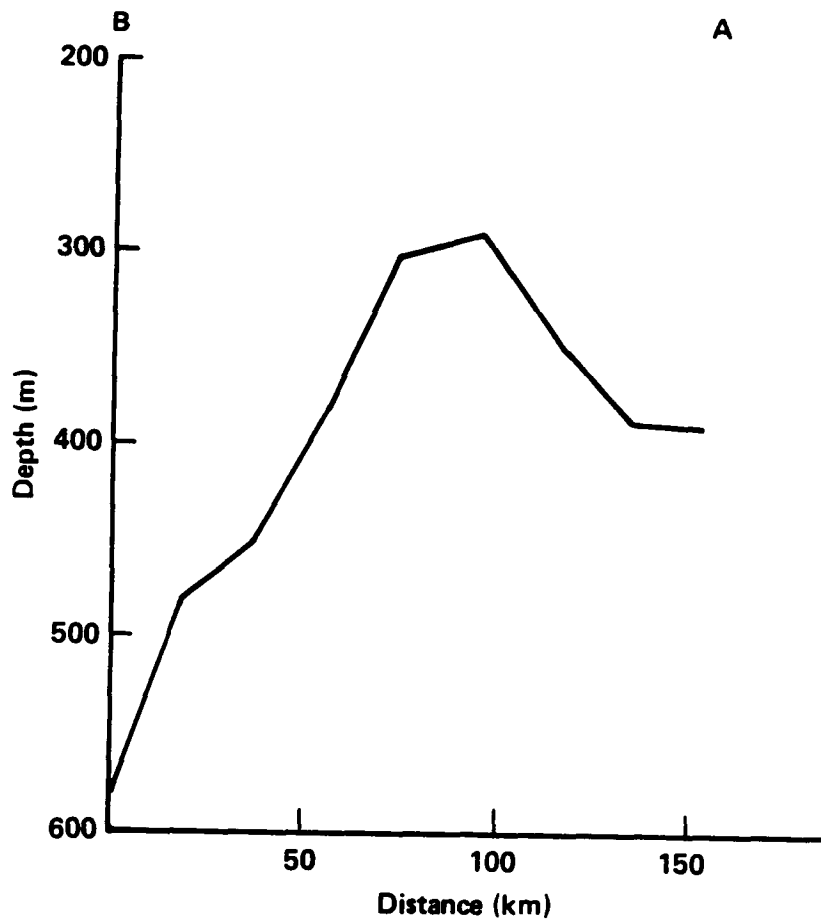


Figure 4.3-18. Analysis of the depth (m) of the 10°C isotherm along transect AB.

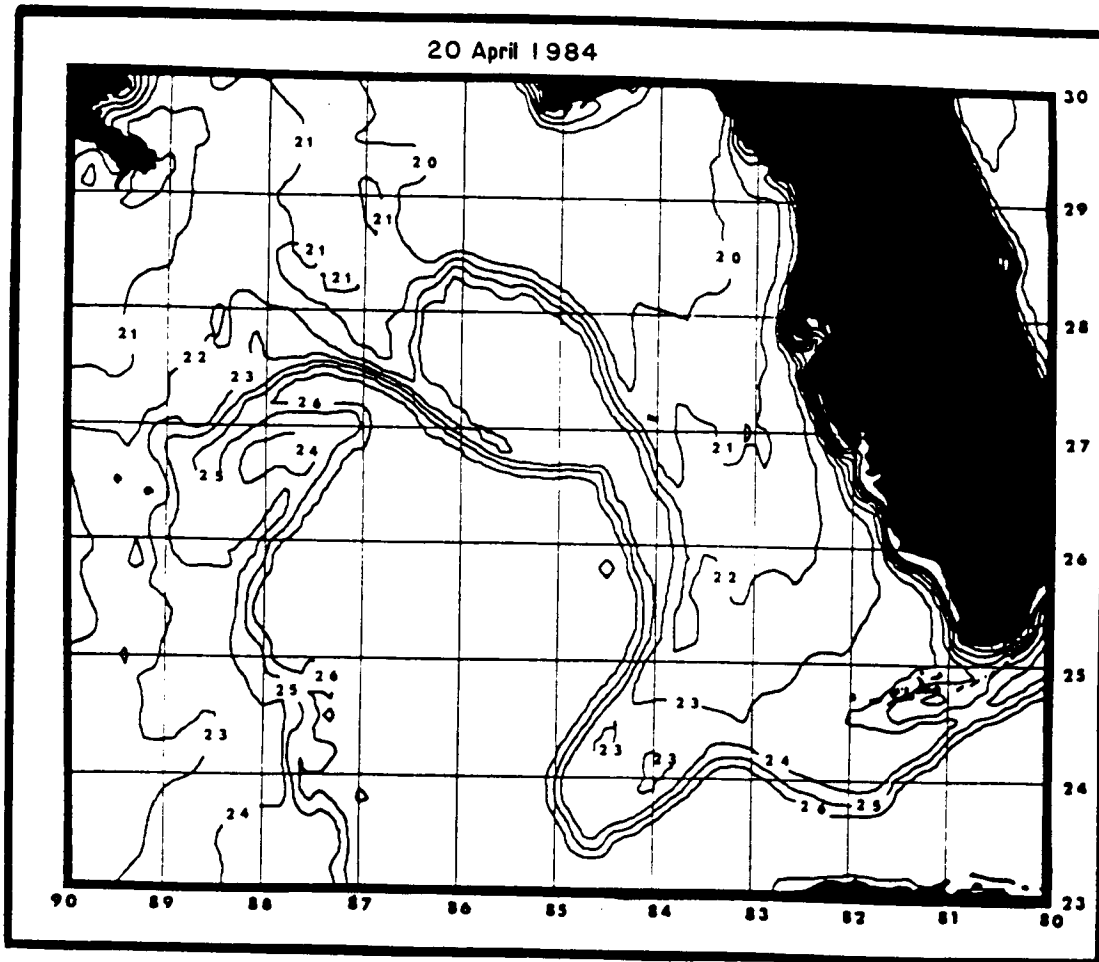


Figure 4.3-19. Sea-surface temperature ($^{\circ}\text{C}$) analysis for 20 April 1984.

when the perturbation moved southward in the region west of the west Florida shelf, its along-flow scale length was greater than its cross-flow scale length. It is possible that when the perturbation reached the Dry Tortugas, it continued to move southward instead of turning eastward, thus producing the large protrusion into the Loop Current (Figure 4.3-19) and an apparent reversal of the magnitude of the two scale lengths. In the region off the Dry Tortugas, the bottom rises by more than 1000 m, and the rise in the bottom depth may have influenced the motion of the perturbation; i.e., preventing it from turning eastward. In more than 10 years of satellite observations, cold perturbations of this size have never been observed to move through the Florida Straits. More research is needed into the cause of the changes in these perturbations in this region.

It is important to note that from the time this perturbation was first observed on the northern boundary of the Loop Current until it reached the Dry Tortugas, there was no significant change in the area of surface expression as it was defined by the along-flow and cross-flow scale lengths. The only change noted was that the cross-flow scale length replaced the along-flow scale length as the major axis (i.e., the scale length having the largest magnitude) when the perturbation reached the Dry Tortugas. Whether the large protrusion into the Loop Current was a result of cold perturbation movement and whether that motion was influenced by the rise in the bottom topography in the Florida Straits could not be established from available data. It was previously thought that either baroclinic and/or barotropic instability were responsible for the development of the large protrusion off the Dry Tortugas (Vukovich and Maul, 1985).

The perturbation drifted slowly eastward at about 3 km day^{-1} and was located at 24°N and 84°W on 28 April (Figure 4.3-20). The along-flow scale length was approximately 130 km and the cross-flow scale length approximately 200 km. These dimensions are consistent with what was observed on 20 April.

Transects CD, DE, and FG were performed in the period 25 to 29 April. The cold dome is well defined in the transect data and exists in the layer from the surface to at least the 900-m depth (Figures 4.3-21a - 4.3-22). The isotherm configuration suggests that the perturbation exceeds the 900-m depth. Analysis of the depth of the 10°C isotherm (Figure 4.3-23) indicates that the isotherm rose from about a maximum depth of 500 m in the Loop Current to the 240-m depth at the cold perturbation's center. Based on the 350-m depth contour for the 10°C isotherm, the cross-flow scale length of the cold dome was approximately 180 km and the along-flow scale length approximately 130 km. These dimensions are consistent with the dimensions of the perturbations at the surface.

The perturbation continued to drift eastward at a speed of about 2 km day^{-1} and by 7 May was located at 24.1°N and 83.8°W (Figure 4.3-24). The size of the perturbation had decreased since 28 April. The cross-shelf scale length was approximately 140 km and the along-shelf scale length was 130 km.

The analysis of the temperature data from transects HI, JK, and LM, performed in the period 5 through 7 May, indicated that the cold dome was not well defined in the surface layer (i.e., in the first 150 to 200 m) (Figures 4.3-25a - c). Apparently, since 28 April, warming occurred in the mixed-layer surface layer as indicated by the larger vertical temperature gradient found

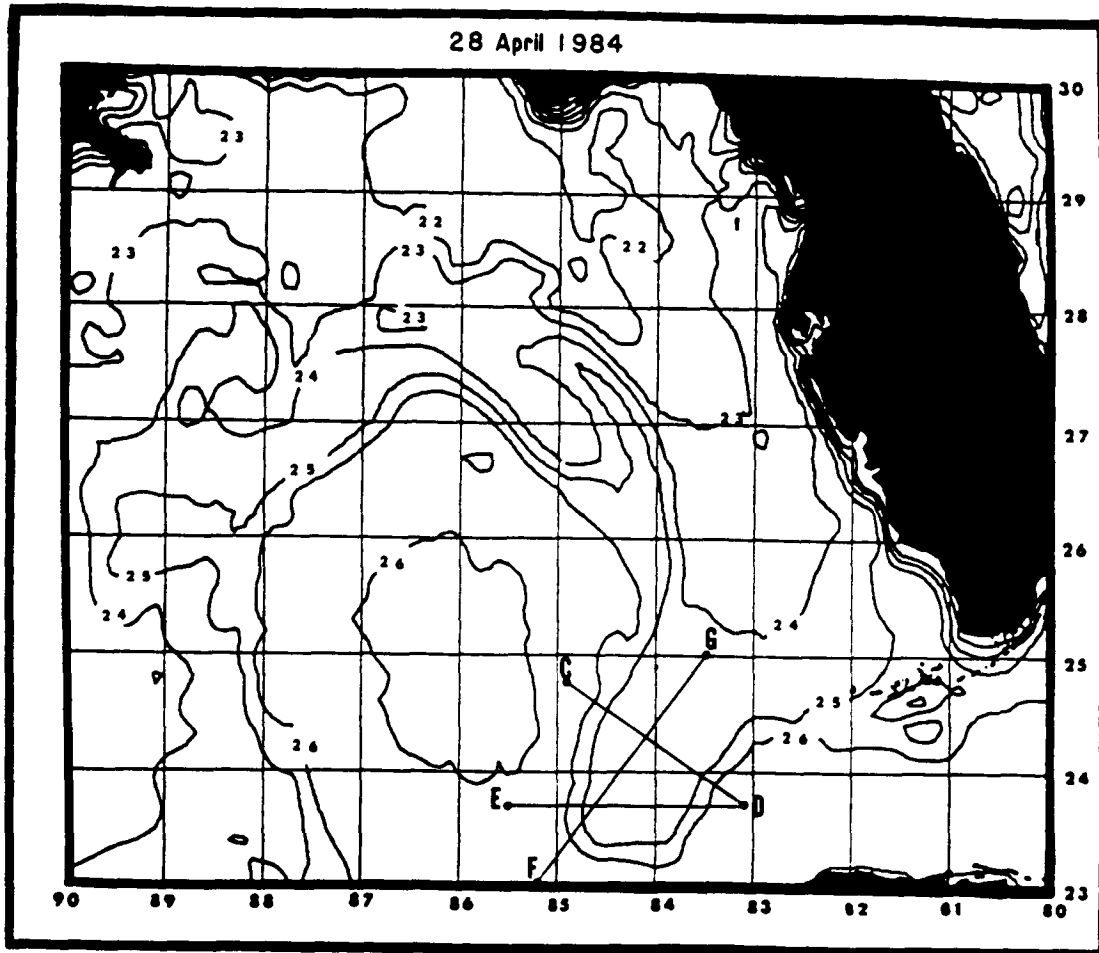


Figure 4.3-20. Sea-surface temperature ($^{\circ}\text{C}$) analysis for 28 April 1984. Transects CD, DE, and FG were performed by F10 in the period of 25-29 April 1984.

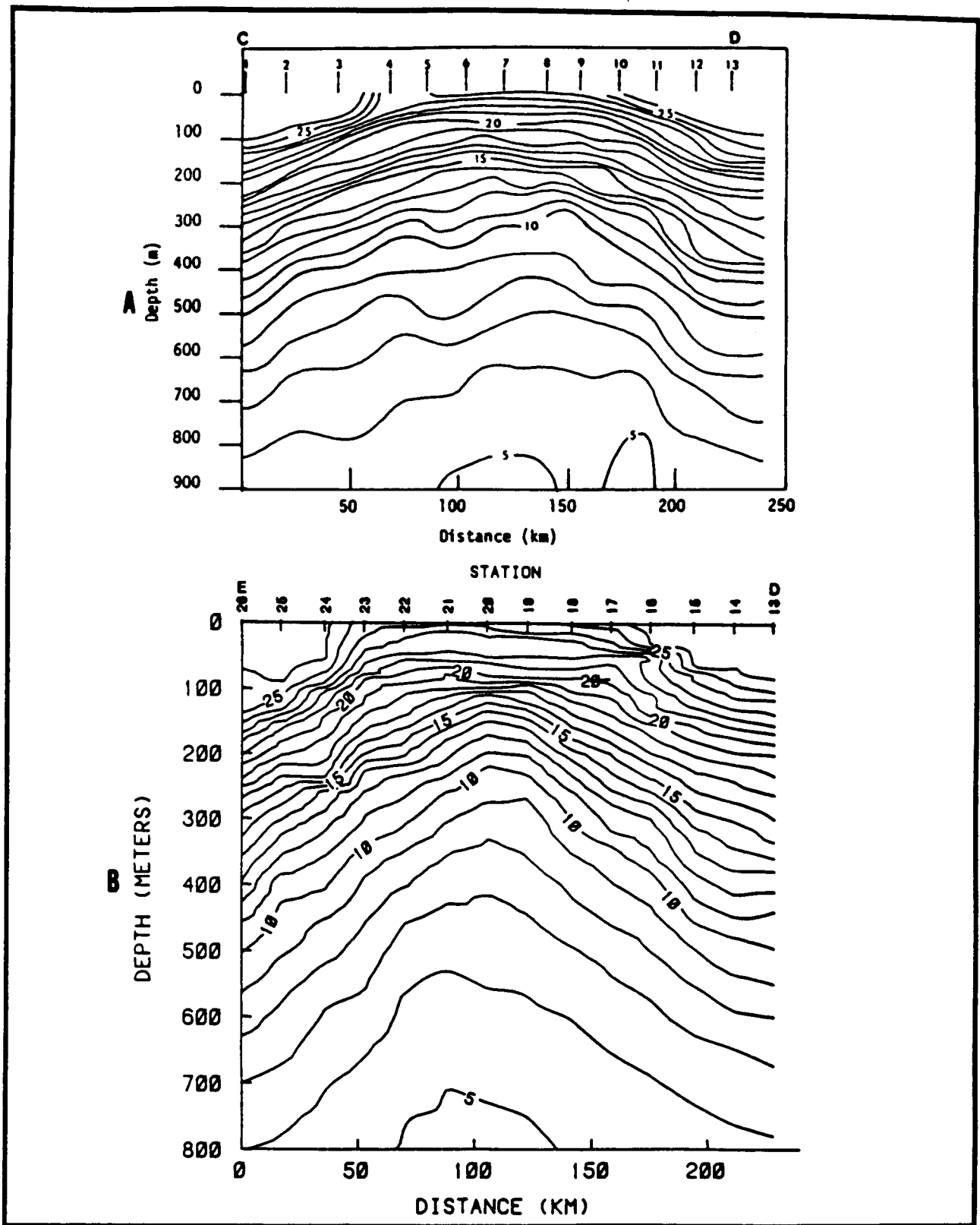


Figure 4.3-21. Temperature ($^{\circ}\text{C}$) analysis along transects (A) CD and (B) DE indicated in Figure 4.3-20.

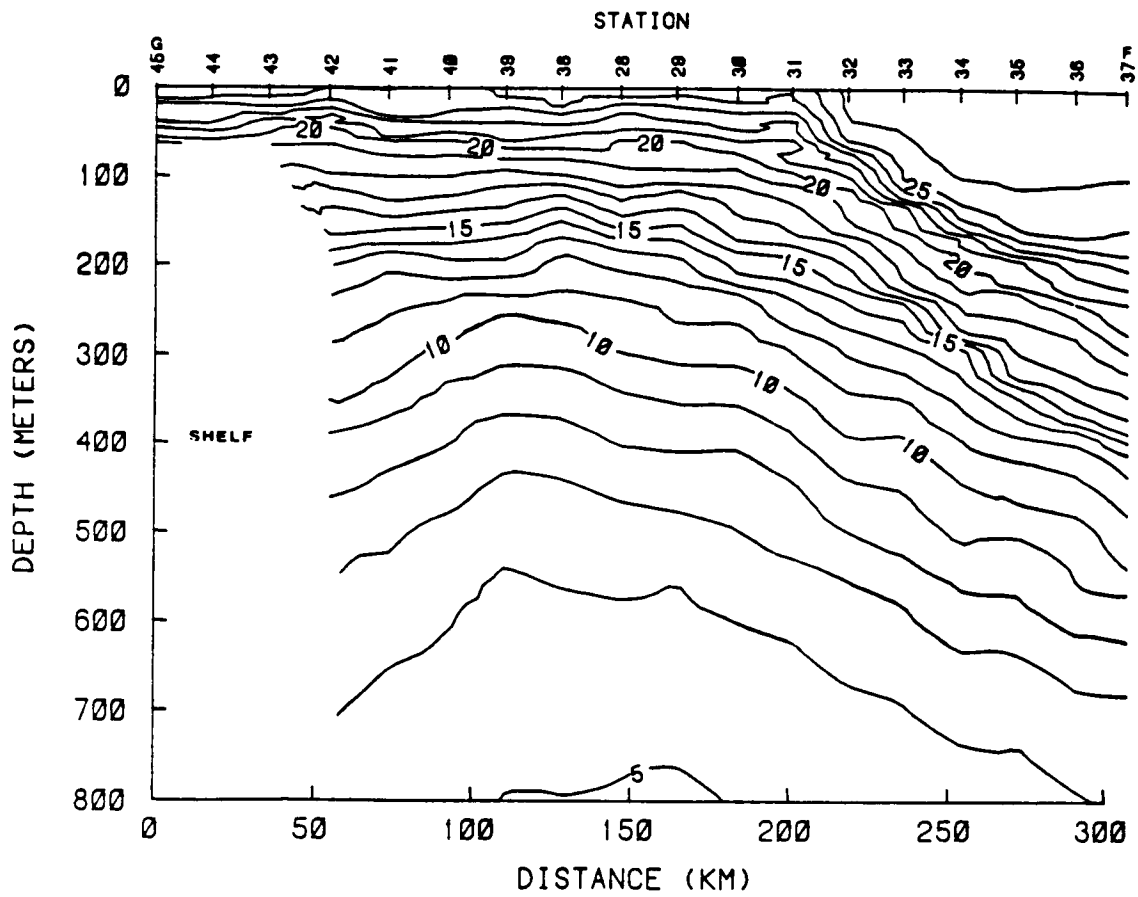


Figure 4.3-22. Temperature ($^{\circ}\text{C}$) analysis along transect FG indicated in Figure 4.3-20.

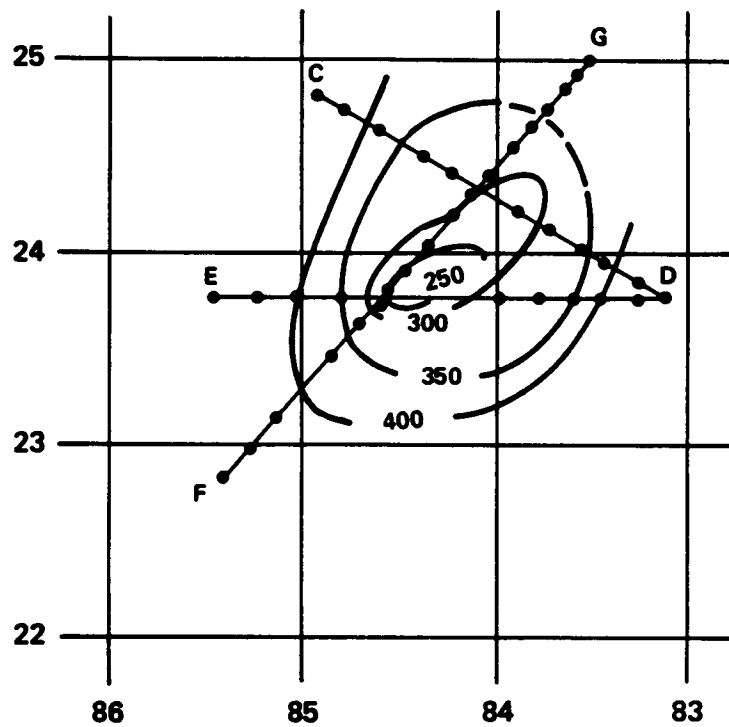


Figure 4.3-23. Analysis of the depth (m) of the 10°C isotherm using data along transects CD, DE, and FG indicated in Figure 4.3-20.

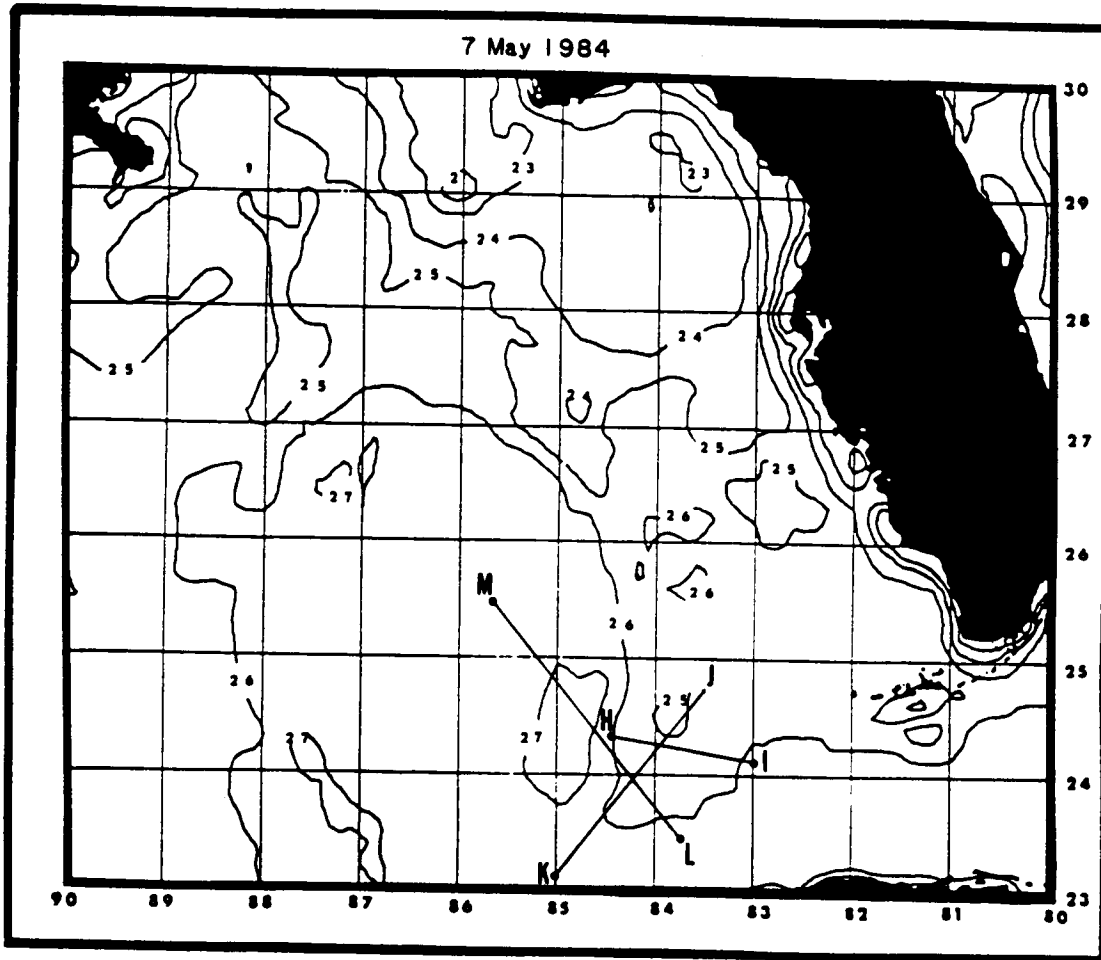


Figure 4.3-24. Sea-surface temperature ($^{\circ}\text{C}$) analysis for 7 May 1984. Transects JK and LM were performed by Science Applications International Corporation (SAIC) in the period of 5-7 May 1984. Transect HI was performed by the Ship-of-Opportunity (RV GYRE) on 5 May 1984.

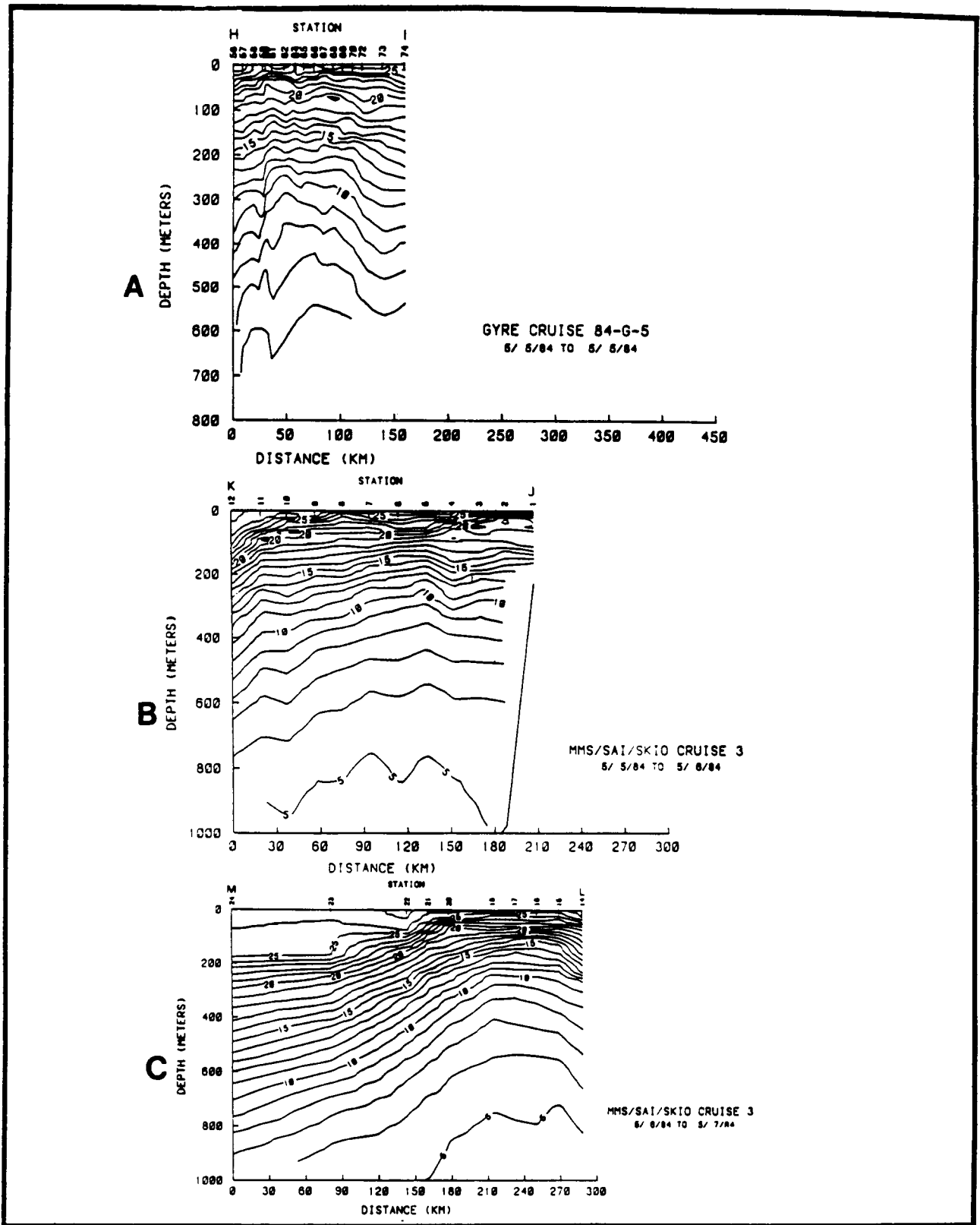


Figure 4.3-25. Temperature ($^{\circ}\text{C}$) analysis along transects (A) HI, (B) JK and (C) LM indicated in Figure 4.3-24.

in that layer in early May as compared to late April (Figures 4.3-21a, 4.3-22). The cold dome is best defined below the 200-m depth.

The analysis of the depth of the 10°C isotherm (Figure 4.3-26) indicated that the isotherm rose from a maximum depth of 480 m in the Loop Current to approximately 280 m in the cold dome. Based on the 350-m contour for the 10°C isotherm, the cross-flow scale length of the cold dome was 140 km and the along-flow scale length, 130 km. These dimensions are equivalent to the surface dimensions of the cold perturbation found on 7 May. A comparison of the dimensions of the cold perturbation between 28 April and 7 May reveals that there was about a 20% decrease in the area of the cold perturbation in the 10-day period. The change in the area of the perturbation is reflected both at the surface and at depth.

The available satellite data suggested that around 22 May this cold perturbation dissipated in the Florida Straits when another cold perturbation moved into the region off the Dry Tortugas. The decrease in the area noted on 7 May suggested that the dissipation process was taking place.

4.3.5 Variations of the Loop Current Boundary (1980-1984)

4.3.5.1 Introduction

Four years of frontal analysis (1980-1984) as derived from satellite data in the Gulf of Mexico were used to study fluctuations of the western and eastern boundaries of the Loop Current. The study focused on the period when usable satellite data were available which was generally November through May. Computations of the fluctuations were made at 25°N, 26°N, and 27°N latitude of the eastern and western boundaries of the Loop Current. Computations were made only when the Loop Current could be identified at all six locations. If a major ring separated from the Loop Current or the Loop Current could not be detected at one of the locations, the entire data set for that particular case was not included in the calculations.

There are two probable causes for the fluctuations of the Loop Current boundary. One is the general east-west drift of the axis of the Loop Current (Vukovich et al., 1979). It has been shown that the Loop Current penetrates to its northernmost position in the eastern Gulf of Mexico when the axis of the Loop Current is near the west Florida shelf. The least northward penetration occurs when the axis of the Loop Current is considerably west of the west Florida shelf. This is a long-term, east-west oscillation that should affect each computation point in a similar manner.

The cold perturbations that have been detected on that boundary are another cause for the variations of the Loop Current boundary (Vukovich and Maul, 1985). These should not affect the calculations in a uniform manner at all locations because they intensify and weaken while moving around the boundary. Generally one perturbation affects one computational position since these features are small compared to the Loop Current. As many as three of these perturbations have been detected on the boundary of the Loop Current at any one time, but usually only one or two are present.

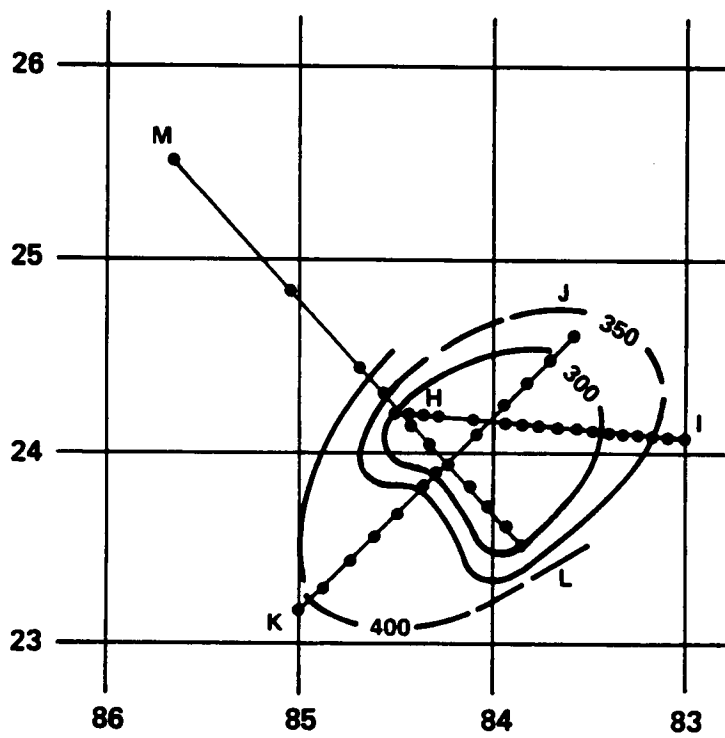


Figure 4.3-26. Analysis of the depth (m) of the 10°C isotherm using data along transects HI, JK, and LM indicated in Figure 4.3-24.

4.3.5.2 Analysis Results

Western and eastern Loop Current boundaries fluctuations were a maximum at 27°N latitude (Figure 4.3-27). Based on the four years of data, the mean position of the northern LC boundary was, on the average, between 27°N and 28°N. Therefore, maximum fluctuations of the western and eastern boundaries of the Loop Current occurred near the northern boundary (Figure 4.3-28). The fluctuations decreased with decreasing latitude. However, fluctuations were larger at 25°N and 26°N on the eastern boundary compared to the western boundary. These results are consistent with previous observations (Vukovich and Maul, 1985) which noted that cold perturbations are initially detected in the satellite data on the northern boundary of the Loop Current, then move eastward along the northern boundary, and then southward along the eastern boundary. They produced large fluctuations of the northern and eastern boundaries of the Loop Current, but no previous evidence shows that they markedly influenced the western boundary south of 27°N.

The largest fluctuations of the eastern boundary of the Loop Current occur in the winter (January through March in the latitude belt 25°N to 27°N) (Figure 4.3-29). In comparison, the fluctuations are smaller in the late fall and early spring. On the western boundary, the fluctuations are also large in the winter compared to late fall and early spring but only at 26°N and 27°N latitude. The fluctuations at 25°N latitude show very little variation from month to month and appear to be a minimum in the winter.

4.3.6 Warm Rings in the Gulf of Mexico

4.3.6.1 Introduction

Large warm masses of water having a diameter ranging from 300-400 km generally separate from the Loop Current when the current has made a deep northward penetration into the Gulf of Mexico (Leipper, 1970; Hurlburt and Thompson, 1982). Penetrations of the Loop Current have extended as far as 29°N latitude (Vukovich, et al., 1979). It is not known precisely what causes the ring or eddy shedding.

After detaching from the Loop Current system, the warm rings move westward into the western Gulf of Mexico (Ichiye, 1962) at speeds estimated to range from 2 to 5 km day⁻¹ (Cochrane, 1972; Elliott, 1982). Elliott has determined that the life span of a ring is approximately one year. Evidence suggests that when a major ring develops in the eastern Gulf, the area of the ring decreases as it moves into the western Gulf. The major rings that develop in the eastern Gulf generally have diameters on the order of 300-400 km (Vukovich, et al., 1979). On the other hand, Elliott has shown that the average ring diameter in the western Gulf is on the order of 185 km. The process by which the ring area decreases is not understood. As many as 3 warm rings have been detected in the western Gulf of Mexico at one time. These are believed to be individual rings that shed from the Loop Current rather than the results of the break-up of a ring.

The warm ring is believed to be a major contributor towards the transport in the western Gulf and the maintenance of an anticyclonic cell along the western boundary of the Gulf of Mexico (Brooks, 1984; Nowlin and McLellan, 1967; Elliott, 1982). The anticyclonic circulation in the warm rings (Leipper,

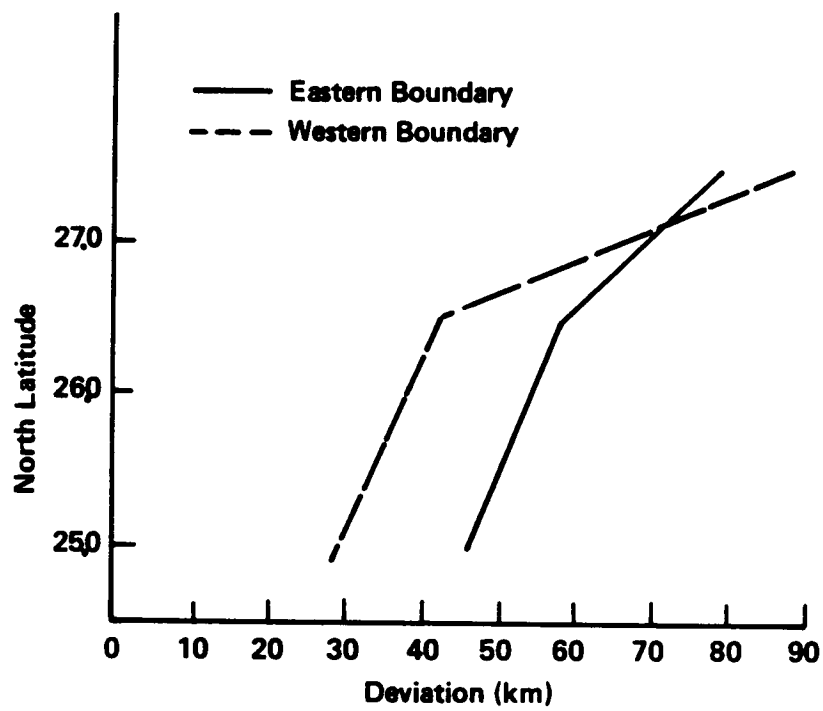


Figure 4.3-27. Mean deviation (km) of the Loop Current western and eastern boundary from their mean position versus latitude based on satellite infrared data from 1980 to 1984 in the period November through May.

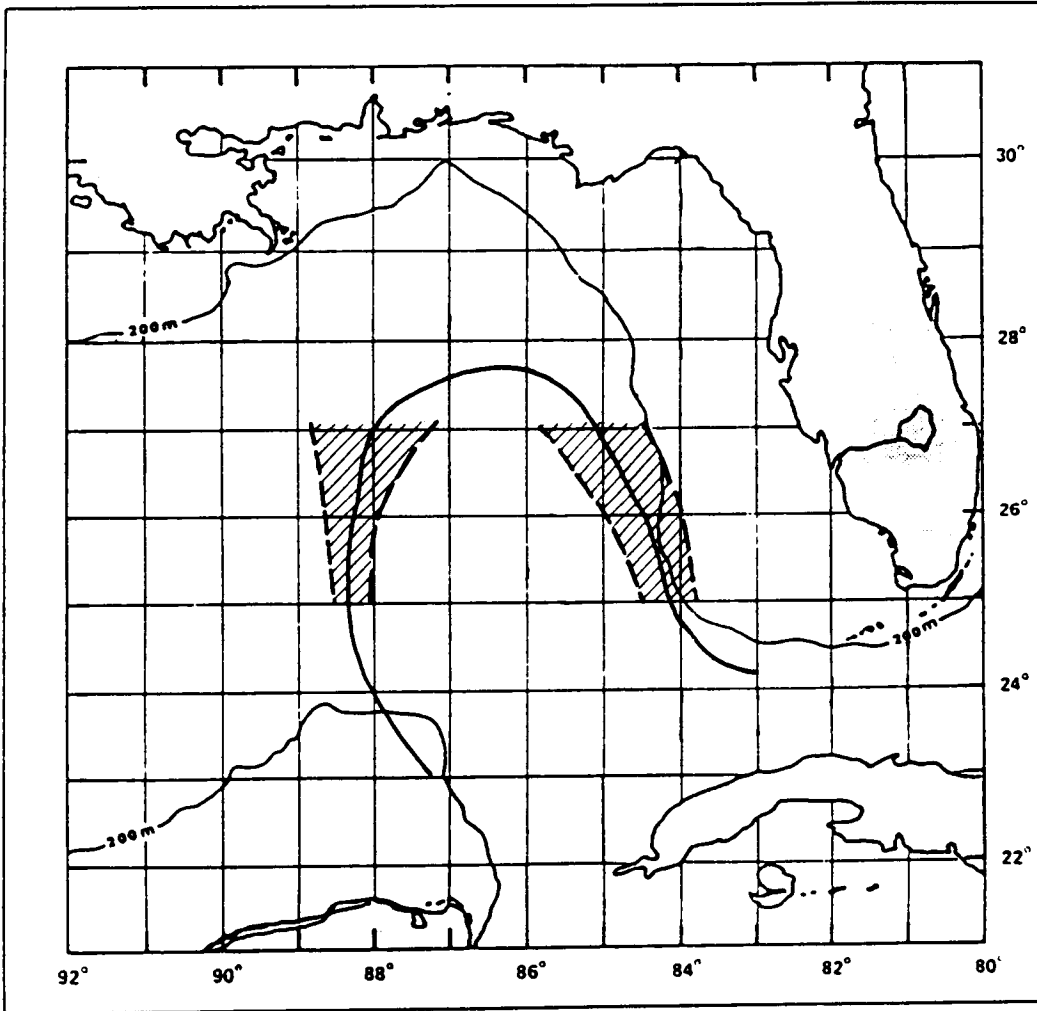


Figure 4.3-28. Mean 4-year position of Loop Current and positive and negative deviations of Loop Current boundary between 25°N and 27° N.

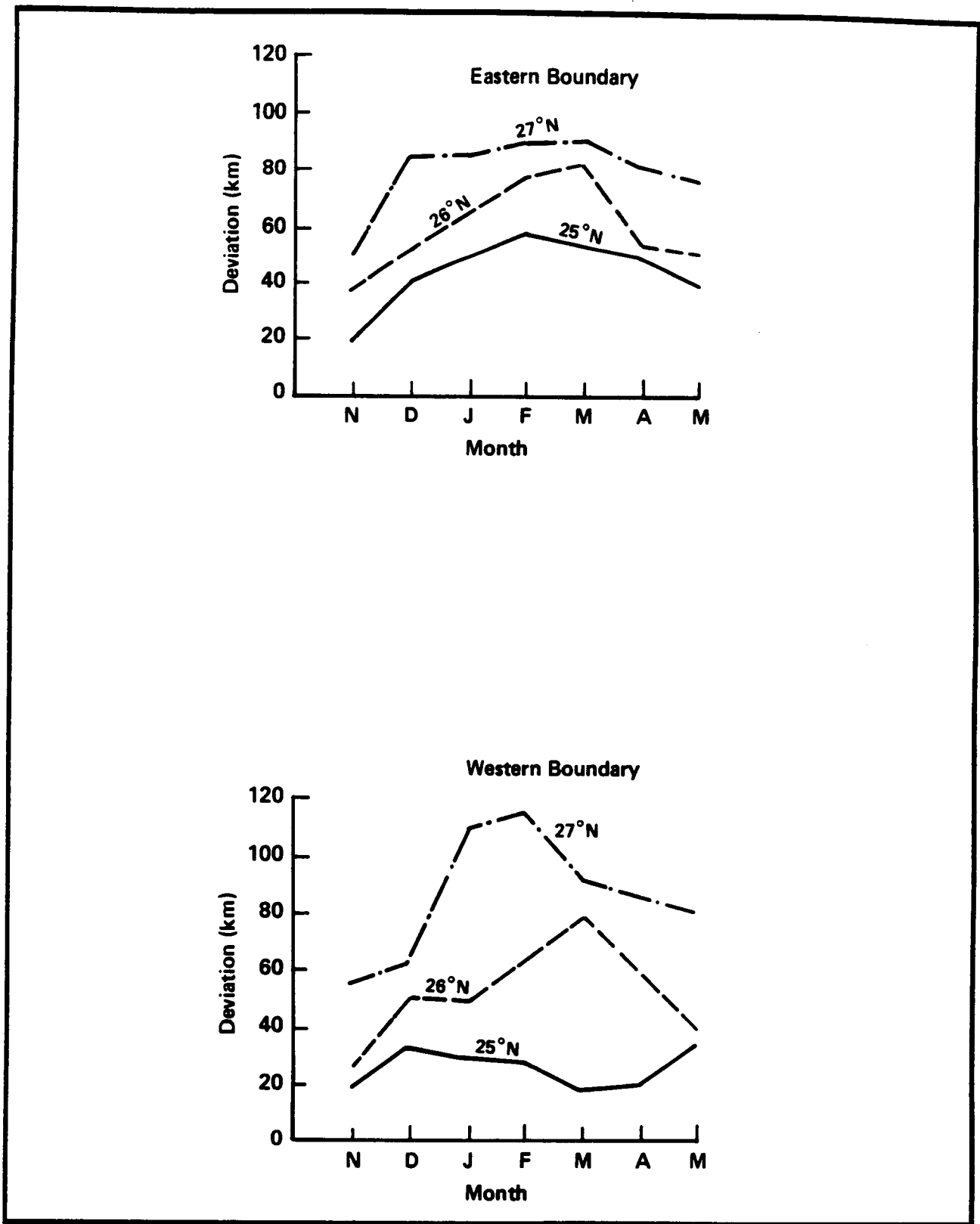


Figure 4.3-29. Mean deviation (km) of the Loop Current's western and eastern boundary from the mean position at 25°N, 26°N, and 27°N for each month in the period November through May based on satellite infrared data for 1980 to 1984.

1970; Elliott, 1982; Molinari, 1977) has a profound effect on surface trajectories and also plays an important role in the heat and salt budget of the western Gulf (Elliott, 1982). It is evident from the literature that the warm rings are a vital part of the oceanography of the Gulf of Mexico.

The following sections discuss the results of a research project which primarily used satellite infrared data to derive various statistics on the warm rings in the western Gulf of Mexico. NOAA satellite infrared data were the primary data source. The data base extended from 1973 through 1984. Various aspects of the temperature structure of the warm rings were derived from Ship-of-Opportunity data obtained in 1982 and 1984.

4.3.6.2 Temperature Structure

On or about 13 December 1983, the NOAA satellite infrared data indicated that a major warm ring (~ 300 km diameter) was separating from the Loop Current (Figure 4.3-30a). By 13 January 1984, the satellite data indicated that the ring had completely separated from the Loop Current (Figure 4.3-30b). In the period from 7-8 January 1984, the NORDIC WASA, a ship involved in the Minerals Management Service's Ship-of-Opportunity program, sailed from the Mississippi Delta southeastward to the Yucatan Strait dropping XBT's. Figure 4.3-31a provides the station locations. The temperature section derived from the XBT data shows the warm ring's center at around Stations 10 or 11 (Figure 4.3-31b). The warm water south of Station 19 is the Loop Current. The cold dome centered at around Station 17 separates the Loop Current from the warm ring. The data show that the ring extends to depths of at least 800 m, and the isotherm configuration suggests that it penetrates to depths below the 800-m level. If the surface temperature gradients at Stations 6 and 7 and Stations 17 and 18 are used to define the boundaries of the ring, then the ring diameter at the surface is on the order of 300 km which is identical to that observed in the satellite data. However, if the horizontal dimensions are based on the shallowest penetration of the 10°C isotherm, then the ring diameter appears to be on the order of 400 km.

On 21 May 1982, a major warm ring (~ 250 km diameter) was observed to be forming in the eastern Gulf of Mexico (Figure 4.3-32a). Two days after that satellite image was obtained, the E. QUEENY sailed east-southeastward across the region of interest (Figure 4.3-32b). The temperature section (Figure 4.3-32c) indicated that the warm ring was centered around Stations 5 and 6 and that the Loop Current was reforming in the eastern part of the eastern Gulf of Mexico at around Station 18. Once again, a major cold dome that was centered at Station 13 separated the Loop Current from the warm ring. The XBT data indicated that the ring diameter at the surface was about 250 km, which is identical to that found in the satellite data. The ring diameter is greater if deep water isotherms are used to define the boundaries of the ring. This was also found in the previous case.

On 8 June 1982, the NOAA satellite infrared data (Figure 4.3-33a) indicated that the ring had not yet completely separated from the Loop Current. The horizontal dimensions of the ring were still around 250 km. In the period 7-8 June 1982, the E. QUEENY sailed west-northwestward across the region of interest (Figure 4.3-33b). The location of the end points of this cruise is approximately the same as that for the May cruise. The temperature section (Figure 4.3-33c) indicated that the warm ring was centered at around Station

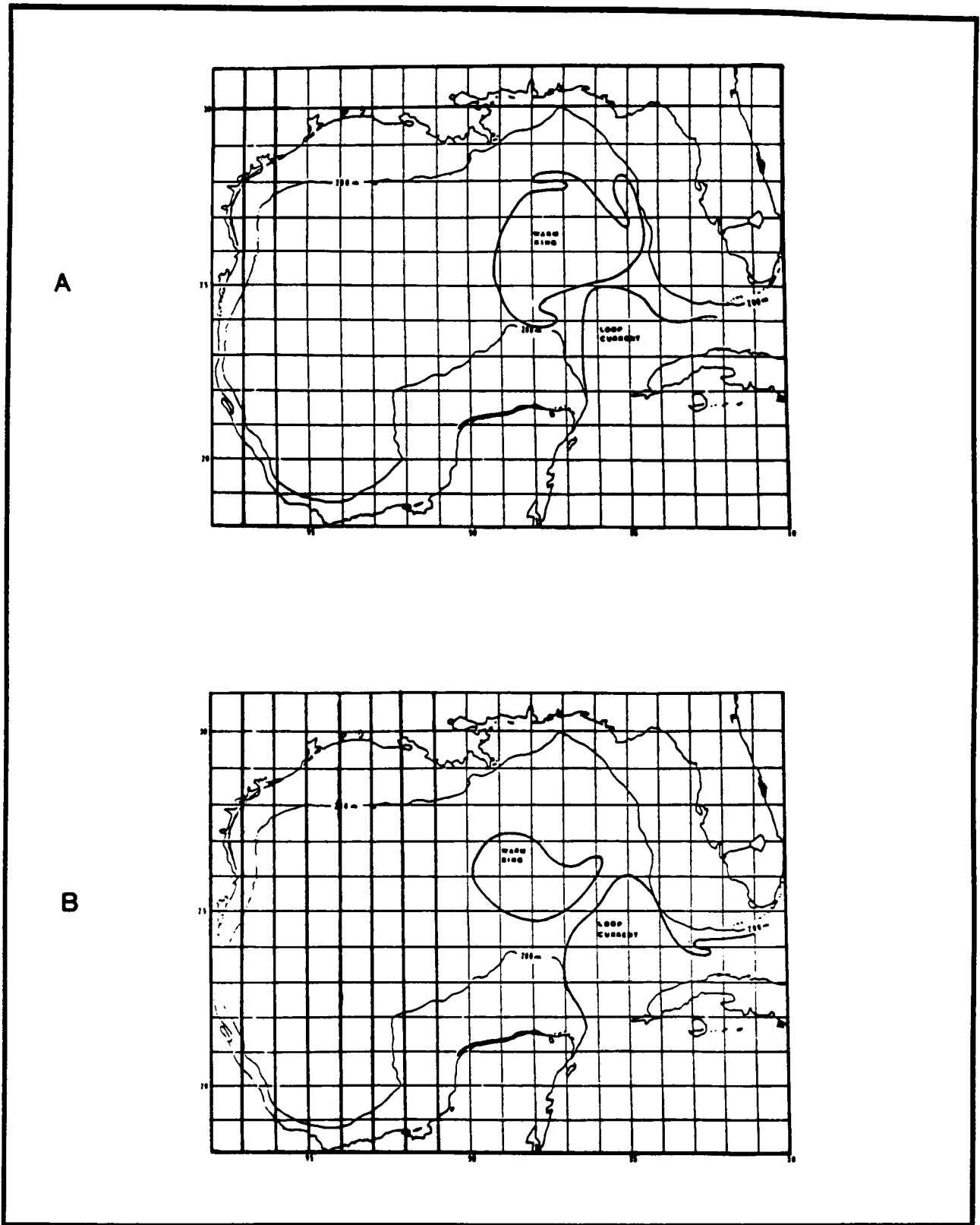


Figure 4.3-30. Surface frontal analysis using NOAA infrared data for (A) 13 December 1983 and (B) 13 January 1984.

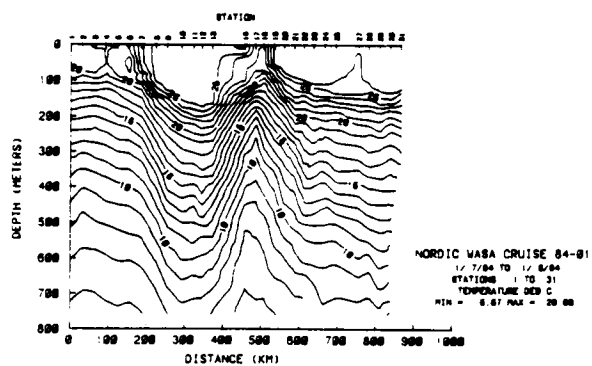
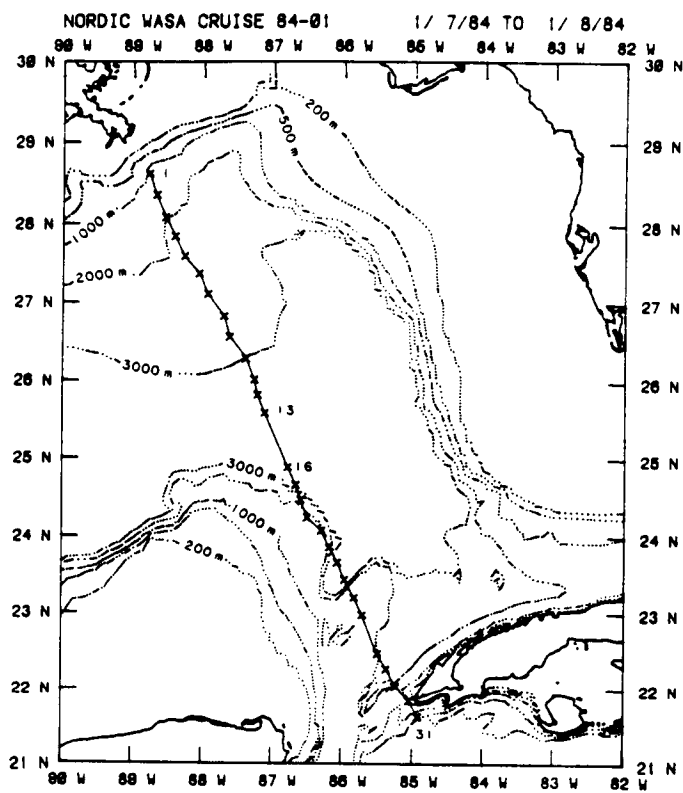


Figure 4.3-31. (A) Cruise path and station location for and (B) temperature ($^{\circ}$ C) section from data collected by the NORDIC WASA on 7-8 January 1984.

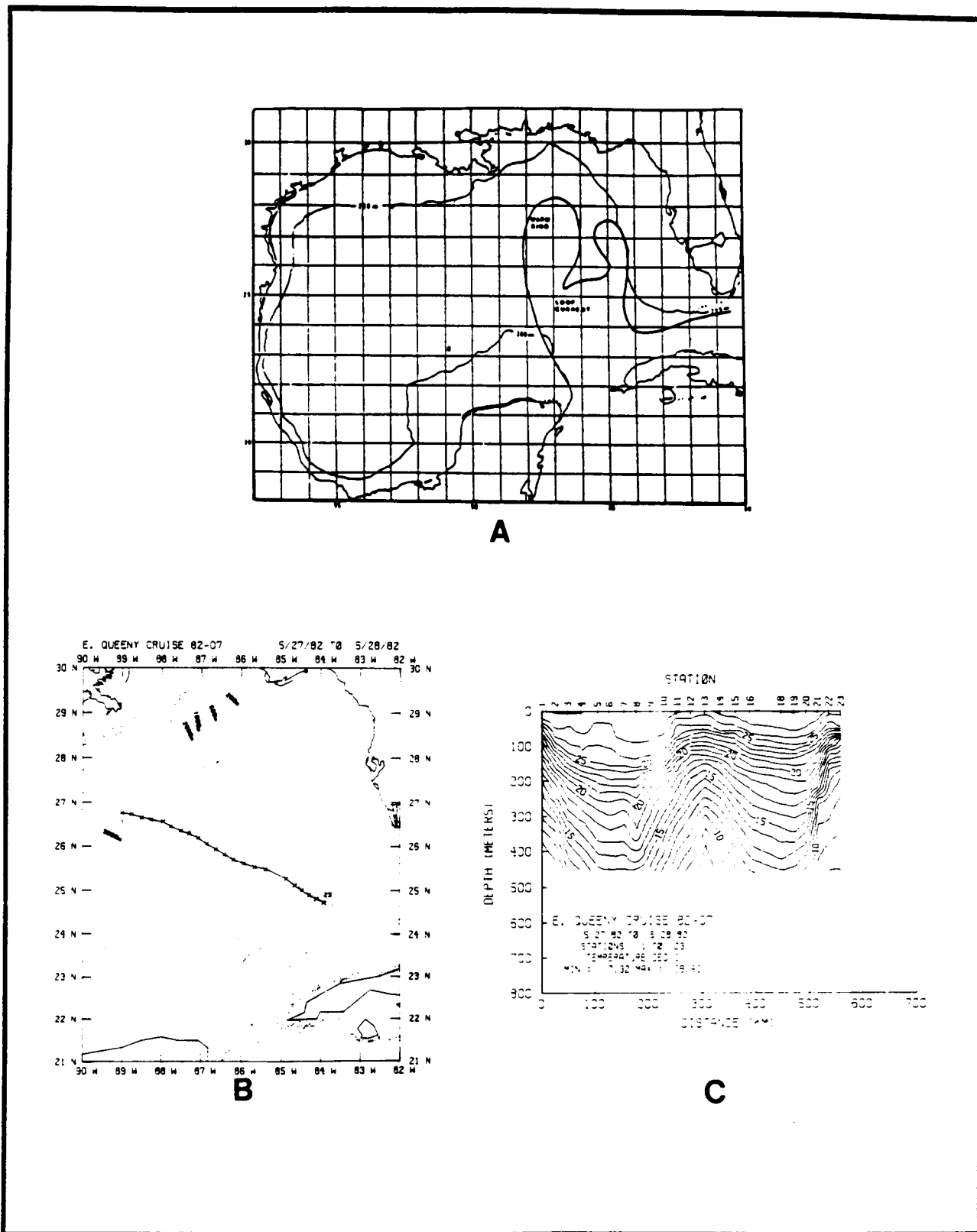


Figure 4.3-32. (A) Surface frontal analysis from the NOAA infrared data for 21 May 1982. (B) Cruise path and station locations for and (C) temperature ($^{\circ}\text{C}$) section from data collected by the E. QUEENY on 7-8 June 1982.

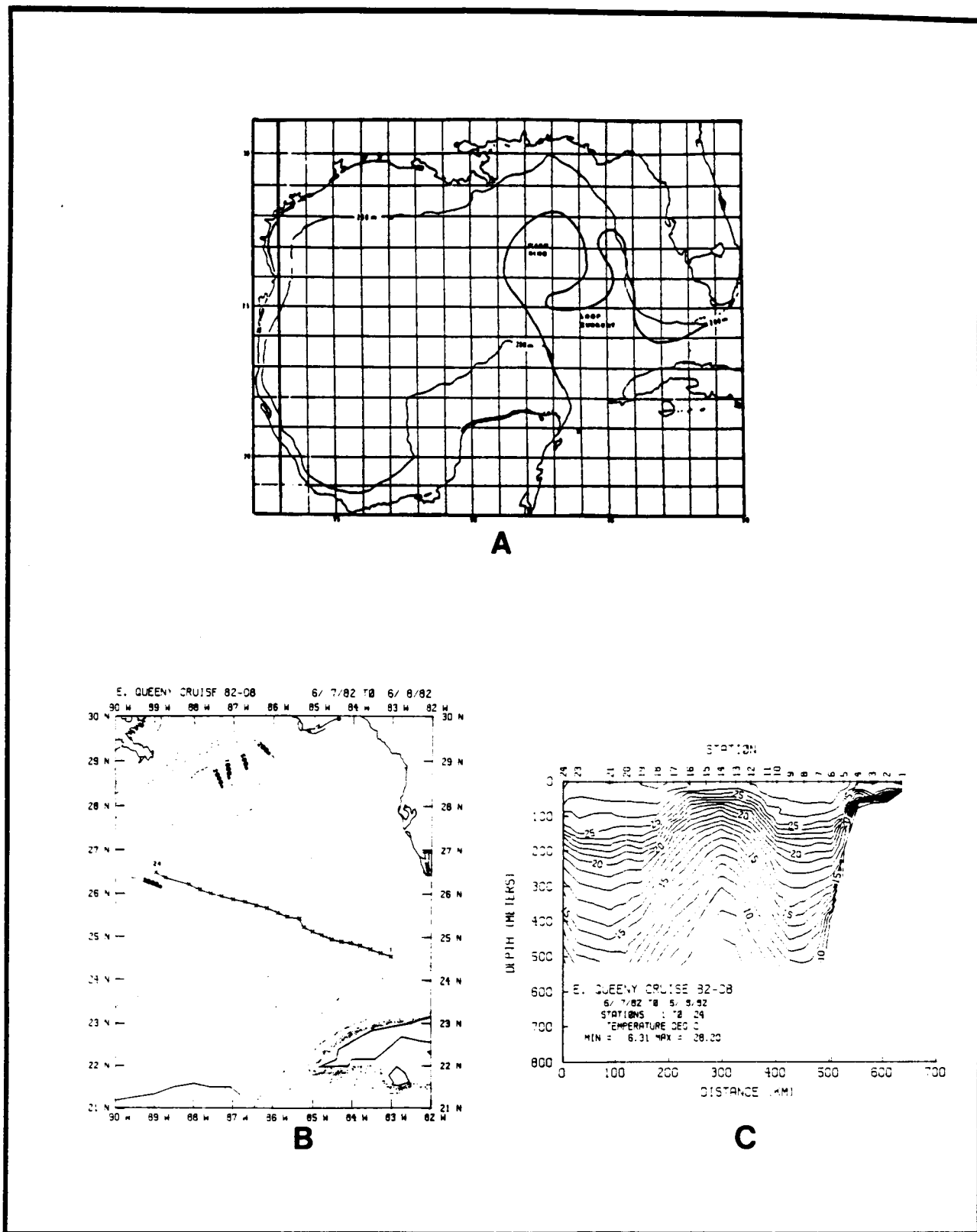


Figure 4.3-33. (A) Surface frontal analysis from the NOAA infrared data for 8 June 1982. (B) Cruise path and station locations for and (C) temperature ($^{\circ}\text{C}$) section from data collected by the E. QUEENY on 7-8 June 1982.

21, the Loop Current at around Station 8, and the cold dome separating the Loop Current from the warm ring at around Station 14. The western boundary of the ring was not depicted in the analysis so the horizontal dimensions of the ring could not be determined. The transect data obtained from the May cruise (Figure 4.3-32c) indicated that the 20°C isotherm penetrated to depths greater than 250 m. However, the June data indicated that the deepest penetration of the 20°C isotherm was about 220 m. The deep water isotherms, on the other hand (for example, 15°C isotherm), had insignificant change and, if they changed at all, were found at greater depths in June than in May.

The cold dome separating the warm ring from the Loop Current seemed to intensify during the May-June period. The shallowest depth of the 20°C isotherm in May was about 110 m, and that for the 15°C isotherm was about 170 m. In June, the shallowest depth for the 20°C isotherm was about 75 m and that for the 15°C isotherm was about 140 m. In May, the width of the Loop Current at the surface was approximately 200 km, and in June, 250 km. These data suggest that the Loop Current was growing in the eastern part of the eastern Gulf of Mexico. By August 1982, the E. QUEENY data (Figures 4.3-34a-b) indicated that the Loop Current had reformed in the eastern Gulf of Mexico and that the eastern extent of the ring edge was further to the west. The temperature contrast at the surface was not sufficient to identify the Loop Current using satellite data at this time of year.

4.3.6.3 Path of the Warm Ring

Figure 4.3-35 presents the path of nine separate rings for which reasonably continuous and long term paths were determined using the available data. In this case, the actual paths are not presented (some of these will be shown later); only a linear plot between endpoints is given in order to provide the general trends of the movement of the rings. The precise details of these movements can only be derived from the actual paths, and the actual paths, at times, show movement that departs significantly from the trends in Figure 4.3-35, which shows a general southwestward movement of the rings. One of the paths shows a general westward movement, and one a northwestward movement.

Though Figure 4.3-35 suggests that there are, at best, two potential warm ring paths, Figure 4.3-36, however, presents three characteristic paths for the warm rings in the western Gulf. All positions of major warm rings determined using the 1973-1984 satellite data base are plotted in the figure and are represented by the dots. The position data are made up of three primary sources:

- (1) Smoothed positions for nine rings for which long-term and continuous paths were determined;
- (2) Warm ring positions associated with short term paths (about four or five continuous positions); and
- (3) Isolated individual positions of a well defined ring (data for items (2) and (3) of the sources were derived from satellite data for the period from 1973-1979).

Three characteristic paths were determined subjectively based on the above mentioned data sources. Path (1), the southwestern Gulf path, was predominant, with six of the long term paths and many of the isolated positions conforming to this path. Only one long term path conformed to

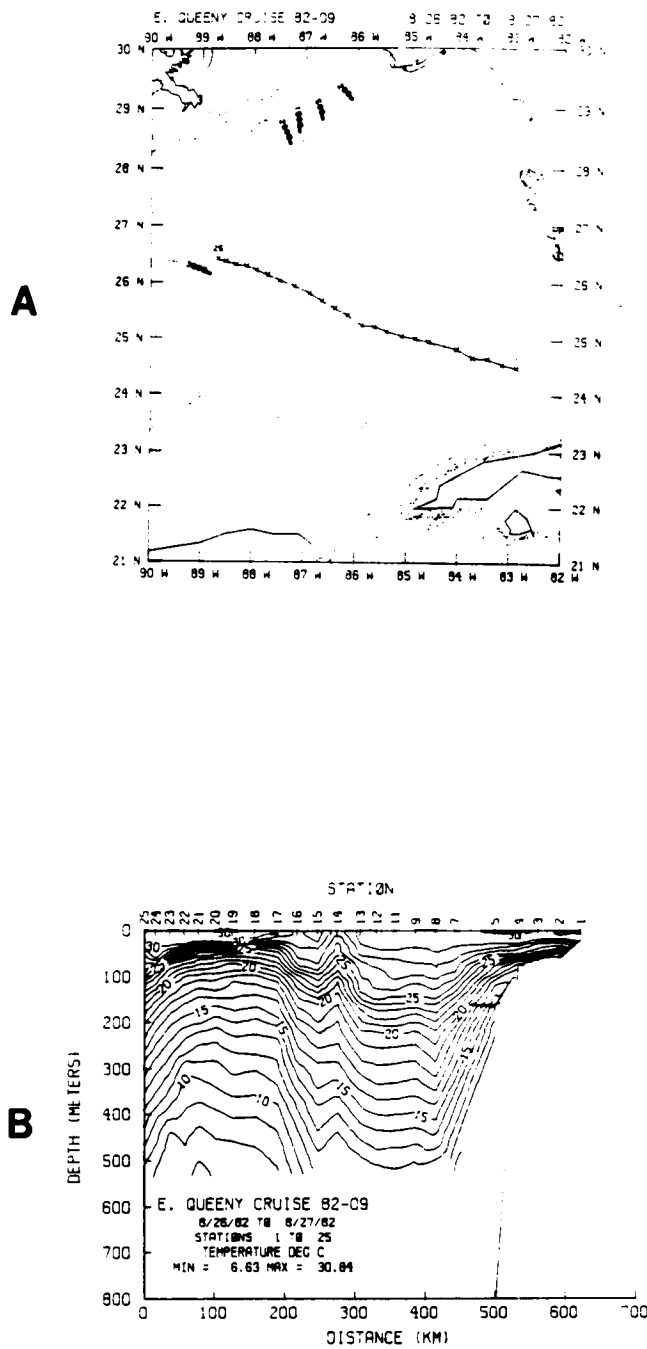


Figure 4.3-34. (A) Cruise path and stations locations for and (B) temperature ($^{\circ}\text{C}$) section from data collected by the E. QUEENY on 26-27 August 1982.

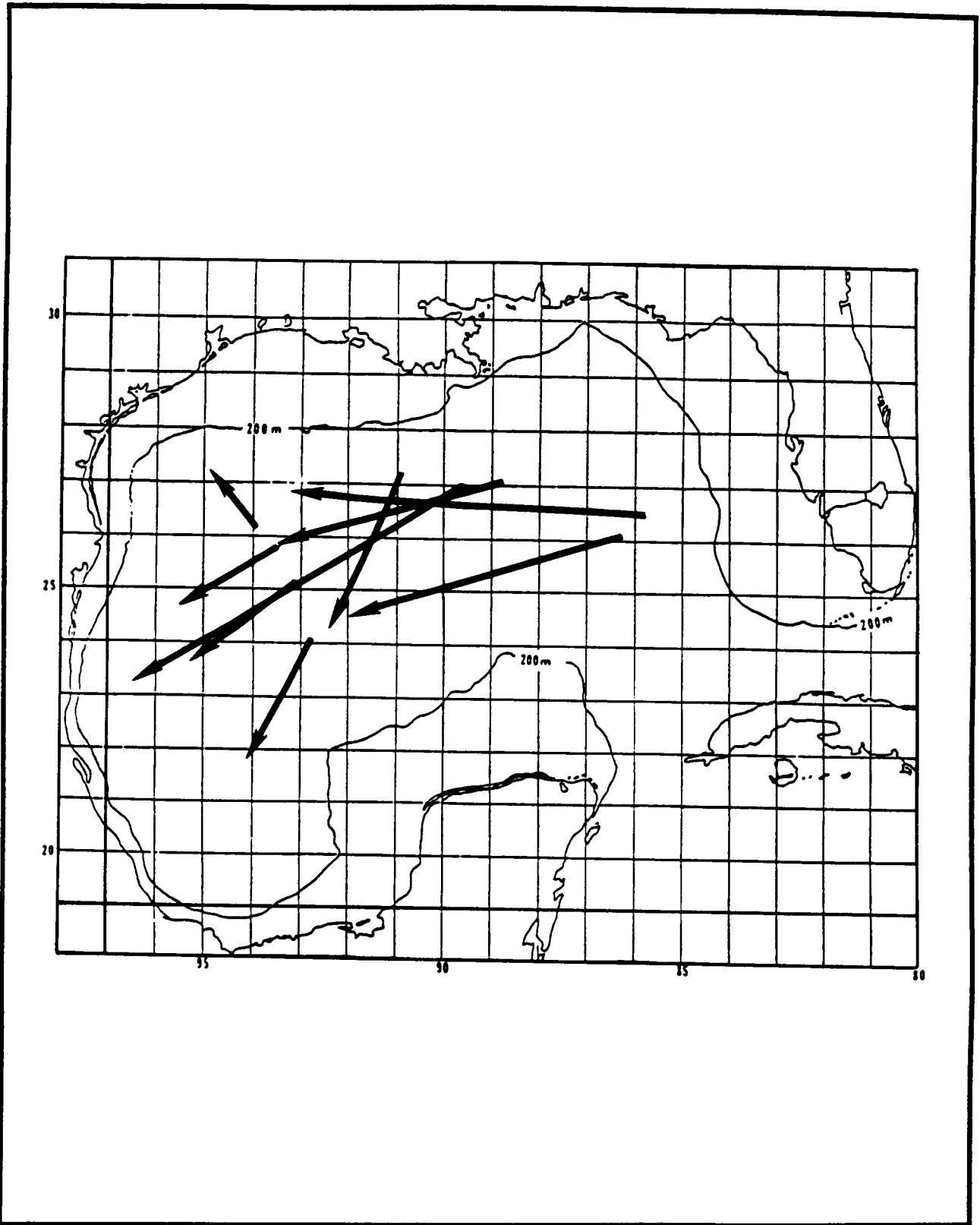


Figure 4.3-35. Linear paths based the connection of endpoints for the long term paths.

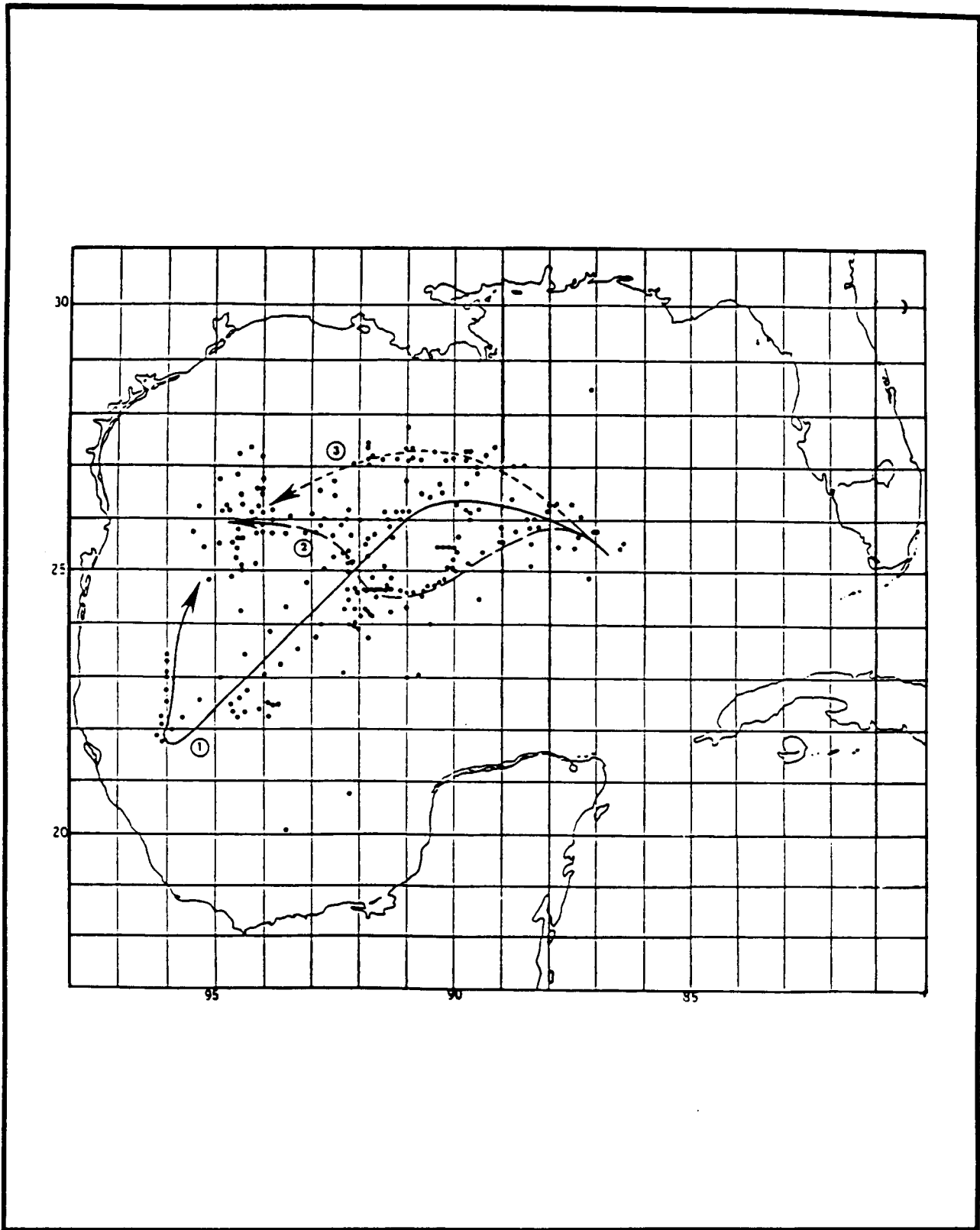


Figure 4.3-36. Characteristic paths of warm rings in the western Gulf of Mexico and the position of warm ring centers obtained using GOES and NOAA satellite data for the periods from 1973 to 1984.

either path 2 or 3. A number of isolated points were found that conformed to path 2 in the period from 1973-1979, and to path 3 in the period from 1976-1979. The isolated points suggested that warm rings moved in accordance to either path 2 or 3 at other times in the past. One (See Figure 4.3-37) of the long term ring paths did not conform to any of the characteristic paths described in Figure 4.3-36. This ring path will be discussed later.

Figure 4.3-38 presents the paths of rings which conform to the three characteristic paths presented in Figure 4.3-36. The position data used to create these paths were smoothed using the polynomial regression procedure. The beginning and ending times of each path are also given. The ending times are the times when the sea-surface temperature lacked sufficient contrast for the satellite data to detect the ring and are not related to the time when dissipation of the ring may have taken place. It can be seen from Figure 4.3-38 that the actual paths are not as smooth as those presented in Figure 4.3-36. Sharp changes in the direction of motion of warm rings are indicated. In most cases, when the sharp changes in the direction of motion of a warm ring were detected, the path of the ring formed a tight loop. The position changes associated with the tight loop were not only present in the smoothed data, but were also present in the raw data. In some cases, the temporal resolution of the raw data was not sufficient to characterize loops. In those cases, a loop is presented (dashed line) as the best interpretation of the changes in the path described by the data. At times, rings undergo marked changes in shape at the surface which can produce artificial changes in the location of the ring's center. These artificial changes could be responsible for the formation of tight loops. However, some of these effects were removed by the smoothing accomplished using polynomial regression.

The data in Figures 4.3-36 and 4.3-38 suggest that all paths converge to a region in the northwestern Gulf of Mexico best defined by 25°N to 28°N and 93°W to 96°W. Figure 4.3-37 gives positional information (the path) for a ring that has reached that region. It can be seen that the ring did not remain stationary and that the path of the ring, even in this region, was characterized by a number of tight loops.

4.3.6.4 Speed of the Warm Rings

Figure 4.3-39 presents the variation of the speed of motion along the path of the three major warm rings whose paths were presented in Figure 4.3-38. The ring speeds are presented as a function of time. In order to emphasize the oscillatory behavior of the speed of movement with time, the speed data in each case were curve fitted using a tenth degree polynomial.

The speed of the warm rings oscillated with periods (periods were defined peak to peak) that ranged from 40 to 100 days. The oscillation is over a speed range of 1 to 8 km day⁻¹, on the average, but ranges were as large as 1 to 14 km day⁻¹. Similar speed oscillations were noted for the ring located in the northwestern part of the Gulf of Mexico (see Figure 4.3-37). The relatively high-speed motion of the rings occurred when the path of the rings was characterized by quasi-linear motion. The relatively low speed motion coincided with the time periods when the ring path was characterized by major changes in direction or by the tight loops.

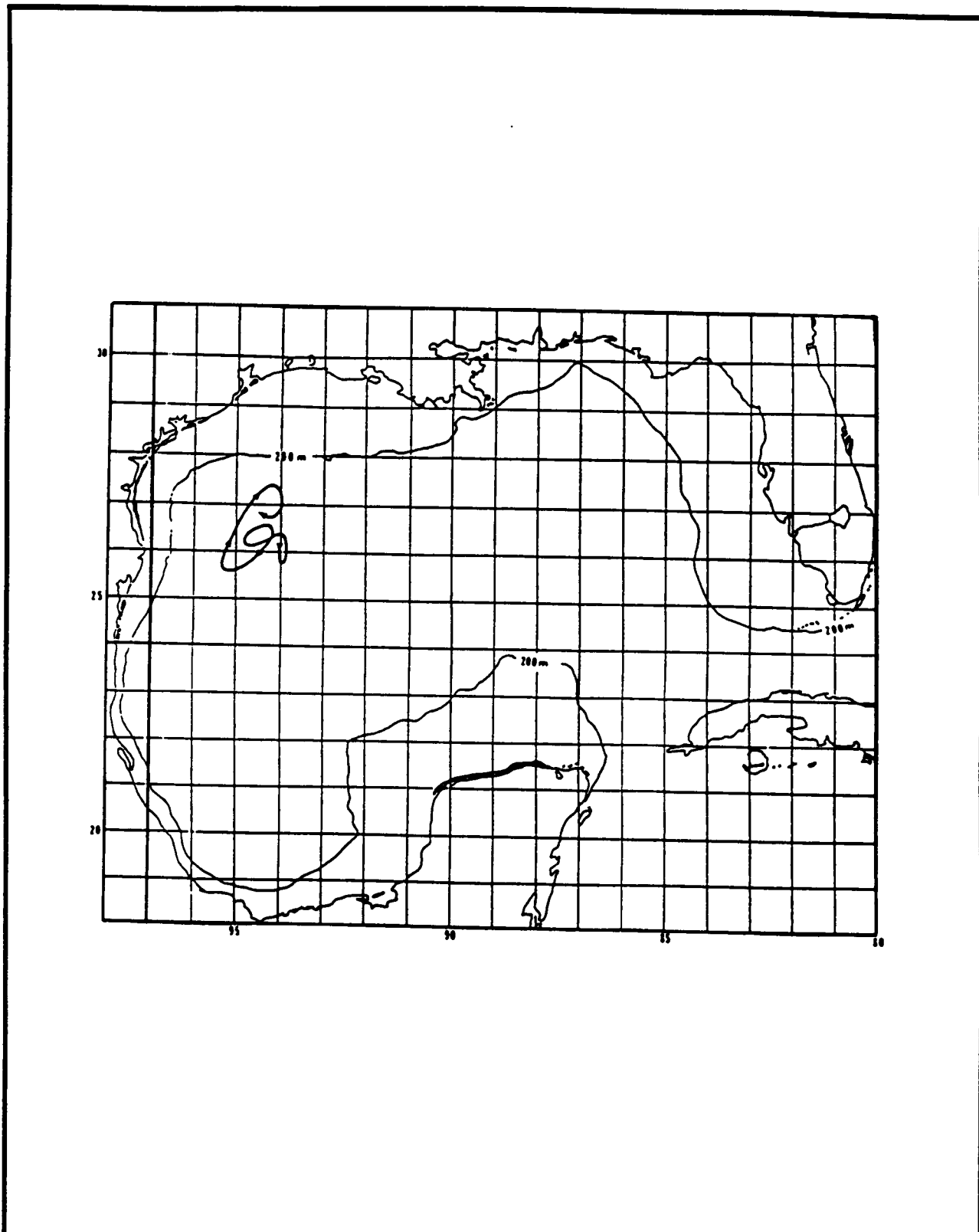


Figure 4.3-37. Path of a warm ring that is located in the northwestern Gulf of Mexico. The period over which the ring was traced is November 1983 to June 1984.

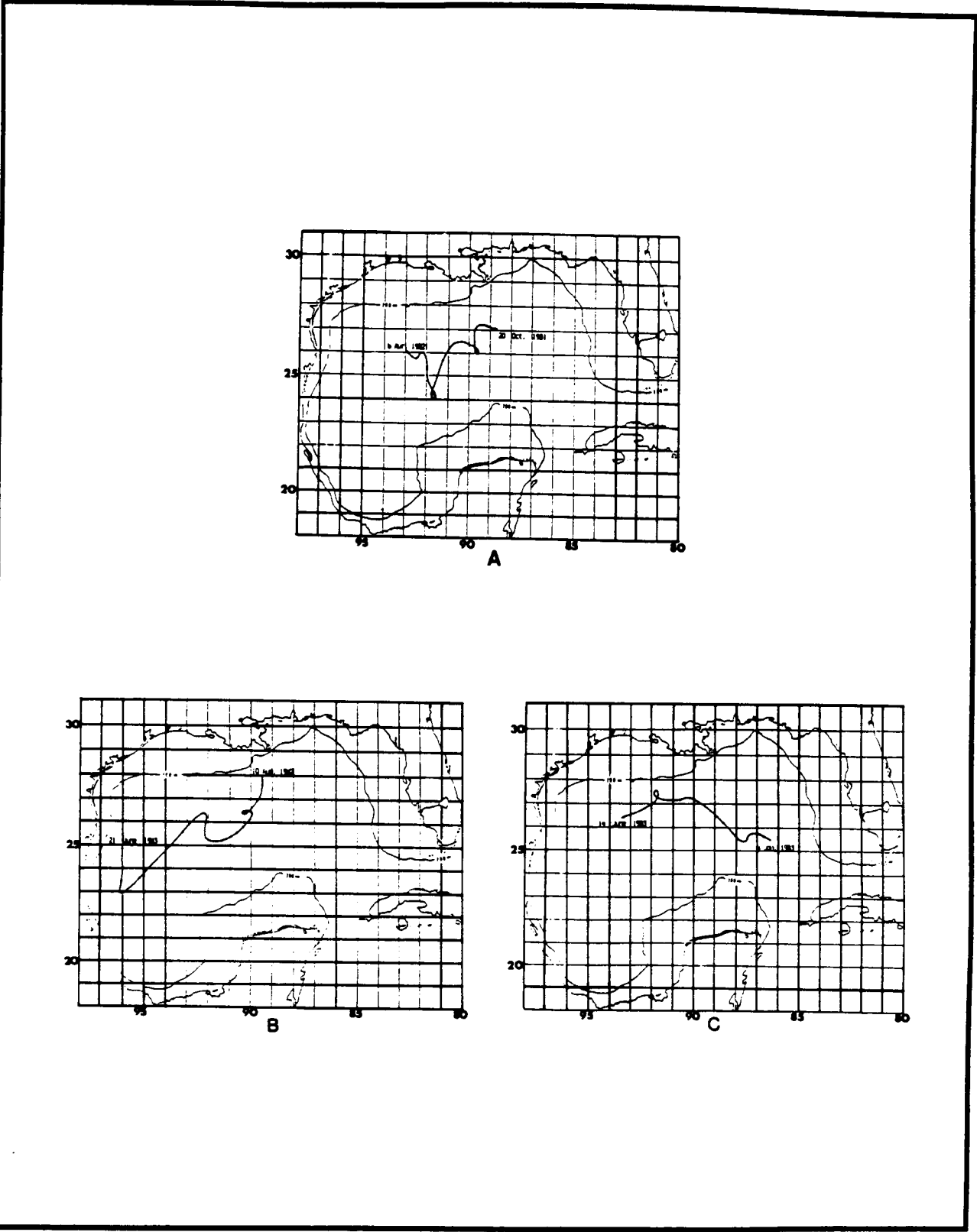


Figure 4.3-38. The path of three warm rings in the Gulf of Mexico which conform to the three characteristic paths presented in Figure 4.3-36. The periods over which the rings were traced are (A) October 1981 to April 1982; (B) August 1982 to June 1983, and (C) January to June 1983.

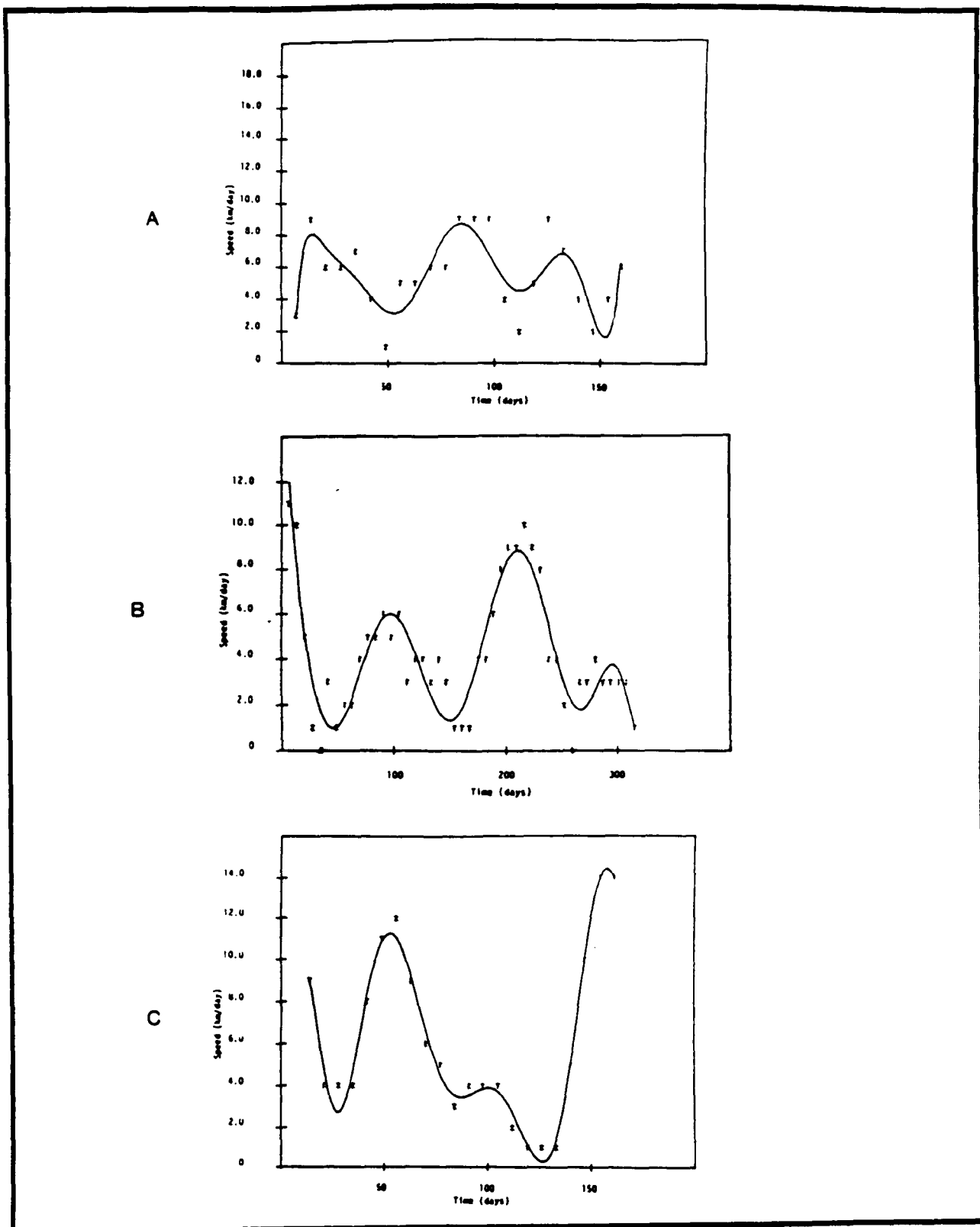


Figure 4.3-39. Speed of the warm rings (km day^{-1}) that are presented in Figure 4.3-38 as a function of time. The time periods as they relate to the lettering (A, B, and C) are the same as in Figure 4.3-38.

The frequency distribution of the speeds of the warm rings (Figure 4.3-40) constructed using data from the 1980 to 1984 period only shows a bimodal distribution. The primary mode occurs at speeds of 4 km day^{-1} , the secondary mode at speeds of 1 km day^{-1} . The primary mode is most probably associated with those time periods when the ring path is characterized by quasi-linear motion, and the secondary mode with those time periods when the ring path is characterized by major directional changes or tight loops. The average speed of the rings along the path is 5 km day^{-1} and the median speed is 4 km day^{-1} .

4.3.6.5 Decay of Ring Size

The decay of the warm ring size was studied by examining the time variations of the ring diameter. The ring diameter, a fictitious parameter inasmuch as the rings seldom have a circular configuration, was chosen on the basis of a best fit circle whose surface area was approximately equal to that of the ring at the given time. It should also be noted that the ring diameter was only defined when the entire ring was visible in the infrared imagery (though it may have been possible to define the position and speed of the ring if only part of the ring was visible). For example, for the 1982-1983 ring (Figure 4.3-38a and 4.3-41b), considerable position data were obtained, but there were only seven observations of the complete ring over a time period. On the other hand, considerable information on the ring diameter was derived for the 1981-1982 ring, as well as for the 1983 ring.

The data in Figure 4.3-41 indicate that in approximately 150 days, the 1981-1982 ring decayed to approximately 52% of its initial size, and the 1983 ring to 54% of its initial size. In the same time period, the 1982-1983 ring decayed to approximately 75% of its initial size; however, the 1982-1983 data are suspect because of the lack of continuous observation of the ring diameter over the period. The ring in the northwestern Gulf (i.e., Figure 4.3-37) did not have appreciable changes in its diameter during the period it was observed.

Two principle methods by which the ring decays have been detected from satellite observations. The first method is by erosion of the ring at the boundaries. Figure 4.3-30 provides an excellent example of this process. On 13 December 1983 (Figure 4.3-30a), the ring was characterized by three filaments at the boundary. These filaments are at most 50- to 300-m deep (Vukovich, 1985). The water in the filaments eventually is isolated and mixes within the environment. The 13 January 1984 frontal analysis (Figure 4.3-30b) shows the same ring, but at reduced size with no filaments at the boundary. The second method involves the separation of a smaller ring from the ring. The larger of the two rings dominates and persists, whereas the smaller ring rapidly loses its surface signature. The rapid loss of the surface signature suggests that the ring might have been dissipating. However, no in situ evidence is available to substantiate that what has been observed by the satellites is in fact a result of the dissipation of the ring.

Reasonably continuous records of the ring diameter versus time were obtained for nine rings over the period of interest. Figure 4.3-42 presents the time variation of the ring diameter averaged over the nine rings. Prior to averaging, ring sizes were normalized by the initial value. The curve fit resembles an exponential decay. The ring diameter was approximately 55% of

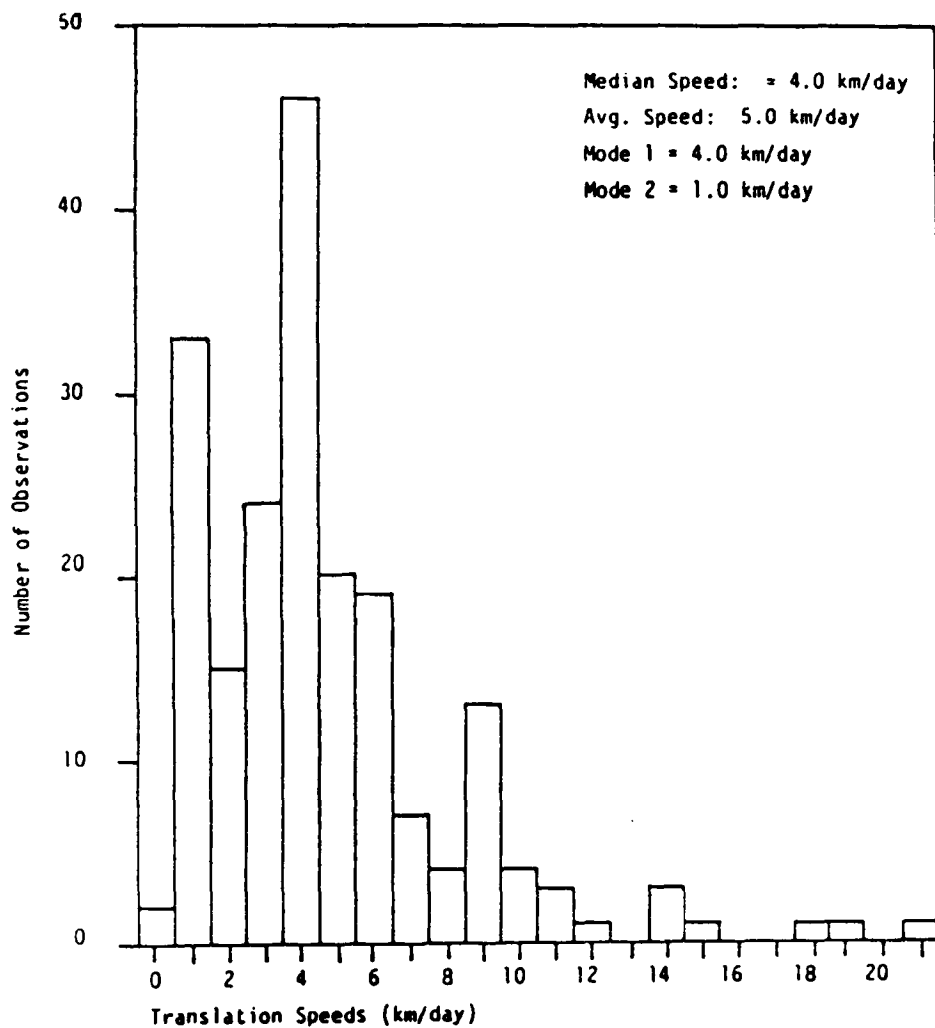
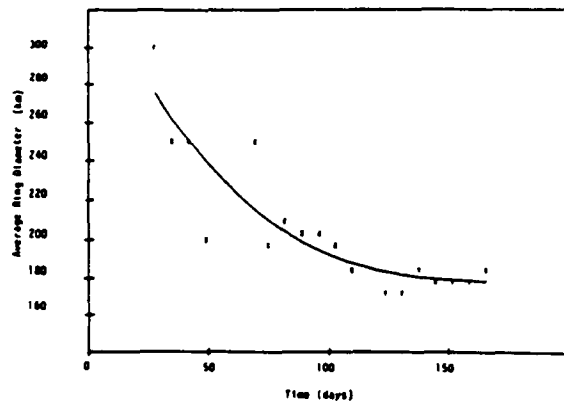
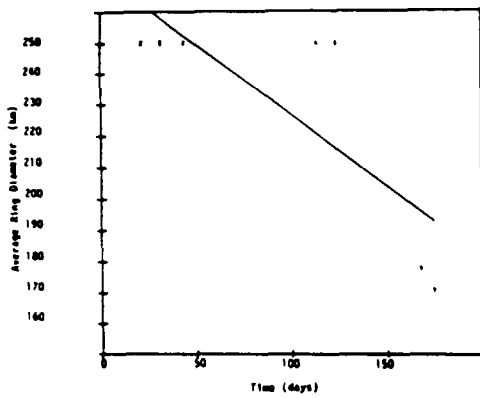


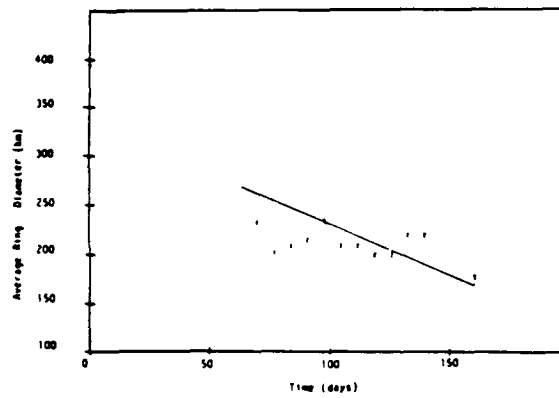
Figure 4.3-40. Frequency distribution of warm ring speeds in the Gulf of Mexico obtained from all continuous ring position data for the period 1973 to 1984.



A



B



C

Figure 4.3-41. Warm ring diameter (km) versus time for the three rings presented in Figure 4.3-38. The time periods as they relate to the lettering (A, B, and C) are the same as in Figure 4.3-38.

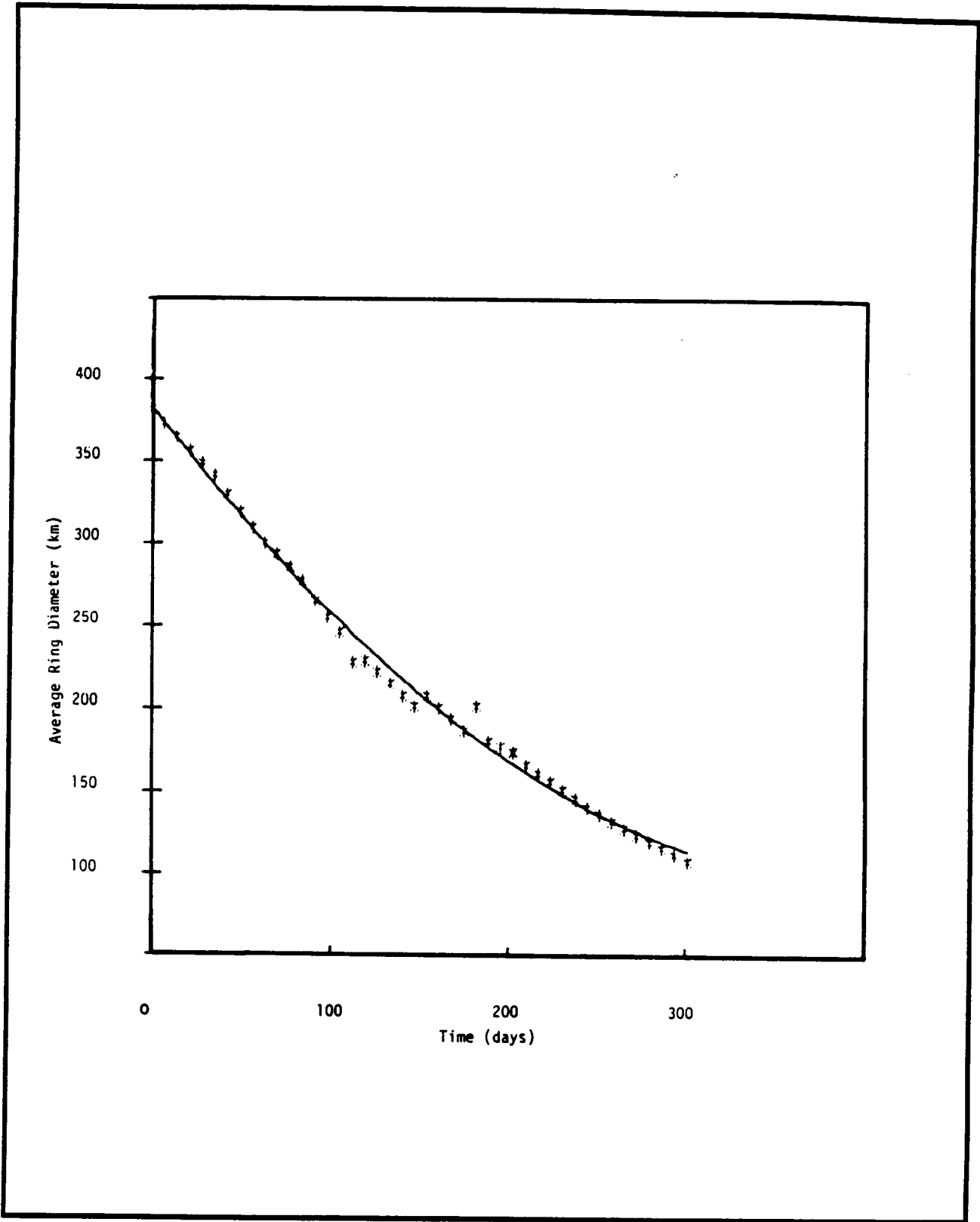


Figure 4.3-42. The time variation of the warm ring diameter averaged over all long term data sets associated with a ring for the period from 1973-1984.

its initial size after 150 days. This corresponds very closely to what was found for the 1981-1982 and the 1983 rings. In 300 days, the ring diameter was approximately 31% of its initial size.

4.3.6.6 Analysis Results

At the time they separate from the Loop Current, the major warm rings have diameters which equal or exceed 250 km and there is usually a major change in the position of the northern boundary of the Loop Current (Vukovich et al., 1979). Evidence presented here suggests that these rings extend to depths greater than 800 m. Very little is known of the vertical extent of the rings after they have had considerable residence in the western Gulf of Mexico. It should be noted that warm rings having diameters less than 250 km also separate from the Loop Current. However, when the smaller rings separate from the Loop Current, there is generally no major change of the position of the northern boundary of the Loop Current.

After these rings have separated from the Loop Current, they move into the western Gulf of Mexico. Three characteristic paths of movement have been determined (Figure 4.3-36): a northern path; a mid-gulf path; and a southwestern path. The southwestern path predominated over the period. The data suggest that all three paths converge to a region in the northwestern portion of the western Gulf of Mexico (the area defined by 25°N to 28°N and 93°W to 96°W). When a ring reaches this region, it is neither stationary nor is its speed steady.

As the ring moves from the eastern Gulf of Mexico into the western Gulf, its speed was observed to oscillate over the speed range from 1-8 km day⁻¹, on the average, but speed ranges as large as 1-14 km per day were detected. The period of the oscillation varied from 40 to 100 days. Based on all continuous data, the average speed of the ring was approximately 5 km day⁻¹. The warm ring moved at a relatively high speed when the ring was in quasi-linear motion, but moved at a relatively low speed when it underwent a major change in direction or when the path formed a tight loop. This behavior accounted for a bimodal distribution of the speeds of the warm ring. The primary mode was at 4 km day⁻¹ and the secondary mode at 1 km day⁻¹. The statistics on the speed of the ring determined using the satellite data were similar to the ring speeds previously determined by Cochrane (1972) and Elliott (1982).

The satellite data indicated that, on the average, the area of the warm ring as defined by a characteristic diameter decreased to about 55% of its initial size in approximately 150 days after separating from the Loop Current. It decreased to about 31% of its initial size in about 300 days with the rate of decrease being greatest in the first 150 days. These results agree with past observations. Vukovich et al. (1979) indicated that at the time when major rings separated from the Loop Current, the characteristic diameters were 300 to 400 km. On the other hand, Elliott (1982) found that the rings in the western Gulf of Mexico had an average diameter of about 185 km. The area of the rings found by Elliott was about 50% to 60% of the initial size of the rings reported by Vukovich et al.

Using satellite data, the size of the ring has been observed to decay by two processes. The most common method is decay by erosion at the boundary. However, it has also been observed that, at times, the major rings will shed

smaller rings thus decreasing the areal extent of the major rings. The larger ring will dominate and persist, and the surface signature of the smaller ring will rapidly decay. It could not be determined whether the loss of the signature in the satellite data was an indication that the smaller ring was dissipating.

This discussion is confined to the decay of the ring in the surface layer since no evidence was available to indicate that this decay also occurs in the deeper structure of the ring. Available hydrographic data from a 1982 case study indicated that a change in the vertical structure of temperature in the near-surface layer of a warm ring occurred soon after it separated from the Loop Current. The isotherms in the ring's near-surface layer (the first 250 m) were observed to rise by as much as 30 m in approximately 10 days. The deeper isotherms did not appear to change substantially. The lifting of the isotherms in the near-surface layer may be associated with the observed decay of the ring size using satellite infrared data, but the evidence is not conclusive.

4.4 Hydrographic Data

4.4.1 March 1983

The station locations for the March 1983 hydrographic cruise are presented in Figure 4.4-1. Temperature, salinity, density and geostrophic velocity (1000-m reference level) plots are shown for Stations 1-38 in Figure 4.4-2 and for Stations 45-76 and 121-148 in Figure 4.4-3. The distributions all confirm the northward flow of water from the Yucatan Straits into the Gulf of Mexico along the western part of the section and the southward flow along the west Florida shelf forming the Florida Current. The geostrophic velocities are not absolute because of the lack of a level surface at 1000 m. However, the relative velocities reached maxima of around 150 cm s^{-1} northward in the flow from the Yucatan Straits and 93 cm s^{-1} in the southward Loop Current flow along the west Florida shelf. These observations suggest that the inflow may have been higher than the outflow, but are not conclusive. Clearly, in the long term volume inflow and outflow are equal.

Boundary currents along shelf break regions often result in upwelling and the intrusion of cold, nutrient-rich, low-oxygen water into adjacent shelf waters; this seems to be the case along the west Florida shelf, and to a lesser degree along the Yucatan shelf. Vertical temperature plots for the southern section (Stations 1-38) (Figure 4.4-2) show 18°C water on the west Florida shelf but water of above 24°C on the Yucatan shelf. This could occur either because the west Florida shelf is deeper than the Yucatan shelf along this section (120 m vs 70 m) or because winds were more favorable for upwelling on the west Florida shelf.

Nutrient concentrations were elevated over the shelf, generally following the isotherms (Figure 4.4-4). Total chlorophyll concentrations were also elevated in the outer waters of both the west Florida and Yucatan shelves. Highest values (2.45 mg m^{-3}) were found on the Yucatan shelf. The distribution of temperature and nutrient parameters along the more northerly section for Stations 45-76 and 121-144 (Figure 4.4-5a,b) is much less different between the two shelves.

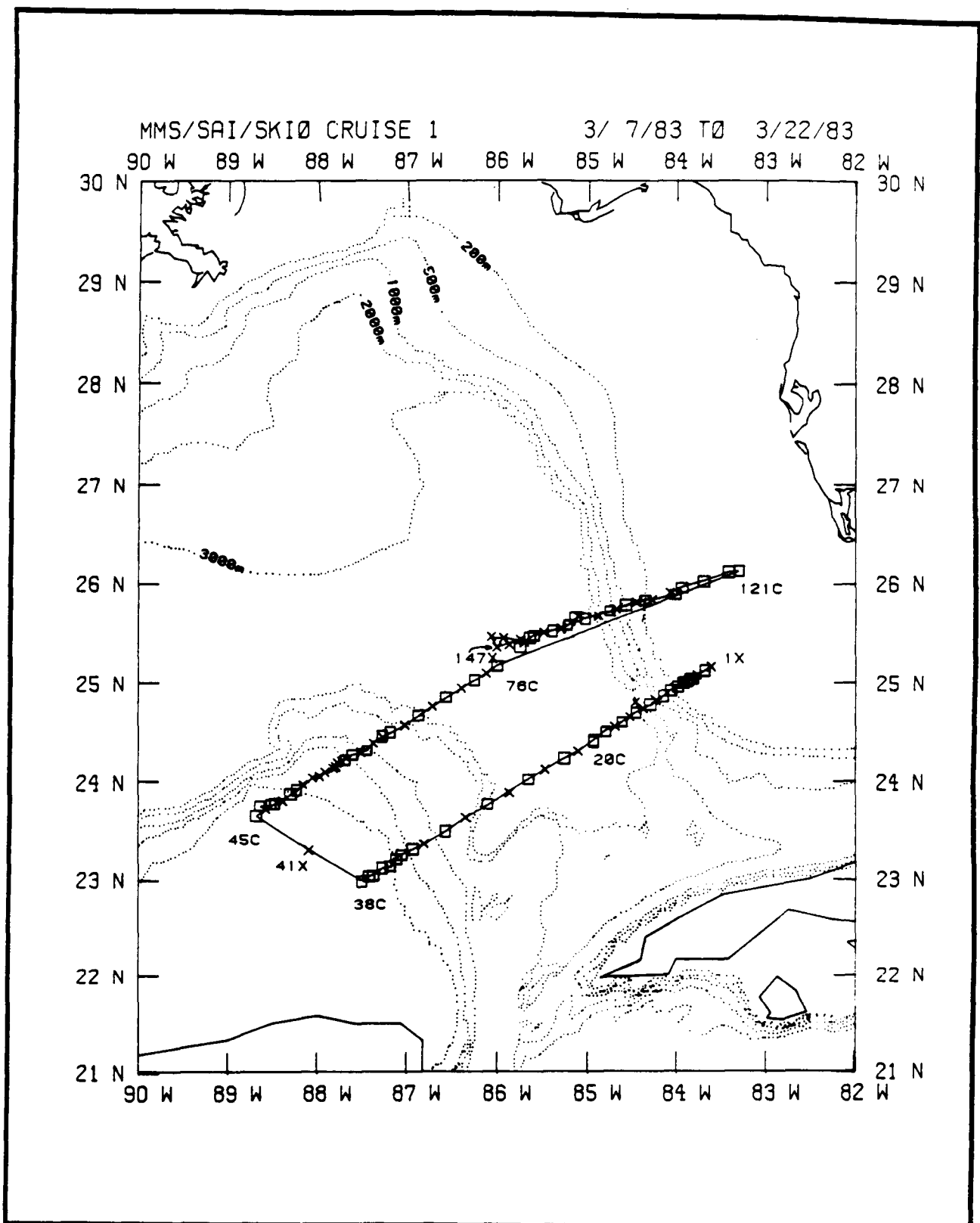


Figure 4.4-1. Cruise track showing XBT and CTD station locations for R/V SUNCOASTER cruise from 7-22 March 1983.

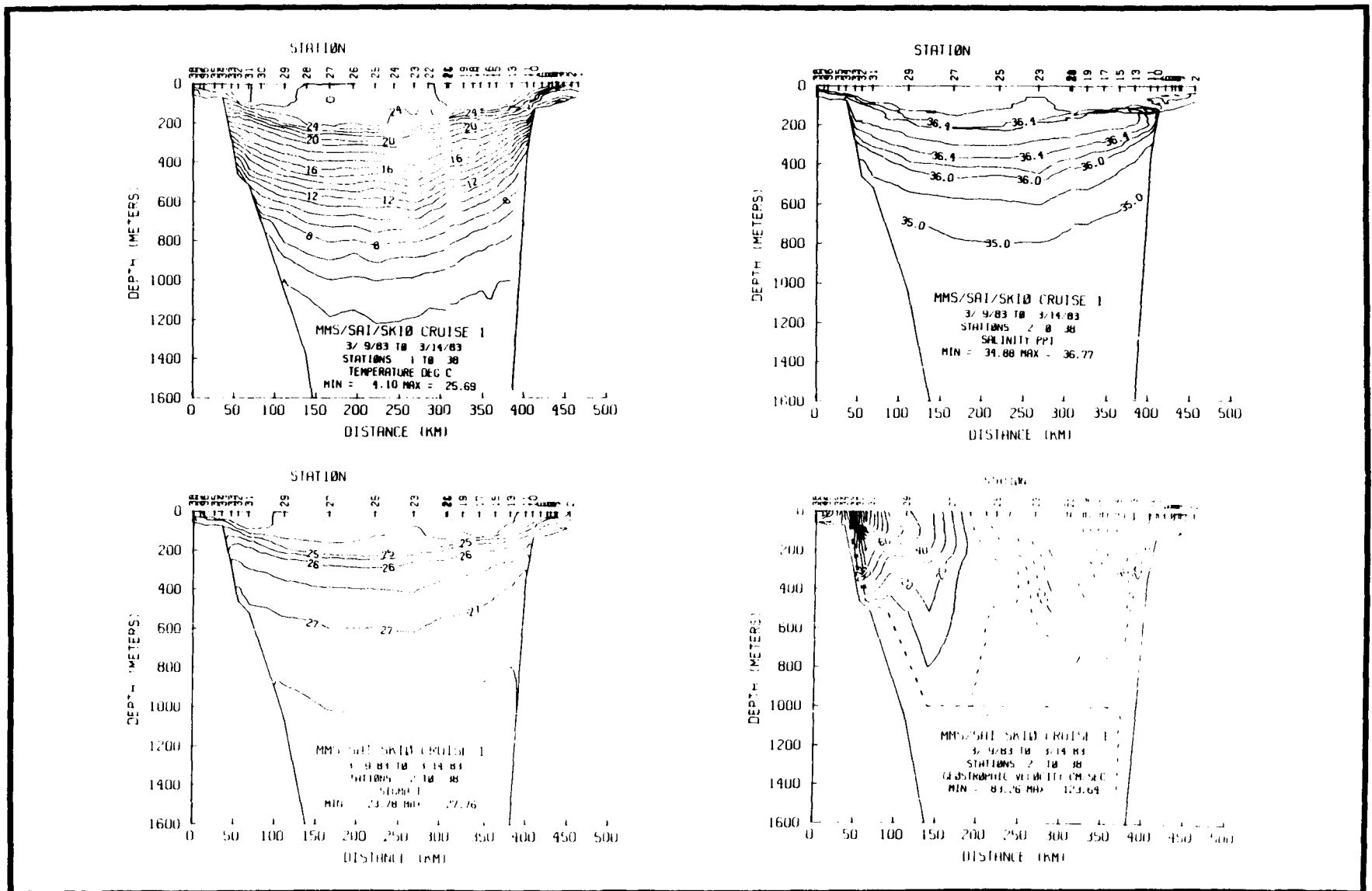


Figure 4.4-2. Temperature, salinity, density, and geostrophic velocities (1000-m level surface) for section Stations 1-38 for 9-14 March 1983. Discontinuity is formed by joining sections done at different times.

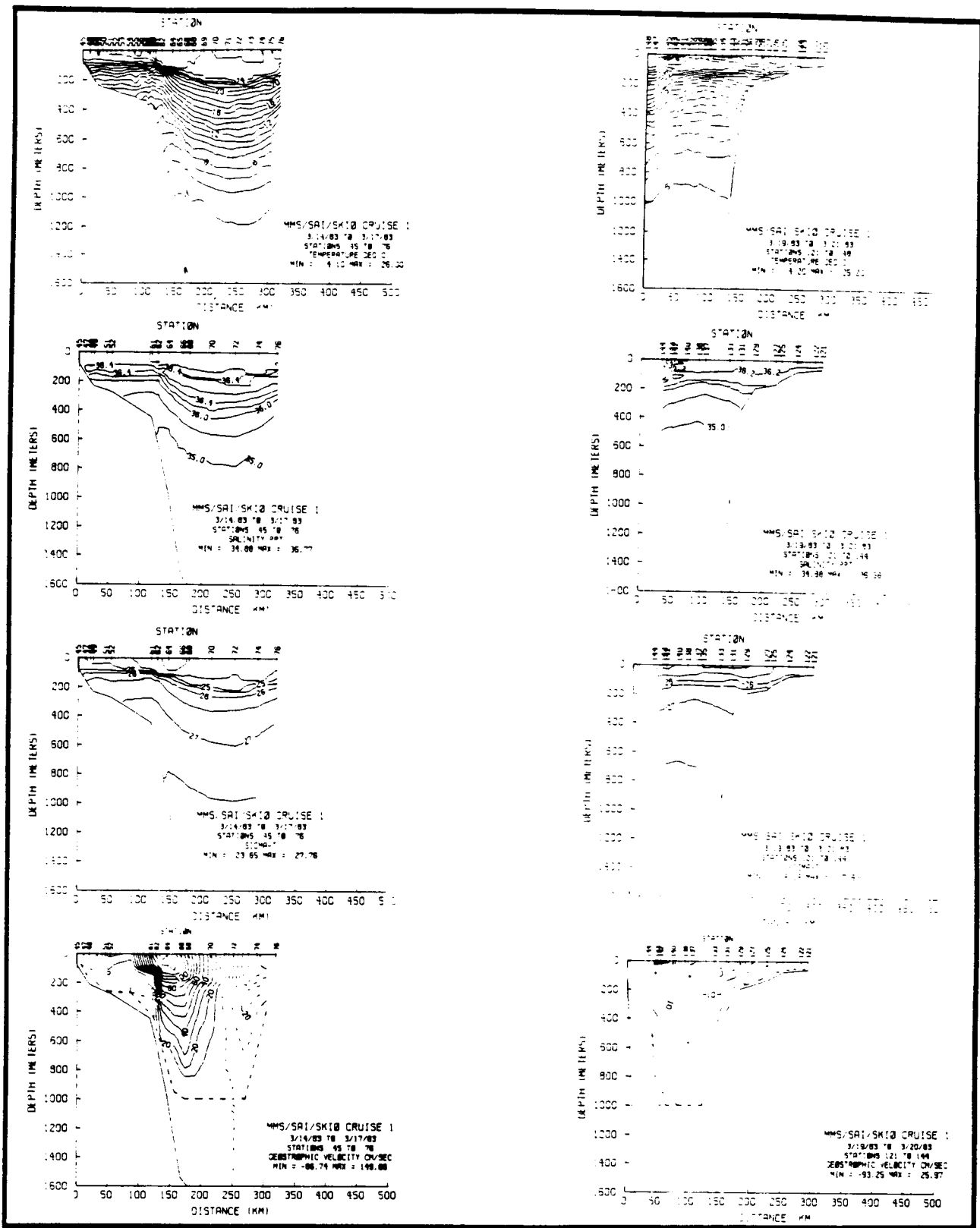


Figure 4.4-3. Temperature, salinity, density, and geostrophic velocities (1000-m reference level surface) for stations 45-76 and 121-144 shown in Figure 4.4-1. The western portion of the section (Stations 45-76) was run on 14-17 March and the eastern portion (Stations 121-148) was run on 19-21 March.

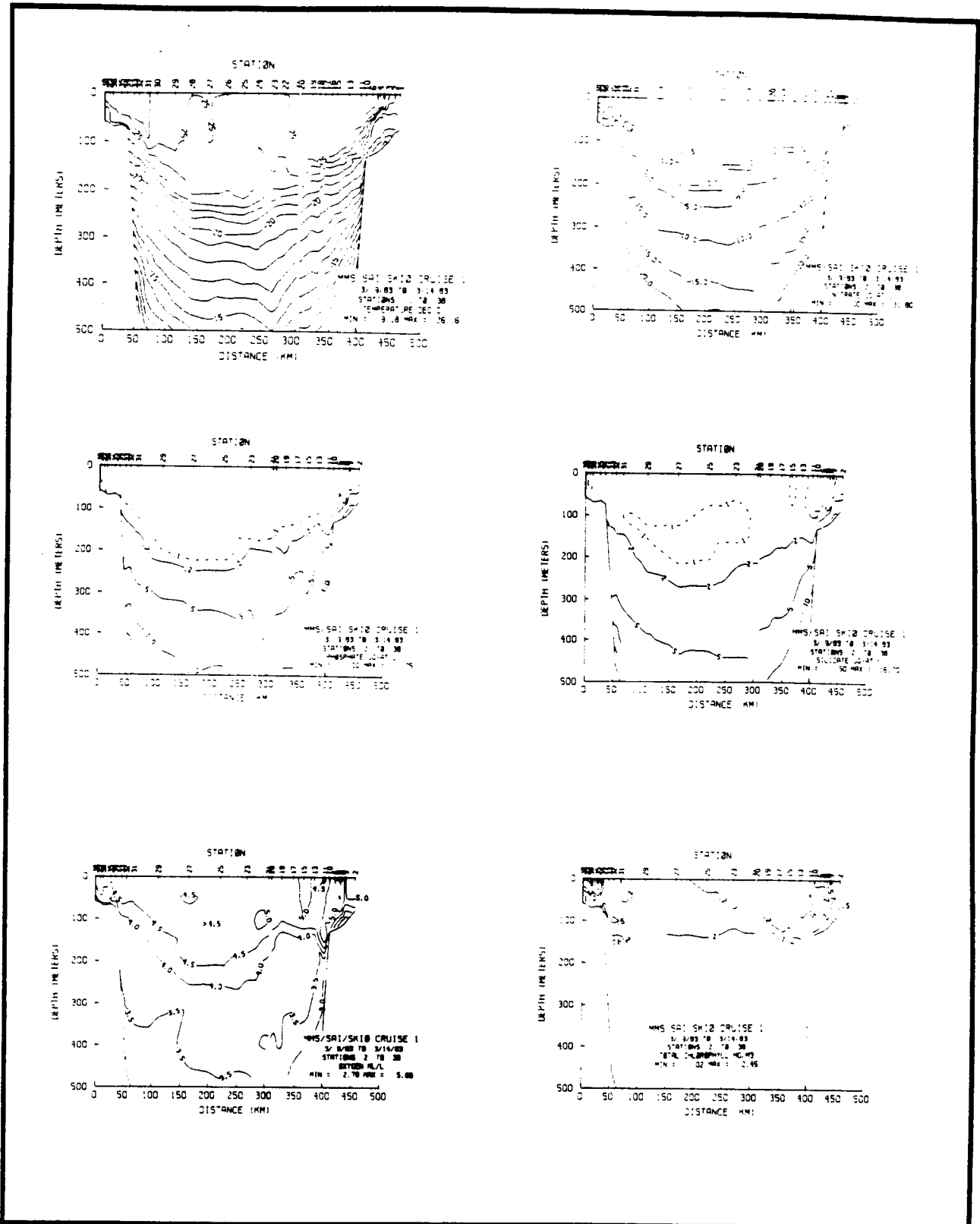


Figure 4.4-4. Temperature, nitrate, phosphate, silicate, oxygen, and total chlorophyll from the southern section in March 1983 (Stations 2-38).

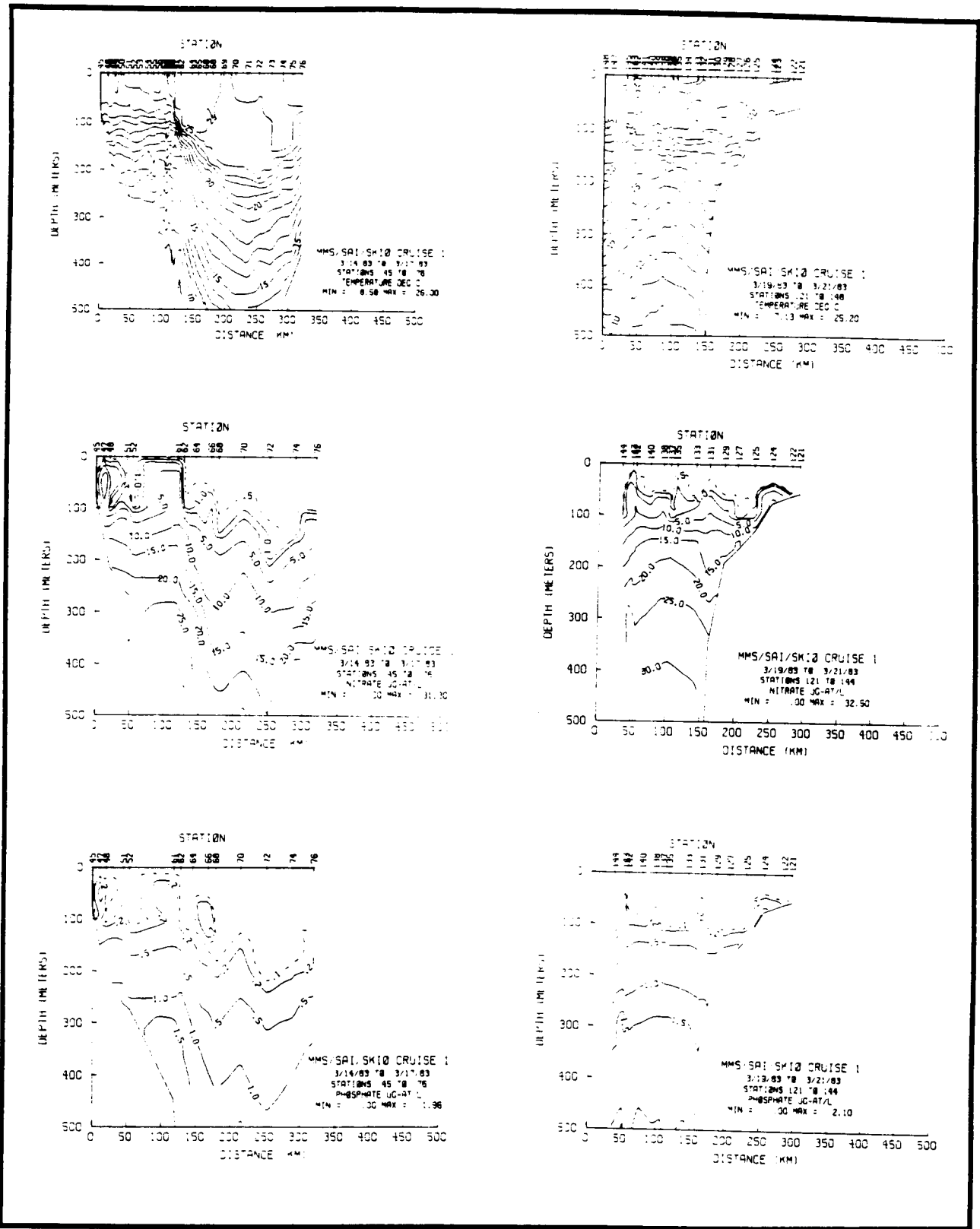


Figure 4.4-5a. Temperature, nitrate, phosphate, silicate, oxygen, and total chlorophyll from the northern section in March 1983 (Stations 45-76 and 121-144).

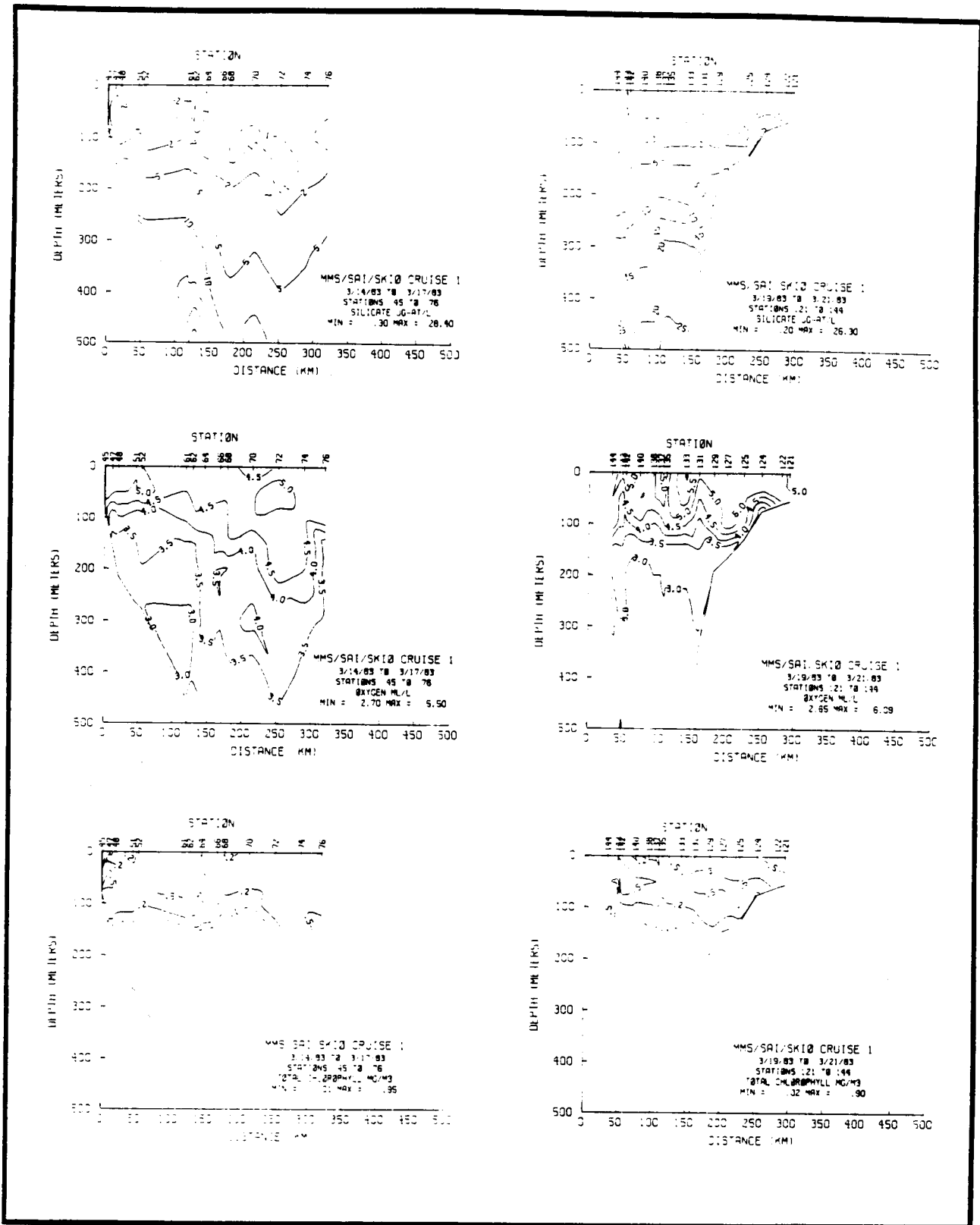


Figure 4.4-5b. (continued).

Along this more northerly section, a cold perturbation was identified along the west Florida shelf. It was first observed in satellite images on 9 March and disappeared between 3 and 12 April. Its life history was discussed in Section 4.3.3. That part of the section formed by Stations 121-148 traversed this cold perturbation on 19-21 March at latitude 26°N (Figure 4.4-6). The temperature, salinity and density sections (Figure 4.4-3) show the cold pool (Stations 136-140) and warm filament (Stations 132-134) which are characteristic of cold frontal eddies. The nutrient and total chlorophyll data (Figure 4.4-5a,b) show no sign of the filament, but the oxygen data are somewhat confusing as lower oxygen values would be expected in the warm filament. Just the reverse is observed.

4.4.2 November 1983

Observations made during the second cruise (November 1983) consisted of long sections across the shelf starting at 24°N and extending north to nearly 29°N (Figure 4.4-7). During this period a cold perturbation was observed in the satellite images and was denoted Event E and F in Table 4.3-1 in Section 4.3.2.

The temperature, salinity and density sections (Figure 4.4-8 through Figure 4.4-11) give little indication of frontal events or eddies. No dramatic dome features were present, nor were downward sloping isotherms present at the shelf edge. At Stations 70-94 and 100-128 there was an indication of doming which could have been the feature identified in the satellite derived SST image. The slope of isopycnals suggests that the Loop Current was flowing along the west Florida shelf and little frontal activity was present.

In spite of the apparent absence of frontal events, considerable deeper Loop Current water was present over the shelf edge. High-nutrient, low-oxygen water intruded over 50 km onto the shelf and in places caused enhanced biological production, suggesting mixing to the euphotic zone (Figure 4.4-12; see chlorophyll at Stations 9-13 and 22-25).

4.4.3 May 1984

4.4.3.1 Aerial Survey

4.4.3.1.1 Introduction

The LC enters the Gulf through the Yucatan Strait which has a sill depth of approximately 2000 m and exits via the Florida Strait which has a nominal sill depth of 800 m. Between these two ports the distribution and location of the LC current patterns can be highly variable. As discussed previously (Section 4.3), both the size and location of the LC can change significantly and at times abruptly, such as with break-off of a major eddy.

The Gulf basin has only these two ports through which exchange occurs. Generally, the assumption has been that the inflow is through the Yucatan Strait and outflow through the Florida Strait. More recently, limited evidence suggests that at-depth the Yucatan Strait may be a net inflow boundary while sustaining a two-way exchange in conjunction with a time-dependent net transport (Maul, et al., 1985). This would be consistent

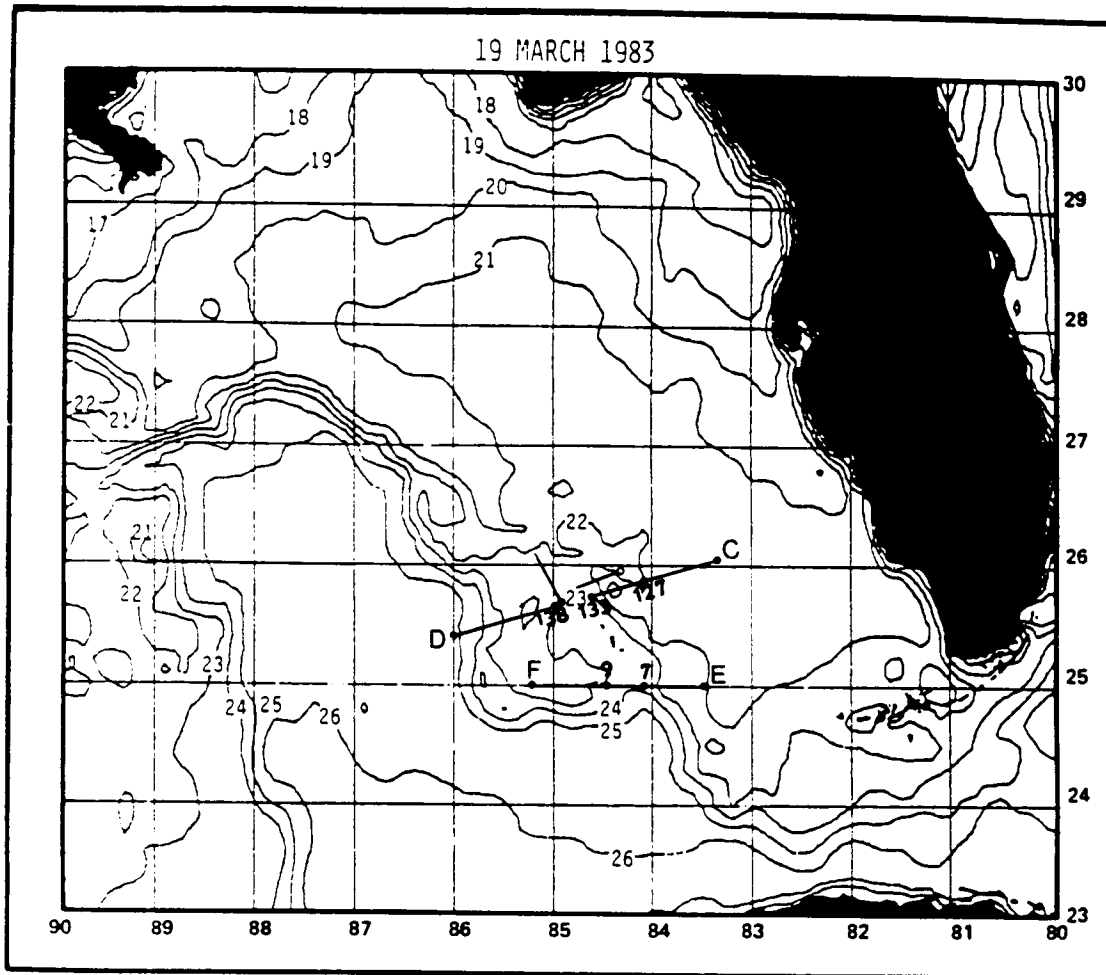


Figure 4.4-6. Sea-surface temperature (C°) analysis for 19 March 1983. Transect CD was performed by FIO in the period of 24-25 March 1983.

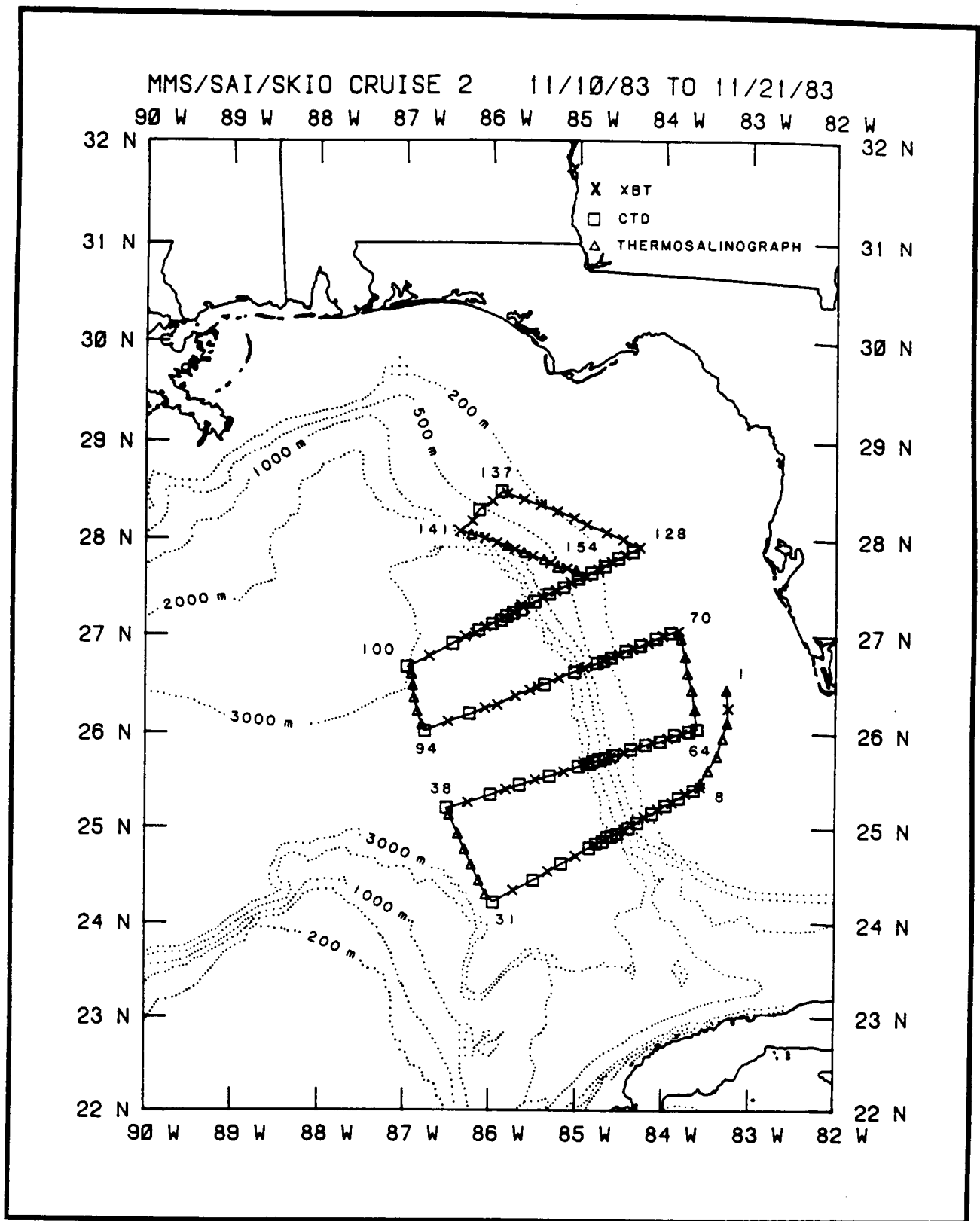


Figure 4.4-7. Cruise track showing XBT, CTD, and thermosalinograph station locations for R/V SUNCOASTER cruise from 10-21 November 1983.

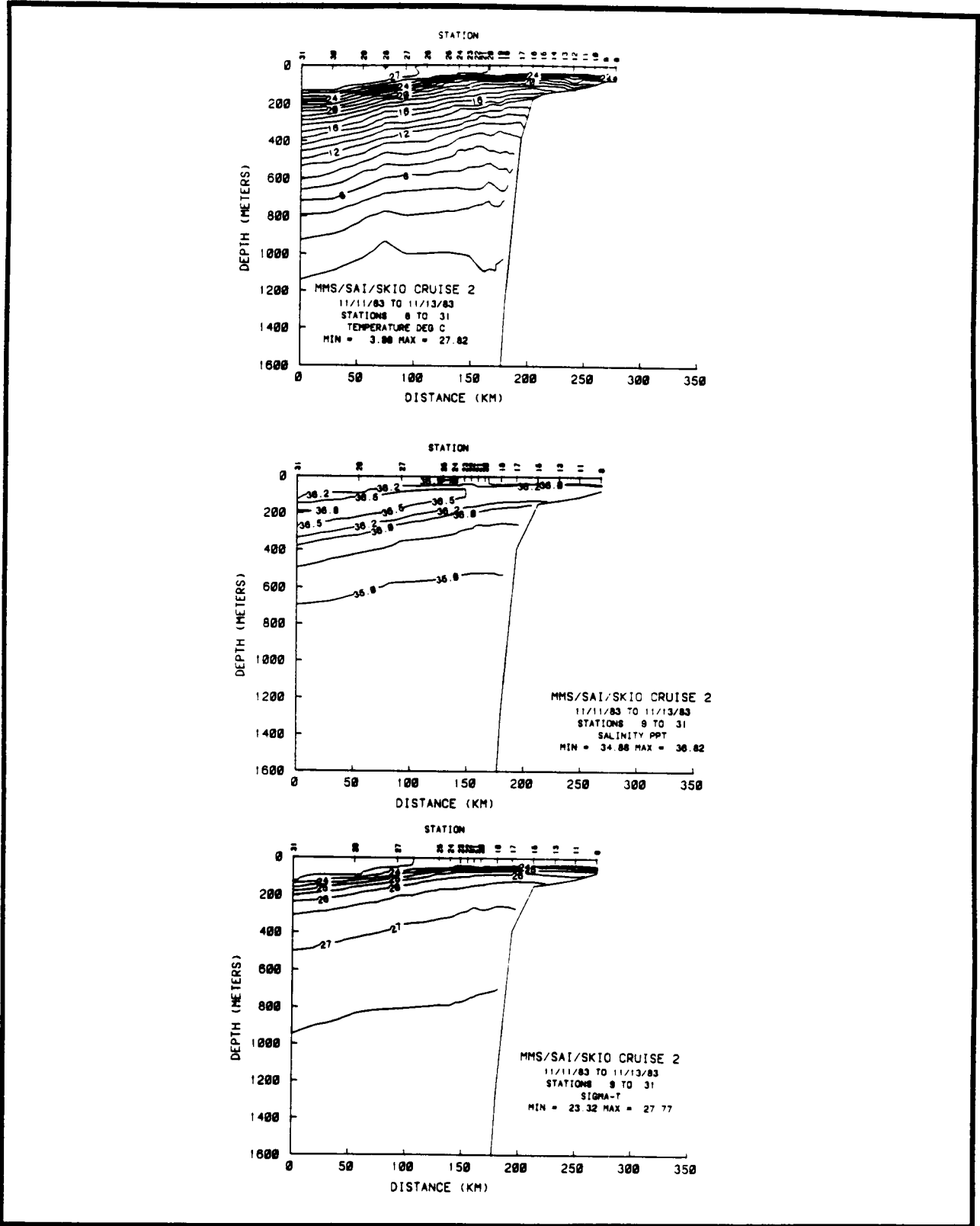


Figure 4.4-8. Vertical plots of temperature, salinity and sigma-t for Stations 8 through 31 for the November 1983 eastern Gulf of Mexico hydrography cruise.

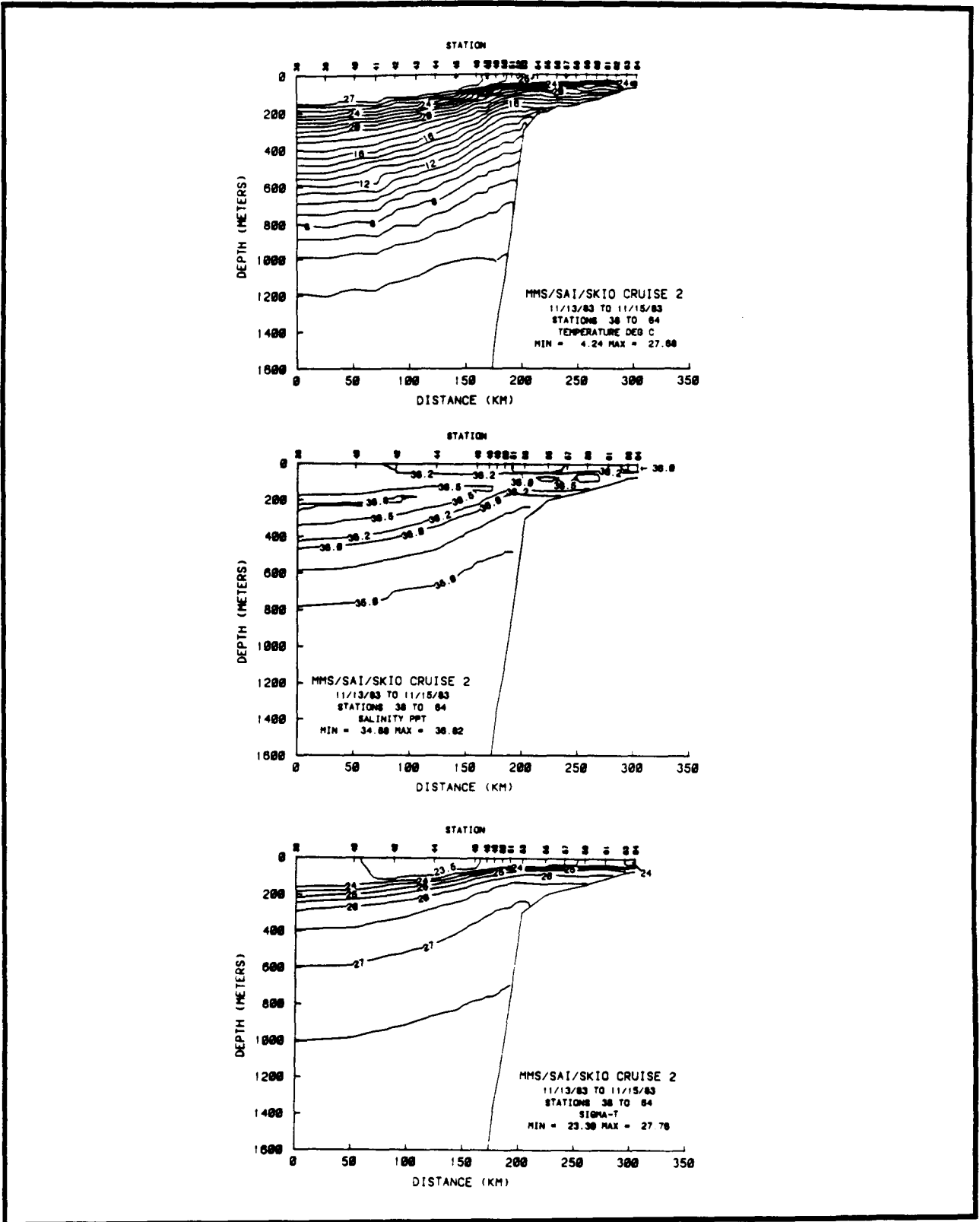


Figure 4.4-9. Vertical plots of temperature, salinity and sigma-t for Stations 38 through 64 for the November 1983 eastern Gulf of Mexico hydrography cruise.

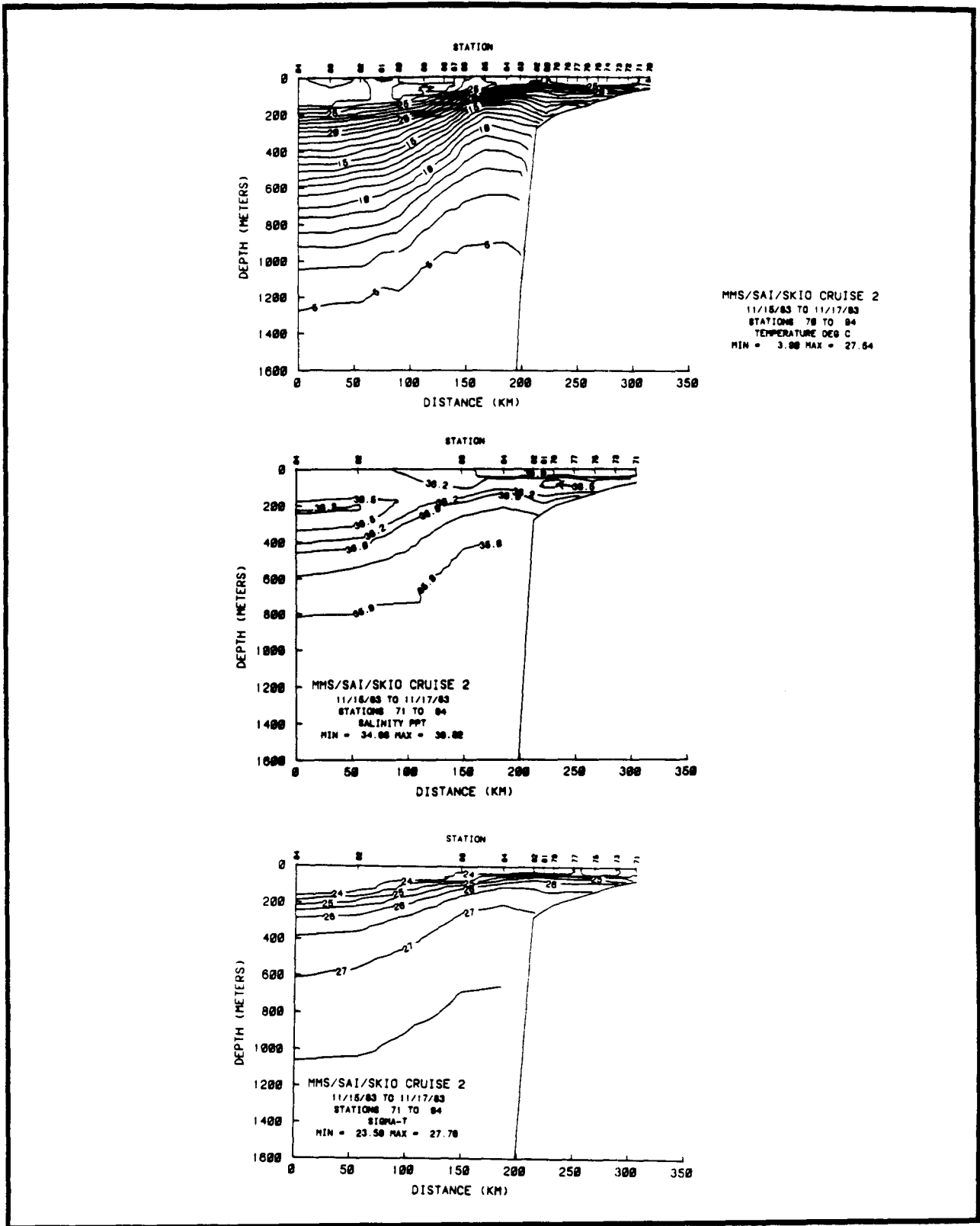


Figure 4.4-10. Vertical plots of temperature, salinity and sigma-t for Stations 70 through 94 for the November 1983 eastern Gulf of Mexico hydrography cruise.

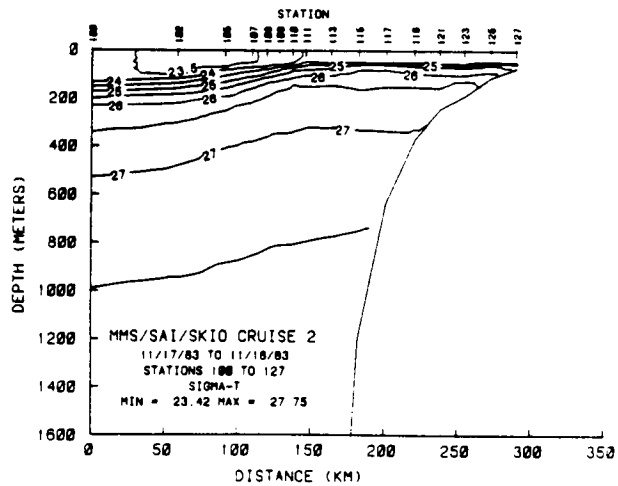
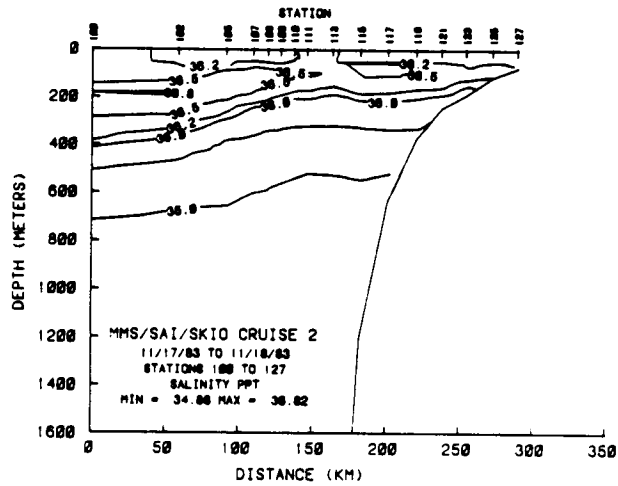
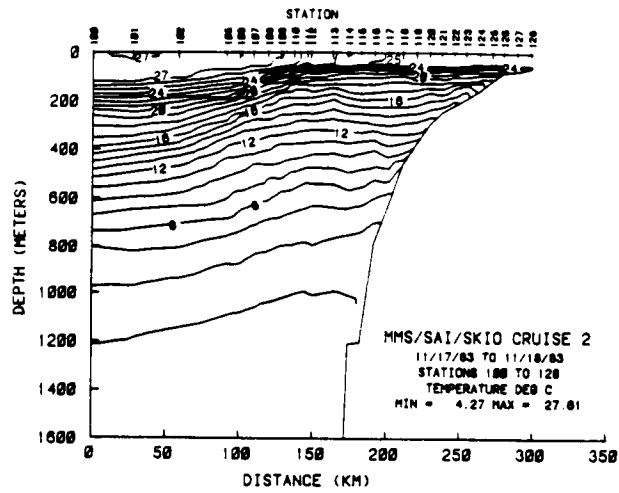


Figure 4.4-11. Vertical plots of temperature, salinity and sigma-t for Stations 100 through 128 for the November 1983 eastern Gulf of Mexico hydrography cruise.

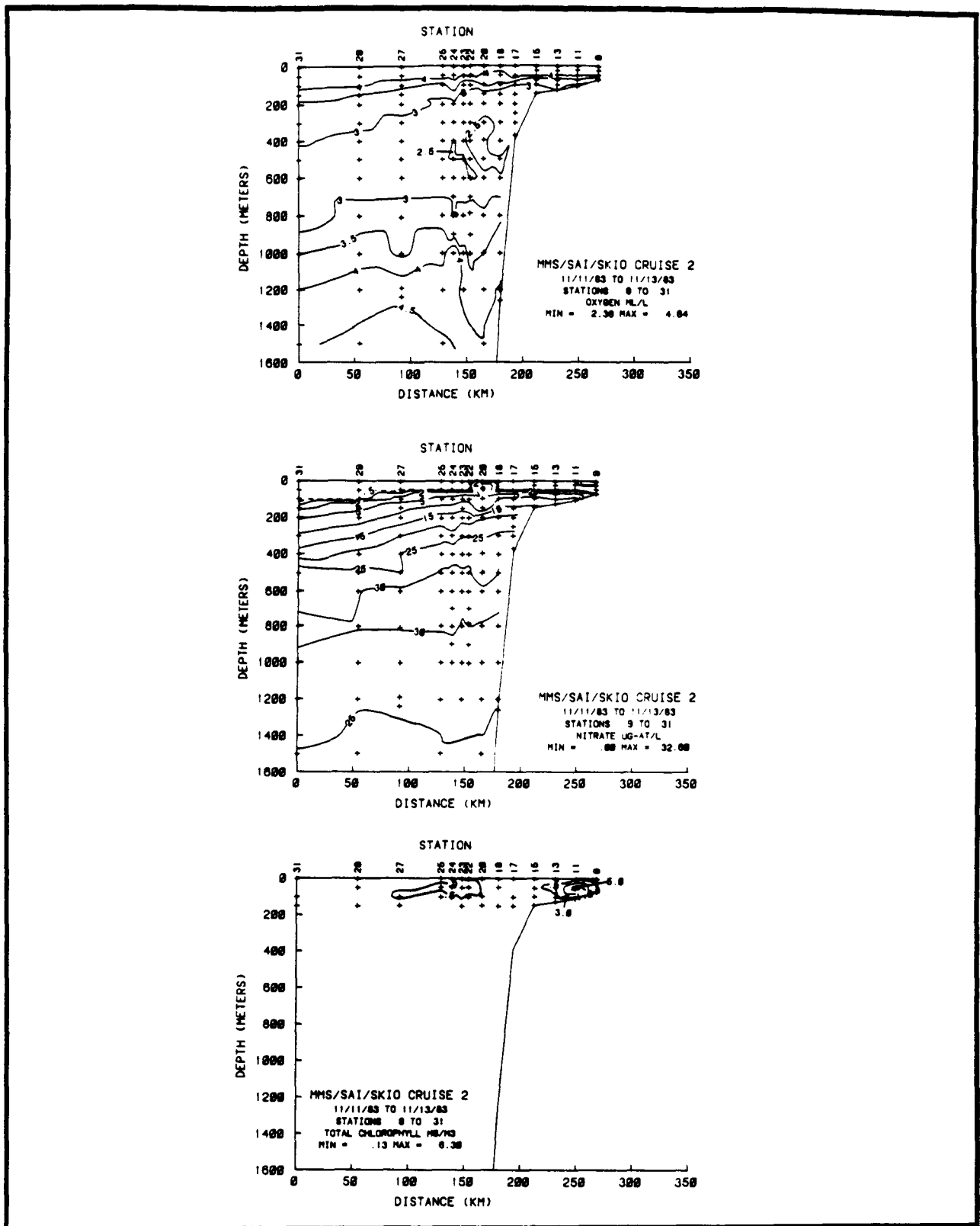


Figure 4.4-12. Vertical plots of oxygen, nitrate and chlorophyll for Stations 9 through 31 for the November 1983 eastern Gulf of Mexico hydrography cruise.

with the time-varying flow of the Gulf Stream; however, it can not be assumed that Gulf inflow and outflow are balanced at a given time since the Gulf basin can act as a buffer to support considerable time-dependent volume storage.

Generally, the LC inflow is composed of several water masses which are partitioned as a function of depth (Morrison and Merrell, 1984); however, the LC water is generally warmer than ambient Gulf water at the corresponding depth. Below the seasonal mixed layer, the constancy of the temperature, salinity, depth triplet in both the LC and Gulf basin water masses allows definition of the subsurface lateral extent by examination of the depth at which selected isotherms occur. One of several general definitions of the lateral LC (and Gulf Stream) extent is when the 15°C isotherm goes below 200-m depth with the LC being on the warmer side. Although other similar definitions may be used, they generally provide comparable boundary locations. As will be seen in the following discussion, this definition of LC extent was slightly less than the sea-surface expression; however, it does coincide with the location of maximum isotherm and isopleth slope which is consistent with the location of the general zone of maximum horizontal currents.

4.4.3.1.2 Horizontal Configuration

The expected LC lateral boundaries are indicated in Figure 4.4-13 as estimated from imagery of sea-surface temperature patterns on 7 May 1984. The boundaries determined by the 15°C temperature at 200-m depth are shown in Figure 4.4-14. Relatively little difference exists in gross configuration; however, subsurface data indicate possible cold pools (e.g. confined areas of 12°C or cooler water) along the eastern boundary which may be associated with periodic frontal perturbations. In addition, the substantial cold pool located southwest of the Dry Tortugas seemed to decrease in size between the 7 May SST imagery and 12 May when that area was studied using aerial deployed probes.

The general configuration of the LC during this study is fairly "typical" in that such a lobate shape extending up to 27°N is observed regularly. Satellite imagery indicated that the LC had not changed substantially for a month prior to the study period.

Figure 4.4-15 provides an example of the flow pattern resulting from a drifter trajectory when the LC had a configuration similar to that during May 1984. Of particular relevance is the cold pool southwest of the Dry Tortugas and the Lagrangian pattern within the fairly high speed currents close to the eastern LC boundary. Coincident satellite imagery confirmed that this buoy moved approximately parallel to eastern Loop Current frontal boundary (Hawkins, personal communication). The buoy path is strong evidence for the presence of the flow rotation as it moves cyclonically around the cold pool while remaining parallel to the front.

4.4.3.1.3 Vertical Configuration

The discussion below focuses on temperature and velocity field along two sections (1A and 2A in Figure 4.4-13) which have particular relevance since they coincide with the following:

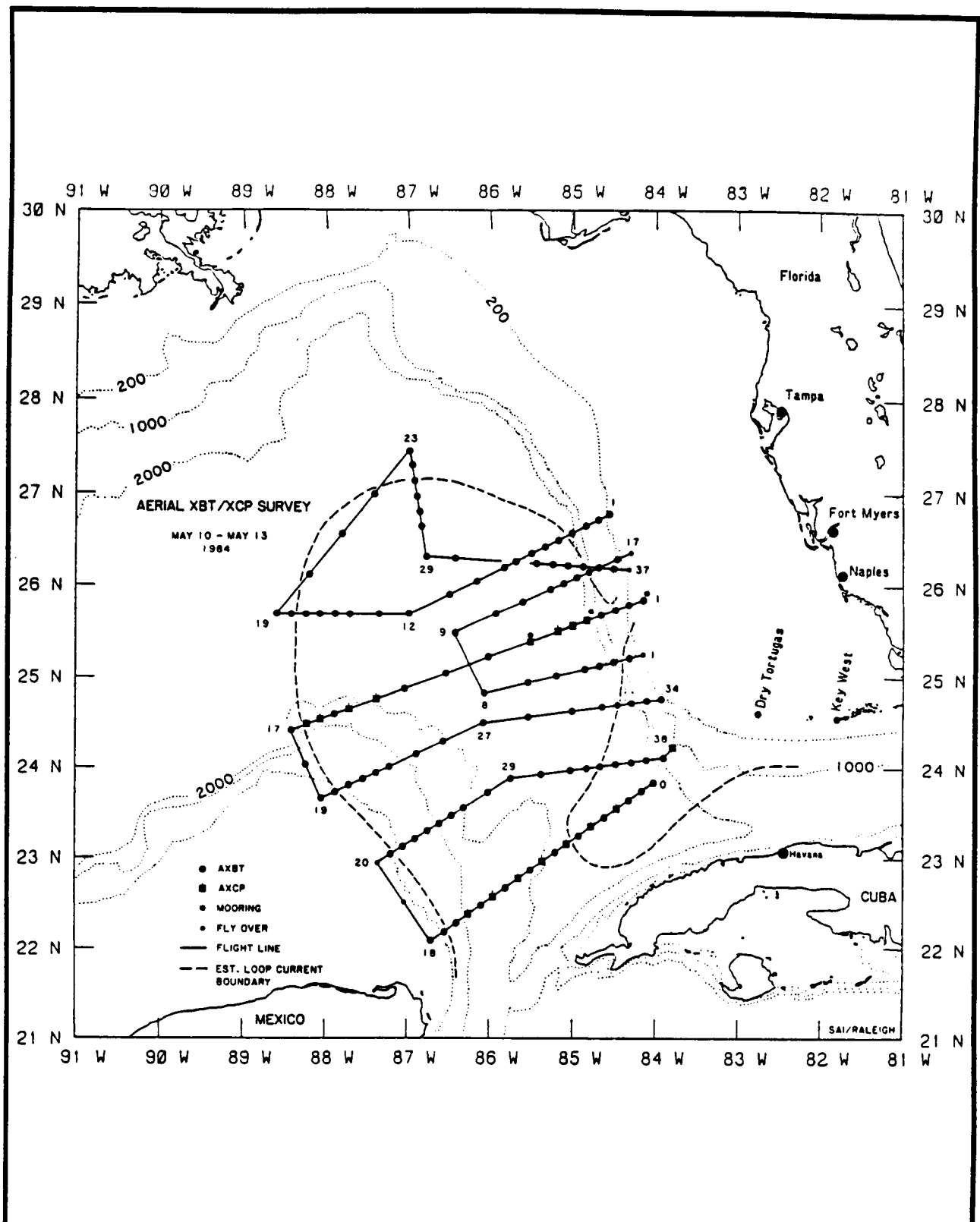


Figure 4.4-13. Sampling scheme for aerial XBT/XCP survey. Section 1A is the southernmost transect and Section 2A is straight transect across the center of the LC which parallels the subsurface mooring line.

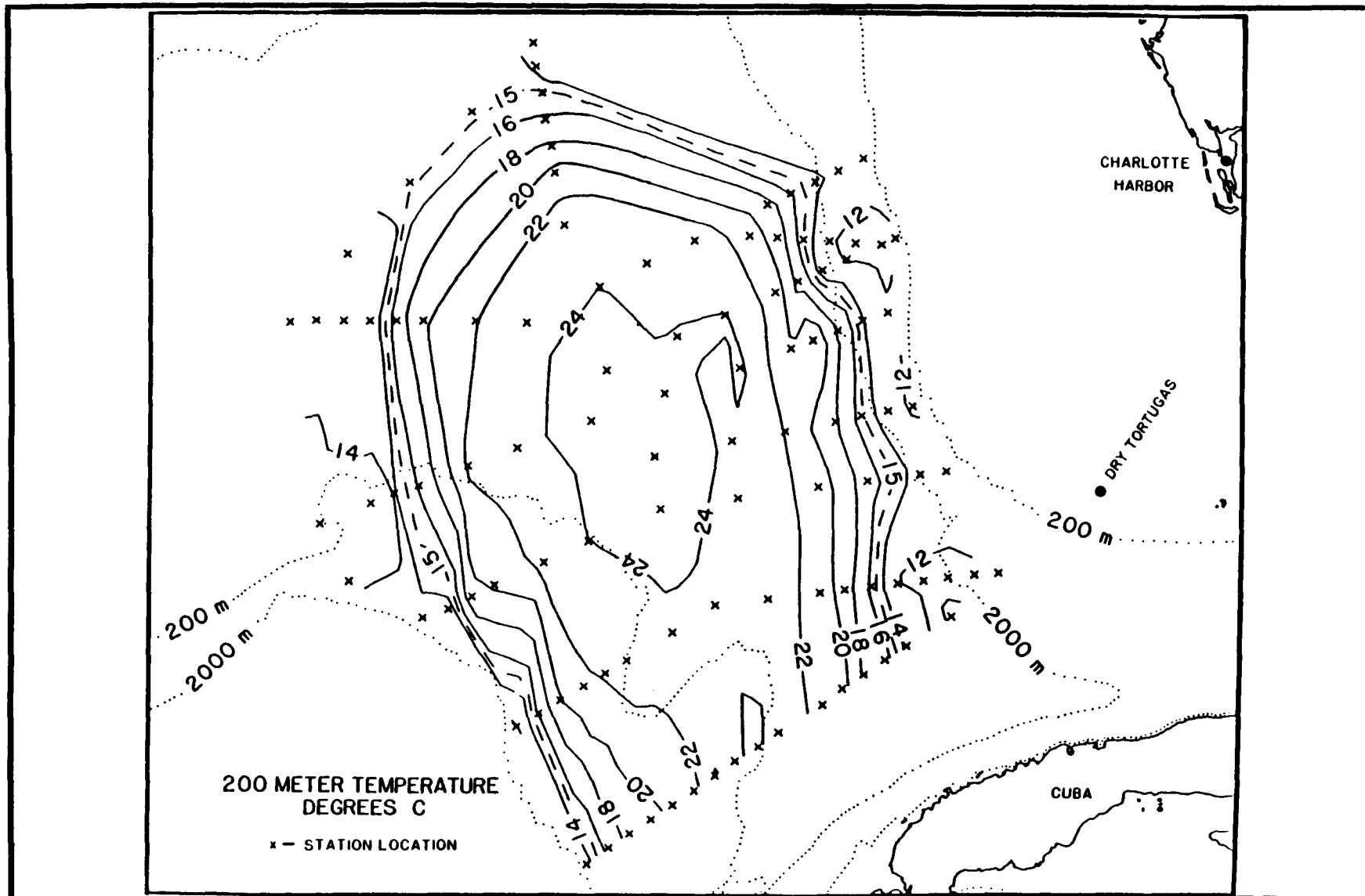


Figure 4.4-14. Horizontal contours of temperatures at 200 m below the surface. The 15°C isotherm is a dashed line. Note the the isolated cold pools along the eastern boundary.

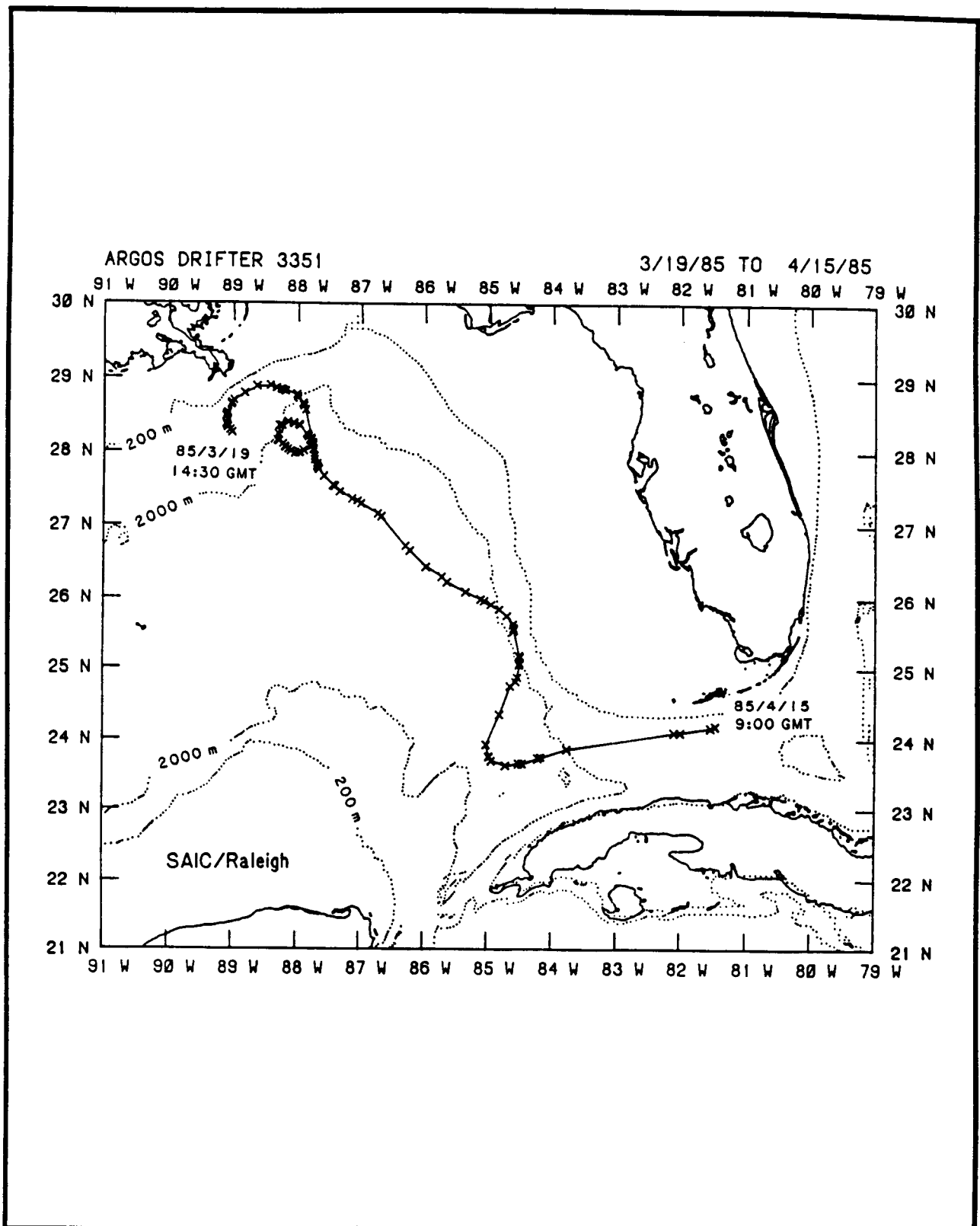


Figure 4.4-15. Trajectory of a drifting buoy around a major cold pool located SW of the southwest Florida shelf. The buoy moved approximately parallel and in fairly close proximity to the LC front.

- Section 1A - goes through a major cold pool and through the "neck" of the LC and hence documents reasonably the inflow and outflow conditions.
- Section 2A - coincides in the east with the subsurface mooring transect and a hydrographic time series taken by the coordinated and concurrent ship-based observations. In the west, Section 2A provides a representation of laterally unbounded LC conditions.

Temperature data does not indicate a substantial difference in conditions between subsurface temperature fields on these transects and the other boundary-normal transects taken.

AXCP profiles provide information regarding relative current magnitude as a function of depth. In many instances the indicated velocity is a reasonable estimate of actual velocity. However, accepting the indicated speeds as absolute could be inappropriate. As with geostrophic currents, it is necessary to know current speed at a known depth to "calibrate" the profile. For geostrophic profiles, a single measured current speed can result from processes other than geostrophy, so velocities at more than one depth should be used to evaluate the assumption that the current field is geostrophic.

The AXCP profiles help define the vertical location of strong shear (relative velocity magnitudes) as well as provide estimates of the absolute velocity magnitude. AXCP measurements suggest a current reversal at depth, i.e. below 500-600 m (Figure 4.4-16). Because of ambiguity as to the exact current speeds, this reversal may be suspect. It is relevant to note that current meters on the indicated mooring along Section 2A showed that in the lower half of the water column northward directed currents dominated with increasing depth until near-bottom when approximately 80% of currents were directed northward. In contrast, in the upper half of the water column, southward directed flow became increasingly dominant with decreasing water depth. An example of this pattern is shown in the 40 HLP stick plots in Figure 4.4-17.

Section 2A

Along Section 2A in Figure 4.4-16 the flow in the high velocity core, i.e. at Station 5, speed is reduced by 65% in the upper 200 m with maximum velocity at or near the surface. In this figure, the apparent distribution of horizontal shear is distorted by the linear interpolation contouring scheme. Surface currents at Station 5 are approximately 50% larger than at Station 7, which is 20 nautical miles further into the Loop Current. A similar current reduction occurs at the surface between Stations 7 and 8. The horizontal surface velocity reduction to the east, i.e. onshore of Station 5, is believed to be much more abrupt with speed changes of several knots over a distance of several kilometers. Such a gradient is also apparent between Stations 13 and 15₁ on the western LC boundary where speeds decrease from over 3 knots ($\sim 150 \text{ cm s}^{-1}$) to less than half a knot in 20 nautical miles. The plotted distribution of surface currents reflects the linear interpolation scheme so there is no way of knowing the detailed along-front speed gradient. Surface currents between Stations 12 and 13 show a change similar to the comparable stations on the eastern side of the Loop Current.

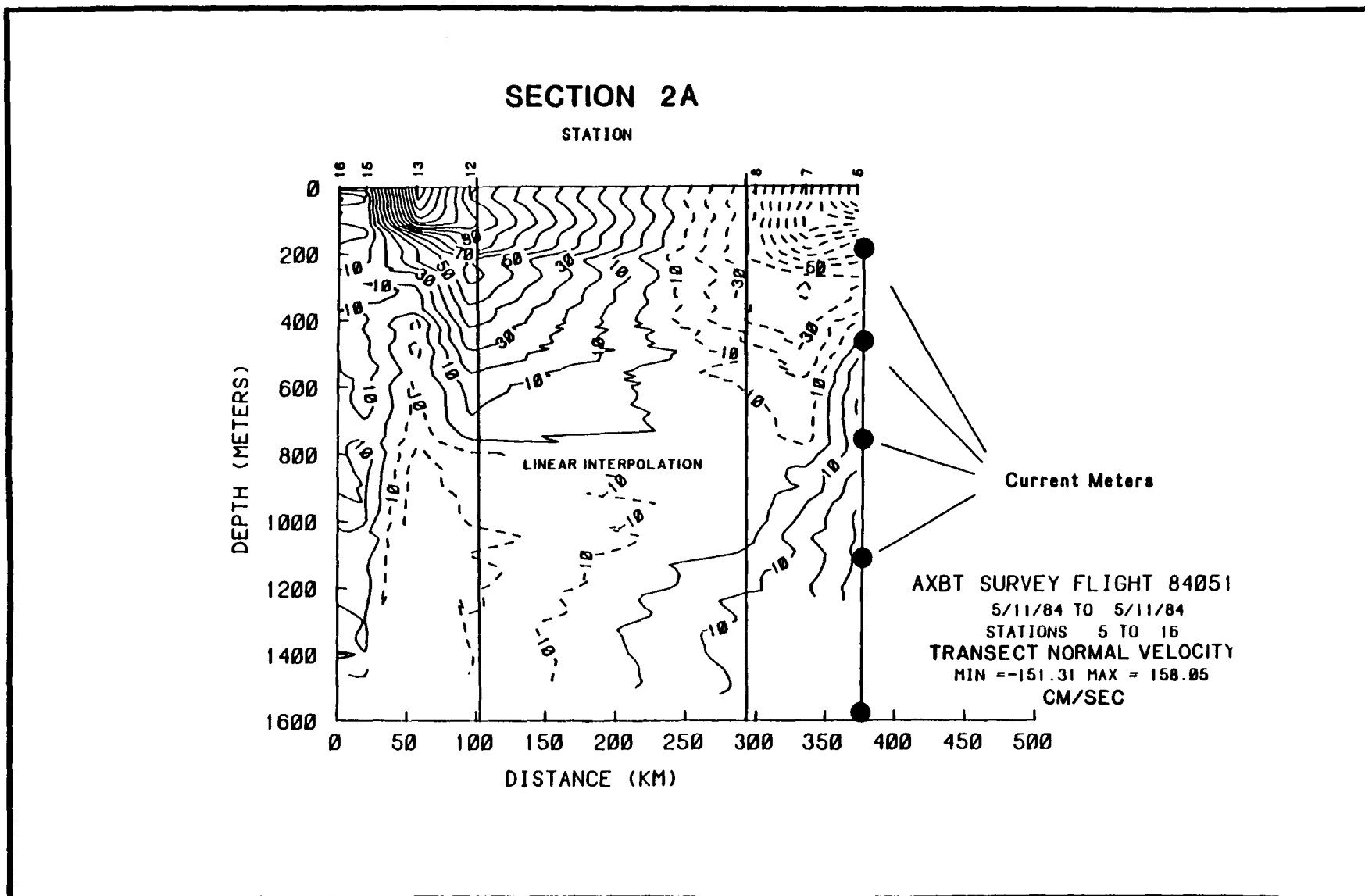


Figure 4.4-16. Contours of transect normal velocity component at indicated stations on Section 2A - see Figure 4.4-13. Mooring A (Figure 4.4-17) is on the onshore end of this section.

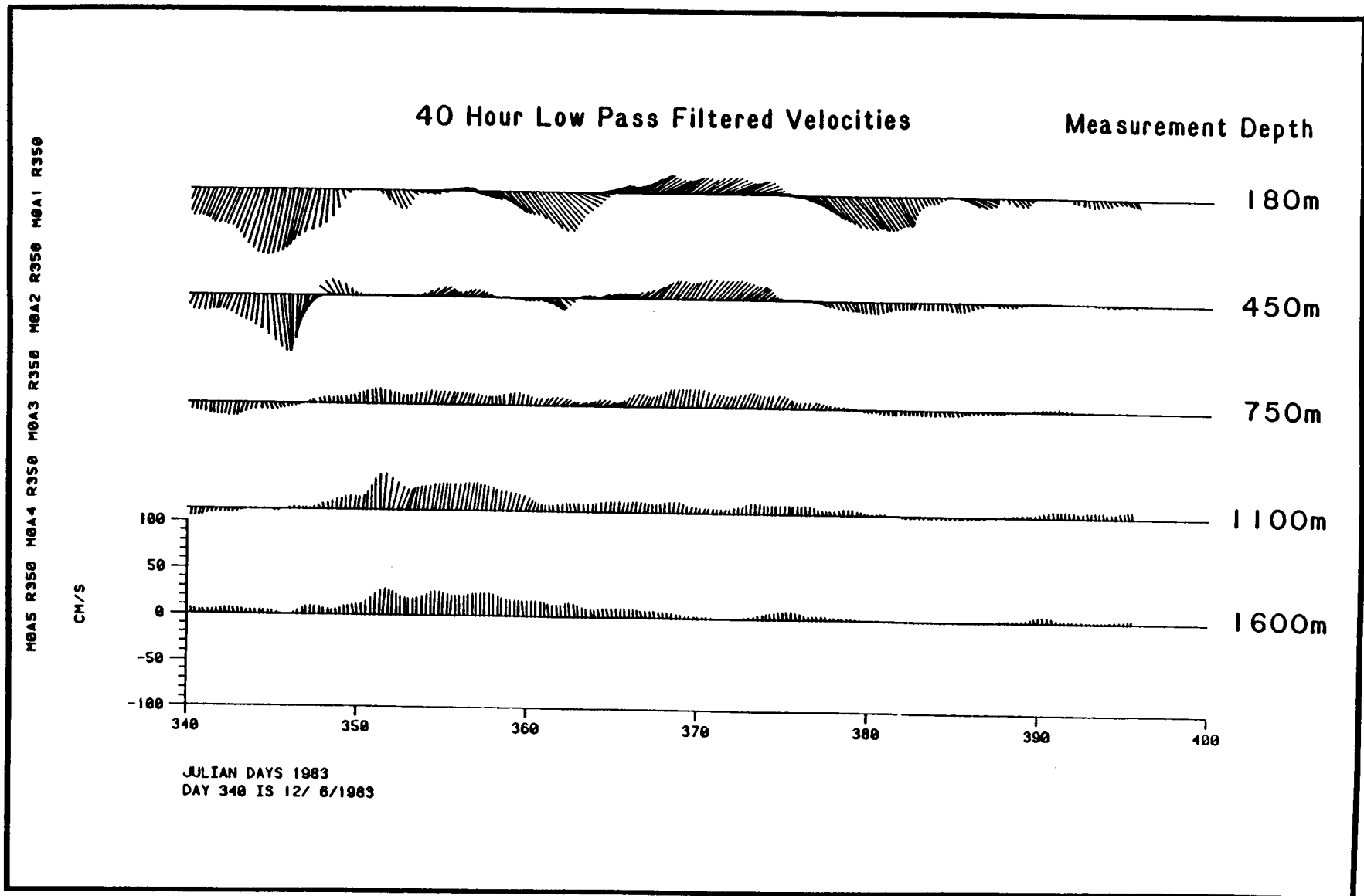


Figure 4.4-17. Representative 40 HLP filtered velocities at mooring indicated in Figure 4.4-16. Vectors pointing up are parallel to the isobaths and approximately to the north. Even though southward directed flows are more prevalent above about 500, northward flows are more prevalent at greater depth.

Section 1A

High velocity inflow and outflow are confined to the upper 200 m of the water column. On the west end of the transect (Station 15) the maximum current occurred at the surface; however, it is quite likely that further westward, velocities were even greater. As shown in Figure 4.4-18, Station 15 was on the slope offshore of the eastern margin of the Campeche escarpment. Examination of Figure 4.4-19 (Section 1A-temp) shows that Station 15 was at the margin of the region of strongest horizontal temperature gradients. Because the maximum currents tend to coincide with this region of greatest spatial change, maximum horizontal currents probably occurred westward of and in shallower water than at Station 15. Some of the strongest spatial gradients observed were near the western end of Section 1A which suggests a correspondingly locally intense current right up against the slope. Note that at the shelf break vertical temperature differences were 10°C with an 8°C change occurring over a few tens of meters (approximately 30-40 meters below the surface).

Along the eastern end of Section 1A, strong horizontal temperature gradients occurred over 20 nautical miles between Stations 3 and 5. Between these two stations very weak horizontal velocity gradients occurred in what was probably the core of the high speed outflow along this section. At the interior LC stations currents were relatively weak with a pattern which could support clockwise (anticyclonic) motion.

4.4.3.2 Ship-Based Hydrography

A cold perturbation (described in Section 4.3.4) was mapped by ship during the 5-18 May period. The cold perturbation appeared off the Dry Tortugas on 20 April. Hydrographic surveys of that area on 5-6 May and again on 17-18 May show the presence of a large dome-like structure either caused by or resulting from the Loop Current being unusually far from the west Florida shelf.

The first two sections across the cold perturbation (5-6 May) were designed to be along and across the axis of the temperature structure (Figure 4.4-20). The first section (Figure 4.4-21), which runs between stations 1 and 12, was all XBT's. All isotherms ascended towards the Keys except for the deeper isotherms (~5°C), where some downwarping was evident. In this direction the cold perturbation featured rather gently sloping isotherms, but when viewed on the 0-200-m scale the situation was more complicated, with features on the scale of 60 km present. At several stations (2,3,4) thermal inversions were observed. The sea-surface temperature profile (Figure 4.4-21) indicated that the cold perturbation was indeed colder than the waters in the front. The second section ran northwestward through the cold perturbation (Figure 4.4-22) and again shows the dome feature. Between LC and adjacent water, isotherms were uplifted over 400 m, which is typical for the Loop Current or Gulf Stream. When viewed on the 0-200 m scale the strength of the feature is appreciated. Note that this cross section shows less structure on the 60-km scale than does the axial section. The profile of sea-surface temperatures shows minimum temperatures to be about 25.7°C. A warm core was present in the Loop Current front with temperatures above 27°C. The sections suggest that the radius of curvature is at least 150 km.

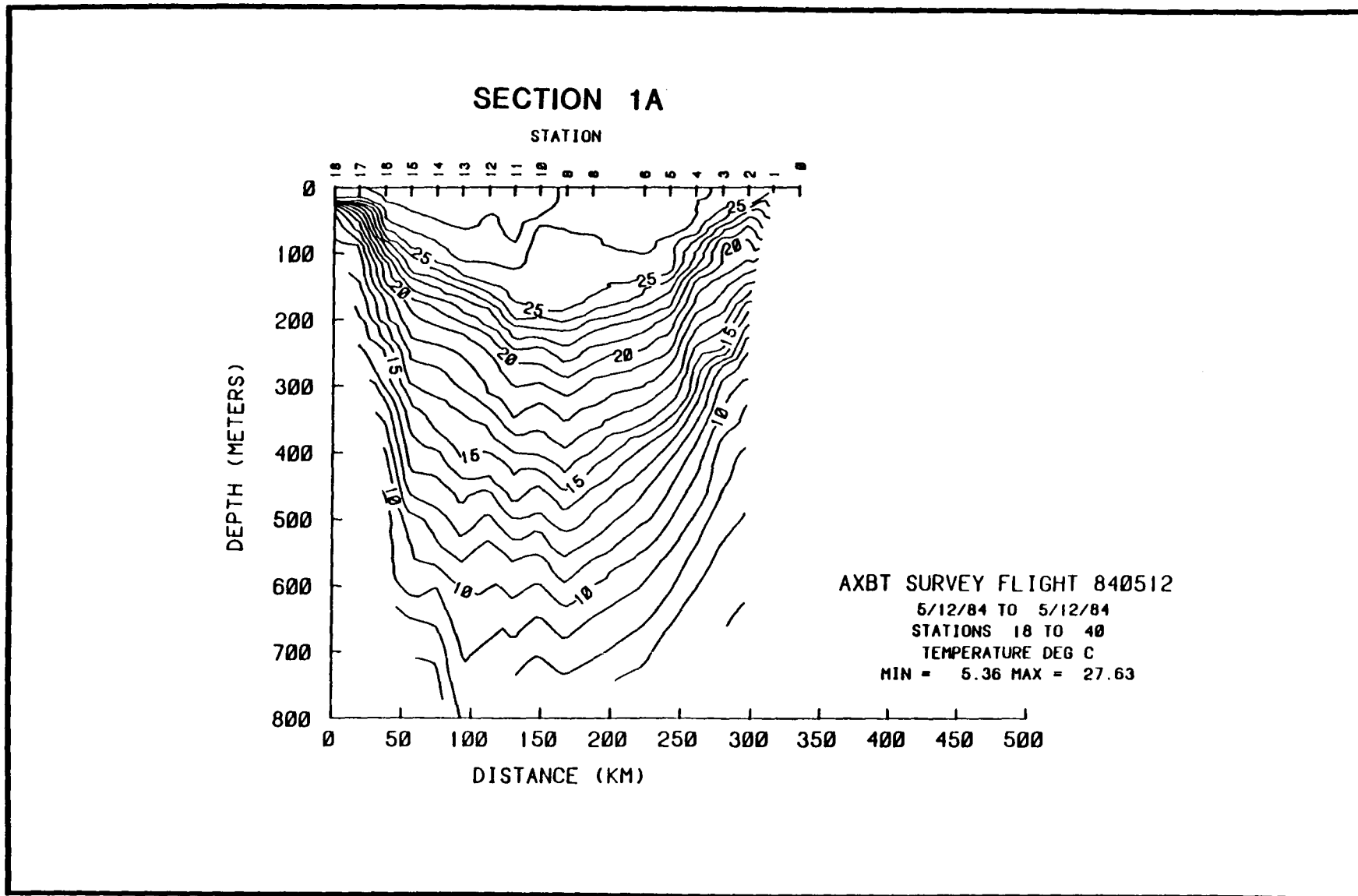


Figure 4.4-19. Temperature along Section 1A.

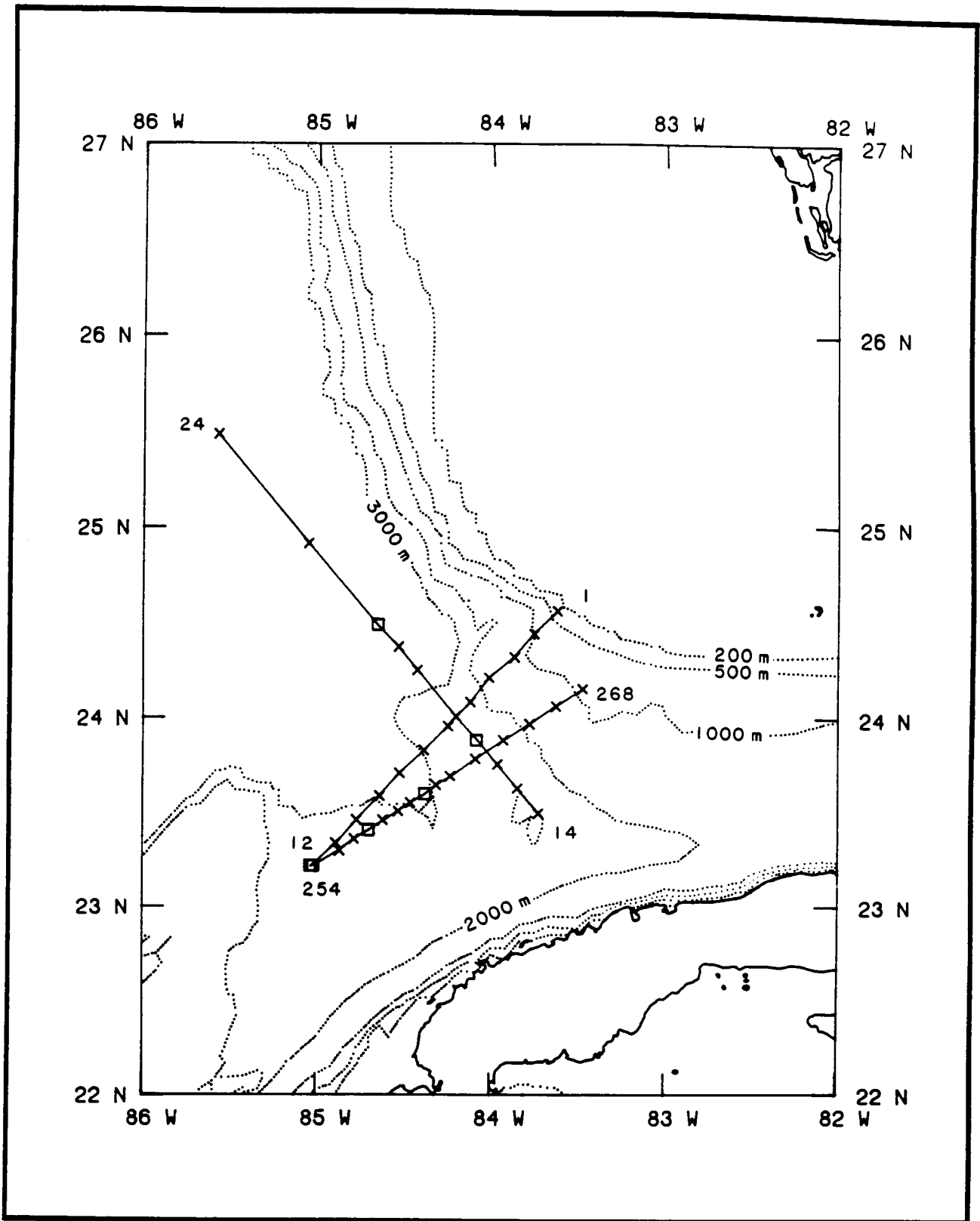


Figure 4.4-20. Three sections through the cold perturbation for period from 5-18 May 1984.

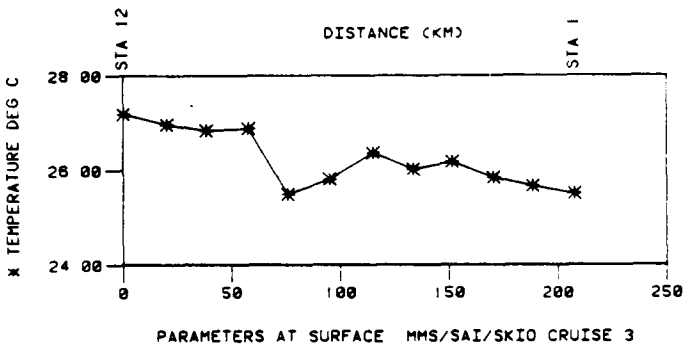
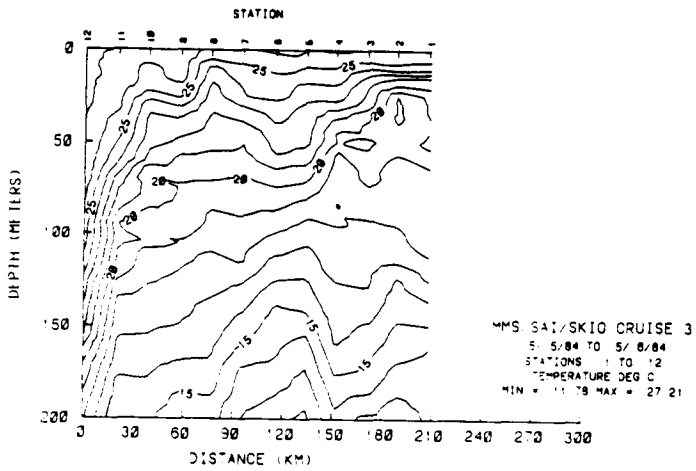
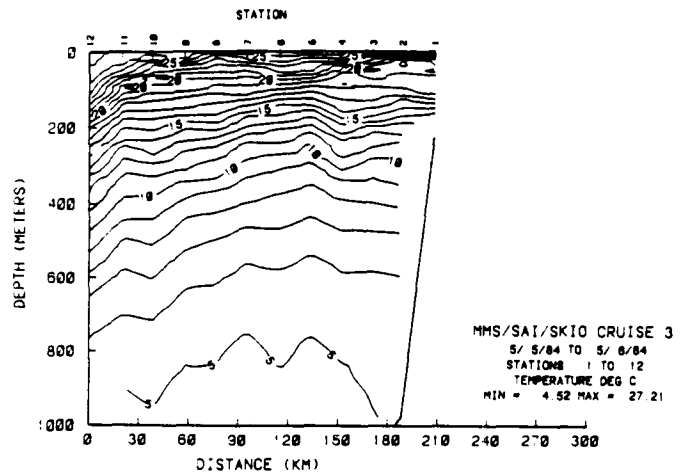


Figure 4.4-21. Temperature section down the axis of the cold perturbation at both 1000-m and 200-m scales with sea-surface temperature profile (Stations 1-12).

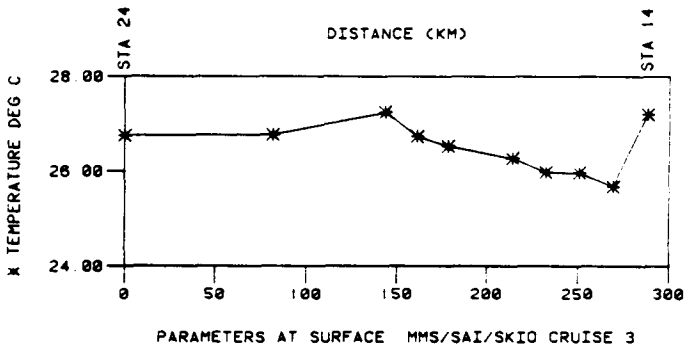
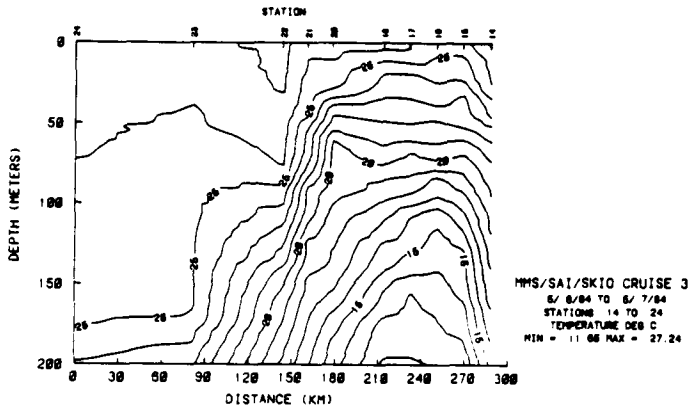
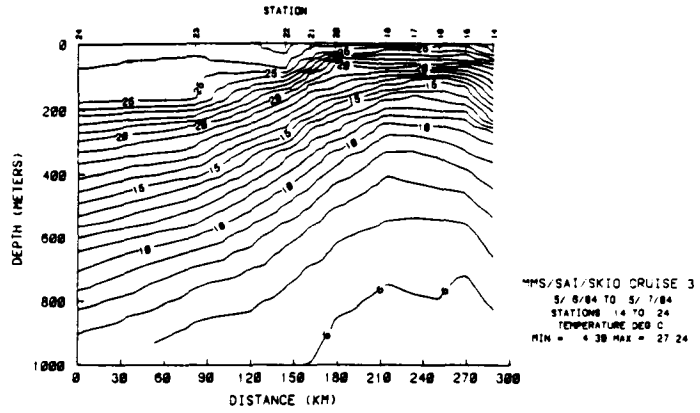


Figure 4.4-22. Temperature section across the cold perturbation of both 1000-m and 200-m scales with sea-surface temperature profile (Stations 14-24).

The cold perturbation was sampled a second time on 17-18 May when a section was made from southwest to northeast on a line close to the first axial line but angling more towards the east (Figure 4.4-23). The Loop Current was still well off from the west Florida shelf and the domed isotherms were present. Sea-surface temperatures (Figure 4.4-23) clearly showed the Loop Current front, a band of cold water embedded in the front and relatively cooler water in the front itself.

Horizontal maps of velocity were generated for this feature from the Ametek Straza data. Figure 4.4-24 shows data obtained at 20-m depth in the cold perturbation for the first sampling on 5-6 May. The northeast-southwest portion of the cruise track was intended to be along the axis of the perturbation, while the southeast-northwest portion was to cut across this axis. The ADCP data confirm the cyclonic circulation around the cold dome of the feature and the strong Loop Current flow into the region from the north. Figures 4.4-25 and 4.4-26 are plots of the velocity field from this feature along the same sections at depths of 100 and 200 m and show that while the magnitude of the velocity vectors decreases with depth, the cyclonic circulation pattern exists at least down to 200-m depth. When this feature was sampled again at the end of the cruise on 17-18 May, the plot in Figure 4.4-27 was generated. The southwest-northeast portion of the track is again along the axis of the feature and also shows a cyclonic circulation. However, comparison of Figures 4.4-24 and 4.4-27 shows that during the cruise this eddy appears to have migrated eastward about one degree of longitude. This is consistent with the interpretation of the hydrographic data.

4.4.3.3 Time Series

During the May 1984 R/V CAPE FLORIDA cruise, two sections were occupied three times each over a seven day period. They are listed in Table 4.4-1 and represented geographically by the two sections shown in Figure 4.4-28 between 25° and 26°N.

This series attempted to sample cold perturbation J described in section 4.3 (see Table 4.3-1, Event J). The sea-surface temperature and vertical temperature sections for the two time series sections are shown in Figures 4.4-29 and 4.4-30. They clearly show the dome structure indicative of the presence of a cold-core frontal eddy on the Loop Current front. The cold core is present with temperatures less than 25°C and the warm filament occurs, although less dramatically, with temperatures about 0.5°C higher than the cold core.

Ametek Straza velocity data at 20-m depth are presented in Figures 4.4-31 through 4.4-33 along the more southerly time series (I). During the first sampling along this line there was a relatively sharp cyclonic shear zone at the Loop Current front near the 400-m isobath (Figure 4.4-31), with little evidence of frontal eddy activity and maximum Loop Current velocities approaching 250 cm s⁻¹ near the 800-m isobath. Two and one half days later the high velocity core of the Loop Current was further offshore, the cyclonic shear zone was significantly wider, and northward flow between the 100- and 400-m isobaths indicated the presence of a frontal eddy. During the third sampling two days later still, the Loop Current was even further offshore and the northward flow in the warm filament of the eddy persisted (Figure 4.4-33).

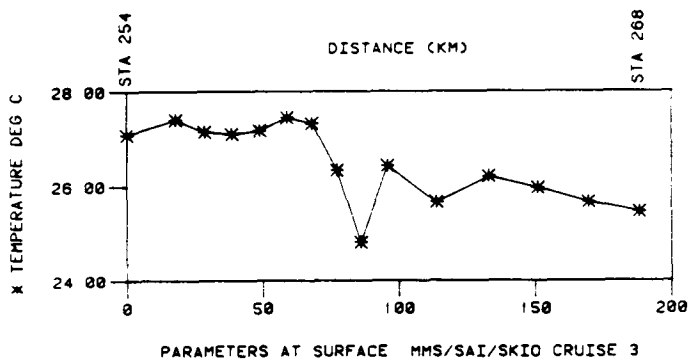
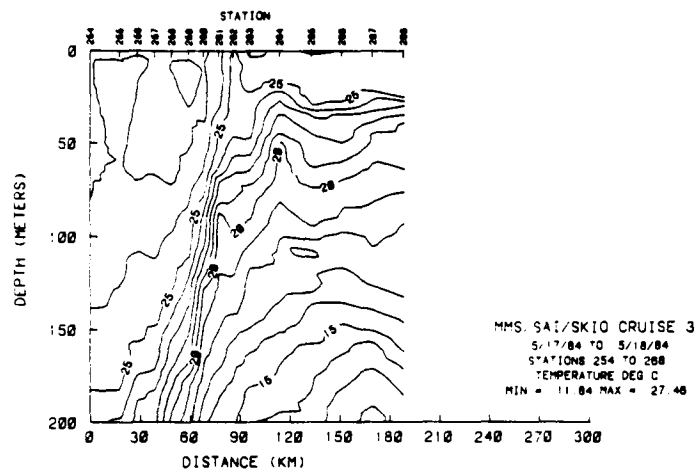
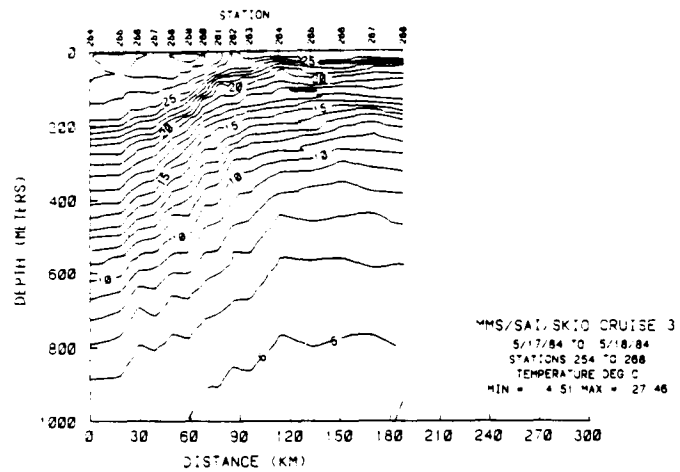


Figure 4.4-23. Temperature section across the cold perturbation at both 1000-m and 200-m scale with sea-surface temperature profile (Stations 254-268).

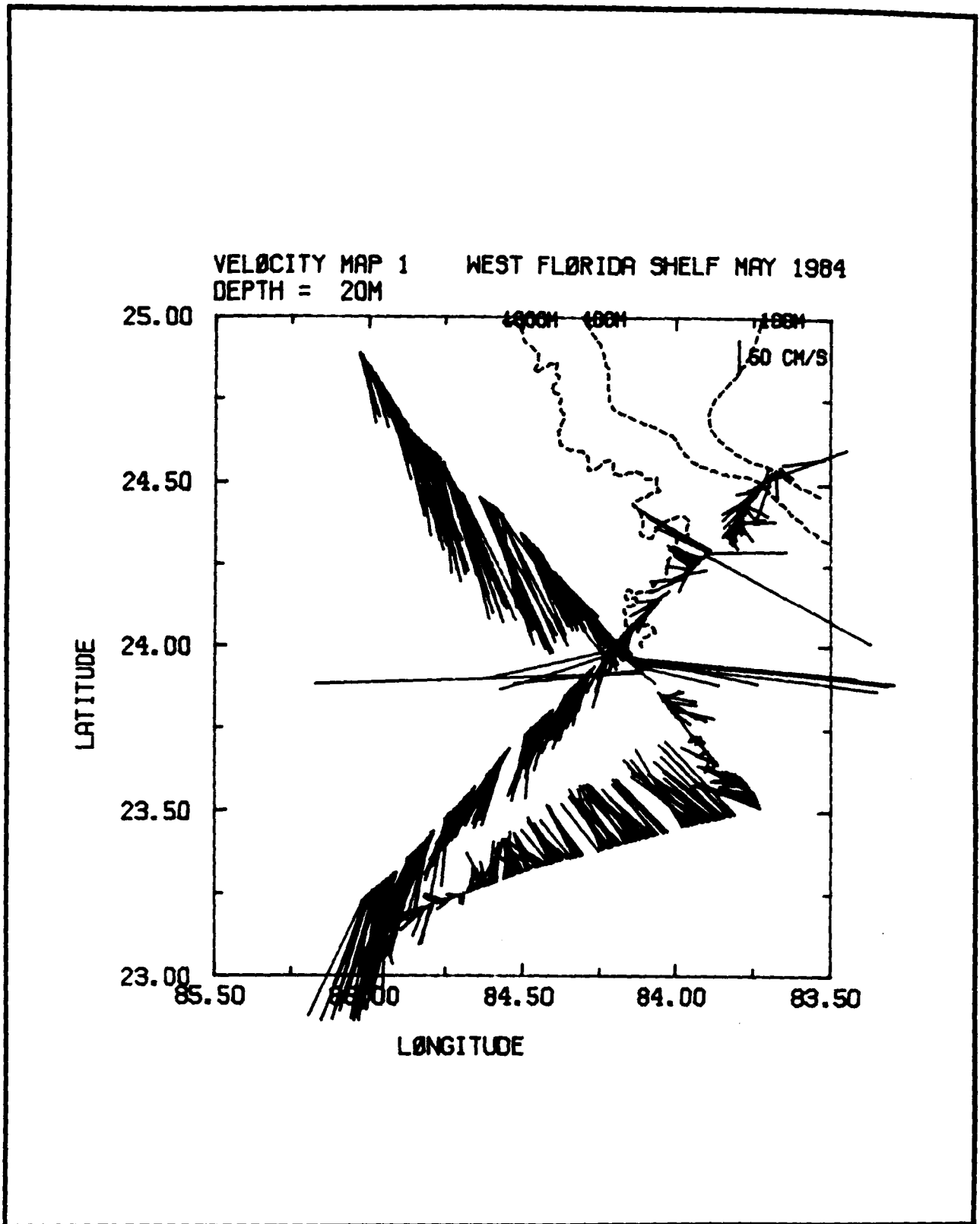


Figure 4.4-24. Stick plots of ADCP velocity at 20-m depth in the cold dome feature southwest of the Dry Tortugas, 6 May 1984. The spurious large magnitude vectors near 24 degrees north are due to imperfections in the process of removing ship motion using LORAN data.

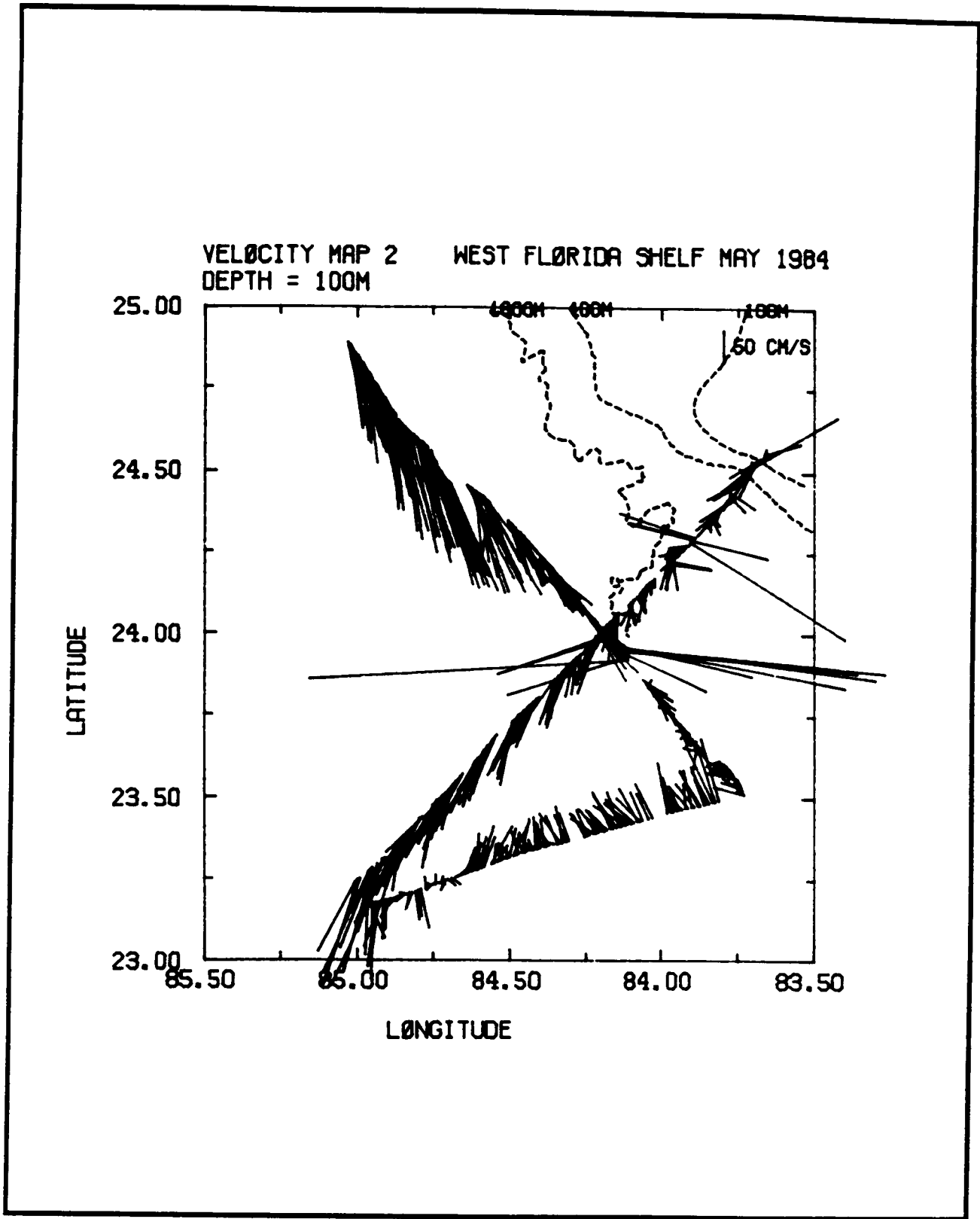


Figure 4.4-25. Stick plots of ADCP velocity at 100-m depth in the cold dome feature southwest of the Dry Tortugas, 6 May 1984. The spurious large magnitude vectors near 24 degrees north are due to imperfections in the process of removing ship motion using LORAN data.

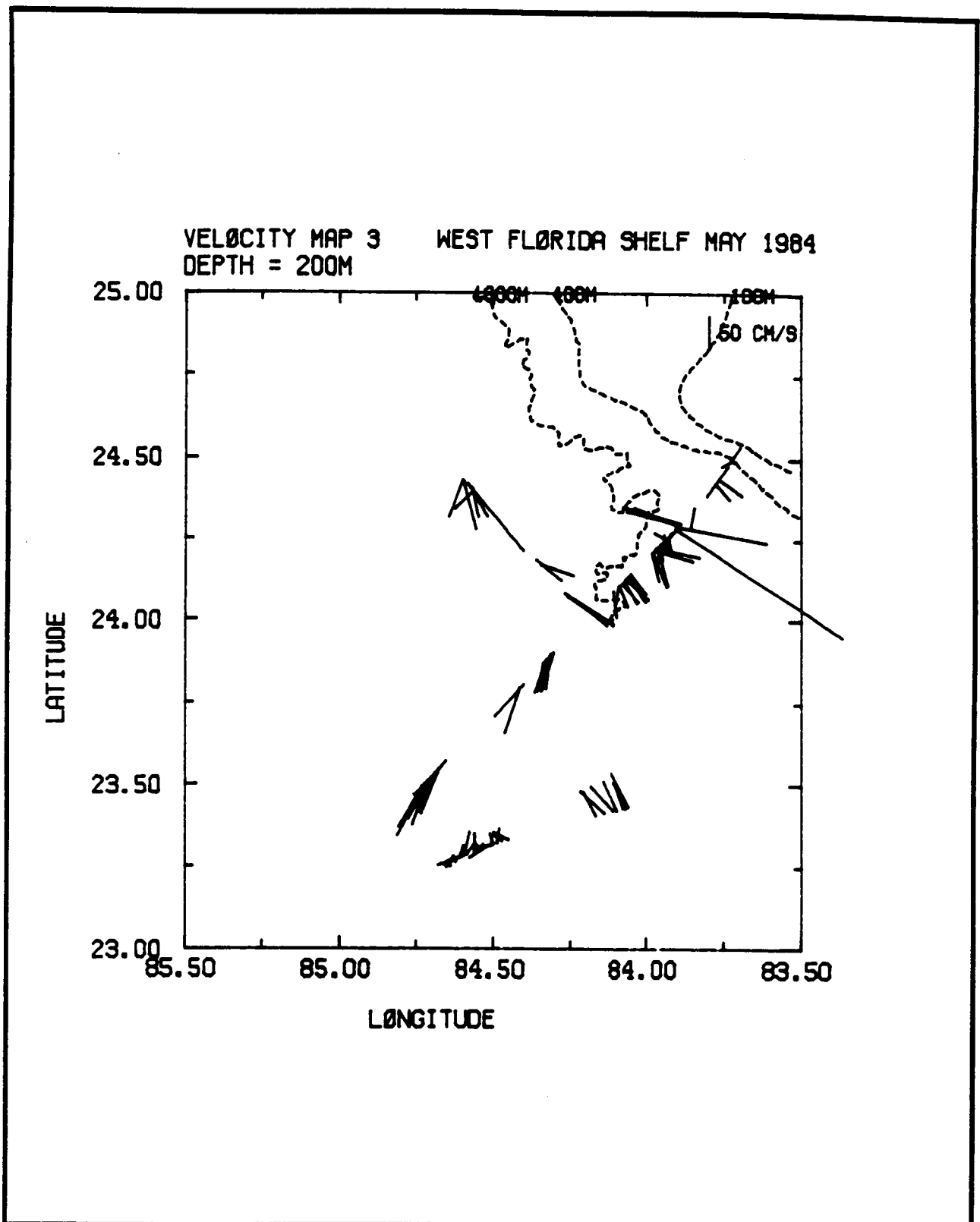


Figure 4.4-26. Stick plots of ADCP velocity at 200-m depth in the cold dome feature southwest of the Dry Tortugas, 6 May 1984. The spurious large magnitude vectors near 24 degrees north are due to imperfections in the process of removing ship motion using LORAN data.

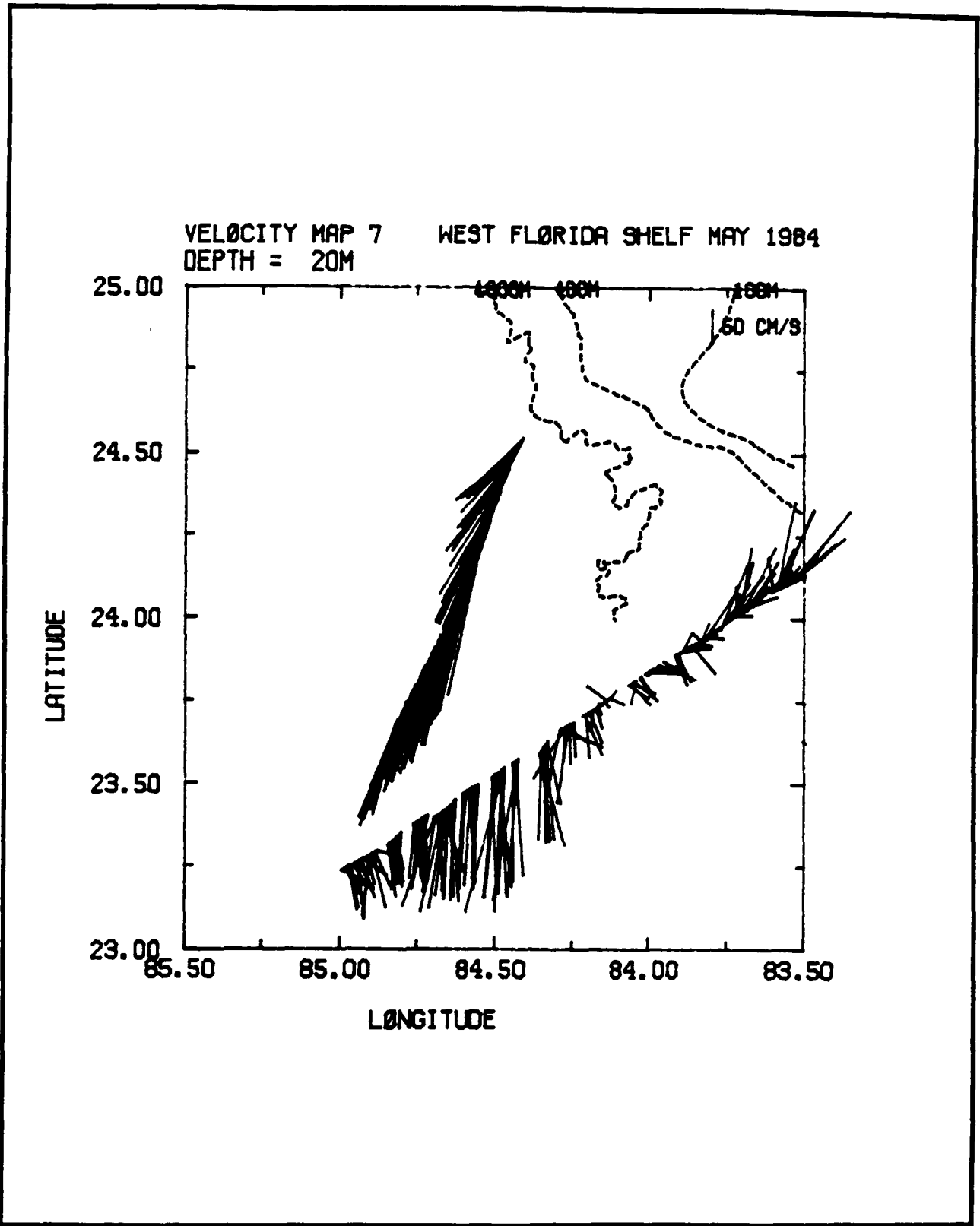


Figure 4.4-27. Stick plots of ADCP velocity at 20-m depth in the cold dome feature southwest of the Dry Tortugas, 17-18 May 1984.

Table 4.4-1. Time Series Sections for R/V CAPE FLORIDA cruise, 4-19 May 1984

SERIES I

Stations 170X-188X
XBT and CTD 13 May

Stations 205C-223C
XBT and CTD 14-15 May

Stations 239X-250X
XBT and CTD 16 May

SERIES II

Stations 130X-146C
XBT 11-12 May

Stations 189C-204C
XBT and CTD 14 May

Stations 224C-238X
XBT 15-16 May

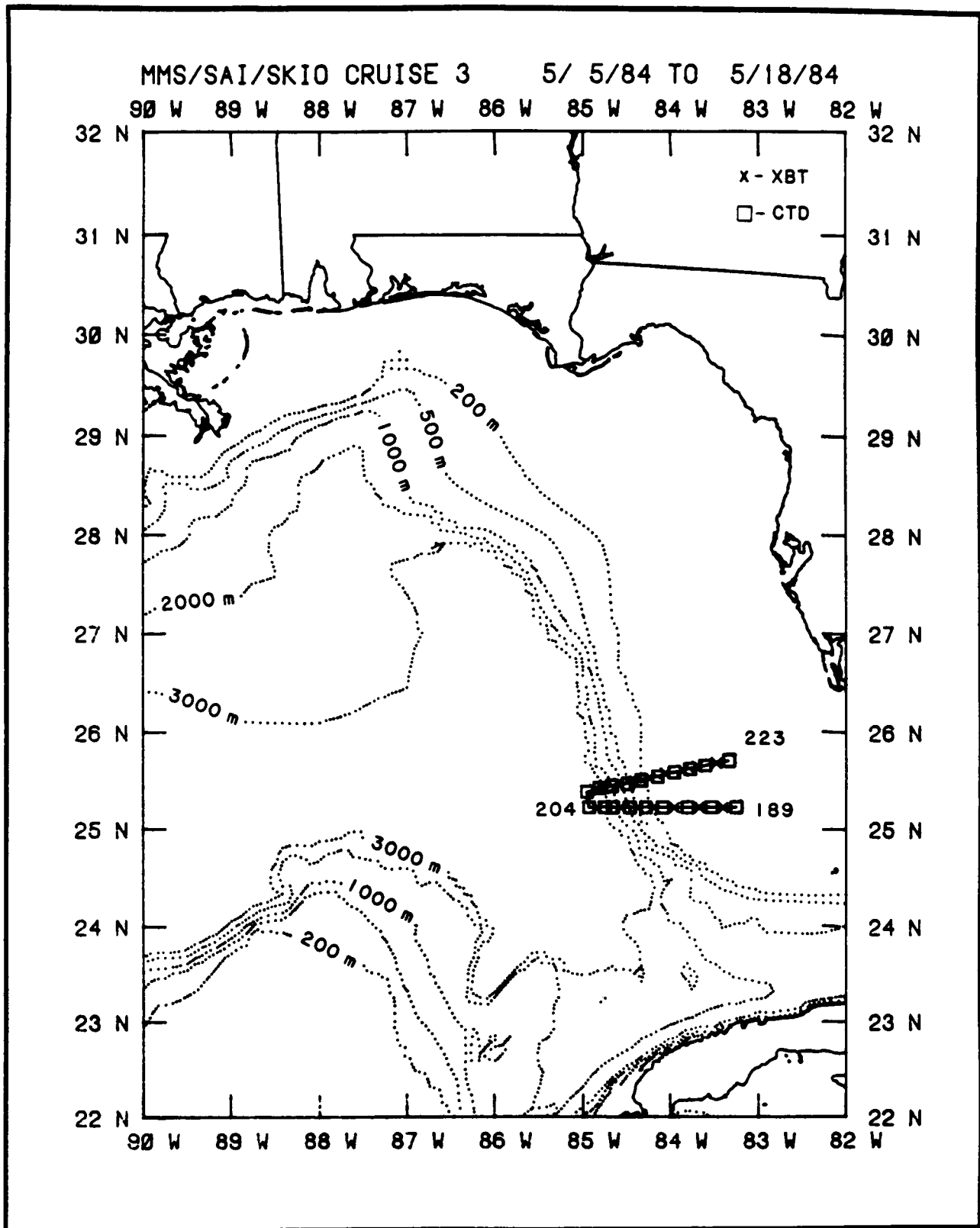


Figure 4.4-28. Cruise track showing XBT and CTD station locations, Stations 189-223, for R/V CAPE FLORIDA cruise from 5-18 May 1984.

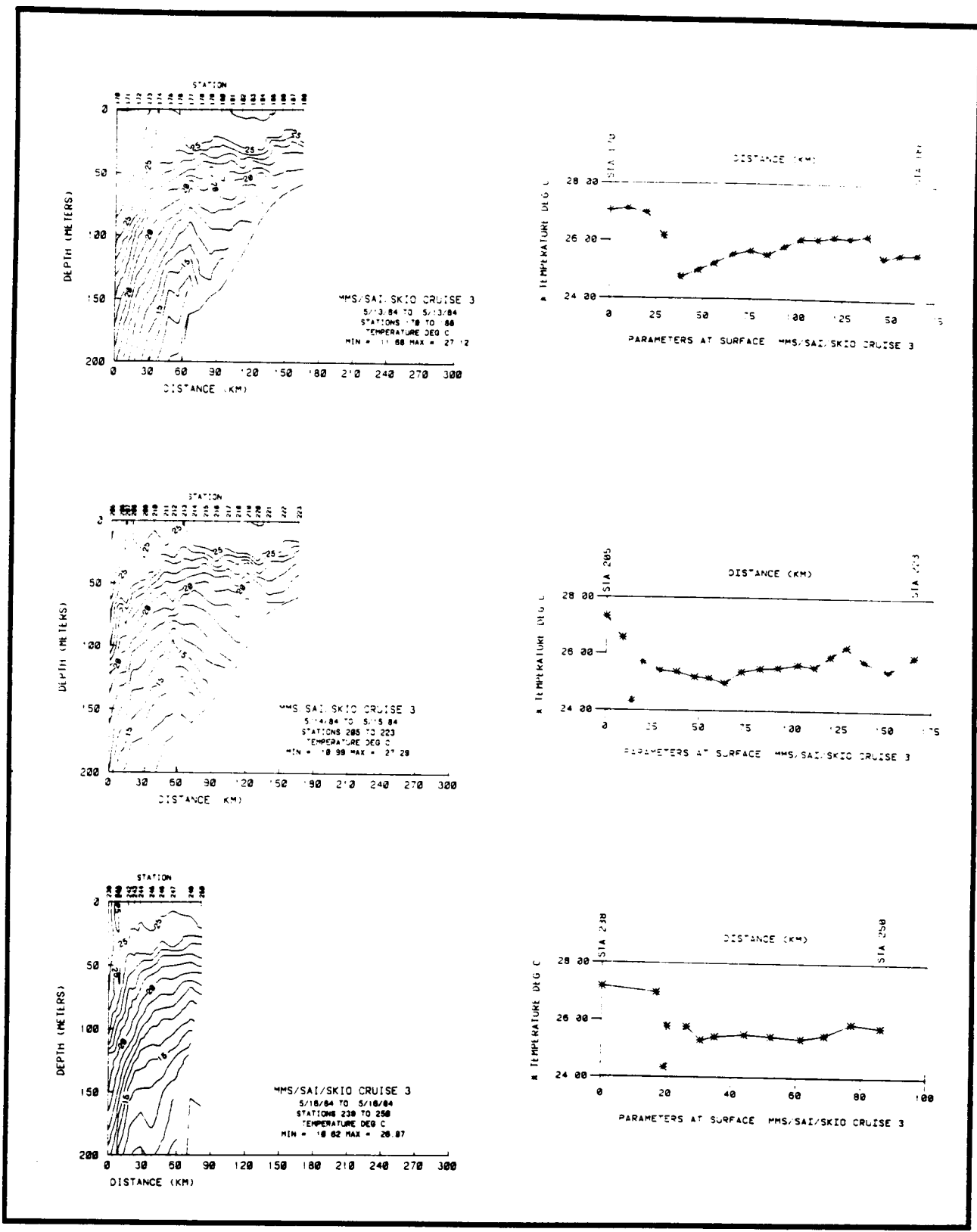


Figure 4.4-29. Temperature sections and sea-surface temperature profiles for time series I.

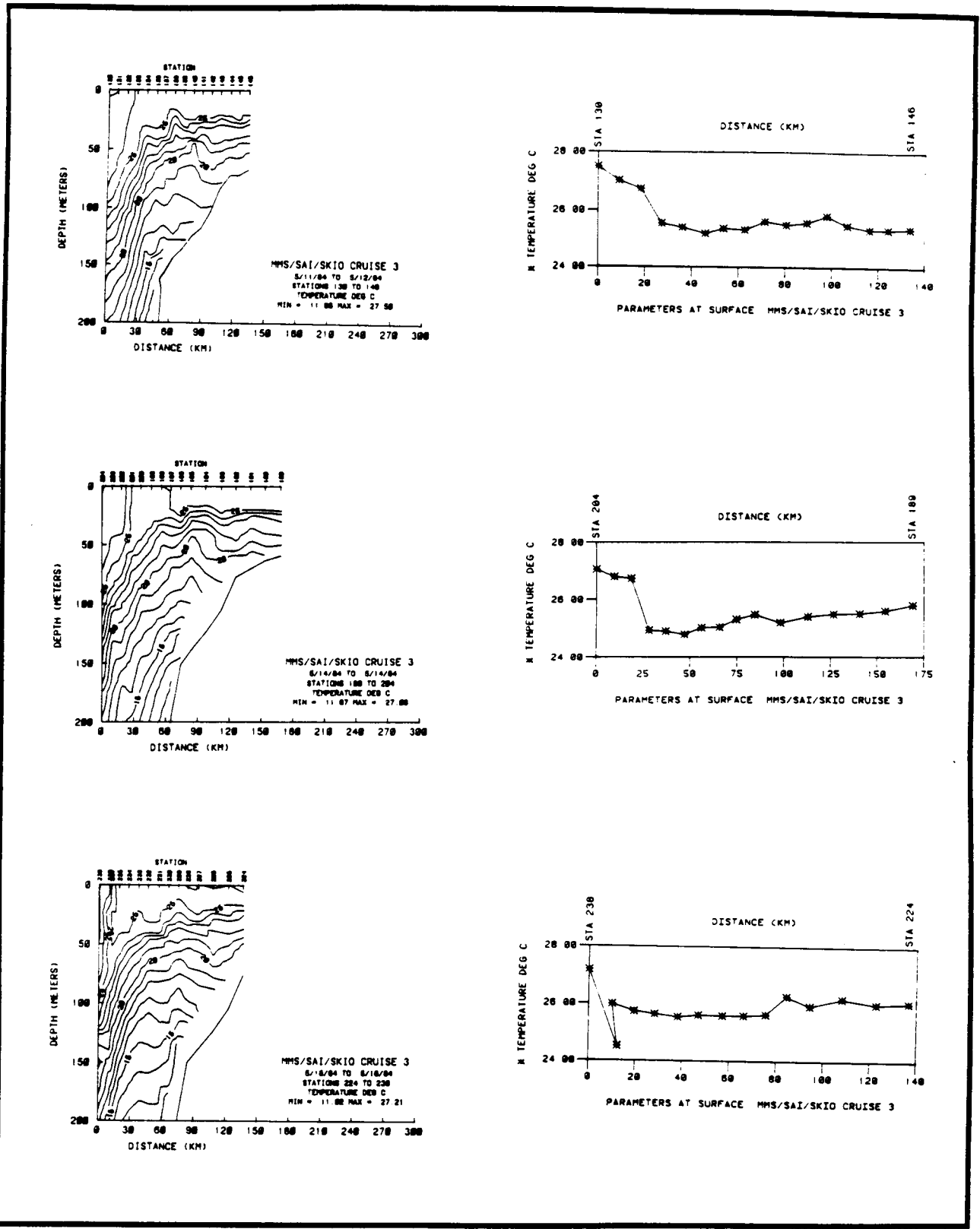


Figure 4.4-30. Temperature sections and sea-surface temperature profiles for time series II.

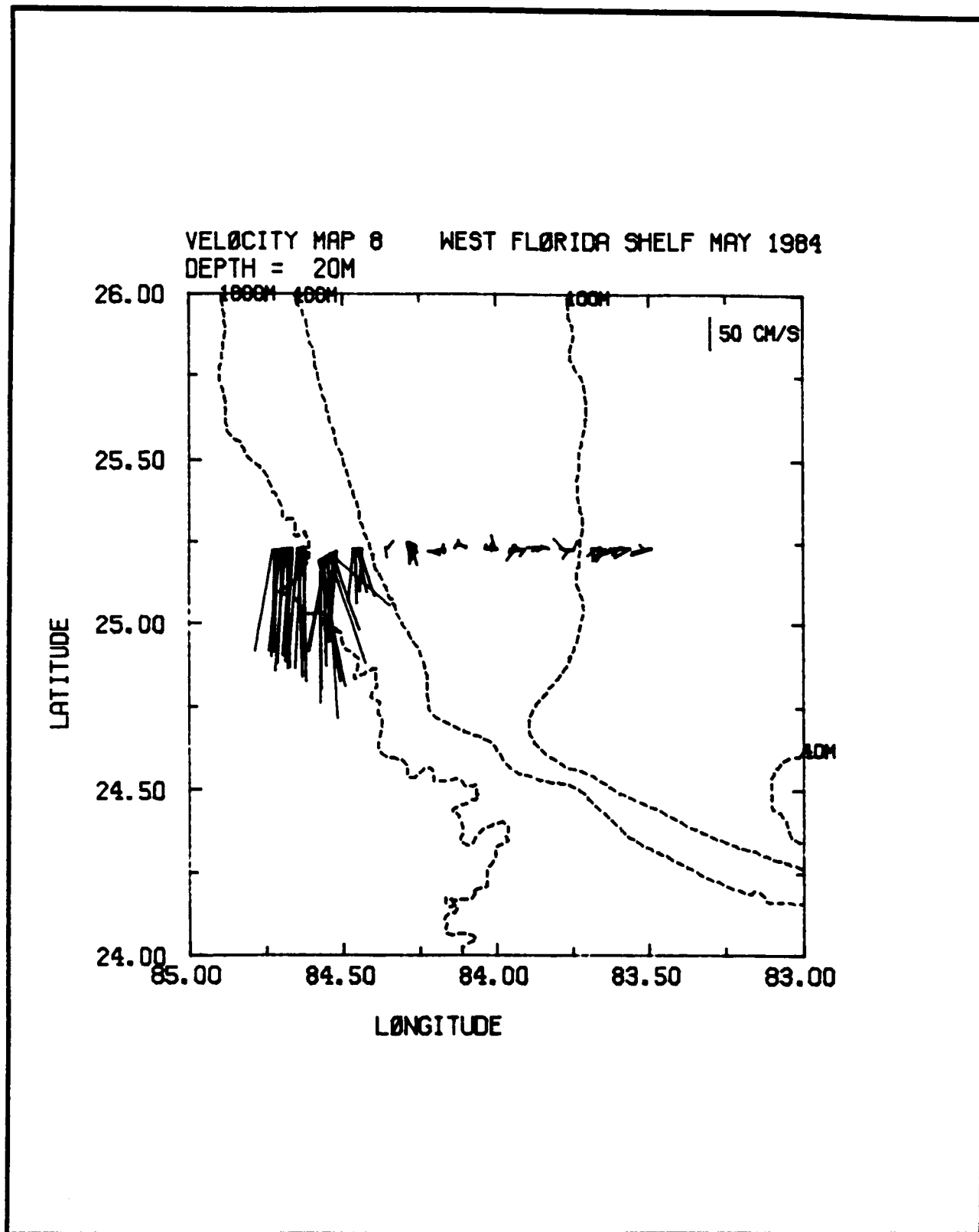


Figure 4.4-31. Stick plots of ADCP velocity at 20-m depth for section XI of time series I obtained before the arrival of a frontal eddy. 11-12 May 1984.

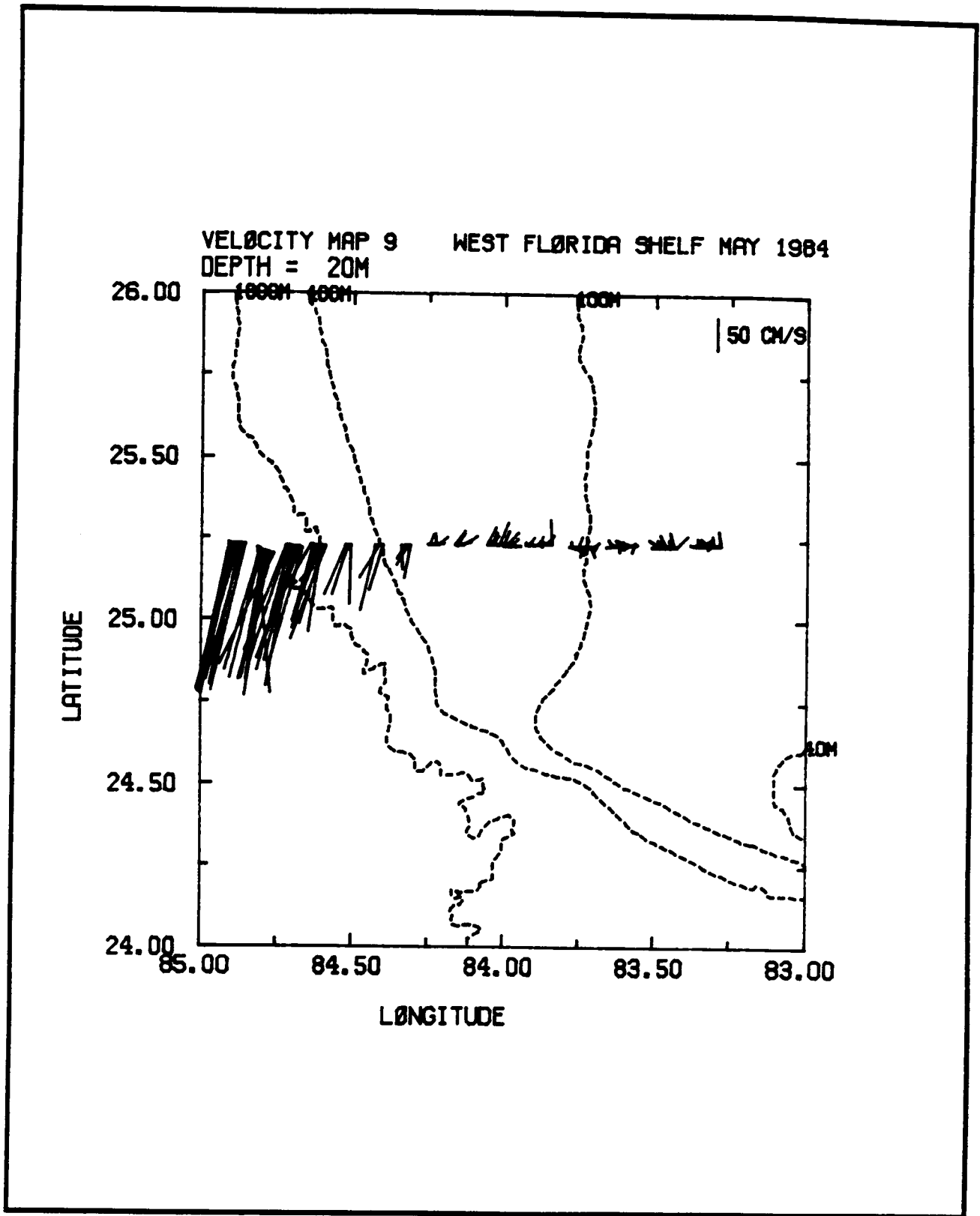


Figure 4.4-32. Stick plots of ADCP velocity at 20-m depth for section XV of time series I obtained just after the arrival of a frontal eddy. 14 May 1984.

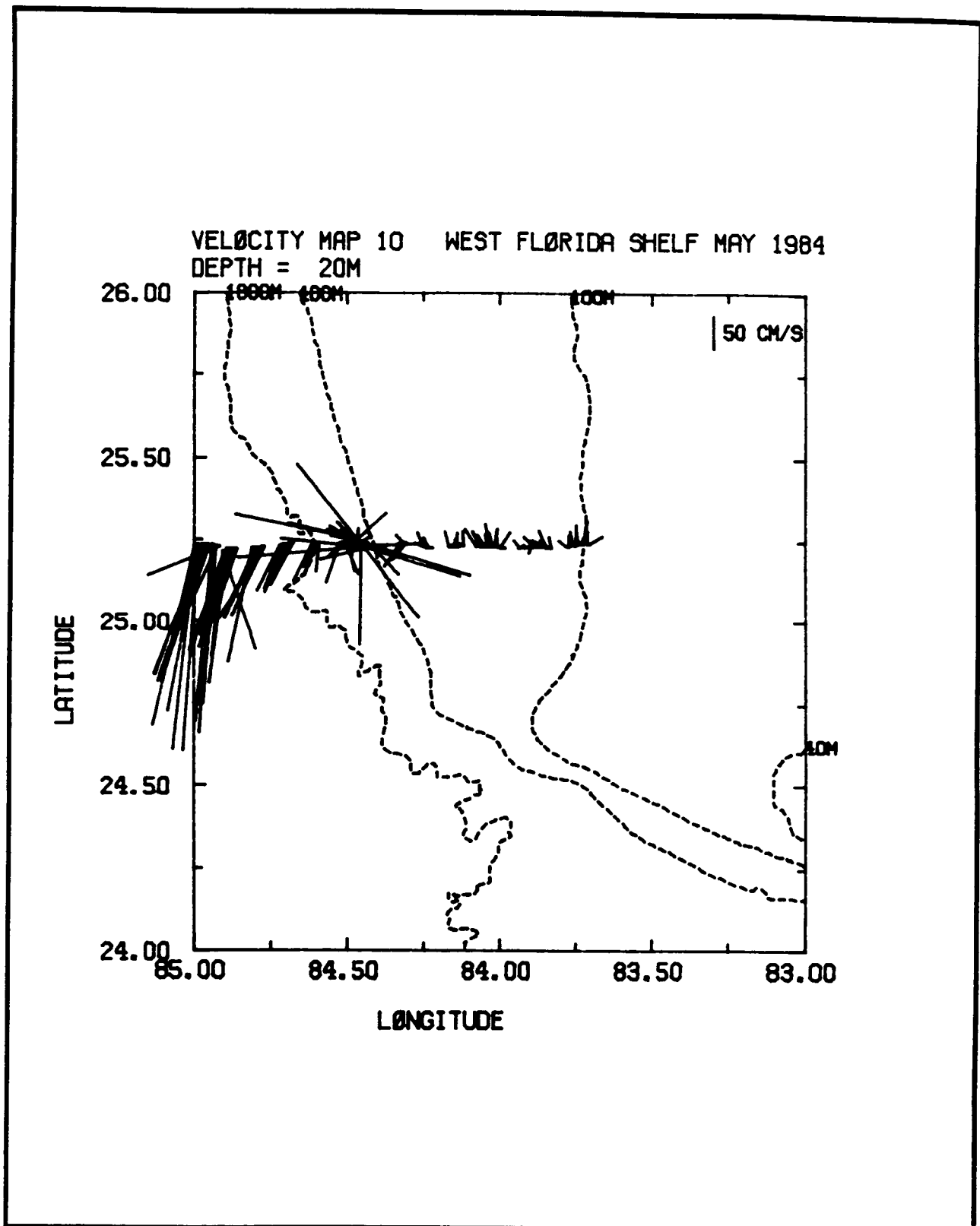


Figure 4.4-33. Stick plots of ADCP velocity at 20-m depth for section XVII of time series I obtained while a frontal eddy was dominating the region. 15-16 May 1984. The spurious large magnitude vectors near 84.5 degrees west are due to imperfections in the process of removing ship motion using LORAN data.

Loop Current velocities approaching 300 cm s^{-1} are indicated.

The vertical structure of this eddy can be seen to extend to 100-m depth. Compare Figures 4.4-32, 4.4-34 and 4.4-35 at 20, 50 and 100 m, respectively. The magnitude of the velocity in the northward flowing warm filament decays with depth as expected from a maximum approaching 40 cm s^{-1} , but the cyclonic shear of the Loop Current front remains strong.

4.5 Subsurface Currents

4.5.1 Introduction

Currents on the west Florida shelf are driven by a combination of forces which include:

- (1) Tides
- (2) Winds
- (3) Eddy-like features, which
 - (a) break off from the Loop Current,
 - (b) originate near the coast,
 - (c) are generated from instabilities at the edge of the Loop Current, and
- (4) Direct forcing by the Loop Current

In the following sections, the observed response to these forces will be discussed. Some of the response seems relatively simple; for example, winds having periods near five days will drive shelf currents having the same period and ordinary cross-spectral analysis will be used to document the response. At slightly lower frequencies, however, at periods of perhaps a week to a month or more, forcing by both the Loop Current and the winds may be important, and it will require other, more complex analysis techniques to separate them clearly.

Local inertial period motion is another important pattern. These motions are usually generated by the passage of strong wind systems. Because they have a period close to the diurnal tides, they will be discussed together with the tidal response.

4.5.2 Tidal and Inertial Currents

The tidal motions are a clear part of each record. The amplitudes are characterized by approximately 5 cm s^{-1} spring tides, with the diurnal (or daily) components being somewhat more prominent than the semidiurnal components. Thus, if there is a wind-induced flow of approximately 5 cm s^{-1} , the flow over a tidal cycle will vary from near zero to near 10 cm s^{-1} .

Tidal analysis using Godin's method (Godin, 1972) has been carried out on long records at three positions: the upper current meter at Mooring C (50-m depth in 180 m of water); the lower instrument at Mooring D (60-m depth in 75 m of water); and the observed tidal heights at Clearwater. The values are

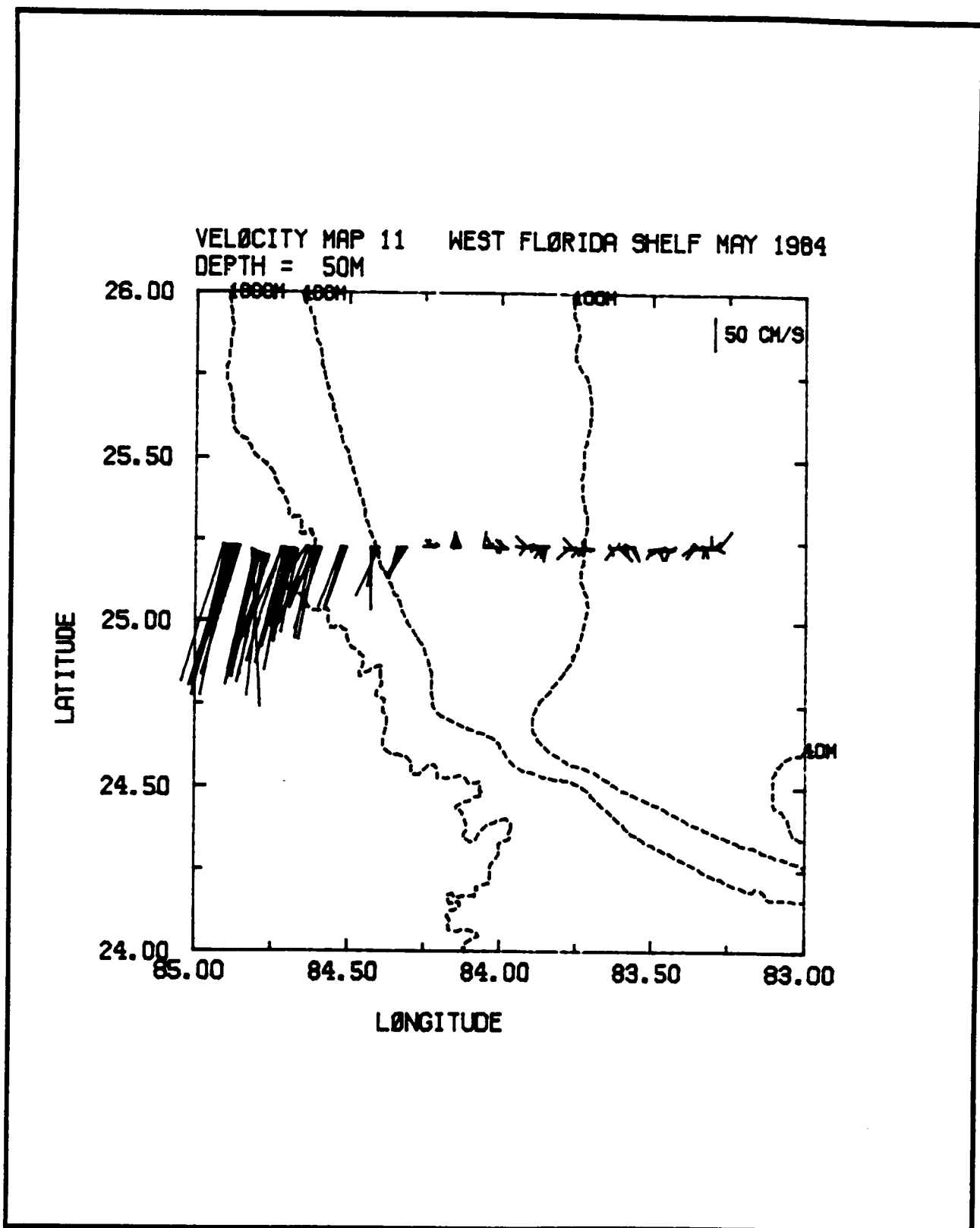


Figure 4.4-34. Stick plots of ADCP velocity at 50-m depth for section XV of time series I obtained just after the arrival of a frontal eddy. 14 May 1984.

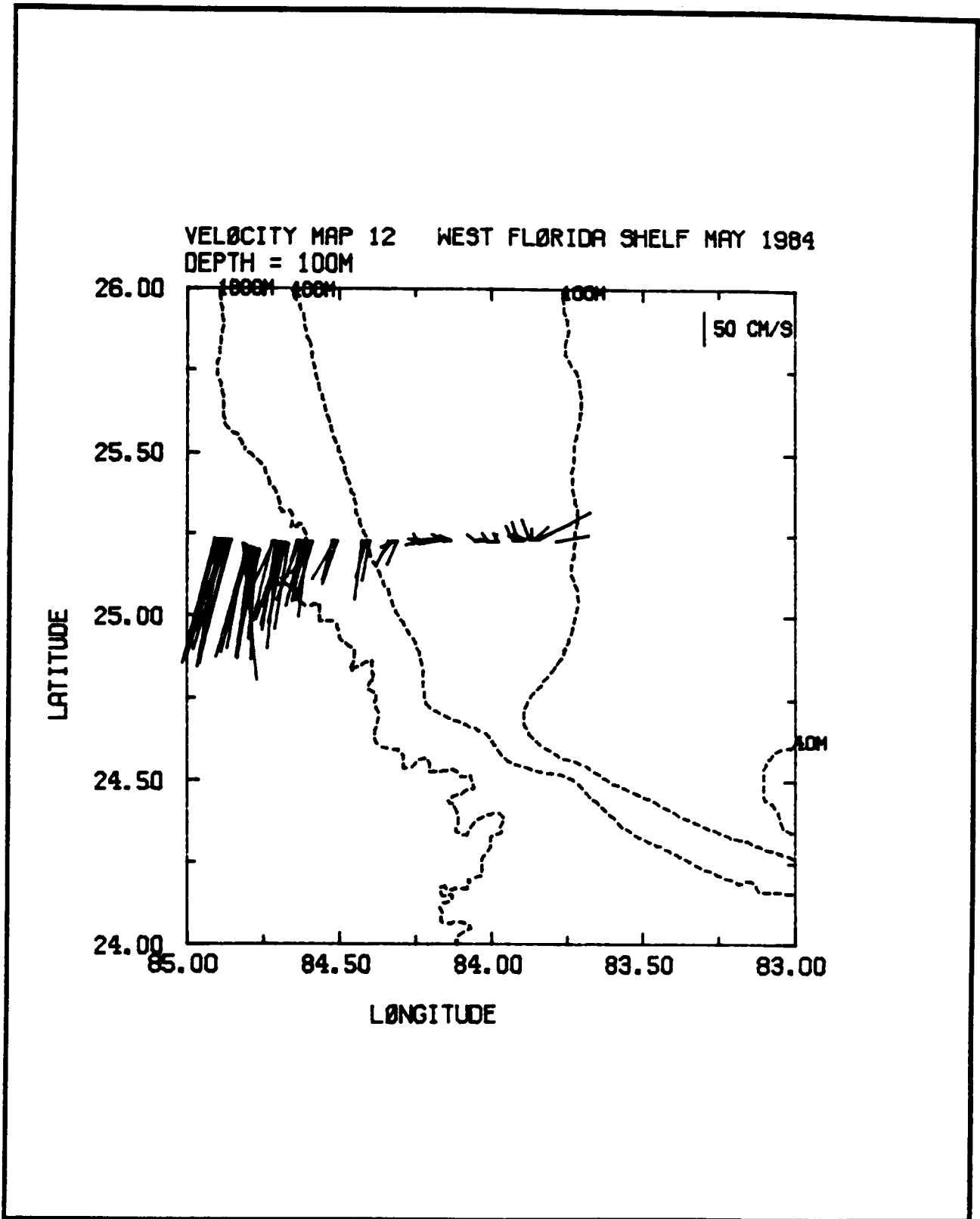


Figure 4.4-35. Stick plots of ADCP velocity at 100-m depth for section XV of time series I obtained just after the arrival of a frontal eddy. 14 May 1984.

calculated for a tidal ellipse. A few of the common constituents are shown in Table 4.5-1. Several terms are omitted, however, which have amplitudes that are within the range of values shown.

In Table 4.5-1, the period is given for each term shown. After that, the term used in tidal analysis is also included. Thus, the nomenclature M2 at a period of 12.42 h is the term arising from the moon's forcing that has two periods per lunar day.

Figure 4.5-1 shows the observations at pressure gauges at the bottom of Moorings C and E (instruments C3 and E3 at 180-m depth) at the edge of the shelf. The most obvious feature is the variation from spring to neap tide (the fortnightly period). Note that a maximum excursion of about 0.8 m occurs as sea level rises and falls 80 cm over a tidal cycle in response to lunar tidal forcing. The tidal excursion, the length of a water parcel's trajectory under a tidal flow of $+5 \text{ cm s}^{-1}$, will be approximately 2.7 km.

When an abrupt wind event passes, transient currents in the "inertial" frequency band can be generated. At a latitude of 26°N this period is about 27.4 h, but the actual frequency observed is slightly shifted about (both + and -) by various processes. At these latitudes, therefore, the inertial motions can be mixed in with the diurnal tidal currents. In a spectra this can cause the low-frequency side of the tidal spectral peak and the high-frequency portion of the inertial peak to coincide or blend additively.

Away from strong topographic influences, tidal motions at any single location tend to be quite predictable. Inertial currents, however, are as random as their forcing. Figures 4.5-2a-b show rotary spectra at instruments C1 (50 m) and D2 (60 m). The tidal constituents are noticeable as small spikes at the appropriate periods. The obvious feature of the figures, however, is the large amount of energy at near-inertial periods (and at twice that frequency, a shallow-water phenomenon). In a spectral plot, the energy (mean-squared velocity) is represented by area. Although it is difficult to judge magnitudes accurately by eye on a logarithmic scale, it should be clear that a major fraction of the current variance is in the inertial band. Figure 4.5-3 shows the observed currents at D2 for a segment of the record. The large bursts of energy are almost entirely inertial motions. Note that the bursts are roughly a week apart, the time between passages of wind events across the shelf.

In a more careful analysis of this record, the calculated tides were subtracted from the observed currents, and the results were then plotted as in Figure 4.5-3. However, scarcely any changes were found. The inertial motions dominate the records at these frequencies. It should be emphasized, therefore, that in a given current-meter record, once it has been processed with a 40-h low-pass filter, a substantial portion (40-60%) of the variance in the record has been suppressed.

4.5.3 Wind-driven Currents

In the absence of other driving forces, synoptic-scale wind events seem to be the dominant forcing mechanism on the inner portion of the shelf at periods longer than a day. In depths less than approximately 30 to 40 m, wind-driven currents are expected to be dominant; the wind-induced amplitudes decrease

Table 4.5-1. Tidal constituents of currents at C1 (the 50-m instrument on Mooring C) and D2 (the 60 m instrument on Mooring D) and the observed tidal heights at Clearwater.

Period. Hrs.	C1		D2		Clearwater Tide Gauge (cm)
	Major Axis (cm s ⁻¹)	Minor Axis	Major Axis (cm s ⁻¹)	Minor Axis	
25.8 (O ₁)	5.43	-4.10	2.92	-1.89	14.86
24.0 (O ₁)	1.66	-1.22	1.80	-1.06	1.63
23.92 (K ₁)	4.52	-3.45	4.76	-3.81	15.45
12.42 (M ₂)	2.29	- .30	5.04	-1.70	24.07
12.0 (S ₂)	.88	- .23	1.72	- .43	9.18

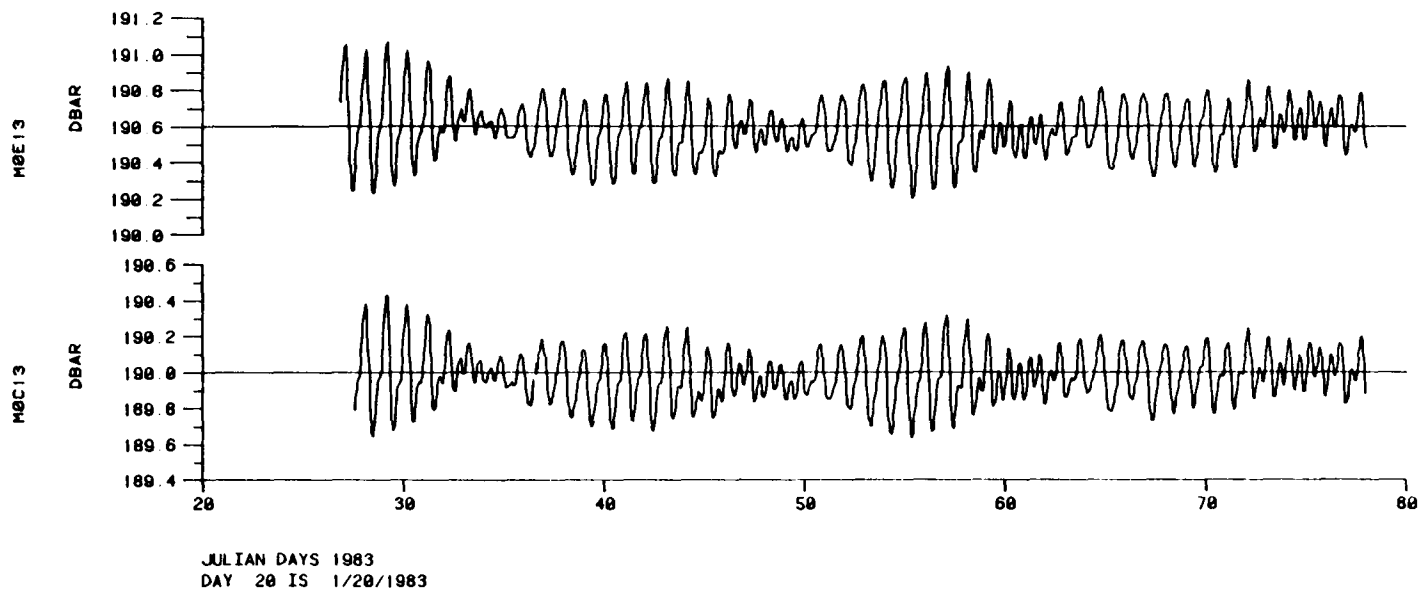


Figure 4.5-1. Fluctuations in pressure at the bottom of Moorings C and E for about the first 50 days, showing dominance of the tides. Samples are recorded every 15 min. The vertical scale, decibars, is absolute pressure and is equivalent to depth in meters.

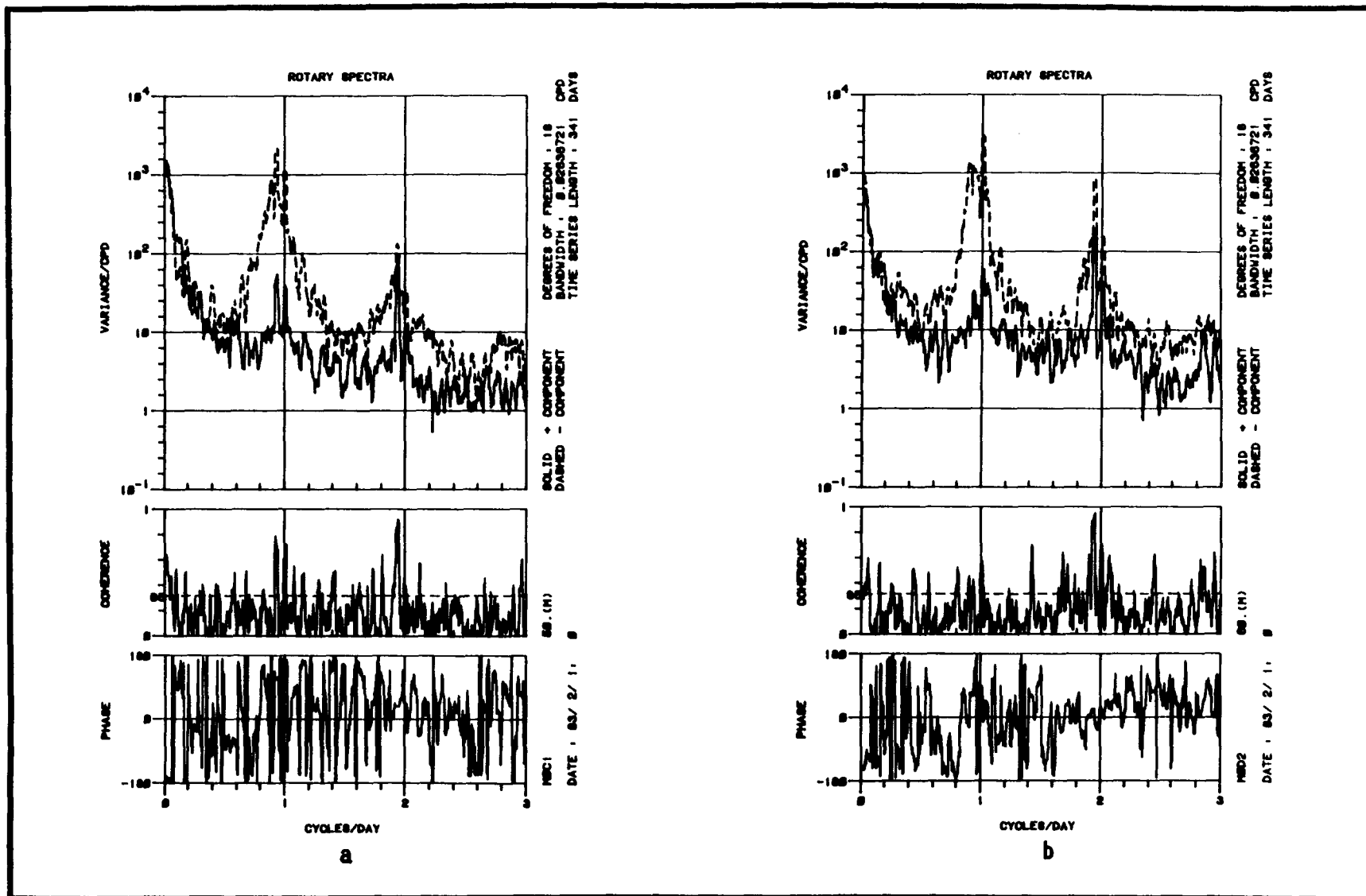


Figure 4.5-2. Rotary spectra of velocity at the upper current meter, depth of 50 m at Mooring C (a) and 60 m at Mooring D (b), for the first 4 moorings. The year of data begins 1 February 1983. The upper panel shows magnitude of the clockwise and counter-clockwise rotating components. The bottom two panels show coherence and phase between them. See sidebar for details.

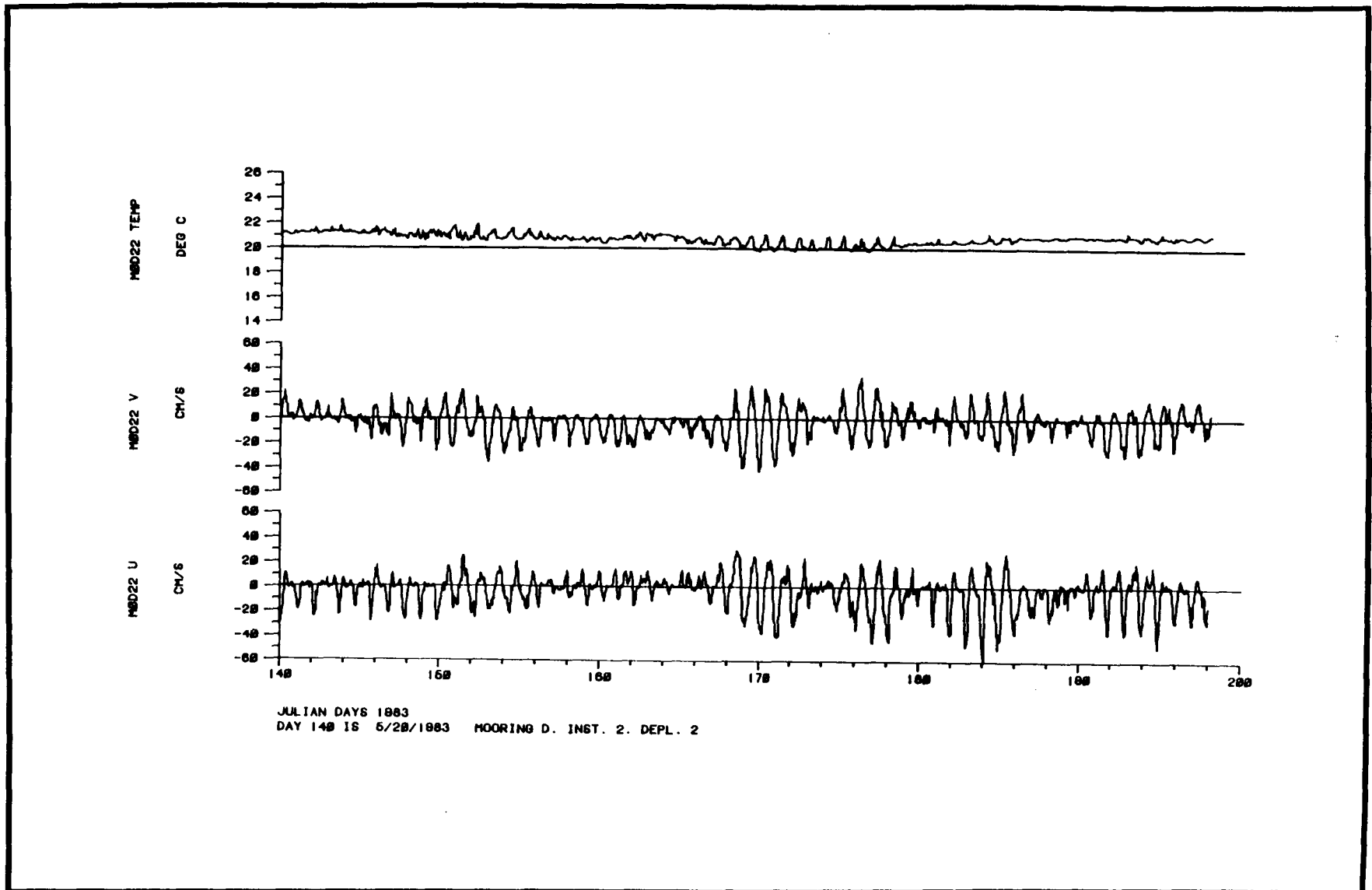


Figure 4.5-3. Velocity components at Mooring D, lower current meter (60 m), during the 2nd setting. The data plotted began on 20 May 1983. The along-shelf and cross-shelf components are in the upper and lower traces. The tidal signal has been removed from the records in a separate analysis, but the near daily signal associated with the inertial motions remains.

from there out to the shelf edge. Because the wind forcing is such an important part of the currents, some brief discussion of the winds is appropriate.

4.5.3.1 Observed Winds

The west Florida shelf has good coastal wind data sets (Key West, Ft. Meyers, Tampa, Pensacola) and at-sea wind data sets from a NDBC Buoy at 26°N, 86°W. Wind spectra were compared between the three stations distributed around the array. Between Tampa and Key West, coherence is uniformly high for periods longer than approximately three days. The Key West winds are stronger than at Tampa in the V (north-south) component by a factor of two or more in the 1983 data, strongly indicating their inappropriateness for characterizing the mid- and north Florida shelf environment.

Phase relationships indicate that the winds at Key West lead the winds at Tampa, in the U and V components, over a wide range of frequencies. This suggests that the frontal systems travel south to north. Conventional wisdom, however, would indicate that the fronts move through from northwest to southeast. The alongshore (V) component of wind is remarkably coherent between the meteorological buoy and Tampa (a distance of about 400 km) from periods longer than 2.5 days. The phase shifts are smaller here than between Key West and Tampa. A comparison of the winds between Pensacola and Tampa reveals that these winds are still coherent (but just barely, in V), but that conventional expectations are met. The wind systems do seem to come out of the northwest; Pensacola leads in both U and V components.

4.5.3.2 Response of Shelf Currents to Wind Forcing

The best coupling between winds and alongshore currents is in the region between the coast and a depth of approximately 30 m. Because alongshore flow is often in geostrophic balance in this region, these nearshore currents contribute most noticeably to water level variations observed at tide gauges. For this reason, it is useful to examine coherence between alongshore winds and the water level heights (adjusted to constant atmospheric pressure). The order of the discussion will be as follows:

- (1) an examination of coherence between winds and coastal sea level,
- (2) an examination of coherence between currents at the most inshore mooring (F) and the appropriate signals (winds, coastal sea level, and the moorings next farther offshore),
- (3) an examination of the moorings farther offshore (C and E) to see to what extent the observed currents there are coherent with wind forcing.

Figures 4.5-4a-d show the variance, coherence squared and phase between the alongshore wind component at Ft. Meyers (V, solid line) and sea level adjusted for atmospheric pressure at Naples, Florida (E, dashed line) for four seasonal divisions. The same comparisons for Clearwater, Florida, using winds from the Tampa airport, are seen in Figures 4.5-5 a-d.

The first result is that coherence between alongshore wind and sea level is high. That is, the near-shore, alongshore currents in the wind-driven band

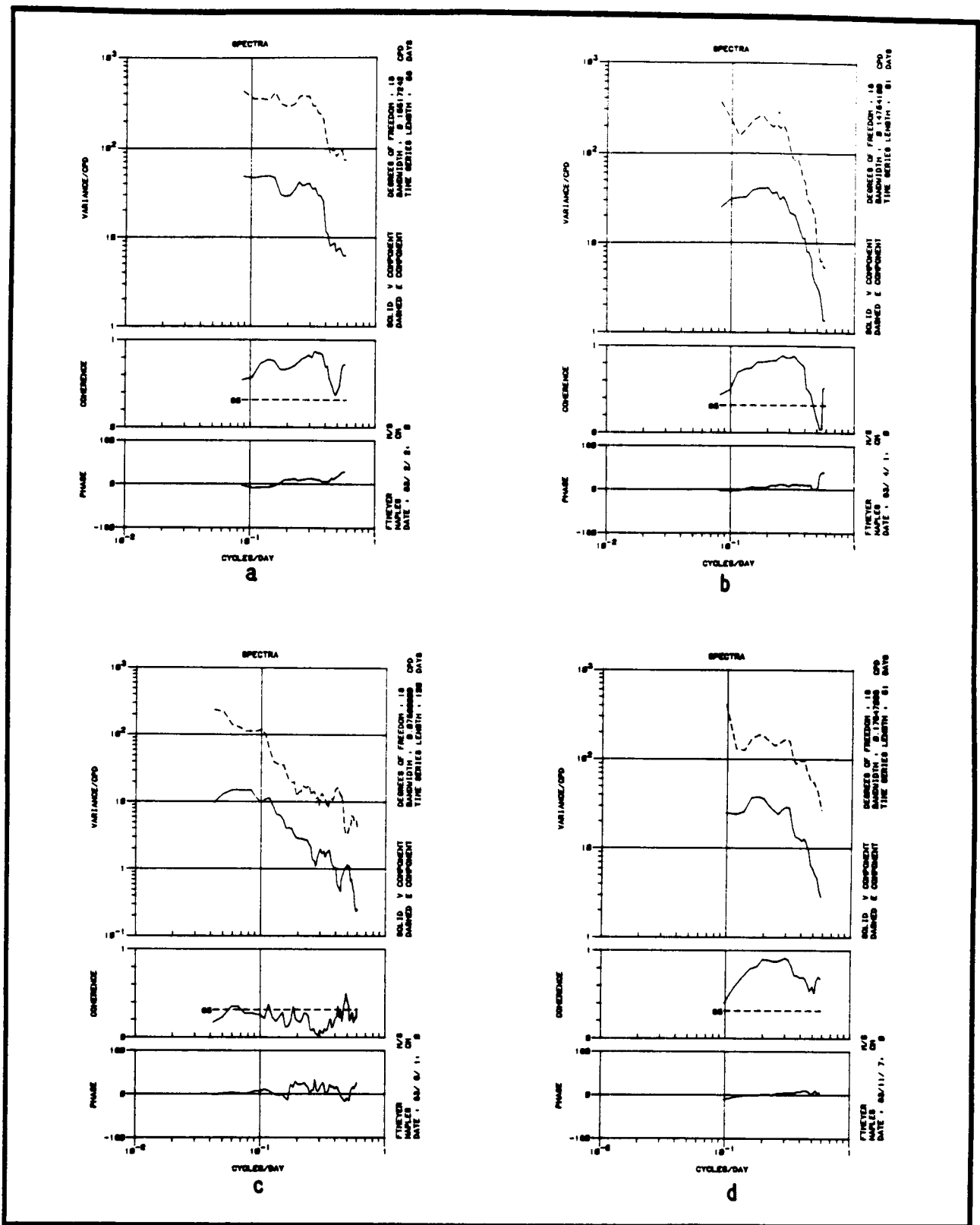


Figure 4.5-4. Cross spectra between longshore wind at Fort Meyers, FL and the tidal height at Naples. (a) winter data, beginning 2 February 1983, (b) spring data, beginning 1 April 1983, (c) 120 days of summer data, beginning 1 June 1983, (d) fall data, beginning 7 November 1983.

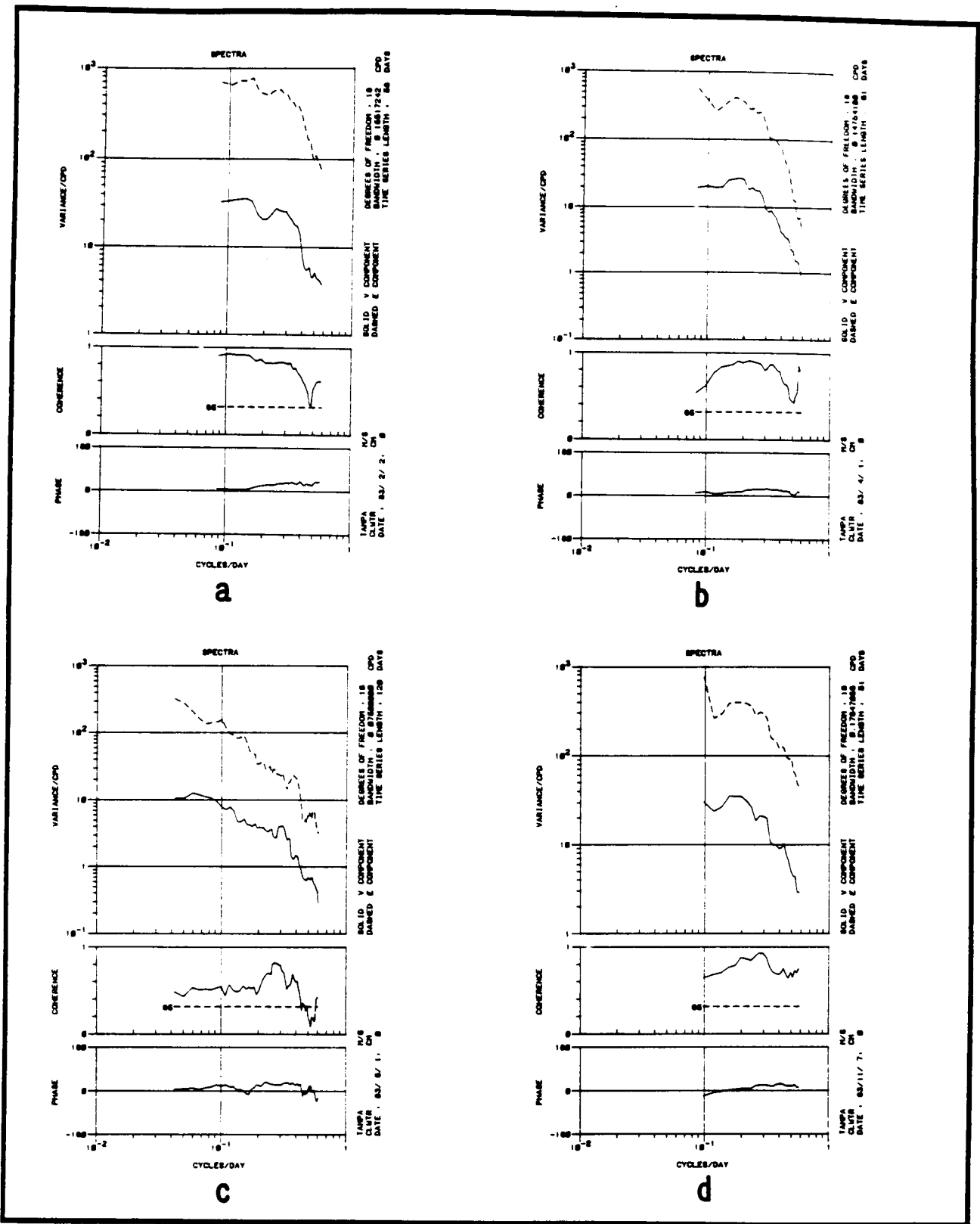


Figure 4.5-5. Cross spectra between longshore wind at Tampa, FL and the tidal height at Clearwater. (a) winter data, beginning 2 February 1983, (b) spring data, beginning 1 April 1983, (c) summer data, beginning 1 June 1983, (d) fall data, beginning 7 November 1983.

(roughly 2-10 days) as seen in the response at the coast are observed to be strongly coherent with the alongshore winds. Coherence is lowest during the summer (Figure 4.5-4c) for two reasons. First, the wind power is much lower, by nearly an order of magnitude, at the wind-driven frequencies. Second, when the water is stratified, wind-induced currents tend to be inhibited. For both reasons, reduced coherency between winds and currents is expected.

Note, however, that coherence is substantially higher between winds and sea level at Tampa than at Naples. This may be due in part because summer winds in 1983 had more power in the 3-5 day band at Tampa. However, it is clear that for the entire summer calculation shown, the sea-level response is greater at Tampa over the whole range of periods from 2-20 days.

This phenomenon presumably results from the fact that the wind-forced motions near Tampa are being forced from north to south. These wave-like motions reflect at the Keys (at the abrupt topographic change). The reflected (free) waves propagate to the north and increase in amplitude from south to north. The signal is reinforced to a greater degree at Tampa than at Naples. Clarke and van Gorder (1985) provide more detail on this theory.

To review, the wind, primarily the alongshore component, drives nearshore currents. The magnitude of the currents decreases toward the edge of the shelf from a maximum in the 20-30 m depth range. As the signal-to-noise ratio decreases, the calculated coherences will decrease, particularly at moorings as far offshore as Moorings D and C.

4.5.3.2.1 Currents at Mooring F: Coherence with Sea Level and with Winds

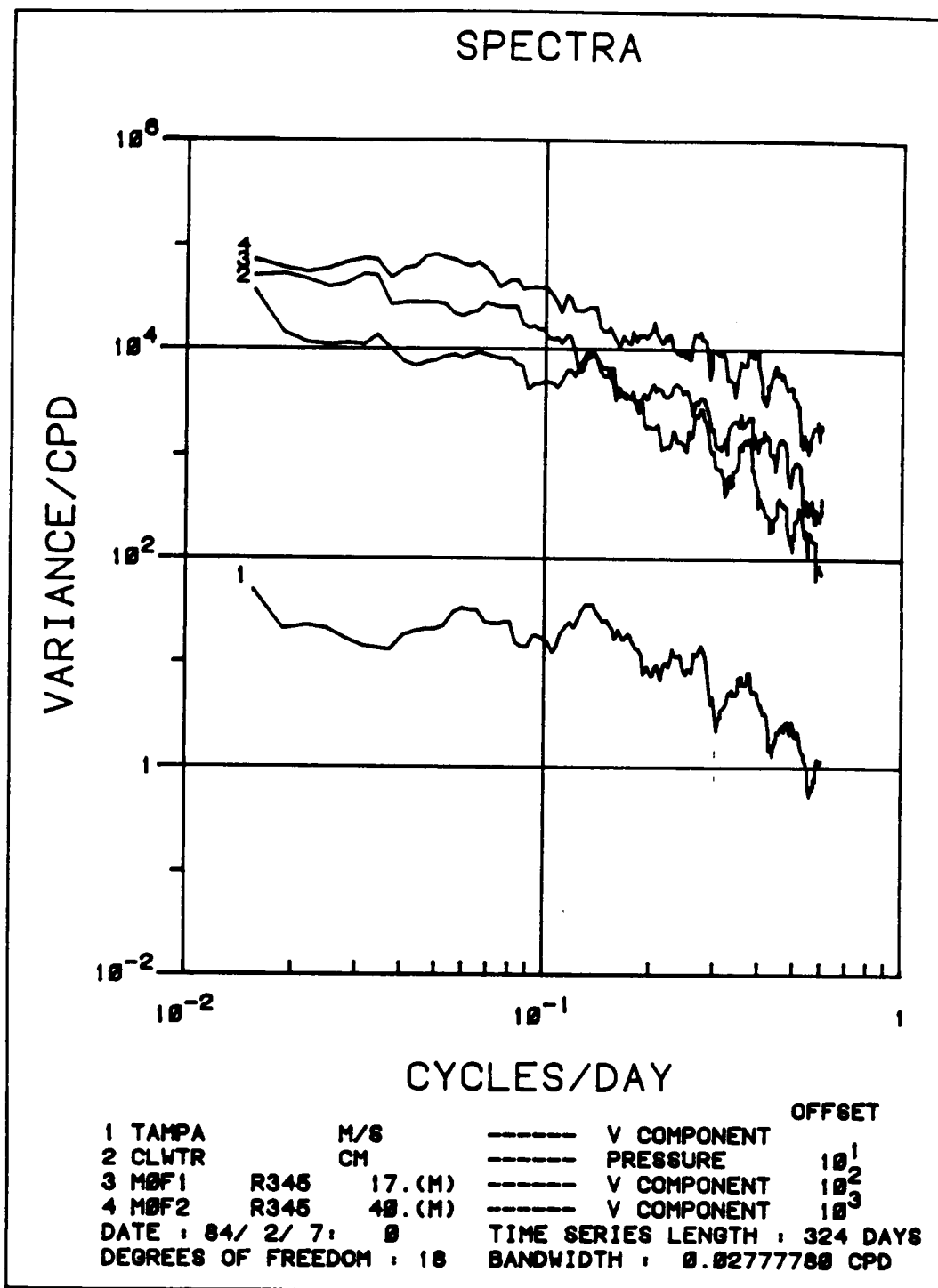
The structure of the winds, currents and sea level linkage is shown in Figure 4.5-6a-c. The spectral amplitudes of

- Tampa winds - V (alongshore) component.
- Clearwater coastal sealevel.
- Mooring F -- V (alongshore) currents at 17 m.
- Mooring F -- V (alongshore) currents at 40 m.

are shown for reference in Figure 4.5-6a.

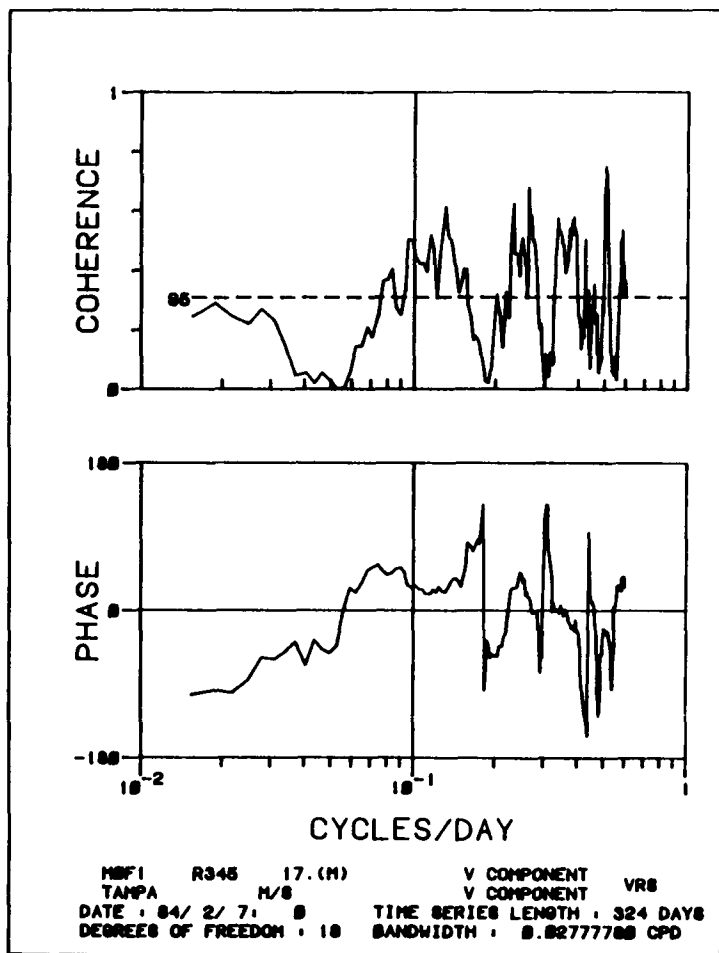
Coherence between alongshore Tampa winds and alongshore currents at 17 and 40 m on Mooring F are shown in Figure 4.5-6b and c. They show a similar pattern with a strong coherent peak at both depths in a band from 7-10 days. In contrast, several significant coherence peaks in Figure 4.5-6b are much less broad at 40 m (Figure 4.5-6c). It is relevant to note that at periods of less than 5 days lack of significant coherence between alongshore currents and winds coincides well with relative minima in alongshore wind forcing (Figure 4.5-6a). In contrast, the strong wind-current coherence at 7-10 days coincides with a peak power in the wind spectra.

When comparing alongshore currents at Mooring F and atmospherically corrected sea level at Clearwater, a pattern of coherence and phase is found which is very similar to that between winds and currents (Figures 4.5-6d and e). This is in keeping with the role of alongshore wind stress driving alongshelf and crossshelf currents which in turn develop adjustments in coastal sealevel. Examination of coherence patterns, especially at periods of 5 days or less,

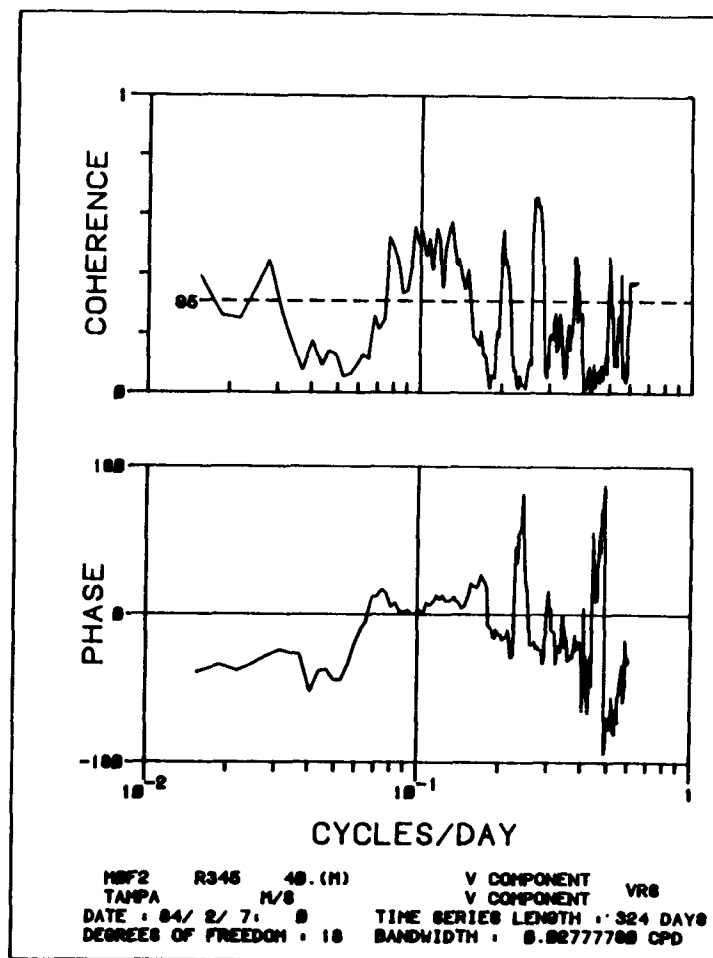


a

Figure 4.5-6. (a) Spectral amplitudes for the second year of data for longshore wind component at Tampa, tidal height at Clearwater, longshore current component at Mooring F (in 50-m depth) at the 17-m and 40-m instruments.

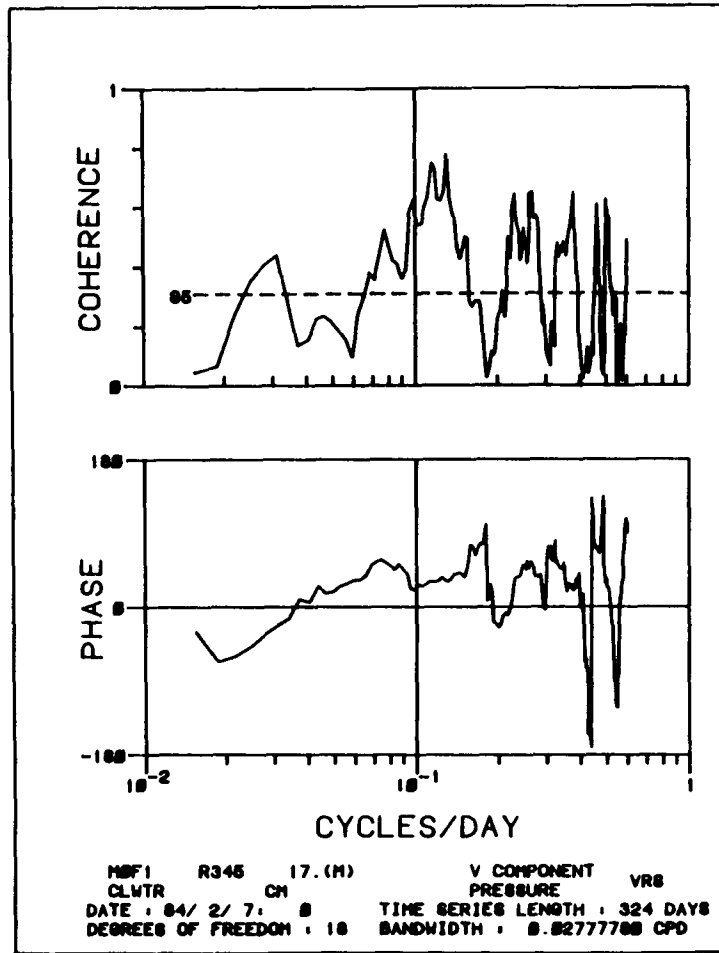


b

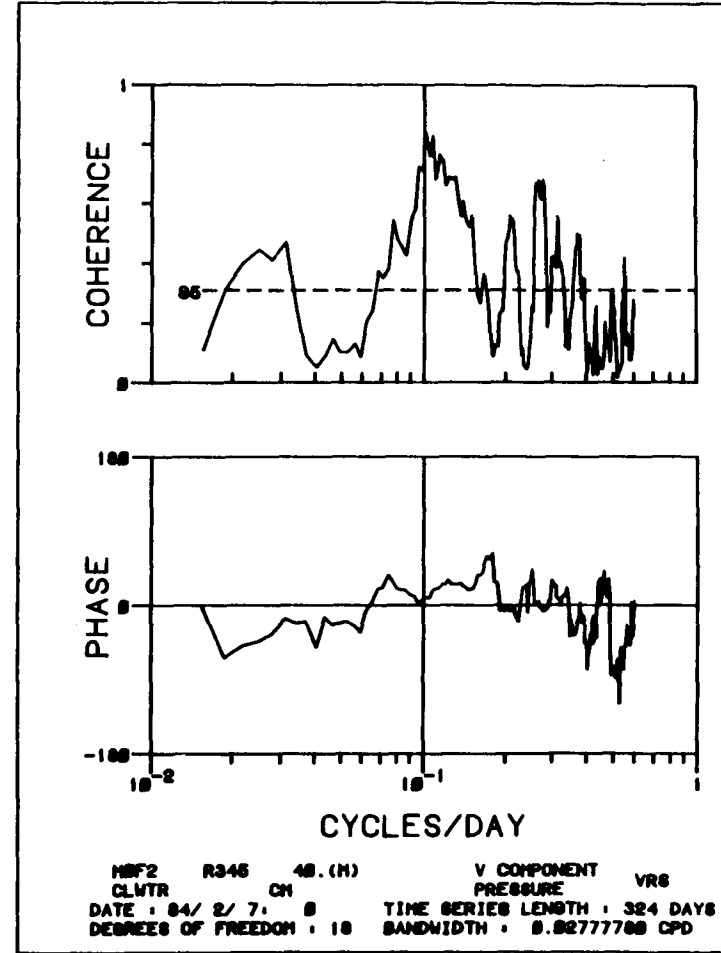


c

Figure 4.5-6. (b) Cross spectral coherence and phase between longshore velocity component at the 17-m instrument at Mooring F and the longshore wind at Tampa for the signals shown in a. (c) same as b, except at the 40-m instrument.



d



e

Figure 4.5-6

(d) Cross spectral coherence and phase between longshore velocity component at the 17-m instrument at Mooring F and the Clearwater tide gauge (adjusted to uniform atmospheric pressure) for the signals shown in a.

(e) same as d, except at the 40-m instrument.

reveals this similarity. In significant coherence bands the phase relationships between winds and currents or coastal sea level are very similar, further suggesting the coupling and simultaneous development of wind-driven transport (currents) and coastal waterlevel.

Calculations between Mooring F currents at 17 m and coastal winds at Tampa using seasonal divisions show that coherence is high at all periods in the winter (Figures 4.5-7b) which allows more current variability to be reasonably accounted for. In the spring (Figures 4.5-8a-c) coherence is lower, but wind power is lower by nearly an order of magnitude over much of the frequency band. Thus, the signal-to-noise ratio is too low to get good estimates of coherence. In summer (Figures 4.5-9a-c) coherence is again at its lowest, as is wind stress. By the fall (Figure 4.5-10a-c), when wind stress is again at about the same level as the winter, coherence between winds and currents is again high.

In the spectra between Mooring F and both winds and coastal sea level for a one year period (Figure 4.5-6), there is lower coherence at periods of four to eight days during the summer than in the fall and winter for at least two reasons. First, because the signals are weak in the summer, the signal-to-noise ratio for the whole year is brought down to a low average value. A second, and perhaps more important reason, is that wind-generated signals have different relative phases if some wind systems come from the north and others come from the south. This question needs continued analysis.

4.5.3.2.2 Coherence between Mooring D and Coastal Sea Level

Coherence between winds at Tampa and the bottom pressure gauge at Mooring E shows the same pattern as at Moorings F and D. This pattern of high coherence for periods near 40 days and near 8-10 days indicates that these signals are coherent across the shelf.

Cross spectra have been examined by seasons between the U and V components of currents at 30 m on Mooring D (D1) and coastal sea level (adjusted to constant atmospheric pressure) at both Naples, the nearest tide gauge, and at Clearwater. The general result is that alongshore currents at D1 are less coherent with winds and sea level than the currents at Mooring F. They are more highly coherent with sea level at Naples than at Clearwater. The cross-shelf component, which is usually smaller than the alongshore component, shows lower coherence.

The results for the four seasons (from February to December 1983) show that coherence is reasonably high in winter and fall, except for the striking gap near 3-5 days (Figures 4.5-11a,d). Since this energy minimum occurs only in currents, not in sea level, the assumption is that it must be associated with the cross-shelf modal structure of either the wind response or the reflected waves at the Florida Keys. It is important to note, however, that the phase difference between the currents and sea level appears to change significantly between the winter and fall periods (Figures 4.5-11a,d). The phase difference is negligible in the fall and 90° in the winter. This shift may be the result of the difference in direction of wind forcing, but this speculation requires further work for confirmation.

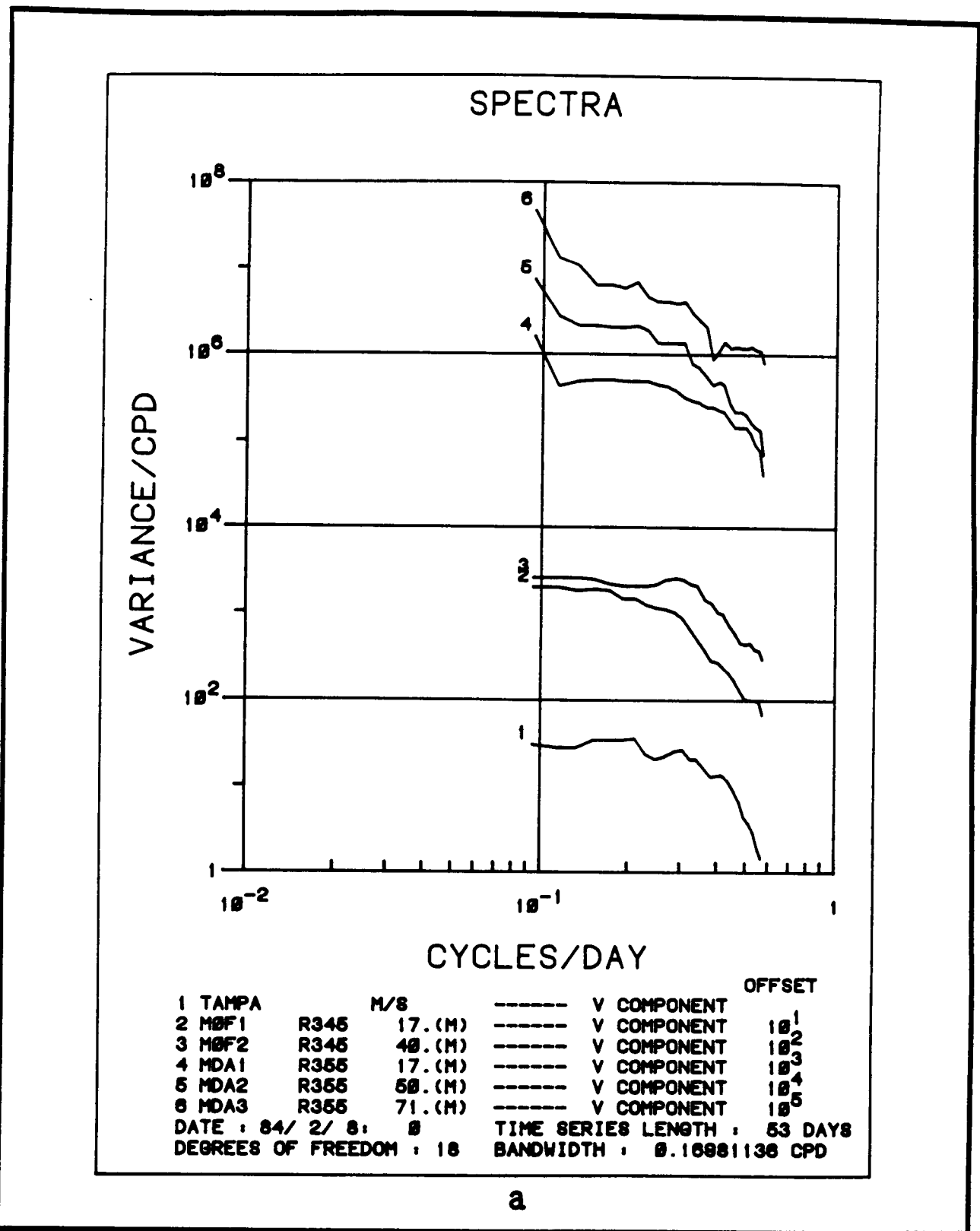
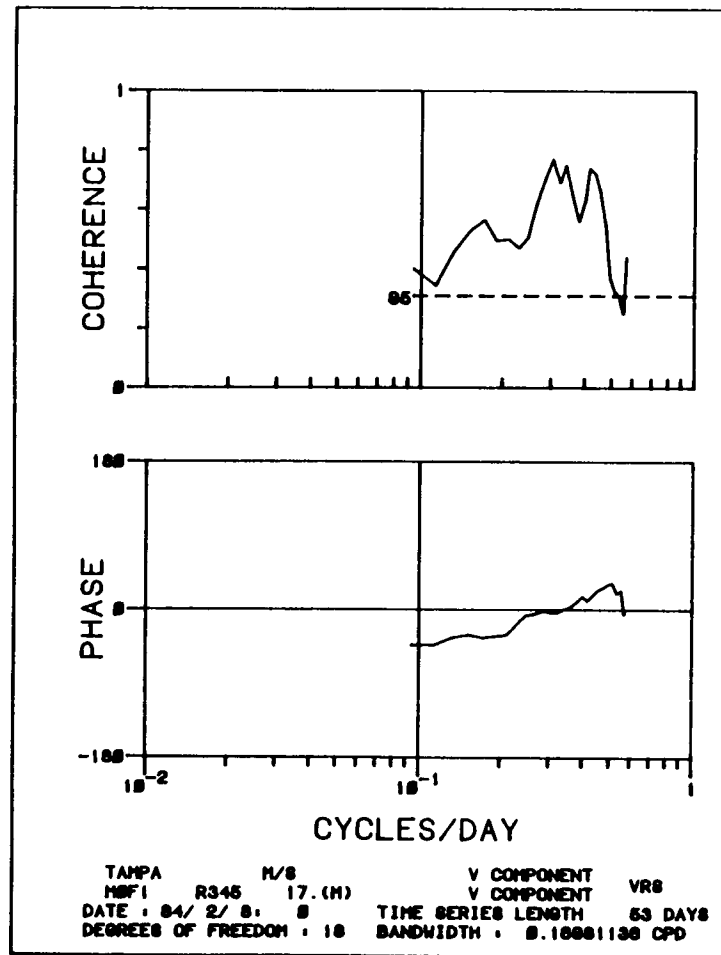
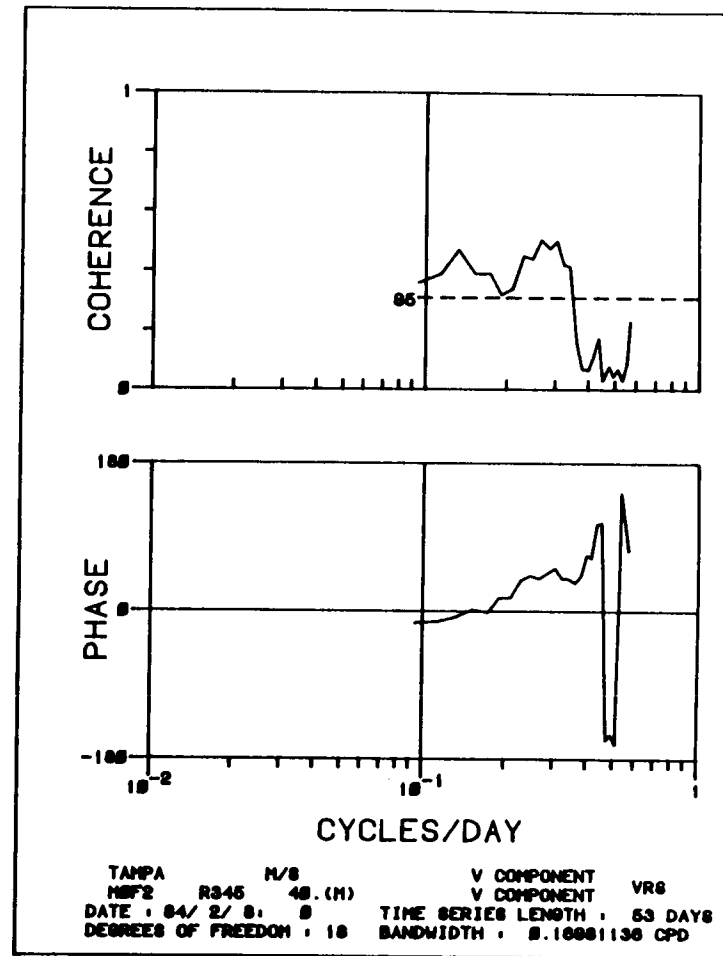


Figure 4.5-7. (a) Spectral amplitudes for the "winter" season of the second year of data, beginning 8 February 1984 for longshore wind component at Tampa, longshore current component at Mooring F (in 50-m depth) at the instruments at 17 m and 40 m and at Mooring D (shows in figure as DA) at depths of 17, 50, and 71 m.

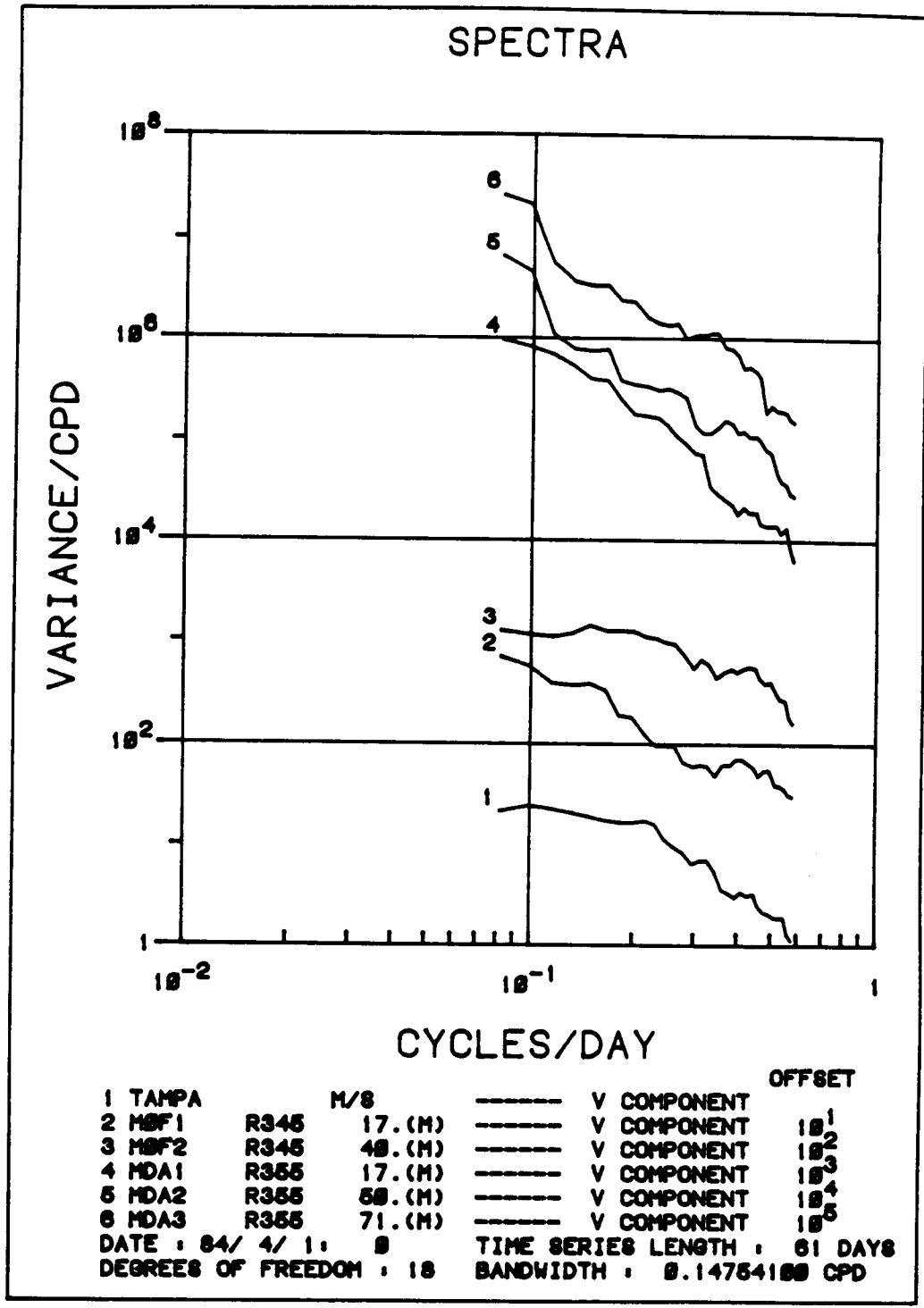


b



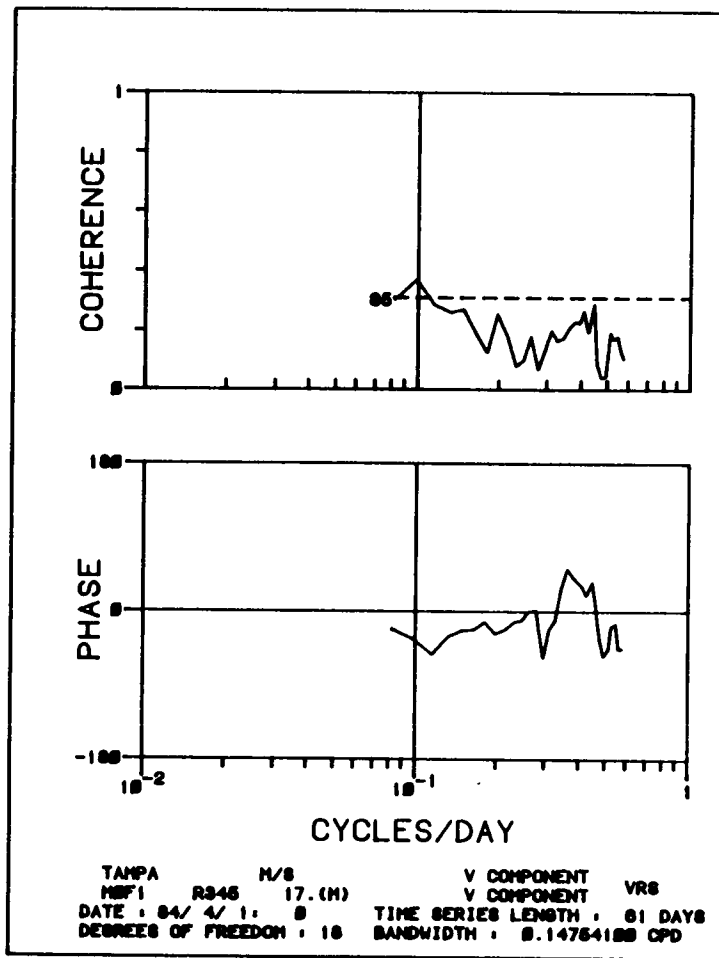
c

Figure 4.5-7. (b) Cross-spectral coherence and phase between longshore velocity component at the 17-m instrument at Mooring F and the winds at Tampa for the signals shown in a.
 (c) same as b, except at the 40-m instrument.

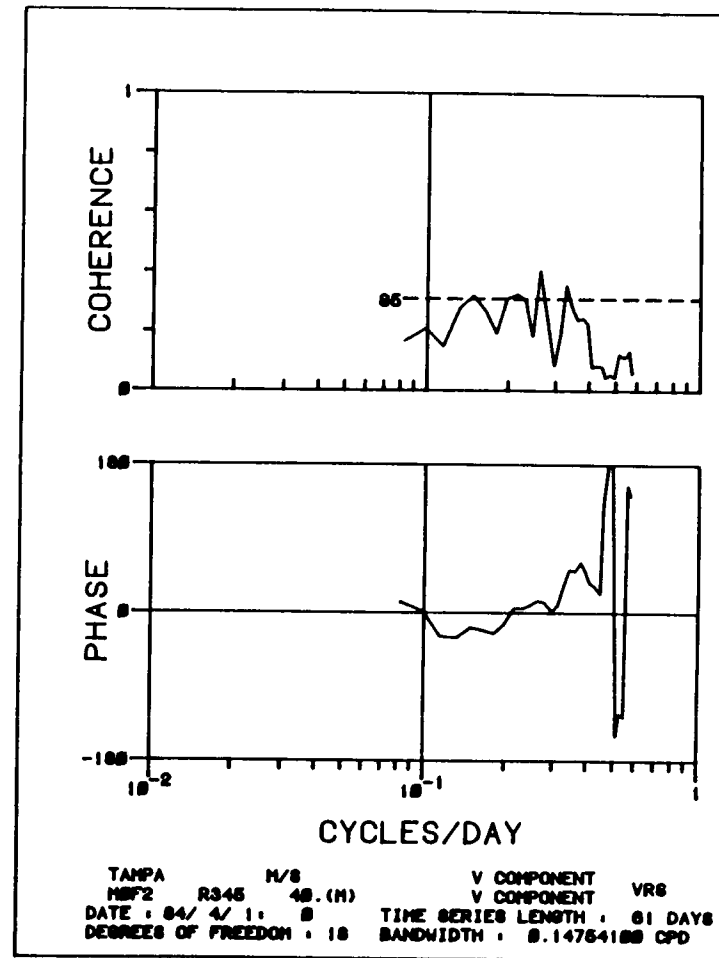


a

Figure 4.5-8. (a) Spectral amplitudes for the "spring" season of the second year of data beginning 1 April 1984, for longshore wind component at Tampa, longshore current component at Mooring F (in 50-m depth) at the instruments at 17 m and 40 m and for Mooring D (shows in figure as DA) at depths of 17, 50, and 71 m.

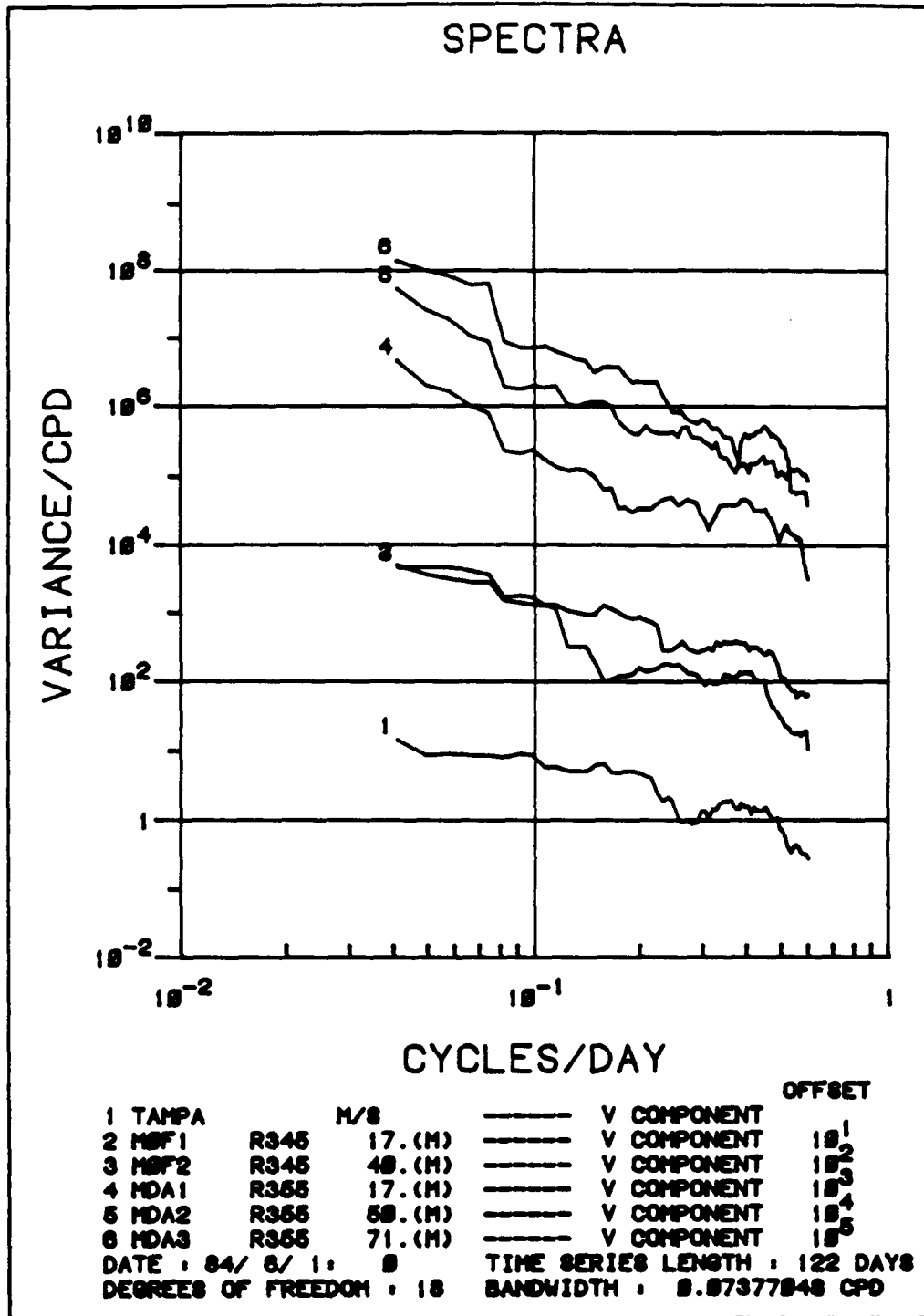


b



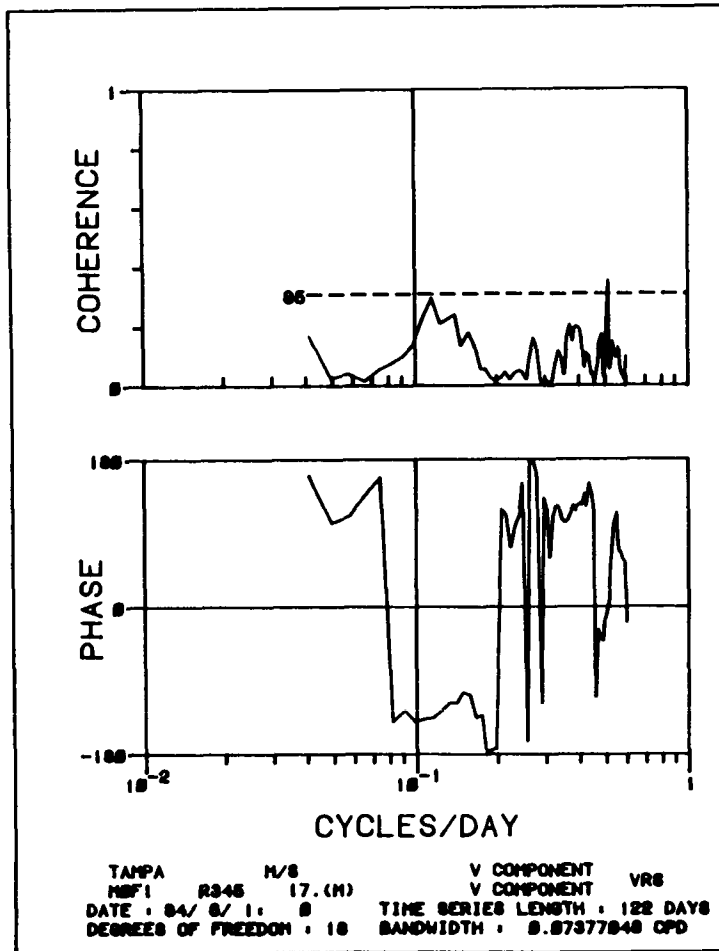
c

Figure 4.5-8. (b) Cross-spectral coherence and phase between longshore velocity component at the 17-m instrument at Mooring F and the winds at Tampa for the signals shown in a. (c) same as b, except at the 40-m instrument.

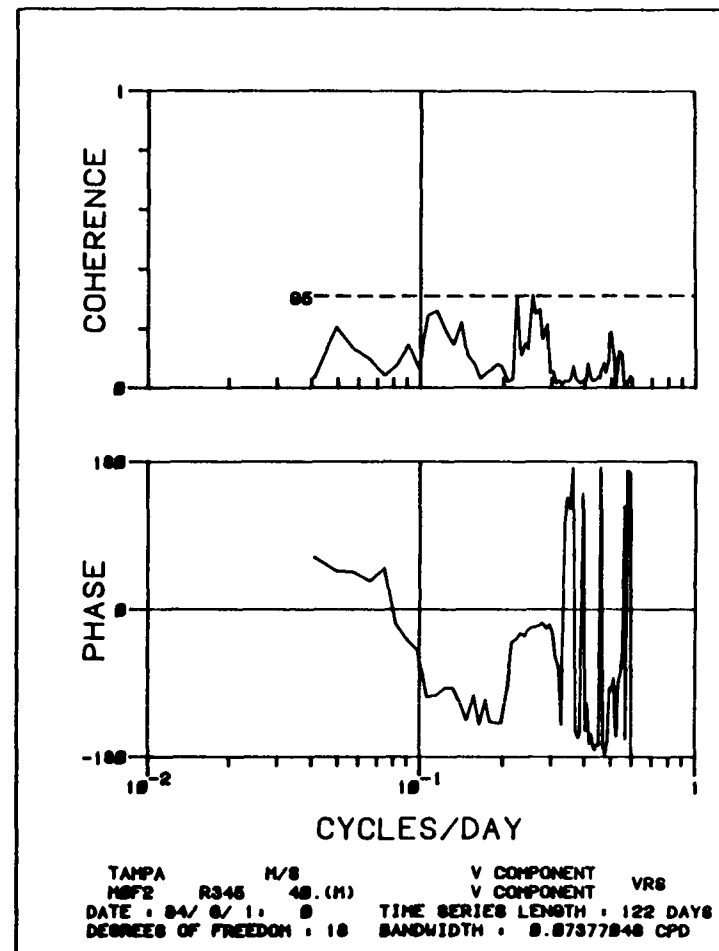


a

Figure 4.5-9. (a) Spectral amplitudes for the "summer" season of the second year of data beginning 1 June 1984 for 122 days of data for longshore wind component at Tampa, longshore current component at Mooring F (in 5-m depth) at the instruments at 17 m and 40 m and for Mooring D (shows in figure as DA) at depths of 17, 50, and 71 m.

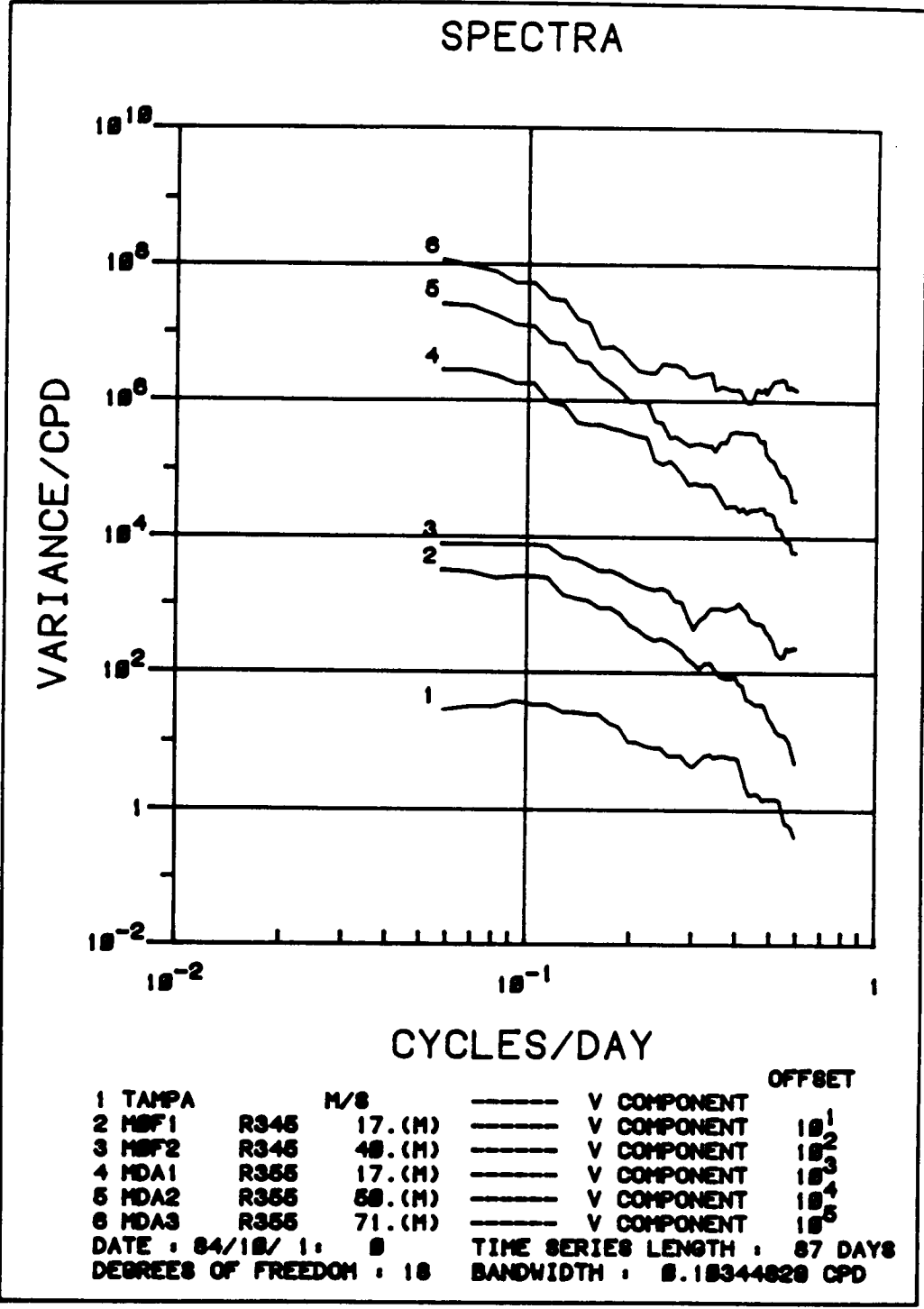


b



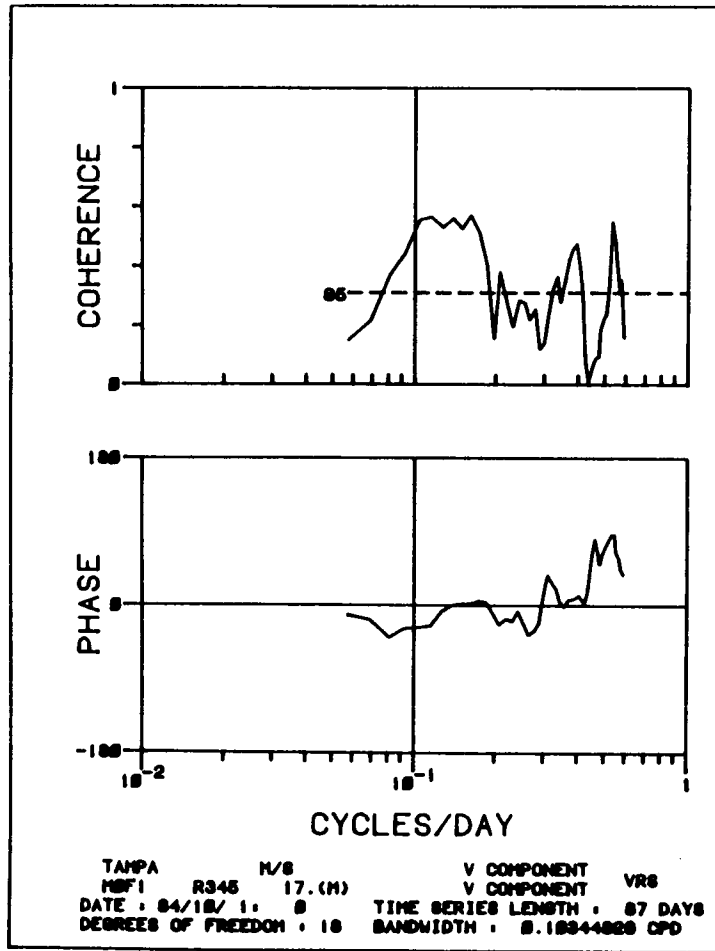
c

Figure 4.5-9. (b) Cross-spectral coherence and phase between longshore velocity component at the 17-m instrument at Mooring F and the winds at Tampa for the signals shown in a. (c) same as b, except at the 40-m instrument.

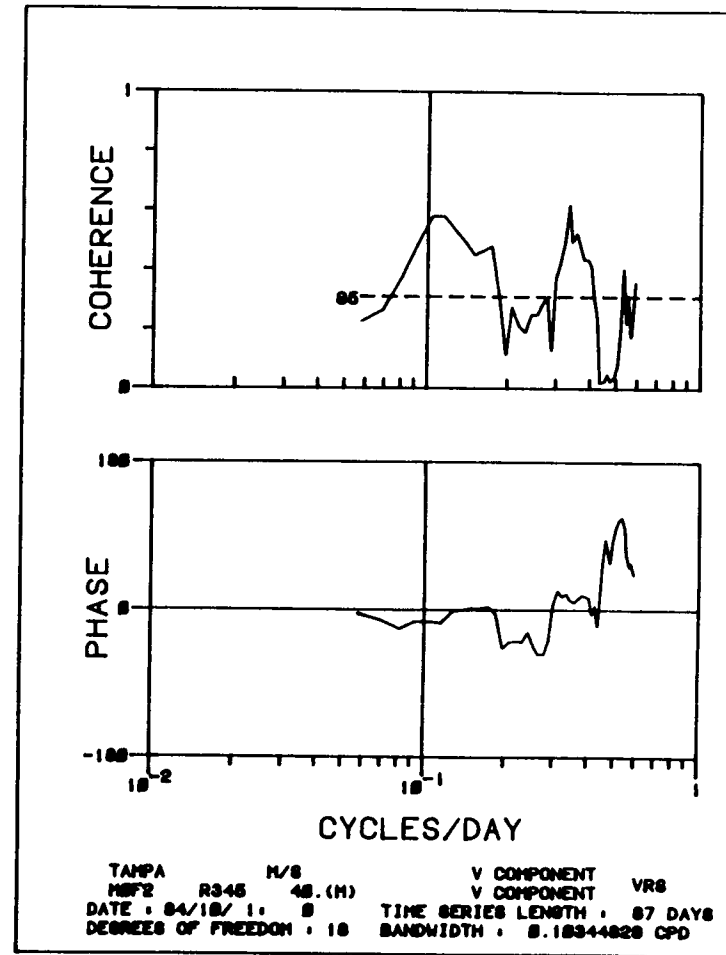


a

Figure 4.5-10. (a) Spectral amplitudes for the "fall" season of the second year of data, beginning 1 October 1984 for 87 days of data, for longshore wind component at Tampa, longshore current component at Mooring F (in 50-m depth) at the instruments at 17 m and 40 m and for Mooring D (shows in figure as DA) at depths of 17, 50, and 71 m.



b



c

Figure 4.5-10. (b) Cross-spectral coherence and phase between longshore velocity component at the 17-m instrument at Mooring F and the winds at Tampa for the signals shown in a. (c) same as b, except at the 40-m instrument.

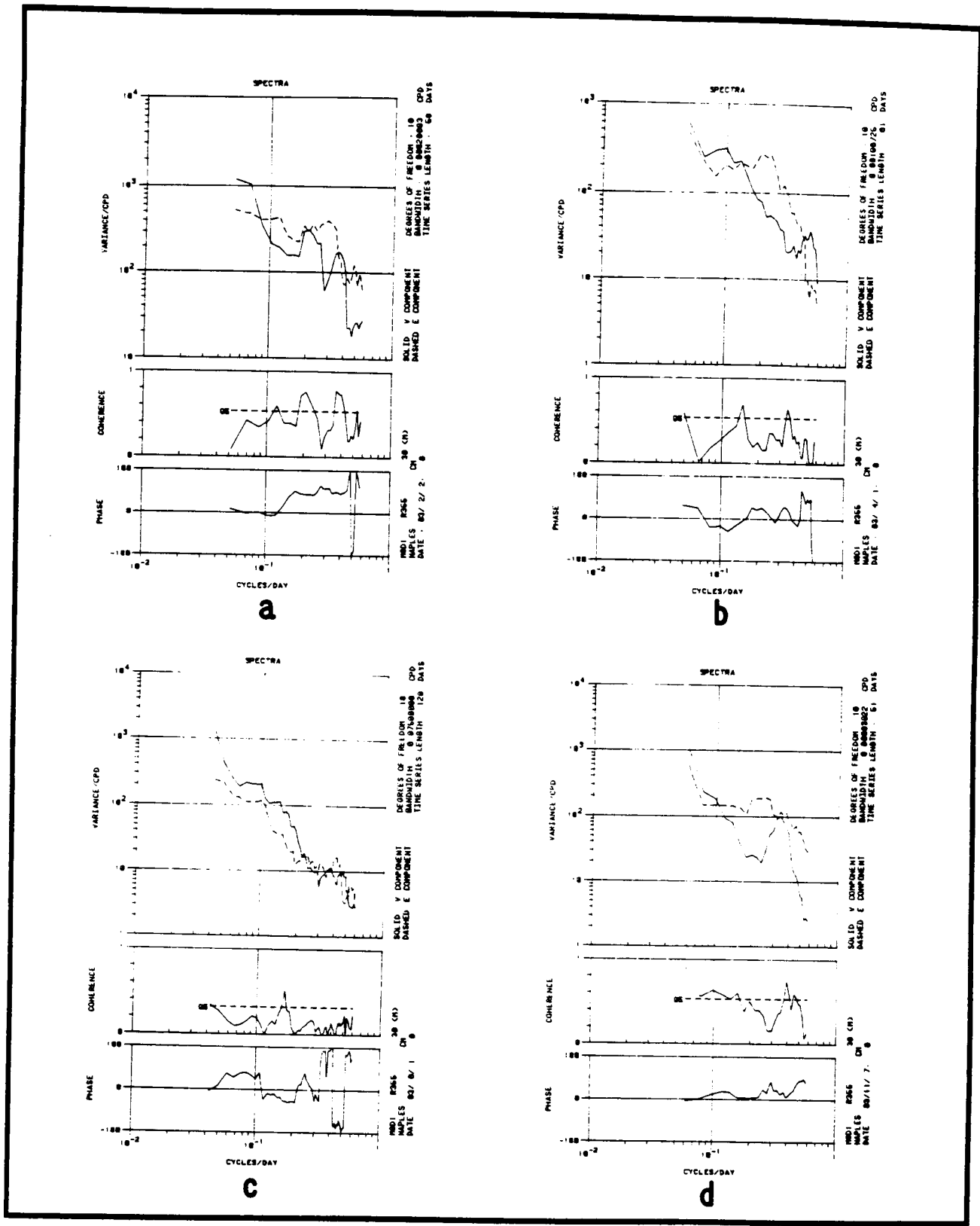


Figure 4.5-11. Cross spectra between the long-shelf current component at Mooring D, upper current meter (30 m) and sea level at the coast (Naples), adjusted to constant atmospheric pressure. If the phase is positive, the currents at D lead the sea level signal. E = Elevation (tide gauges).

Coherence is lower in spring and much lower in summer (Figures 4.5-11b,c). This result is the same as was found at Mooring F, and presumably for the same reasons, i.e. vertical stratification and weaker forcing. Figure 4.5-12 shows cross spectra between the U component of current and sea level at Naples for the two seasons of highest (in V component) coherence. As suspected, the gap near 3 days in the previous plots (V components) is manifest as a relative high in the U component. Nevertheless, the energy level is low in U relative to the V component.

Surprisingly, a moderate coherence is seen from ~3 to 8 days between the U component at D1 (30 m) and Clearwater sea level (Figure 4.5-13a). In most cases, coherence is higher with the Naples gauge. For this season, however, it is suspected that the dominant wind forcing must have been from storms that moved from north to south, so the reflection at the Keys played a significant role. Coherence with the alongshore (v) component is low across the entire frequency range (Figure 4.5-13b). Although not shown, this difference is suspected to be associated with the cross-shelf modal structure.

4.5.3.2.3 Coherence between Moorings F and D

In order to understand the currents on the middle and outer shelf, it is necessary to begin with the currents observed during the 5th deployment (February - April 1984). For the first four mooring periods, the shallowest mooring was at D in a depth of 75 m, which appears to be near the outer limits of obvious wind coherence. As seen in Chapter 2, for the fifth deployment (the beginning of year 2), an additional inshore mooring was installed (Mooring F) in approximately 50-m depth and an additional instrument was added to Mooring D and the instrument depths adjusted. This change provided an improvement in vertical resolution and in understanding flow.

At Mooring F, the V component of currents measured at 17 and 40 m is coherent over the entire frequency range while the U components are coherent in two narrow bands (Figure 4.5-14a). This latter pattern is expected in part if only as a result of a lower signal-to-noise ratio resulting from the lower power content of the cross-shelf (U) velocity component at 40-m depth (U 40 in Figure 4.5-14a). In the higher frequency U versus U coherence band (.2-3 day period), upper and lower layers are approximately 180° (π) out-of-phase as would result from frictional, wind-induced upper and lower layer Ekman transport. In the lower frequency, coherence band for U versus U where offshore forcing or other mechanism may be more important, this phase relation does not occur. Note that in linear systems analysis such as used here, for variance at a given frequency to be coherent, the phase of the two signals being compared should remain the same rather than changing for differing occurrences.

At Mooring D (75 m) during Deployment 5 (Figure 4.5-14b), coherence and phase between U and V velocity components at 17 and 50 m of water showed a pattern similar to that which occurred at 17 and 40 m on Mooring F (50 m) in 50-m water depth. Note, however, that lower frequency U versus U coherence is greater which may result from stronger cross-shelf velocity components or a more consistent forcing mechanism. This latter may be the case of the low-frequency signal results from forcing which originates offshore or beyond the shelf break.

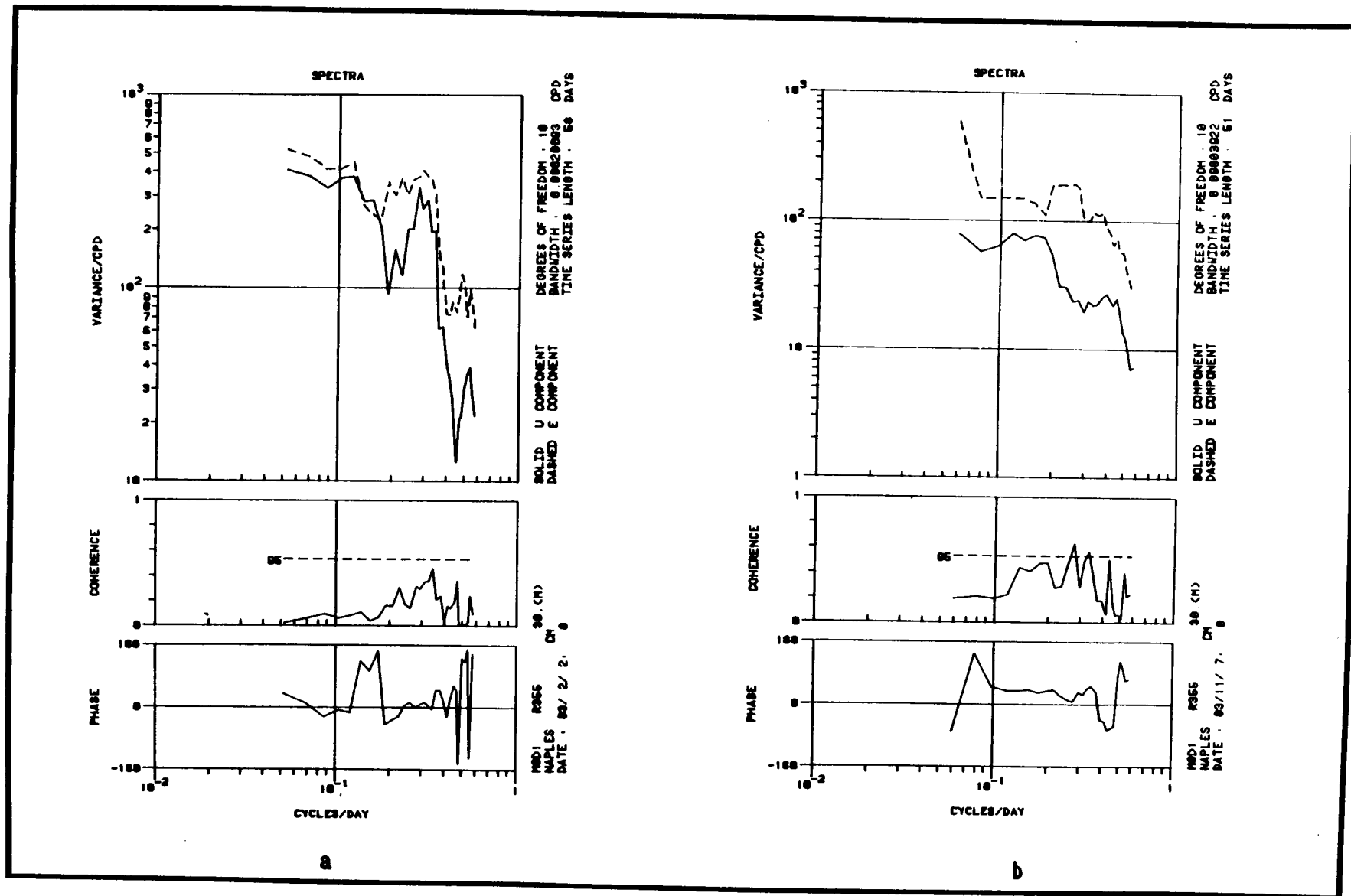


Figure 4.5-12. Cross spectra between the cross-shelf current component at Mooring D, upper current meter (30 m) and sea level at the coast (Naples), adjusted to constant atmospheric pressure. (a) for "winter" season, February - March 1983. (b) for "fall" season beginning 7 November 1983. E = Elevation (tide gauges).

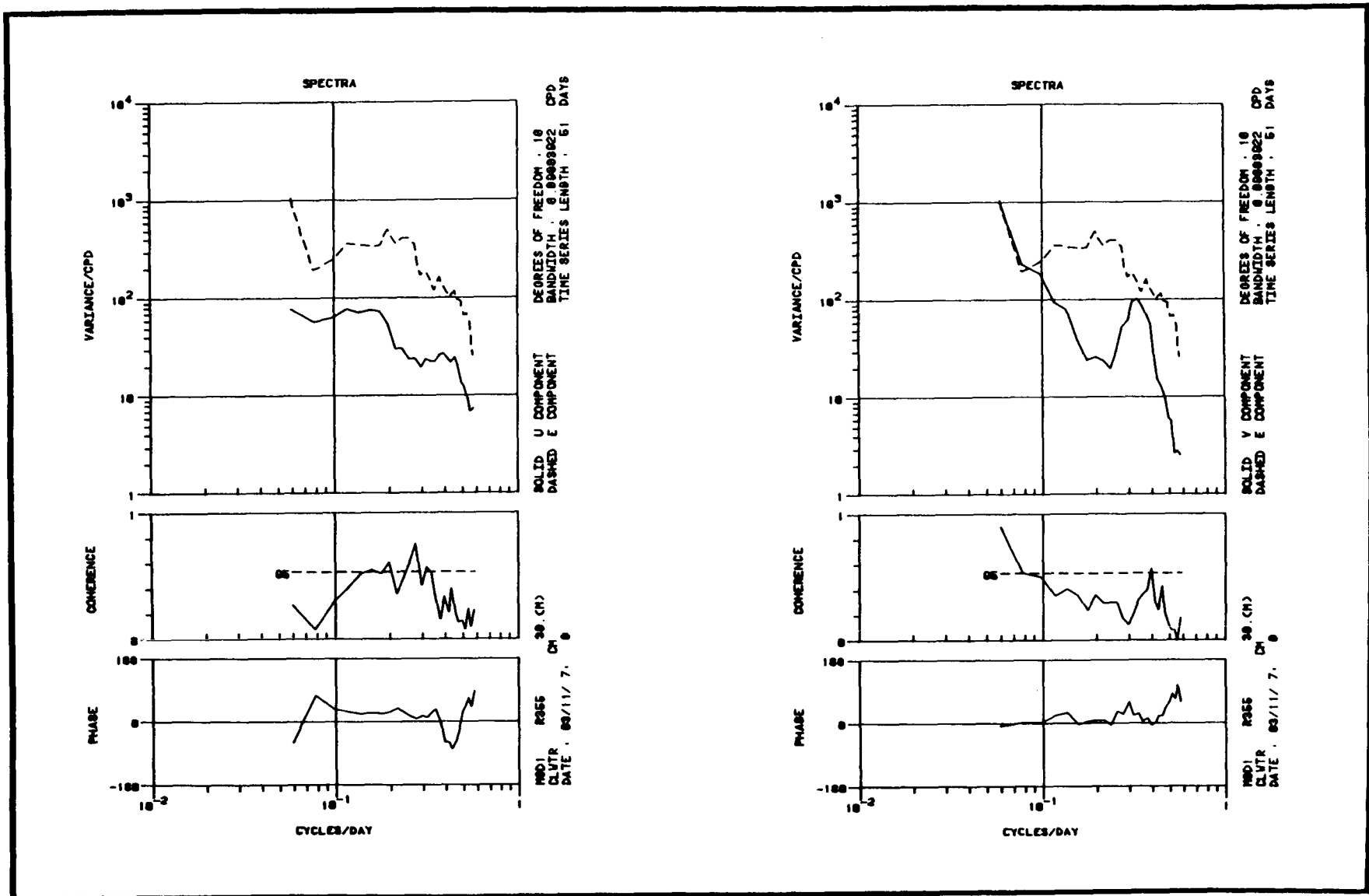


Figure 4.5-13. Cross spectra between the (a) cross shelf and (b) long shelf current component at Mooring D, upper current meter (30 m) and sea level at the coast, but at Clearwater for "fall" season, beginning 7 November 1983. E = Elevation (tide gauges).

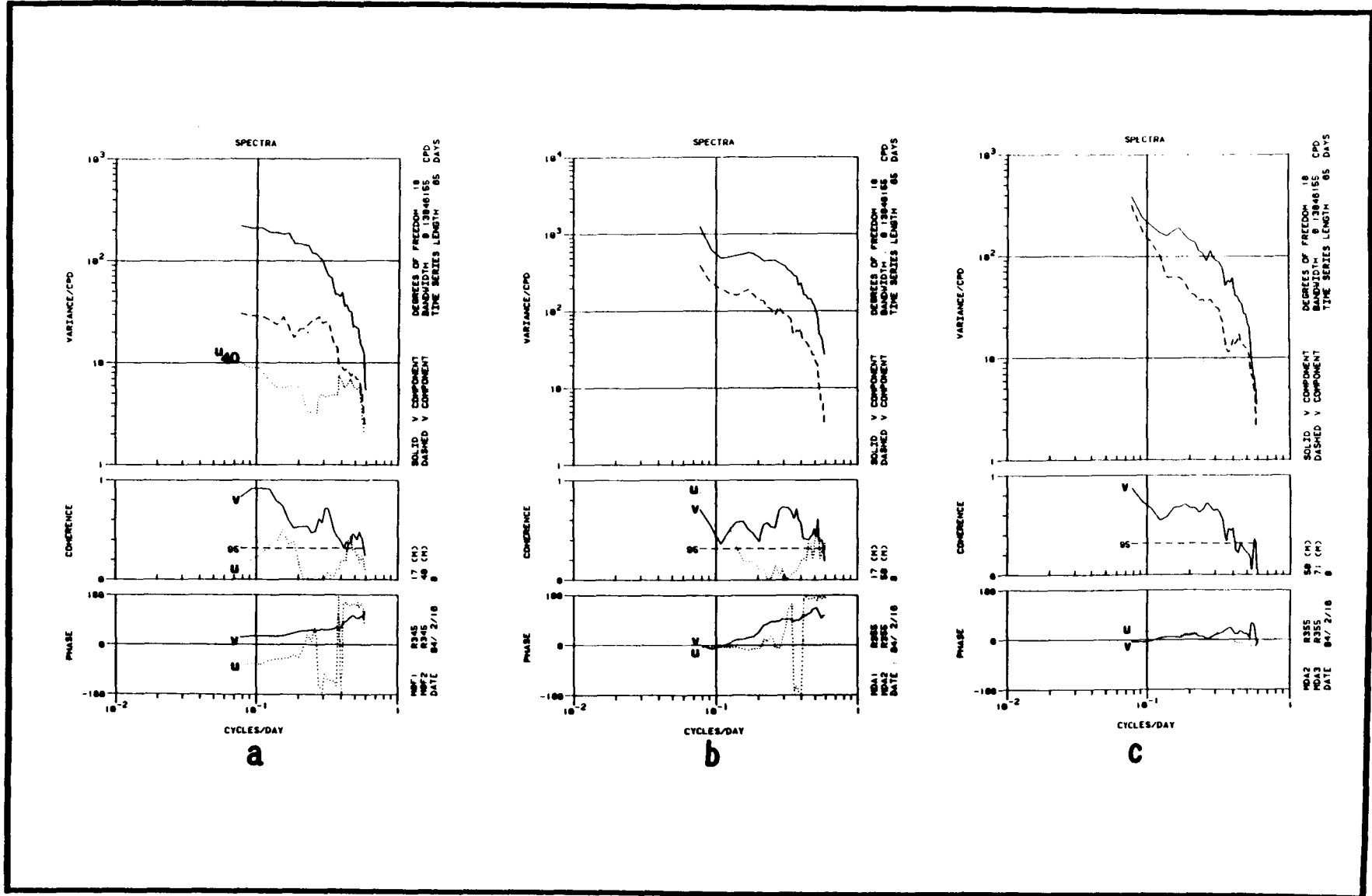


Figure 4.5-14 (a) Spectra, phase and coherence at upper and lower instruments on Mooring F; dotted spectra is for U-component at 40 m, (b) same analysis for Mooring D between the 17- and 50-m instruments, (c) C at Mooring D, between 50- and 71-m instruments. Solid and dashed line spectra are for the shallow and deeper V-components of the instruments being compared. Dotted coherence and phase are between comparable U-components.

During the same measurement interval, alongshelf (V) velocity components at 50 and 71 m on Mooring F were coherent and in-phase over the frequency band containing meaningful variation. Although not significantly coherent, the two U components (U in Figure 4.5-14c) were also in-phase.

Coherence between the V-component of currents at the upper current meters on Moorings DA and F (17 m) is seen in Figure 4.5-15a. Perhaps one of the most encouraging spectra from this experiment, it is a clearly understandable result: the water column at the two locations responds similarly. A comparable result was found using currents at the lower instruments on Moorings DA and F (Figure 4.5-15b). The level of energy at 50 m (DA2) on Mooring DA is similar to that at 17 m (F1) on Mooring F. However, the energy level at 40 m (F2) is lower by almost an order of magnitude from 17 m (F1). Thus the lack of coherence at periods longer than eight days is presumably a result of lower power at Mooring F. (Note that on this diagram in Figure 4.5-15b, the spectral level must increase toward low frequencies at a rate of $1/f$ to remain at a constant level with frequency). Figure 4.5-15c compares U components at the upper instruments. There is some coherence but the signal is weak at F1.

4.5.3.3 Response Between Wind and Currents: Selected Details

In this section cross-spectra are examined in detail and meaningful coherence identified. The shallowest mooring during the first year was at 75-m depth, which is offshore of where currents might be highly coherent with winds. It is more fruitful to compare Mooring D with Mooring F than with winds, but during year 1, F was not in place. Fortunately, during the best of the well-mixed season, the longshore currents are coherent with wind at D2 (60 m), 15 m above the bottom as shown in Figure 4.5-16. The best coherence between winds and currents is found in winter, when wind stress is highest and stratification is least. Coherence and phase are shown for winter 1983; phases are also shown for the other seasons at frequencies where coherence is significant. As in previous discussions, this illustrates that seasonal phases change, presumably as the direction of frontal passages varies. At D1 (30 m), coherence is much lower which could be the result of substantial wave-induced noise at the upper instrument, as the energy level is quite a bit higher, or there could be a substantial amount of baroclinic structure. At the lower current meter (D2), the gain between wind and current is larger than at the upper current meter (D1) by a factor of two near periods of about three and a half days and 10 days.

At Mooring C in 180 m at the shelf break, coherence with the wind is expected to be lower than at Mooring D. In the alongshore component, it is near the 95% confidence level in the three to six day band at the 100-m level (see Figure 4.5-17), and the phase information is consistent enough between the 50-m and 100-m instruments. Coherence is slightly higher for the onshore components since during February - March this wind component was stronger.

On Moorings C and E in 180-m depth at an instrument 1 m above the bottom (C3 and E3 respectively), the noise level is low. During the first deployment there was good coherence between the winds and currents at E in the longshore direction, but there was none at C.

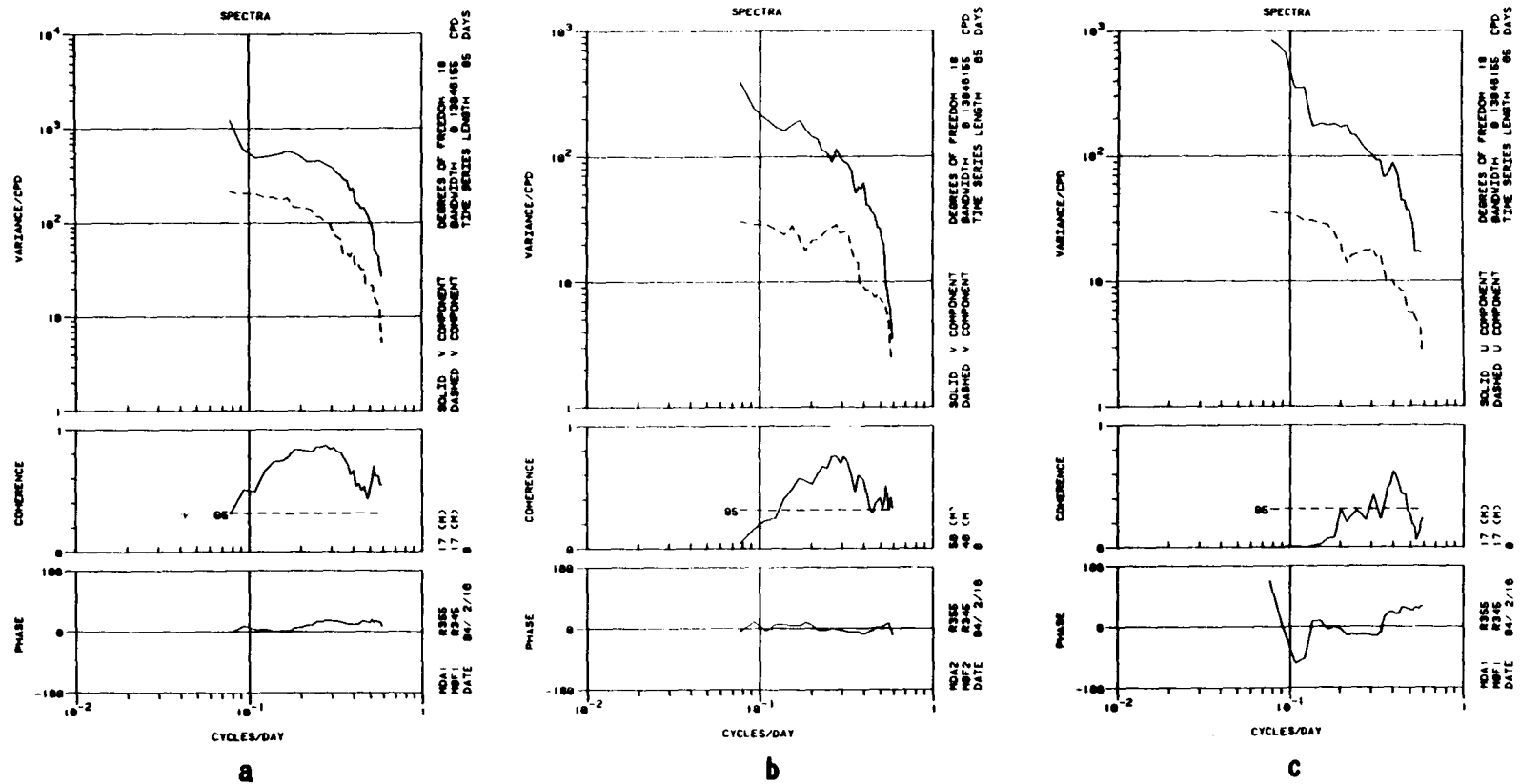


Figure 4.5-15. Cross spectra between long-shelf components at (a) the upper current meters (17m), (b) the lower current meters 40 m, 50 m), and (c) and between cross-shelf components at the upper current meters (17 m), at Moorings D and F for winter 1984 data beginning 16 February. The phase is positive if currents lead at Mooring D.

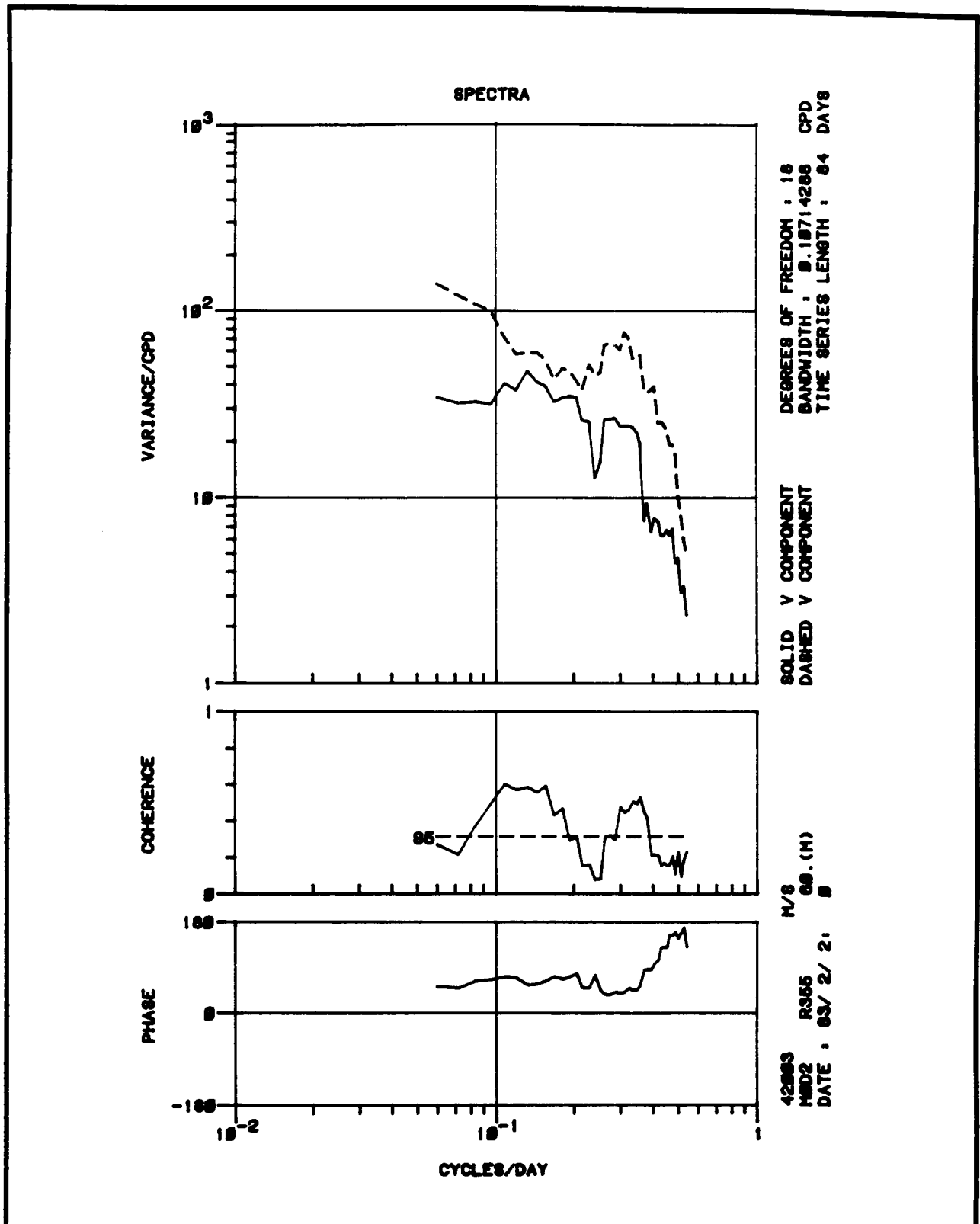


Figure 4.5-16. Cross spectra between longshore wind component at the Met Buoy and currents at 60 m, Mooring D. Coherence is shown for the winter season; phases are shown for "seasons" using the same data divisions as in previous figures. The phase is shown only for frequencies where coherence is above 95% and is positive when the winds lead.

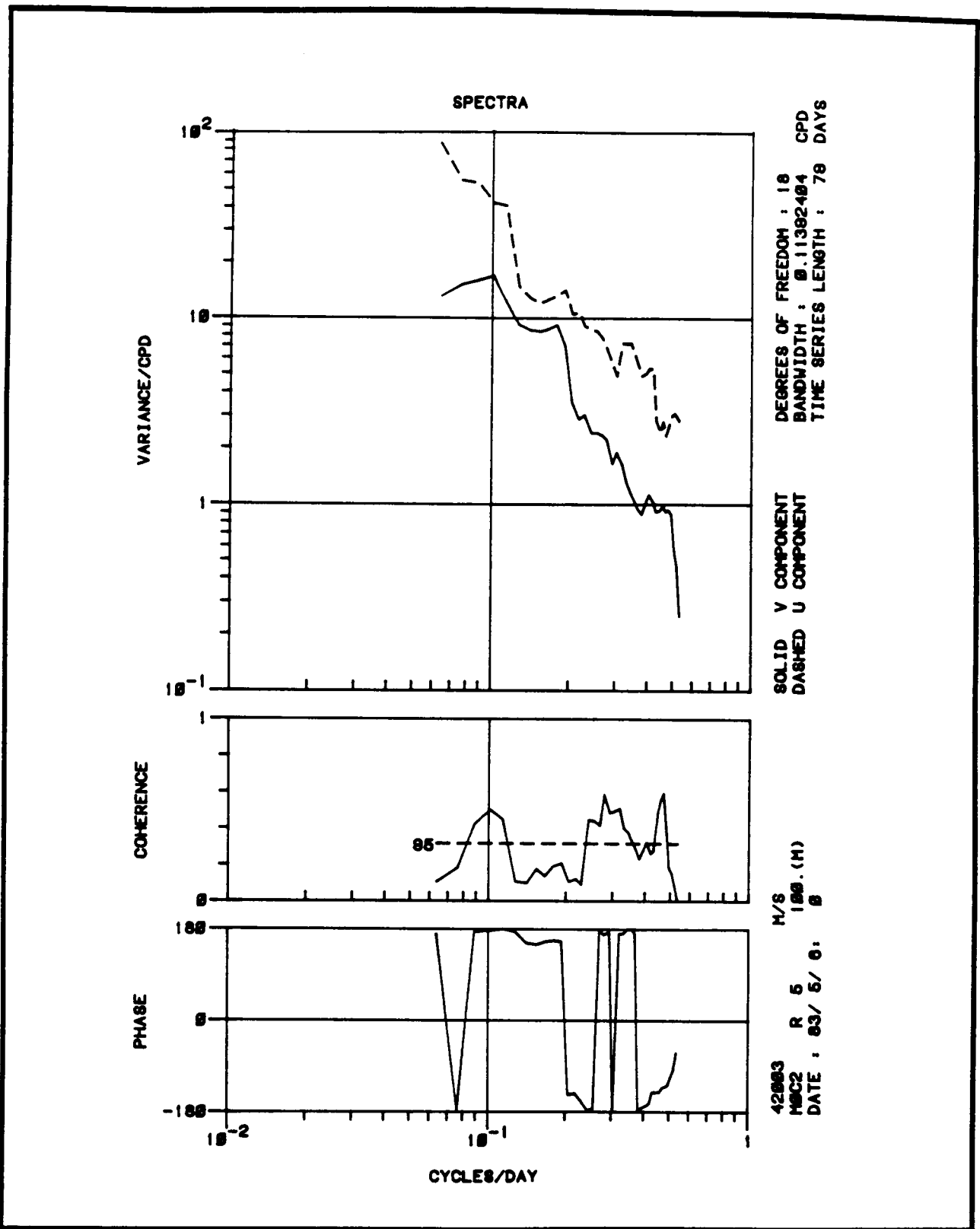


Figure 4.5-17. Cross spectra between longshore wind component at the Met Buoy and the cross-shelf currents at 100 m, Mooring C. The amplitude is shown for Mooring E for comparison. Coherence is shown for the spring season; phases are shown only between the winds and currents at C and for frequencies where coherence is above 95%.

4.5.3.3.1 Response of Currents to Winds: Second Deployment, May - July 1983

Cross spectra between the buoy winds and the shallow Mooring D (in 75 m) show that coherence is lower than it was previously. The winds, however, are weaker by about a factor of three in the 5-10 day band and by nearly an order of magnitude near three days.

At Mooring C the only coherence with wind in the normal wind band of less than 10 days is in the onshore direction. In the alongshore, coherence (even if marginal) is found at periods of 10 to 16 days. This result is even more surprising since the wind power is less during the second deployment period. Coherence with wind at Mooring E is lower than at C. In the longshore components, marginal coherence (near 90%) is found at 14-16 days at the upper instrument (50 m).

Interestingly, the coherence is much higher between the V winds and the U currents at mid-depth (100 m) at C and E (Figure 4.5-17). The nearly constant 180° phase shift at C suggests an Ekman-layer-like response where northerly (positive) winds induce offshore (negative) currents. Thus the 100-m instrument is in the return flow, not the directly-forced layer.

4.5.3.3.2 Response of Currents to Winds: Third Deployment, August - October 1983

During the third deployment the water column was stratified. At Mooring D, some coherence is found at the lower instrument in the alongshore direction between the wind and currents in the normal wind band near six days and three days. As seen earlier, the currents lag the winds slightly near six days, but the phase shift goes to 180° for periods shorter than three days at this lower meter (60 m in 75-m depth). During the first (winter) deployment, the wind stress was much larger than during the spring. At the upper current meter (30 m), almost no coherence is found with wind. There is, however, a small amount of coherence between across-shelf winds and currents for periods between 2.5 and four days.

At the upper current meter (50 m) on Mooring C, coherence between alongshore currents and winds occurs at near four days. The region of coherence near four days in V is associated with a small region of V-component energy that is not present in the U component, presumably related to a wave pattern associated with the modal structure set up on the shelf.

The same kind of result is seen at the lower instrument (100 m) on Mooring C, with higher coherence between the across-shelf (U) and the alongshore (V) wind components. The V current has about the same energy level. The cross spectra between the U wind and U currents show less coherence. At the bottom current meter on C, there is a narrow band of alongshore coherence near five days, just as at Mooring D. In the U component, there is coherence at lower frequencies and a lower energy level at E. In the V component, however, the energy level is much higher at E, but no coherence with wind is found.

At the upper current meter at Mooring E, there is marginal alongshore coherence with wind from 3.5-7 days. At the near-bottom instrument, some coherence is found near 5-7 days and near 2.5 days.

4.5.3.3.3 Response of Currents to Winds: Fourth Deployment, November 1983 - January 1984

Winds at the offshore meteorological buoy are not available for this period, so the winds from Fort Myers, Florida, are used. This should have little effect since the two wind records are highly coherent and nearly in-phase. Highest coherences between wind and currents at Mooring D were between the U currents and V winds. There is little overlap between the periods at which the two instruments are coherent, although the phases seem stable even for lower coherence. At Mooring C, the only coherence is found at periods shorter than 3 days. Coherence is higher at the 100-m instrument, but the current energy level is greater by about six times at the upper meter. The U component of current is coherent over a wide range at the lowest instrument, but higher coherence is found with the V winds in a narrow band. At Mooring E, coherence is found at all three instruments in the V,V calculation.

4.5.3.3.4 Wind Forcing at Mooring D: Summary

It is moderately instructive to compare the spectra from the first four deployments. For the normal wind band near five days there is a bit of coherence that is more or less consistent from one deployment to the next. However, there is just not much coherence. At the band near three days, the phase shift is about the same for the first and fourth deployments, in winter conditions. For the two deployments in between, there appears to be a difference of about 180°, presumably resulting from stratification.

4.5.4 Coherence Across the Shelf: Tide Gauge to the Shelf Break

Coherence between fluctuations in pressure at the shelf break and coastal sea level at Naples and Clearwater is shown in Figures 4.5-18a-c (the coastal gauges have been adjusted to uniform atmospheric pressure). The winter (1983) deployment at Mooring C (Figure 4.5-18a) shows high coherence between currents and sea level at Naples, for periods of 9-16 days and approximately two to four days, suggesting that these motions are coherent across the shelf. Where coherence is highest, Figures 4.5-18a,b show 90° phase shift and Figure 4.5-18c shows 45°. A 90° phase difference means that when one instrument is recording its mean value, the other is recording a maximum value, for a large pressure difference. Figure 4.5-18b again shows the phenomenon that in the wind band (near five days) coherence is higher at the northern mooring (E) while no coherence is found at C. Presumably this is the effect of reflections at the keys, but such comments are very speculative at this writing. At E this coherence remains high in the fall season also (Figure 4.5-18c).

Figure 4.5-19 shows coherence and phase between alongshore currents at E at 179 m and the winds at Tampa. Despite the loss of the data during which best coherence is found, this figure shows fairly high coherence across an encouragingly broad range of frequencies.

4.5.5 Mean Values Over Two Years: 1983-1984

It is of considerable interest to know what the mean of the observed flow field is and to determine how reliable and stable this estimate is. To

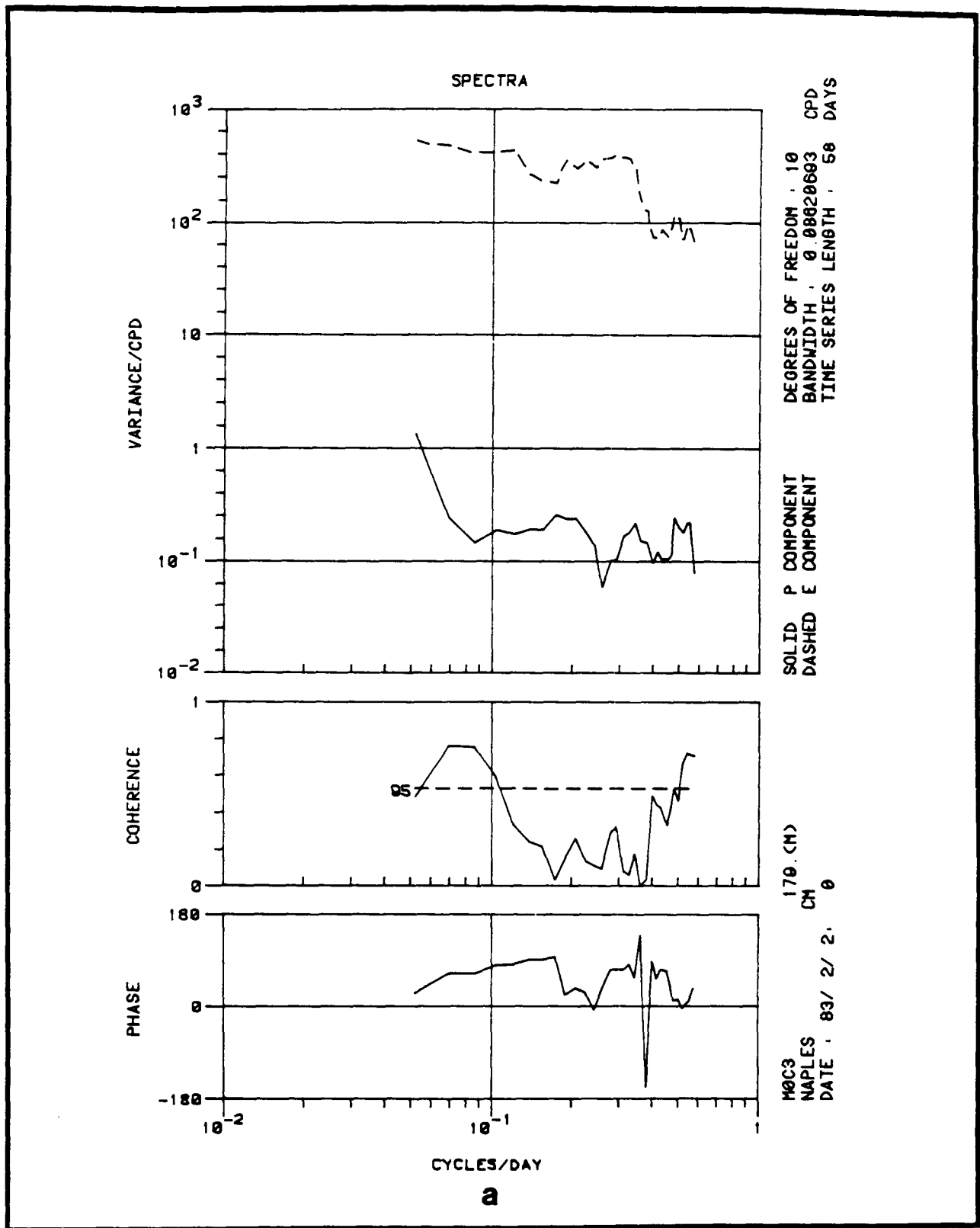


Figure 4.5-18. (a) Cross spectra between bottom pressure at Mooring C (179 m) and sea level at Naples, FL, for "winter" data, beginning 2 February 1983, for a 58-day record. The sea-level spectrum is shown dashed, and has been adjusted to constant atmospheric pressure. Phase is positive if bottom pressure at C leads.

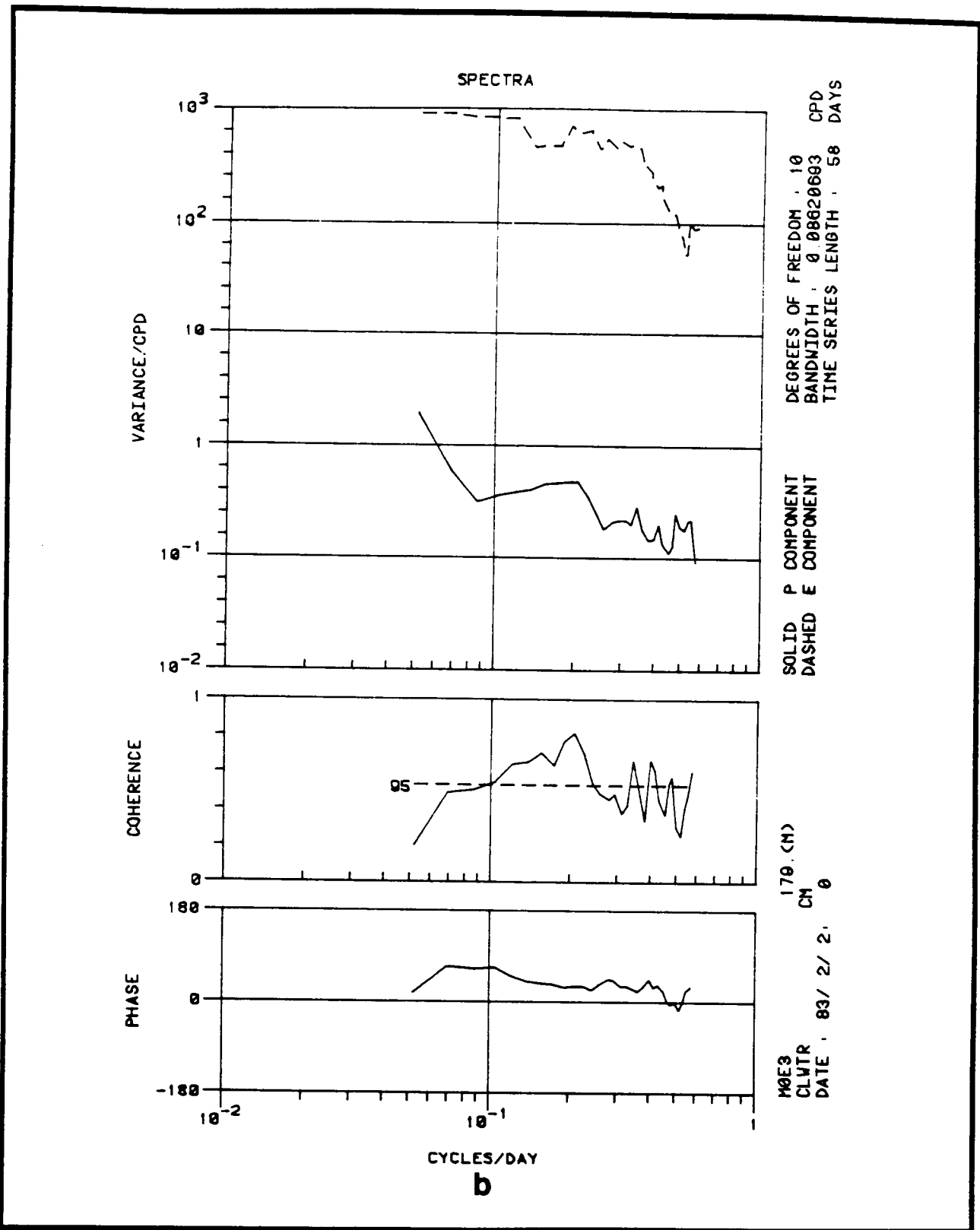


Figure 4.5-18 (continued)

(b) Cross spectra between bottom pressure at Mooring E (179 m) and sea level at Clearwater, FL, for "winter" data, beginning 2 February 1983, for a 58-day record. The sea-level spectrum is shown dashed, and has been adjusted to constant atmospheric pressure. Phase is positive if bottom pressure at E leads.

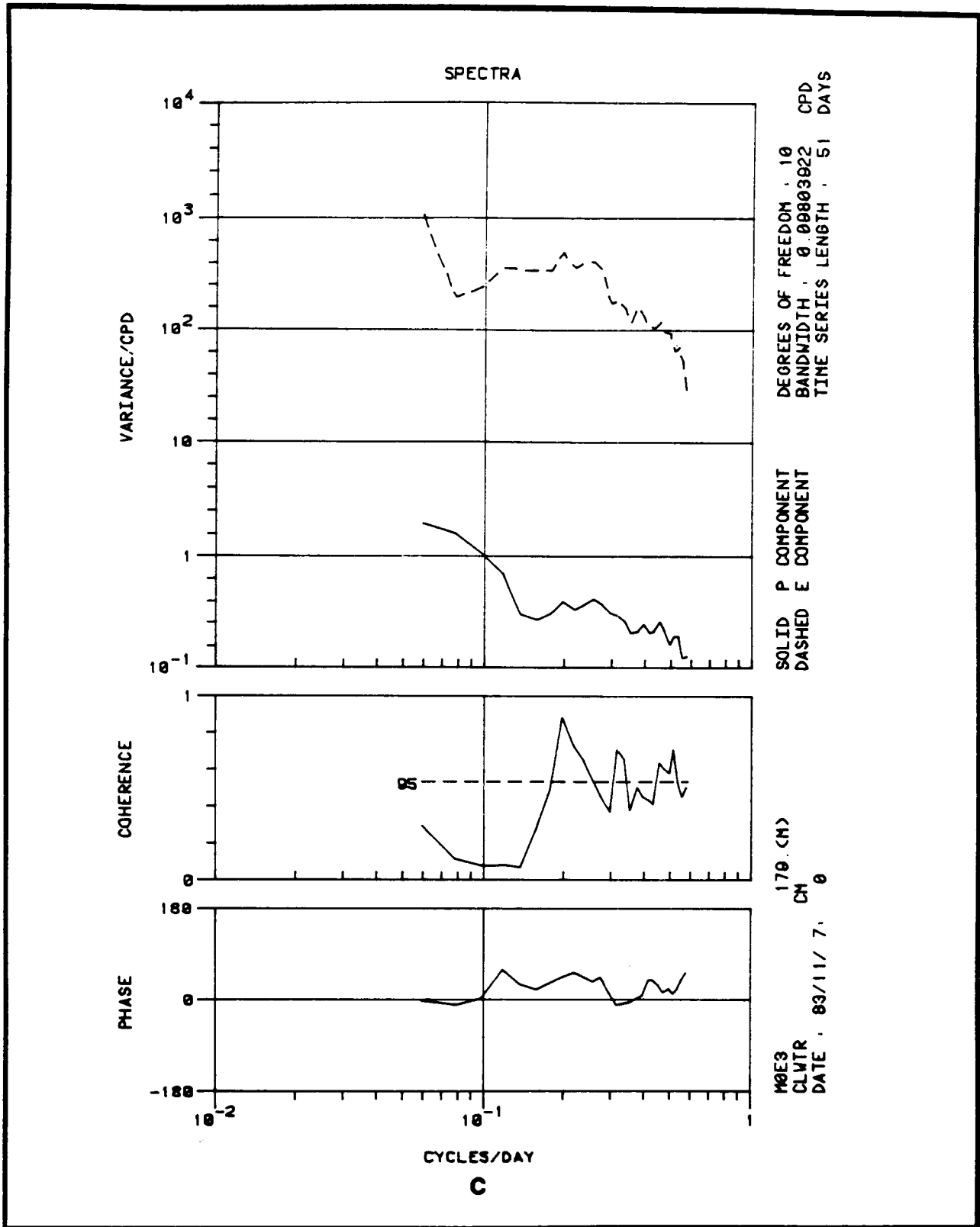


Figure 4.5-18
(continued)

(c) Cross spectra between bottom pressure at Mooring E (179 m) and sea level at Clearwater, FL for "fall" data, beginning 7 November 1983, for a 51-day record. The sea-level spectrum is shown dashed, and has been adjusted to constant atmospheric pressure. Phase is positive if bottom pressure at E leads.

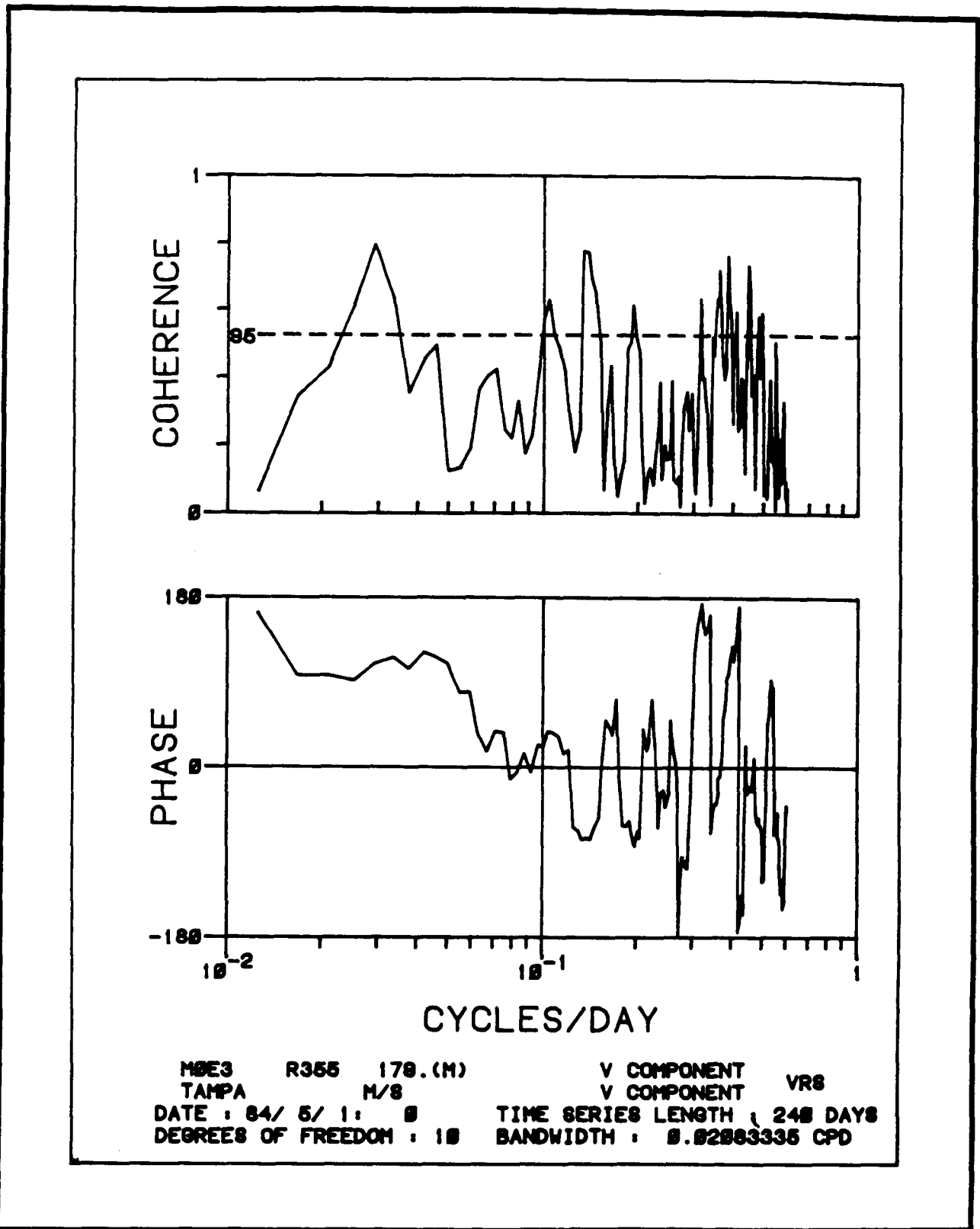


Figure 4.5-19. Cross spectra between currents 1 m above the bottom at Mooring E (179 m) and winds at Tampa, FL, for 8 months of data, beginning 1 May 1984 for the long-shelf components. Phase is positive if bottom currents at E lead.

emphasize the variability of the flow, Figures 4.5-20 and 4.5-21 show scatter-plots of the 40-h low-passed daily values from the upper instruments at Moorings C and D at 50 m and 30 m, respectively, during the first deployment. Although it is clear that a mean can be computed, it is equally clear that the mean is small and "buried" in the noise. It is of some concern, then, to determine how long the records need to be in order to secure a reliable mean. Available data suggest that the two year records provide good estimates of the mean.

The mean value at the upper instrument on Mooring C changed over the course of the first two years (Figure 4.5-22). For each three-month deployment the mean is shown (pluses) together with the accumulating long-term mean. The standard error (two standard deviations) of the mean is also shown. The total variance of the signal is crucial in estimating the error of the mean. The calculation here is done using the method described by Bendat & Piersol (1966), assuming that the variability is concentrated at periods longer than six days.

What is not known, in general, is whether the process being observed will change significantly if examined during other periods of comparable length. In Figure 4.5-22 it is clear that the last two deployments gave values that were far outside anything that would have been expected on the basis of the previous 18 months of data. It is disconcerting to find such a large fraction of the total variance in the record contributed by only a few mooring emplacements. Nevertheless, the mean value appears to be stable after 24 months of data.

Table 4.5-2 shows a compilation of means over the available record lengths for the moorings on the shelf. The moorings off the shelf are so affected by the presence or absence of the Loop Current that a similar calculation is of little value.

Results of these calculations show that from Mooring F to the edge of the shelf the mean flow is to the south, with the exception of the bottom instruments at the shelf break. These are positions which would be the most likely to differ from typical shelf values.

At the edge of the shelf Moorings C and E show an onshore directed mean flow at mid-depth. The mean is also onshore at the upper instrument on D and offshore below; the means are barely at two sigma reliability, but the pattern is consistent.

The mean values at Mooring F are too small to be reliable. The record there is only half as long. The problem appears to be not that the variability is larger than at the other instruments, but that the mean values are small.

4.5.6 Variability at Moorings A and G

The currents at Mooring A have a bimodal structure depending on whether the Loop Current has meandered that far to the east, close to the edge of the continental shelf. During February 1983, shortly after the mooring program was begun, Mooring A appeared to be well within the Loop Current. The U and V velocity components at the 172-m instrument both exceeded 40 cm s^{-1} (with flow toward the southeast). However, the V component was just as strong in the

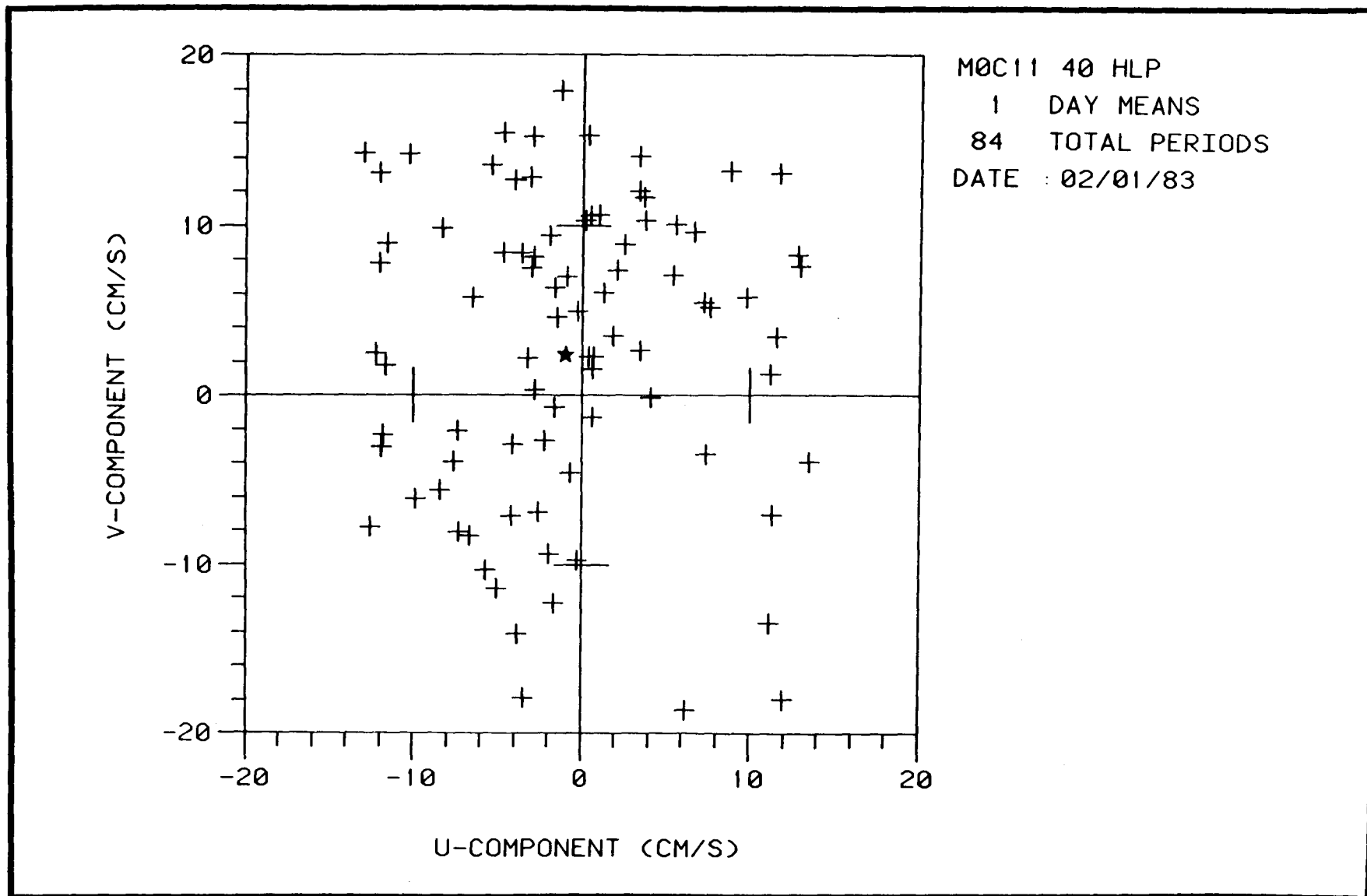


Figure 4.5-20. Scatter plot of velocity (U, V components) at the upper current meter (50 m) at Mooring C for the first emplacement, beginning 1 February 1983, for 84 days. The data have been treated with a 40-hr low-pass filter and sampled once a day. The small star near the center of the figure ($U = -0.92$; $V = 2.66$) shows the mean over the data.

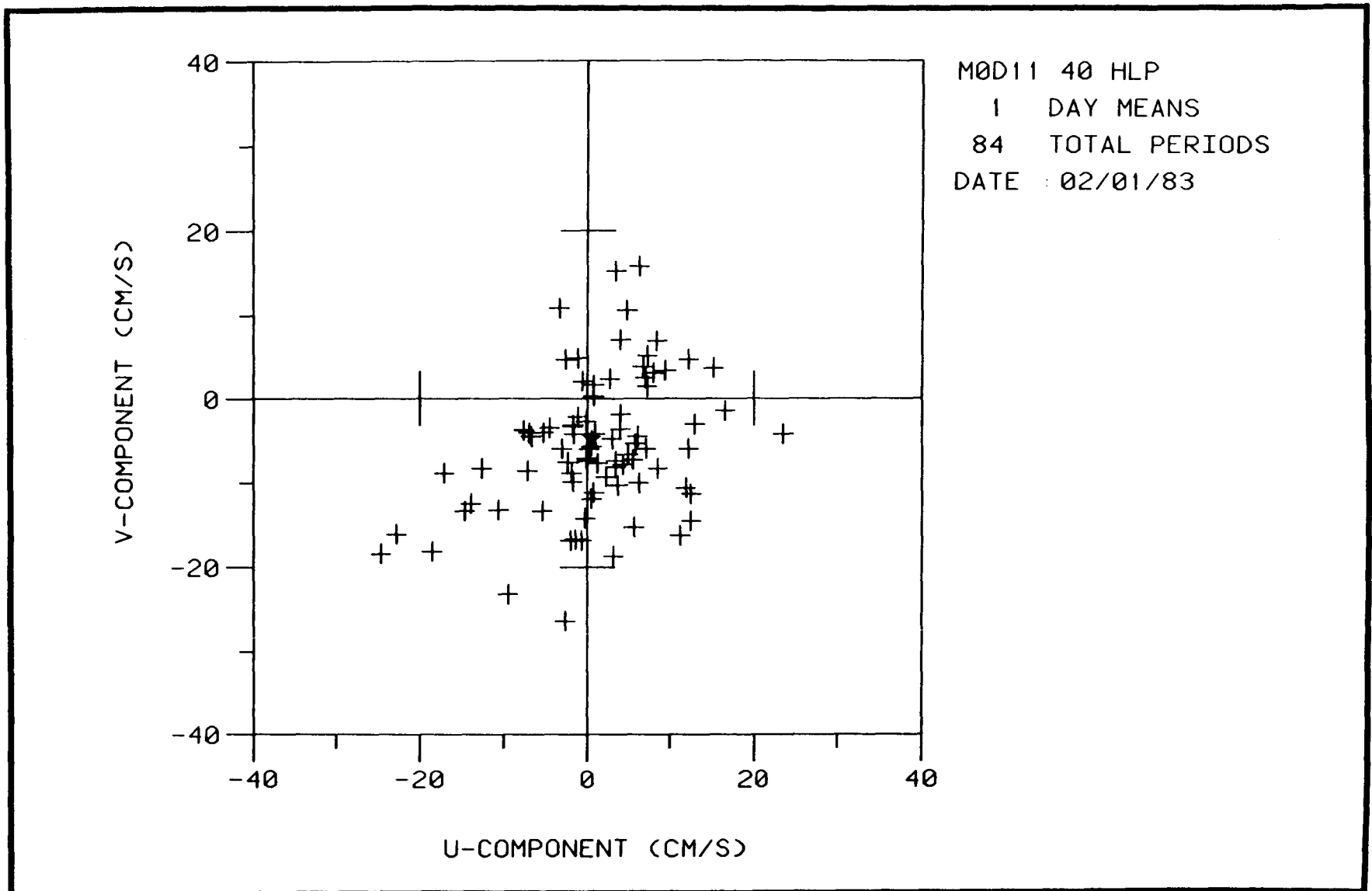


Figure 4.5-21. Scatter plot of velocity (U, V components) at the upper current meter (30 m) at Mooring D, for the first emplacement, beginning February 1983, for 84 days. The data have been treated with a 40-hr low-pass filter and sampled once a day. The small star near the center of the figure ($U = .46$; $V = -5.68$) shows the mean over the data.

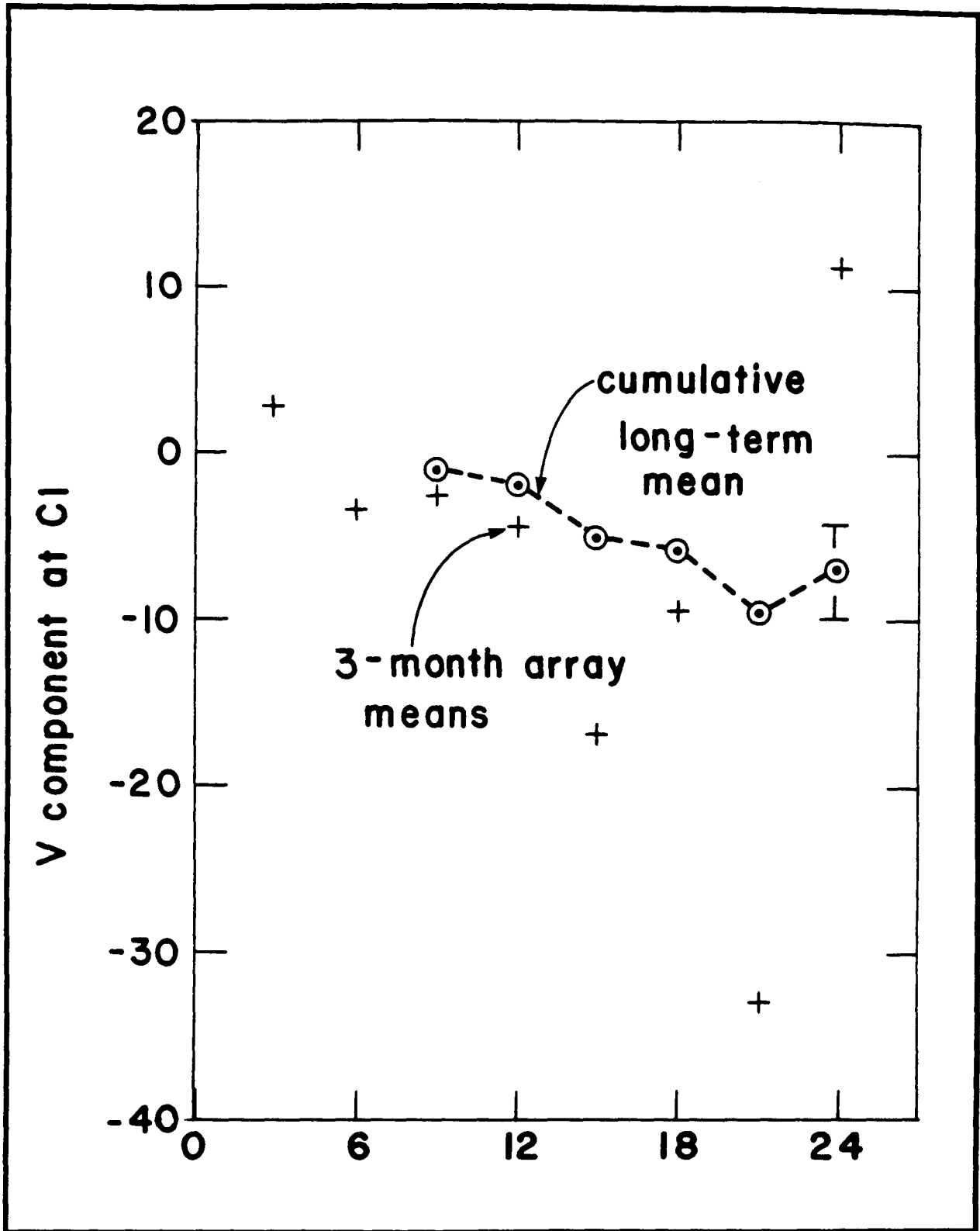


Figure 4.5-22. A comparison between mean values computed from individual 3-month mooring records (plus signs) and the cumulative mean from the entire record up to that time for long-shelf component, upper current meter (50 m), Mooring C.

Table 4.5-2. Compilation of means over the available record lengths for the shelf moorings.

Instrument	Orientation of V Component (°+)	Depth(m)	U	V
C1	+5°	50	3.0 (1.5)	-7.0 (2.7)
C2	+5°	100	1.9 (.9)	-5.5 (1.8)
C3	+5°	179	-.4 (.6)	1.9 (.8)
D1*	+355°	17	.8 (.8)	-2.8 (1.4)
D2*	+355°	50	-1.0 (.6)	-2.2 (1.2)
D3*	+355°	71	-.8 (.8)	-1.1 (1.3)
E1	+355°	50	2.0 (1.3)	-6.3 (7.8)
E2	+355°	100	0.4 (.9)	-3.2 (1.2)
E3	+355°	179	0.8 (.4)	+1.5 (1.0)
F1*	+345°	17	-.4 (.2)	-.2 (.8)

* These instruments were in place for only one year.

V = Along isobath

U = Across Isobath (directed onshore)

opposite direction a month later when a large meander passed across the mooring. Both these events are clearly observable in the satellite data (See Section 4.5.8).

A promising method for determining the horizontal position of the Loop Current might be by examining the temperature at a depth within the main thermocline from mooring records. The temperature at 172 m was greater than 18°C when the edge of the Loop Current had meandered to the east. The temperature then dropped to a minimum of 14°C when the flow was to the north. Likewise, the currents at Mooring G seem to be either high or low, depending upon whether the Loop Current is present.

One of the most spectacular events seen in the data occurred during late July - August 1984 when no satellite SST imagery was available. Figures 4.5-23a-c show stick plots at the deeper current meters at Mooring G and all instruments at C and D. Under normal flow conditions, the Loop Current would be expected to flow to the south, or out, over Mooring G. However, it appears that at the beginning of the record shown in Figure 4.5-23a, the Loop Current at G was going to the north. By day 260 the flow was again to the South. Figure 4.5-23b shows that the currents at the shelf break (Mooring C) were strong (nearly 100 cm sec⁻¹) to the south, when the currents at G were to the north. The obvious inference is that the Loop Current had meandered enough to the east that the inflowing part was over G, and the return flow was firmly against the continental shelf and slope. Note that it is just over 100 km between Moorings G and C. The currents at D reached approximately 40 cm s⁻¹ at both upper current meters. Currents at A were to the south from day 220 to 280. They reached 50 cm sec⁻¹ at 400 m near day 240.

Variations at Mooring A usually have seemed to be in phase vertically, with the exception of the occasional finding of a northward flowing deep counter current. Figures 4.5-24a,b show examples of the high coherence between currents and temperature at 172 m and 400 m. Coherence is high in the V (along-shelf) component from periods of five days out to 16 days; in U there is coherence at periods as short as three days. The phase change between 172 and 400 m is small, but coherence between temperature fluctuations is high at approximately four days and longer. Coherence remains high, between 400 m and 738 m, particularly in the U component. Coherence is high in the V component only for periods >10 days (see Figure 4.5-25). Even as deep as 1100-1600-m there is significant coherence between V components at periods near three days, suggesting that the wind-forced motions may extend to this depth, although at reduced magnitudes.

The variability at Mooring G is a great deal like that at Mooring A. Coherence is significant across the thermocline at periods longer than eight days, and high at periods of approximately two weeks or longer (Figure 4.5-26). The phase shift is small, considering stratification, only ~30°. A comparison between 1565 m and 2364 m for two mooring emplacements yielded quite similar results (Figures 4.5-27a-d). Because there is still an ample signal at these depths, but less noise (presumably from surface waves), the coherence looks remarkably high. A similar result between the deepest instruments, 2364 m and 3174 m, is seen in Figures 4.5-28a-d. Figure 4.5-29 shows that coherence in the V-component is significant across the total column, from 357 m to 3174 m, with small phase change, almost all of which occurred above 1500 m.

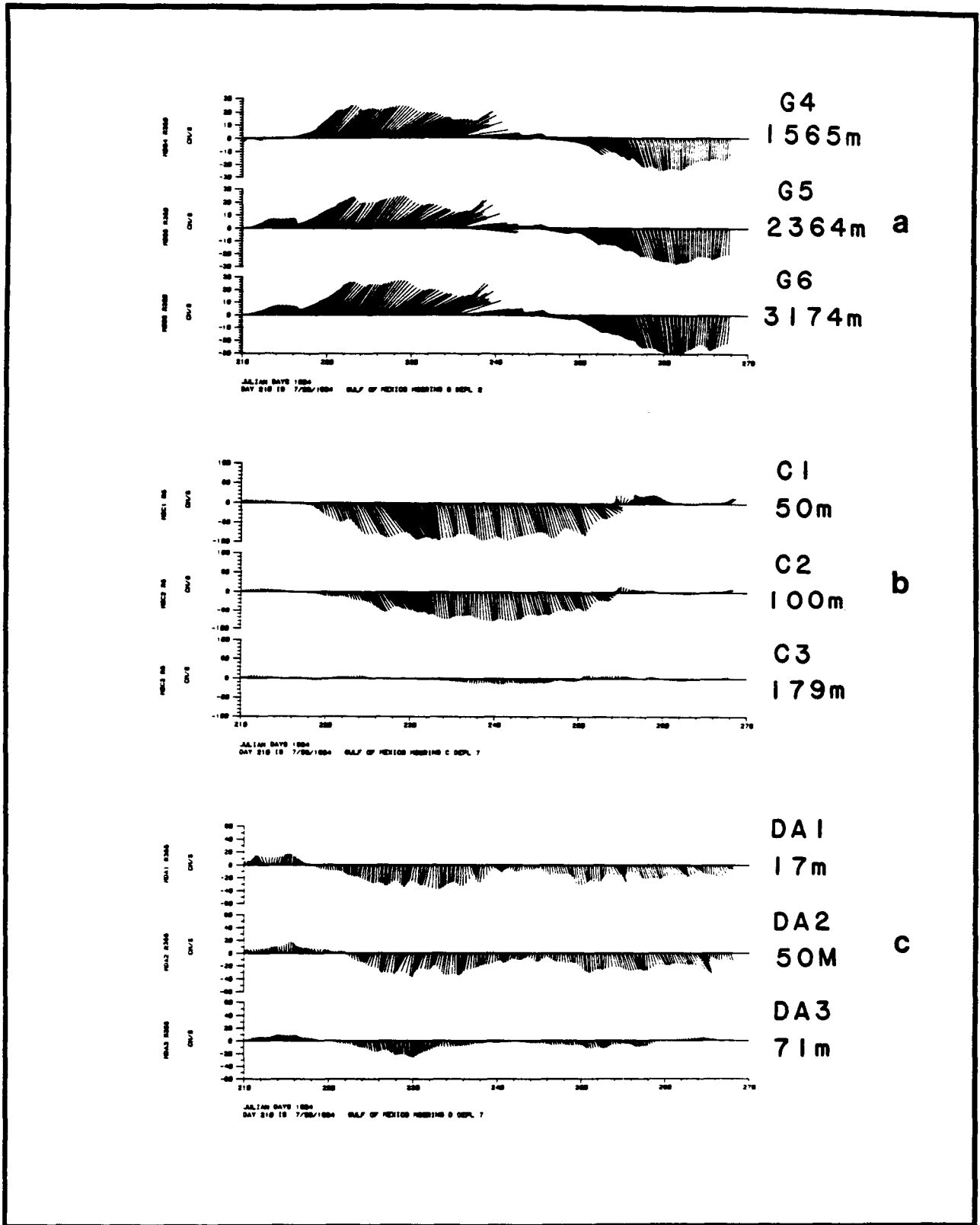
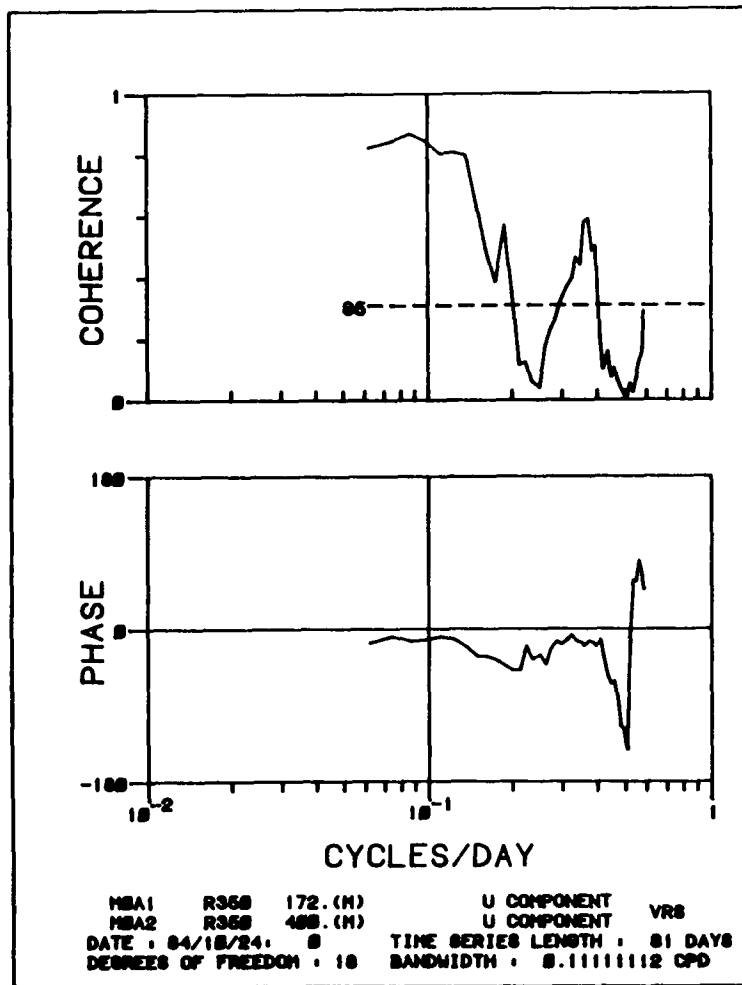
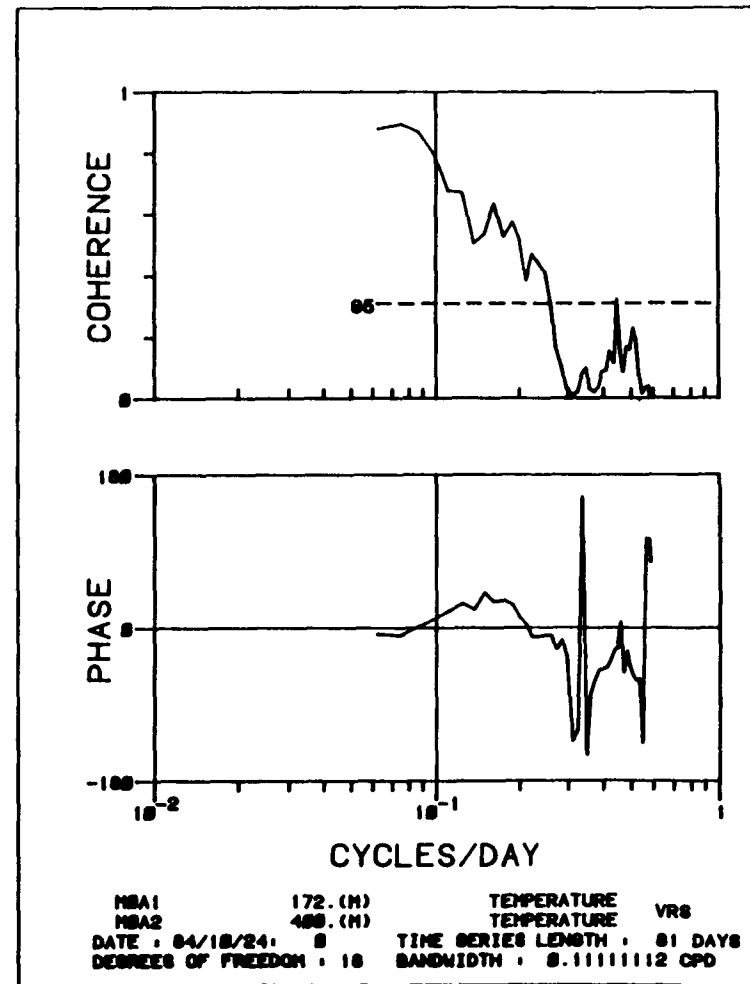


Figure 4.5-23. (a) Stick plots of currents at Mooring G (in 3200 m), (b) at Mooring C (in 180 m), (c) at Mooring D (in 75 m), summer 1984. The long-shelf direction is up in the figure.



a



b

Figure 4.5-24. Vertical coherence at Mooring A, (a) between currents at 170 m and 400 m, in the long-shelf component, (b) between temperature measured at 170 m and 400 m.

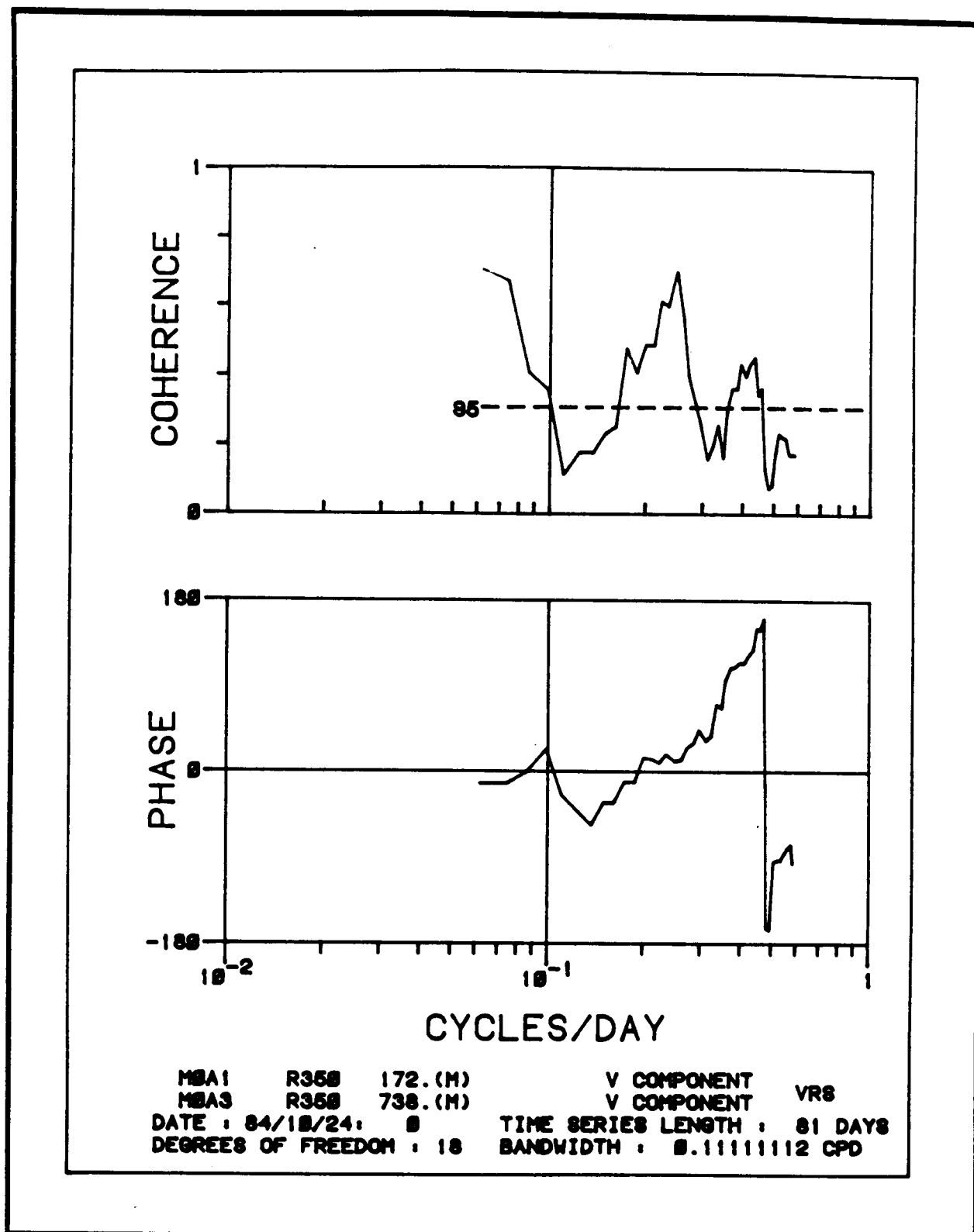


Figure 4.5-25. Vertical coherence at Mooring A between currents at 400 m and 740 m in the long-shelf component.

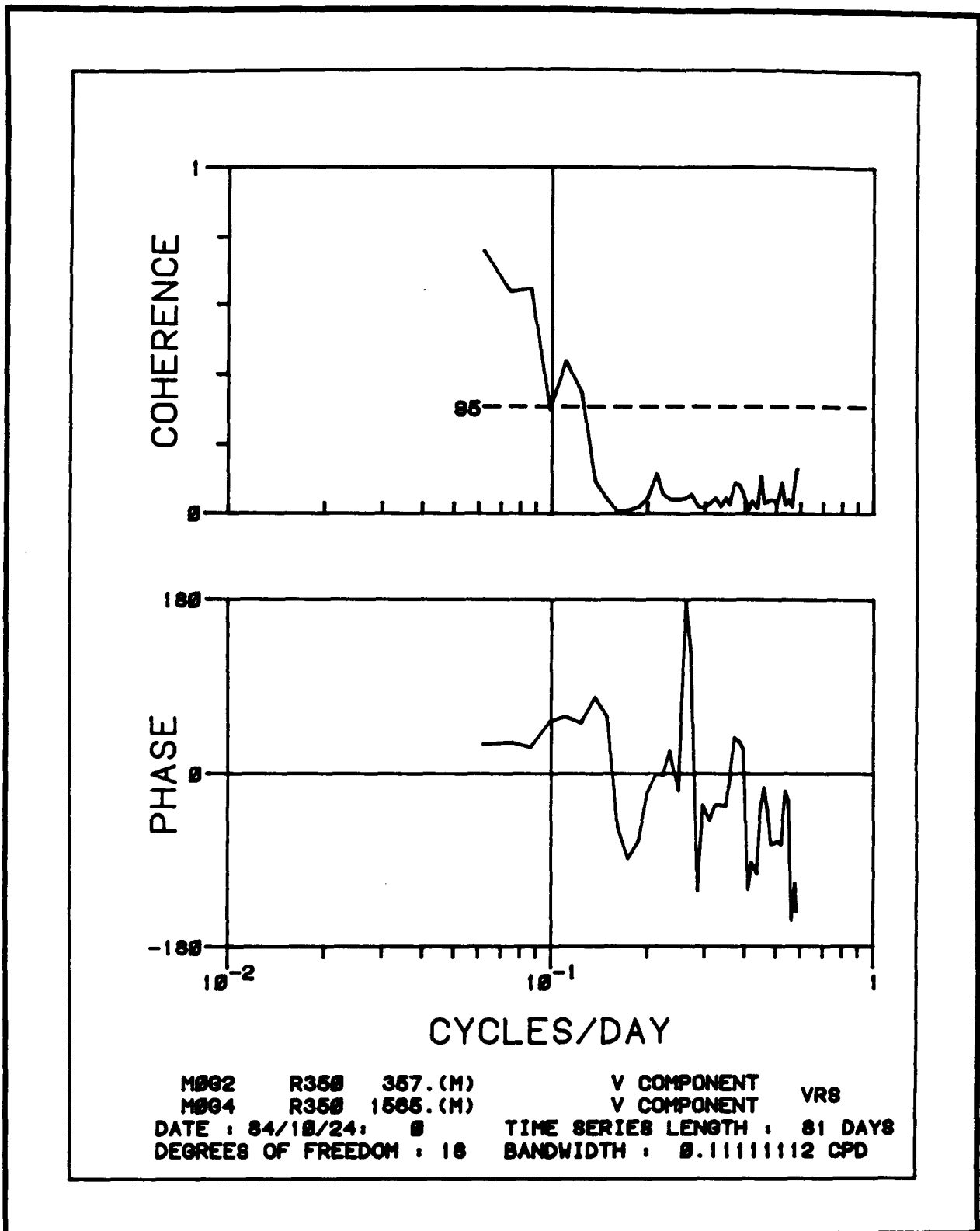


Figure 4.5-26. Vertical coherence at Mooring G between currents at 357 m and 1565 m in the long-shelf component.

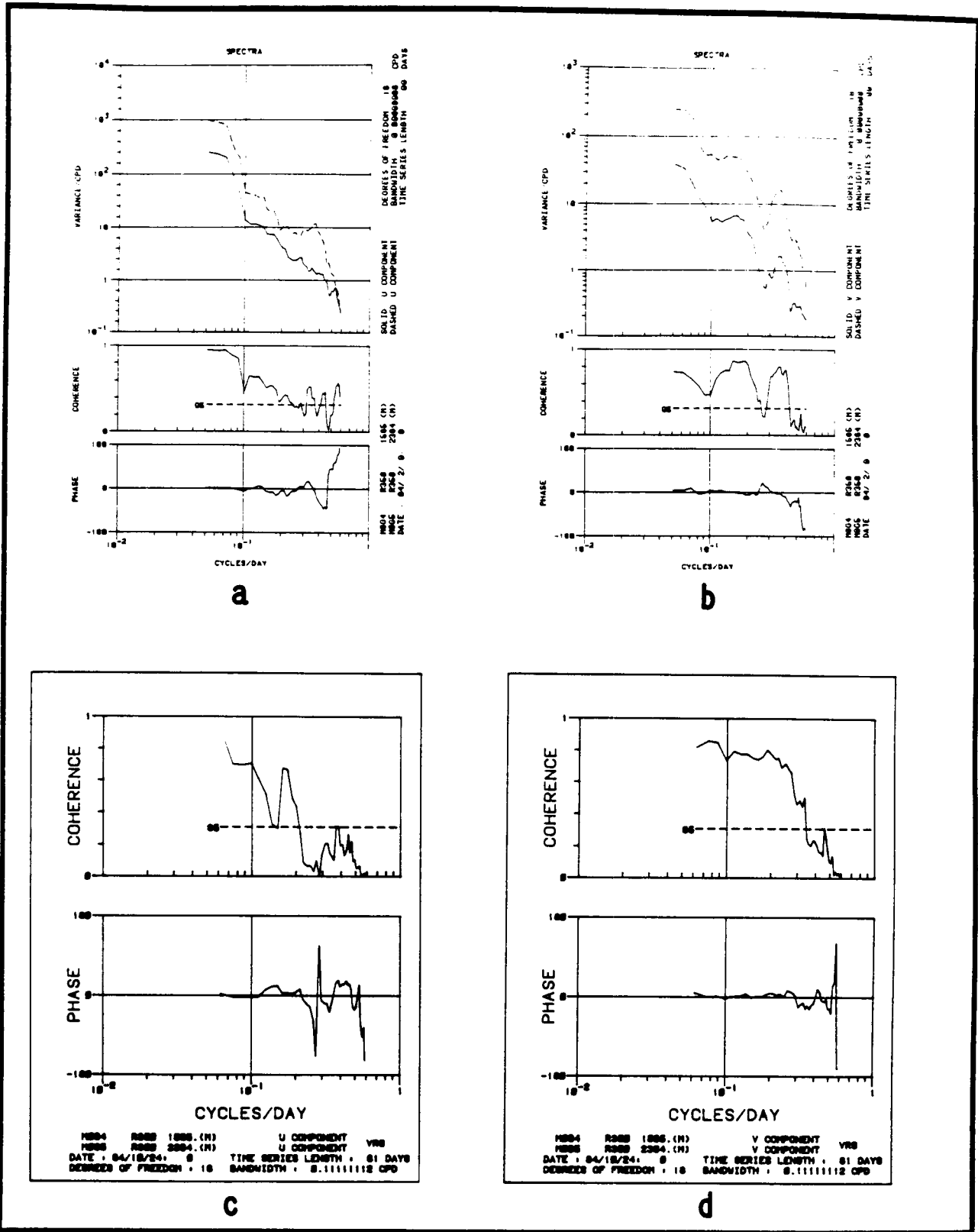


Figure 4.5-27. (a) Vertical coherence of U components at Mooring G between currents at 1565 m and 2364 m for the period beginning on 9 February 1984. (b) for V components, (c) for U components for the period beginning 24 October 1984, (d) for V components for the period beginning 24 October 1984.

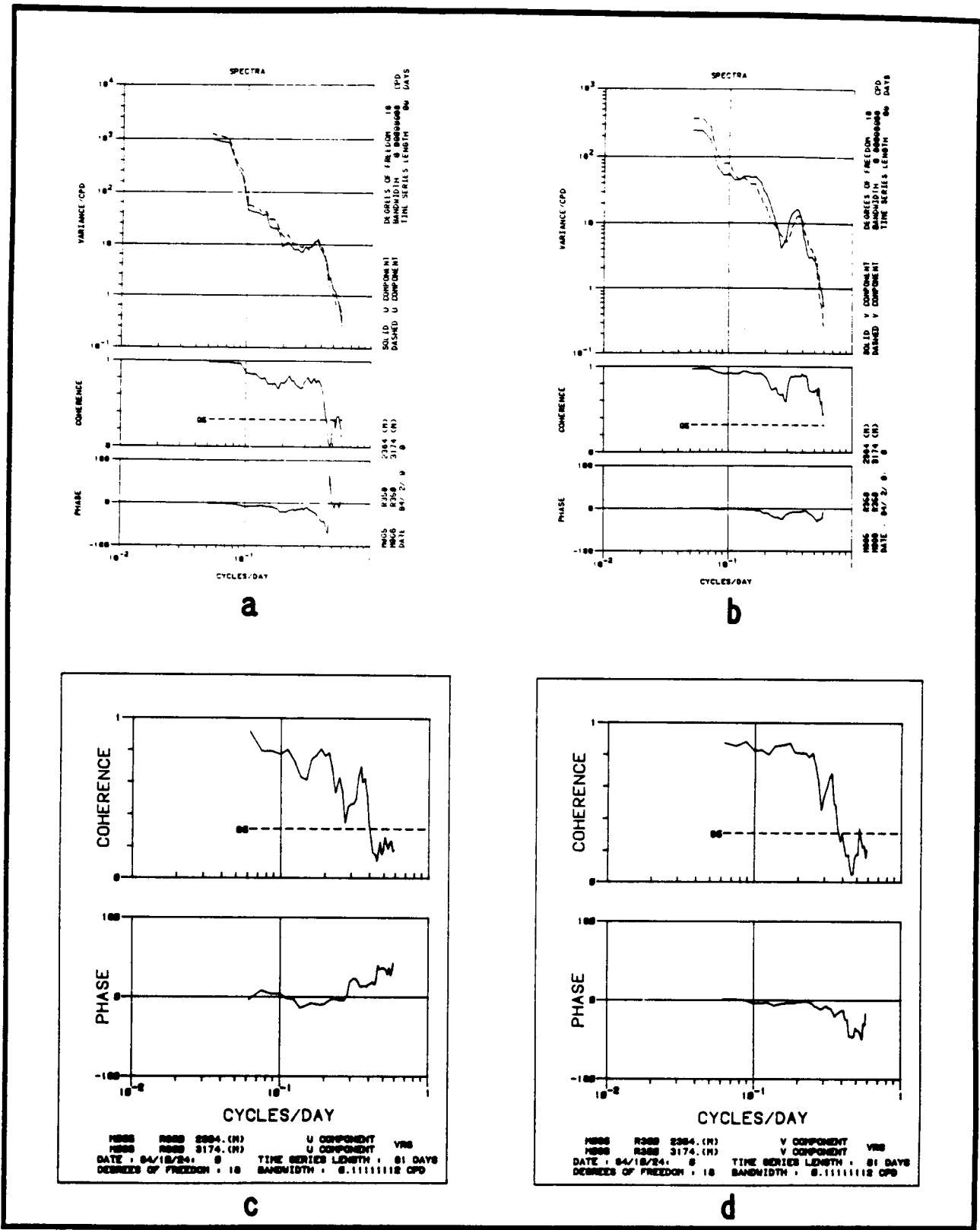


Figure 4.5-28. (a) Vertical coherence of u components at Mooring G between currents at 2364 and 3174 m for the period beginning on 9 February 1984. (b) for V components, (c) for U components for the period beginning 24 October 1984, (d) for V components for the period beginning 24 October 1984.

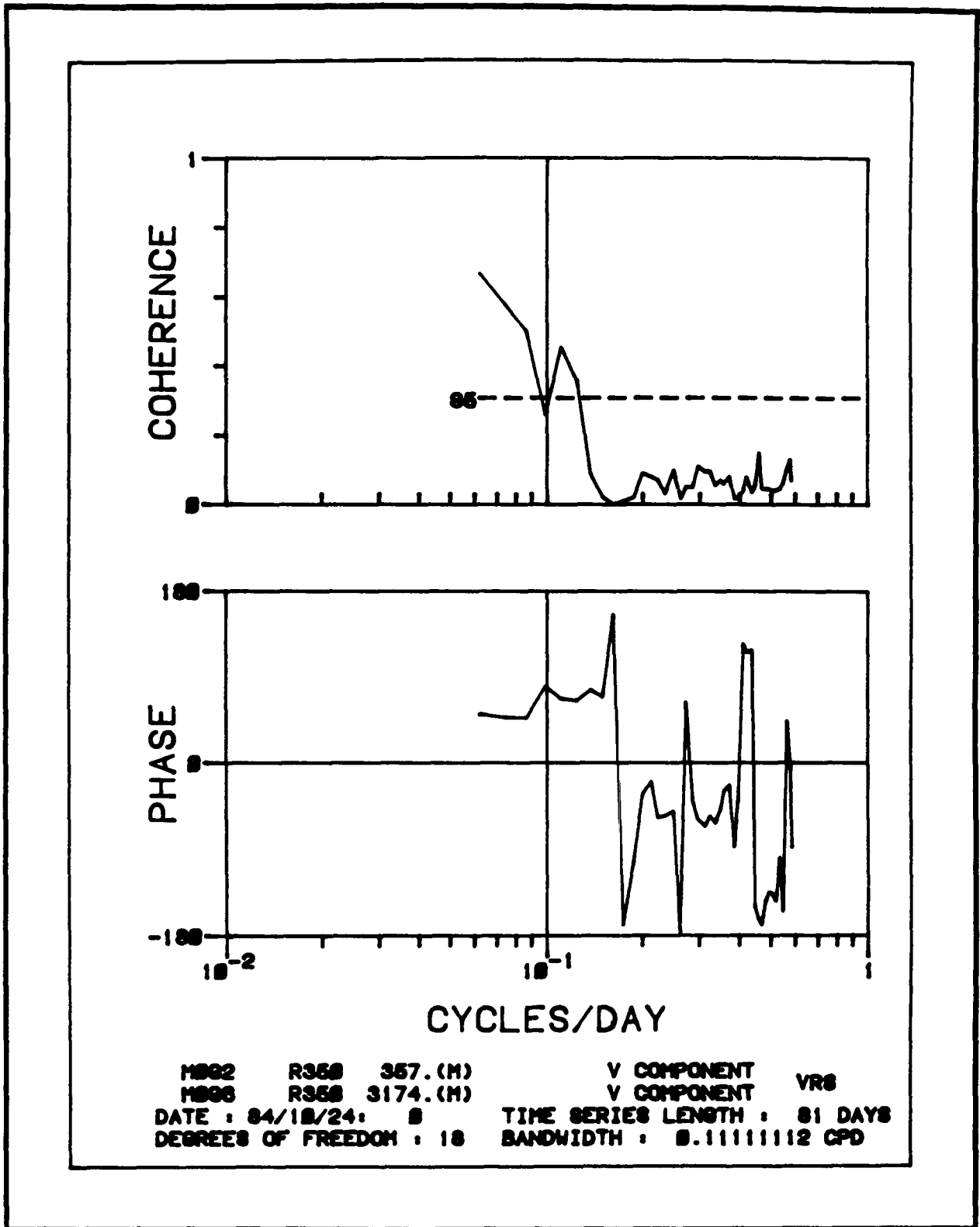


Figure 4.5-29. Coherence of the V components at Mooring G between currents at 357 m and 3174 m for the period beginning on 24 October 1984.

In correlations involving temperatures at 1565 m, the V, T correlation is high, even in the wind-driven bands near five and three days (Figure 4.5-30). A similar calculation at 2364 m is seen in Figure 4.5-31. Surprisingly, the temperature fluctuations are 180° out-of-phase between the two deepest instruments even though the velocity is in phase (Figure 4.5-32). An examination of data between the 1565-m and 2364-m instruments shows that temperature is in-phase between them. Therefore, the phase shift must occur below 2364 m.

4.5.7 Motions at Longer Periods: 30 Days or More

Most of the previous discussion has concentrated on fluctuations at periods normally associated with synoptic scale wind events, roughly two weeks or less. The wind spectra, however, show a significant amount of energy at longer periods. The relative amounts vary from season to season, but, as seen from the available records, the variability is sufficiently large so that seasonal means can not be reliably determined.

The fraction of low-frequency motions that may be wind generated can be examined in Figures 4.5-33 through 4.5-37, which show scatter plots between alongshore currents and alongshore winds at Tampa. The data were filtered with a 30-day, low-pass filter to suppress fluctuations at periods shorter than a month. The resulting series were subsampled every five days.

The results at the upper instrument at Mooring D (30 m, 1983; 17 m, 1984) (Figure 4.5-33a, b) show a correlation consistent with a number of the spectra in the preceding sections. They show that the correlation is positive. Low-frequency wind events to the south are correlated with currents to the south, although causality has yet to be shown. Figures 4.5-34a,b show a similar plot for the next lower instrument in the water column (60 m, 1983; 50 m, 1984). Obviously some fluctuations at low wind speeds, particularly in the 1984 data, are uncorrelated with wind. Yet the overall correlation is apparent. It appears that low-frequency wind events are correlated with current fluctuations on the order of 20 cm s⁻¹. The southerly directed fluctuations seem to be larger.

An important result found in these data is in the net horizontal advection associated with wind events. For a given amplitude of current fluctuation, the horizontal length of an excursion is directly proportional to the period of the event. Therefore, for a current amplitude of ~20 cm s⁻¹, an event having a period of ~40 days (as found in the spectra discussed previously) will be associated with horizontal displacements approximately eight times as large as for the five-day wind events.

At the mooring closest to shore (F) the apparent correlation is similar to that at D, but is not significantly different than zero. The maximum speeds at these frequencies are only a few cm s⁻¹. A similar plot at Mooring E is seen in Figure 4.5-35. While the correlation is significant, the scatter is larger than at Mooring D. This result is to be expected, as E is much closer to direct forcing by the Loop Current. In a similar plot for Mooring C, in the upper water column, the scatter obscures any correlation. Figure 4.5-36 shows a plot of this type at the upper current meter (172 m) at Mooring A. The correlation is positive, as at most of the other instruments, but the amplitude is smaller by at least a factor of two compared with the flow on the

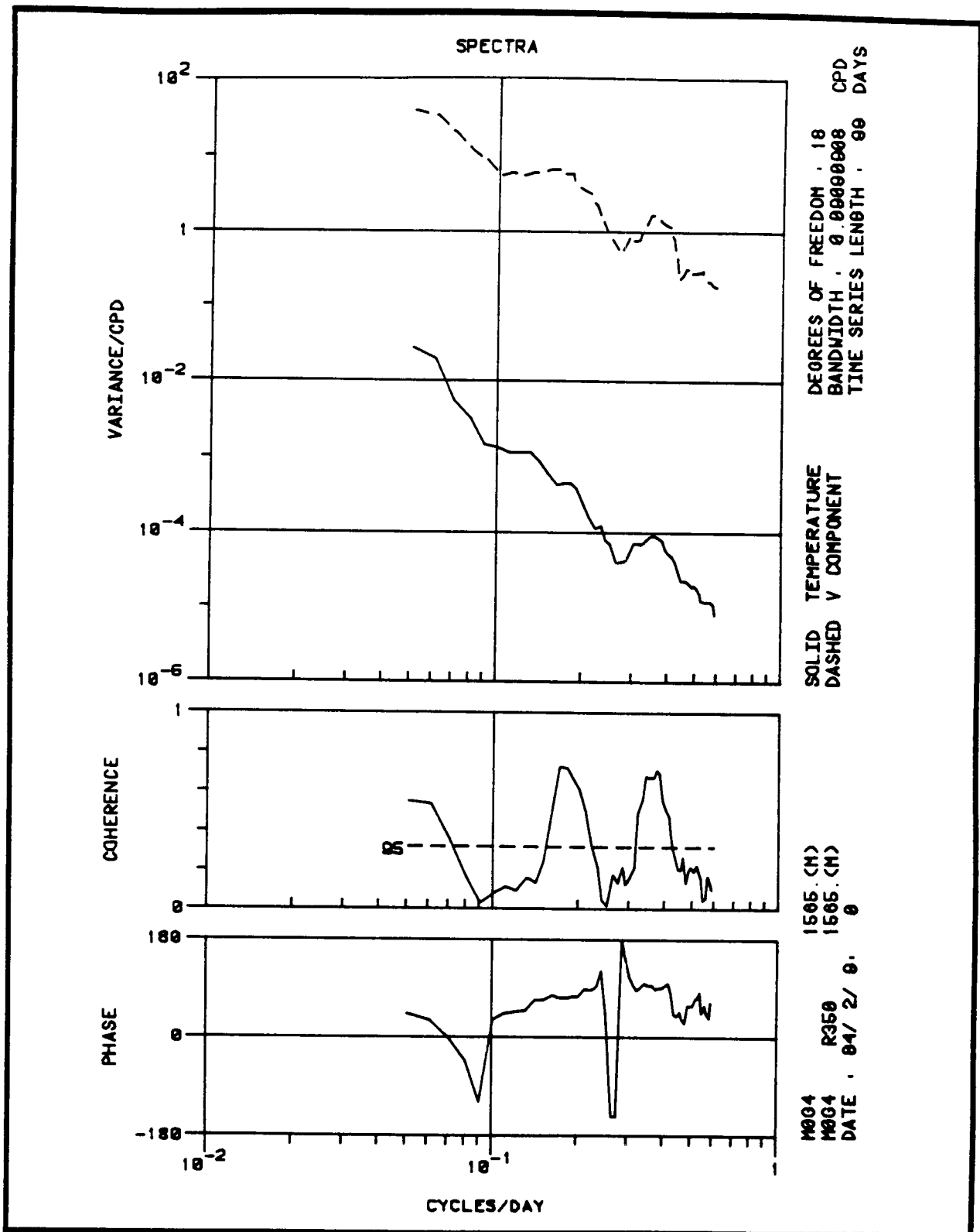


Figure 4.5-30. Coherence between the long-shelf velocity component (V) and temperature at Mooring G, 1565 m for the period beginning on 9 February 1984.

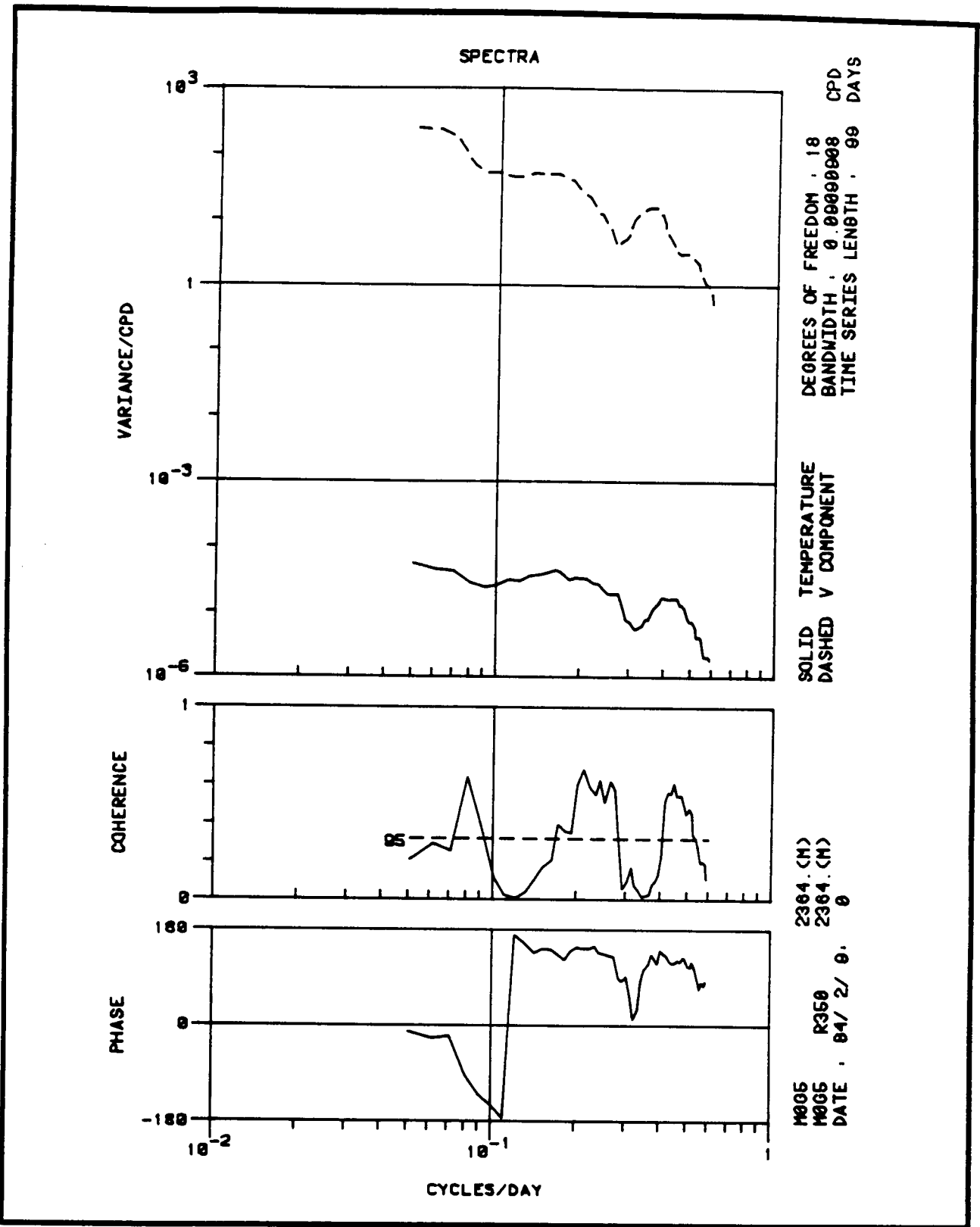


Figure 4.5-31. Coherence between the long-shelf velocity component (V) and temperature at Mooring G, 2364 m for the period beginning on 9 February 1984.

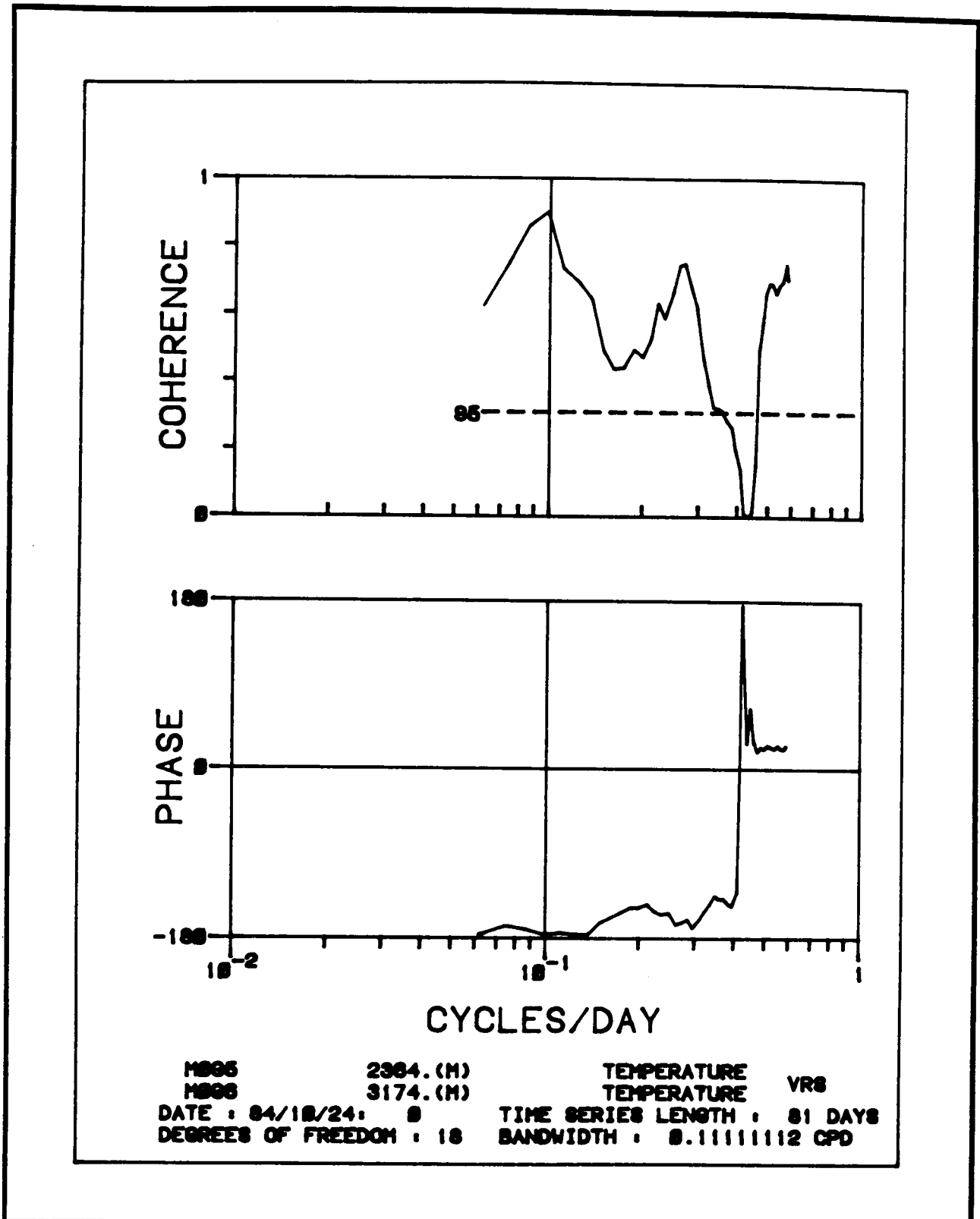


Figure 4.5-32. Coherence in temperature at Mooring G between observations at 2364 m and 3174 m for the period beginning on 24 October 1984.

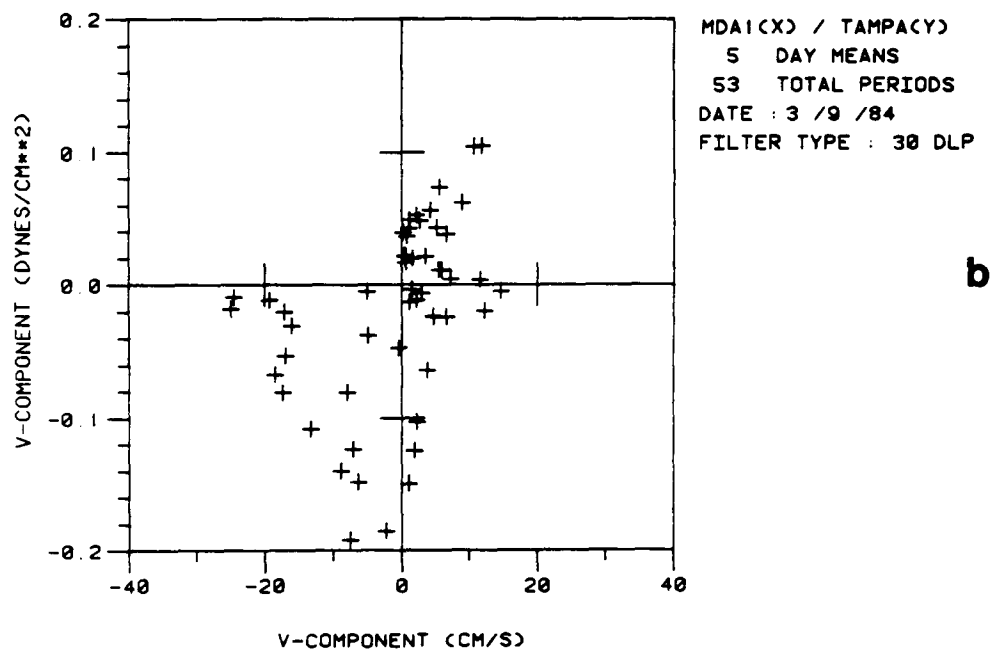
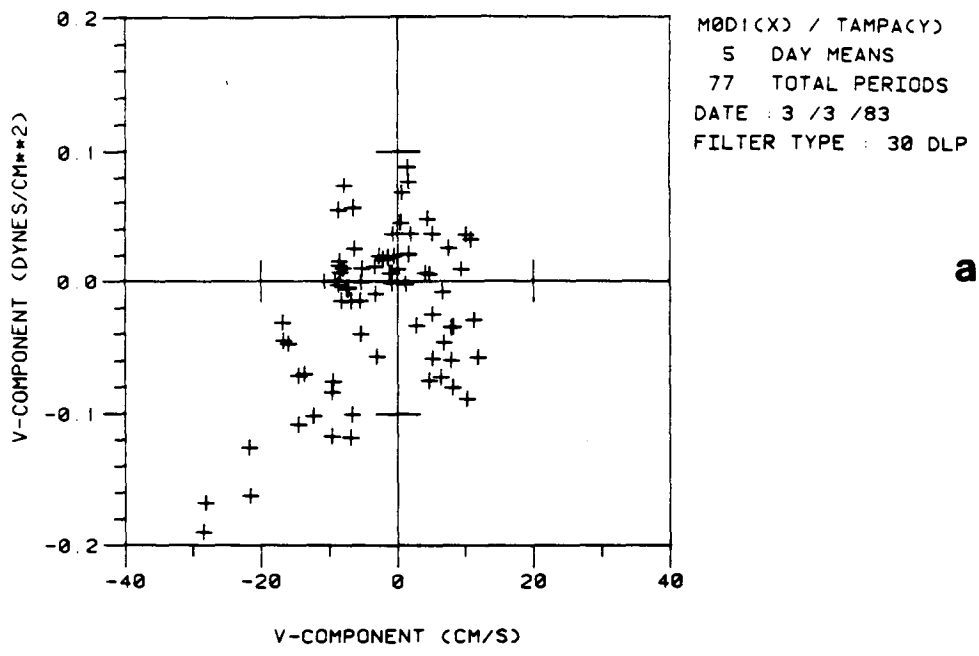


Figure 4.5-33. Very low frequency scatter plot of wind stress at Tampa versus currents at Mooring D, upper current meter (30 m), for the long-shelf components. (a) The first year of data beginning 3 March 1983, (b) the second year of data beginning 9 March 1984 at Mooring D upper current meter (17m).

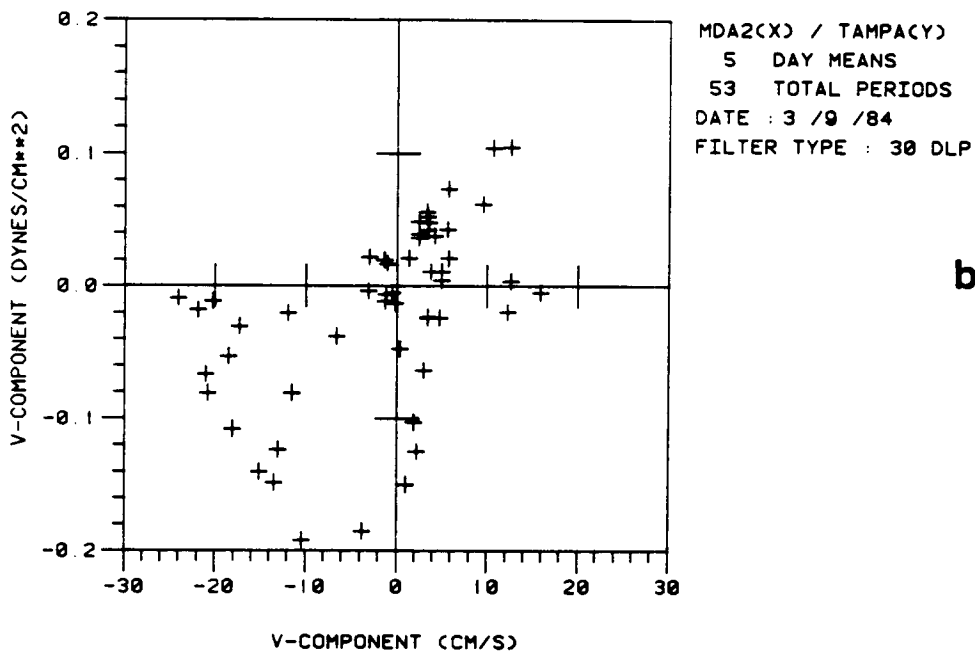
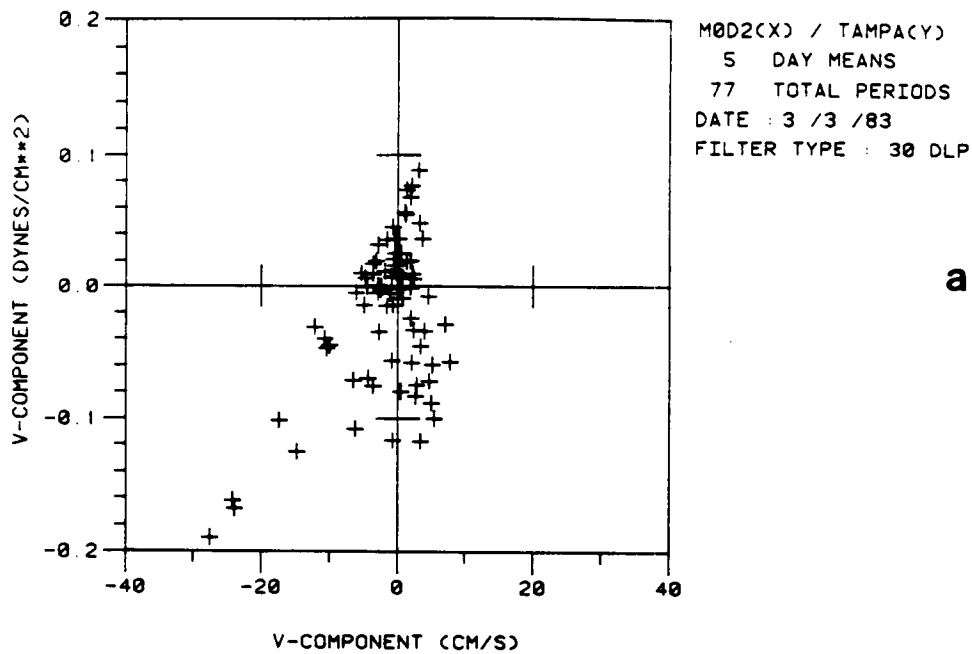


Figure 4.5-34. Very low frequency scatter plot of wind stress at Tampa versus currents at Mooring D, (a) lower current meter (60 m) for the first year of data beginning 3 March 1983, and (b) middle current meter (50 m), for the long-shelf components, for the second year of data beginning 9 March 1984.

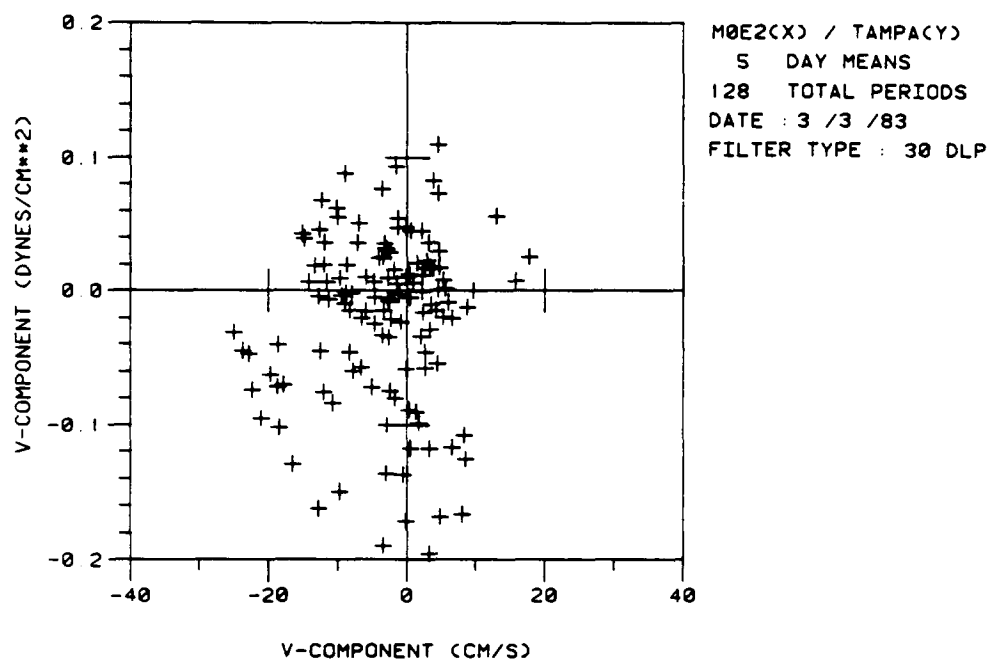


Figure 4.5-35. Very low frequency scatter plot of wind stress at Tampa versus currents at Mooring E, middle current meter (100 m) for the long-shelf components. A 30-day low-pass filter is used, and the data is sub-sampled every 5 days; for the first year of data, beginning 3 March 1983.

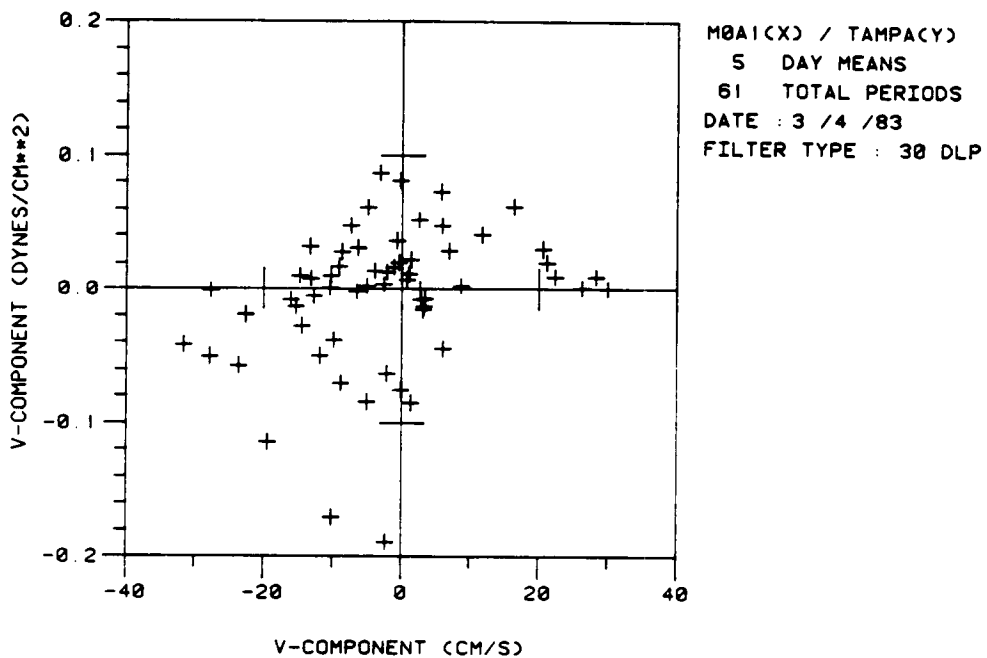


Figure 4.5-36. Very low frequency scatter plot of wind stress at Tampa versus currents at Mooring A, upper current meter (170 m) for the long-shelf components. A 30-day low-pass filter is used, and the data is sub-sampled every 5 days; for the first year of data, beginning 4 March 1983.

shelf. It would be expected that shelf motions would decay toward smaller values in deeper water. This instrument, 172 m from the surface, is well below the depth of any direct frictional influence of local wind.

Figures 4.5-37a-c show results from the near-bottom instruments on Moorings E and C. (There are breaks in the record at E3, hence two plots). The correlation is the opposite of what has been seen in the previous plots. The flow associated with southerly wind events near the bottom at the shelf break is to the north. This result is found at both Moorings E and C. One suspects immediately that this is a return flow of some sort. However, a wave-like motion that has a phase reversal at the shelf break would be equally plausible.

4.5.8 Forcing by the Loop Current

Figures 4.5-38a,b show a sampling of positions of the Loop Current from satellite observations during the first year of the array. In many of the daily images, several finger-like extensions can be seen at the edge of the Loop Current. In images a few days apart, these sometimes can be seen to move downstream. Coherence is less than perfect, as some of the features are not found in the next image.

The position of the inshore edge of the current at several latitudes has been examined using all available maps for the first year through mid-June. Using the normally produced NOAA images, the spacing between data points is two days, then five days. For 12-day periods, the two-day data points are fine. The five-day gap may be a bit long, but it turns out to be adequate for these purposes (e.g., Sturges 1983). The positions were digitized, and a smooth curve was forced through them using a cubic spline.

In a spectrum from the E-W variation of Loop Current positions along 25°N, the relevant feature is the concentration of energy at periods near 10-16 days (Figure 4.5-39). The longer periods (30-40 days) are more energetic, but they are not resolved well in this relatively short record. In the cross spectra from one latitude to the next (not shown), the fluctuations are coherent between latitudes and the phase delay is such that they propagate downstream, i.e., from north to south with the current.

Another aspect of this finding is of a substantial amount of power at periods of 10-14 days. This finding should affect the ideas about the periods with which a reasonable sampling strategy must deal. If this power at $T > 10$ days is not sampled adequately, it will, of course, be aliased to lower frequencies.

In order to test for a simple, direct forcing mechanism, cross spectra between different positions of the Loop Current, as the assumed forcing, and the currents observed at the moorings will be computed in an analysis presently under way. As a first step, cross spectra have been computed between the data whose spectrum is shown here and the onshore component of velocity at Mooring A. Significant coherence is found at periods just longer than 10 days. This result suggests that some fraction of the variability at these periods is associated with Loop Current motions. It should be emphasized, however, that the direction of the forcing is unclear. That is, the wind may force these fluctuations on the shelf; these fluctuations may then cause the variations in

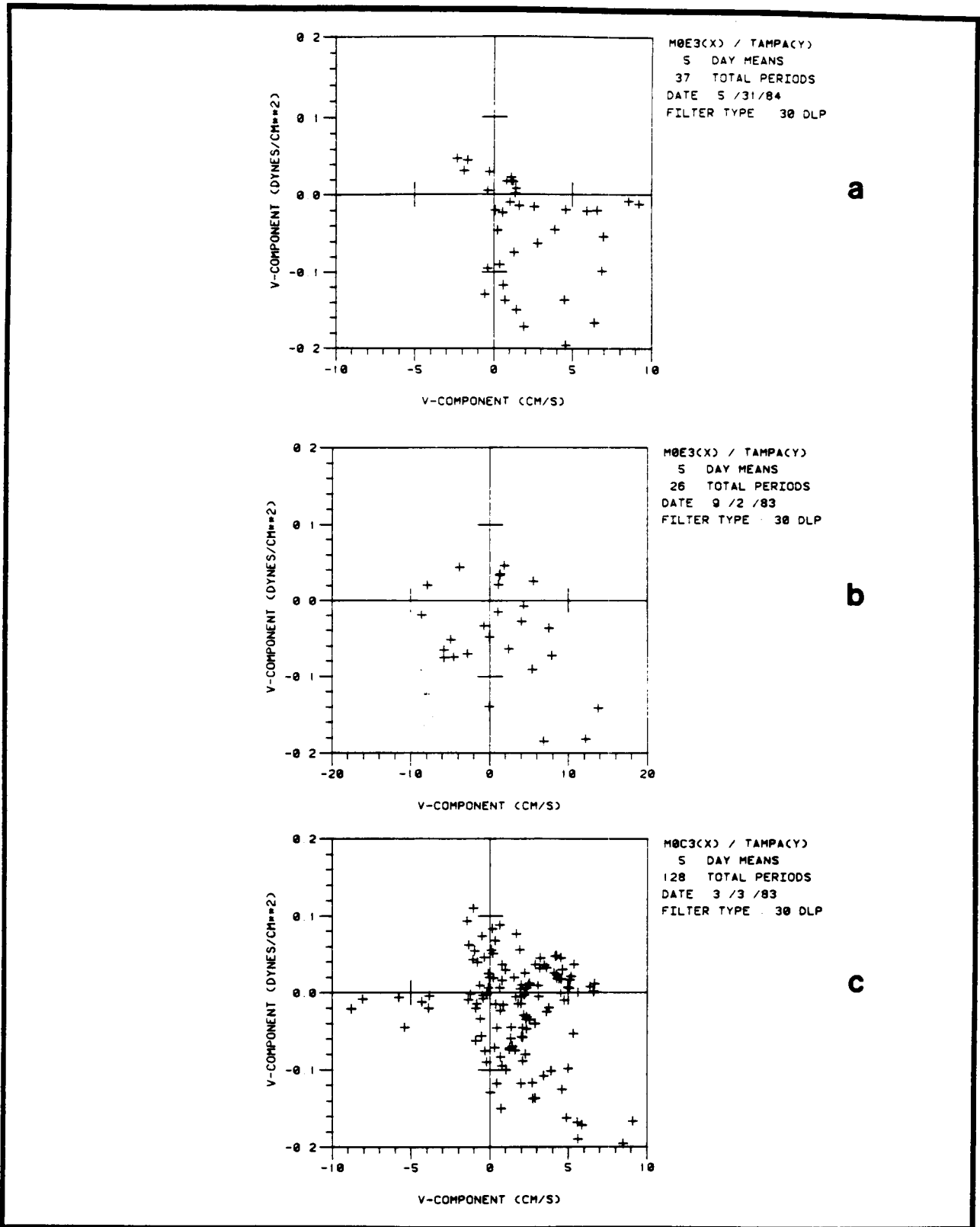


Figure 4.5-37. Very low frequency scatter plot of wind stress at Tampa versus currents at Mooring E, bottom current meter (179 m) for the long-shelf components: (a) for data during the first year, beginning 2 September 1983, (b) for the data, during the second year, beginning 31 May 1984, (c) at Mooring C, for the two year-long record, beginning 3 March 1983.

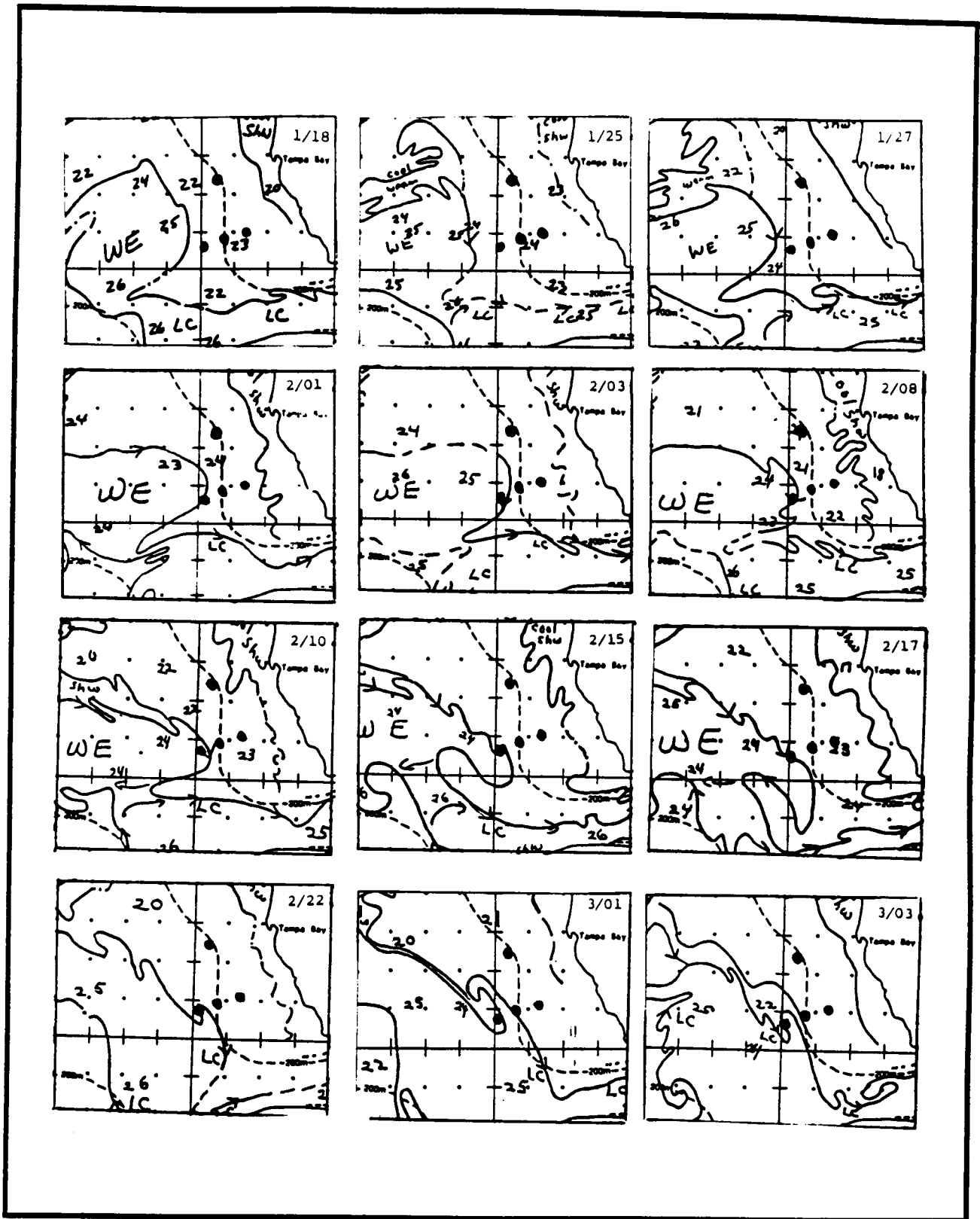


Figure 4.5-38a. Positions of the Loop Current near the mooring array from the NOAA satellite images, January - March 1983. Moorings A, C, D and E are shown by the small dots.

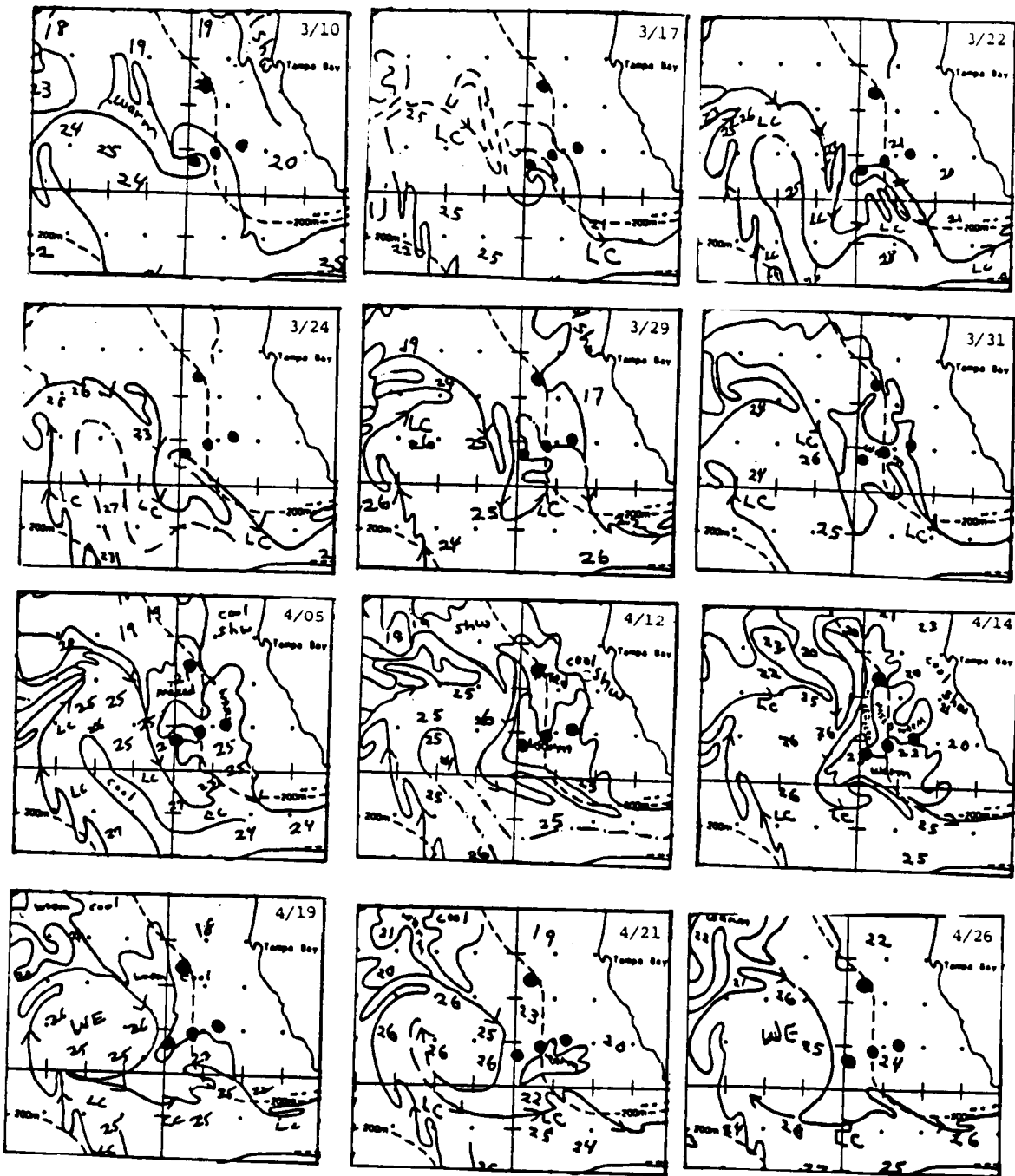


Figure 4.5-38b. Positions of the Loop Current near the mooring array from the NOAA satellite images, March - April 1983. The moorings are shown by the small dots.

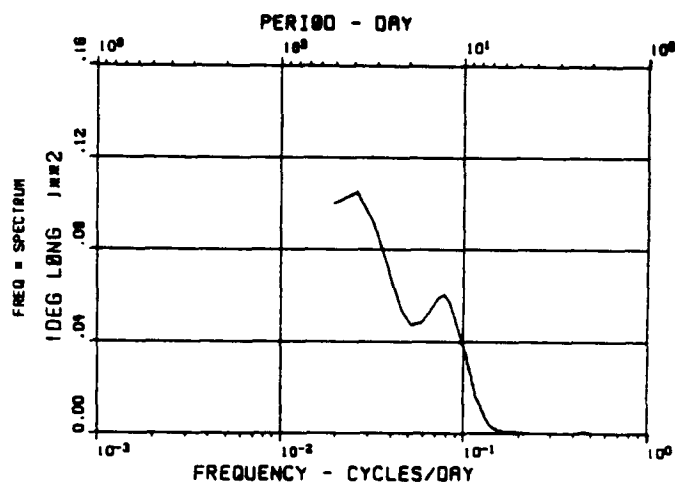
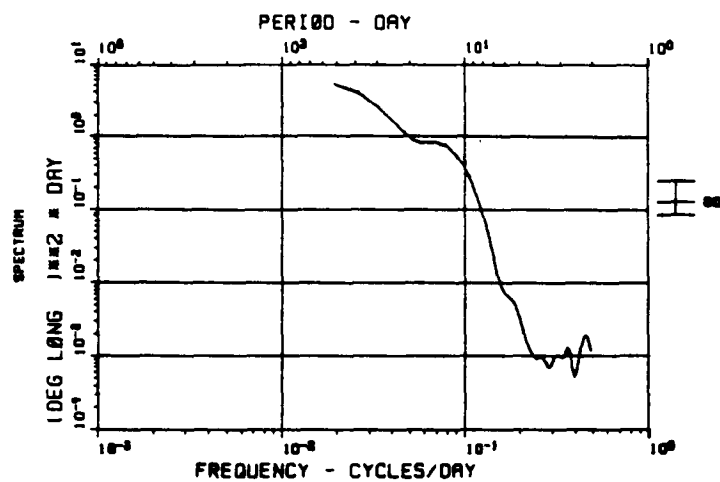


Figure 4.5-39. Spectrum of east-west fluctuations of inshore edge of the Loop Current at 25°N from the maps of Figure 4.5-38 et. seq. Spectrum is shown in the normal fashion above and in the variance-preserving form below. Degrees of freedom = 12; 7 Hanning passes were used. After the cubic spline fit, each end of original data series was tapered 10%.

Loop Current position. This effect is being explored. The Loop Current positions (from maps such as Figure 4.5-38) are being digitized with greater spatial resolution to allow further calculations of this type. However, because there is also coherence with wind at these same frequencies, a multiple input spectral model will be necessary. Such models allow a separation of the response into parts that are forced by different mechanisms. It is anticipated that it will be possible to determine what fractions of the currents are forced by wind and by the Loop Current independently.

4.6 Analysis of Louisiana Shelf Current Meter Observations

4.6.1 Introduction

As discussed in Chapter 3, data from Louisiana shelf Mooring MD in 81-m depth off the Mississippi River delta were collected over the following three periods:

- 23 February to 10 May 1984
- 10 May to 27 July 1984
- 27 July to 8 November 1984

Instruments were deployed at depths of 13, 25, 45 and 70 m on each occasion. The only current data obtained from the initial deployment were at the 70-m level and it is suspected that wear on the current meter impeller bearings may have resulted in low readings. During the third deployment the upper instrument at 13 m recorded temperature only.

4.6.2 Discussion

Energy spectra for currents at 70 m decreased with increasing frequency except at the lowest spectral estimate, where an energy plateau is suggested (Figures 4.6-1 through 4.6-3). Both diurnal and semi-diurnal peaks are apparent. The energy levels across the spectrum at the 70-m level are an order of magnitude or more greater during the second and third deployments than they were during the first. This suggests that the readings from the first deployment were biased low. The spectral shape and phase and coherence-squared estimates, however, appear reliable. The second and third deployments also revealed that the energy levels at the lowest frequencies decay with depth.

Energy spectra of temperature fluctuations at different meters are similar to those for currents with energy peaks or plateaus in the diurnal and semi-diurnal bands. The definition of these peaks increases with depth and from the first to the third deployment as the summer thermal structure develops (Figures 4.6-4 to 4.6-6).

The two components of current from the 70-m level during the first deployment are coherent up to frequencies slightly greater than 0.3 cpd (Figure 4.6-7). At the low frequency end of this band, the phase is near zero, implying elongated current ellipses, due to topographic steering. At the higher frequencies, the phase approaches $\pi/2$ as the currents become more nearly circularly polarized.

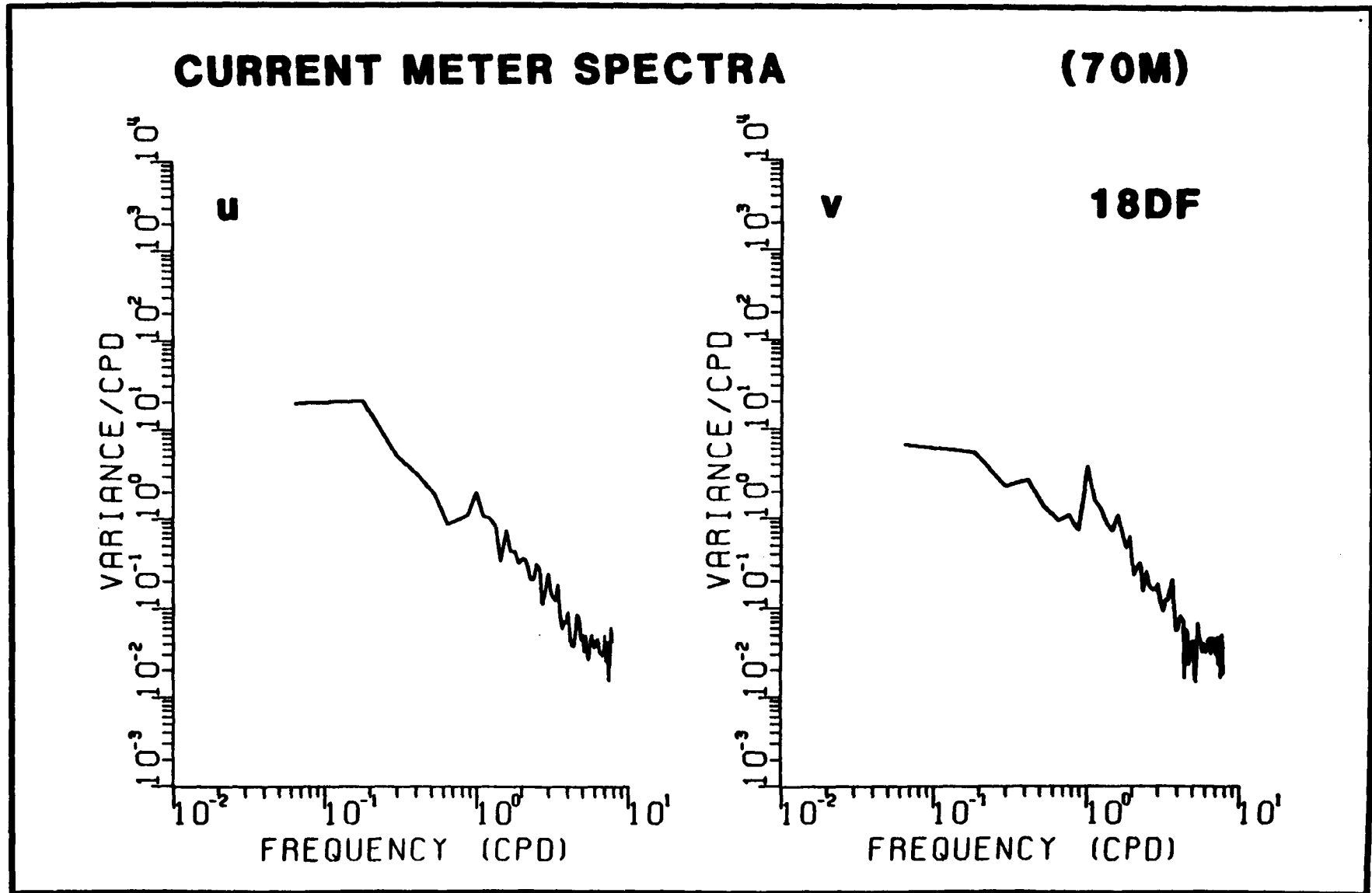


Figure 4.6-1. Spectra of current velocity components for meter MD 4 (70 m) from 23 February to 10 May. The u component is positive toward the east; the v component is positive toward the north. Spectral estimates have 18 degrees of freedom.

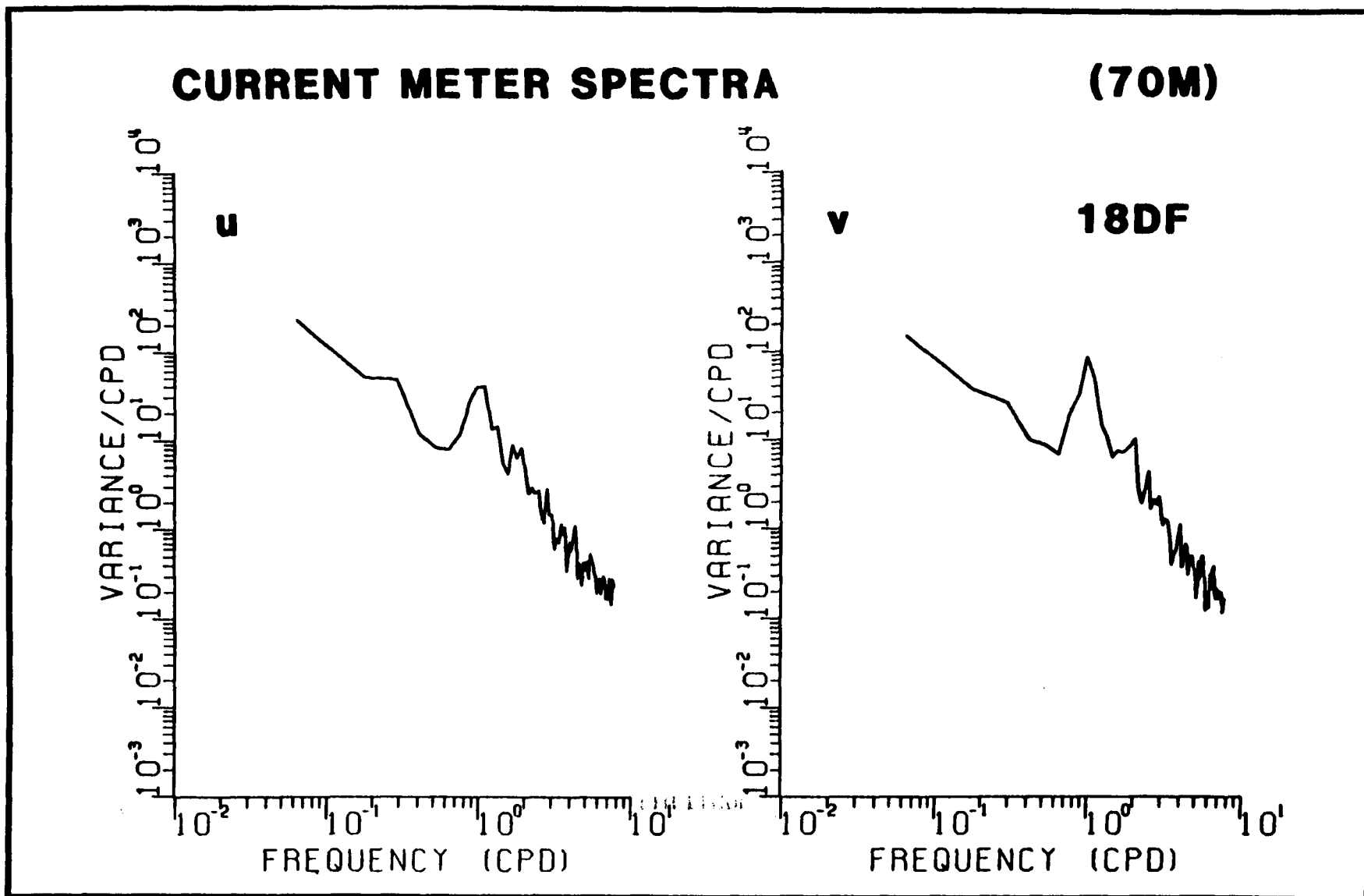


Figure 4.6-2. Spectra of current velocity components for meter MD 4 (70 m) from 10 May to 27 July. The u component is positive toward the east; the v component is positive toward the north. Spectral estimates have 18 degrees of freedom.

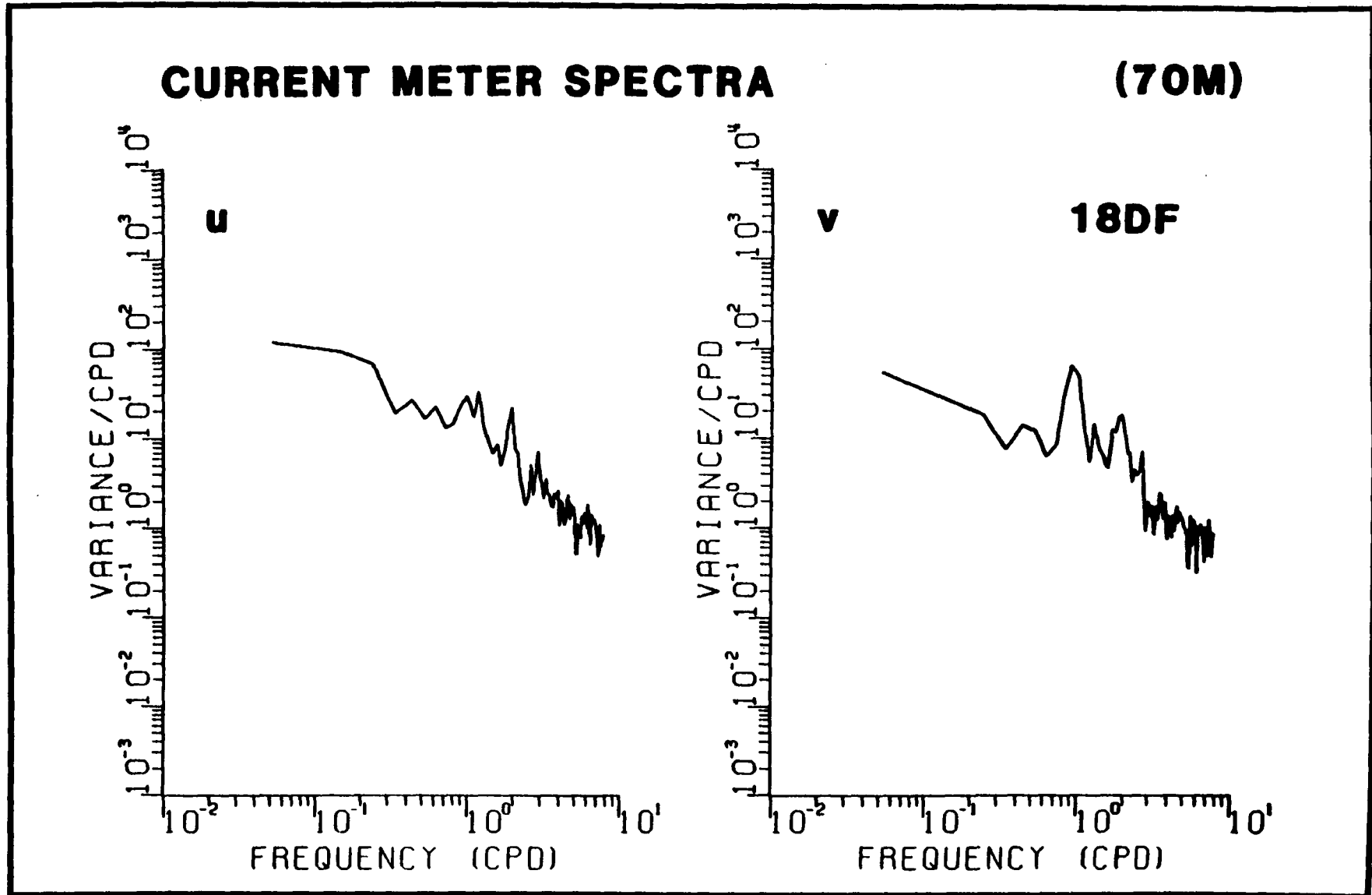


Figure 4.6-3. Spectra of current velocity components for meter MD 4 (70 m) from 27 July to 29 October. The u component is positive toward the east; the v component is positive toward the north. Spectral estimates have 18 degrees of freedom.

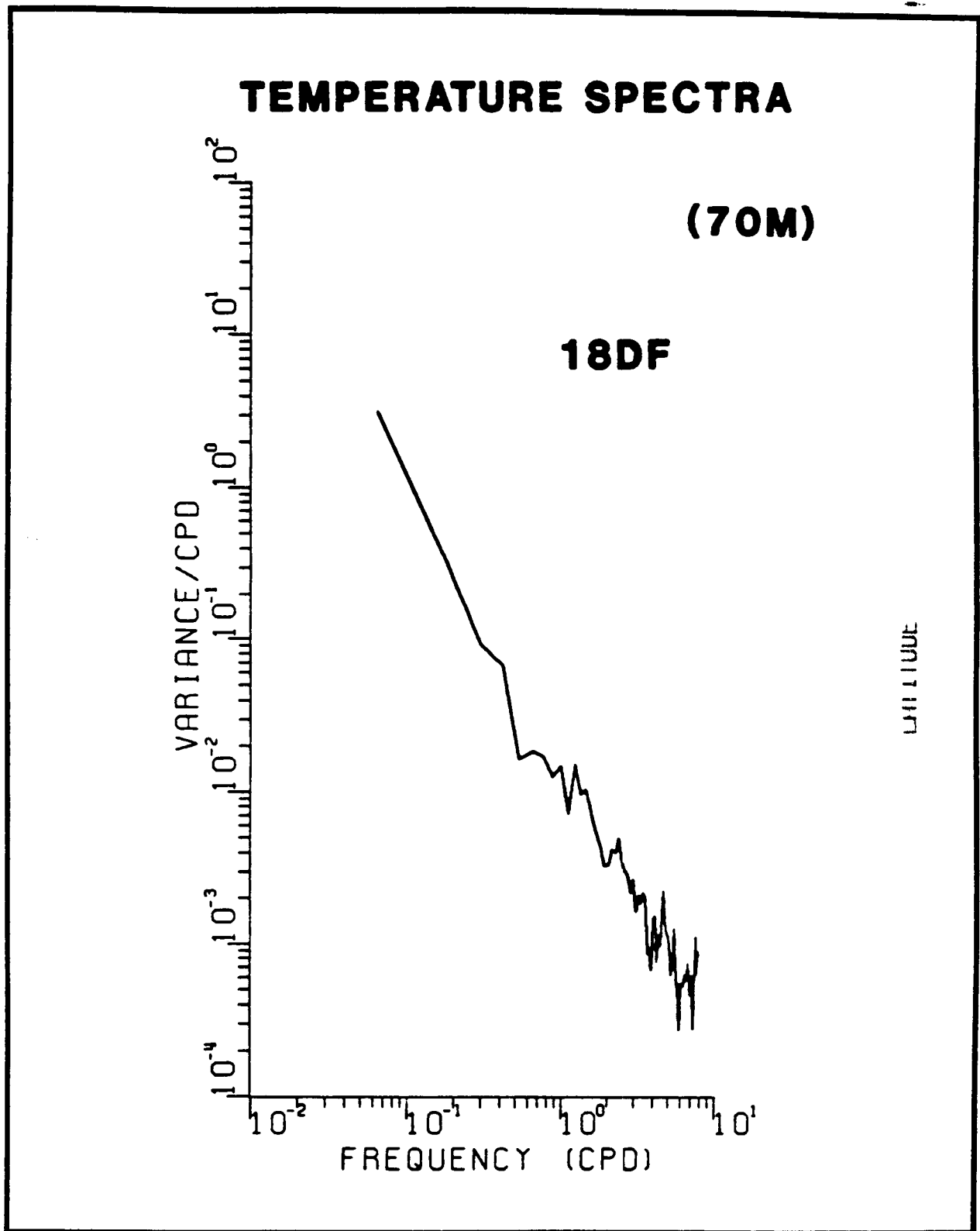


Figure 4.6-4. Spectra of temperature for meter MD 4 (70 m) from 23 February to 20 May. The spectral estimates have 18 degrees of freedom.

TEMPERATURE SPECTRA

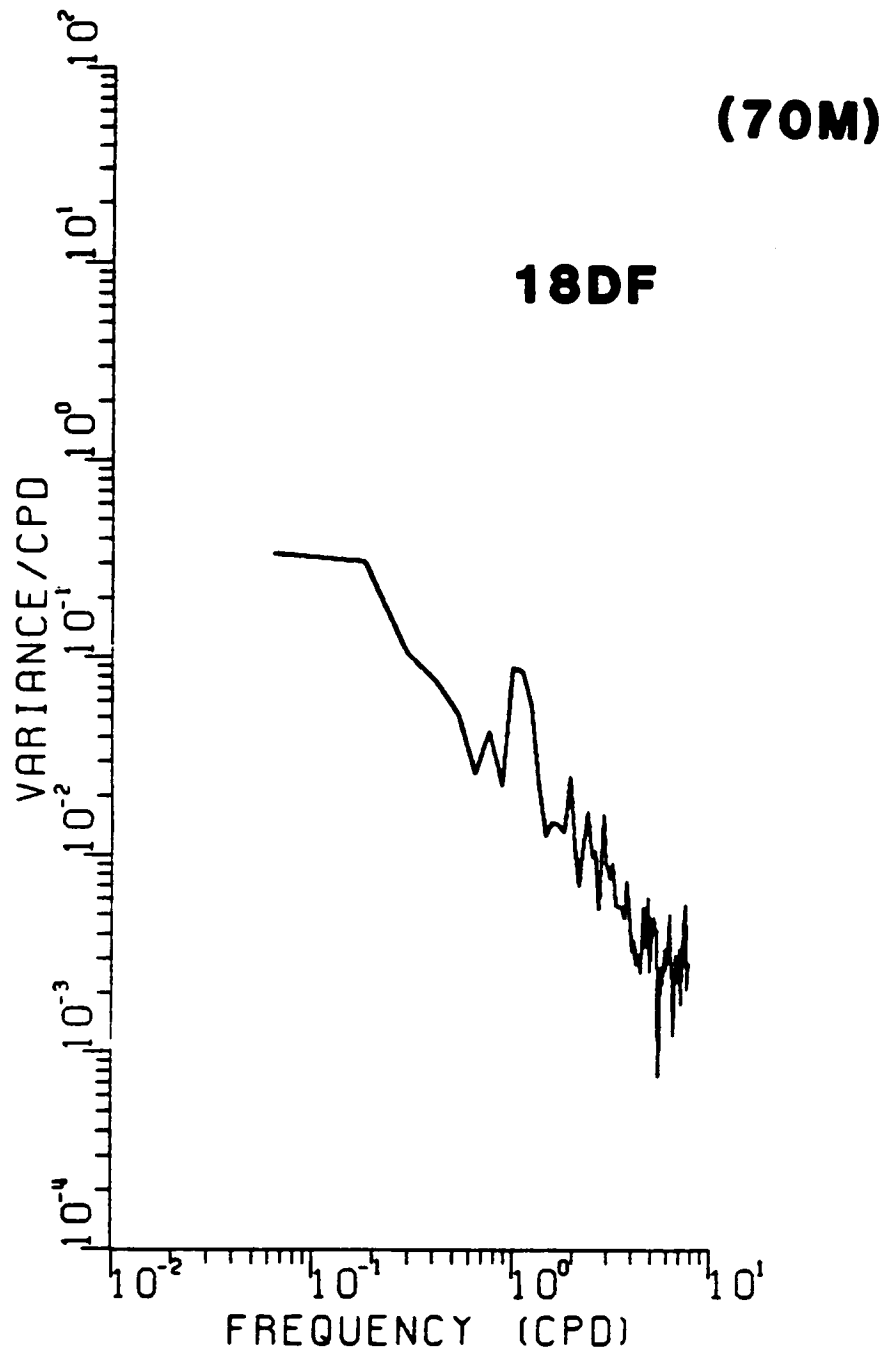
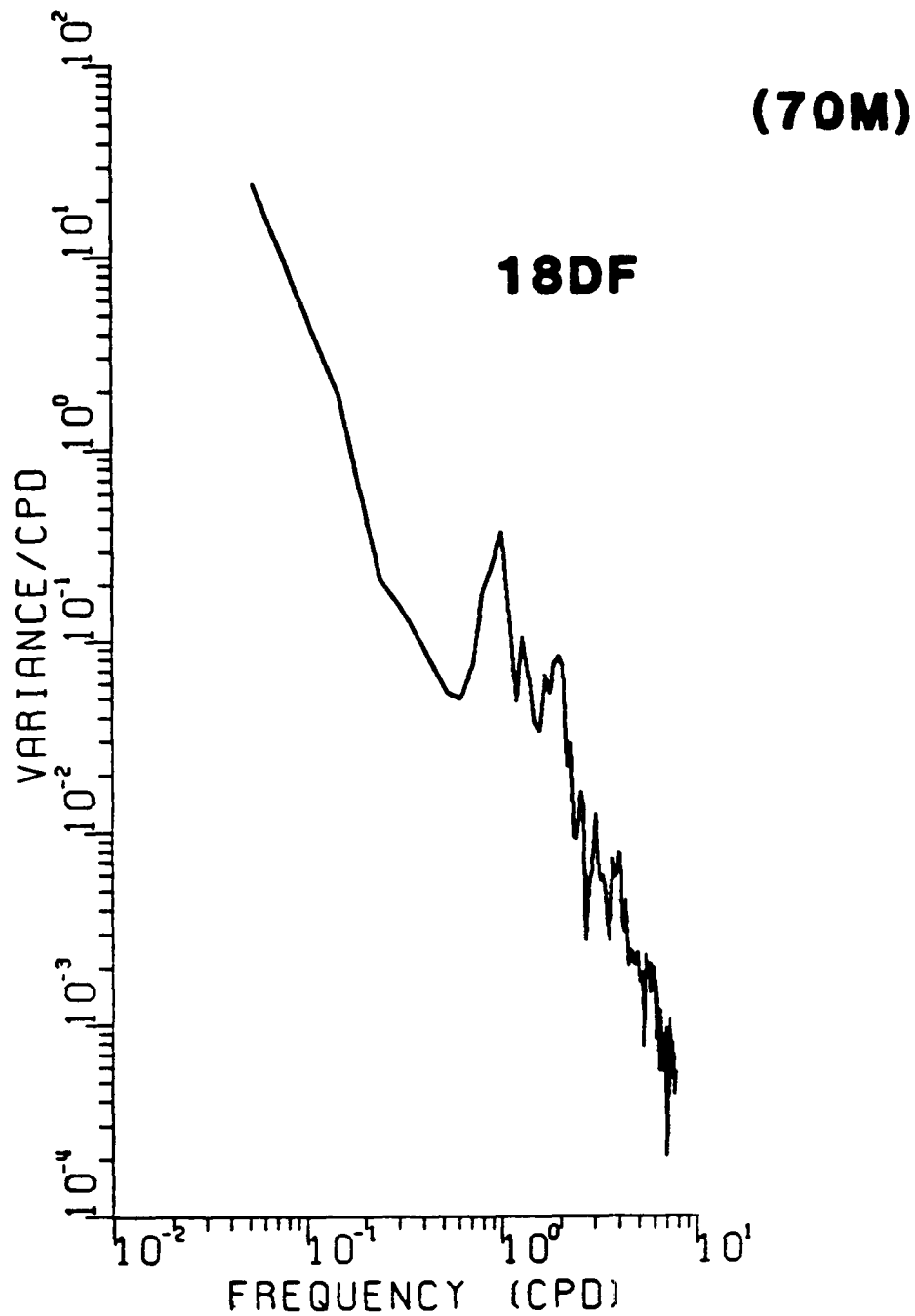


Figure 4.6-5. Spectra of temperature for meter MD 4 (70 m) from 10 May to 27 July. The spectral estimates have 18 degrees of freedom.

TEMPERATURE SPECTRA



AMPLITUDE

Figure 4.6-6. Spectra of temperature for meter MD 4 (70 m) from 27 July to 29 October. The spectral estimates have 18 degrees of freedom.

3112

COHERENCE AND PHASE VELOCITY COMPONENTS (70M) 18DF

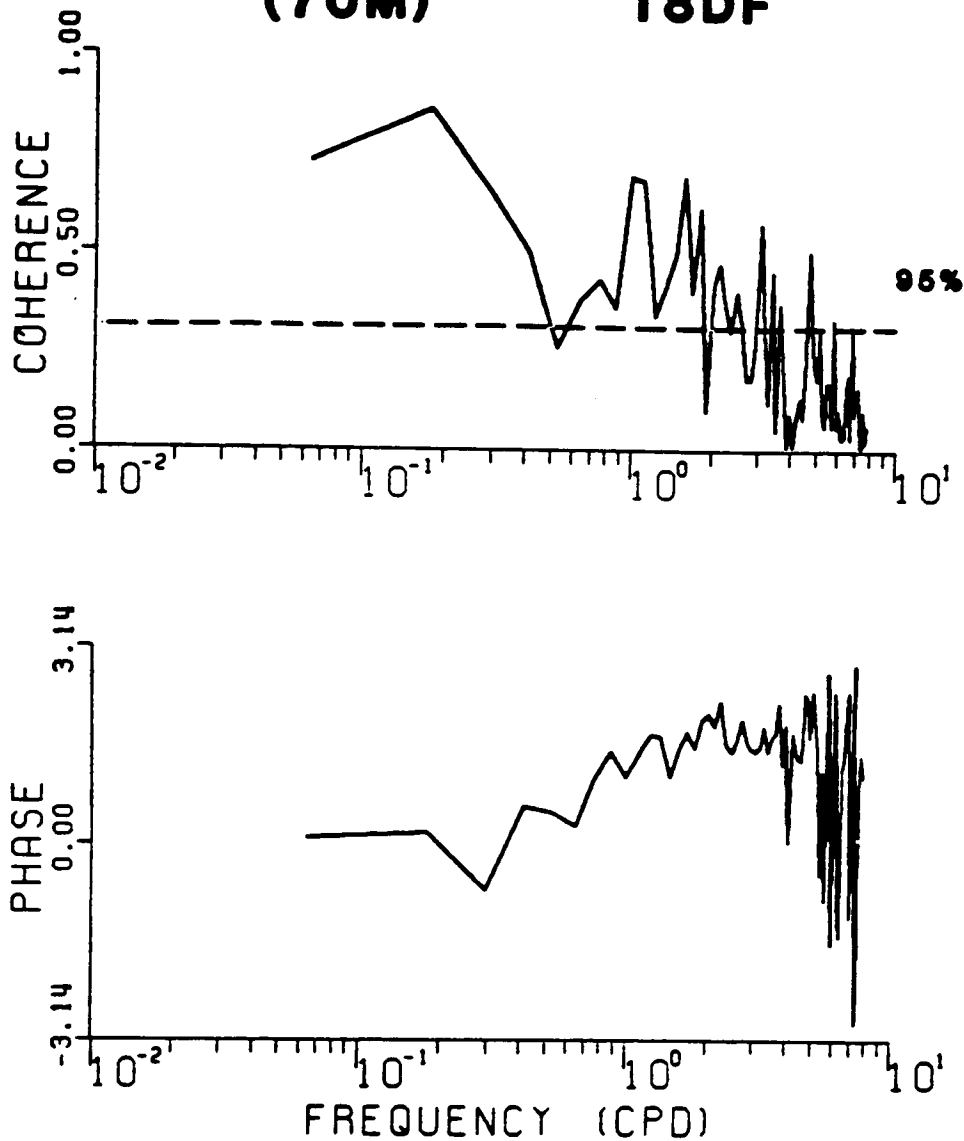


Figure 4.6-7. Coherence squared (above) and phase (below) between velocity components at meter MD 4 (70 m) from 23 February to 10 May. The spectral estimates have 18 degrees of freedom. The 95% significance level is 0.31.

During the second and third deployments, at all depths, the lowest frequency fluctuations are coherent between components and with near-zero phase as earlier. The diurnal fluctuations are coherent with a phase near $\pi/2$ and the level of coherence-squared and the width of the bands of significant coherence increase with depth.

Statistics for the current and temperature records are presented in Tables 4.6-1 and 4.6-2 respectively. Most noteworthy is the large increase in variance at 25- and 45-m depths from the second and third deployments. The variances about the mean for each current component, by frequency band, are presented in Table 4.6-3. The principal contribution to the total variance, in all cases, is from the low-passed part of the spectrum where the distribution of energy is very anisotropic because of bottom steering. Subsequently, the bottom slope appears to be an important control throughout the year. This is in contrast to the situation on the west Louisiana shelf where the water column density structure during the summer is similar to that near the Mississippi River delta below the low-salinity effluent plume and appears to be sufficient to decouple all but the deepest currents from the influence of the weak bottom slope. During winter, however, when the water column is more homogeneous, the bottom topography there becomes an important control on the low-passed current structure as well.

While the low-passed currents are anisotropic, the tidal/inertial band current energy is evenly distributed between components, reflecting the rotary nature of the currents. The total energy in the current fluctuations decreases with depth and while all records exhibit a weak mean westerly drift, few of the means are statistically reliable at any reasonable significance level.

Stick plots of the low-passed current time series and line plots of low-passed temperatures are shown in Figures 4.6-8 through 4.6-13. Once again, steering of the low-frequency currents by the bottom topography is apparent.

The strong current events seen on the records from the third deployment (Figure 4.6-10) do not appear to be related to local meteorological forcing or runoff events. They represent the strongest events recorded and yet occur during a meteorologically uneventful period. They are also strongly sheared in the vertical and are associated with significant thermal variability, although the thermal variations do not always extend throughout the entire water column (e.g., the second half of this deployment in Figure 4.6-13). Although an intense thermal signal is apparent at 70-m depth, the velocity signal at this depth is weak.

Ebbesmeyer et al. (1982) report current events greater than 30 cm s^{-1} at the Cognac site and the OTEC site south of Mobile, Alabama. Many of the characteristics are similar to those observed. Their events occurred below 100-m depth, were strongly sheared in the vertical, and occurred on time scales similar to those observed here. They suggest the structures they measured were associated with Loop Current intrusions into the northern Gulf. In contrast, events observed here were somewhat stronger, farther up on the shelf, and at slightly shallower depth in the water column. They were also associated with stronger thermal variation than were those of Ebbesmeyer et al. The observed current/temperature relation is inappropriate for a westward-propagating, anti-cyclonic ring, but may be associated with smaller scale cyclonic features on the edge of the Loop Current and rings.

Table 4.6-1. Velocity Component Statistics for 3-Hour Low-Passed Records for Louisiana shelf Mooring MD.

Meter (Deployment)	Depth (m)	Mean (cm s ⁻¹)	Variance (cm ² s ⁻²)	Standard Deviation (cm s ⁻¹)	Maximum (cm s ⁻¹)	Minimum (cm s ⁻¹)
MD4(1)-u	70	-1.34	7.94	2.82	6.67	- 9.39
MD4(1)-v	70	-0.02	4.41	2.10	7.36	- 8.65
MD1(2)-u	13	-5.57	390.14	19.75	38.07	-79.05
MD1(2)-v	13	-1.21	117.18	10.82	37.81	-42.79
MD2(2)-u	25	-4.19	335.86	18.33	51.03	-60.54
MD2(2)-v	25	-0.07	109.35	10.46	53.60	-37.54
MD3(2)-u	45	-3.53	185.84	13.63	42.38	-49.56
MD3(2)-v	45	-0.08	57.34	7.57	26.88	-25.46
MD4(2)-u	70	-2.10	69.30	8.32	21.45	-25.14
MD4(2)-v	70	-1.34	61.63	7.85	20.04	-28.21
MD2(3)-u	25	-1.05	1096.55	33.11	94.12	-142.67
MD2(3)-v	25	2.92	260.27	16.13	44.87	-59.07
MD3(3)-u	45	-3.65	408.58	20.21	64.31	-70.89
MD3(3)-v	45	-0.28	132.84	11.53	29.84	-39.39
MD4(3)-u	70	-3.52	67.69	8.23	25.96	-33.65
MD4(3)-v	70	-1.74	48.76	6.98	21.01	-43.30

NOTE: u component is positive east, v component is positive north.

Table 4.6-2. Temperature Statistics for 3-Hour Low-Passed Records for Louisiana shelf Mooring MD

Meter (Deployment)	Depth (m)	Mean (°C)	Variance (°C ²)	Standard Deviation (°C)	Maximum (°C)	Minimum (°C)
MD3(1)	45	18.18	0.40	0.63	20.20	16.58
MD4(1)	70	17.09	0.46	0.68	18.83	14.92
MD1(2)	13	23.62	2.75	1.66	27.83	18.96
MD2(2)	25	21.69	3.81	1.95	26.28	18.35
MD3(2)	45	19.83	1.52	1.23	24.73	17.82
MD4(2)	70	19.21	0.25	0.50	21.48	17.79
MD1(3)	13	27.08	2.15	1.47	30.81	21.72
MD2(3)	25	24.76	5.38	2.32	28.49	19.51
MD3(3)	45	23.40	7.00	2.65	27.47	18.59
MD4(3)	70	20.47	3.52	1.88	25.80	17.85

Table 4.6-3. Velocity Component Variances ($\text{cm}^2 \text{s}^{-2}$) within Three Frequency Bands for Total 3-Hour Low-Pass Filtered Records for each of three deployments on the Louisiana shelf.

Frequency Band	DM1 (13m)		DM2 (25m)		DM3 (45m)		DM4 (70m)	
	u	v	u	v	u	v	u	v
HP (3-10 hr)							0.42	0.42
BP (10-38 hr)							1.25	1.66
LP (>38 hr)							6.27	2.33
Total (Deployment 1)	No Data		No Data		No Data		7.94	4.41

Frequency Band	DM1 (13m)		DM2 (25m)		DM3 (45m)		DM4 (70m)	
	u	v	u	v	u	v	u	v
HP (3-10 hr)	5.84	6.26	5.29	5.57	3.63	3.56	3.67	3.62
BP (10-38 hr)	35.57	25.93	32.92	37.61	21.33	19.05	22.47	30.70
LP (>38 hr)	348.73	84.99	297.65	66.17	160.88	34.73	43.16	27.31
Total (Deployment 2)	390.14	117.18	335.86	109.35	185.84	57.34	69.30	61.63

Frequency Band	DM1 (13m)		DM2 (25m)		DM3 (45m)		DM4 (70m)	
	u	v	u	v	u	v	u	v
HP (3-10 hr)			16.64	15.13	6.37	12.01	9.58	7.55
BP (10-38 hr)			57.08	43.13	45.19	40.05	23.49	27.66
LP (>38 hr)			1022.83	202.01	357.02	80.78	34.62	13.55
Total (Deployment 3)	No Data		1096.55	260.27	408.58	132.84	67.69	48.76

NOTE: u component is positive east, v component is positive north.

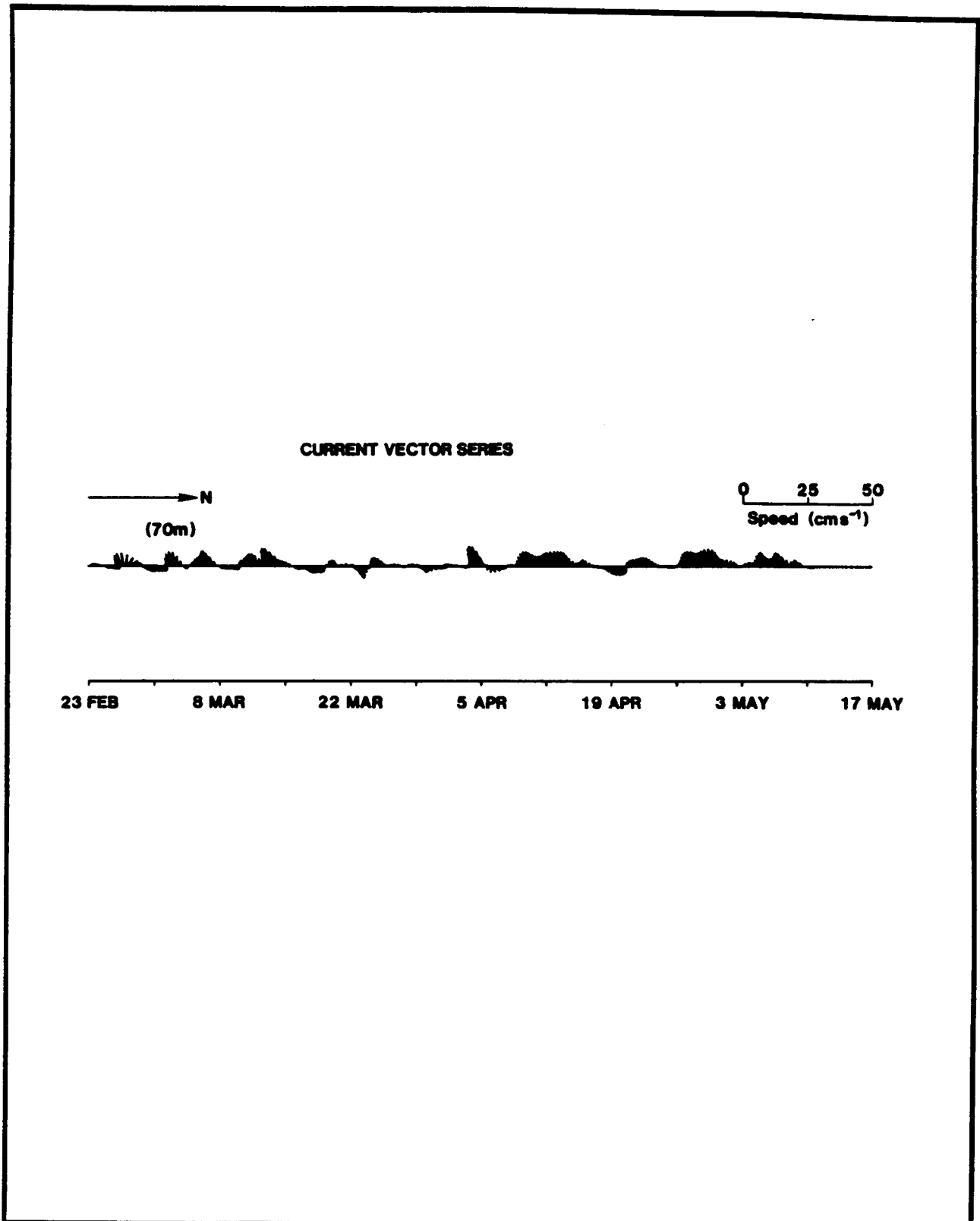


Figure 4.6-8. 38-hour low-passed current stick plots from the initial MD deployment (23 February to 10 May 1984).

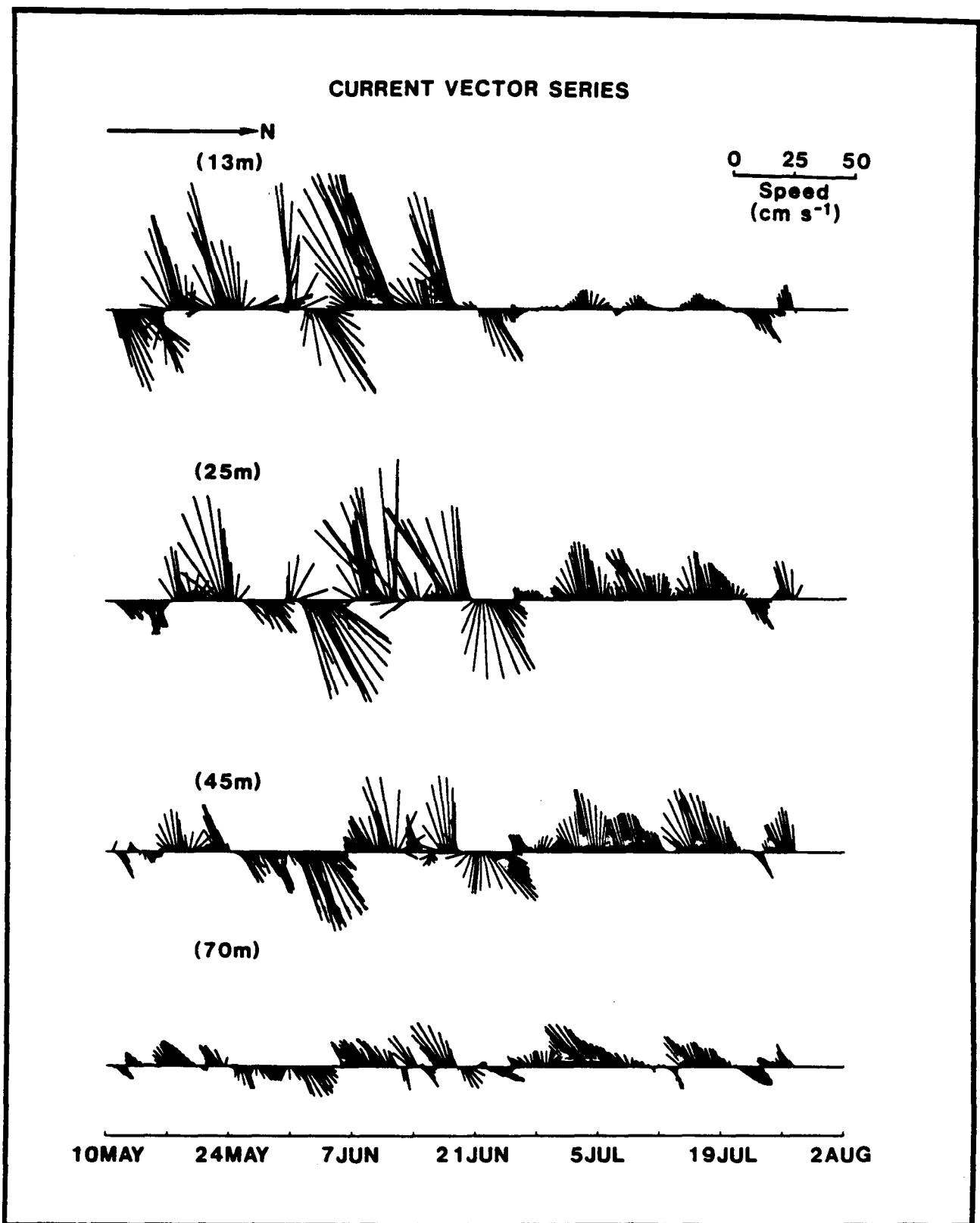


Figure 4.6-9. 38-hour low-passed current stick plots from the second MD deployment (10 May to 27 July 1984).

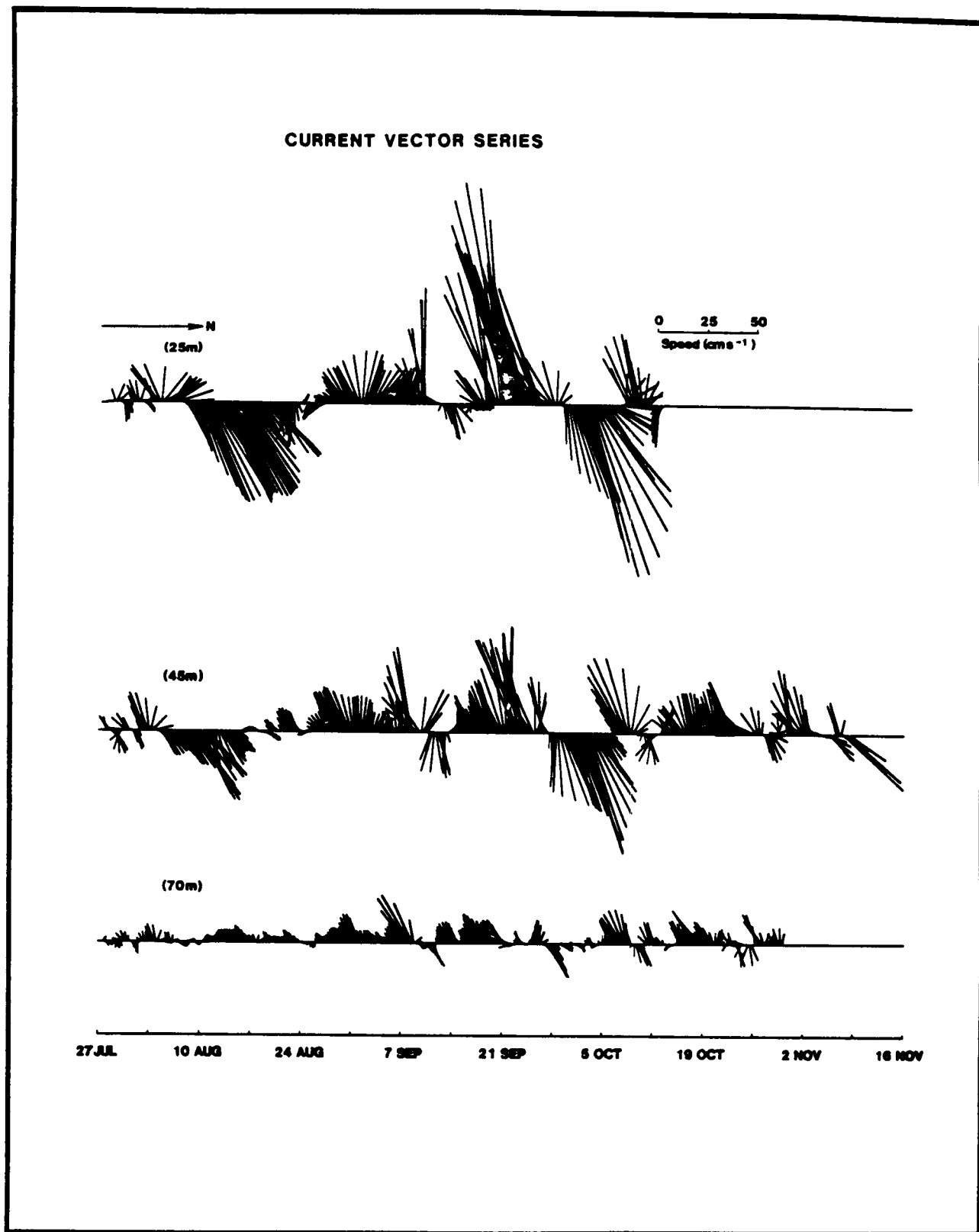


Figure 4.6-10. 38-hour low-passed current stick plots from the third MD deployment (27 July to 8 November 1984).

38-HR LOW PASS TEMPERATURE

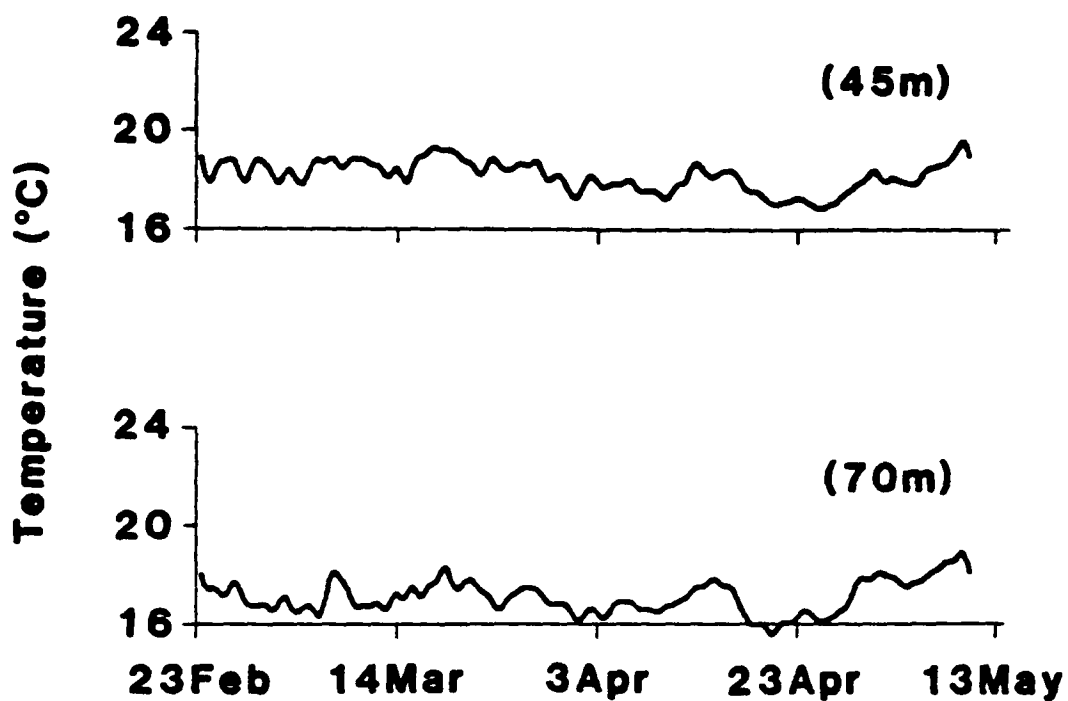


Figure 4.6-11. Line plots of the 38-hour low-passed temperature records from the initial MD deployment (23 February to 10 May 1984).

38-HR LOW PASS TEMPERATURE

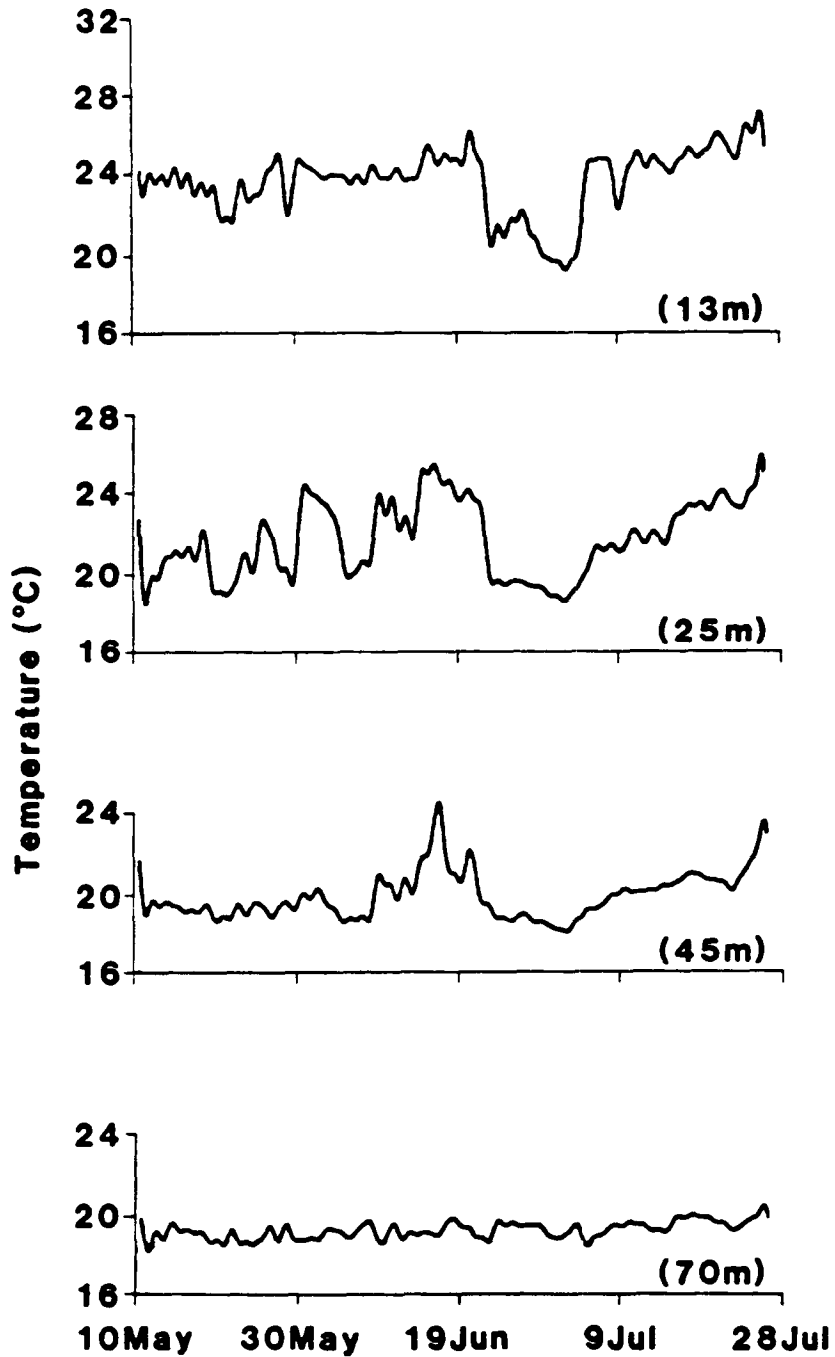


Figure 4.6-12. Line plots of the 38-hour low-passed temperature records from the second MD deployment (10 May to 27 July 1984).

38-HR LOW PASS TEMPERATURE

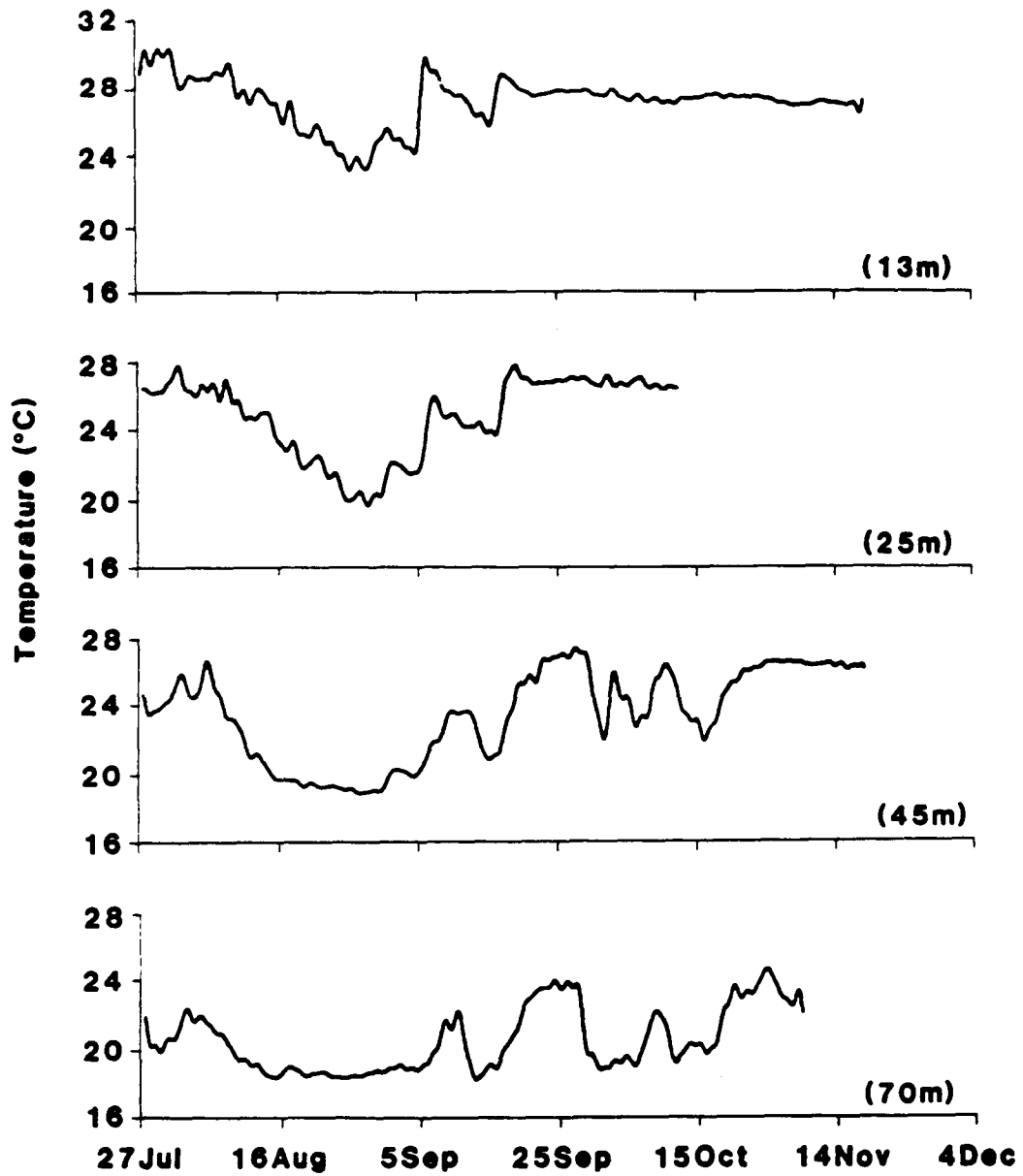


Figure 4.6-13. Line plots of the 38-hour low-passed temperature records from the third MD deployment (27 July to 8 November 1984).

Unfortunately, there is no evidence of the presence of the Loop Current or rings near the Mississippi Delta during the third deployment, so verification of the causes of the observed events must await further field work.

4.7 Analysis of South Texas Continental Shelf Current Meter Observations: July to December, 1984

4.7.1 Introduction

This study concerns the driving forces behind shelf circulation and the transport of sand and silt. Near-surface modern sediments of the south Texas Continental shelf (STOCS) are known to contain thin, discrete sand beds intercalated with mud (Berryhill et al., 1976; Figure 4.7-1). Some controversy surrounds the origin of these beds. They have been attributed variously to turbidity currents (Hayes, 1967) and wind force currents (Morton, 1981). However, previous studies have been plagued by a lack of data on the processes which operate upon the shelf. Some Eulerian measurements have been taken for short periods of time in water depths of less than 35 m (Smith, 1975, 1977, 1978, 1979), but no large-scale, long-period study has been previously conducted upon the STOCS, nor has there been any prior study of the kinematics and dynamics of sediment transport on this shelf.

4.7.2 General Geologic and Oceanographic Setting

The South Texas continental shelf represents an offshore extension of the gently seaward sloping coastal plain. During the late Pleistocene, sea level stood essentially at what is now the shelf break near 100 m (Figure 4.7-2). Examination of the isobath map reveals obvious protuberances on the northwest and south which seismic evidence suggests are buried Wisconsinian shelf-margin deltas (Suter and Berryhill, 1985). This project was most concerned with the portion of the STOCS situated between those two Pleistocene sand dispersal systems. This area represents what truly can be considered a muddy shelf. The mean grain size of surficial sediments in this embayment is well into the silt and clay range (Schideler, 1978).

Hydrographically, the STOCS is highly influenced by three factors: local river discharge during the spring and other periods, the freshwater plume of the Mississippi river delta, and cold air outbreaks. Figure 4.7-3 shows water discharge records for three Texas rivers at three representative nearcoastal sites. This two-year record shows that the highest rates occur typically in the spring, although heavy rains during other periods can occasionally cause high discharges such as seen in the Brazos valley during the fall of 1981. The spring-time peak discharges of Texas rivers occur somewhat later than with the maximum outflow of the Mississippi and Atchafalaya rivers. Smith (1980b) discovered from hydrographic measurements across the STOCS that a salinity minimum occurs in the late spring, suggesting westward advection of the Mississippi freshwater plume. In addition, a late summer salinity decrease was noted, which Lewis (1980) also attributed to the Mississippi-Atchafalaya outflow.

Frontal passages are thought to be responsible for the formation in late fall/early winter of a high density water mass in the central portion of the east Texas/western Louisiana shelf (Crout, 1983). Calculations by Crout (1983) reveal that this density gradient may drive westward baroclinic flow on

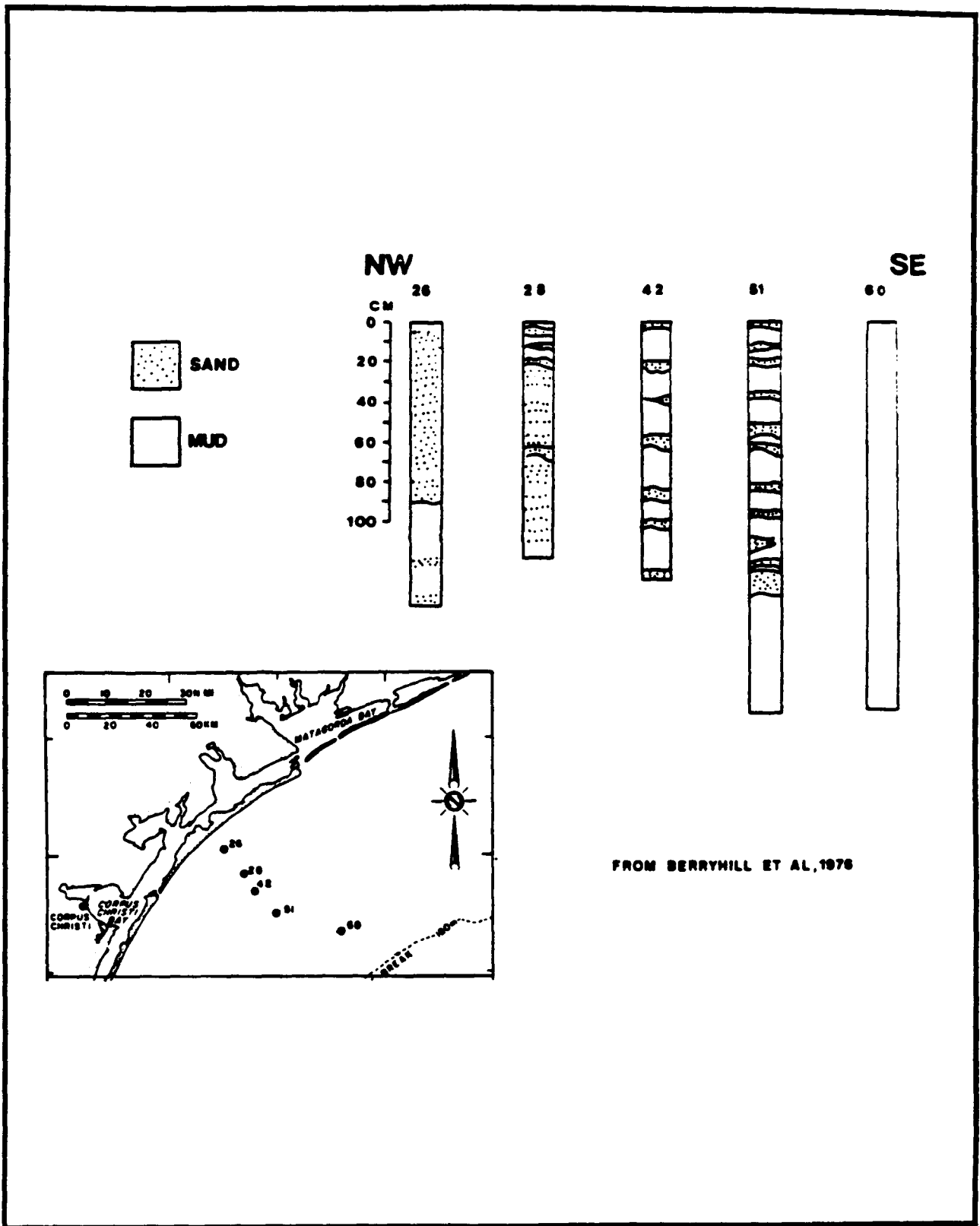


Figure 4.7-1. Gravity core transect across the STOCS near the study area (from Berryhill et al., 1976).

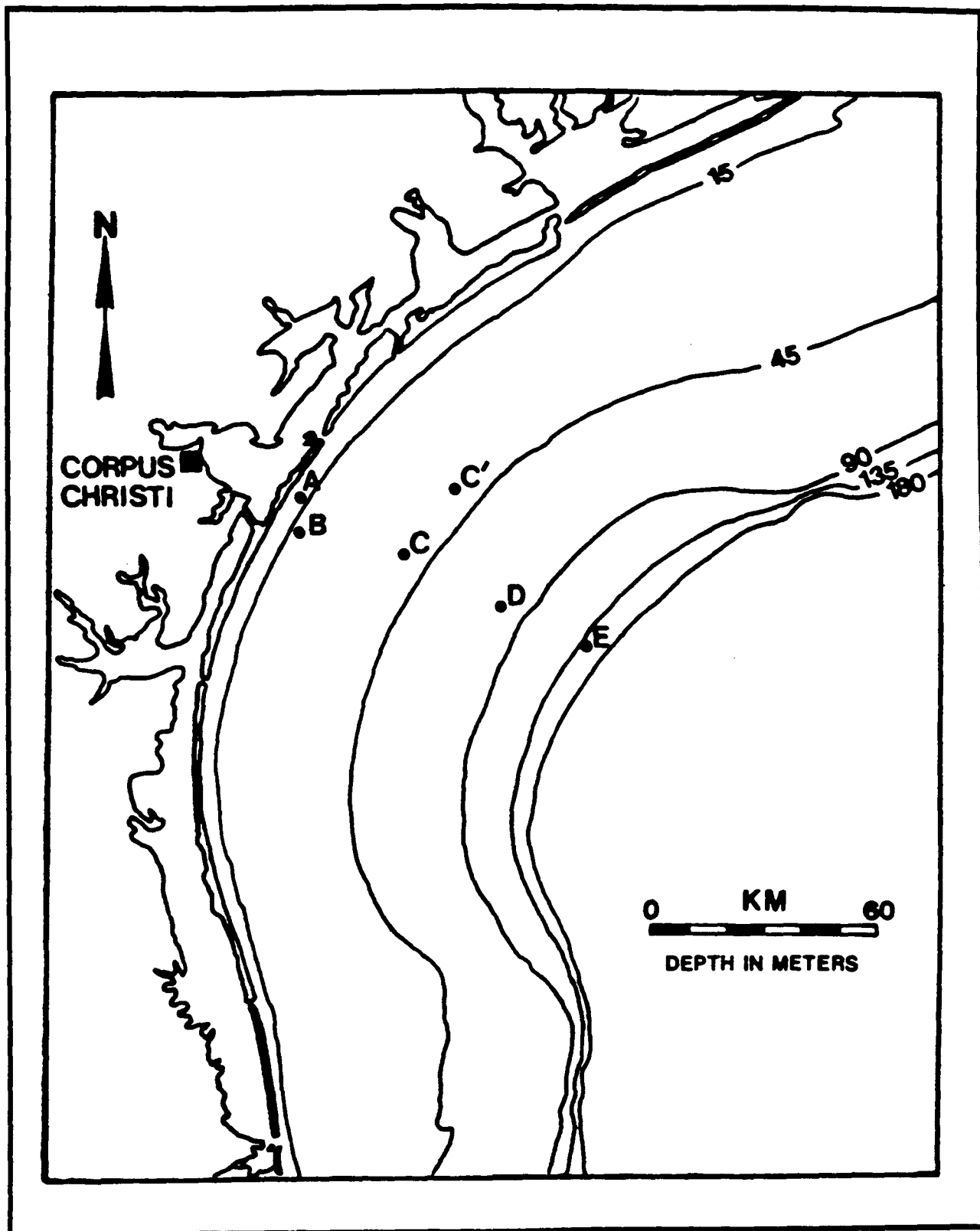


Figure 4.7-2. General bathymetric map of STOCS showing locations of current meters.

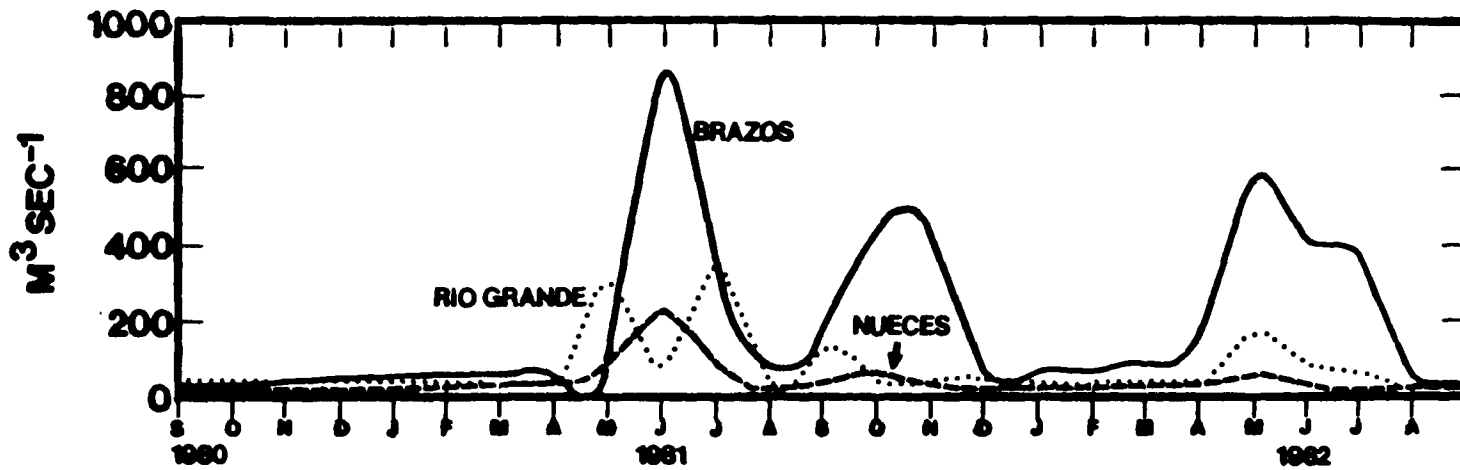


Figure 4.7-3. Monthly mean water discharges for the Brazos River near Richmond, Texas, the Nueces River at Mathis, Texas, and the Rio Grande River at Brownsville, Texas from September 1980 to September 1982. Data from Dept. of Interior.

the innershelf two to nine cm s^{-1} and on the outer shelf 1.5 to six cm s^{-1} eastward. However, these values are relatively insignificant compared to speeds recorded during this study and will not be discussed further. The most important physical effect of these cold air outbreaks lies in their ability to create virtually isothermal and isohaline conditions in nearshore waters (Smith, 1977, 1979). Outer shelf waters are less affected by these fronts, the major change being a slight deepening of the pycnocline and depth to the base of the mixed layer (Nowlin and Parker, 1974).

Other forces to consider are the anti-cyclonic rings which are known to pinch off the Loop Current and migrate westward toward the STOCS area (Elliott, 1982). Surface velocities associated with these features can get as high as 50 cm s^{-1} . However, most of these rings appear to dissipate their energy on the Mexican shelf, well south of the STOCS study area (Kirwan et al., 1984).

The wind stress and general circulation of the STOCS appear to have a seasonal pattern. Due to the almost year-round influence of the Bermuda High, the prevailing winds are southeasterly except for brief periods during the fall and winter when the trailing edges of cold fronts intrude upon the area. Along the north-south trending portion of the Texas coast, the result is a general northerly flow (Smith, 1980a). Along the more east-west trending Louisiana and east Texas coasts the result is more often a westerly current. Clearly the two must converge somewhere. Drifter data suggest a convergence near 27°N latitude (Hill and Garrison, 1978). However, this convergence appears to be more of a net annual condition. What appears to be more typical of a specific area like that offshore from Mustang Island, Texas, is a seasonal pattern where summer along-shelf current flow is to the north under the influence of southeast winds and to the south under more northerly winds associated with cold air outbreaks (Watson and Behrens, 1970; Smith, 1975). A further examination shows that the flow during both summer and winter alternates from northeast to southwest along-shelf depending on the orientation of the wind with respect to the coast. This is intimately related to the well-known fact that the most important driving force in general circulation on this shelf is the wind and its orientation.

4.7.3 Low Frequency Currents and Winds

For the purpose of analysis, the study period has been divided into two parts. In the first period, 16 July to 4 October 1984, all five meters were in operation for the majority of this time. In the second period, 4 October to 8 December, 1984, only meters C (34 m) and E (140 m) were in operation.

4.7.3.1 July to October

The 40 HRLP data for the first period are characterized by typical summer wind conditions and alternating along-shelf flow (Figure 4.7-4). Except for discrete periods of northerly winds, the wind was primarily from the south-southeast and southeast. Flow during the times of southerly winds was generally along-shelf to the northeast. Motion was fairly coherent across the shelf, although at 140 m there are some differences. The strength of the flow generally decreased offshore, with some exceptions. Current speeds at the nearshore locations peaked at 20 cm s^{-1} . Deep water waves recorded by Buoy 42002 had periods of five to six seconds and heights of less than a meter.

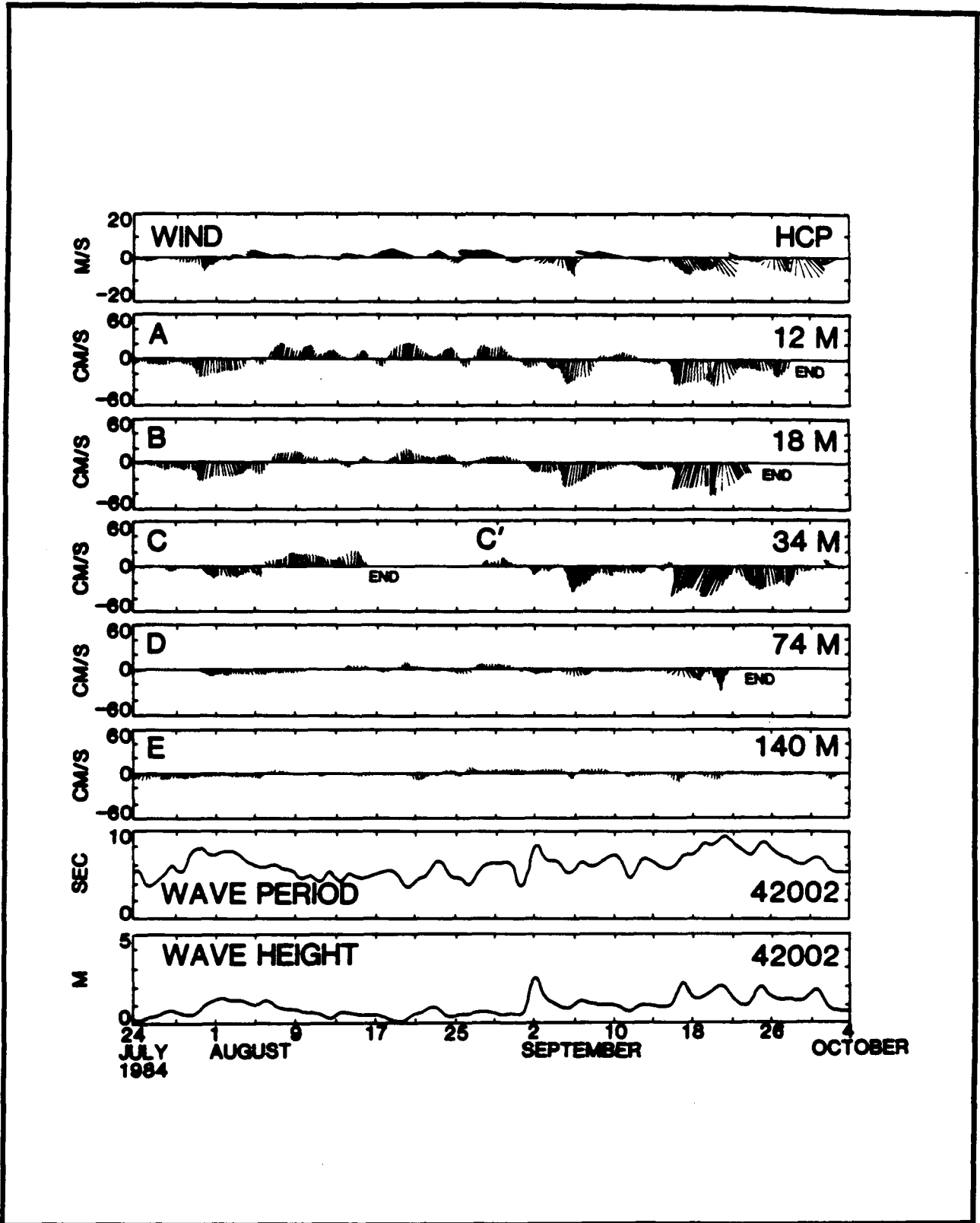


Figure 4.7-4. 40-h low-passed Eulerian data, 24 July to 4 October 1984. Wind data from Horace Caldwell Pier (HCP), Port Aransas, Texas. 40 HRLP wave data from Buoy 42002 is also shown. Vertical axis is along-shelf (V) motion, positive toward the NE. Cross-shelf (U) motion is positive offshore (SE). Wind is direction "towards", same as that of the currents.

Sturges and Blaha (1976) recognized that such southerly winds constitute a negative wind curl and can give rise to a western boundary current which they called the Mexican current. Although there has been some question as to the exact origin of this northerly current (e.g. Elliott, 1982), its presence has been well established. Indeed, this data set provides further evidence of its existence.

In between these periods of southerly winds, discrete intervals of northerly winds serve to drive flow on the STOCS. Occasionally these can be quite intense. The most important of these was an event on 16-24 September. Synoptic weather maps indicate that beginning on 16 September a stationary front became situated over the Gulf of Mexico midway between Buoy 42002 and the Texas coast. A low pressure center developed on its trailing edge at latitude 27°N and longitude 95°W. Although this center did not show any tropical characteristics, it did exhibit the cyclonic wind pattern typical of tropical storms (Figure 4.7-5). The northeasterly along-shelf winds produced a dramatic water level set-up at Mustang Island, with a rise of 1.5 m in 24 h. Waves were observed breaking at the toe of the dune line (Anthony Amos, 1984, pers. comm.). The storm deepened and wandered to the north, eventually making landfall on 22 September near Galveston, Texas. The highest tides recorded during September at Freeport, Texas (the nearest operative tide gauge), occurred at 0200 hours on 21 September. A dramatic change occurred in the beach topography for some 200 miles along the Texas coast as a result of the superelevated tides. Wave period and height as measured at Buoy 42002 increased substantially during this storm (Figure 4.7-4). Deep water wave period reached almost ten seconds with wave heights up to two m. Current speeds recorded at nearshore locations peaked at 40 cm s⁻¹. Flow was highly coherent all the way out to 140 m. Generally, motion was to the southwest, along-shelf.

Progressive vectors of the inferred Lagrangian motion during the July to October period show clearly the differences in the nature of water parcel displacement between the fair weather and storm conditions (Figure 4.7-6). During the fairweather period of southerly winds, motion is weak, meandering, and often oriented towards deeper water. This is similar to the weak bottom water return flow recognized by Smith (1977) to be a response to the onshore winds and presumably onshore-driven surface waters. Hydrographic data indicate that a well-developed pycnocline was present during this time which could be responsible for this inferred directional shear (A. Amos, 1984, pers. comm.). This weak offshore meandering contrasts sharply with the well-defined motion imposed by the storm event of 16-24 September. Flow is generally to the southwest, along-shelf. As will be discussed later, this displacement appears to be in phase with the northeasterly winds and the cross-shelf pressure gradient they induced.

4.7.3.2 October to July

During the second part of the study, 4 October to 7 December 1984 (Figure 4.7-7), current meters were operative at C' (34 m) and E (140 m). The wind record shows a pattern more typical of the fall and winter: the response to the passage of the trailing margins of migrated low pressure centers. Typically, as a front approaches a fixed location, barometric pressure falls and winds increase out of the southeast quadrant. Winds then rotate clockwise and become northwesterly following the passage of the front. Because the low

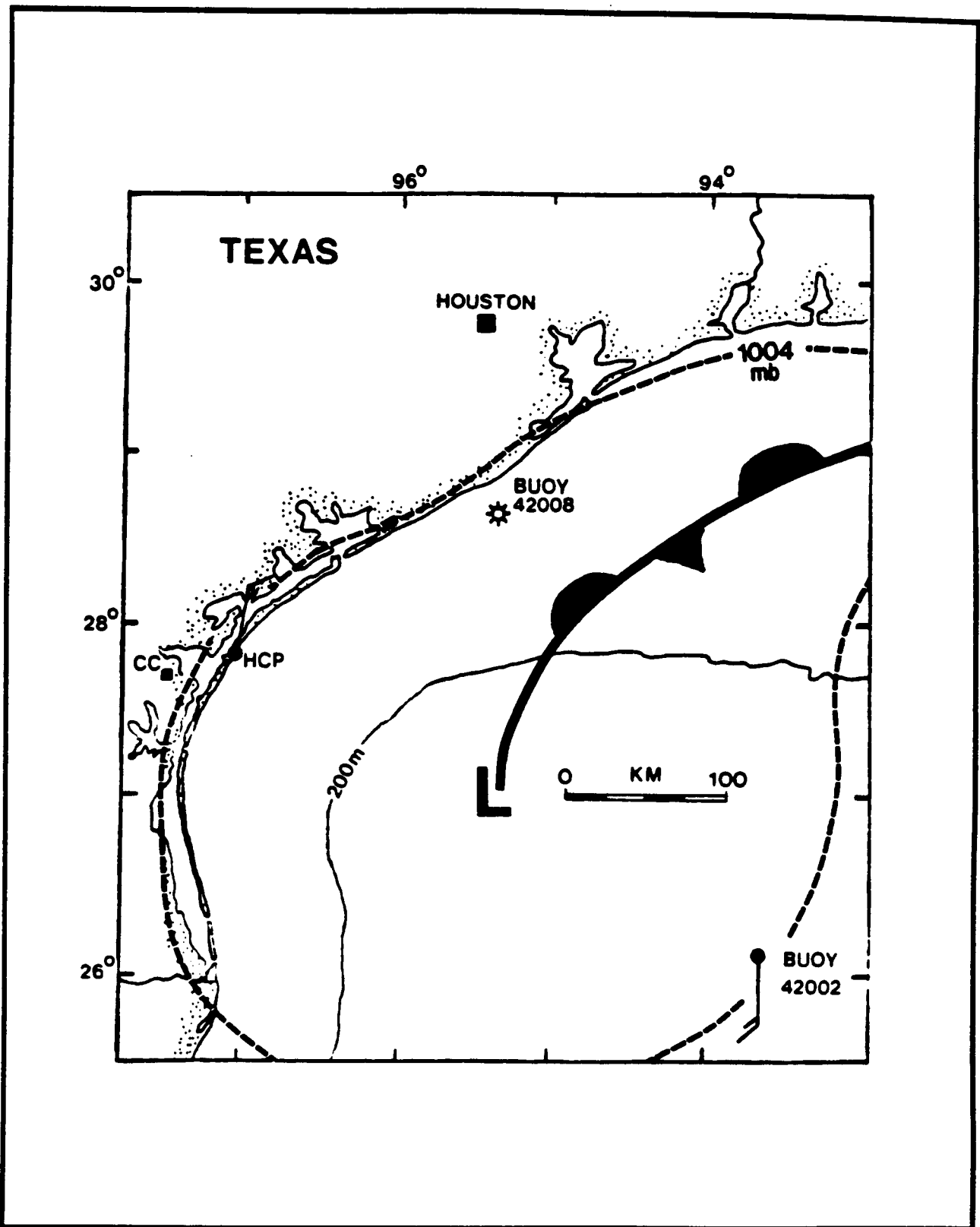


Figure 4.7-5. Extratropical storm on 19 September 1984. Data from U. S. Weather Bureau synoptic weather maps.

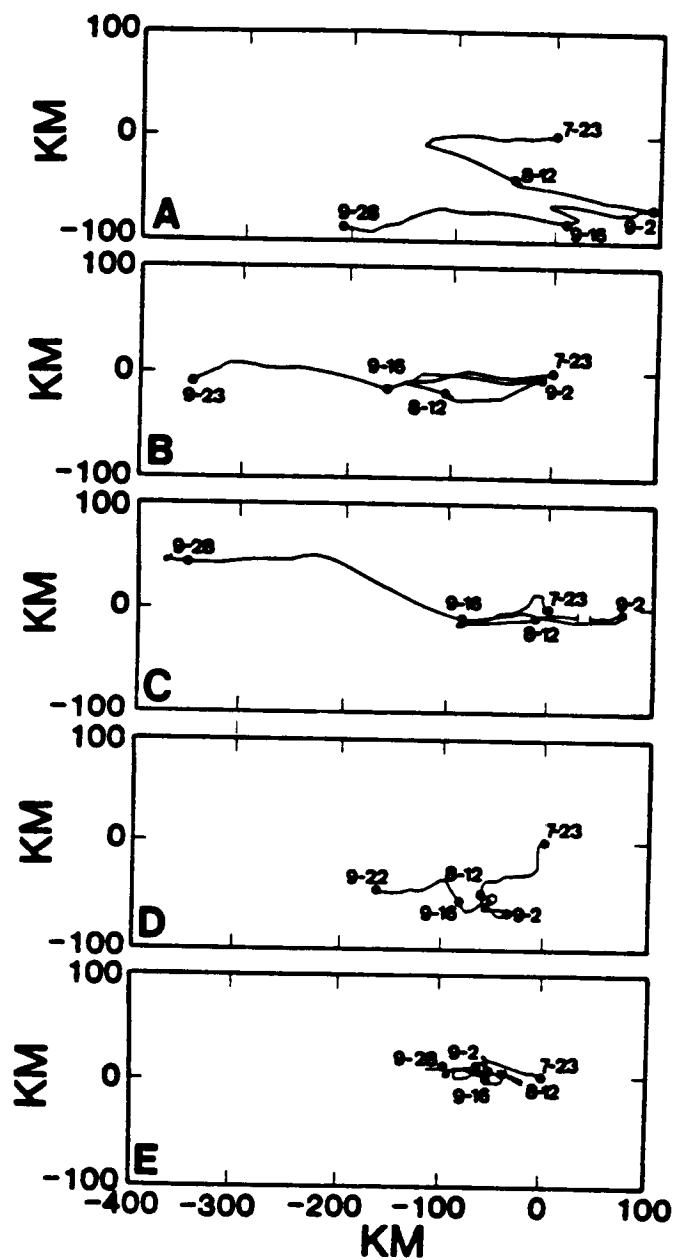


Figure 4.7-6. Inferred low frequency Lagrangian motion at current meter A (12 m), B (18 m), C (34 m), D (74 m) and E (140 m), 23 July to 4 October 1984. Vertical axis is cross-shelf (U) motion, positive towards the coast. Horizontal axis is along-shelf (V) motion, positive toward NE. Gap in motion at C represents period when meter was out of water prior to redeployment.

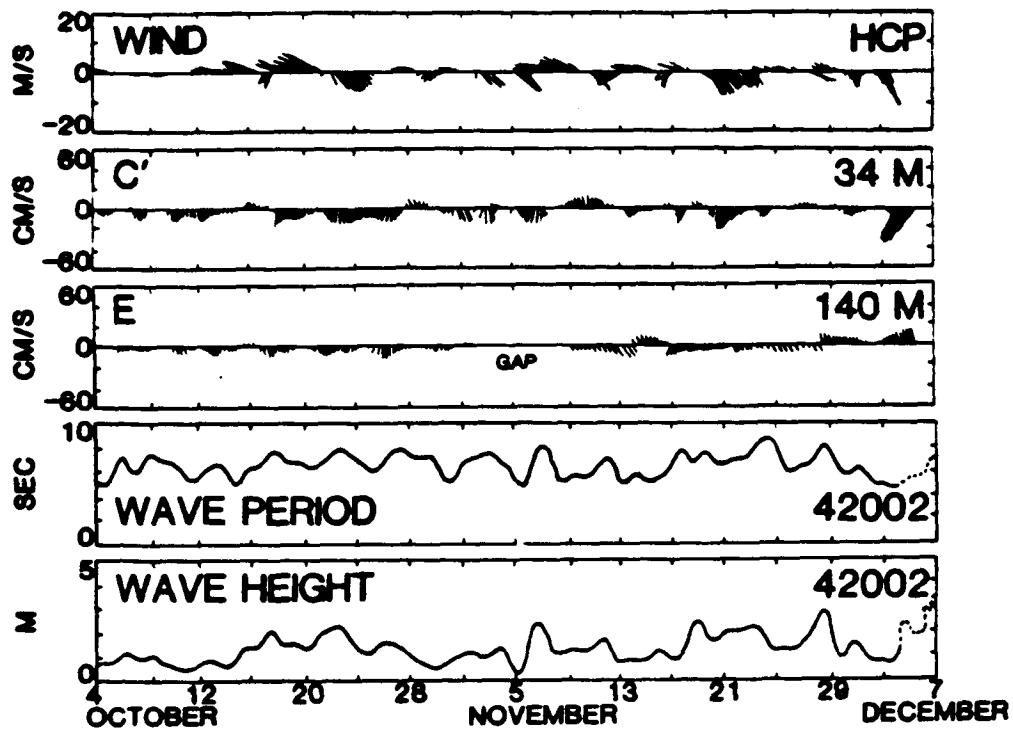


Figure 4.7-7. 40-h low-passed Eulerian data, 4 October to 7 December 1984. 40 HRLP wave data from Buoy 42002 is also shown. Eulerian data has been rotated 35 degrees. Vertical axis is along-shore (V) motion, positive toward the northeast. Crossshelf (U) motion is positive offshore (SE). Wind is direction "towards".

pressure centers generally migrate well to the north of the STOCS, northeasterly winds are generally weak or non-existent.

As expected, current flow at 34 m responded to these changes in the overlying wind field. Generally, southeasterly winds appear to drive weak northeasterly along-shelf motion. Northwesterly winds appear to force motion to the southwest, although there is a pronounced onshore component. At 140 m, there is considerably less coherence with wind and motion at 34 m. Certainly, there is a much slower response to the rapid changes in the wind field, suggesting forcing is more by lateral friction with shallower water motion than by any direct coupling with the wind.

The most significant record occurred toward the very end. On 3 December, a well-developed wave cyclone migrated across the midwestern states, its trailing cold front skirting the STOCS. However, as the low pressure center became disorganized along the Atlantic seaboard, the trailing margin stalled over the Gulf of Mexico. Like the storm of 20 September, a secondary low pressure center developed offshore from Brownsville, Texas. Again, this produced cyclonic wind circulation and along-shelf winds across the study area. The net result was water level set-up at the coast. The swash zone was about 1 m above fairly normal fair weather levels.

Progressive vectors of the inferred lagrangian motion recorded at C' (34 m) show a consistent onshore motion at the bottom (Figure 4.7-8). Flow at E (140 m) tends to parallel that motion, but is smaller in magnitude. During the storm of 4-6 December, bottom water movement at 34 m appears to be oriented onshore to the west-southwest, a pattern similar to that of the September event. However, motion at 140 m is directed towards the north, suggesting some divergence of bottom water flow.

4.7.4 Boundary Shear Stress

Eulerian data such as these have often been used to make inferences concerning the nature of sediment transport in a given area (e.g. Adams et al., 1982). Such inferences must be made in the light of present knowledge of geophysical fluid boundary layers. Because of the no-slip condition at the seawater-sea bottom boundary, the flow directly above the bottom is modified in speed and direction (Pedlosky, 1979). The typical ocean boundary layer consists of two parts: the logarithmic layer, where current speed increases logarithmically upwards from the boundary, and the much larger Ekman layer. Above this point, where flow is unaffected by friction, is the geostrophic interior. Directional shear in the boundary layer theoretically occurs only in the logarithmic layer although there have been some reports of veering in the Ekman layer (e.g. Weatherly, 1972).

The flow of sea water past this sea bottom boundary generates shear stress, commonly measured in dynes cm^{-2} . Early flume experiments have shown that the entrainment of clastic particles is related to the magnitude of this quantity. Commonly, the boundary shear stress can be calculated by the use of the quadratic stress law:

$$T_o = C_d P U^2_{100}$$

where T is the boundary shear stress, C_d is the drag coefficient (here 0.001),

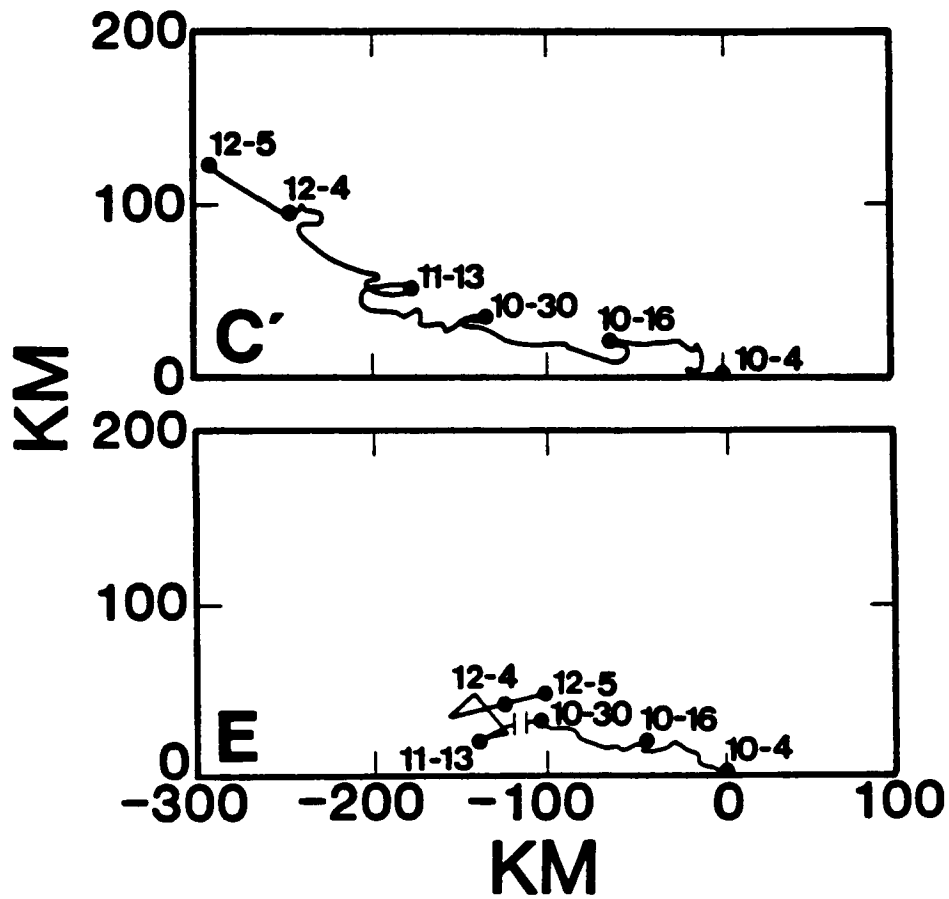


Figure 4.7-8. Inferred low frequency Lagrangian motion at current meter C' (34 m) and E (140 m), 4 October to 7 December 1984. Orientation of axes same as in Figure 4.7-6.

P is the fluid density (1.027 g cm^{-3}) and U_{100}^2 the velocity measured one meter above the bottom.

However, in the coastal ocean, currents are not the sole source of shear stress. Surface gravity waves generated by the wind and other sources also exert force upon the boundary, particularly in shallow water (Madsen, 1976). It has also been shown that the non-linear interaction of waves and currents contributes to the total shear stress. This total may be many times greater than the simple addition of the shear stress due to the waves and currents alone (Grant and Madsen, 1979).

With this in mind, the total boundary shear stress at each location has been calculated for the two time periods (Figures 4.7-9 and 4.7-10). The deep water wave data have been adjusted for phase velocity lag, bottom refraction and shoaling, bottom friction, and energy dissipation upon the muddy shelf bottom typical of the STOCS using the guidelines of Komar (1976), Madsen (1976), Tubman and Suhayda (1976), and Hsiao and Shemdin (1978, 1980). Of particular importance was the energy dissipation in the muddy shelf bottom which can result in considerable wave attenuation in some cases (Forristall and Reece, 1985).

Superimposed upon the diagrams is a dashed line representing the critical threshold for 68 micron sand. Analysis of the grain size distribution of discrete sand layers in boxcores taken on the shelf during this project indicates that 68 microns (about four phi) is the modal peak of the size distribution (Figure 4.7-11). This is slightly finer than the modal peak of beach sands of adjacent Mustang Island.

Flume experiments by Shields (1936) established the numerical conditions necessary for the initiation of sediment motion. In his work, he constructed diagrams of dimensionless fluid stress, theta, and boundary Reynolds number. From a given grain size, the threshold shear stress can be calculated. Bagnold (1966) later revised this diagram, putting grain size on the horizontal axis. He also established criteria for determining the mode of sediment transport (i.e. suspension versus bedload). These suspension criteria were later modified by McCave (1971), based upon measurements in the North Sea (Figure 4.7-12). Use of this diagram indicates that 68 micron (.068) sand will be transported entirely in suspension and will have a threshold shear stress of $1.4 \text{ dynes cm}^{-2}$. It should be mentioned that Shields (1936) did not actually have measurements of the threshold values for sand grains finer than 0.1 mm. Later work by Vanoni (1964) and White (1970) suggested that Shields' (1936) extrapolation is a little pessimistic in the fine sizes. However, the error is greatest at the finest sizes and for 68 micron sand is less than 10%.

It appears from Figures 4.7-9 and 4.7-10 that the most important sedimentological events in the time series occurred during the September and December storms mentioned previously. However, even during these events, the threshold was not exceeded at locations D (74 m) and E (140 m). This is not surprising, considering that it is unlikely that surface gravity waves will feel bottom in such water depths in less than "hurricane" conditions. It is also important to note that boundary stress recorded at the shallower locations often exceeds the wind stress values, further emphasizing the contribution of other factors which will be discussed later.

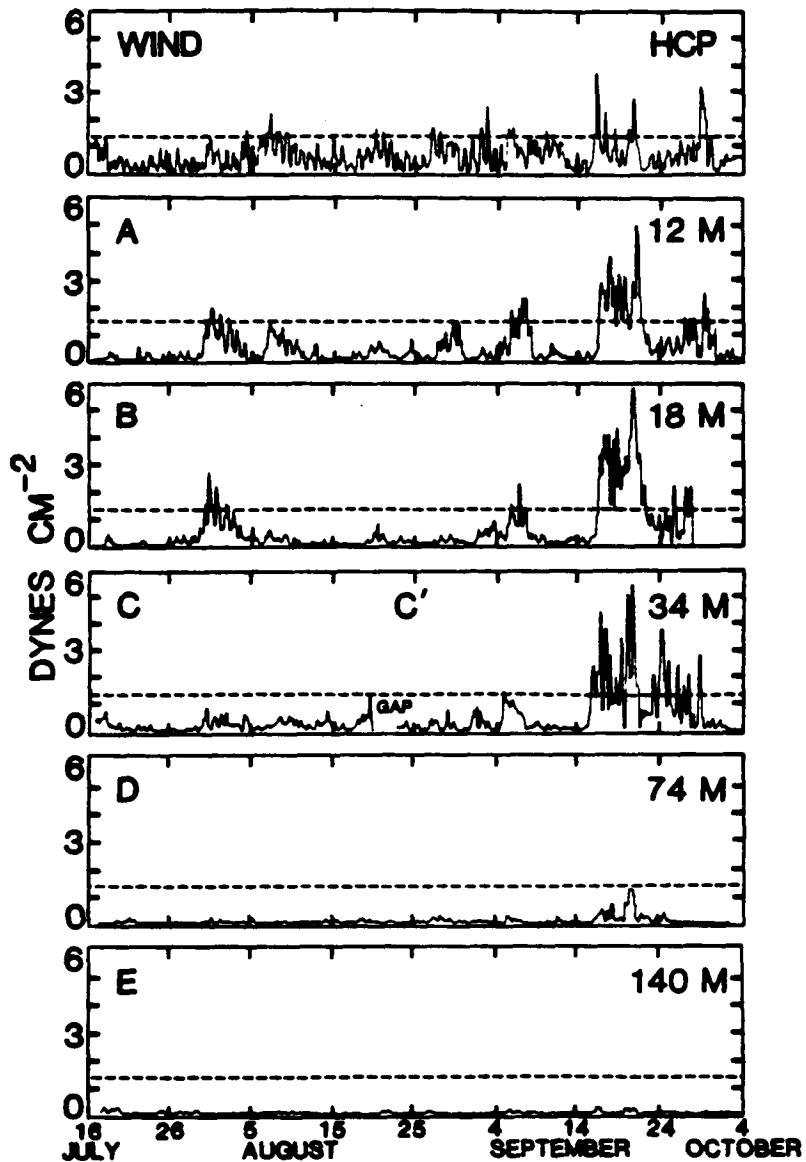


Figure 4.7-9. Boundary shear stress due to combined wave and current interaction at current meter locations on the STOCS 16 July to 4 October 1984. Wind stress is also shown. Dotted line is the critical threshold for initiation of motion of 68 micron sand (based upon McCave, 1971; see Figure 4.7-12).

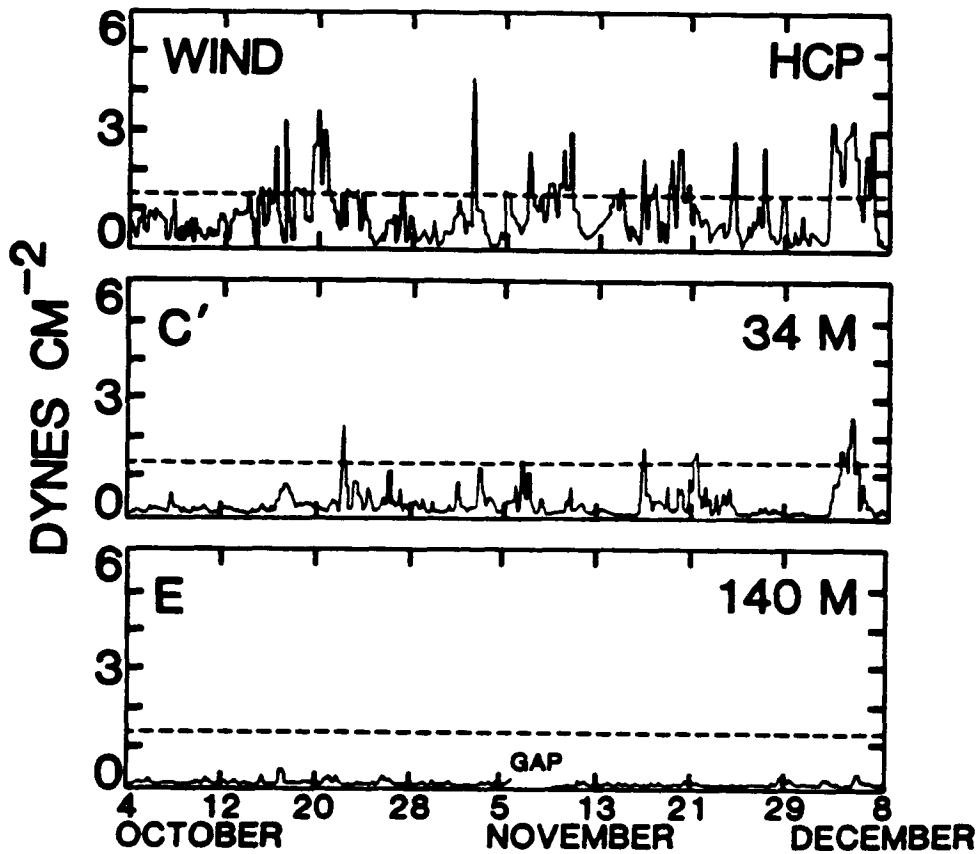


Figure 4.7-10. Boundary shear stress due to combined wave and current interaction at current meter locations on the STOCS 16 October to 9 December 1984. Wind stress is also shown. Dashed line is the critical threshold for initiation of motion of 68 micron sand (based upon McCave, 1971; see Figure 4.7-12).

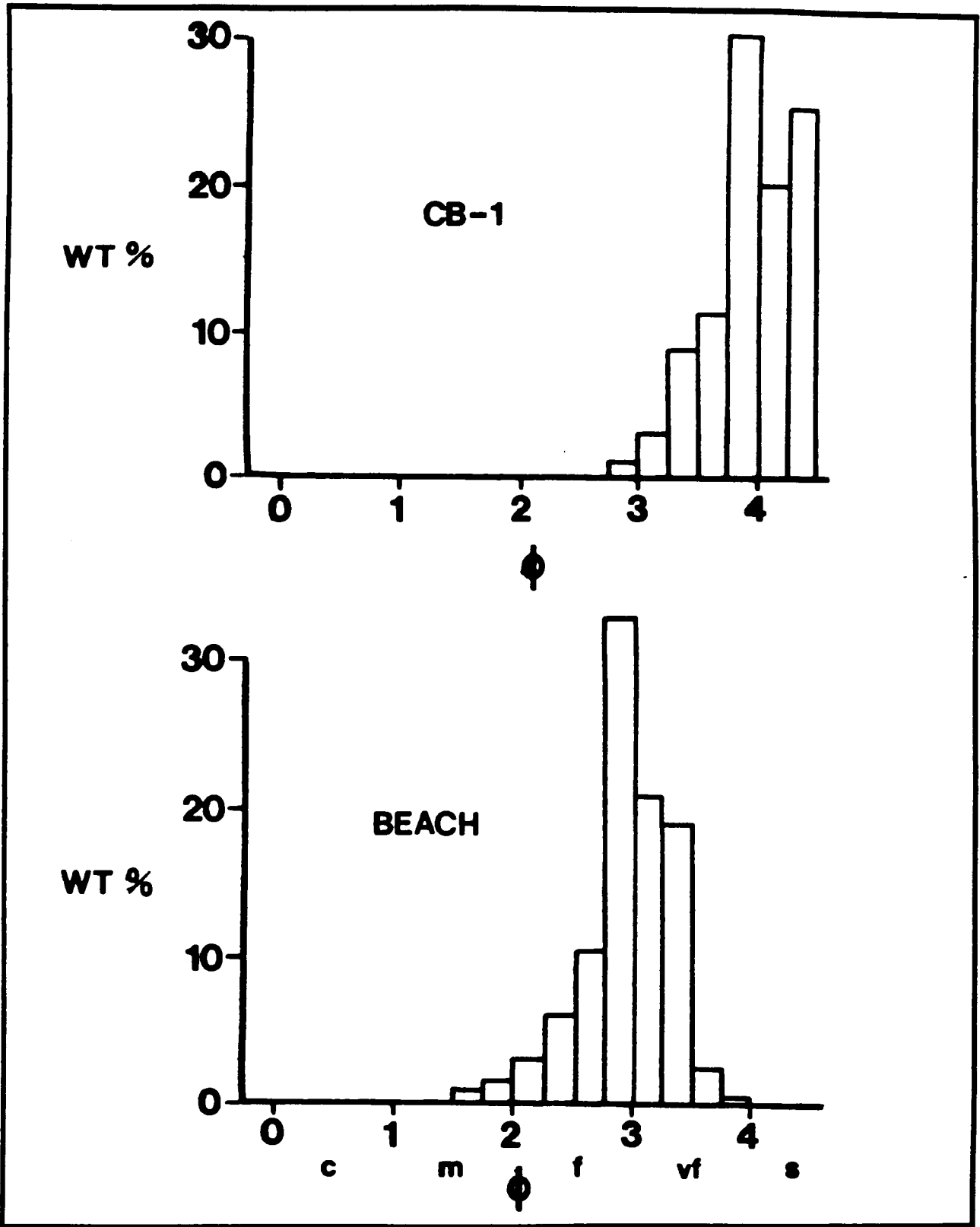
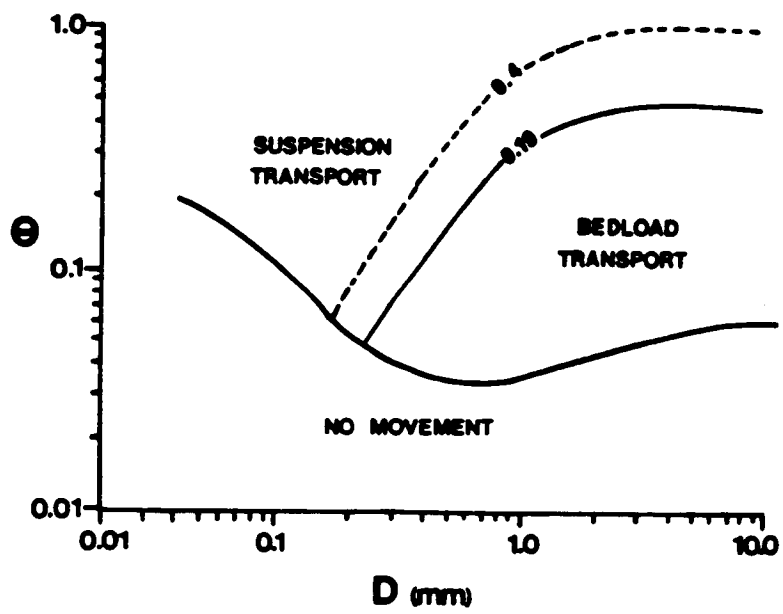


Figure 4.7-11. Grain size distributions of samples from boxcore CB-1 (26 m) and from beach at Mustang Island.



FROM MCCAVE, 1971

Figure 4.7-12. Modified Shields diagram (from McCave, 1971). Dashed line is critical suspension curve of Bagnold (1966).

Adams et al. (1982) found that values calculated from the quadratic stress law tend to be 20% higher than those actually present in the sediment-laden flow. This apparent reduction in boundary shear stress is related to the dynamics of sediment-current interaction. Without measurements at several different levels above the boundary, it is difficult to determine whether a flow has taken on such characteristics. However, as an adjustment for this phenomenon, a threshold of $1.68 \text{ dynes cm}^{-2}$ was superimposed upon periods where there appears to be just such a flow. As Figures 4.7-9 and 4.7-10 suggest, the September and December storms are still sedimentologically important events.

Once it has been determined that the threshold of sediment motion has been exceeded during an event, the most critical question concerns the kinematics of sediment transport. To answer this question, progressive displacement vectors were plotted for the periods during which the boundary shear stress was in excess of the threshold of motion (Figures 4.7-13, 4.7-14). Motion was assumed to continue until the shear stress values fell below 0.9 times the threshold. Because 0.068 mm sand is transported entirely in suspension, the progressive vectors are considered to represent the motion of this sand upon the STOCs during periods of elevated shear stress. During the first period, it appears that sand transport is along-shelf to the southwest (Figure 4.7-13). There is a noticeable cross-shelf gradient in transport. Bottom transport appears to become more onshore the further out toward deeper water. The cause of the gradient is being investigated. During the second period, sand transport is almost entirely confined to a two-day period in December (Figure 4.7-14). Like the response to the storm in September, motion at 34 m is largely onshore to the west-southwest.

4.7.5 Forcing Mechanisms

Without some analysis of the possible driving forces behind the transport of sand on the STOCs, only kinematics of that transport would be revealed. Toward this end, the two storms which occurred during the study period have been studied closely. Figure 4.7-15 shows the low frequency (40 HLP) progressive displacement vectors of the wind during the study period. As mentioned, the wind was out of the southeasterly quadrant for the majority of the study period. However, two important departures occurred during 16-24 September and 4-5 December 1984 when winds came out of the northeast quadrant.

During these two events, surface water was presumably driven toward shore where it met the constraint of the coastal boundary. The result was a rise in sea level as measured by the nearest operative tide gauge at Freeport, Texas, 200 km to the northeast. In the case of the September event, the highest water level occurred at 0200 CST on the 21st (Figure 4.7-16). The peak in the water level coincides roughly with the maximum current speeds and thus the shear stress due to currents. The slight time lag may be attributed to the distance between the study site and the Freeport gauge. The boundary shear stress due to the currents is numerically greater than the wind stress, suggesting the presence of a cross-shelf pressure gradient. Since the time scale of the motion was considerably in excess of the inertial period, it is likely that the rotation of the earth played a role in deflecting flow to the southwest. In other words, motion was in geostrophic balance.

The December storm shows similar characteristics, although the difference between the values of wind stress and shear stress is smaller. The lack of

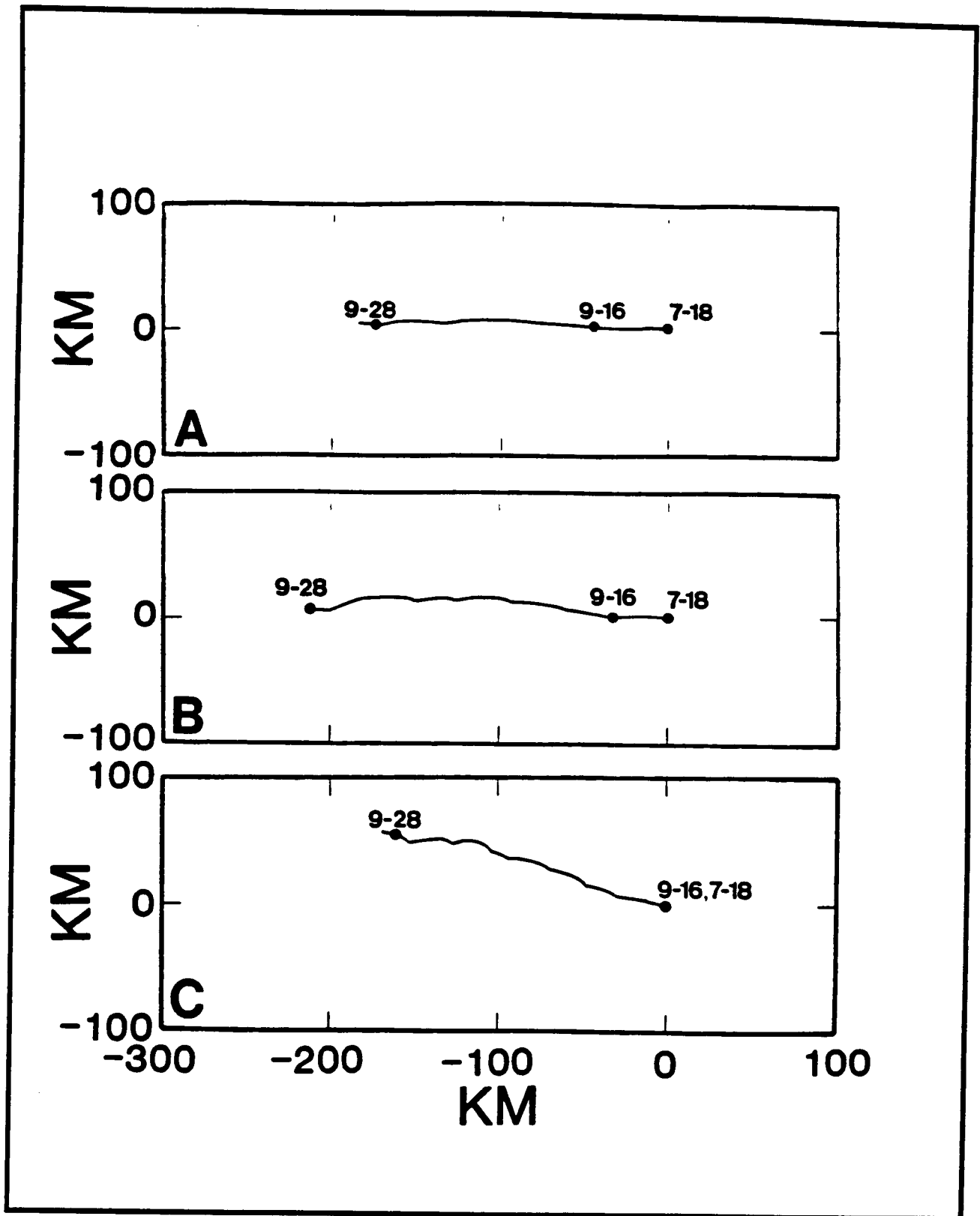


Figure 4.7-13. Inferred Lagrangian displacement of sand, 16 July to 4 October 1984. Orientation of axes same as Figure 4.7-6.

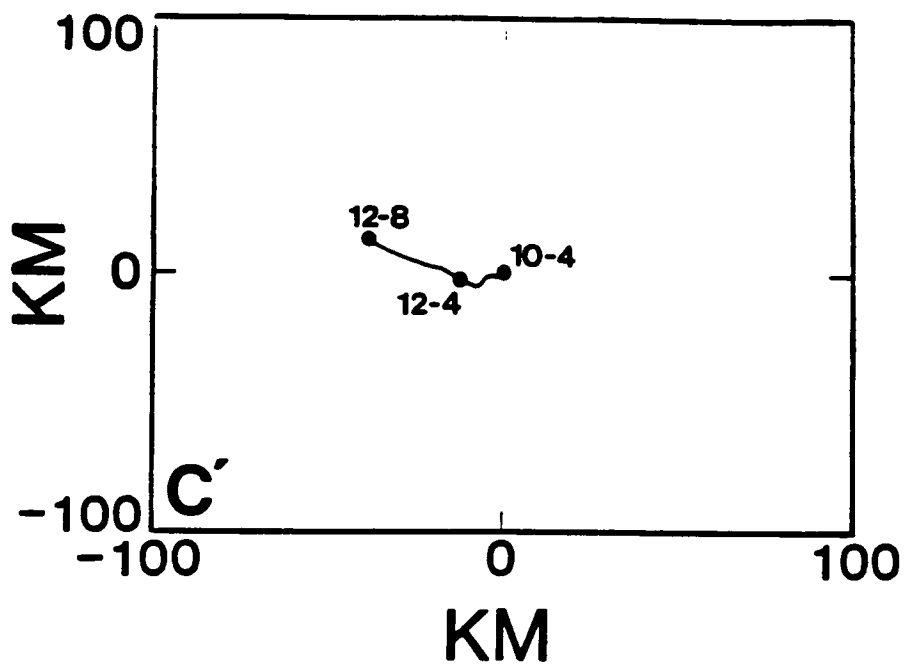


Figure 4.7-14. Inferred Lagrangian displacement of sand, 4 October to 8 December 1984. Orientation of axes same as Figure 4.7-6.

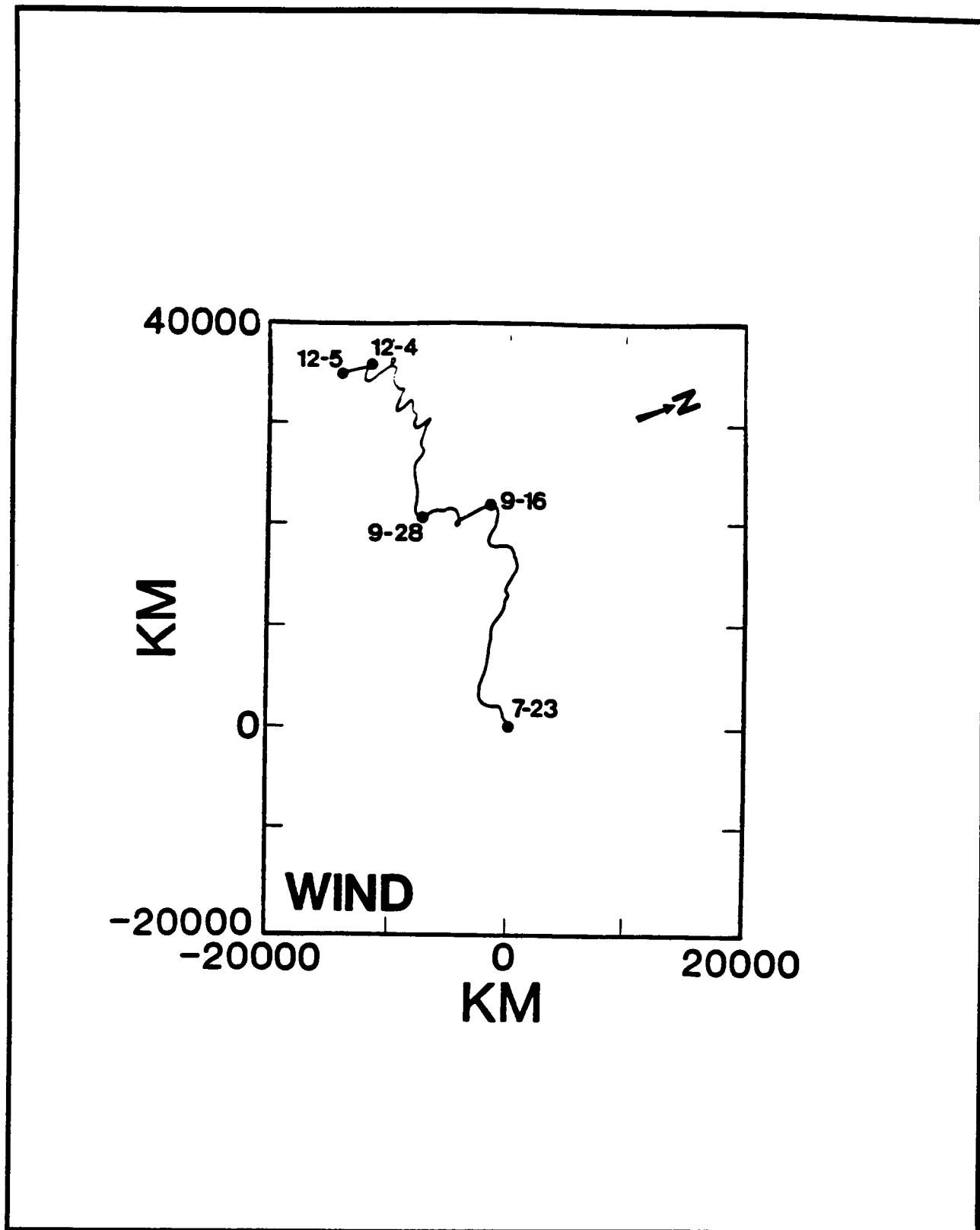


Figure 4.7-15. Inferred Lagrangian motion of low frequency wind, 23 July to 5 December 1984. Wind measured at Horace Caldwell Pier, Port Aransas, Texas. Orientation of axes is the same as Figure 4.7-6.

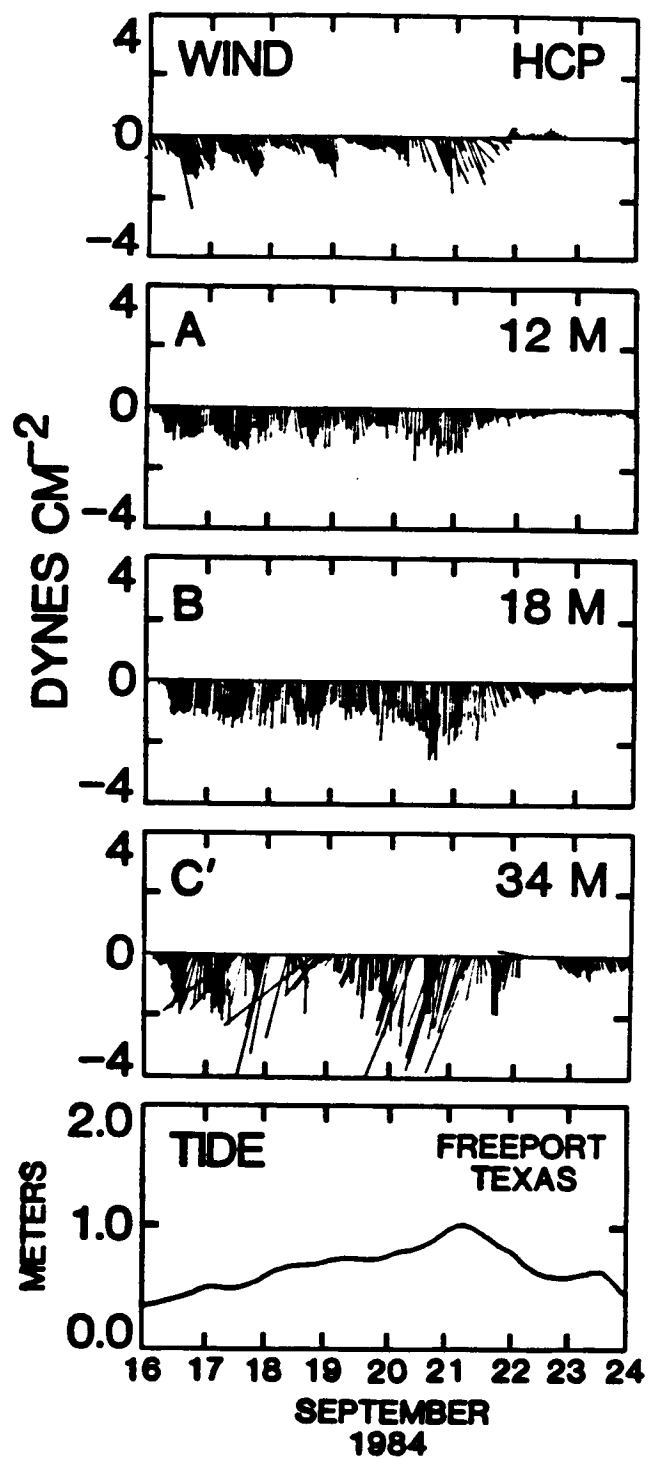


Figure 4.7-16. Unfiltered shear stress due to currents at 12 m, 18 m, and 34 m. Wind stress is also shown. Tidal data is 40-hour filtered record from Freeport, Texas. Height is distance above NGVD.

Eulerian measurements at 12 and 18 m precludes discussion of the effectiveness of this higher wind stress in driving motion in shallow water, particularly during a period when the water column was largely unstratified. However, the fact that the motion at 34 m during this event is so similar to its response during the September event when the water column was stably stratified leads to the belief that the inshore response was also similar.

4.7.6 Conclusions

In hopes of gaining some knowledge about the nature of shelf water circulation and sediment transport, five ENDECO 105 current meters were deployed across the south Texas continental shelf (STCS) for a 145 day period from July 16 to December 8, 1984. Analysis of these data suggests the following:

- 1) At the lower frequencies, coherence between the overlying wind field and the bottom current structure decreases in an offshore direction. However, there is still some coherence even at the shelf break, indicating that lateral friction between shallow and deep water plays a role in generating motion.
- 2) The July-October time period is often characterized by southerly winds and weak northerly offshore motion. This "fairweather" flow is occasionally interrupted by periods of intense southwesterly flow driven by northerly winds.
- 3) The October-December time period also shows alternation in along-shelf flow but this time the flow is driven by the wind field associated with the passage of the trailing margins of mid-latitude lows.
- 4) Two events, the first lasting from 16 to 24 September and the second from 4 to 6 December, appear to be quite important in terms of shelf sediment transport. In both cases, a low developed offshore and to the south of the study area. The cyclonic wind circulation associated with the two produced unusual NE winds. To some degree, the wind fields are similar to that of a tropical storm or hurricane. The NE winds caused a water level set-up at the coast and a general downwelling situation upon the shelf. Flow during the events was southwesterly and apparently in geostrophic balance with the cross-shelf pressure gradient and Coriolis force.

4.8 References for Chapter 4

- Adams, E. E., J. T. Wells, and J. M. Coleman, 1982. Sediment transport on the central Louisiana continental shelf: Implications for the developing Atchafalaya River delta. *Contrib. Mar. Sci.* 25: 23-40.
- Bahnold, R. A., 1966. An approach to the sediment transport problem from general physics. U.S.G.S. Prof. Paper 422-I, 40 pp.
- Behringer, D. W., R. L. Molinari, and J. F. Festa, 1977. The variability of anticyclonic current patterns in the Gulf of Mexico. *J. Geophys. Res.* 82: 5469-5478.
- Bendat, J. S. and A. G. Piersol, 1966. *Measurement and Analysis of Random Data.* Wiley & Sons, New York, 184-185, 390 pp.
- Berryhill, H. L. et al., 1976. Environmental studies, south Texas outer continental shelf (Geology). Available only U. S. Dept. Commerce, Nat's Tech. Inf. Serv., Springfield, Virg. Report PB 289-144/AS. 306 pp.
- Brooks, D. A., and R. V. Legeckis, 1982. A ship and satellite view of hydrographic features in the western Gulf of Mexico. *J. Geophys. Res.* 87(C6): 4195-4206.
- Brooks, P. A., 1984. Current and hydrographic variability in the northwestern Gulf of Mexico. *J. Geophys. Res.* 89(C5): 8022-8032.
- Clark A. J. and Stephen Van Gorder, 1985. A method for estimating wind driven shelf and slope water flow. *J. Phys. Oceanogr.*, in press.
- Cochrane, J. D. and F. J. Kelly, 1982. Proposed annual mean progression in the mean Texas-Louisiana shelf circulation. *Trans. Am Geop. Union.* 63(45): 1012.
- Cochrane, J. D., 1972. Separation of an Anticyclone and Subsequent Developments in the Loop Current (1969). In: L. R. A. Capurro and J. L. Reid (eds.), *Contributions on the Physical Oceanography of the Gulf of Mexico.* Gulf Publishing, pp 91-106.
- Crout, R. L., 1983. Wind-driven, near-bottom currents over the western Louisiana inner continental shelf. Unpublished Ph.D Dissertation, Louisiana State Univ., 117 pp.
- Csanady, G. T., 1982. *Circulation in the Coastal Ocean.* Reidel Pub. Co., London, 280 pp.
- Ebbesmeyer, C. C., G. N. Williams, R. C. Hamilton, C. E. Abbott, B. C. Collipp, and C. F. McFarlane, 1982. Strong persistent currents at depth off the Mississippi River delta. *Proc. Offshore Technology Conf.* 259-267 pp.
- Elliott, B. A., 1982. Anticyclonic rings in the Gulf of Mexico. *Phys. Oceanogr.* 12: 1293-1309.

- Forristall, G. Z., and A. M. Reece, 1985. Measurements of wave attenuation due to a soft bottom: The SWAMP experiment. *Geophys. Res.* 90(C2): 3367-3380.
- Grant, W. D. and O. S. Madsen, 1979. Combined wave and current interaction with a rough bottom. *J. Geophys. Res.* 84(C4): 1797-1808.
- Godin, G., 1972. *The Analysis of Tides.* University of Toronto Press, Toronto.
- Hayes, M. O., 1967. Hurricanes as geologic agents; case studies of Hurricane Carla, 1961 and Cindy, 1963. *Univ. Tex. Bur. Econ. Geol. Rept. Inv. No 61*, 56 p.
- Hill, G. W., and L. E. Garrison, 1978. Maps showing seasonal drift patterns along the Texas coast, 1970-1975. *U.S.G.S. Misc. Field Inv. Map MF-982.*
- Hsaio, S. V., and O. H. Shemdin, 1978. Bottom dissipation in finite-depth water waves. *Proc. 16th Coastal Engin. Conf., ASCE, Hamburg*, 434-448 pp.
- Hsaio, S. V., and O. H. Shemdin, 1980. Interaction of ocean waves with a soft bottom. *J. Phys. Oceanogr.* 10: 605-610.
- Hurlburt, H. E., and J. D. Thompson, 1982. The Dynamics of the Loop Current and Shed Eddies in a Numerical Model of the Gulf of Mexico. In: J. C. J. Nihoul (ed.), *Hydrodynamics of Semi-enclosed Seas.* Elsevier, pp. 243-298.
- Hurlburt, H. E., and J. D. Thompson, 1980. A numerical study of Loop Current intrusions and eddy shedding. *J. Phys. Oceanogr.* 10: 1611-1651.
- Ichiye, T., 1962. Circulation and water mass distribution in the Gulf of Mexico. *Geofis. Int.* 2: 47-76.
- Kirwan, A. D., W. J. Merrell, Jr., J. K. Lewis, and R. E. Whitaker, 1984. Lagrangian observations of an anticyclonic ring in the western Gulf of Mexico. *J. Geophys. Oceanogr.* 89(C3): 3417-3424.
- Komar, P. D., 1976. *Beach Processes and Sedimentation.* Prentice-Hall, New Jersey, 426 p.
- Leipper, D. F., 1970. A sequence of current patterns in the Gulf of Mexico. *J. Geophys. Res.* 75(3): 637-657.
- Lewis, J. K., 1980. Comments on "The hydrography of shelf waters off the central Texas Gulf coast." *J. Phys. Oceanogr.* 10: 2121-2122.
- Madsen, O. S., 1976. Wave Climate of the Continental Margin: Elements of its Mathematical Description. In: D. J. Stanley and D. J. P. Swift (eds.), *Marine Sediment Transport and Environmental Management.* John Wiley and Sons, New York, 255-310 pp.

- Maul, G. A., 1977. The annual cycle of the Loop Current, Part I: Observations during a one-year time series. *J. Marine Res.* 35: 29-47.
- Maul, G. A., D. A. Mayer and S. R. Baig, 1985. Comparisons between a continuous 3-year current-meter observation at the sill of the Yucatan Strait, satellite measurements of Loop Current area and regional sea level. *J. of Geophys. Res.* 90 (C5): 9090-9096.
- McCave, I. N., 1971. Sand waves in the North Sea of the coast of Holland. *Marine Geol.* 10: 199-225.
- Merrell, W. J., and J. M. Morrison, 1981. On the circulation of the western Gulf of Mexico with observations from April 1978. *J. Geophys. Res.* 86(C5): 4181-4185.
- Merrell, W. J., and A. M. Vazquez, 1983. Observations of changing mesoscale circulation patterns in the western Gulf of Mexico. *J. of Geophys. Res.* 88(C12): 7721-7723.
- Molinari, R. L., 1977. Synoptic and mean monthly 20°C topographies in the eastern Gulf of Mexico. NOAA Tech. Mem. ERL AOML-27, 33 pp.
- Morton, R. A., 1981. Formation of Storm Deposits by Wind-forced Currents in the Gulf of Mexico and the North sea. In: S. D. Nio et al. (eds.), *Holocene Marine Sedimentation in the North Sea Basin*. Int. Assoc. Sed. Spec. Publ. no. 5, 385-96 pp.
- Nowlin, W. D., and C. A. Parker, 1974. Effects of a cold-air outbreak on shelf waters of the Gulf of Mexico. *J. Phys. Oceanogr.* 4: 467-486.
- Nowlin, W. D., and H. J. McClellan, 1967. A characterization of the Gulf of Mexico waters in winter. *J. Mar. Res.* 25: 29-59.
- Pedlosky, J., 1979. *Geophysical Fluid Dynamics*. Springer-Verlag, New York, 624 pp.
- Ropelewski, C. F., 1984. The climate of summer 1983 - a season of contrasts and extremes. *Mon. Wea. Rev.* 112(3): 591-609.
- Schideler, G. L., 1978. A sediment-dispersal model for the south Texas continental shelf, northwest Gulf of Mexico. *Mar. Geol.* 26: 289-313.
- Shields, A., 1936. "Anwendung der Aehnlichkeitsmechanik und der turbulenzforschung auf die Geschiebebewegung," *Mitt, der Preuss., Veruchsanstalt fur Wasserbau and Schiffbua, Berlin* (see Vanoni, 1964 for brief description of work).
- Smith, D. C., IV, 1985. A numerical study of Loop Current eddy interaction with topography in the Western Gulf of Mexico. *J. Phys. Oceanogr.*, in press.

- Smith, D. C., IV, and J. J. O'Brien, 1983. The interaction of a two-layer isolated mesoscale eddy with bottom topography. *J. Phys. Oceanogr.* 13: 1681-1697.
- Smith, N. P., 1975. Seasonal variations in nearshore circulation in the northwestern Gulf of Mexico. *Contrib. Mar. Sci.* 19: 49-65.
- Smith, N. P., 1977. Near-bottom cross-shelf currents in the northwestern Gulf of Mexico: a response to wind-forcing. *J. Phys. Oceanogr.* 7: 615-620.
- Smith, N. P., 1978. Low-frequency reversals of nearshore currents in the northwestern Gulf of Mexico. *Contrib. Mar. Sci.* 21: 104-115.
- Smith, N. P., 1979. An investigation of the vertical structure in shelf circulation. *J. Phys. Oceanogr.* 9: 624-630.
- Smith, N. P., 1980a. Temporal and spatial variability in longshore motion along the Texas Gulf coast. *J. Geophys. Res.* 85(C3): 1531-36.
- Smith, N. P., 1980b. On the hydrography of shelf waters off the central Texas Gulf coast. *J. Geophys. Oceanogr.* 10: 806-813.
- Sturges, W. and J. P. Blaha, 1976. A western boundary current in the Gulf of Mexico. *Science.* 192: 367-69.
- Sturges, W., 1983. On interpolating gappy records for time-series analysis. *J. Geophys. Res.* 88: 9736-9740.
- Suter, J. R. and H. F. Berryhill, 1985. Late Quaternary shelf-margin deltas, northwest Gulf of Mexico. *Bull. Am. Assoc. Pet. Geol.* 69: 77-91.
- Thompson, J. D., 1985. Altimeter data and geoid error in mesoscale ocean prediction: some results from a primitive equation model. *J. Geophys. Res.*, in press.
- Tubman, M. W., and J. N. Suhayda, 1976. Wave action and bottom movements in fine sediments. *Proc. 15th Coastal Engin. Conf. ASCE, Honolulu,* 1168-1183 pp.
- Vanoni, V. A., 1964. Measurements of critical shear stress for entraining fine sediments in a boundary layer. *W. M. Keck Lab Hydraulics, Calif. Inst. Tech., Report KH-R-7,* 47 pp.
- Vukovich, F. M., and B. W. Crissman, 1985. Some aspects of warm rings in the Gulf of Mexico. *Report for Sci. Appls. Int'l Corp., Offc. of Geosciences Programs, Res. Triangle, Inst., Res. Triangle Park, N. Car.* 31 pp.
- Vukovich, F. M., 1985. Aspects of the behavior of cold perturbation in the Eastern Gulf of Mexico: A case study. *Submitted to J. Phys. Oceanogr.,* 25 pp.

- Vukovich, F. M., and G. A. Maul, 1985. Cyclonic eddies in the eastern Gulf of Mexico. *J. Phys. Oceanogr.* 15(1): 105-117.
- Vukovich, F. M., and B. W. Crissman, 1985. Aspects of warm rings in the Gulf of Mexico. To be submitted to *J. Geophys. Res.*
- Vukovich, F. M., B. W. Crissman, and D. Erlich, 1980. Sea-surface temperature variability analysis of potential OTEC sites in the eastern Gulf of Mexico utilizing satellite data. Interim Report, National Oceanic and Atmospheric Administration, Contract No. 03-78-B01-72, 37 pp.
- Vukovich, F. M., and B. W. Crissman, 1980. Some aspects of Gulf Stream western boundary eddies from satellite and in situ data. *J. Phys. Oceanogr.* 10(11): 1792-1813.
- Vukovich, F. M., W. J. King, J. W. Dunn, and J. B. Worth, 1979. Observations and simulations of the diurnal variation of the urban heat island circulation and associated variations of the ozone distribution: a case study. *J. Appl. Meteorol.* 18(7): 836-854.
- Vukovich, F. M., B. W. Crissman, M. Bushnell, and W. J. King, 1979. Some aspects of the oceanography of the Gulf of Mexico using satellite and in situ data. *J. Geophys. Res.* 84(C12): 7749-7768.
- Vukovich, F. M., B. W. Crissman, M. Bushnell, and W. J. King, 1978. Sea-surface temperature variability analysis of potential OTEC sites utilizing satellite data. Final Report DOE Contract No. EG-77-C-05-0544. Research Triangle Institute, Research Triangle Park, N. C. 17709, 153 pp.
- Vukovich, F. M., and B. W. Crissman, 1975. Quasi-realtime oceanographic experiment using NOAA satellite data and ship data. Final Report, NOAA Contract No.3-35402, Research Triangle Institute, 57 pp.
- Watson, R. L., and E. W. Behrens, 1970. Nearshore surface currents, southeastern Texas Gulf coast. *Contrib. Mar. Sci.*, 15: 133-143.
- Weatherly, G. L., 1972. A study of the bottom boundary layer of the Florida current. *J. Phys. Oceanogr.* 2: 54-72.
- White, S. J., 1970. Plane bed thresholds of fine-grained sediments. *Nature.* 228: 152-53.



The Department of the Interior Mission

As the Nation's principal conservation agency, the Department of the Interior has responsibility for most of our nationally owned public lands and natural resources. This includes fostering sound use of our land and water resources; protecting our fish, wildlife, and biological diversity; preserving the environmental and cultural values of our national parks and historical places; and providing for the enjoyment of life through outdoor recreation. The Department assesses our energy and mineral resources and works to ensure that their development is in the best interests of all our people by encouraging stewardship and citizen participation in their care. The Department also has a major responsibility for American Indian reservation communities and for people who live in island territories under U.S. administration.



The Minerals Management Service Mission

As a bureau of the Department of the Interior, the Minerals Management Service's (MMS) primary responsibilities are to manage the mineral resources located on the Nation's Outer Continental Shelf (OCS), collect revenue from the Federal OCS and onshore Federal and Indian lands, and distribute those revenues.

Moreover, in working to meet its responsibilities, the **Offshore Minerals Management Program** administers the OCS competitive leasing program and oversees the safe and environmentally sound exploration and production of our Nation's offshore natural gas, oil and other mineral resources. The MMS **Minerals Revenue Management** meets its responsibilities by ensuring the efficient, timely and accurate collection and disbursement of revenue from mineral leasing and production due to Indian tribes and allottees, States and the U.S. Treasury.

The MMS strives to fulfill its responsibilities through the general guiding principles of: (1) being responsive to the public's concerns and interests by maintaining a dialogue with all potentially affected parties and (2) carrying out its programs with an emphasis on working to enhance the quality of life for all Americans by lending MMS assistance and expertise to economic development and environmental protection.